Ab initio construction of symmetry-adapted k · p Hamiltonians for the electronic structure of semiconductors

Milan Jocić* and Nenad Vukmirović†
Institute of Physics Belgrade, University of Belgrade, Pregrevica 118, 11080 Belgrade, Serbia

(Received 30 April 2020; revised 26 June 2020; accepted 27 July 2020; published 11 August 2020)

While **k** · **p** Hamiltonians are frequently used for the description of electronic states in quantum nanostructures, a method is lacking to obtain them in their symmetrized form directly from *ab initio* band structure calculations of bulk material. We developed a method for obtaining the parameters and the symmetry-adapted form of the **k** · **p** Hamiltonian from the output of an *ab initio* band structure calculation. The method consists of (i) evaluation of momentum matrix elements between the wave functions obtained from band structure calculation; (ii) identification of the unitary transformation that transforms these wave functions to the symmetry-adapted basis; (iii) transformation of the **k** · **p** Hamiltonian to the symmetry-adapted basis. We illustrate the methodology by obtaining **k** · **p** Hamiltonians that describe the band structure of zinc-blende CdSe and then we use the Hamiltonians obtained to calculate the electronic states in CdSe quantum wells. Excellent agreement between density functional theory and **k** · **p** is obtained for the electronic structure, even for quite thin wells.

DOI: 10.1103/PhysRevB.102.085121

I. INTRODUCTION

Semiconductor materials and nanostructures based upon them are at the heart of the operation of almost all electronic and optical devices. For this reason, there is a significant interest in understanding the electronic states in these materials. The progress in developments of methodologies for *ab initio* electronic structure calculations has led us to the point where it is relatively straightforward to perform band structure calculations of bulk semiconducting materials. Density functional theory (DFT) calculations based on local or semilocal approximations for the exchange-correlation functional give band gaps that are significantly smaller than experimental band gaps [1]. However, improved treatments based on the use of hybrid functionals [2,3] or many body perturbation theory in GW (where G stands for the Green's function and W for screened Coulomb interaction) approximation [4] give rather accurate band gaps and band structure of the bulk material [5–7]. On the other hand, it is rather difficult to perform *ab initio* calculations of semiconductor nanostructures because the calculation needs to be performed for a supercell containing a very large number of atoms.

The method that proved to be both practical and successful in treating the electronic states in semiconductor nanostructures is the **k** · **p** method [8–11]. It is based on the representation of the single-particle wave function in terms of Bloch functions of the bulk material at a certain point in the Brillouin zone (typically the Γ point) and slowly varying envelope functions. The **k** · **p** Hamiltonian for a nanostructure is then an operator that acts on the column of envelope functions corresponding to each of the bulk bands.

Despite the success in using the **k** · **p** method for description of bulk band structure around a certain point in the Brillouin zone (usually the Γ point) and for treating the semiconductor nanostructures, there is still no systematic way to construct the **k** · **p** Hamiltonian for a given material and obtain the parameters of the Hamiltonian. The parameters of most conventional **k** · **p** Hamiltonians (such as the eight-band Hamiltonian [10,12,13]) for a few most common classes of semiconductors can be found in the literature [14,15] and were obtained from the band gap and effective masses in the valence and conduction band. Parameters of **k** · **p** Hamiltonians with larger number of bands (such as, for example, the 30-band Hamiltonian [16–20]) and recently introduced atomistic **k** · **p** [21] are typically obtained by fitting to the calculated band structure of the material or to experimental data. However, given a relatively large number of fitting parameters, it is questionable if the fit gives unique parameters. It is also not clear what part of the Brillouin zone should be used in the fitting procedure, since it is not expected that the **k** · **p** method describes the bulk band structure throughout the whole Brillouin zone.

Given the fact that new classes of semiconductor materials and nanostructures based upon them emerge or find new applications quite often, it would be of significant interest to develop the procedure for construction of desired **k** · **p** Hamiltonians. Since all parameters of the **k** · **p** Hamiltonian are related to momentum matrix elements between single-particle wave functions of the bulk, it is in principle possible to obtain them from electronic structure calculation of the bulk material. This is indeed done when **k** · **p** is used as a method for interpolation of *ab initio* calculated band structure to a more dense grid of **k** points [22–25]. However, there is a certain shortcoming of this approach when it comes to the construction of **k** · **p** Hamiltonians that should be used in future applications. Namely, due to the symmetry of the

*milan.jocic@ipb.ac.rs
†nenad.vukmirovic@ipb.ac.rs

crystalline material the energy levels in characteristic points in the Brillouin zone are degenerate and for this reason the choice of Bloch wave functions from the Hilbert space spanned by the degenerate states is not unique. As a consequence, one may end up with different forms of the final $\mathbf{k}\cdot\mathbf{p}$ Hamiltonian depending on the particular choice of Bloch functions from this space. The number of Hamiltonian parameters in these forms might be significantly larger than the true number of parameters imposed by the symmetry of the crystal.

In this work, we develop the procedure for construction of the $\mathbf{k}\cdot\mathbf{p}$ Hamiltonian in the symmetrized form with a minimal number of parameters imposed by crystal symmetry. In Sec. II we give a brief overview of the $\mathbf{k}\cdot\mathbf{p}$ method and present our approach for the construction of the Hamiltonian. In Sec. III we illustrate the method by applying it to bulk zinc-blende CdSe and to CdSe quantum wells.

II. THEORETICAL APPROACH

A. k · p equation

We start this section by briefly reviewing the $\mathbf{k}\cdot\mathbf{p}$ method to set the stage for description of our procedure for construction of $\mathbf{k}\cdot\mathbf{p}$ Hamiltonian. We start with the equation for an electron in the periodic crystal that reads

$$\left[\frac{p^2}{2m_0}+U+T_{\rm rk}+H_{\rm D}+H_{\rm soc}\right]|\Psi_{n\mathbf{k}}\rangle=E_n(\mathbf{k})|\Psi_{n\mathbf{k}}\rangle, \quad (1)$$

where $p^2/(2m_0)=-\hbar^2\nabla^2/(2m_0)$ is the kinetic energy operator and m_0 is the free electron mass, U is the periodic crystal potential (including nuclei, core and valence electrons), while $E_n(\mathbf{k})$ and $|\Psi_{n\mathbf{k}}\rangle$ are the corresponding energy and wave function for the electron in band n at wave vector $\mathbf{k}$ in the Brillouin zone. When the effects of spin-orbit interaction are included, $|\Psi_{n\mathbf{k}}\rangle$ is a two-component spinor. The last three terms in brackets are the relativistic corrections accounting for kinetic energy $T_{\rm rk}=-p^4/(8m_0^3c^2)$, fine structure through the Darwin term $H_{\rm D}=\hbar^2\nabla\cdot\nabla U/(8m_0^2c^2)$ and spin-orbit coupling (SOC) $H_{\rm soc}=\hbar(\sigma\times\nabla U)\cdot\mathbf{p}/(4m_0^2c^2)$, where $\sigma=(\sigma_x,\sigma_y,\sigma_z)$ denotes a vector with Pauli matrices as its components.

For an electron in a periodic potential, the Bloch theorem holds, by which the components of $|\Psi_{n\mathbf{k}}\rangle$ are of the form

$$\Psi^{(a)}_{n\mathbf{k}}(\mathbf{r})=e^{i\mathbf{k}\cdot\mathbf{r}}u^{(a)}_{n\mathbf{k}}(\mathbf{r}), \quad (2)$$

where $u^{(a)}_{n\mathbf{k}}(\mathbf{r})$ are periodic Bloch functions satisfying the condition $u^{(a)}_{n\mathbf{k}}(\mathbf{r}+\mathbf{R})=u^{(a)}_{n\mathbf{k}}(\mathbf{r})$, with $\mathbf{R}$ being the direct lattice vector. Inserting Eq. (2) into Eq. (1), we obtain the one-electron equation in terms of periodic Bloch functions:

$$\left[H+\frac{\hbar^2k^2}{2m_0}+T'_{\rm rk}(\mathbf{k})+\frac{\hbar\mathbf{k}\cdot\mathbf{p}_{\rm soc}}{m_0}\right]|u_{n\mathbf{k}}\rangle=E_n(\mathbf{k})|u_{n\mathbf{k}}\rangle, \quad (3)$$

where $H=p^2/(2m_0)+U+T_{\rm rk}+H_{\rm D}+H_{\rm soc}$ is the initial Hamiltonian from Eq. (1), $\mathbf{p}_{\rm soc}=\mathbf{p}+\hbar(\sigma\times\nabla U)/(4m_0c^2)$ is the momentum modified with the SOC part and $T'_{\rm rk}(\mathbf{k})$ is given as

$$T'_{\rm rk}(\mathbf{k})=-\frac{1}{8m_0^3c^2}[4(\hbar\mathbf{k}\cdot\mathbf{p})p^2+4(\hbar\mathbf{k}\cdot\mathbf{p})^2+4(\hbar\mathbf{k})^2(\hbar\mathbf{k}\cdot\mathbf{p})+2(\hbar k)^2p^2+(\hbar k)^4]. \quad (4)$$

We further express $|u_{a\mathbf{k}}\rangle$ in the basis of orthonormal functions $|u_{m\mathbf{k}_0}\rangle$:

$$|u_{a\mathbf{k}}\rangle=\sum_m B^{(a)}_m(\mathbf{k})|u_{m\mathbf{k}_0}\rangle, \quad (5)$$

which are solutions of eigenproblem given by Eq. (3) at a certain $\mathbf{k}_0$ with eigenvalues $E_n(\mathbf{k}_0)$. Inserting Eq. (5) into Eq. (3), multiplying from the left by $\langle u_{n\mathbf{k}_0}|$ and exploiting the orthonormality condition we arrive at the equation

$$\sum_m\left[\left(E_n(\mathbf{k}_0)+\frac{\hbar^2(k^2-k_0^2)}{2m_0}\right)\delta_{nm}+\frac{\hbar(\mathbf{k}-\mathbf{k}_0)}{m_0}\cdot\langle u_{n\mathbf{k}_0}|\mathbf{p}|u_{m\mathbf{k}_0}\rangle\right]B^{(a)}_m(\mathbf{k})=E^{(a)}(\mathbf{k})B^{(a)}_n(\mathbf{k}). \quad (6)$$

We have omitted $T'_{\rm rk}(\mathbf{k},\mathbf{k}_0)$ that would appear in Eq. (6) because its contribution depends directly on the distance between $\mathbf{k}$ and $\mathbf{k}_0$ and becomes significant at distances far greater than the one where $\mathbf{k}\cdot\mathbf{p}$ theory is applicable. We have performed a numerical check of this claim in case of zinc-blende CdSe and we have shown that the influence of this term on bulk eigenenergies is smaller than 0.3 meV throughout the whole Brillouin zone. For similar reasons, we neglected SOC modification to momentum (i.e., we take $\mathbf{p}_{\rm soc}\approx\mathbf{p}$). We note that SOC is fully included in our approach unlike in many theoretical treatments where it is treated as a perturbation. We further rewrite Eq. (6) in somewhat more convenient form by exploiting the relation

$$\langle\Psi_{n\mathbf{k}_0}|\mathbf{p}|\Psi_{m\mathbf{k}_0}\rangle=\hbar\mathbf{k}\delta_{nm}+\langle u_{n\mathbf{k}_0}|\mathbf{p}|u_{m\mathbf{k}_0}\rangle. \quad (7)$$

We then obtain

$$\sum_m\left[\left(E_n(\mathbf{k}_0)+\frac{\hbar^2(\mathbf{k}-\mathbf{k}_0)^2}{2m_0}\right)\delta_{nm}+\frac{\hbar(\mathbf{k}-\mathbf{k}_0)}{m_0}\cdot\langle\Psi_{n\mathbf{k}_0}|\mathbf{p}|\Psi_{m\mathbf{k}_0}\rangle\right]B^{(a)}_m(\mathbf{k})=E^{(a)}(\mathbf{k})B^{(a)}_n(\mathbf{k}), \quad (8)$$

which takes the form of an eigenproblem:

$$\sum_m H^{(1)}_{nm}B^{(a)}_m=E^{(a)}B^{(a)}_n, \quad (9)$$

where $H^{(1)}_{nm}$ is given by the term in square brackets in Eq. (8). The indices m and n in Eq. (9) go over the bands that were included in the expansion in Eq. (5). The accuracy of $\mathbf{k}\cdot\mathbf{p}$ Hamiltonian can further be improved by adding the effect of remote bands [the bands not included in the expansion in Eq. (5)] perturbatively using the Löwdin's perturbation theory [11,26]. This yields additional term in the $\mathbf{k}\cdot\mathbf{p}$ Hamiltonian which reads

$$H^{(2)}_{nm}=\frac{\hbar^2}{m_0^2}\sum_l\frac{\langle u_{n\mathbf{k}_0}|\mathbf{K}\cdot\mathbf{p}|u_{l\mathbf{k}_0}\rangle\langle u_{l\mathbf{k}_0}|\mathbf{K}\cdot\mathbf{p}|u_{m\mathbf{k}_0}\rangle}{[E_n(\mathbf{k}_0)+E_m(\mathbf{k}_0)]/2-E_l(\mathbf{k}_0)}, \quad (10)$$

with $\mathbf{K}=\mathbf{k}-\mathbf{k}_0$ and the summation goes over the bands l that were not included in the expansion in Eq. (5).

B. Construction of symmetrized k · p Hamiltonian

The expression (8) can be, in principle, used to construct the $\mathbf{k}\cdot\mathbf{p}$ Hamiltonian directly from *ab initio* calculation of band structure of bulk. Namely, all Hamiltonian matrix elements can be calculated from band energies $E_n(\mathbf{k}_0)$ at point $\mathbf{k}_0$ and momentum matrix elements $\langle\Psi_{n\mathbf{k}_0}|\mathbf{p}|\Psi_{m\mathbf{k}_0}\rangle$ between the wave functions at $\mathbf{k}_0$. However, an issue arises regarding the uniqueness of the constructed Hamiltonian matrix as a consequence of the fact that some of the eigenstates $|\Psi_{n\mathbf{k}_0}\rangle$ are degenerate. A typical choice for the $\mathbf{k}_0$ point is some high symmetry point where band dispersions exhibit minima or maxima (such as for example the Γ point) and the group $G_{\mathbf{k}_0}$ of the wave vector $\mathbf{k}_0$ is some high symmetry point group. For this reason, there is a degeneracy between the eigenstates at $\mathbf{k}_0$, where the degree of degeneracy is determined by the dimensions of irreducible representations (irreps) of the group $G_{\mathbf{k}_0}$ corresponding to each of the states. For example, in the case of zinc-blende CdSe material used as an example in this work, the top valence band is threefold degenerate and the bottom conduction band is nondegenerate when spin degrees of freedom are not taken into account and the effect of spin-orbit interaction is not included. When spin-orbit interaction is included, the bottom conduction band is twofold degenerate, while two top valence bands are twofold and fourfold degenerate.

Let d be the degeneracy of the set of eigenstates $|\phi_1\rangle, |\phi_2\rangle, \ldots, |\phi_d\rangle$ at $\mathbf{k}_0$ at let $\mathcal{H}_d$ be the Hilbert space spanned by these states. The states $|\phi_1\rangle, |\phi_2\rangle, \ldots, |\phi_d\rangle$ form an orthonormal basis of $\mathcal{H}_d$ but any other orthonormal basis may well have been chosen. With the use of different basis, the momentum matrix elements in Eq. (8) would be different and the $\mathbf{k}\cdot\mathbf{p}$ Hamiltonian would have a different form. Moreover, it might even appear that the Hamiltonian has a different number of parameters. Our goal is to overcome this issue by fixing the choice of the degenerate states and obtaining the $\mathbf{k}\cdot\mathbf{p}$ Hamiltonian in the form where it has a minimal number of parameters imposed by the symmetry group $G_{\mathbf{k}_0}$ of the wave vector $\mathbf{k}_0$.

The set $|\phi_1\rangle, |\phi_2\rangle, \ldots, |\phi_d\rangle$ is obtained from DFT and they form $d\times d$ matrices $\Gamma(g)$ of the irrep of group $G_{\mathbf{k}_0}$ that are given as

$$\Gamma_{mn}(g) = \langle\phi_m|P(g)|\phi_n\rangle, \tag{11}$$

where g is an element of the group $G_{\mathbf{k}_0}$ and $P(g)$ is the operator that applies the symmetry operation g on the given wave function. The matrices $\Gamma(g)$ are then obtained by directly calculating the matrix elements in Eq. (11). We then calculate the characters of Γ to match it with one of the equivalent conventional irreps Γ′ of the point group $G_{\mathbf{k}_0}$. The matrices of irreps Γ′ can be found in databases of irreps of point groups, for example in Bilbao crystallographic data server [27]. The matrices $\Gamma(g)$ and $\Gamma'(g)$ are connected via a unitary transformation

$$U^\dagger\Gamma(g)U = \Gamma'(g), \tag{12}$$

which is satisfied for each $g\in G_{\mathbf{k}_0}$. Therefore, to obtain the basis of states in $\mathcal{H}_d$ which is adapted to conventional matrices $\Gamma'(g)$ in databases of irreps, one has to make a unitary transformation of the basis

$$|\psi_j\rangle = \sum_{i=1}^{d} U_{ij}|\phi_i\rangle. \tag{13}$$

Now, the representation of the operator $P(g)$ from Eq. (11) in the new basis set $|\psi_j\rangle$ is the conventional representation Γ′. In the $|\psi_j\rangle$ basis, the $\mathbf{k}\cdot\mathbf{p}$ Hamiltonian has a convenient, symmetry-adapted form, in which relevant parameters of the Hamiltonian can be straightforwardly identified.

It remains to define a procedure for obtaining the unitary matrix U that connects the two representations Γ and Γ′. Such a procedure has recently been developed in Ref. [28] and we outline it here. One first obtains a set of coefficients r_{ab} as

$$r_{ab} = \sqrt{\frac{n_\Gamma}{|G|}}\left(\sum_{g\in G}\Gamma_{aa}(g)\Gamma'_{bb}(g^{-1})\right)^{1/2}, \tag{14}$$

where $\Gamma_{aa}(g)$ and $\Gamma'_{bb}(g^{-1})$ are known matrix elements for symmetry operation (group element) g and its inverse g^{-1}, respectively, $|G|$ is the order of group G while n_Γ is the dimension of representations Γ and Γ′. Then, one chooses the pair (a, b) for which $r_{ab} > 0$. The existence of such a pair has been proven in Ref. [28]. The matrix U is then given as

$$U_{ij} = \frac{1}{r_{ab}}\frac{n_\Gamma}{|G|}\sum_{g\in G}\Gamma_{ia}(g^{-1})\Gamma'_{bj}(g). \tag{15}$$

With this, we complete our procedure for construction of symmetrized $\mathbf{k}\cdot\mathbf{p}$ Hamiltonian. For clarity, we review all steps of the procedure here:

(i) Perform *ab initio* calculation of band structure for bulk, using DFT with local functionals, hybrid functional DFT, or by including quasiparticle energy correction within the GW approximation.

(ii) Choose the point $\mathbf{k}_0$ in the Brillouin zone, that is most suited for $\mathbf{k}\cdot\mathbf{p}$ expansion and extract band energies $E_n(\mathbf{k}_0)$ and their eigenstates $|\Psi_{n\mathbf{k}_0}\rangle$ from desired *ab initio* method.

(iii) Identify the groups of degenerate states at $\mathbf{k}_0$ and the symmetry point group $G_{\mathbf{k}_0}$. Select the groups of degenerate states (usually those around the gap) that will form the $\mathbf{k}\cdot\mathbf{p}$ Hamiltonian. Extract these groups of degenerate states $|\phi_i\rangle$ from *ab initio* eigenstates $|\Psi_{n\mathbf{k}_0}\rangle$.

(iv) For each of selected groups of degenerate states calculate the matrices $\Gamma(g)$ of corresponding irrep Γ using Eq. (11). Using characters of $\Gamma(g)$, match Γ to the equivalent conventional representation Γ′ found in databases of irreps of point groups.

(v) For each of selected groups of degenerate states, calculate the unitary matrices U using sets of matrices $\Gamma(g)$ and $\Gamma'(g)$ as inputs for Eqs. (14) and (15).

(vi) Proceed with calculation of the new, symmetry-adapted basis, consisting of selected groups of degenerate states $|\psi_j\rangle$ using matrices U, obtained from the previous step, and corresponding groups of degenerate states $|\phi_i\rangle$ with Eq. (13).

(vii) Evaluate the momentum matrix elements in the new basis using Eqs. (7) (8), (9), and (10) which then

give all parameters of the symmetrized $\mathbf{k}\cdot\mathbf{p}$ Hamiltonian $H_{nm} = H^{(1)}_{nm} + H^{(2)}_{nm}$.

It is important to note that these steps constitute a well-defined and straightforward procedure that gives the desired $\mathbf{k}\cdot\mathbf{p}$ Hamiltonian starting from output of an *ab initio* calculation. It does not involve any kind of fitting which would introduce certain arbitrariness.

Next, we discuss the form of the Hamiltonian that we obtain and its relation to the form of the Hamiltonian that would be obtained using Luttinger's method of invariants [11,29]. The form of the Hamiltonian that we obtain consists of blocks $\mathcal{B}(\Gamma'_a, \Gamma'_b)$, where each block originates from two groups of states: the states $|\psi^{(a)}_1\rangle, \ldots, |\psi^{(a)}_{d_a}\rangle$ that transform in accordance with the representation Γ'_a of dimension d_a and the states $|\psi^{(b)}_1\rangle, \ldots, |\psi^{(b)}_{d_b}\rangle$ that transform in accordance with the representation Γ'_b of dimension d_b. The Hamiltonian consists of the terms quadratic in electronic momentum K, the terms linear in K and the terms that do not contain K. Luttinger's method of invariants [11,29] gives a systematic way to obtain the form of each $\mathcal{B}(\Gamma'_a, \Gamma'_b)$ for terms of given order in K. For this reason, our procedure yields the same form of the Hamiltonian as Luttinger's method of invariants applied to obtain the terms up to second order in K. By its construction, Luttinger's method fully exploits the point group symmetry and yields the Hamiltonian in the form where a minimal number of parameters appears. On the other hand, it is clear that Luttinger's method cannot give the values of these parameters, since it exploits the symmetry of the system only and does not consider other details of the system. Our procedure in some sense links Luttinger's method from 1950's to modern *ab initio* calculations as it enables to obtain the form of the Hamiltonian that would be obtained using Luttinger's method and additionally gives the values of these parameters starting from *ab initio* wave functions and energies.

In Sec. III we apply our procedure to zinc-blende CdSe crystal whose point group at the Γ point is the T_d group. However, we note that our procedure is by no means limited to this particular crystal symmetry. It can be used for crystals of any kind of symmetry, at any point $\mathbf{k}_0$ in the Brillouin zone. Of course, benefits of this method will be greater if the symmetry point group $G_{\mathbf{k}_0}$ at $\mathbf{k}_0$ is of higher order. Having a symmetry-adapted form of the Hamiltonian also gives great advantage when it comes to calculation of nanostructures. Numerical codes for calculating nanostructures using $\mathbf{k}\cdot\mathbf{p}$ Hamiltonians could be easily adapted to another material of the same symmetry by just changing the numerical values of the parameters, that can be straightforwardly obtained using *ab initio* calculation for bulk material and the procedure described in the paper.

Finally, we briefly discuss on the conventions for matrices of the representations Γ'. In all examples in this work we have taken the matrices from Bilbao crystallographic data server [27] and consequently we used the conventions used therein. Unfortunately, this is not the only convention in the literature. The discussion on the effect of the choice of the convention for Γ' on the form of basis states $|\psi_i\rangle$ and the form of $\mathbf{k}\cdot\mathbf{p}$ Hamiltonian is given at the end of Secs. II B and II C of Ref. [30].

III. RESULTS

In this section, we apply the methodology described in Sec. II to bulk zinc-blende CdSe crystal and to zinc-blende CdSe quantum well. We apply the methodology to obtain the form and the parameters of the 8×8 (4×4) and 26×26 (13×13) symmetry adapted $\mathbf{k}\cdot\mathbf{p}$ Hamiltonian with (without) spin-orbit interaction included for CdSe in the zinc-blende structure. We will refer to the 8×8 (4×4) Hamiltonian as the standard Hamiltonian, while 26×26 (13×13) Hamiltonian will be referred to as the extended Hamiltonian.

The band energies and wave functions were obtained from DFT where exchange-correlation energy was modeled using the Perdew-Burke-Ernzerhof generalized gradient approximation revised for solids (PBEsol) [31]. Calculations were performed using the Quantum Espresso code [32,33]. Core electrons were modeled using fully relativistic optimized normconserving Vanderbilt pseudopotentials [34,35]. The $10\times 10\times 10$ grid in reciprocal space of the Brillouin zone was used, while the kinetic energy cutoff of the plane waves used to represent the wave functions was 90 Ry. The lattice constant of $a = 6.096$ Å, obtained by minimization of the energy of the structure, was used in all subsequent calculations.

Since local and semilocal approximations in DFT do not give accurate values of the band gap [1], we have also performed the band structure calculation using many-body perturbation theory in the GW approximation [4]. Within this approach, the electron self-energy is approximated using the expression containing the Green's function G and the screened Coulomb interaction W. In this work, we used the G_0W_0 variant of GW approximation in which the self-energy is obtained from Green's function G_0 of an electron in DFT Kohn-Sham potential, without further iterations. The calculations were performed using the YAMBO code [36,37], with input Kohn-Sham wave functions obtained from a previous DFT calculation on the $4\times 4\times 4$ grid in reciprocal space. Plasmon-pole approximation was used to account for the frequency dependence of the dielectric function. Kinetic energy cutoff used for the calculation of dielectric function in G_0W_0 calculation was 50 Ry. The corresponding number of bands was 400 (800), while the number of bands used in the evaluation of self-energy was 300 (600) in the case when spin-orbit interaction is omitted (included). We estimate that these values yield numerical accuracy of 20 meV or better for band energy corrections.

A. Bulk zinc-blende CdSe

We used the procedure described in Sec. II to obtain the standard and extended $\mathbf{k}\cdot\mathbf{p}$ Hamiltonian in symmetry-adapted form. Γ point was chosen as the point $\mathbf{k}_0$ in our procedure, since zinc-blende CdSe exhibits a direct gap at the Γ point. The corresponding group $G_{\mathbf{k}_0}$ is then the point symmetry group of the crystal, which is the T_d group in the case of zinc-blende structures. We will denote irreps of this group using the convention of Ref. [38].

We will refer to the states that are included in the standard $\mathbf{k}\cdot\mathbf{p}$ Hamiltonian as the main states, while remaining states included in the extended Hamiltonian will be referred to as

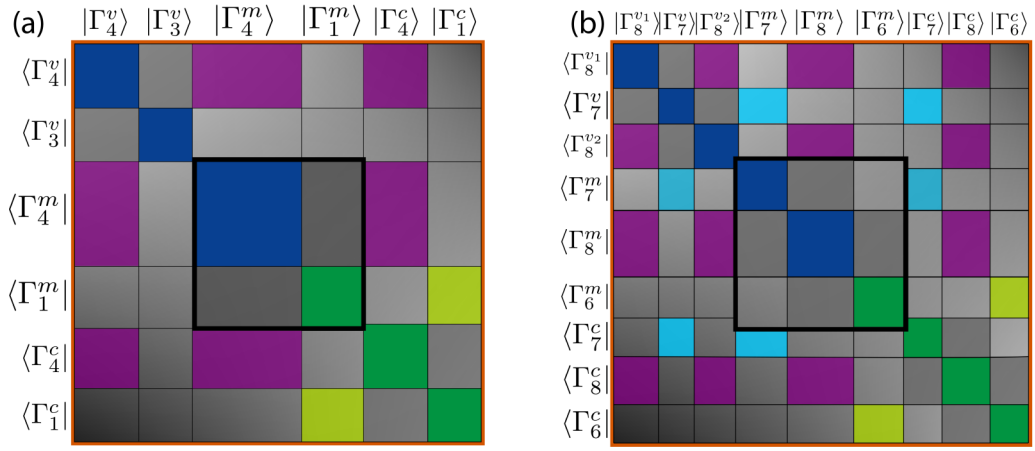

FIG. 1. The form of $\mathbf{k}\cdot\mathbf{p}$ Hamiltonian obtained when spin-orbit interaction is (a) omitted; (b) included. Each block of the matrix contains the terms that originate from matrix elements between the states that transform according to irrep specified on the left and above the matrix. The superscripts v, m, and c denote the lower valence band states, the main states, and the higher conduction band states. The central square marked with thick black lines denotes the standard Hamiltonian.

lower valence band and higher conduction band states. When spin-orbit interaction is omitted, main states used to construct the standard Hamiltonian are the threefold degenerate Γ_4 and nondegenerate Γ_1 states that lie below and above the gap, respectively, giving a total of four states. Extended Hamiltonian is constructed by adding the twofold degenerate Γ_3 and threefold degenerate Γ_4 valence states and Γ_4 and Γ_1 conduction states, yielding a total of 13 states. When spin-orbit interaction is included, the states transform according to irreps of the double T_d group. The states corresponding to Γ_4 will split into fourfold Γ_8 and twofold degenerate Γ_7 state, the states corresponding to Γ_3 become fourfold degenerate Γ_8 and the states corresponding to Γ_1 become twofold degenerate Γ_6 states. The characters of the irreps of the single and the double point group T_d are given in Sec. I of Ref. [30].

In Fig. 1, we show the form of both extended and standard Hamiltonian, in cases when the effects of spin-orbit interaction are omitted and included. The Hamiltonian is divided into blocks, where each block originates from two groups of degenerate states with the corresponding irrep shown on the left and above the matrix. These blocks can be absolutely diagonal (connecting same irreps from same states), irrep-diagonal (connecting same irreps from different states) and off-diagonal. When our procedure is applied, each block is obtained in the form with smallest number of parameters in the block, determined by the point group of the crystal. Analytical expressions for the elements of all blocks of the $\mathbf{k}\cdot\mathbf{p}$ Hamiltonian are given in Sec. II of Ref. [30]. We have checked that the same form of the blocks of the Hamiltonian is obtained when Luttinger's method of invariants [11,29] is applied. Numerical values of each parameter appearing in the blocks of the Hamiltonian are given in Sec. III of Ref. [30]. We note that the standard four-band Hamiltonian that we obtain coincides with the second-order four-band Kane Hamiltonian [11]. The standard eight-band Hamiltonian that we obtain coincides with Weiler eight-band Hamiltonian [11,12] after an appropriate unitary transformation is made. The details of this unitary transformation are given in Sec. II B of Ref. [30].

To better illustrate the advantage of using a symmetry-adapted form of the $\mathbf{k}\cdot\mathbf{p}$ Hamiltonian (that is obtained from symmetrized wave functions $|\psi_i\rangle$) rather than the form of the $\mathbf{k}\cdot\mathbf{p}$ Hamiltonian that would be obtained directly from DFT wave functions $|\phi_i\rangle$, we compare the number of parameters in the two forms of the Hamiltonian. The two forms of the four-band Hamiltonian are presented in Sec. II C of Ref. [30]. The number of parameters of the symmetrized form is significantly smaller (1 versus 9 parameters for the terms linear in k and 5 versus 46 parameters for the terms quadratic in k), which clearly shows its advantage in terms of simplicity for further use in the study of nanostructures.

In Fig. 2 we plot the band structure of zinc-blende CdSe obtained from DFT calculation and by diagonalizing the standard and extended $\mathbf{k}\cdot\mathbf{p}$ Hamiltonian in cases with and without the effects of spin-orbit interaction. As expected, extended Hamiltonian gives results that are qualitatively and quantitatively closer to full DFT than the standard one. It should be noted that it is preferable to add the states in extended Hamiltonian symmetrically around the main states. We found that expanding the standard Hamiltonian by a noneven number of valence and conduction states can lead to closing of the gap at points far away from Γ point. This was more prone to happen if the number of conduction states added was greater than number of valence states added. The presence of such spurious states then prevents the application of the $\mathbf{k}\cdot\mathbf{p}$ Hamiltonian to the nanostructure. Our choice of 13 (26) bands used to construct the extended Hamiltonian was therefore a compromise between (i) the goal to accurately describe the band structure within the part of the Brillouin zone which is as large as possible; (ii) the desire to use the number of bands (and therefore the number of parameters of the $\mathbf{k}\cdot\mathbf{p}$ Hamiltonian) that is not extremely large; (iii) the aim to avoid the appearance of spurious states that close the gap. To quantify in more detail the ability of derived $\mathbf{k}\cdot\mathbf{p}$ Hamiltonians to reproduce the *ab initio* calculated band structure, we plot in Fig. 3 the maximal difference between $\mathbf{k}\cdot\mathbf{p}$ and DFT results within the sphere of radius k_r (which is centered at the Γ point) for main bands. We find that standard

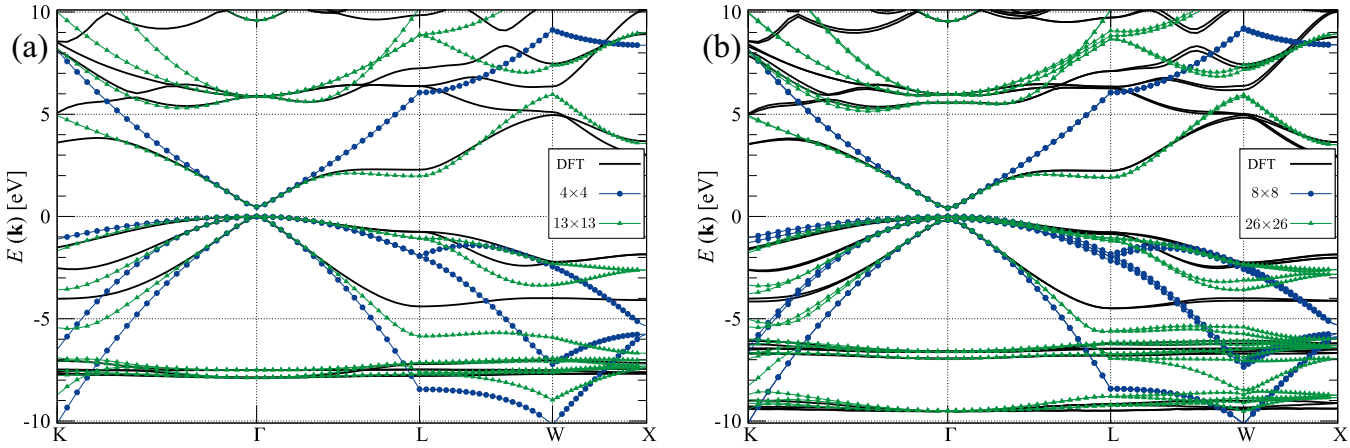

FIG. 2. Band structure of zinc-blende CdSe calculated using DFT and using standard and extended $\mathbf{k}\cdot\mathbf{p}$ Hamiltonian when the effects of spin-orbit interaction are (a) omitted; (b) included.

(extended) $\mathbf{k}\cdot\mathbf{p}$ results differ no more than 4 eV (1.75 eV) inside the sphere inscribed in the first Brillouin zone, with a difference not greater than 45 meV (35 meV) inside a sphere of radius $k_r = 0.2$ in units of $2\pi/a$, where a is the lattice constant. Figure 3 shows that in the reasonable vicinity of Γ point, in any direction, extended $\mathbf{k}\cdot\mathbf{p}$ Hamiltonians produce a band structure that is significantly closer to DFT results, than the standard $\mathbf{k}\cdot\mathbf{p}$ Hamiltonians. The use of extended Hamiltonians is necessary in many practical cases. If one wishes to study only the low field electrical properties or the optical properties at photon energies just above the band gap, the standard Hamiltonians are usually sufficient. However, if one is interested in optical properties in a wider energy range (which is relevant, for example, for solar cells) or transport at larger electrical fields (which is relevant in field-effect transistors) extended Hamiltonians are required to properly describe all relevant electronic states.

For the results presented so far, the $\mathbf{k}\cdot\mathbf{p}$ Hamiltonian was constructed starting from the wave functions and energies of Kohn-Sham orbitals obtained from DFT using the PBEsol functional. It is well known that the DFT band gap is typically significantly smaller from experimental gap and for this reason the same applies to $\mathbf{k}\cdot\mathbf{p}$ band structure obtained starting from DFT wave functions and energies. The methodology that we described is by no means limited to using the DFT wave functions and energies. To demonstrate this, we have calculated the self-energy corrections to energies $E_n(\mathbf{k}_0)$ within the G_0W_0 approximation. The G_0W_0 calculation gives the band gap values of 1.77 and 1.60 eV without and with inclusion of spin-orbit interaction, respectively. These results are in good agreement with experimental value of 1.71 eV [39]. As expected, this is a great improvement over DFT, which underestimates the gap at 0.47 eV (without spin-orbit interaction) and 0.40 eV (with spin-orbit interaction).

The energies $E_n(\mathbf{k}_0)$ obtained from G_0W_0 calculation were then used in Eqs. (10) and (8) to construct the standard and extended $\mathbf{k}\cdot\mathbf{p}$ Hamiltonian. The parameters of these Hamiltonians are given in Secs. III G and III H of Ref. [30], while the band structure obtained from diagonalization of these Hamiltonians is presented in Fig. 4.

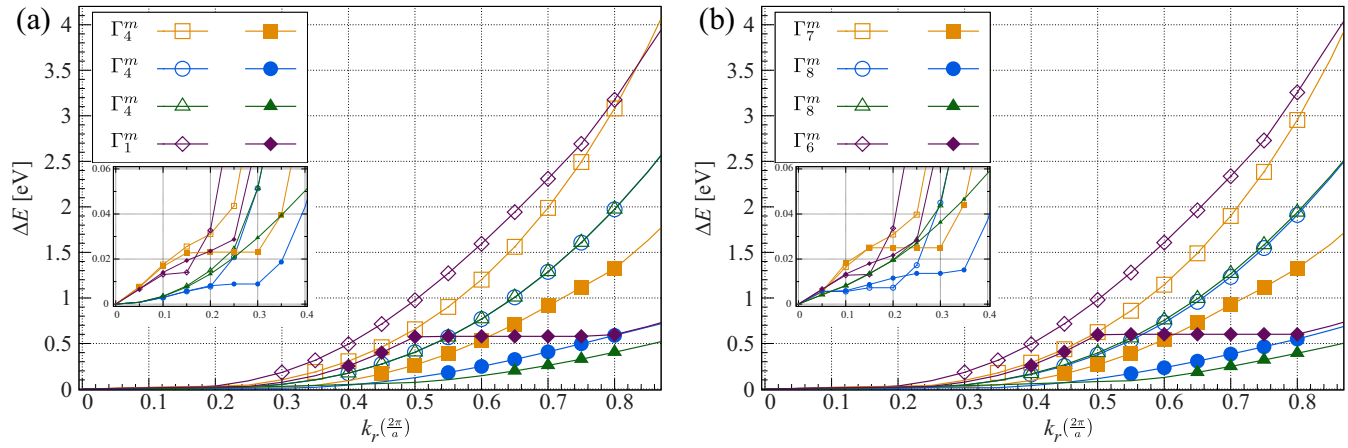

FIG. 3. Maximal absolute difference ΔE between the band energy obtained from DFT and $\mathbf{k}\cdot\mathbf{p}$ within the region of the Brillouin zone in the shape of a sphere of radius k_r centered at Γ when the effects of spin-orbit interaction are (a) omitted; (b) included. The difference is shown for main bands where the results obtained using standard $\mathbf{k}\cdot\mathbf{p}$ Hamiltonian are shown using empty symbols, while the results obtained using the extended $\mathbf{k}\cdot\mathbf{p}$ Hamiltonian are shown using filled symbols. Insets show a zoom of the same graph in the region around $k_r = 0$.

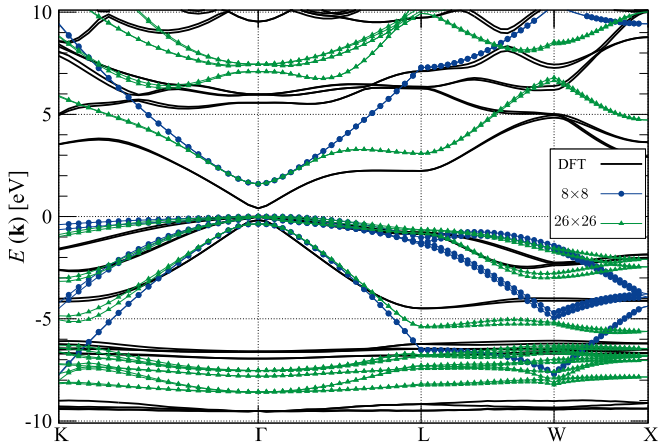

FIG. 4. Band structure of zinc-blende CdSe calculated using standard and extended $\mathbf{k}\cdot\mathbf{p}$ Hamiltonian parametrized starting from band energies obtained in G_0W_0 calculation. DFT results are given for comparison.

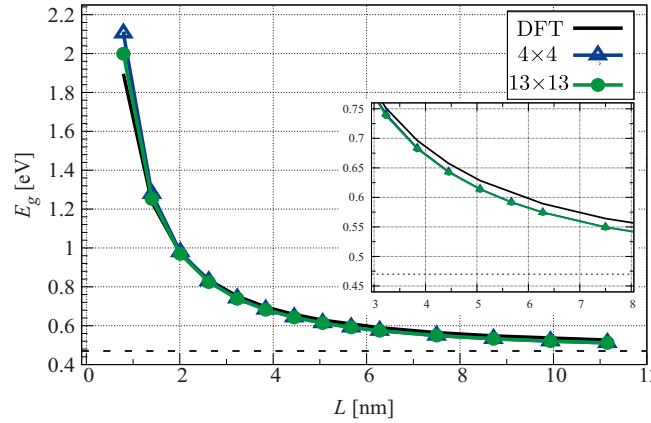

FIG. 5. Dependence of zinc-blende CdSe quantum well band gap on well width. The results obtained from DFT without the effects of spin-orbit coupling and from standard 4×4 and extended 13×13 $\mathbf{k}\cdot\mathbf{p}$ models are presented. The inset shows the zoom of the same dependence to the narrower range in the figure. The horizontal dashed line denotes the bulk DFT band gap.

B. CdSe quantum well

We finally demonstrate the usefulness of the procedure developed and the Hamiltonians derived by applying them to calculate the electronic states in zinc-blende CdSe quantum wells of various well widths. We perform the calculation both using the $\mathbf{k}\cdot\mathbf{p}$ method and using DFT and we compare the results that we obtain using the two approaches.

Within DFT, we perform the calculation of electronic states of a quantum well by considering the slab of CdSe material whose surfaces are perpendicular to the [001] direction. We terminate the slab with Cd layer at both surfaces and add pseudohydrogen atoms of charge 1.5 to passivate the dangling bonds at surfaces. Pseudohydrogen atoms are positioned at a distance of 1.58 Å from the corresponding Cd atom. For slabs of the width $\leqslant 6a$ ($>6a$), the vacuum region of the width equal to $3a$ (half of the slab width) was added on both sides of the quantum well, to avoid the interaction of the quantum well with its images caused by periodic boundary conditions in the calculation. The calculation was performed for quantum wells containing from 1 to 18 CdSe unit cells. We define the quantum well width as the distance between the two pseudohydrogen passivating layers. We performed the calculation without the effect of spin-orbit interaction included to lower the computational cost and therefore extend the range of well widths for comparison of DFT and $\mathbf{k}\cdot\mathbf{p}$ results.

In the case of a quantum well whose plane is perpendicular to the z direction, electronic states within the $\mathbf{k}\cdot\mathbf{p}$ model can be obtained by solving the eigenvalue problem

$$\sum_n H_{mn}\left(k_x, k_y, -i\frac{d}{dz}\right)\Psi_n^{(a)}(z) = E^{(a)}\Psi_m^{(a)}(z), \tag{16}$$

where $H_{mn}(k_x, k_y, -i\frac{d}{dz})$ is the $\mathbf{k}\cdot\mathbf{p}$ Hamiltonian of the bulk with k_z component of the wave vector replaced by the differential operator $-i\frac{d}{dz}$, $\Psi_n^{(a)}(z)$ is the envelope function corresponding to the state (a) of band n, while $E^{(a)}$ is the energy of that state. We solve the eigenvalue problem using the plane wave expansion method [40–45]. The well is embedded in the region of length L_z and the envelope functions are expanded into a linear combination of plane waves

$$\Psi_n^{(a)}(z) = \frac{1}{\sqrt{L_z}}\sum_{n_z=-N_z}^{N_z} c_{n,n_z}^{(a)} e^{i\frac{2\pi}{L_z}n_z z}, \tag{17}$$

where $c_{n,n_z}^{(a)}$ are expansion coefficients that have to be determined and N_z is an integer that defines the total number of plane waves. After substitution of Eq. (17) into Eq. (16) we obtain the eigenvalue problem of the Hermitian matrix that we diagonalize using standard numerical routines to obtain the coefficients $c_{n,nz}^{(a)}$ and the energies $E^{(a)}$. For a fair comparison with DFT calculation of CdSe slab in vacuum, we perform the calculation for a quantum well inside a large energy barrier. We therefore model the region outside the quantum well as an artificial material whose all parameters are the same as CdSe parameters except the band energies at the Γ point. In this artificial material, we increase all energies of conduction bands by ΔE with respect to corresponding energies in CdSe and decrease all energies of valence bands by the same amount ΔE. In the calculation we use the values $\Delta E = 5$ eV, $L_z = 20$ nm and $N_z = 50$. We have checked that these are sufficiently large values whose further increase would not affect the results.

In Fig. 5 we present the dependence of the band gap on well width obtained within DFT and within the $\mathbf{k}\cdot\mathbf{p}$ model. For a fair comparison, the results of DFT calculation without the effects of spin-orbit interaction were compared with $\mathbf{k}\cdot\mathbf{p}$ models without spin-orbit interaction; the 4×4 and the 13×13 model. The agreement between DFT and $\mathbf{k}\cdot\mathbf{p}$ results and between the results of the two $\mathbf{k}\cdot\mathbf{p}$ models is excellent. For quantum well widths of three lattice constants and larger the band gap differences are smaller than 20 meV. The agreement is quite satisfactory even for rather thin wells of 1 and 2 unit cells, where one might not have expected that $\mathbf{k}\cdot\mathbf{p}$ performs so well. It is also important to note that the calculation of electronic structure of the quantum well using the $\mathbf{k}\cdot\mathbf{p}$ approach takes only up to a few seconds on a single-core desktop

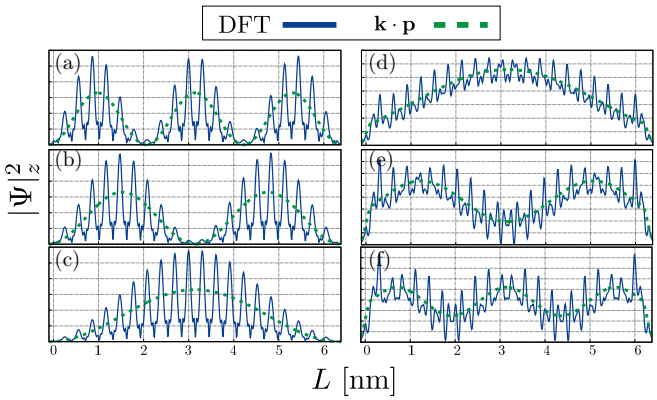

FIG. 6. The wave-function moduli squared of quantum well states obtained from DFT without the effects of spin-orbit coupling and the four-band $\mathbf{k}\cdot\mathbf{p}$ model. The DFT wave functions are presented by performing the in-plane average of wave-function moduli squared. The $\mathbf{k}\cdot\mathbf{p}$ wave functions are presented by a sum $\sum_n |\Psi_n(z)|^2$. The wave functions that are presented in the figure correspond to the following states: (a) VBM-4, (b) degenerate VBM-3 and VBM-2, (c) degenerate VBM-1 and VBM, (d) CBM, (e) CBM + 1, (f) CBM + 2, where VBM (valence band maximum) denotes the highest energy state in the valence band, while CBM (conduction band minimum) denotes the lowest energy state in the conduction band.

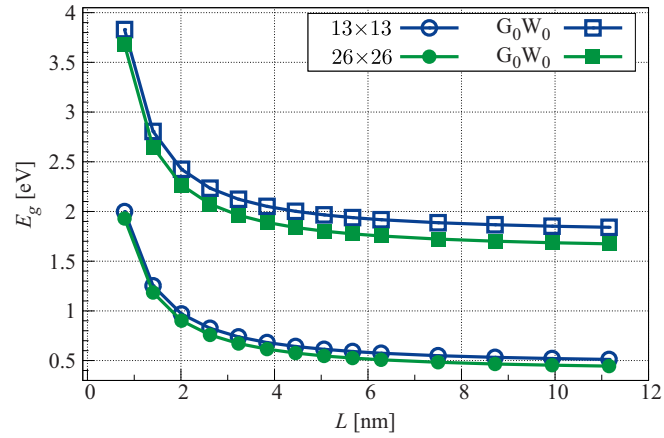

FIG. 7. Well width dependence of zinc-blende CdSe quantum well band gap calculated using the $\mathbf{k}\cdot\mathbf{p}$ method. The parameters of the $\mathbf{k}\cdot\mathbf{p}$ Hamiltonian were extracted from G_0W_0 calculation of bulk band structure. The results obtained with and without the effects of spin-orbit interaction are shown, respectively, in full and empty squares. The results obtained from $\mathbf{k}\cdot\mathbf{p}$ Hamiltonians parametrized from DFT are shown for comparison in full (the case with spin-orbit interaction) and empty (the case without spin-orbit interaction) circles.

computer, regardless of the width of the quantum well. DFT calculations, however, take minutes or hours depending on the width of the quantum well on a computing cluster with several nodes. For example, our calculation times range from approximately 3 min (using 32 cores) to 21 h (using 64 cores) for narrowest and widest quantum wells calculated by DFT, respectively. In the case of nanostructures confined in all three spatial directions, such as quantum dots, the advantages of $\mathbf{k}\cdot\mathbf{p}$ over DFT become even more pronounced. Due to a lack of periodicity in any direction, one needs to calculate supercells with quite a large number of atoms in DFT and the problem becomes computationally intractable for DFT. On the other hand, $\mathbf{k}\cdot\mathbf{p}$ is almost routinely used to study quantum dots, see for example, Refs. [40–45].

We next discuss the origin of somewhat surprisingly good agreement between DFT and $\mathbf{k}\cdot\mathbf{p}$ for thin wells. Within $\mathbf{k}\cdot\mathbf{p}$ the atomistic wave function (shown in Fig. 6 in full lines) is represented in terms of the product of slowly varying envelope functions (shown in Fig. 6 in dashed lines) and rapidly varying bulk Bloch functions, while the only additional approximation in $\mathbf{k}\cdot\mathbf{p}$ with respect to the atomistic method (DFT in our case) comes from truncation of the wave-function expansion to a limited set of bands. For this reason, we believe that excellent agreement between $\mathbf{k}\cdot\mathbf{p}$ and DFT results for wide wells is expected because basis functions used in $\mathbf{k}\cdot\mathbf{p}$ provide a good basis set in this case. In the case of very thin wells, one could argue that the representation of the wave function in terms of the product of envelope functions and bulk Bloch functions for a few bands only cannot be a good representation because the system is rather different from bulk and therefore the basis formed from bulk Bloch functions cannot be a good basis. Our results for CdSe wells confirm that such an argument is certainly valid to some extent because the agreement between DFT and $\mathbf{k}\cdot\mathbf{p}$ becomes somewhat worse for quite thin wells. Nevertheless, we find that the agreement between DFT and $\mathbf{k}\cdot\mathbf{p}$ is quite satisfactory even then and we note that it would be quite interesting to investigate in the future if this is also the case for other materials. It should be noted as well that the use of pseudohydrogen surface passivation also contributes in making the wave functions of thin wells closer to wave functions of bulk material.

We finally present the results of the calculation of CdSe quantum well electronic states, using the $\mathbf{k}\cdot\mathbf{p}$ Hamiltonians parametrized from G_0W_0 calculation of bulk band structure (the parameters of these Hamiltonians are given in Secs. III F and III H of Ref. [30]). To obtain an accurate quasiparticle band gap, we add to the band gap obtained from $\mathbf{k}\cdot\mathbf{p}$ Hamiltonian the correction which takes into account the dielectric mismatch between the quantum well and the vacuum, i.e., the image charge effect. The correction was added using the analytical formula presented in Ref. [46], which was also recently applied in a DFT study of CdSe nanoplatelets [47]. The results obtained are presented in Fig. 7 along with the results obtained from $\mathbf{k}\cdot\mathbf{p}$ Hamiltonians parametrized from DFT, which are given for comparison. As expected, we obtain significantly larger band gaps using $\mathbf{k}\cdot\mathbf{p}$ Hamiltonians parametrized from G_0W_0 calculation of bulk. We note that we focused in this work on single particle energies and the reported gaps are the quasiparticle band gaps. To obtain the optical gap, one would additionally need to consider excitonic effects, which was also recently done for CdSe nanoplatelets in Ref. [47].

IV. CONCLUSION

In conclusion, we presented the method that allows automatic construction of $\mathbf{k}\cdot\mathbf{p}$ Hamiltonians in their symmetry-adapted form starting from output of *ab initio* band structure calculation of bulk material. We then presented

the application of the method to construct the $\mathbf{k}\cdot\mathbf{p}$ Hamiltonians for zinc-blende CdSe material. These Hamiltonians were subsequently used to calculate the electronic states in CdSe quantum wells. Interestingly, excellent agreement was obtained between the results obtained from $\mathbf{k}\cdot\mathbf{p}$ and DFT calculations of quantum wells, even for rather thin wells. While construction and parametrization of $\mathbf{k}\cdot\mathbf{p}$ Hamiltonians is usually believed to be a rather difficult and time consuming task, we expect that the method that we presented will change this situation and that it will be straightforward in the future to obtain $\mathbf{k}\cdot\mathbf{p}$ Hamiltonians for new materials and apply them to study electronic properties of nanostructures based on these materials without the need to perform any kind of fitting.

ACKNOWLEDGMENTS

The authors acknowledge funding provided by the Institute of Physics Belgrade, through the grant by Ministry of Education, Science and Technological Development of the Republic of Serbia. Numerical simulations were run on the PARADOX-IV supercomputing facility at the Scientific Computing Laboratory, National Center of Excellence for the Study of Complex Systems, Institute of Physics Belgrade.

[1] J. P. Perdew, Density functional theory and the band gap problem, Int. J. Quantum Chem. **28**, 497 (1985).

[2] J. P. Perdew, M. Ernzerhof, and K. Burke, Rationale for mixing exact exchange with density functional approximations, J. Chem. Phys. **105**, 9982 (1996).

[3] C. Adamo and V. Barone, Toward reliable density functional methods without adjustable parameters: The PBE0 model, J. Chem. Phys. **110**, 6158 (1999).

[4] L. Hedin, New method for calculating the one-particle Green's function with application to the electron-gas problem, Phys. Rev. **139**, A796 (1965).

[5] M. Shishkin and G. Kresse, Self-consistent *GW* calculations for semiconductors and insulators, Phys. Rev. B **75**, 235102 (2007).

[6] W. Chen and A. Pasquarello, Band-edge levels in semiconductors and insulators: Hybrid density functional theory versus many-body perturbation theory, Phys. Rev. B **86**, 035134 (2012).

[7] Y. Hinuma, Y. Kumagai, I. Tanaka, and F. Oba, Band alignment of semiconductors and insulators using dielectric-dependent hybrid functionals: Toward high-throughput evaluation, Phys. Rev. B **95**, 075302 (2017).

[8] J. M. Luttinger and W. Kohn, Motion of electrons and holes in perturbed periodic fields, Phys. Rev. **97**, 869 (1955).

[9] E. Kane, Energy band structure in p-type germanium and silicon, J. Phys. Chem. Solids **1**, 82 (1956).

[10] C. R. Pidgeon and R. N. Brown, Interband magneto-absorption and Faraday rotation in InSb, Phys. Rev. **146**, 575 (1966).

[11] L. C. Lew Yan Voon and M. Willatzen, *The* $\mathbf{k}\cdot\mathbf{p}$ *Method: Electronic Properties of Semiconductors* (Springer-Verlag, Berlin, 2009).

[12] M. H. Weiler, R. L. Aggarwal, and B. Lax, Warping- and inversion-asymmetry-induced cyclotron-harmonic transitions in InSb, Phys. Rev. B **17**, 3269 (1978).

[13] T. B. Bahder, Eight-band k · p model of strained zinc-blende crystals, Phys. Rev. B **41**, 11992 (1990).

[14] I. Vurgaftman, J. R. Meyer, and L. R. Ram-Mohan, Band parameters for III-V compound semiconductors and their alloys, J. Appl. Phys. **89**, 5815 (2001).

[15] I. Vurgaftman and J. R. Meyer, Band parameters for nitrogen-containing semiconductors, J. Appl. Phys. **94**, 3675 (2003).

[16] M. El Kurdi, G. Fishman, S. Sauvage, and P. Boucaud, Band structure and optical gain of tensile-strained germanium based on a 30 band k · p formalism, J. Appl. Phys. **107**, 013710 (2010).

[17] S. Richard, F. Aniel, and G. Fishman, Energy-band structure of Ge, Si, and GaAs: A thirty-band $\mathbf{k}\cdot\mathbf{p}$ method, Phys. Rev. B **70**, 235204 (2004).

[18] S. Boyer-Richard, F. Raouafi, A. Bondi, L. Pédesseau, C. Katan, J.-M. Jancu, and J. Even, 30-band k · p method for quantum semiconductor heterostructures, Appl. Phys. Lett. **98**, 251913 (2011).

[19] Z. Song, W. Fan, C. S. Tan, Q. Wang, D. Nam, D. H. Zhang, and G. Sun, Band structure of $Ge_{1-x}Sn_x$ alloy: A full-zone 30-band k · p model, New J. Phys. **21**, 073037 (2019).

[20] N. A. Čukarić, M. Ž. Tadić, B. Partoens, and F. M. Peeters, 30-band $\mathbf{k}\cdot\mathbf{p}$ model of electron and hole states in silicon quantum wells, Phys. Rev. B **88**, 205306 (2013).

[21] C. E. Pryor and M.-E. Pistol, Atomistic k · p theory, J. Appl. Phys. **118**, 225702 (2015).

[22] C. Persson and C. Ambrosch-Draxl, A full-band FPLAPW + k · p-method for solving the Kohn-Sham equation, Comput. Phys. Commun. **177**, 280 (2007).

[23] K. Berland and C. Persson, Enabling accurate first-principle calculations of electronic properties with a corrected k · p scheme, Comput. Mater. Sci. **134**, 17 (2017).

[24] T. Shishidou and T. Oguchi, $\mathbf{k}\cdot\mathbf{p}$ formula for use with linearized augmented plane waves, Phys. Rev. B **78**, 245107 (2008).

[25] C. J. Pickard and M. C. Payne, Extrapolative approaches to Brillouin-zone integration, Phys. Rev. B **59**, 4685 (1999).

[26] P. Löwdin, A note on the quantum-mechanical perturbation theory, J. Chem. Phys. **19**, 1396 (1951).

[27] M. I. Aroyo, A. Kirov, C. Capillas, J. M. Perez-Mato, and H. Wondratschek, Bilbao Crystallographic Server. II. Representations of crystallographic point groups and space groups, Acta Crystallogr. Sect. A **62**, 115 (2006).

[28] M. Mozrzymas, M. Studziński, and M. Horodecki, Explicit constructions of unitary transformations between equivalent irreducible representations, J. Phys. A. **47**, 505203 (2014).

[29] J. M. Luttinger, Quantum theory of cyclotron resonance in semiconductors: General theory, Phys. Rev. **102**, 1030 (1956).

[30] See Supplemental Material at http://link.aps.org/supplemental/10.1103/PhysRevB.102.085121 for characters of irreducible representations of the T_d group, analytical expressions for the elements of all blocks of the $\mathbf{k}\cdot\mathbf{p}$ Hamiltonians and numerical values of the parameters of the Hamiltonians.

[31] J. P. Perdew, A. Ruzsinszky, G. I. Csonka, O. A. Vydrov, G. E. Scuseria, L. A. Constantin, X. Zhou, and K. Burke, Restoring the Density-Gradient Expansion for Exchange in Solids and Surfaces, Phys. Rev. Lett. **100**, 136406 (2008).

[32] P. Giannozzi, S. Baroni, N. Bonini, M. Calandra, R. Car, C. Cavazzoni, D. Ceresoli, G. L. Chiarotti, M. Cococcioni, I. Dabo, A. Dal Corso, S. de Gironcoli, S. Fabris, G. Fratesi, R. Gebauer, U. Gerstmann, C. Gougoussis, A. Kokalj, M. Lazzeri, L. Martin-Samos, N. Marzari, F. Mauri, R. Mazzarello, S. Paolini, A. Pasquarello, L. Paulatto, C. Sbraccia, S. Scandolo, G. Sclauzero, A. P. Seitsonen, A. Smogunov, P. Umari, and R. M. Wentzcovitch, QUANTUM ESPRESSO: A modular and open-source software project for quantum simulations of materials, J. Phys.: Condens. Matter **21**, 395502 (2009).

[33] P. Giannozzi, O. Andreussi, T. Brumme, O. Bunau, M. B. Nardelli, M. Calandra, R. Car, C. Cavazzoni, D. Ceresoli, M. Cococcioni, N. Colonna, I. Carnimeo, A. D. Corso, S. de Gironcoli, P. Delugas, R. A. D. Jr, A. Ferretti, A. Floris, G. Fratesi, G. Fugallo, R. Gebauer, U. Gerstmann, F. Giustino, T. Gorni, J. Jia, M. Kawamura, H.-Y. Ko, A. Kokalj, E. Kucukbenli, M. Lazzeri, M. Marsili, N. Marzari, F. Mauri, N. L. Nguyen, H.-V. Nguyen, A. O. de-la Roza, L. Paulatto, S. Poncé, D. Rocca, R. Sabatini, B. Santra, M. Schlipf, A. P. Seitsonen, A. Smogunov, I. Timrov, T. Thonhauser, P. Umari, N. Vast, X. Wu, and S. Baroni, Advanced capabilities for materials modeling with Quantum ESPRESSO, J. Phys.: Condens. Matter **29**, 465901 (2017).

[34] D. R. Hamann, Optimized norm-conserving Vanderbilt pseudopotentials, Phys. Rev. B **88**, 085117 (2013).

[35] M. van Setten, M. Giantomassi, E. Bousquet, M. Verstraete, D. Hamann, X. Gonze, and G.-M. Rignanese, The pseudodojo: Training and grading a 85 element optimized norm-conserving pseudopotential table, Comp. Phys. Comm. **226**, 39 (2018).

[36] D. Sangalli, A. Ferretti, H. Miranda, C. Attaccalite, I. Marri, E. Cannuccia, P. Melo, M. Marsili, F. Paleari, A. Marrazzo, G. Prandini, P. Bonfà, M. O. Atambo, F. Affinito, M. Palummo, A. Molina-Sánchez, C. Hogan, M. Grüning, D. Varsano, and A. Marini, Many-body perturbation theory calculations using the Yambo code, J. Phys.: Condens. Matter **31**, 325902 (2019).

[37] A. Marini, C. Hogan, M. Grüning, and D. Varsano, Yambo: An *ab initio* tool for excited state calculations, Comp. Phys. Comm. **180**, 1392 (2009).

[38] A. P. Cracknell, B. L. Davies, S. C. Miller, and W. F. Love, *Kronecker Product Tables, 1, General Introduction and Tables of Irreducible Representations of Space groups* (IFI/Plenum, New York, 1979).

[39] S. Ninomiya and S. Adachi, Optical properties of cubic and hexagonal CdSe, J. Appl. Phys. **78**, 4681 (1995).

[40] M. A. Cusack, P. R. Briddon, and M. Jaros, Electronic structure of InAs/GaAs self-assembled quantum dots, Phys. Rev. B **54**, R2300 (1996).

[41] S.-S. Li, J.-B. Xia, Z. L. Yuan, Z. Y. Xu, W. Ge, X. R. Wang, Y. Wang, J. Wang, and L. L. Chang, Effective-mass theory for InAs/GaAs strained coupled quantum dots, Phys. Rev. B **54**, 11575 (1996).

[42] A. D. Andreev and E. P. O'Reilly, Theory of the electronic structure of GaN/AlN hexagonal quantum dots, Phys. Rev. B **62**, 15851 (2000).

[43] S. Tomić, A. G. Sunderland, and I. J. Bush, Parallel multi-band $\mathbf{k}\cdot\mathbf{p}$ code for electronic structure of zinc blend semiconductor quantum dots, J. Mater. Chem. **16**, 1963 (2006).

[44] N. Vukmirović, D. Indjin, V. D. Jovanović, Z. Ikonić, and P. Harrison, Symmetry of $\mathbf{k}\cdot\mathbf{p}$ Hamiltonian in pyramidal InAs/GaAs quantum dots: Application to the calculation of electronic structure, Phys. Rev. B **72**, 075356 (2005).

[45] N. Vukmirović and S. Tomić, Plane wave methodology for single quantum dot electronic structure calculations, J. Appl. Phys. **103**, 103718 (2008).

[46] Y. Cho and T. C. Berkelbach, Environmentally sensitive theory of electronic and optical transitions in atomically thin semiconductors, Phys. Rev. B **97**, 041409(R) (2018).

[47] Q. Zhou, Y. Cho, S. Yang, E. A. Weiss, T. C. Berkelbach, and P. Darancet, Large band edge tunability in colloidal nanoplatelets, Nano Lett. **19**, 7124 (2019).

Supplementary material for: Ab-initio construction of symmetry-adapted $\mathbf{k} \cdot \mathbf{p}$ Hamiltonians for electronic structure of semiconductors

Milan Jocić* and Nenad Vukmirović†
Institute of Physics Belgrade, University of Belgrade, Pregrevica 118, 11080 Belgrade, Serbia

* milan.jocic@ipb.ac.rs
† nenad.vukmirovic@ipb.ac.rs

I. CHARACTER TABLES OF THE T_d POINT SINGLE AND DOUBLE GROUP

T_d	E	$3C_2$	$6S_4$	$6\sigma_d$	$8C_3$
Γ_1 (A_1) $x^2+y^2+z^2$	1	1	1	1	1
Γ_2 (A_2)	1	1	-1	-1	1
Γ_3 (E) $(x^2-y^2,$ $3z^2-r^2)$	2	2	0	0	-1
Γ_4 (T_2) (z,x,y)	3	-1	-1	1	0
Γ_5 (T_1) (xy,yz,zx)	3	-1	1	-1	0

TABLE I. Character table for the T_d point group [1, 2].

T_d	E	$3C_2$ $3\overline{C}_2$	$6S_4$	$6\sigma_d$ $6\overline{\sigma}_d$	$8C_3$	$\overline{E}$	$6\overline{S}_4$	$8\overline{C}_3$
Γ_1 (A_1) $x^2+y^2+z^2$	1	1	1	1	1	1	1	1
Γ_2 (A_2)	1	1	-1	-1	1	1	-1	1
Γ_3 (E) $(x^2-y^2,$ $3z^2-r^2)$	2	2	0	0	-1	2	0	-1
Γ_4 (T_2) (z,x,y)	3	-1	-1	1	0	3	-1	0
Γ_5 (T_1) (xy,yz,zx)	3	-1	1	-1	0	3	1	0
Γ_6 $(\overline{E}_1)$	2	0	$\sqrt{2}$	0	1	-2	$-\sqrt{2}$	-1
Γ_7 $(\overline{E}_2)$	2	0	$-\sqrt{2}$	0	1	-2	$\sqrt{2}$	-1
Γ_8 $(\overline{F})$	4	0	0	0	-1	-4	0	1

TABLE II. Character table for the double T_d point group [1].

II. ANALYTICAL EXPRESSIONS FOR THE ELEMENTS OF ALL BLOCKS OF THE $\mathbf{k}\cdot\mathbf{p}$ HAMILTONIAN

In this section, we list the Hamiltonian matrix elements arising from the term $\frac{\hbar(\mathbf{k}-\mathbf{k}_0)}{m_0}\cdot\langle\Psi_{n\mathbf{k}_0}|\,\mathbf{p}\,|\Psi_{m\mathbf{k}_0}\rangle$ in Eq. (8) and the $H^{(2)}_{nm}$ term in Eq. (10) of the main part of the paper. To obtain the full $\mathbf{k}\cdot\mathbf{p}$ Hamiltonian these terms should be complemented with the diagonal term $\left[E_n(\mathbf{k}_0)+\frac{\hbar^2(\mathbf{k}-\mathbf{k}_0)^2}{2m_0}\right]\delta_{nm}$.

A. Single group T_d

We now list analytical expressions for all possible blocks $\mathcal{B}(\Gamma_m,\Gamma_n)$ of the $\mathbf{k}\cdot\mathbf{p}$ Hamiltonian in the case of single T_d group:

$$\mathcal{B}(\Gamma_1,\Gamma_1)=C_1k^2, \tag{1}$$

$$\mathcal{B}(\Gamma_1,\Gamma_2)=0, \tag{2}$$

$$\mathcal{B}(\Gamma_1,\Gamma_3)=C_2\left[(k_z^2+\omega^2k_x^2+\omega k_y^2)\;\;(k_z^2+\omega k_x^2+\omega^2k_y^2)\right],\quad \omega=e^{i2\pi/3}, \tag{3}$$

$$\mathcal{B}(\Gamma_1,\Gamma_4)=C_3\left[k_z\;\;k_x\;\;k_y\right]+C_4\left[k_xk_y\;\;k_yk_z\;\;k_zk_x\right], \tag{4}$$

$$\mathcal{B}(\Gamma_1,\Gamma_5)=0, \tag{5}$$

$$\mathcal{B}(\Gamma_2,\Gamma_2)=C_5k^2, \tag{6}$$

$$\mathcal{B}(\Gamma_2,\Gamma_3)=C_6\left[-(k_z^2+\omega^2k_x^2+\omega k_y^2)\;\;(k_z^2+\omega k_x^2+\omega^2k_y^2)\right], \tag{7}$$

$$\mathcal{B}(\Gamma_2,\Gamma_4)=0, \tag{8}$$

$$\mathcal{B}(\Gamma_2,\Gamma_5)=C_7\left[k_z\;\;k_x\;\;k_y\right]+C_8\left[k_xk_y\;\;k_yk_z\;\;k_zk_x\right], \tag{9}$$

$$\begin{aligned}\mathcal{B}(\Gamma_3,\Gamma_3)=&C_9\begin{bmatrix}k^2&0\\0&k^2\end{bmatrix}\\&+C_{10}\begin{bmatrix}0&(k_z^2+\omega^2k_x^2+\omega k_y^2)\\(k_z^2+\omega k_x^2+\omega^2k_y^2)&0\end{bmatrix},\end{aligned} \tag{10}$$

$$\begin{aligned}\mathcal{B}(\Gamma_3,\Gamma_4)=&C_{11}\begin{bmatrix}k_z&\omega k_x&\omega^2k_y\\k_z&\omega^2k_x&\omega k_y\end{bmatrix}\\&+C_{12}\begin{bmatrix}k_xk_y&\omega k_yk_z&\omega^2k_zk_x\\k_xk_y&\omega^2k_yk_z&\omega k_zk_x\end{bmatrix},\end{aligned} \tag{11}$$

$$\begin{aligned}\mathcal{B}(\Gamma_3,\Gamma_5) = C_{13}&\begin{bmatrix} k_z & \omega k_x & \omega^2 k_y \\ -k_z & -\omega^2 k_x & -\omega k_y \end{bmatrix} \\ &+ C_{14}\begin{bmatrix} k_x k_y & \omega k_y k_z & \omega^2 k_z k_x \\ -k_x k_y & -\omega^2 k_y k_z & -\omega k_z k_x \end{bmatrix}\end{aligned} \tag{12}$$

$$\begin{aligned}\mathcal{B}(\Gamma_4,\Gamma_4) = C_{15}&\begin{bmatrix} 0 & k_y & k_x \\ k_y & 0 & k_z \\ k_x & k_z & 0 \end{bmatrix} \\ &+ C_{16}\begin{bmatrix} 0 & k_z k_x & k_y k_z \\ k_z k_x & 0 & k_x k_y \\ k_y k_z & k_x k_y & 0 \end{bmatrix} \\ &+ C_{17}\begin{bmatrix} 2k_z^2 - k_x^2 - k_y^2 & 0 & 0 \\ 0 & 2k_x^2 - k_y^2 - k_z^2 & 0 \\ 0 & 0 & 2k_y^2 - k_z^2 - k_x^2 \end{bmatrix} \\ &+ C_{18}\begin{bmatrix} k^2 & 0 & 0 \\ 0 & k^2 & 0 \\ 0 & 0 & k^2 \end{bmatrix},\end{aligned} \tag{13}$$

$$\begin{aligned}\mathcal{B}(\Gamma_4,\Gamma_5) = C_{19}&\begin{bmatrix} 0 & k_y & -k_x \\ -k_y & 0 & k_z \\ k_x & -k_z & 0 \end{bmatrix} \\ &+ C_{20}\begin{bmatrix} 0 & k_z k_x & -k_y k_z \\ -k_z k_x & 0 & k_x k_y \\ k_y k_z & -k_x k_y & 0 \end{bmatrix} \\ &+ C_{21}\begin{bmatrix} k_x^2 - k_y^2 & 0 & 0 \\ 0 & k_y^2 - k_z^2 & 0 \\ 0 & 0 & k_z^2 - k_x^2 \end{bmatrix},\end{aligned} \tag{14}$$

$$\begin{aligned}\mathcal{B}(\Gamma_5,\Gamma_5) = C_{22}&\begin{bmatrix} 0 & k_y & k_x \\ k_y & 0 & k_z \\ k_x & k_z & 0 \end{bmatrix} \\ &+ C_{23}\begin{bmatrix} 0 & k_z k_x & k_y k_z \\ k_z k_x & 0 & k_x k_y \\ k_y k_z & k_x k_y & 0 \end{bmatrix} \\ &+ C_{24}\begin{bmatrix} 2k_z^2 - k_x^2 - k_y^2 & 0 & 0 \\ 0 & 2k_x^2 - k_y^2 - k_z^2 & 0 \\ 0 & 0 & 2k_y^2 - k_z^2 - k_x^2 \end{bmatrix} \\ &+ C_{25}\begin{bmatrix} k^2 & 0 & 0 \\ 0 & k^2 & 0 \\ 0 & 0 & k^2 \end{bmatrix},\end{aligned} \tag{15}$$

To form the $\mathbf{k}\cdot\mathbf{p}$ Hamiltonian based on a chosen set of bands, one should simply combine all relevant blocks. For example, to obtain the 4×4 Hamiltonian based on the Γ_1^m and Γ_4^m bands, one should take the blocks $\mathcal{B}(\Gamma_1,\Gamma_1)$,

$\mathcal{B}(\Gamma_1,\Gamma_4)$, $\mathcal{B}(\Gamma_4,\Gamma_1)$ and $\mathcal{B}(\Gamma_4,\Gamma_4)$. The Hamiltonian that we obtain in this case (taking into account that $C_{15}=0$ as shown in Section III A) corresponds exactly to the second-order four-band Kane Hamiltonian [3].

It is common in the literature to choose the states that transform as x, y and z as the basis of the three-dimensional manifold of Γ_4 states. On the other hand, we pointed out at the end of Section II-B in the main part of the paper that this basis $|\psi_i\rangle$ [Eq. (13) of the paper] depends on the convention for matrices of irreps, Γ_4 in this case. We find that the convention for matrices of irrep Γ_4 that we used leads exactly to the basis states that transform as x, y and z. For this reason, we obtain the form of the Hamiltonian that is identical to the second-order four-band Kane Hamiltonian which is formulated in x, y, z basis.

B. Double group T_d

When spin-orbit interaction is included, the states transform according to the representations of the double point group T_d, which means that only the Γ_6,Γ_7 and Γ_8 states are relevant. Since the matrices that we obtained have some parts that appear more than once, we introduce the following shortened notation:

$$\Upsilon = \omega^2 k_x^2 + \omega k_y^2 + k_z^2, \tag{16}$$

$$\Sigma(z,x,y) = \begin{bmatrix} z & x-iy \\ x+iy & -z \end{bmatrix}, \tag{17}$$

$$\Delta(z,x,y) = \begin{bmatrix} ze^{i45^\circ} & xe^{-i75^\circ}+ye^{i75^\circ} \\ xe^{-i75^\circ}+ye^{-i105^\circ} & ze^{-i135^\circ} \end{bmatrix}, \tag{18}$$

$$\Lambda(z,x,y) = \begin{bmatrix} xe^{i30^\circ}+ye^{i60^\circ} & z \\ ze^{i90^\circ} & xe^{i120^\circ}+ye^{-i30^\circ} \end{bmatrix}, \tag{19}$$

$$\Xi(z,x,y) = \begin{bmatrix} ze^{-i135^\circ} & xe^{i105^\circ}+ye^{-i105^\circ} \\ xe^{i105^\circ}+ye^{i75^\circ} & ze^{i45^\circ} \end{bmatrix}. \tag{20}$$

$$\begin{aligned} \Omega_1(z,x,y) &= \begin{bmatrix} xe^{i60^\circ}+ye^{-i150^\circ} & -iz \\ z & xe^{i150^\circ}+ye^{i120^\circ} \end{bmatrix} \\ \Omega_2(z,x,y) &= \begin{bmatrix} xe^{i30^\circ}+ye^{-i120^\circ} & iz \\ -z & xe^{-i60^\circ}+ye^{-i30^\circ} \end{bmatrix} \end{aligned} \tag{21}$$

Using the notation from equations (16) through (21) we write down the relevant blocks of the Hamiltonian in case of double point group T_d:

$$\mathcal{B}(\Gamma_6,\Gamma_6) = C_1^d k^2, \tag{22}$$

$$\mathcal{B}(\Gamma_7,\Gamma_7) = C_2^d k^2, \tag{23}$$

$$\mathcal{B}(\Gamma_6,\Gamma_7) = C_3^d \Sigma(k_z,k_x,k_y) + C_4^d \Sigma(k_x k_y, k_y k_z, k_z k_x) \tag{24}$$

$$\begin{aligned}\mathcal{B}(\Gamma_6,\Gamma_8) &= C_5^d \begin{bmatrix} -\frac{1+i}{2}\Upsilon & 0 & 0 & \frac{1}{\sqrt{2}}\Upsilon^* \\ 0 & -\frac{1+i}{2}\Upsilon & -\frac{i}{\sqrt{2}}\Upsilon^* & 0 \end{bmatrix} \\ &+ C_6^d \begin{bmatrix} \Delta(k_z,k_x,k_y) & \Lambda(k_z,k_x,k_y) \end{bmatrix} \\ &+ C_7^d \begin{bmatrix} \Delta(k_xk_y,k_yk_z,k_zk_x) & \Lambda(k_xk_y,k_yk_z,k_zk_x) \end{bmatrix}\end{aligned} \tag{25}$$

$$\begin{aligned}\mathcal{B}(\Gamma_7,\Gamma_8) &= +C_8^d \begin{bmatrix} \frac{1+i}{2}\Upsilon & 0 & 0 & \frac{1}{\sqrt{2}}\Upsilon^* \\ 0 & \frac{1+i}{2}\Upsilon & -\frac{i}{\sqrt{2}}\Upsilon^* & 0 \end{bmatrix} \\ &+ C_9^d \begin{bmatrix} \Xi(k_z,k_x,k_y) & \Lambda(k_z,k_x,k_y) \end{bmatrix} \\ &+ C_{10}^d \begin{bmatrix} \Xi(k_xk_y,k_yk_z,k_zk_x) & \Lambda(k_xk_y,k_yk_z,k_zk_x) \end{bmatrix}\end{aligned}, \tag{26}$$

$$\begin{aligned}\mathcal{B}(\Gamma_8,\Gamma_8) &= C_{11}^d k^2 \\ &+ C_{12}^d \begin{bmatrix} 0 & 0 & 0 & -\Upsilon \\ 0 & 0 & i\Upsilon & 0 \\ 0 & \Upsilon^* & 0 & 0 \\ -i\Upsilon^* & 0 & 0 & 0 \end{bmatrix} \\ &+ C_{13}^d \begin{bmatrix} \Sigma(k_z,k_x,k_y) & 0 \\ 0 & \Sigma(k_z,k_y,k_x) \end{bmatrix} \\ &+ C_{14}^d \begin{bmatrix} 0 & \Omega_1(k_z,k_x,k_y) \\ \Omega_2(k_z,k_x,k_y) & 0 \end{bmatrix} \\ &+ C_{15}^d \begin{bmatrix} \Sigma(k_xk_y,k_yk_z,k_zk_x) & 0 \\ 0 & \Sigma(k_xk_y,k_zk_x,k_yk_z) \end{bmatrix} \\ &+ C_{16}^d \begin{bmatrix} 0 & \Omega_1(k_xk_y,k_yk_z,k_zk_x) \\ \Omega_2(k_xk_y,k_yk_z,k_zk_x) & 0 \end{bmatrix}\end{aligned}, \tag{27}$$

It is common in the literature to choose the states that transform as 1/2 angular momentum states in the two-dimensional manifolds of Γ_6 and Γ_7 states and the states that transform as 3/2 angular momentum states in the four-dimensional manifold of Γ_8 states. On the other hand, we pointed out at the end of Section II-B in the main part of the paper that the basis $|\psi_i\rangle$ [Eq. (13) of the paper] in these manifolds depends on the convention for matrices of irreps, Γ_6-Γ_8 in this case. We find that the convention for matrices of irreps Γ_6 and Γ_7 that we used leads exactly to the basis states that transform as 1/2 angular momentum states. However, the convention for matrices of irrep Γ_8 does not yield the basis states that transform as 3/2 angular momentum states. For this reason, we do not get the same form of Hamiltonian that is obtained in the literature when the basis of 3/2 angular momentum states is used. In particular, the 8-band Hamiltonian that we obtain by taking the highest valence bands that transform as Γ_7 and Γ_8 and the lowest conduction band that transforms as Γ_6 coincides with Weiler 8-band Hamiltonian [3, 4] only after an appropriate unitary transformation is made. This unitary transformation consists of a transformation to 3/2 angular momentum basis in the Γ_8 manifold and additionally it has some trivial phase factor multiplications (the terms $e^{j\phi_1}$ and $e^{j\phi_2}$). The transformation is given as

$$H_8' = U^\dagger H_8 U. \tag{28}$$

In this equation H_8 is the eight-band Hamiltonian that we obtain from our procedure and H_8' is the 8-band Hamiltonian

reported in Ref. [4] (also reproduced in Ref. [3]). The matrix U reads

$$U = \begin{bmatrix} 0 & 0 & 0 & 0 & 0 & 0 & 0 & e^{j\phi_1} \\ 0 & 0 & 0 & e^{j\phi_1} & 0 & 0 & 0 & 0 \\ 0 & 0 & 0 & 0 & 0 & \frac{\sqrt{2}}{2} & \frac{j\sqrt{2}}{2} & 0 \\ 0 & -\frac{j\sqrt{2}}{2} & -\frac{\sqrt{2}}{2} & 0 & 0 & 0 & 0 & 0 \\ 0 & -\frac{1}{2}-\frac{j}{2} & \frac{1}{2}-\frac{j}{2} & 0 & 0 & 0 & 0 & 0 \\ 0 & 0 & 0 & 0 & 0 & \frac{1}{2}+\frac{j}{2} & \frac{1}{2}-\frac{j}{2} & 0 \\ e^{j\phi_2} & 0 & 0 & 0 & 0 & 0 & 0 & 0 \\ 0 & 0 & 0 & 0 & e^{j\phi_2} & 0 & 0 & 0 \end{bmatrix}. \tag{29}$$

The phase factors $e^{j\phi_1}$ and $e^{j\phi_2}$ adjust the phases so that all parameters of the Weiler Hamiltonian become real. For the parameters given in Section III C these phase factors read $e^{j\phi_1} = 0.93659 + 0.35042 \cdot j$ and $e^{j\phi_2} = -0.98853 - 0.15103 \cdot j$. After performing the transformation given in Eq. (28) we obtain the Weiler Hamiltonian with parameters (for the parameters given in Section III C): $\gamma_1 = 3.82622$, $\gamma_2 = -0.32116$, $\gamma_3 = 0.39693$, $\gamma_1' = 3.84008$, $\gamma_2' = -0.28179$, $\gamma_3' = 0.43182$, $P = 0.40682$, $P' = 0.38616$, $G = 0.26536$, $G' = 0.00000$, $F = 0.12078$, $C = -0.00931$, $C' = -0.00042$, $N_2 = 0.02090$. These parameters were given in Hartree atomic units.

We have also checked that our procedure yields directly the Weiler Hamiltonian (up to phase factors $e^{j\phi_1}$ and $e^{j\phi_2}$ that need to be fixed) if we use from the beginning the matrices of irrep Γ_8 that transform as 3/2 angular momentum states.

C. Comparison of DFT-obtained and symmetry-adapted 4×4 Hamiltonian

Two analytical forms of the 4×4 Hamiltonian, made from degenerate states corresponding to Γ_4 and Γ_1 irreps that lie below and above the gap respectively, in the case of CdSe, are presented here. Both Hamiltonians give the same physics, overall, and they are connected by an unitary transformation U, that is used to transform initial DFT basis $|\phi_i\rangle$ to the symmetry-adapted basis $|\psi_j\rangle$. To give more clarity and justify the whole procedure of transforming the initial DFT basis, we will compare inital DFT-form $H^{\text{init}}_{\text{DFT}}$, obtained from groups of degenerate states $|\phi_i\rangle$ and symmetry-adapted form $H^{\text{sym}}_{\text{adap}}$, that is made out of transformed groups of degenerate states $|\psi_j\rangle$.

Initial DFT-form $H^{\text{init}}_{\text{DFT}}$ of the 4×4 Hamiltonian is given as:

$$H^{\text{init}}_{\text{DFT}} = \frac{\hbar^2 k^2}{2m_0} + \begin{bmatrix} E_{\Gamma_4} & 0 & 0 & 0 \\ 0 & E_{\Gamma_4} & 0 & 0 \\ 0 & 0 & E_{\Gamma_4} & 0 \\ 0 & 0 & 0 & E_{\Gamma_1} \end{bmatrix} + \frac{\hbar}{m_0} \begin{bmatrix} 0 & 0 & 0 & P^{(1)}_{03} \\ 0 & 0 & 0 & P^{(1)}_{13} \\ 0 & 0 & 0 & P^{(1)}_{23} \\ P^{(1)*}_{03} & P^{(1)*}_{13} & P^{(1)*}_{23} & 0 \end{bmatrix} + \frac{\hbar^2}{m_0^2} \begin{bmatrix} P^{(2)}_{00} & P^{(2)}_{01} & P^{(2)}_{02} & P^{(2)}_{03} \\ P^{(2)*}_{01} & P^{(2)}_{11} & P^{(2)}_{12} & P^{(2)}_{13} \\ P^{(2)*}_{02} & P^{(2)*}_{12} & P^{(2)}_{22} & P^{(2)}_{23} \\ P^{(2)*}_{03} & P^{(2)*}_{13} & P^{(2)*}_{23} & P^{(2)}_{33} \end{bmatrix},$$

where:

$$\begin{aligned} P^{(1)}_{i3} &= C^{x(1)}_{i3} k_x + C^{y(1)}_{i3} k_y + C^{z(1)}_{i3} k_z, \quad i = 0, 1, 2; \\ P^{(2)}_{i3} &= C^{xy(2)}_{i3} k_x k_y + C^{yz(2)}_{i3} k_y k_z + C^{zx(2)}_{i3} k_z k_x, \quad i = 0, 1, 2; \\ P^{(2)}_{ij} &= C^{xx(2)}_{ij} k_x^2 + C^{yy(2)}_{ij} k_y^2 + C^{zz(2)}_{ij} k_z^2 + C^{xy(2)}_{ij} k_x k_y + C^{yz(2)}_{ij} k_y k_z + C^{zx(2)}_{ij} k_z k_x, \quad i, j = 0, 1, 2; \\ P^{(2)}_{33} &= C^{zz(2)}_{33} k^2. \end{aligned}$$

If we count the number of parameters $C^{m(1)}_{i3}$ for 1st order and $C^{mn(2)}_{ij}$ for 2nd order terms $(m, n = x, y, z)$ in the last four expressions, we can tell that $H^{\text{init}}_{\text{DFT}}$ has a total number of $3 \times 3 + 3 \times 3 + 6 \times 6 + 1 = 55$ parameters. Of course, this number can be reduced but the procedure could be rather cumbersome especially if a great number of materials with different symmetries is considered.

Symmetry-adapted form $H^{\text{sym}}_{\text{adap}}$ of the 4×4 Hamiltonian is given as:

$$H^{\text{sym}}_{\text{adap}} = \frac{\hbar^2 k^2}{2m_0} + \begin{bmatrix} E_{\Gamma_4} & 0 & 0 & 0 \\ 0 & E_{\Gamma_4} & 0 & 0 \\ 0 & 0 & E_{\Gamma_4} & 0 \\ 0 & 0 & 0 & E_{\Gamma_1} \end{bmatrix} + \frac{\hbar}{m_0} \begin{bmatrix} 0 & C_{15} k_y & C_{15} k_x & C_3 k_z \\ C_{15} k_y & 0 & C_{15} k_z & C_3 k_x \\ C_{15} k_x & C_{15} k_z & 0 & C_3 k_y \\ C_3^* k_z & C_3^* k_x & C_3^* k_y & 0 \end{bmatrix}$$
$$+ \frac{\hbar^2}{m_0^2} \begin{bmatrix} C_{17}(2k_z^2 - k_x^2 - k_y^2) + C_{18} k^2 & C_{16} k_z k_x & C_{16} k_y k_z & C_4^* k_x k_y \\ C_{16} k_z k_x & C_{17}(2k_x^2 - k_y^2 - k_z^2) + C_{18} k^2 & C_{16} k_x k_y & C_4^* k_y k_z \\ C_{16} k_y k_z & C_{16} k_x k_y & C_{17}(2k_y^2 - k_z^2 - k_x^2) + C_{18} k^2 & C_4^* k_z k_x \\ C_4 k_x k_y & C_4 k_y k_z & C_4 k_z k_x & C_1 k^2 \end{bmatrix},$$

where $C_{15} = 0$ if the block is formed from two same Γ_4 irreps as it is in the 4×4 case. This gives for $H^{\text{sym}}_{\text{adap}}$, a total number of $1 + 5 = 6$ parameters, for 1st and 2nd order $\mathbf{k} \cdot \mathbf{p}$ terms. This way, if we were to consider a large number of crystals, we could group them according to their symmetry group, and compare the individual parameters.

Unlike symmetry-adapted form $H^{\text{sym}}_{\text{adap}}$, initial DFT-form $H^{\text{init}}_{\text{DFT}}$ clearly demonstrates much more parameters than symmetry of the crystal CdSe would suggest, even for the simplest 4×4 case.

III. NUMERICAL VALUES OF THE PARAMETERS

In this Section, we present the numerical values of the parameters of the Hamiltonians obtained. All quantities are given in Hartree atomic units, while relevant energies are additionally also given in electron volts. Table III gives a summary of different parametrizations of the Hamiltonian and the sections where the parametrizations are given.

Section	Hamiltonian
Section III A	Standard 4×4 Hamiltonian parametrized from DFT without SOC
Section III B	Extended 13×13 Hamiltonian parametrized from DFT without SOC
Section III C	Standard 8×8 Hamiltonian parametrized from DFT with SOC
Section III D	Extended 26×26 Hamiltonian parametrized from DFT with SOC
Section III E	Standard 4×4 Hamiltonian parametrized from DFT without SOC with quasiparticle energies taken from G_0W_0 calculation
Section III F	Extended 13×13 Hamiltonian parametrized from DFT without SOC with quasiparticle energies taken from G_0W_0 calculation
Section III G	Standard 8×8 Hamiltonian parametrized from DFT with SOC with quasiparticle energies taken from G_0W_0 calculation
Section III H	Extended 26×26 Hamiltonian parametrized from DFT with SOC with quasiparticle energies taken from G_0W_0 calculation

TABLE III. A summary of different parametrizations of the Hamiltonian and the sections where the parametrizations are given.

A. Standard 4×4 Hamiltonian

	E[eV]	E[Hartree]
Γ_4^m	0.0	0.0
Γ_1^m	0.46821	0.01721

	$\mathcal{B}(\Gamma_1^m, \Gamma_1^m)$
C_1	0.03880

	$\mathcal{B}(\Gamma_1^m, \Gamma_4^m)$
C_3	$0.29213 + 0.28073j$
C_4	$0.22183 - 0.23083j$

	$\mathcal{B}(\Gamma_4^m, \Gamma_4^m)$
C_{15}	0
C_{16}	-0.68794
C_{17}	0.16303
C_{18}	-1.04656

B. Extended 13×13 Hamiltonian

	E[eV]	E[Hartree]
Γ_4^v	-7.88140	-0.28964
Γ_3^v	-7.50786	-0.27591
Γ_4^m	0.0	0.0
Γ_1^m	0.46821	0.01721
Γ_4^c	5.87086	0.21575
Γ_1^c	9.58302	0.35217

	$\mathcal{B}(\Gamma_1^m, \Gamma_1^m)$	$\mathcal{B}(\Gamma_1^c, \Gamma_1^c)$	$\mathcal{B}(\Gamma_1^c, \Gamma_1^m)$
C_1	0.01616	0.01635	$-0.00653 - 0.03685j$

	$\mathcal{B}(\Gamma_1^c, \Gamma_3^v)$	$\mathcal{B}(\Gamma_1^m, \Gamma_3^v)$
C_2	$-0.13097 - 0.07961j$	$0.10099 - 0.11476j$

	$\mathcal{B}(\Gamma_1^m, \Gamma_4^v)$	$\mathcal{B}(\Gamma_1^m, \Gamma_4^m)$	$\mathcal{B}(\Gamma_1^m, \Gamma_4^c)$
C_3	$-0.16939 - 0.05120j$	$0.29213 + 0.28073j$	$-0.12171 + 0.03090j$
C_4	$-0.09935 + 0.32871j$	$-0.08738 + 0.09093j$	$-0.00165 - 0.00649j$

	$\mathcal{B}(\Gamma_1^c, \Gamma_4^v)$	$\mathcal{B}(\Gamma_1^c, \Gamma_4^m)$	$\mathcal{B}(\Gamma_1^c, \Gamma_4^c)$
C_3	$0.00690 - 0.05817j$	$0.00911 - 0.01361j$	$0.23220 + 0.51426j$
C_4	$0.41908 + 0.04970j$	$0.12813 + 0.08580j$	$0.00524 - 0.00237j$

	$\mathcal{B}(\Gamma_3^v, \Gamma_3^v)$
C_9	-0.33898
C_{10}	0.12786

	$\mathcal{B}(\Gamma_3^v, \Gamma_4^v)$	$\mathcal{B}(\Gamma_3^v, \Gamma_4^m)$	$\mathcal{B}(\Gamma_3^v, \Gamma_4^c)$
C_{11}	$0.00272 + 0.00595j$	$0.00154 - 0.03508j$	$-0.19430 - 0.13307j$
C_{12}	$0.12304 - 0.05616j$	$0.03769 + 0.00165j$	$-0.06773 + 0.09889j$

	$\mathcal{B}(\Gamma_4^v, \Gamma_4^v)$	$\mathcal{B}(\Gamma_4^m, \Gamma_4^m)$	$\mathcal{B}(\Gamma_4^c, \Gamma_4^c)$
C_{15}	0	0	0
C_{16}	0.29432	0.39888	-0.47968
C_{17}	-0.00204	-0.20023	0.07955
C_{18}	-0.29136	-0.32823	-0.55226

	$\mathcal{B}(\Gamma_4^m, \Gamma_4^v)$	$\mathcal{B}(\Gamma_4^c, \Gamma_4^v)$	$\mathcal{B}(\Gamma_4^c, \Gamma_4^m)$
C_{15}	$0.05946 + 0.11647j$	$0.03891 - 0.06460j$	$0.42118 - 0.26210j$
C_{16}	$-0.16023 + 0.08180j$	$0.15739 + 0.09480j$	$-0.08474 - 0.13617j$
C_{17}	$-0.02788 + 0.01423j$	$-0.04879 - 0.02939j$	$0.08051 + 0.12937j$
C_{18}	$-0.16355 + 0.08349j$	$0.03718 + 0.02240j$	$0.06582 + 0.10577j$

C. Standard 8×8 Hamiltonian

	E[eV]	E[Hartree]
Γ_7^m	-0.16924	-0.00622
Γ_8^m	0.0	0.0
Γ_6^m	0.40085	0.01473

	$\mathcal{B}(\Gamma_6^m, \Gamma_6^m)$
C_1^d	0.06588

	$\mathcal{B}(\Gamma_7^m, \Gamma_7^m)$
C_2^d	-1.04722

	$\mathcal{B}(\Gamma_6^m, \Gamma_7^m)$
C_3^d	$-0.21822 + 0.04568j$
C_4^d	$0.03234 + 0.15448j$

	$\mathcal{B}(\Gamma_6^m, \Gamma_8^m)$
C_5^d	$0.01350 + 0.01837j$
C_6^d	$0.18927 - 0.13908j$
C_7^d	$-0.09896 - 0.13467j$

	$\mathcal{B}(\Gamma_7^m, \Gamma_8^m)$
C_8^d	$-0.19781 + 0.09009j$
C_9^d	$-0.00009 - 0.00019j$
C_{10}^d	$0.37124 - 0.16908j$

	$\mathcal{B}(\Gamma_8^m, \Gamma_8^m)$
C_{11}^d	-1.04344
C_{12}^d	$-0.12387 + 0.12387j$
C_{13}^d	0
C_{14}^d	$-0.00658 + 0.00658j$
C_{15}^d	-0.37497
C_{16}^d	0

D. Extended 26×26 Hamiltonian

	E[eV]	E[Hartree]
$\Gamma_8^{v_1}$	-9.50287	-0.34922
Γ_7^{v}	-6.94697	-0.25530
$\Gamma_8^{v_2}$	-6.60685	-0.24280
Γ_7^{m}	-0.16924	-0.00622
Γ_8^{m}	0.0	0.0
Γ_6^{m}	0.40085	0.01473
Γ_7^{c}	5.56618	0.20455
Γ_8^{c}	5.97379	0.21953
Γ_6^{c}	9.53629	0.35045

	$\mathcal{B}(\Gamma_6^m,\Gamma_6^m)$	$\mathcal{B}(\Gamma_6^c,\Gamma_6^m)$	$\mathcal{B}(\Gamma_6^c,\Gamma_6^c)$
C_1^d	0.01863	$0.02546+0.03002j$	0.01738

	$\mathcal{B}(\Gamma_7^v,\Gamma_7^v)$	$\mathcal{B}(\Gamma_7^m,\Gamma_7^v)$	$\mathcal{B}(\Gamma_7^c,\Gamma_7^v)$
C_2^d	-0.26310	$0.15491+0.11684j$	$0.02861-0.02945j$

	$\mathcal{B}(\Gamma_7^m,\Gamma_7^m)$	$\mathcal{B}(\Gamma_7^c,\Gamma_7^m)$	$\mathcal{B}(\Gamma_7^c,\Gamma_7^c)$
C_2^d	-0.36390	$-0.01605+0.12791j$	-0.51997

	$\mathcal{B}(\Gamma_6^m,\Gamma_7^v)$	$\mathcal{B}(\Gamma_6^m,\Gamma_7^m)$	$\mathcal{B}(\Gamma_6^m,\Gamma_7^c)$
C_3^d	$-0.10904-0.05132j$	$-0.21822+0.04568j$	$-0.02093-0.06086j$
C_4^d	$-0.08139+0.17295j$	$-0.01709-0.08162j$	$-0.00481+0.00165j$

	$\mathcal{B}(\Gamma_6^c,\Gamma_7^v)$	$\mathcal{B}(\Gamma_6^c,\Gamma_7^m)$	$\mathcal{B}(\Gamma_6^c,\Gamma_7^c)$
C_3^d	$0.00855+0.03169j$	$-0.01216-0.00946j$	$0.16439-0.27667j$
C_4^d	$-0.22411+0.06048j$	$0.06612-0.08502j$	$-0.01687-0.01002j$

	$\mathcal{B}(\Gamma_6^m,\Gamma_8^{v_1})$	$\mathcal{B}(\Gamma_6^m,\Gamma_8^{v_2})$
C_5^d	$-0.08794-0.08322j$	$-0.15106+0.08260j$
C_6^d	$0.04906-0.05184j$	$0.03470+0.06346j$
C_7^d	$-0.11283-0.10676j$	$0.10096-0.05520j$

	$\mathcal{B}(\Gamma_6^m,\Gamma_8^m)$	$\mathcal{B}(\Gamma_6^m,\Gamma_8^c)$
C_5^d	$-0.00953-0.01296j$	$-0.00537+0.00572j$
C_6^d	$0.18927-0.13908j$	$0.05385+0.05061j$
C_7^d	$0.04030+0.05485j$	$-0.00588+0.00626j$

	$\mathcal{B}(\Gamma_6^c, \Gamma_8^{v1})$	$\mathcal{B}(\Gamma_6^c, \Gamma_8^{v2})$
C_5^d	$0.00696 - 0.12794j$	$-0.15674 - 0.06024j$
C_6^d	$-0.02513 - 0.00137j$	$0.00701 - 0.01823j$
C_7^d	$0.01060 - 0.19485j$	$0.13521 + 0.05197j$

	$\mathcal{B}(\Gamma_6^c, \Gamma_8^m)$	$\mathcal{B}(\Gamma_6^c, \Gamma_8^c)$
C_5^d	$0.00378 - 0.01590j$	$-0.02377 - 0.00121j$
C_6^d	$0.00866 + 0.00206j$	$-0.01685 + 0.33051j$
C_7^d	$-0.01955 + 0.08214j$	$-0.01545 - 0.00079j$

	$\mathcal{B}(\Gamma_7^v, \Gamma_8^{v1})$	$\mathcal{B}(\Gamma_7^v, \Gamma_8^{v2})$
C_8^d	$0.00039 - 0.00117j$	$-0.00096 - 0.00070j$
C_9^d	$0.00272 + 0.00090j$	$-0.00280 + 0.00384j$
C_{10}^d	$-0.03069 + 0.09326j$	$-0.13829 - 0.10095j$

	$\mathcal{B}(\Gamma_7^v, \Gamma_8^m)$	$\mathcal{B}(\Gamma_7^v, \Gamma_8^c)$
C_8^d	$-0.01475 + 0.02717j$	$0.08938 + 0.02908j$
C_9^d	$-0.06796 - 0.03688j$	$0.00602 - 0.01850j$
C_{10}^d	$-0.05483 + 0.10103j$	$-0.11487 - 0.03737j$

	$\mathcal{B}(\Gamma_7^m, \Gamma_8^{v1})$	$\mathcal{B}(\Gamma_7^m, \Gamma_8^{v2})$
C_8^d	$-0.03485 + 0.02419j$	$-0.00500 - 0.01650j$
C_9^d	$0.02810 + 0.04050j$	$-0.06265 + 0.01897j$
C_{10}^d	$-0.07114 + 0.04937j$	$-0.01250 - 0.04129j$

	$\mathcal{B}(\Gamma_7^m, \Gamma_8^m)$	$\mathcal{B}(\Gamma_7^m, \Gamma_8^c)$
C_8^d	$0.25682 - 0.11697j$	$0.11600 + 0.16596j$
C_9^d	$-0.00009 - 0.00019j$	$-0.23577 + 0.16480j$
C_{10}^d	$-0.20194 + 0.09197j$	$-0.04193 - 0.05999j$

	$\mathcal{B}(\Gamma_7^c, \Gamma_8^{v1})$	$\mathcal{B}(\Gamma_7^c, \Gamma_8^{v2})$
C_8^d	$-0.02450 - 0.04686j$	$0.05328 - 0.00910j$
C_9^d	$0.10802 - 0.05649j$	$-0.01634 - 0.09568j$
C_{10}^d	$0.05044 + 0.09647j$	$-0.00961 + 0.00164j$

	$\mathcal{B}(\Gamma_7^c, \Gamma_8^m)$	$\mathcal{B}(\Gamma_7^c, \Gamma_8^c)$
C_8^d	$-0.06033 - 0.19331j$	$-0.09941 + 0.05241j$
C_9^d	$-0.26218 + 0.08183j$	$-0.00437 - 0.00829j$
C_{10}^d	$0.02882 + 0.09235j$	$0.24092 - 0.12702j$

	$\mathcal{B}(\Gamma_8^{v_1}, \Gamma_8^{v_1})$	$\mathcal{B}(\Gamma_8^{v_2}, \Gamma_8^{v_1})$
C_{11}^d	-0.28902	$-0.00696 - 0.02152j$
C_{12}^d	$0.02918 - 0.02918j$	$0.05393 + 0.02759j$
C_{13}^d	0	$-0.00655 + 0.00212j$
C_{14}^d	$-0.00148 + 0.00148j$	$-0.00064 - 0.00033j$
C_{15}^d	0.18072	$-0.01765 - 0.05462j$
C_{16}^d	0	$-0.03641 + 0.07119j$

	$\mathcal{B}(\Gamma_8^m, \Gamma_8^{v_1})$	$\mathcal{B}(\Gamma_8^c, \Gamma_8^{v_1})$
C_{11}^d	$0.13348 - 0.02419j$	$0.00012 - 0.03541j$
C_{12}^d	$-0.01469 + 0.02119j$	$-0.02594 - 0.02611j$
C_{13}^d	$-0.01220 - 0.06732j$	$0.03234 + 0.00011j$
C_{14}^d	$-0.00593 + 0.00856j$	$-0.05535 - 0.05573j$
C_{15}^d	$0.06877 - 0.01246j$	$0.00014 - 0.03990j$
C_{16}^d	$0.01221 + 0.00846j$	$0.02512 - 0.02495j$

	$\mathcal{B}(\Gamma_8^{v_2}, \Gamma_8^{v_2})$	$\mathcal{B}(\Gamma_8^m, \Gamma_8^{v_2})$
C_{11}^d	-0.30823	$-0.01543 + 0.11501j$
C_{12}^d	$0.05971 - 0.05971j$	$-0.01187 - 0.01555j$
C_{13}^d	0	$0.02416 + 0.00324j$
C_{14}^d	$0.00399 - 0.00399j$	$0.01190 + 0.01558j$
C_{15}^d	-0.01283	$-0.01215 + 0.09055j$
C_{16}^d	0	$0.00727 - 0.00555j$

	$\mathcal{B}(\Gamma_8^c, \Gamma_8^{v_2})$	$\mathcal{B}(\Gamma_8^m, \Gamma_8^m)$
C_{11}^d	$0.02899 + 0.00948j$	-0.32179
C_{12}^d	$0.03694 - 0.01874j$	$0.14004 - 0.14004j$
C_{13}^d	$0.03764 - 0.11510j$	0
C_{14}^d	$-0.09818 + 0.04980j$	$-0.00658 + 0.00658j$
C_{15}^d	$0.12964 + 0.04239j$	0.22602
C_{16}^d	$-0.02793 - 0.05507j$	0

	$\mathcal{B}(\Gamma_8^c, \Gamma_8^m)$	$\mathcal{B}(\Gamma_8^c, \Gamma_8^c)$
C_{11}^d	$-0.02317 + 0.12545j$	-0.57103
C_{12}^d	$-0.08829 - 0.12830j$	$-0.06365 + 0.06365j$
C_{13}^d	$0.28896 + 0.05338j$	0
C_{14}^d	$-0.00592 - 0.00860j$	$-0.00004 + 0.00004j$
C_{15}^d	$0.01451 - 0.07853j$	-0.30114
C_{16}^d	$0.01504 - 0.01035j$	0

E. Standard 4×4 + GW

	E[eV]	E[Hartree]
Γ_4^m	0.0	0.0
Γ_1^m	1.76931	0.06502

	$\mathcal{B}(\Gamma_1^m, \Gamma_1^m)$
C_1	0.02705

	$\mathcal{B}(\Gamma_1^m, \Gamma_4^m)$
C_3	$0.29213 + 0.28073j$
C_4	$0.16975 - 0.17664j$

	$\mathcal{B}(\Gamma_4^m, \Gamma_4^m)$
C_{15}	0
C_{16}	-0.47738
C_{17}	0.11355
C_{18}	-0.84096

F. Extended 13×13 + GW

	E[eV]	E[Hartree]
Γ_4^v	-8.14820	-0.29944
Γ_3^v	-7.83478	-0.28792
Γ_4^m	0.0	0.0
Γ_1^m	1.76931	0.06502
Γ_4^c	7.52506	0.27654
Γ_1^c	11.16596	0.41034

	$\mathcal{B}(\Gamma_1^m, \Gamma_1^m)$	$\mathcal{B}(\Gamma_1^c, \Gamma_1^c)$	$\mathcal{B}(\Gamma_1^c, \Gamma_1^m)$
C_1	0.01567	0.01478	$-0.00646 - 0.03643j$

	$\mathcal{B}(\Gamma_1^c, \Gamma_3^v)$	$\mathcal{B}(\Gamma_1^m, \Gamma_3^v)$
C_2	$-0.13113 - 0.07971j$	$0.10078 - 0.11452j$

	$\mathcal{B}(\Gamma_1^m, \Gamma_4^v)$	$\mathcal{B}(\Gamma_1^m, \Gamma_4^m)$	$\mathcal{B}(\Gamma_1^m, \Gamma_4^c)$
C_3	$-0.16939 - 0.05120j$	$0.29213 + 0.28073j$	$-0.12171 + 0.03090j$
C_4	$-0.09967 + 0.32976j$	$-0.08734 + 0.09089j$	$-0.00172 - 0.00677j$

	$\mathcal{B}(\Gamma_1^c, \Gamma_4^v)$	$\mathcal{B}(\Gamma_1^c, \Gamma_4^m)$	$\mathcal{B}(\Gamma_1^c, \Gamma_4^c)$
C_3	$0.00690 - 0.05817j$	$0.00911 - 0.01361$	$0.23220 + 0.51426j$
C_4	$0.41786 + 0.04955j$	$0.12719 + 0.08516j$	$0.00359 - 0.00162j$

	$\mathcal{B}(\Gamma_3^v, \Gamma_3^v)$
C_9	-0.30827
C_{10}	0.14407

	$\mathcal{B}(\Gamma_3^v, \Gamma_4^v)$	$\mathcal{B}(\Gamma_3^v, \Gamma_4^m)$	$\mathcal{B}(\Gamma_3^v, \Gamma_4^c)$
C_{11}	$0.00272 + 0.00595j$	$0.00154 - 0.03508j$	$-0.19430 - 0.13307j$
C_{12}	$0.13632 - 0.06214j$	$0.04124 + 0.00183j$	$-0.06481 + 0.09462j$

	$\mathcal{B}(\Gamma_4^v, \Gamma_4^v)$	$\mathcal{B}(\Gamma_4^m, \Gamma_4^m)$	$\mathcal{B}(\Gamma_4^c, \Gamma_4^c)$
C_{15}	0	0	0
C_{16}	0.32363	0.36031	-0.51563
C_{17}	-0.00691	-0.16664	0.09072
C_{18}	-0.26036	-0.28849	-0.57456

	$\mathcal{B}(\Gamma_4^m, \Gamma_4^v)$	$\mathcal{B}(\Gamma_4^c, \Gamma_4^v)$	$\mathcal{B}(\Gamma_4^c, \Gamma_4^m)$
C_{15}	$0.05946 + 0.11647j$	$0.03891 - 0.06460j$	$0.42118 - 0.26210j$
C_{16}	$-0.15214 + 0.07767j$	$0.14989 + 0.09029j$	$-0.07498 - 0.12046j$
C_{17}	$-0.03336 + 0.01703j$	$-0.04548 - 0.02740j$	$0.07282 + 0.11701j$
C_{18}	$-0.15886 + 0.08110j$	$0.03496 + 0.02106j$	$0.05809 + 0.09335j$

G. Standard 8×8 + GW

	E[eV]	E[Hartree]
Γ_7^m	-0.35663	-0.01311
Γ_8^m	0.0	0.0
Γ_6^m	1.60110	0.05884

	$\mathcal{B}(\Gamma_6^m, \Gamma_6^m)$
C_1^d	0.04692

	$\mathcal{B}(\Gamma_7^m, \Gamma_7^m)$
C_2^d	-0.84410

	$\mathcal{B}(\Gamma_6^m, \Gamma_7^m)$
C_3^d	$-0.21822 + 0.04568j$
C_4^d	$0.02561 + 0.12234j$

	$\mathcal{B}(\Gamma_6^m, \Gamma_8^m)$
C_5^d	$0.01200 + 0.01638j$
C_6^d	$0.18927 - 0.13908j$
C_7^d	$-0.07907 - 0.10747j$

	$\mathcal{B}(\Gamma_7^m, \Gamma_8^m)$
C_8^d	$-0.14870 + 0.06776j$
C_9^d	$-0.00009 - 0.00019j$
C_{10}^d	$0.26240 - 0.11980j$

	$\mathcal{B}(\Gamma_8^m, \Gamma_8^m)$
C_{11}^d	-0.84342
C_{12}^d	$-0.09171 + 0.09171j$
C_{13}^d	0
C_{14}^d	$-0.00658 + 0.00658j$
C_{15}^d	-0.25600
C_{16}^d	$-0.00010 - 0.00003j$

H. Extended 26×26 + GW

	E[eV]	E[Hartree]
$\Gamma_8^{v_1}$	-8.57873	-0.31526
Γ_7^{v}	-7.80871	-0.28696
$\Gamma_8^{v_2}$	-7.52888	-0.27668
Γ_7^{m}	-0.35663	-0.01311
Γ_8^{m}	0.0	0.0
Γ_6^{m}	1.60110	0.05884
Γ_7^{c}	7.08839	0.26049
Γ_8^{c}	7.45201	0.27386
Γ_6^{c}	10.94474	0.40221

	$\mathcal{B}(\Gamma_6^m, \Gamma_6^m)$	$\mathcal{B}(\Gamma_6^c, \Gamma_6^m)$	$\mathcal{B}(\Gamma_6^c, \Gamma_6^c)$
C_1^d	0.01787	$0.02517 + 0.02968j$	0.01622

	$\mathcal{B}(\Gamma_7^v, \Gamma_7^v)$	$\mathcal{B}(\Gamma_7^m, \Gamma_7^v)$	$\mathcal{B}(\Gamma_7^c, \Gamma_7^v)$
C_2^d	-0.23320	$0.15446 + 0.11650j$	$0.02601 - 0.02676j$

	$\mathcal{B}(\Gamma_7^m, \Gamma_7^m)$	$\mathcal{B}(\Gamma_7^c, \Gamma_7^m)$	$\mathcal{B}(\Gamma_7^c, \Gamma_7^c)$
C_2^d	-0.31525	$-0.01412 + 0.11250j$	-0.52764

	$\mathcal{B}(\Gamma_6^m, \Gamma_7^v)$	$\mathcal{B}(\Gamma_6^m, \Gamma_7^m)$	$\mathcal{B}(\Gamma_6^m, \Gamma_7^c)$
C_3^d	$-0.10904 - 0.05132j$	$-0.21822 + 0.04568j$	$-0.02093 - 0.06086j$
C_4^d	$-0.07496 + 0.15929j$	$-0.01593 - 0.07609j$	$-0.00452 + 0.00155j$

	$\mathcal{B}(\Gamma_6^c, \Gamma_7^v)$	$\mathcal{B}(\Gamma_6^c, \Gamma_7^m)$	$\mathcal{B}(\Gamma_6^c, \Gamma_7^c)$
C_3^d	$0.00855 + 0.03169j$	$-0.01216 - 0.00946j$	$0.16439 - 0.27667j$
C_4^d	$-0.20847 + 0.05626j$	$0.06220 - 0.07998j$	$-0.01632 - 0.00970j$

	$\mathcal{B}(\Gamma_6^m, \Gamma_8^{v_1})$	$\mathcal{B}(\Gamma_6^m, \Gamma_8^{v_2})$
C_5^d	$-0.09464 - 0.08979j$	$-0.14089 + 0.07718j$
C_6^d	$0.04906 - 0.05184j$	$0.03470 + 0.06346j$
C_7^d	$-0.12041 - 0.11423j$	$0.09121 - 0.04970j$

	$\mathcal{B}(\Gamma_6^m, \Gamma_8^m)$	$\mathcal{B}(\Gamma_6^m, \Gamma_8^c)$
C_5^d	$-0.00692 - 0.00935j$	$-0.00540 + 0.00576j$
C_6^d	$0.18927 - 0.13908j$	$0.05385 + 0.05061j$
C_7^d	$0.03989 + 0.05442j$	$-0.00600 + 0.00639j$

	$\mathcal{B}(\Gamma_6^c, \Gamma_8^{v1})$	$\mathcal{B}(\Gamma_6^c, \Gamma_8^{v2})$
C_5^d	$0.00764 - 0.13736j$	$-0.14748 - 0.05656j$
C_6^d	$-0.02513 - 0.00137j$	$0.00701 - 0.01823j$
C_7^d	$0.01135 - 0.20448j$	$0.12410 + 0.04787j$

	$\mathcal{B}(\Gamma_6^c, \Gamma_8^m)$	$\mathcal{B}(\Gamma_6^c, \Gamma_8^c)$
C_5^d	$0.00272 - 0.01162j$	$-0.02515 - 0.00128j$
C_6^d	$0.00866 + 0.00206j$	$-0.01685 + 0.33051j$
C_7^d	$-0.01939 + 0.08107j$	$-0.01749 - 0.00090j$

	$\mathcal{B}(\Gamma_7^v, \Gamma_8^{v1})$	$\mathcal{B}(\Gamma_7^v, \Gamma_8^{v2})$
C_8^d	$-0.00414 + 0.01232j$	$-0.01149 - 0.00684j$
C_9^d	$0.00272 + 0.00090j$	$-0.00280 + 0.00384j$
C_{10}^d	$-0.03263 + 0.09720j$	$-0.13961 - 0.10233j$

	$\mathcal{B}(\Gamma_7^v, \Gamma_8^m)$	$\mathcal{B}(\Gamma_7^v, \Gamma_8^c)$
C_8^d	$-0.01982 + 0.03607j$	$0.08224 + 0.02674j$
C_9^d	$-0.06796 - 0.03688j$	$0.00602 - 0.01850j$
C_{10}^d	$-0.05602 + 0.10399j$	$-0.10628 - 0.03469j$

	$\mathcal{B}(\Gamma_7^m, \Gamma_8^{v1})$	$\mathcal{B}(\Gamma_7^m, \Gamma_8^{v2})$
C_8^d	$-0.03271 + 0.02272j$	$-0.00680 - 0.02378j$
C_9^d	$0.02810 + 0.04050j$	$-0.06265 + 0.01897j$
C_{10}^d	$-0.06765 + 0.04739j$	$-0.01399 - 0.04525j$

	$\mathcal{B}(\Gamma_7^m, \Gamma_8^m)$	$\mathcal{B}(\Gamma_7^m, \Gamma_8^c)$
C_8^d	$0.20749 - 0.09443j$	$0.10528 + 0.15070j$
C_9^d	$-0.00009 - 0.00019j$	$-0.23577 + 0.16480j$
C_{10}^d	$-0.18687 + 0.08485j$	$-0.03553 - 0.05067j$

	$\mathcal{B}(\Gamma_7^c, \Gamma_8^{v1})$	$\mathcal{B}(\Gamma_7^c, \Gamma_8^{v2})$
C_8^d	$-0.02363 - 0.04506j$	$0.04854 - 0.00825j$
C_9^d	$0.10802 - 0.05649j$	$-0.01634 - 0.09568j$
C_{10}^d	$0.05062 + 0.09761j$	$-0.00680 + 0.00146j$

	$\mathcal{B}(\Gamma_7^c, \Gamma_8^m)$	$\mathcal{B}(\Gamma_7^c, \Gamma_8^c)$
C_8^d	$-0.05385 - 0.17267j$	$-0.12004 + 0.06312j$
C_9^d	$-0.26218 + 0.08183j$	$-0.00437 - 0.00829j$
C_{10}^d	$0.02444 + 0.07796j$	$0.25733 - 0.13537j$

	$\mathcal{B}(\Gamma_8^{v_1}, \Gamma_8^{v_1})$	$\mathcal{B}(\Gamma_8^{v_2}, \Gamma_8^{v_1})$
C_{11}^d	-0.24713	$-0.00492 - 0.01847j$
C_{12}^d	$0.06463 - 0.06424j$	$0.05715 + 0.02905j$
C_{13}^d	0	$-0.00655 + 0.00212j$
C_{14}^d	$-0.00148 + 0.00148j$	$-0.00064 - 0.00033j$
C_{15}^d	0.25098	$-0.01534 - 0.04886j$
C_{16}^d	$0.00006 + 0.00049j$	$-0.02898 + 0.05775j$

	$\mathcal{B}(\Gamma_8^m, \Gamma_8^{v_1})$	$\mathcal{B}(\Gamma_8^c, \Gamma_8^{v_1})$
C_{11}^d	$0.12348 - 0.02266j$	$0.00007 - 0.03685j$
C_{12}^d	$-0.01977 + 0.02825j$	$-0.02563 - 0.02567j$
C_{13}^d	$-0.01220 - 0.06732j$	$0.03234 + 0.00011j$
C_{14}^d	$-0.00593 + 0.00856j$	$-0.05535 - 0.05573j$
C_{15}^d	$0.05326 - 0.00974j$	$0.00011 - 0.04091j$
C_{16}^d	$0.00987 + 0.00652j$	$0.02545 - 0.02532j$

	$\mathcal{B}(\Gamma_8^{v_2}, \Gamma_8^{v_2})$	$\mathcal{B}(\Gamma_8^m, \Gamma_8^{v_2})$
C_{11}^d	-0.28674	$-0.01600 + 0.11728j$
C_{12}^d	$0.05141 - 0.05145j$	$-0.01350 - 0.01758j$
C_{13}^d	0	$0.02416 + 0.00324j$
C_{14}^d	$0.00399 - 0.00399j$	$0.01190 + 0.01558j$
C_{15}^d	-0.00501	$-0.01246 + 0.09213j$
C_{16}^d	$-0.00043 - 0.00053j$	$0.00590 - 0.00469j$

	$\mathcal{B}(\Gamma_8^c, \Gamma_8^{v_2})$	$\mathcal{B}(\Gamma_8^m, \Gamma_8^m)$
C_{11}^d	$0.02620 + 0.00864j$	-0.27831
C_{12}^d	$0.03349 - 0.01703j$	$0.11463 - 0.11460j$
C_{13}^d	$0.03764 - 0.11510j$	0
C_{14}^d	$-0.09818 + 0.04980j$	$-0.00658 + 0.00658j$
C_{15}^d	$0.12014 + 0.03925j$	0.21144
C_{16}^d	$-0.02627 - 0.05172j$	$-0.00010 - 0.00003j$

	$\mathcal{B}(\Gamma_8^c, \Gamma_8^m)$	$\mathcal{B}(\Gamma_8^c, \Gamma_8^c)$
C_{11}^d	$-0.02085 + 0.11282j$	-0.59150
C_{12}^d	$-0.08063 - 0.11724j$	$-0.07212 + 0.07314j$
C_{13}^d	$0.28896 + 0.05338j$	0
C_{14}^d	$-0.00592 - 0.00860j$	$-0.00004 + 0.00004j$
C_{15}^d	$0.01242 - 0.06655j$	-0.32318
C_{16}^d	$0.01612 - 0.01110j$	$-0.00006 - 0.00004j$

IV. REFERENCES

[1] L. Elcoro, B. Bradlyn, Z. Wang, M. G. Vergniory, J. Cano, C. Felser, B. A. Bernevig, D. Orobengoa, G. de la Flor, and M. I. Aroyo, Double crystallographic groups and their representations on the Bilbao Crystallographic Server, J. Appl. Crystallogr. **50**, 1457 (2017).

[2] M. S. Dresselhaus, G. Dresselhaus, and A. Jorio, *Group Theory: Application to the Physics of Condensed Matter* (Springer-Verlag Berlin Heidelberg, 2008).

[3] L. C. Lew Yan Voon and M. Willatzen, *The k·p Method: Electronic Properties of Semiconductors* (Springer-Verlag Berlin Heidelberg, 2009).

[4] M. H. Weiler, R. L. Aggarwal, and B. Lax, Warping- and inversion-asymmetry-induced cyclotron-harmonic transitions in InSb, Phys. Rev. B **17**, 3269 (1978).

THE JOURNAL OF PHYSICAL CHEMISTRY C
A JOURNAL OF THE AMERICAN CHEMICAL SOCIETY

pubs.acs.org/JPCC

Article

Electronic Properties of Silver–Bismuth Iodide Rudorffite Nanoplatelets

Danijela Danilović, Aleksandar R. Milosavljević,* Pitambar Sapkota, Radovan Dojčilović, Dragana Tošić, Nenad Vukmirović, Milan Jocić, Vladimir Djoković, Sylwia Ptasinska, and Dušan K. Božanić*

Cite This: J. Phys. Chem. C 2022, 126, 13739–13747

Read Online

ACCESS | Metrics & More | Article Recommendations | Supporting Information

ABSTRACT: Silver–bismuth iodide (Ag–Bi–I) rudorffites are chemically stable and non-toxic materials that can act as a possible lead-free replacement for methylammonium lead halides in optoelectronic applications. We report on a simple route for fabricating Ag–Bi–I colloidal nanoplatelets approximately 160 nm in lateral dimensions and 1–8 nm in thickness via exfoliation of Ag–Bi–I rudorffite powders in acetonitrile. The valence band electronic structure of isolated Ag–Bi–I nanoplatelets was investigated using synchrotron radiation to perform X-ray aerosol photoelectron spectroscopy (XAPS). The ionization energy of the material was found to be 6.1 ± 0.2 eV with respect to the vacuum level. UV–vis absorption and photoluminescence spectroscopies of the Ag–Bi–I colloids showed that the optical properties of the nanoplatelets originate from I 5p to Bi 6p and I 5p to I 5p transitions, which is further confirmed by density functional theory (DFT) calculations. Finally, calculations based on the DFT and $\mathbf{k}\cdot\mathbf{p}$ theoretical methods showed that the quantum confinement effect is very weak in the system studied.

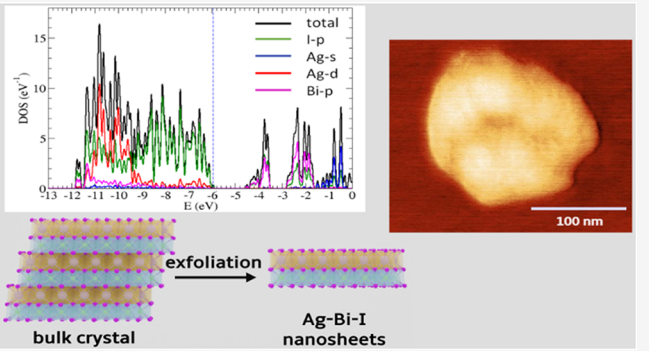

INTRODUCTION

Hybrid perovskite materials have attracted extensive research interest in recent years as they exhibit optical and semiconducting properties favorable for the fabrication of optoelectronic devices such as solar cells, light-emitting diodes, and photodetectors.[1−5] Among them, lead-based halide perovskites are the most studied systems since their application as absorbers in solar cells has resulted in the highest value of power conversion efficiency (PCE) of 25%.[6,7] The exceptional performance of this type of material arises from its large absorption coefficient, low effective masses, and high mobility of charge carriers. It has been proposed that these properties originate mainly from the partially oxidized Pb^{2+} state with $6s^26p^0$ configuration.[8] However, lead-based perovskite materials are unstable and easily degrade after exposure to high temperatures, electromagnetic radiation, moisture, and oxygen.[9−12] Our previous study also showed that low-energy electrons can affect the structural and chemical properties of methylammonium lead iodide ($MAPbI_3$).[13] Furthermore, lead toxicity is a serious predicament for large-scale applications.[14] Thus, continuous research efforts are seeking to develop more stable and less toxic perovskite materials.

Transition metal cations, such as Bi^{3+}, Sn^{2+}, Ge^{2+}, and Sb^{3+}, also have stable, partially oxidized states, with the same ns^2np^0 configuration as the lead ion. Consequently, these elements could act as suitable replacements for lead in emergent solar cell absorber materials. Compared to tin-, germanium-, and antimony-based materials, bismuth-based halide perovskites appear to be the most chemically stable and the least toxic. Incorporating an Ag^+ or Cu^+ cation in the bismuth–halide lattice can lead to the formation of a new type of material with edge-shared $[AX_6]$ and $[BiX_6]$ octahedra (A = Ag, Cu, X = I, Br) named rudorffites.[15] These metal halides may appear in many compositions that vary depending on the number of occupied sites in the cation sublattice. Several methods for fabricating silver–bismuth iodide (Ag–Bi–I) have been proposed.[15−22] Most of these procedures were oriented toward the synthesis of bulk material. For example, Ag–Bi–I powders were produced by heating a mixture of the precursor powders at temperatures above 600 °C under vacuum,[15,18,23] while the thin films can be fabricated via spin-coating or dynamic hot-casting of precursor solutions in organic solvents.[16,21,24−26] In our previous study, we fabricated Ag_3BiI_6 spherical nanoparticles in the form of aerosols and investigated their

Received: May 9, 2022
Revised: July 28, 2022
Published: August 9, 2022

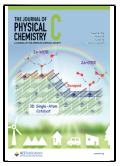

https://doi.org/10.1021/acs.jpcc.2c03208
J. Phys. Chem. C 2022, 126, 13739–13747

electronic properties via synchrotron radiation X-ray aerosol photoelectron spectroscopy (XASP).[27]

The band structure of 2D perovskite materials may depend on the size of the particles and structural modification induced by various factors.[28−37] For example, Kanatzidis and co-workers[28] used organic spacer cations to create separation between adjacent layers in Ag−Bi−I particles. It was shown that the optical properties depended on the type of spacer cations used, i.e., the changes in the distances between the layers. Also, previous studies on layered semiconducting colloidal nanoparticles showed a strong effect of size reduction on their optical properties due to the confinement effect,[38−41] which initiated the same type of research in layered perovskite nanomaterials. It was observed that Pb- and Sn-based nanoplatelets also display a strong quantum confinement effect with optical properties that depend on the particle thickness, i.e., the number of layers.[29−33] Conversely, in the most-studied 2D lead-free systems Cs_2AgBiX_6 (X = Cl, Br, or I), the quantum confinement is rather weak.[34,36,42] Pal et al.[37] also showed that $Rb_3Bi_2I_9$ 2D colloidal nanoparticles have the same band structure characteristics as their bulk counterparts.

In this work, we present a simple method for the preparation of colloidal 2D layered Ag−Bi−I rudorffite nanostructures based on the exfoliation of Ag−Bi−I powders. The study focused on the optical properties and valence band electronic structure of the resulting nanoplatelets. The valence band structure of isolated Ag−Bi−I nanoplatelets was studied using synchrotron radiation XASP. Obtained electronic spectra were discussed and interpreted with the results from density functional theory calculations.

EXPERIMENTAL SECTION

Materials. Bismuth(III) iodide (BiI_3, purity: 99%), silver iodide (AgI, purity: 99%), and sodium citrate tribasic dihydrate ($C_6H_5Na_3O_7{\cdot}2H_2O$) were purchased from Sigma Aldrich and used as received. Dimethyl sulfoxide (DMSO) and acetonitrile were used as solvents.

Synthesis. Ag−Bi−I nanopowder was prepared from 234 mg of AgI and 295 mg of BiI_3 powders (molar ratio of AgI/BiI_3 = 2:1) mixed and ground with a mortar until the mixture became light gray. The resulting powder was dissolved in 50 mL of DMSO (0.01 M). Subsequently, 10 mL of sodium citrate (0.3 M DMSO solution) was added to the solution as a stabilizing agent. The solution was stirred for 15 min, cast in a Petri dish, and heated to 120 °C in a vacuum oven to evaporate the solvent. The prepared nanopowders were characterized either in the dry state or dispersed in acetonitrile (0.6 mg/mL) to obtain the colloids. Photographs of the Ag−Bi−I powder and the Ag−Bi−I colloid are shown in Supporting Information Figure S1. For comparison with Ag−Bi−I, BiI_3 nanopowders and colloids were fabricated using the same procedure.

Characterization. X-ray diffraction (XRD) measurements of the samples deposited on an oriented Si wafer were performed using a Rigaku SmartLab system using Cu K_α radiation (1.5406 Å, 30 mA, 40 kV) and operated in the 2θ range from 10 to 50°.

Scanning electron microscopy (SEM) analyses of powdered samples were performed with a JEOL JSM-6390 LV instrument using a 30 kV acceleration voltage. Before analysis, the samples were deposited onto an adhesive carbon tape and coated with a thin gold layer. Transmission electron microscopy (TEM) was carried out with a JEOL JEM-1400 operating at 120 kV. For the analyses, the colloidal samples were deposited onto a carbon-coated copper grid with 300 mesh and dried in vacuum.

Surface topography investigations were performed using a Quesant atomic force microscope (AFM). Colloids were deposited on freshly cleaved mica substrates by spin-coating (3500 rpm, 1 min) and investigated immediately. Measurements were made in AFM tapping mode at room temperature, using standard silicon probes Q-WM300 (force constant 40 N/m).

The UV−vis diffuse reflectance and absorption spectra of the nanopowders and dispersed colloid samples were measured with a Shimadzu UV-2600 (Shimadzu Corporation, Japan) spectrophotometer equipped with an integrating sphere (ISR-2600 Plus) over the 220−800 nm range. Photoluminescence spectra (PL) of the colloidal samples were recorded with a PerkinElmer LS45 fluorescence spectrophotometer.

Surface X-ray photoelectron spectroscopy (XPS) measurements were carried out on an ambient pressure SPECS Surface Nano Analysis GmbH X-ray photoelectron spectrometer with a monochromatic Al K_α X-ray source (1486.6 eV). For the analysis, the acetonitrile dispersions were deposited onto a glass substrate following the procedure described in the literature by Sansom et al.[23] High-resolution spectra were recorded with a pass energy of 20 eV, which gave a full width at half-maximum of ∼0.5 eV for the Au $4f_{7/2}$ peak. The binding energy was calibrated with respect to the Fermi level by adjusting the position of the adventitious C 1s peak to 284.8 eV.[23]

X-ray aerosol photoelectron spectroscopy (XAPS) was performed at the PLEIADES beamline of the SOLEIL synchrotron using the Multi-Purpose Source Chamber (MPSC) and the Scienta hemispherical electron analyzer. A detailed description of the experimental setup is provided in our previous study.[27] For these measurements, the Ag−Bi−I aerosols were generated from acetonitrile dispersions of Ag−Bi−I nanoparticles using a TSI 3076 atomizer. Carried by 2.5 bar of Ar gas, the aerosols were transported through a metallic tube, heated to a temperature of ∼80 °C, and then cooled to 0 °C via a cold trap to remove excess acetonitrile. Subsequently, the free aerosols were introduced through a pressure-limiting orifice (250 μm in diameter) into an aerodynamic lens system and placed inside the differentially pumped stage of the MPSC. The aerodynamic lens focused the nanoparticle beam into the high-vacuum interaction region of the photoelectron spectrometer through a skimmer (1.5 mm diameter). The particle beam was ionized with 100 eV monochromatic synchrotron radiation. Gas-phase XPS spectra were recorded using a wide-angle-lens VG-Scienta R4000 electron energy analyzer. The overall resolution of the valence electron spectra was about 170 meV. Spectra were calibrated relative to the vacuum level using the binding energy of $3p_{3/2}$ Ar carrier gas at 15.76 eV[1,43] with an overall uncertainty of less than 0.2 eV.

Calculation Methods. *Density Functional Theory Calculations with the PBE Functional.* Density functional theory (DFT) calculations were performed by modeling the exchange-correlation functional using the Perdew−Burke−Ernzerhof (PBE) generalized gradient approximation (GGA).[44] Norm-conserving fully relativistic pseudopotentials[45,46] were used to model the effect of core electrons, and the effects of spin-orbit interaction were fully included. A Quantum Espresso code,[47,48] which is based on the representation of wave functions in the basis of plane waves,

https://doi.org/10.1021/acs.jpcc.2c03208
J. Phys. Chem. C 2022, 126, 13739−13747

was used to perform these calculations. The kinetic energy cutoff for the plane-wave representation of wave functions was 50 Ry. Relaxation of lattice parameters and atomic coordinates were performed until the atomic forces were smaller than 10^{-3} Ry/bohr.

Density Functional Theory Calculation with the Hybrid PBE0 Functional. Since local and semilocal functionals in DFT (such as the PBE functional) do not result in accurate values of the band gap,[49] we also performed the calculation of bulk band structure using the hybrid PBE0 functional.[50,51] This functional modeled the correlation energy as the PBE correlation energy, while the exchange energy was modeled as the sum of three-fourths of the PBE exchange energy and one-fourth of the Hartree−Fock exchange energy. It is known that the calculations with this functional yield band gap values that correlate significantly better with experimental band gaps of semiconducting materials than those carried out with the PBE functional (see for example refs 52 and 53). However, calculations based on the PBE0 functional are computationally significantly more demanding since they also request calculations of the Hartree−Fock exchange energy. For this reason, we used this functional only to perform bulk band structure calculations of a given bulk atomic structure. The calculation was performed using the Quantum Espresso code, where the adaptively compressed exchange operator approach for calculating exchange energy[54] is implemented.

***k · p* Calculations of the Electronic Structure.** To calculate larger nanoplatelets (quantum wells), we constructed the **k · p** Hamiltonian following the approach presented in ref 55, where its parameters are determined by ab initio calculations (using either DFT/PBE or the hybrid PBE0 functional methods) of bulk material. **k·p** calculations are numerically very cheap and can therefore easily be applied to larger nanoplatelets for which DFT/PBE calculation is computationally very demanding and hybrid functional calculation is practically impossible to perform. Additional details related to **k·p** calculations are presented in the Supporting Information.

Determination of Absolute Positions of Bulk Energy Levels with Respect to Vacuum. DFT calculations with plane-wave basis and periodic boundary conditions do not yield the absolute value of the position of the energy levels with respect to vacuum. These positions were determined by performing the calculation of the interface of the material slab with vacuum as described in more detail in the Supporting Information. All the energies that we subsequently report are with vacuum as the zero energy.

RESULTS AND DISCUSSION

Characterization of the Ag−Bi−I Nanoplatelets. The results of the X-ray diffraction measurements of the Ag−Bi−I powders are presented in Figure 1a. The XRD pattern of the sample shows diffraction maxima at 2θ angles of 12.7, 23.9, 25.1, 25.6, 29.2, 32.0, 41.4, 42.2, and 43.5°, which correspond to the $CdCl_2$-type rhombohedral structure of a silver-rich Ag−Bi−I rudorffite system.[15,19,56] In addition, low-intensity peaks at 22.3, 23.7, 39.2, and 46.3° indicate a small contribution of the γ-AgI phase.[20] Similar diffraction patterns were observed in various other types of Ag−Bi−I structures, for example, Ag_3BiI_6 nanoparticles produced in the gas phase from iodide precursors,[27] Ag−Bi−I nanoparticles fabricated from nitrate salts,[57] Ag−Bi−I thin films produced by the dynamic hot-casting method,[21] and Ag−Bi−I thin films produced on a TiO_2/FTO/glass substrate.[58] The appearance of the AgI phase

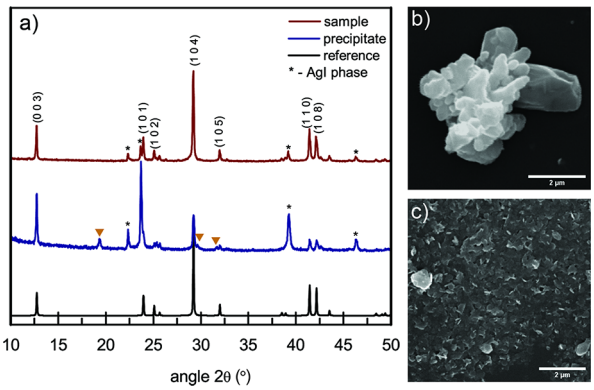

Figure 1. (a) XRD patterns of Ag−Bi−I powder (red line) and the precipitate sample obtained by drying Ag−Bi−I acetonitrile dispersion under ambient conditions (blue line). The black line represents the Ag_3BiI_6 reference pattern.[56] The asterisks and triangles mark the 2θ angles corresponding to the diffraction maxima of the AgI phase[20] and the BiOI phase,[58] respectively. SEM images of (b) Ag−Bi−I powder and (c) precipitate samples.

in the sample is expected since in the Ag-rich Ag−Bi−I solids, the excess of Ag ions are delocalized and occupy the sites between the $(Ag/Bi)I_6$ octahedral layers.[19] The XRD measurements were performed on a precipitate of the Ag−Bi−I sample in order to check its structure after dispersion in acetonitrile. This sample is prepared by drying the colloid in the dark under ambient conditions. The XRD pattern of the precipitate (Figure 1a, blue line) shows that in addition to the increase in the AgI content, the sample retained its Ag−Bi−I phase. Changes in morphology were also investigated by SEM, and the images of two samples are shown in Figure 1b,c. These analyses showed that exfoliation of Ag−Bi−I sheets upon dispersion in acetonitrile takes place, which is consistent with an increase in the intensity of (0 0 3) diffraction maximum relative to the (1 0 4) peak in the diffractogram of the precipitate. In addition, the presence of the bismuth oxyiodide (BiOI) phase in the diffraction pattern can be seen, resulting from drying the sample in air. This result indicates that oxidation occurs at the outmost layers of the exfoliated particles.

Further analyses of the size and morphology of the dispersed-phase Ag−Bi−I particles were carried out by transmission electron microscopy on the colloidal samples dried in a vacuum. Typical TEM images of the sample are presented in Supporting Information Figure S2. For comparison, the results for BiI_3 particles, prepared using the same procedure, are also given. The micrographs show that the Ag−Bi−I particles have a plate-like morphology with average lateral dimensions of ∼160 nm. A similar morphology was also observed for BiI_3 nanoparticles; however, their lateral dimensions were in the 40−60 nm range. The observed morphology is characteristic of binary metal iodides (such as BiI_3[41,59]) and occurs because of a relatively large difference in distance between cations in edge-sharing octahedra and the distance between cations in adjacent layers. In rudorffite $Ag_{2-3x}Bi_xI_2$ (x = 0.33−0.60) ternary halides, Ag and Bi ions occupy similar edge-sharing octahedral sites $(Ag/Bi)I_6$,[15,19] which results in the formation of the Ag−Bi−I nanoplatelets. The HRTEM/EDS mapping of Ag−Bi−I nanoplatelets (Supporting information Figure S2c) showed that the elements were uniformly distributed in the particles. The distribution of the thicknesses of the nanoplatelets was determined from their

https://doi.org/10.1021/acs.jpcc.2c03208
J. Phys. Chem. C 2022, 126, 13739−13747

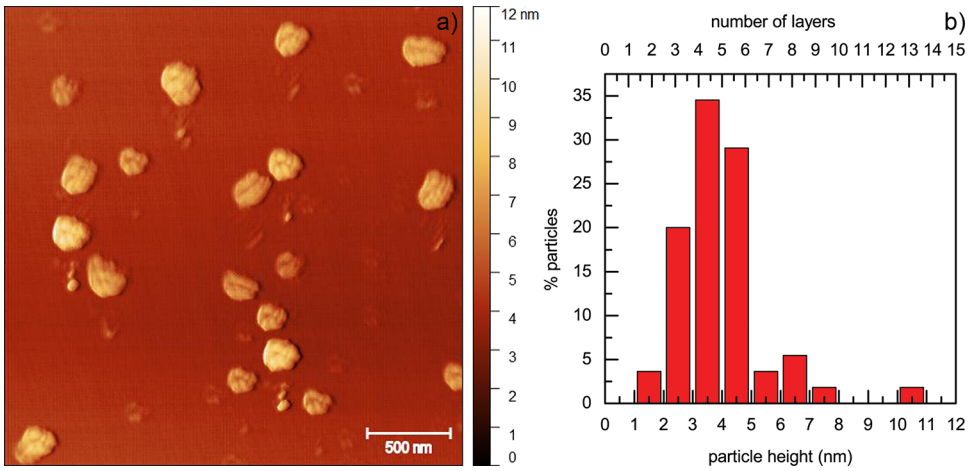

Figure 2. (a) AFM image of Ag−Bi−I nanoplatelets and (b) corresponding distribution of particles' heights. The number of Ag−Bi−I monolayers in the nanoplatelets was estimated assuming a monolayer thickness of 0.66 nm.

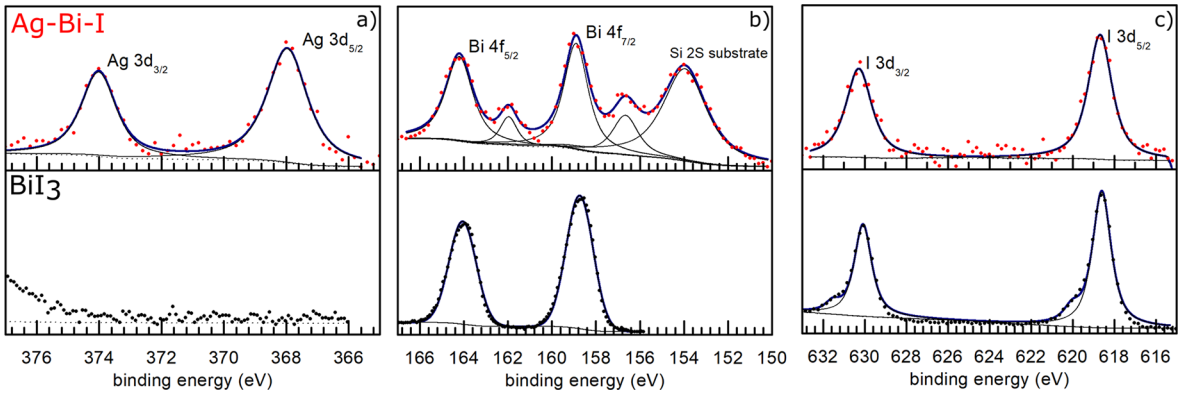

Figure 3. High-resolution XPS spectra of (a) Ag 3d, (b) Bi 4f, and (c) I 3d core levels of Ag−Bi−I (top) and BiI_3 (bottom) colloidal nanoplatelets.

height profiles obtained by AFM. The AFM image of the Ag−Bi−I sample and the particle height distribution are presented in Figure 2a,b, respectively, while the details of the height profile analyses are given in the Supporting Information (Figure S3). The average thickness of the nanoplatelets was found to be 3.9 ± 0.2 nm. Taking into account that the thickness of the monolayer is ~0.66 nm, the nanoplatelets, on average, have six layers.

The chemical environment of the ions in the Ag−Bi−I nanoplatelets was investigated by surface X-ray photoelectron spectroscopy. High-resolution XPS spectra of the Ag 3d, Bi 4f, and I 3d core levels of the Ag−Bi−I nanoplatelets are presented in Figure 3. The survey scan of the sample is given in Supporting Information Figure S4. For comparison, the results for the BiI_3 sample are also shown. For the Ag−Bi−I sample, Ag $3d_{3/2}$ and Ag $3d_{5/2}$ levels are observed at 374.0 and 368.0 eV, respectively (Figure 3a). These values match the binding energies obtained for Ag 3d levels in AgI.[60] For Bi, 4f levels (Figure 3b) are assigned to peaks at 164.2 and 158.9 eV, corresponding to Bi $4f_{5/2}$ and Bi $4f_{7/2}$ levels. The spectrum shows additional peaks at lower binding energies that are not present for the BiI_3 sample. These features were previously reported for the Ag−Bi−I films prepared by thermal evaporation[61] as well as for the oriented BiI_3 single crystals in contact with Pd and Pt.[62] The peaks were assigned to bismuth ions that are not in a complete $6I^+$ coordination and therefore approach binding energies characteristic for metallic bismuth. The binding energies of I $3d_{3/2}$ and I $3d_{5/2}$ levels are observed at 630.3 and 618.7 eV (Figure 3c). It should be noticed that the I 3d levels in the Ag−Bi−I sample are slightly broader than in the BiI_3 sample, suggesting possible effects of changes in the chemical environment. The XPS results suggest that a redox solid-state reaction between Ag and BiI_3 is taking place in the system, resulting in the formation of Ag−Bi−I and AgI phases, as well as metallic Bi (which can proceed to the formation of BiOI in the presence of oxygen), noticed in the XRD pattern (Figure 1). A similar redox reaction was observed at the interfaces between Ag and Bi_2Se_3 single crystals.[63]

Electronic Properties of the Ag−Bi−I Nanoplatelets. To study the electronic properties of Ag−Bi−I nanoplatelets in the valence region, we used a similar approach as in our previous study of $MAPbBr_3$ nanoparticles.[1] Two complementary X-ray photoemission spectroscopy techniques were employed. For XPS measurements, the colloids were deposited onto a Si substrate. The XAPS measurements were carried out on isolated Ag−Bi−I particles, where synchrotron radiation was used as the X-ray source.

The photoemission spectrum of Ag−Bi−I nanoplatelets obtained by the XAPS technique is presented in Figure 4, while the corresponding spectrum of the BiI_3 sample is given in the Supporting Information (Figure S5a). Contrary to XPS measurements, where the band energies are referenced with respect to the Fermi level (E_F), all energies in the XAPS technique are measured with respect to the vacuum level (E_0).[1]

https://doi.org/10.1021/acs.jpcc.2c03208
J. Phys. Chem. C 2022, 126, 13739−13747

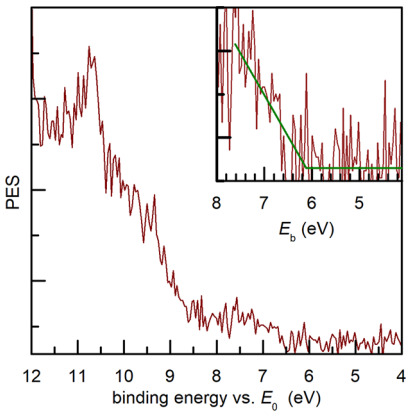

Figure 4. Valence region photoemission spectrum of Ag−Bi−I nanoplatelets measured by XAPS using 100 eV photon energy. The inset shows the zoom-in region around the ionization energy value.

The ionization energy of Ag−Bi−I nanoplatelets determined by XAPS is 6.1 ± 0.2 eV relative to E_0. This is in good agreement with the ionization energies reported for 3D Ag_3BiI_6 aerosol particles[27] and Ag_3BiI_6 thin films[58] as well as those reported for rhombohedral $Ag_{0.65}Bi_{0.45}I_2$ materials.[19] This indicates a negligible influence of the size and morphology of Ag−Bi−I particles on the position of the valence band maxima. The ionization energy is also in good agreement with our calculated value of −5.95 eV for the valence band maximum. The ionization energy obtained by surface XPS was 1.4 ± 0.2 eV relative to E_F (Supporting Information Figure S5b). By comparing the values of the ionization energies obtained by these two techniques, the estimated value of the work function (ϕ) of Ag−Bi−I nanoplatelets was found to be 4.7 eV. It should be noted, however, that in the XAPS of isolated nanoparticles, the near-surface vacuum level cannot be perfectly defined, which results in additional uncertainty in the determination of the ionization energy.[64,65]

The optical properties of the Ag−Bi−I powder and the colloidal dispersion in acetonitrile are presented in Figure 5. The diffuse reflectance spectrum of the Ag−Bi−I powder samples (dashed black line) displays an onset of absorption at 732 nm (~1.7 eV), which is a typical value for the band gap of Ag−Bi−I thin films and powder samples.[15,21,23] After exfoliation, the UV−vis absorption spectrum of the Ag−Bi−I

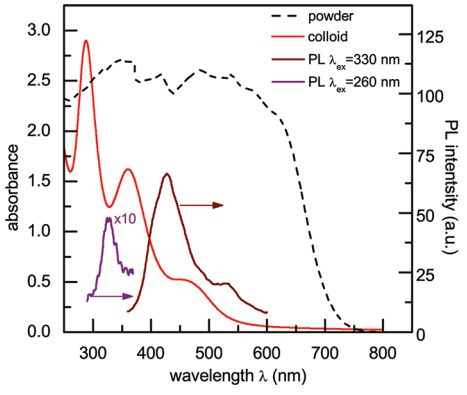

Figure 5. UV−vis absorption (red line) and photoluminescence (PL) (purple and brown lines) spectra of Ag−Bi−I nanoplatelets dispersed in acetonitrile and the diffuse reflectance spectrum of Ag−Bi−I powders (dashed black line).

colloid (solid red line) shows three bands at 288 nm (4.30 eV), 360 nm (3.44 eV), and 457 nm (2.71 eV). The bands in the spectra of the Ag−Bi−I colloid originate mainly from I 5p to Bi 6p and I 5p to I 5p transitions in $(BiI_6)^{3-}$ octahedra. It should be noted that the absorption spectra obtained for BiI_3 powder and its dispersion in acetonitrile are similar to those obtained for corresponding Ag−Bi−I samples (Supporting Information Figure S7). The absorption spectrum of the BiI_3 powder (Figure S7) exhibited a slightly lower band gap value, which is in accordance with the results presented in the literature.[61] On the other hand, the absorption spectrum of the BiI_3 dispersion has similar features as the spectrum of the Ag−Bi−I colloid, although the absorption peaks appear at slightly different energies. It seems that the changes induced by the additional element in the structure affect I 5p to Bi 6p and I 5p to I 5p transitions to a certain extent. A recent study by Kanatzidis et al.[28] may support this conclusion. They showed that the optical properties of 2D Ag−Bi−I layered materials significantly depend on both the distance between the layers and the arrangement and orientation of $(AgI_6)^{5-}$ and $(BiI_6)^{3-}$ octahedra.

Recently, Premkumar et al. synthesized Ag−Bi−I quantum dots and noticed that they exhibited blueshifted absorption with respect to the bulk material.[66] The observed shift is attributed to the size confinement effect. However, because the effective masses of the charge carriers in Ag−Bi−I material are relatively large,[58] it can be expected that the quantum confinement effects in the Ag−Bi−I nanoplatelets are relatively weak. Indeed, our calculations (see Figure 7 below) showed that the nanoplatelet band gap changes by only about 50 meV in the range of thicknesses from 2 to 5 nm. This suggests that the three peaks at 2.71, 3.44, and 4.30 eV are the internal transitions already present in the bulk sample as well, which become more pronounced after exfoliation. To check this, we made a rough calculation of the optical absorption for the bulk Ag−Bi−I (see Supporting Information Figure S6). The theoretical absorption curve in Figure S6 exhibits a similar trend as the experimental absorption spectrum of Ag−Bi−I colloid in the UV−vis range.

The photoluminescence spectra of the Ag−Bi−I nanoplatelets dispersed in acetonitrile, recorded with 260 nm (purple solid line) and 330 nm (brown solid line) excitations, are also presented in Figure 5. The emission bands at around 326, 430, and 530 nm are Stokes-shifted with respect to the band observed in the absorption spectrum. The excitation of the colloids by the light of different wavelengths did not affect the position of the emission bands (Supporting Information Figure S8). Notably, the emission at the photon energy of the band gap was not detected in either powder or colloid samples.

DFT was used to calculate the electronic structure of Ag−Bi−I nanoplatelets. The calculations of the electronic structure of the platelets with larger lateral dimensions were performed by the $\mathbf{k} \cdot \mathbf{p}$ method, and the Hamiltonian parameterization was carried out using the results obtained by the DFT. As a model for the atomic structure of the Ag−Bi−I material, we used the rhombohedral $AgBiI_4$ configuration. The details about its atomic structure, corresponding lattice parameters, and atomic positions are given in the Supporting Information.

The electronic band structure of bulk $AgBiI_4$ obtained from DFT/PBE calculations is presented in Figure 6a. A direct band gap can be observed at the Y_2 point in the Brillouin zone with a band gap energy of 0.33 eV was found. As expected, the DFT/PBE calculation yields a significantly lower value of the band

https://doi.org/10.1021/acs.jpcc.2c03208
J. Phys. Chem. C 2022, 126, 13739−13747

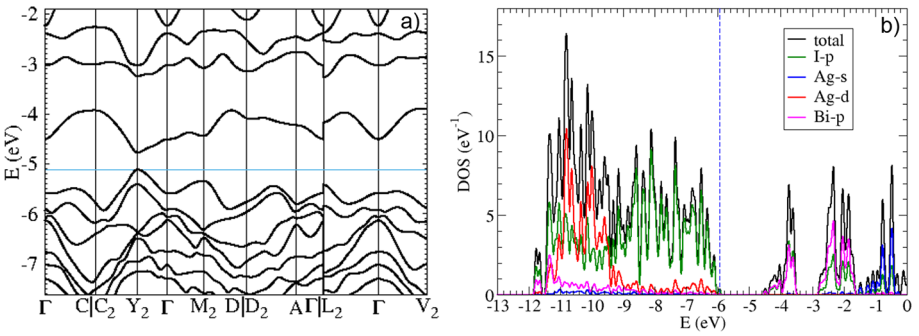

Figure 6. (a) Electronic band structure of $AgBiI_4$ obtained from DFT/PBE calculations. The blue horizontal line represents the valence band maximum energy. The choice of the path in the Brillouin zone was made using the SeeK-path tool.[67] (b) Density of electronic states (total density of states and orbital projected density of states) of $AgBiI_4$ obtained from hybrid PBE0 functional calculations. The vertical dashed line denotes the energy of the valence band maximum. The reported energy values in figures (a) and (b) are given with respect to the vacuum level.

gap than the energy value established in the experiment. For this reason, an additional approach was considered, and the calculation was performed using the hybrid PBE0 functional. In this calculation, the band gap energy of 1.3 eV was obtained, which is much closer to the experimental result of 1.7 eV. The calculated densities of electronic states are presented in Figure 6b. The results suggest that the highest states in the valence band (in the energy interval of ∼3 eV below the valence band maximum) originate from p-orbitals of the I atom, while the lowest states in the conduction band (in the energy interval of ∼2.5 eV above the conduction band minimum) originate from p-orbitals of the Bi and I atoms. This result is in agreement with the previous reports[23,28] and supports the claim that the optical transitions in Ag−Bi−I are dominated by I 5p to Bi 6p and by I 5p to I 5p transitions in the $(BiI_6)^{3-}$.

Since the lateral dimensions of the Ag−Bi−I nanoplatelets are much larger than vertical dimensions (Figure 2), they were modeled as quantum wells infinite in the *xy* plane with width *L* in the *z*-direction. The procedure for constructing their atomic structure is presented in the Supporting Information. Three different methods were employed to calculate the electronic structure of $AgBiI_4$ quantum wells: (i) DFT/PBE; (ii) $\mathbf{k}\cdot\mathbf{p}$ method with parameterization based on DFT/PBE calculations of bulk $AgBiI_4$; (iii) $\mathbf{k}\cdot\mathbf{p}$ calculations with parameterization based on hybrid PBE0 functional calculations of bulk $AgBiI_4$.

The results obtained by using method (i) are presented in the Supporting Information. This method cannot give accurate values of the band gap, but it is still useful for gaining insight into the overall role of quantum confinement effects. The results indicate that these effects are quite weak. In the range of well widths of 2 to 5 nm (corresponding to the range of the heights of the nanoplatelets that were observed), the band gap changes for about 50 meV only (see Figure S12 in the Supporting Information). The comparison of the band structures of quantum wells with different widths (Figures S13 and S14 in the Supporting Information) also suggests that the electronic structure is only weakly dependent on the well width. Therefore, within a reasonably good approximation, it follows that the electronic structure of the nanoplatelet is rather similar to the electronic structure of the bulk material.

The calculations using method (ii) were used to confirm that the $\mathbf{k}\cdot\mathbf{p}$ method is reliable for the calculation of electronic states in quantum wells. Details of this calculation are reported in the Supporting Information. The results suggest that $\mathbf{k}\cdot\mathbf{p}$ and DFT/PBE yield essentially the same results for well widths above 2 nm, which implies that $\mathbf{k}\cdot\mathbf{p}$ can be safely used then.

Finally, method (iii) was employed to calculate the band gap, conduction band minimum (CBM), and valence band maximum (VBM) of the quantum wells of various sizes. The results (Figure 7) indicate a rather weak dependence of

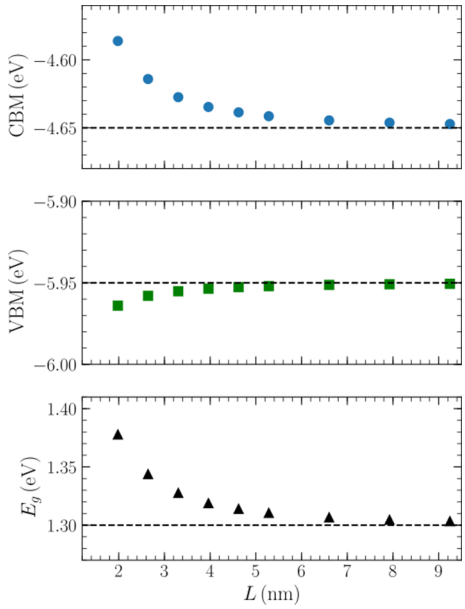

Figure 7. The dependence of CBM, VBM, and energy gap (E_g) on quantum well width. The results were obtained from the $\mathbf{k}\cdot\mathbf{p}$ Hamiltonian parameterized using the data from hybrid PBE0 functional calculations of bulk Ag−Bi−I. Horizontal dashed lines denote the bulk values.

electronic states energies on the well width, consistent with previous conclusions obtained by using less accurate methods. It was also estimated that the dielectric contrast between the nanoplatelet and the solvent does not affect the energy levels of the nanoplatelet to a significant extent (see the Supporting Information for details).

CONCLUSIONS

In summary, we report a simple procedure for the chemical exfoliation of sliver/bismuth iodide powders into Ag−Bi−I nanoplatelets dispersible in acetonitrile together with results of characterization and electronic structure determination.

https://doi.org/10.1021/acs.jpcc.2c03208
J. Phys. Chem. C 2022, 126, 13739−13747

The XRD results showed that the material prepared is composed of a rhombohedral Ag-rich rudorffite phase with minor traces of the γ-AgI phase. The results of the morphological characterization revealed that the material is in the form of layered two-dimensional nanoplatelets with lateral dimensions of ~160 nm and thicknesses in the 1−8 nm range, indicating that the prepared nanoplatelets consist of 1−10 Ag−Bi−I monolayers. XPS analyses of the Ag 3d, Bi 4f, and I 3d core levels suggested that the Ag−Bi−I rudorffite phase is being formed by a redox reaction between Ag and BiI_3, which also results in the formation of γ-AgI and metallic Bi phases. The valence band electronic structure of isolated Ag−Bi−I nanoplatelets was investigated by synchrotron radiation X-ray aerosol photoelectron spectroscopy. An ionization energy of 6.1 ± 0.2 eV was obtained with respect to the vacuum level. The value of the ionization energy was found to be 1.4 ± 0.2 eV with respect to the Fermi level by standard XPS. We therefore estimated the work function of Ag−Bi−I nanoplatelets to be 4.7 eV. The band gap value of Ag−Bi−I powder was estimated to be ~1.7 eV based on the diffuse reflectance spectrum. The UV−vis absorption spectroscopy of the Ag−Bi−I colloids showed that the optical properties of the nanoplatelets originate mainly from I 5p to Bi 6p and I 5p to I 5p transitions, which is further confirmed by DFT calculations. To interpret the electronic properties of the Ag−Bi−I nanoplatelets with larger lateral dimensions, we performed electronic structure calculations using the density functional theory and $\mathbf{k} \cdot \mathbf{p}$ methods. The DFT results showed weak dependence of the ionization energy and the band gap values of Ag−Bi−I nanoplatelets on their thickness.

This work demonstrates a simple and innovative route for the preparation of colloidal 2D layered Ag−Bi−I nanomaterials. In addition, the study offers a deeper insight into the understanding of the electronic structure of the Ag−Bi−I nanoplatelets, which were further correlated with the particle size.

■ ASSOCIATED CONTENT

Supporting Information

The Supporting Information is available free of charge at https://pubs.acs.org/doi/10.1021/acs.jpcc.2c03208.

Images of Ag−Bi−I powder and Ag−Bi−I dispersed in acetonitrile; results of TEM and EDS analyses; AFM images with AFM profile analysis of Ag−Bi−I nanoplatelets; XPS survey scan of Ag−Bi−I nanoplatelets; valence region XPS spectra of Ag−Bi−I and BiI_3 nanoparticles; comparison of calculations with experimental absorption spectra; absorption spectra of Ag−Bi−I and BiI_3 powders and their dispersion in acetonitrile; PL spectra of Ag−Bi−I dispersed in acetonitrile; details of DFT calculations (PDF)

■ AUTHOR INFORMATION

Corresponding Authors

Aleksandar R. Milosavljević − *Synchrotron SOLEIL, l'Orme des Merisiers, 91192 Gif sur Yvette Cedex, France;* orcid.org/0000-0003-3541-8872; Email: milosavljevic@synchrotron-soleil.fr

Dušan K. Božanić − *Department of Radiation Chemistry and Physics, "Vinča" Institute of Nuclear Sciences - National Institute of the Republic of Serbia and Center of Excellence for Photoconversion, "Vinča" Institute of Nuclear Sciences - National Institute of the Republic of Serbia, University of Belgrade, 11001 Belgrade, Serbia;* orcid.org/0000-0001-8246-9635; Email: bozanic@vin.bg.ac.rs

Authors

Danijela Danilović − *Department of Radiation Chemistry and Physics, "Vinča" Institute of Nuclear Sciences - National Institute of the Republic of Serbia and Center of Excellence for Photoconversion, "Vinča" Institute of Nuclear Sciences - National Institute of the Republic of Serbia, University of Belgrade, 11001 Belgrade, Serbia*

Pitambar Sapkota − *Radiation Laboratory, University of Notre Dame, Notre Dame, Indiana 46556, United States; Department of Physics, University of Notre Dame, Notre Dame, Indiana 46556, United States*

Radovan Dojčilović − *Department of Radiation Chemistry and Physics, "Vinča" Institute of Nuclear Sciences - National Institute of the Republic of Serbia and Center of Excellence for Photoconversion, "Vinča" Institute of Nuclear Sciences - National Institute of the Republic of Serbia, University of Belgrade, 11001 Belgrade, Serbia; Department of Experimental and Health Sciences, Pompeu Fabra University, 08003 Barcelona, Spain*

Dragana Tošić − *Department of Radiation Chemistry and Physics, "Vinča" Institute of Nuclear Sciences - National Institute of the Republic of Serbia, University of Belgrade, 11001 Belgrade, Serbia*

Nenad Vukmirović − *Institute of Physics Belgrade, University of Belgrade, 11080 Belgrade, Serbia;* orcid.org/0000-0002-4101-1713

Milan Jocić − *Institute of Physics Belgrade, University of Belgrade, 11080 Belgrade, Serbia*

Vladimir Djoković − *Department of Radiation Chemistry and Physics, "Vinča" Institute of Nuclear Sciences - National Institute of the Republic of Serbia and Center of Excellence for Photoconversion, "Vinča" Institute of Nuclear Sciences - National Institute of the Republic of Serbia, University of Belgrade, 11001 Belgrade, Serbia*

Sylwia Ptasinska − *Radiation Laboratory, University of Notre Dame, Notre Dame, Indiana 46556, United States; Department of Physics, University of Notre Dame, Notre Dame, Indiana 46556, United States;* orcid.org/0000-0002-7550-8189

Complete contact information is available at: https://pubs.acs.org/10.1021/acs.jpcc.2c03208

Notes

The authors declare no competing financial interest.

■ ACKNOWLEDGMENTS

The authors acknowledge funding from the Ministry of Education, Science, and Technological Development of the Republic of Serbia. The authors are grateful for the support of the entire staff of the Synchrotron SOLEIL for smooth operation during beamtime no. 20190421. Numerical simulations were performed on the PARADOX supercomputing facility at the Scientific Computing Laboratory, National Center of Excellence for the Study of Complex Systems, Institute of Physics Belgrade. P.S. and S.P. acknowledge the US Department of Energy Office of Science, Office of Basic Energy Sciences under award number DE-FC02-04ER15533 (NDRL no. 5356).

REFERENCES

(1) Milosavljević, A. R.; Božanić, D. K.; Sadhu, S.; Vukmirović, N.; Dojčilović, R.; Sapkota, P.; Huang, W.; Bozek, J.; Nicolas, C.; Nahon, L.; et al. Electronic Properties of Free-Standing Surfactant-Capped Lead Halide Perovskite Nanocrystals Isolated in Vacuo. *J. Phys. Chem. Lett.* **2018**, *9*, 3604−3611.

(2) Mei, A.; Li, X.; Liu, L.; Ku, Z.; Liu, T.; Rong, Y.; Xu, M.; Hu, M.; Chen, J.; Yang, Y.; et al. A Hole-Conductor−Free, Fully Printable Mesoscopic Perovskite Solar Cell with High Stability. *Science* **2014**, *345*, 295−298.

(3) Leung, S.-F.; Ho, K.-T.; Kung, P.-K.; Hsiao, V. K. S.; Alshareef, H. N.; Wang, Z. L.; He, J.-H. A Self-Powered and Flexible Organometallic Halide Perovskite Photodetector with Very High Detectivity. *Adv. Mater.* **2018**, *30*, 1704611.

(4) Chen, Q.; de Marco, N.; Yang, Y. M.; Song, T.-B.; Chen, C.-C.; Zhao, H.; Hong, Z.; Zhou, H.; Yang, Y. Under the Spotlight: The Organic-Inorganic Hybrid Halide Perovskite for Optoelectronic Applications. *Nano Today* **2015**, *10*, 355−396.

(5) Yuan, M.; Quan, L. N.; Comin, R.; Walters, G.; Sabatini, R.; Voznyy, O.; Hoogland, S.; Zhao, Y.; Beauregard, E. M.; Kanjanaboos, P.; et al. Perovskite Energy Funnels for Efficient Light-Emitting Diodes. *Nat. Nanotechnol.* **2016**, *11*, 872−877.

(6) Yang, W. S.; Park, B.-W.; Jung, E. H.; Jeon, N. J.; Kim, Y. C.; Lee, D. U.; Shin, S. S.; Seo, J.; Kim, E. K.; Noh, J. H.; Seok, S. I. Iodide Management in Formamidinium-Lead-Halide−Based Perovskite Layers for Efficient Solar Cells. *Science* **2017**, *356*, 1376−1379.

(7) NREL. Best Research-Cell Efficiency Chart. https://www.nrel.gov/pv/cell-efficiency.html (accessedFebruary 2, 2022).

(8) Brandt, R. E.; Stevanović, V.; Ginley, D. S.; Buonassisi, T. Identifying Defect-Tolerant Semiconductors with High Minority-Carrier Lifetimes: Beyond Hybrid Lead Halide Perovskites. *MRS Commun.* **2015**, *5*, 265−275.

(9) Aristidou, N.; Sanchez-Molina, I.; Chotchuangchutchaval, T.; Brown, M.; Martinez, L.; Rath, T.; Haque, S. A. The Role of Oxygen in the Degradation of Methylammonium Lead Trihalide Perovskite Photoactive Layers. *Am. Ethnol.* **2015**, *127*, 8326−8330.

(10) Habisreutinger, S. N.; Leijtens, T.; Eperon, G. E.; Stranks, S. D.; Nicholas, R. J.; Snaith, H. J. Carbon Nanotube/Polymer Composites as a Highly Stable Hole Collection Layer in Perovskite Solar Cells. *Nano Lett.* **2014**, *14*, 5561−5568.

(11) Bag, M.; Renna, L. A.; Adhikari, R. Y.; Karak, S.; Liu, F.; Lahti, P. M.; Russell, T. P.; Tuominen, M. T.; Venkataraman, D. Kinetics of Ion Transport in Perovskite Active Layers and Its Implications for Active Layer Stability. *J. Am. Chem. Soc.* **2015**, *137*, 13130−13137.

(12) Chaudhary, B.; Kulkarni, A.; Jena, A. K.; Ikegami, M.; Udagawa, Y.; Kunugita, H.; Ema, K.; Miyasaka, T. Poly(4-Vinylpyridine)-Based Interfacial Passivation to Enhance Voltage and Moisture Stability of Lead Halide Perovskite Solar Cells. *ChemSusChem* **2017**, *10*, 2473−2479.

(13) Milosavljević, A. R.; Huang, W.; Sadhu, S.; Ptasinska, S. Low-Energy Electron-Induced Transformations in Organolead Halide Perovskite. *Angew. Chem., Int. Ed.* **2016**, *55*, 10083−10087.

(14) Babayigit, A.; Ethirajan, A.; Muller, M.; Conings, B. Toxicity of Organometal Halide Perovskite Solar Cells. *Nat. Mater.* **2016**, *15*, 247−251.

(15) Turkevych, I.; Kazaoui, S.; Ito, E.; Urano, T.; Yamada, K.; Tomiyasu, H.; Yamagishi, H.; Kondo, M.; Aramaki, S. Photovoltaic Rudorffites: Lead-Free Silver Bismuth Halides Alternative to Hybrid Lead Halide Perovskites. *ChemSusChem* **2017**, *10*, 3754−3759.

(16) Oh, J. T.; Kim, D. H.; Kim, Y. Solution-Processed ″silver-Bismuth-Iodine″ Ternary Thin Films for Lead-Free Photovoltaic Absorbers. *J. Visualized Exp.* **2018**, *2018*, No. e58286.

(17) Hosseini, S. S.; Adelifard, M.; Ataei, M. An Investigation on Physical Properties of Ag_2BiI_5 Absorber Layers Synthesized by Microwave Assisted Spin Coating Technique. *J. Mater. Sci.: Mater. Electron.* **2019**, *30*, 5021−5029.

(18) Jung, K. W.; Sohn, M. R.; Lee, H. M.; Yang, I. S.; Sung, S. D.; Kim, J.; Wei-Guang Diau, E.; Lee, W. I. Silver Bismuth Iodides in Various Compositions as Potential Pb-Free Light Absorbers for Hybrid Solar Cells. *Sustainable Energy Fuels* **2018**, *2*, 294−302.

(19) Koedtruad, A.; Goto, M.; Amano Patino, M.; Tan, Z.; Guo, H.; Nakamura, T.; Handa, T.; Chen, W. T.; Chuang, Y. C.; Sheu, H. S.; et al. Structure-Property Relations in Ag−Bi−I Compounds: Potential Pb-Free Absorbers in Solar Cells. *J. Mater. Chem. A* **2019**, *7*, 5583−5588.

(20) Mashadieva, L. F.; Aliev, Z. S.; Shevelkov, A. V.; Babanly, M. B. Experimental Investigation of the Ag−Bi−I Ternary System and Thermodynamic Properties of the Ternary Phases. *J. Alloys Compd.* **2013**, *551*, 512−520.

(21) Ghosh, B.; Wu, B.; Guo, X.; Harikesh, P. C.; John, R. A.; Baikie, T.; Wee, A. T.; Guet, C.; Sum, T. C.; et al. Superior Performance of Silver Bismuth Iodide Photovoltaics Fabricated via Dynamic Hot-Casting Method under Ambient Conditions. *Adv. Energy Mater.* **2018**, *8*, 1802051.

(22) Lu, C.; Zhang, J.; Sun, H.; Hou, D.; Gan, X.; Shang, M. H.; Li, Y.; Hu, Z.; Zhu, Y.; Han, L. Inorganic and Lead-Free AgBiI4 Rudorffite for Stable Solar Cell Applications. *ACS Appl. Energy Mater.* **2018**, *1*, 4485−4492.

(23) Sansom, H. C.; Whitehead, G. F. S.; Dyer, M. S.; Zanella, M.; Manning, T. D.; Pitcher, M. J.; Whittles, T. J.; Dhanak, V. R.; Alaria, J.; Claridge, J. B.; et al. $AgBiI_4$ as a Lead-Free Solar Absorber with Potential Application in Photovoltaics. *Chem. Mater.* **2017**, *29*, 1538−1549.

(24) Zhang, Q.; Wu, C.; Qi, X.; Lv, F.; Zhang, Z.; Liu, Y.; Wang, S.; Qu, B.; Chen, Z.; Xiao, L. Photovoltage Approaching 0.9 v for Planar Heterojunction Silver Bismuth Iodide Solar Cells with Li-TFSI Additive. *ACS Appl. Energy Mater.* **2019**, *2*, 3651−3656.

(25) Zhu, H.; Pan, M.; Johansson, M. B.; Johansson, E. M. J. High Photon-to-Current Conversion in Solar Cells Based on Light-Absorbing Silver Bismuth Iodide. *ChemSusChem* **2017**, *10*, 2592−2596.

(26) Iyoda, F.; Nishikubo, R.; Wakamiya, A.; Saeki, A. Ag-(Bi, Sb, In, Ga)-I Solar Cells: Impacts of Elemental Composition and Additives on the Charge Carrier Dynamics and Crystal Structures. *ACS Appl. Energy Mater.* **2020**, *3*, 8224−8232.

(27) Danilović, D.; Božanić, D. K.; Dojčilović, R.; Vukmirović, N.; Sapkota, P.; Vukašinović, I.; Djoković, V.; Bozek, J.; Nicolas, C.; Ptasinska, S.; et al. Aerosol Synthesis and Gas-Phase Photoelectron Spectroscopy of Ag−Bi−I Nanosystems. *J. Phys. Chem. C* **2020**, *124*, 23930−23937.

(28) Li, X.; Traoré, B.; Kepenekian, M.; Li, L.; Stoumpos, C. C.; Guo, P.; Even, J.; Katan, C.; Kanatzidis, M. G. Bismuth/Silver-Based Two-Dimensional Iodide Double and One-Dimensional Bi Perovskites: Interplay between Structural and Electronic Dimensions. *Chem. Mater.* **2021**, *33*, 6206−6216.

(29) Tyagi, P.; Arveson, S. M.; Tisdale, W. A. Colloidal Organohalide Perovskite Nanoplatelets Exhibiting Quantum Confinement. *J. Phys. Chem. Lett.* **2015**, *6*, 1911−1916.

(30) Huang, C.; Gao, Y.; Wang, S.; Zhang, C.; Yi, N.; Xiao, S.; Song, Q. Giant Blueshifts of Excitonic Resonances in Two-Dimensional Lead Halide Perovskite. *Nano Energy* **2017**, *41*, 320−326.

(31) Ding, Y.-F.; Zhao, Q.-Q.; Yu, Z.-L.; Zhao, Y.-Q.; Liu, B.; He, P.-B.; Zhou, H.; Li, K.; Yin, S.-F.; Cai, M.-Q. Strong Thickness-Dependent Quantum Confinement in All-Inorganic Perovskite Cs_2PbI_4 with a Ruddlesden−Popper Structure. *J. Mater. Chem. C* **2019**, *7*, 7433−7441.

(32) Connor, B. A.; Leppert, L.; Smith, M. D.; Neaton, J. B.; Karunadasa, H. I. Layered Halide Double Perovskites: Dimensional Reduction of $Cs_2AgBiBr_6$. *J. Am. Chem. Soc.* **2018**, *140*, 5235−5240.

(33) Gelmetti, I.; Cabau, L.; Montcada, N. F.; Palomares, E. Selective Organic Contacts for Methyl Ammonium Lead Iodide (MAPI) Perovskite Solar Cells: Influence of Layer Thickness on Carriers Extraction and Carriers Lifetime. *ACS Appl. Mater. Interfaces* **2017**, *9*, 21599−21605.

(34) Bekenstein, Y.; Dahl, J. C.; Huang, J.; Osowiecki, W. T.; Swabeck, J. K.; Chan, E. M.; Yang, P.; Alivisatos, A. P. The Making and Breaking of Lead-Free Double Perovskite Nanocrystals of Cesium

https://doi.org/10.1021/acs.jpcc.2c03208
J. Phys. Chem. C 2022, 126, 13739−13747

Silver−Bismuth Halide Compositions. *Nano Lett.* **2018**, *18*, 3502−3508.
(35) Tan, Z.; Wu, Y.; Hong, H.; Yin, J.; Zhang, J.; Lin, L.; Wang, M.; Sun, X.; Sun, L.; Huang, Y.; et al. Two-Dimensional $(C_4H_9NH_3)_2PbBr_4$ Perovskite Crystals for High-Performance Photodetector. *J. Am. Chem. Soc.* **2016**, *138*, 16612−16615.
(36) Creutz, S. E.; Crites, E. N.; de Siena, M. C.; Gamelin, D. R. Colloidal Nanocrystals of Lead-Free Double-Perovskite (Elpasolite) Semiconductors: Synthesis and Anion Exchange To Access New Materials. *Nano Lett.* **2018**, *18*, 1118−1123.
(37) Pal, J.; Bhunia, A.; Chakraborty, S.; Manna, S.; Das, S.; Dewan, A.; Datta, S.; Nag, A. Synthesis and Optical Properties of Colloidal M3Bi2I9 (M = Cs, Rb) Perovskite Nanocrystals. *J. Phys. Chem. C* **2018**, *122*, 10643−10649.
(38) Brus, L. E. Electron-Electron and Electron-Hole Interactions in Small Semiconductor Crystallites: The Size Dependence of the Lowest Excited Electronic State. *Chem. Phys.* **1984**, *80*, 4403−4409.
(39) Sandroff, C. J.; Kelty, S. P.; Hwang, D. M. Clusters in Solution: Growth and Optical Properties of Layered Semiconductors with Hexagonal and Honeycombed Structures. *Chem. Phys.* **1986**, *85*, 5337−5340.
(40) Micic, O. I.; Nenadovic, M. T.; Peterson, M. W.; Nozik, A. J. Size Quantization in Layered Semiconductor Colloids with Tetrahedral Bonding: Mercury Diiodide. *J. Phys. Chem.* **1987**, *91*, 1295−1297.
(41) Micic, O. I.; Li, Z.; Mills, G.; Sullivan, J. C.; Meisel, D. Formation of Small Particles of Lead Iodide, Mercuric Iodide, and Bismuth Iodide Layered Semiconductors. *J. Phys. Chem.* **1987**, *91*, 6221−6229.
(42) Liu, Z.; Yang, H.; Wang, J.; Yuan, Y.; Hills-Kimball, K.; Cai, T.; Wang, P.; Tang, A.; Chen, O. Synthesis of Lead-Free Cs_2AgBix_6 (X = Cl, Br, I) Double Perovskite Nanoplatelets and Their Application in CO_2 Photocatalytic Reduction. *Nano Lett.* **2021**, *21*, 1620−1627.
(43) Božanić, D. K.; Garcia, G. A.; Sublemontier, O.; Pajović, J.; Djoković, V.; Nahon, L. Velocity Map Imaging VUV Angle-Resolved Photoemission on Isolated Nanosystems: Case of Gold Nanoparticles. *J. Phys. Chem. C* **2020**, *124*, 24500−24512.
(44) Perdew, J. P.; Burke, K.; Ernzerhof, M. Generalized Gradient Approximation Made Simple. *Phys. Rev. Lett.* **1996**, *77*, 3865−3868.
(45) van Setten, M. J.; Giantomassi, M.; Bousquet, E.; Verstraete, M. J.; Hamann, D. R.; Gonze, X.; Rignanese, G.-M. The PseudoDojo: Training and Grading a 85 Element Optimized Norm-Conserving Pseudopotential Table. *Comput. Phys. Commun.* **2018**, *226*, 39−54.
(46) Hamann, D. R. Optimized Norm-Conserving Vanderbilt Pseudopotentials. *Phys. Rev. B* **2013**, *88*, 085117.
(47) Giannozzi, P.; Andreussi, O.; Brumme, T.; Bunau, O.; Buongiorno Nardelli, M.; Calandra, M.; Car, R.; Cavazzoni, C.; Ceresoli, D.; Cococcioni, M.; et al. Advanced Capabilities for Materials Modelling with Quantum ESPRESSO. *J. Phys.: Condens. Matter* **2017**, *29*, 465901.
(48) Garrity, K. F.; Bennett, J. W.; Rabe, K. M.; Vanderbilt, D. Pseudopotentials for High-Throughput DFT Calculations. *Comput. Mater. Sci.* **2014**, *81*, 446−452.
(49) Perdew, J. P. Density Functional Theory and the Band Gap Problem. *Int. J. Quantum Chem.* **1985**, *28*, 497−523.
(50) Perdew, J. P.; Ernzerhof, M.; Burke, K. Rationale for Mixing Exact Exchange with Density Functional Approximations. *J. Chem. Phys.* **1996**, *105*, 9982−9985.
(51) Adamo, C.; Barone, V. Toward Reliable Density Functional Methods without Adjustable Parameters: The PBE0 Model. *J. Chem. Phys.* **1999**, *110*, 6158−6170.
(52) Chen, W.; Pasquarello, A. Band-Edge Levels in Semiconductors and Insulators: Hybrid Density Functional Theory versus Many-Body Perturbation Theory. *Phys. Rev. B* **2012**, *86*, No. 035134.
(53) Steiner, K.; Chen, W.; Pasquarello, A. Band Offsets of Lattice-Matched Semiconductor Heterojunctions through Hybrid Functionals and G0W0. *Phys. Rev. B* **2014**, *89*, 205309.
(54) Lin, L. Adaptively Compressed Exchange Operator. *J. Chem. Theory Comput.* **2016**, *12*, 2242−2249.
(55) Jocić, M.; Vukmirović, N. Ab Initio Construction of Symmetry-Adapted k · p Hamiltonians for the Electronic Structure of Semiconductors. *Phys. Rev. B* **2020**, *102*, 085121.
(56) Oldag, T.; Aussieker, T.; Keller, H. L.; Preitschaft, C.; Pfitzner, A. Solvothermale Synthese Und Bestimmung Der Kristallstrukturen von $AgBiI_4$ Und Ag_3BiI_6. *Z. Anorg. Allg. Chem.* **2005**, *631*, 677−682.
(57) Prasad, M. D.; Krishna, M. G.; Batabyal, S. K. Silver Bismuth Iodide Nanomaterials as Lead-Free Perovskite for Visible Light Photodetection. *ACS Appl. Nano Mater.* **2021**, *4*, 1252−1259.
(58) Crovetto, A.; Hajijafarassar, A.; Hansen, O.; Seger, B.; Chorkendorff, I.; Vesborg, P. C. K. Parallel Evaluation of the BiI3, BiOI, and Ag3BiI6Layered Photoabsorbers. *Chem. Mater.* **2020**, *32*, 3385−3395.
(59) Sengupta, A.; Mandal, K. C.; Zhang, J. Z. Ultrafast Electronic Relaxation Dynamics in Layered Iodide Semiconductors: A Comparative Study of Colloidal BiI_3 and PbI_2 Nanoparticles. *J. Phys. Chem. B* **2000**, *104*, 9396−9403.
(60) Gaarenstroom, S. W.; Winograd, N. Initial and Final State Effects in the ESCA Spectra of Cadmium and Silver Oxides. *J. Chem. Phys.* **1977**, *67*, 3500−3506.
(61) Khazaee, M.; Sardashti, K.; Chung, C. C.; Sun, J. P.; Zhou, H.; Bergmann, E.; Dunlap-Shohl, W. A.; Han, Q.; Hill, I. G.; Jones, J. L.; et al. Dual-Source Evaporation of Silver Bismuth Iodide Films for Planar Junction Solar Cells. *J. Mater. Chem. A* **2019**, *7*, 2095−2105.
(62) Qiu, W.; Dudder, G. J.; Zhao, X.; Perry, S. S.; Nino, J. C. Interfacial Reactivity of Au, Pd, and Pt on BiI_3 (001): Implications for Electrode Selection. *ACS Appl. Mater. Interfaces* **2011**, *3*, 1910−1917.
(63) Ferfolja, K.; Valant, M.; Mikulska, I.; Gardonio, S.; Fanetti, M. Chemical Instability of an Interface between Silver and Bi_2Se_3 Topological Insulator at Room Temperature. *J. Phys. Chem. C* **2018**, *122*, 9980−9984.
(64) Pignié, M.-C.; Patra, S.; Huart, L.; Milosavljević, A. R.; Renault, J. P.; Leroy, J.; Nicolas, C.; Sublemontier, O.; le Caër, S.; Thill, A. Experimental Determination of the Curvature-Induced Intra-Wall Polarization of Inorganic Nanotubes. *Nanoscale* **2021**, *13*, 19650−19662.
(65) Schürmann, R.; Titov, E.; Ebel, K.; Kogikoski, S.; Mostafa, A.; Saalfrank, P.; Milosavljević, A. R.; Bald, I. The Electronic Structure of the Metal-Organic Interface of Isolated Ligand Coated Gold Nanoparticles. *Nanoscale Adv.* **2022**, *4*, 1599−1607.
(66) Premkumar, S.; Liu, D.; Zhang, Y.; Nataraj, D.; Ramya, S.; Jin, Z.; Mamba, B. B.; Kuvarega, A. T.; Gui, J. Stable Lead-Free Silver Bismuth Iodide Perovskite Quantum Dots for UV Photodetection. *ACS Appl. Nano Mater.* **2020**, *3*, 9141−9150.
(67) Hinuma, Y.; Pizzi, G.; Kumagai, Y.; Oba, F.; Tanaka, I. Band Structure Diagram Paths Based on Crystallography. *Comput. Mater. Sci.* **2017**, *128*, 140−184.

https://doi.org/10.1021/acs.jpcc.2c03208
J. Phys. Chem. C 2022, 126, 13739−13747

Electronic Properties of Silver-Bismuth Iodide Rudorffite Nanoplatelets

Danijela Danilović[1,2], Aleksandar R. Milosavljević[3*], Pitambar Sapkota[4,5], Radovan Dojčilović[1,2,6], Dragana Tošić[1], Nenad Vukmirović[7], Milan Jocić[7], Vladimir Djoković[1,2], Sylwia Ptasinska[4,5], and Dušan K. Božanić[1,2*]

[1] Department of Radiation Chemistry and Physics, "Vinča" Institute of Nuclear Sciences - National Institute of the Republic of Serbia, University of Belgrade, P.O. Box 522, 11001 Belgrade, Serbia

[2] Center of Excellence for Photoconversion, Vinča" Institute of Nuclear Sciences - National Institute of the Republic of Serbia, University of Belgrade, P.O. Box 522, 11001 Belgrade, Serbia

[3] Synchrotron SOLEIL, l'Orme des Merisiers, St. Aubin, BP48, 91192 Gif sur Yvette Cedex, France

[4] Radiation Laboratory, University of Notre Dame, Notre Dame, IN 46556, USA

[5] Department of Physics, University of Notre Dame, Notre Dame, IN 46556, USA

[6] Department of Experimental and Health Sciences (DCEXS), Pompeu Fabra University (UPF), 08003 Barcelona, Spain

[7] Institute of Physics Belgrade, University of Belgrade, Pregrevica 118, 11080, Belgrade, Serbia

Corresponding authors: *A.R.M. milosavljevic@synchrotron-soleil.fr; *D.K.B. bozanic@vin.bg.ac.rs

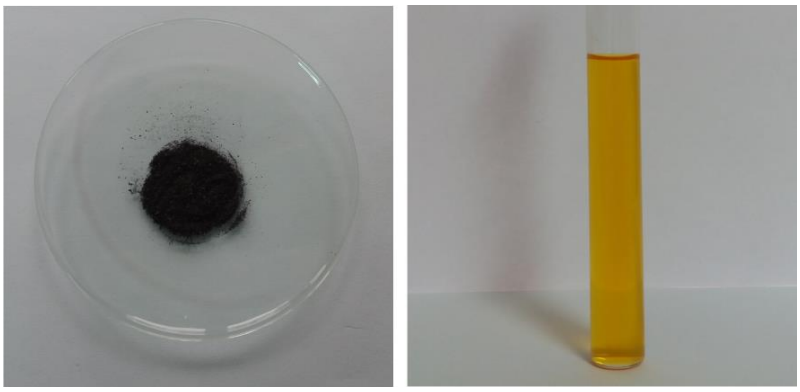

Figure S1. Photographs of Ag-Bi-I powder, and the Ag-Bi-I dispersed in acetonitrile.

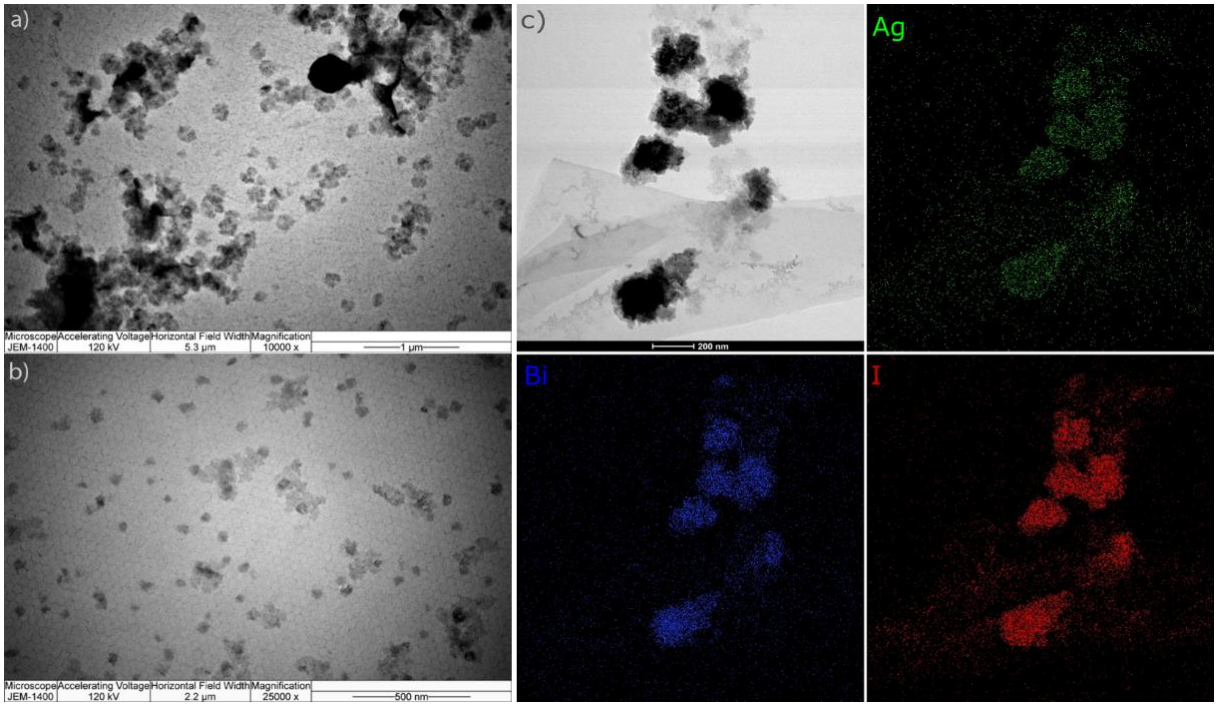

Figure S2. TEM images of a) Ag-Bi-I and b) BiI_3 nanoplatelets and c) HRTEM/EDS mapping of Ag-Bi-I nanoplatelets for silver, bismuth, and iodine.

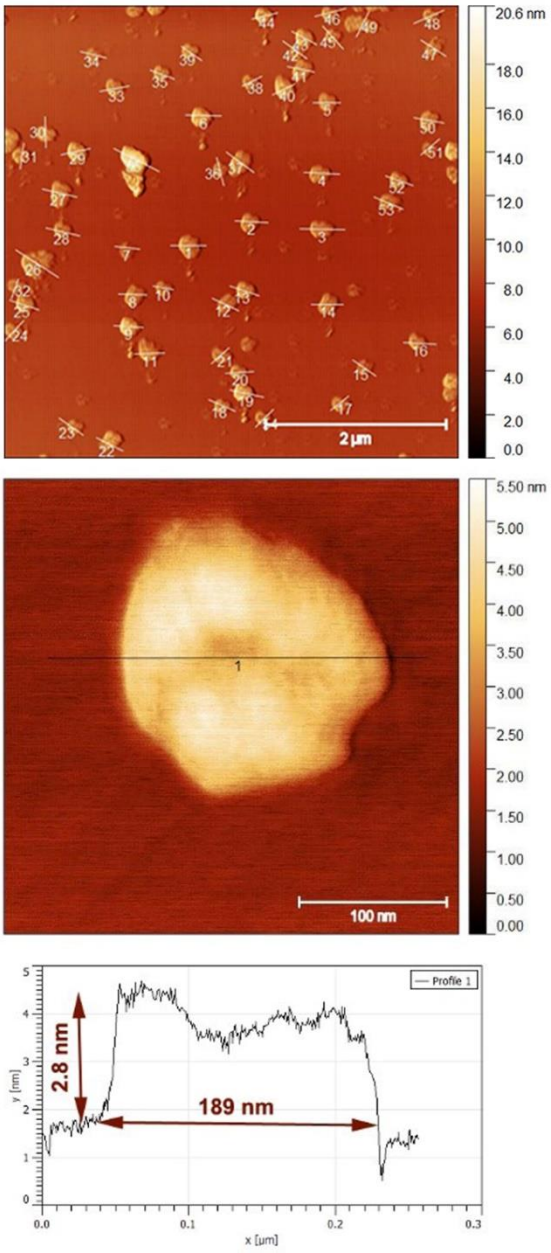

Particle number	Height (nm)	Particle number	Height (nm)
1.	4.61	29.	4.22
2.	3.67	30.	3.63
3.	3.52	31.	3.96
4.	3.59	32.	3.41
5.	4.26	33.	3.20
6.	4.96	34.	1.52
7.	3.13	35.	3.19
8.	4.44	36.	2.63
9.	5.56	37.	4.44
10.	2.22	38.	4.03
11.	7.11	39.	4.17
12.	4.36	40.	6.37
13.	2.36	41.	6.08
14.	4.44	42.	1.82
15.	2.63	43.	4.14
16.	3.82	44.	5.35
17.	2.49	45.	3.16
18.	2.52	46.	2.82
19.	4.44	47.	2.31
20.	6.67	48.	3.40
21.	2.81	49.	3.32
22.	4.68	50.	3.46
23.	2.09	51.	4.11
24.	3.79	52.	3.20
25.	4.74	53.	3.86
26.	3.98	54.	2.95
27.	4.96	55.	10.04
28.	3.85		

Figure S3. AFM profile analysis procedure for determination of the height distribution of Ag-Bi-I nanoplatelets and the corresponding results table. The height profile in the random direction of the observed particles was evaluated and maximum height was considered as the thickness of the particle.

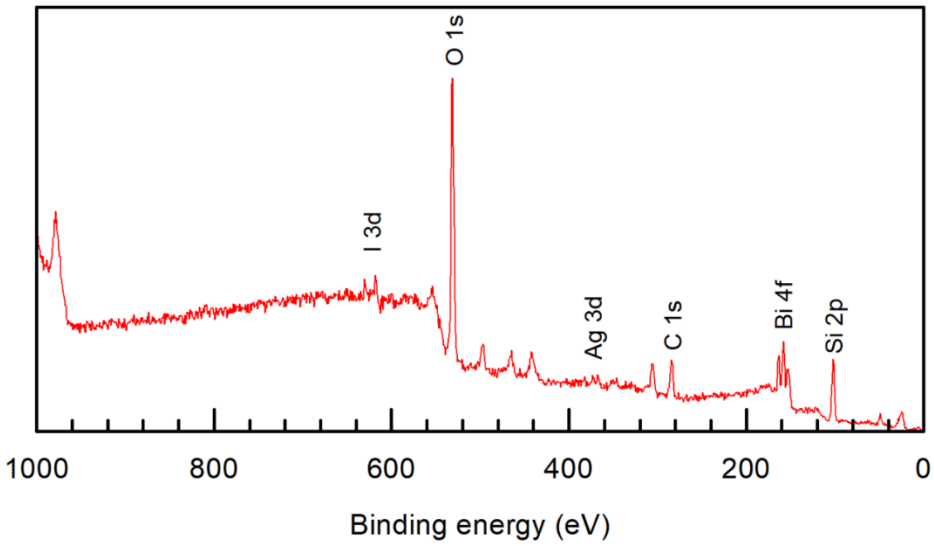

Figure S4. XPS survey scan of Ag-Bi-I nanoplatelets.

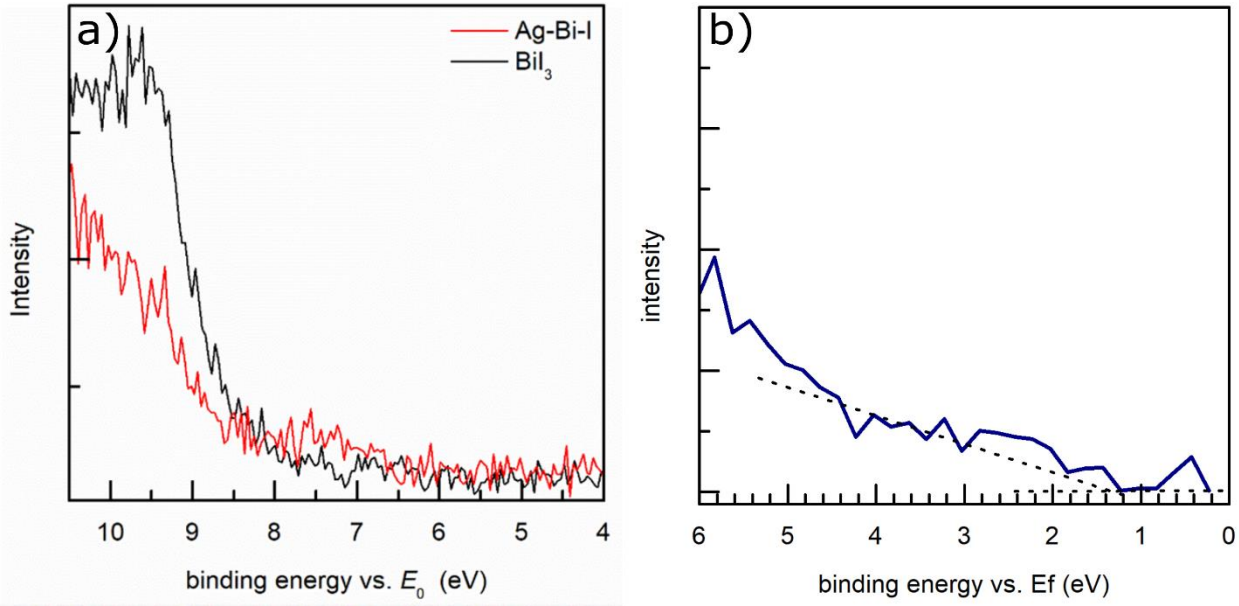

Figure S5. (a) Valence region photoemission spectra of Ag-Bi-I and BiI_3 aerosol particles recorded at 100 eV using XAPS. (b) Valence region photoemission spectrum of Ag-Bi-I measured using XPS at 1486.6 eV.

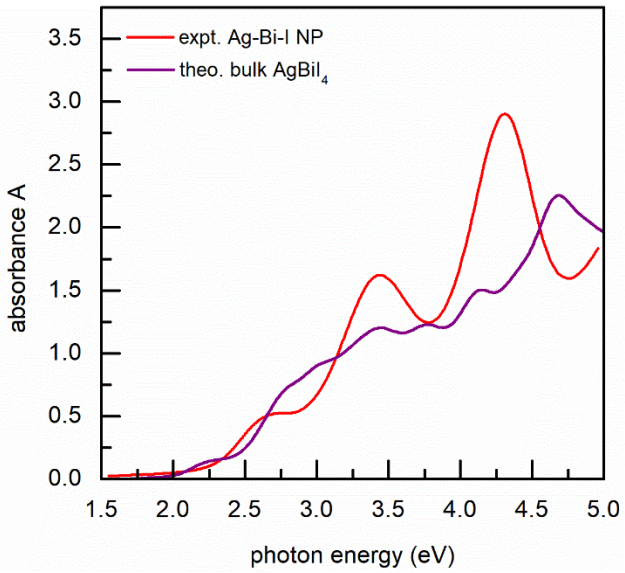

Figure S6. UV-vis absorption spectrum of Ag-Bi-I nanoplatelets dispersed in acetonitrile (red line) and the theoretical absorption of bulk $AgBiI_4$ material (purple line) calculated by the procedure described in Section A8. The theoretical curve was shifted by 0.4 eV to match the theoretical value of the band gap with the experimental one.

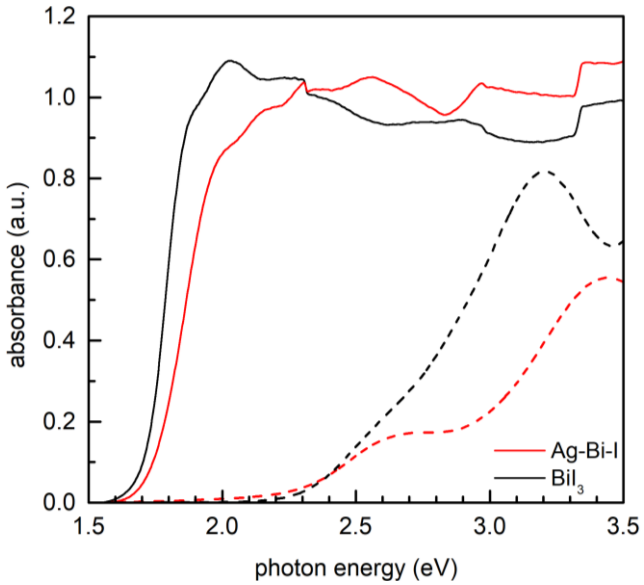

Figure S7. Absorption spectra of Ag-Bi-I and BiI_3 powders (dashed lines) and their colloidal dispersions in acetonitrile (solid lines).

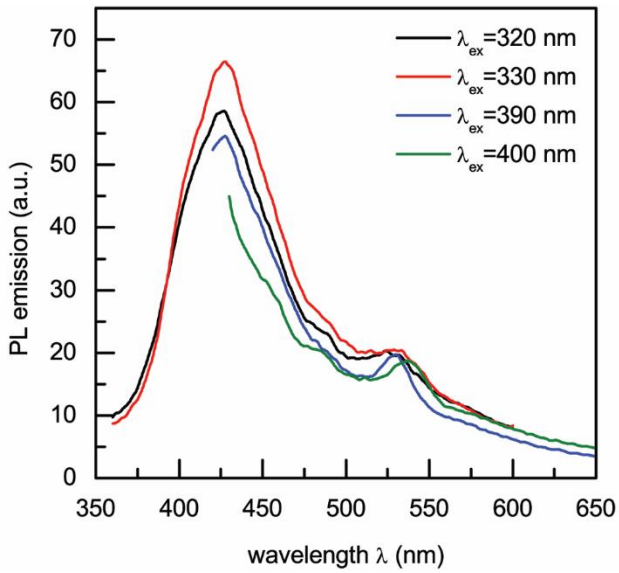

Figure S8. Photoluminescence emission spectra of Ag-Bi-I nanoplatelets dispersed in acetonitrile.

A1 Parametrization of $\mathbf{k}\cdot\mathbf{p}$ Hamiltonian using the data obtained from DFT calculations

To enable accurate calculations of wider quantum wells, we constructed the $\mathbf{k}\cdot\mathbf{p}$ Hamiltonian following the approach of Ref [1]. Namely, the Hamiltonian matrix takes the form

$$H_{mn}(\mathbf{k}) = H_{mn}^{(1)}(\mathbf{k}) + H_{mn}^{(2)}(\mathbf{k}),$$

where

$$H_{mn}^{(1)}(\mathbf{k}) = \left[E_n(\mathbf{k}_0) + \frac{\hbar^2(\mathbf{k}-\mathbf{k}_0)^2}{2m_0}\right]\delta_{mn} + \frac{\hbar(\mathbf{k}-\mathbf{k}_0)}{m_0}\langle\Psi_{n\mathbf{k}_0}|\mathbf{p}|\Psi_{m\mathbf{k}_0}\rangle,$$

$$H_{mn}^{(2)}(\mathbf{k}) = \frac{\hbar^2}{m_0^2}\sum_l \frac{\langle\Psi_{m\mathbf{k}_0}|(\mathbf{k}-\mathbf{k_0})\cdot\mathbf{p}|\Psi_{l\mathbf{k}_0}\rangle\langle\Psi_{l\mathbf{k}_0}|(\mathbf{k}-\mathbf{k_0})\cdot\mathbf{p}|\Psi_{n\mathbf{k}_0}\rangle}{[E_n(\mathbf{k}_0)+E_m(\mathbf{k}_0)]/2 - E_l(\mathbf{k}_0)},$$

$E_n(\mathbf{k}_0)$ is the energy of band n at the wave vector $\mathbf{k}_0$, $|\Psi_{n\mathbf{k}_0}\rangle$ is the corresponding wave function, and $\mathbf{p}$ is the momentum operator. The indices m and n denote the main bands that are used to construct the $\mathbf{k}\cdot\mathbf{p}$ Hamiltonian, while the index l denotes the remaining bands. The effects of the later bands are included in calculations perturbatively . The $\mathbf{k}\cdot\mathbf{p}$ Hamiltonian is constructed by calculating all the elements of the Hamiltonian matrix starting from calculated energies $E_n(\mathbf{k}_0)$ and wave functions $|\Psi_{n\mathbf{k}_0}\rangle$ of the bulk material. One can use either the energies and wave functions obtained from DFT/PBE calculation, or the ones obtained from the hybrid PBE0 functional calculation. In the latter case, it is expected that band gap of quantum wells would be significantly more accurate. Once the $\mathbf{k}\cdot\mathbf{p}$ Hamiltonian is obtained, the electronic structure of the quantum well can be calculated according to the procedure described in Section III B of Ref [1].

A2 Model for atomic structure of bulk Ag-Bi-I material

As a model for atomic structure of the Ag-Bi-I material we used the rhombohedral $AgBiI_4$ material. We constructed its atomic structure as follows. We started with an atomic structure of the rhombohedral $CdCl_2$, and lattice parameters given in Ref. [2] (Table I therein). We replaced Cl atoms with I, while we replaced the Cd atom in one primitive cell with Ag atom and the Cd atom in the neighboring primitive cell with the Bi atom. We then performed DFT/PBE based relaxation of lattice parameters and atomic positions. The final atomic structure that we obtained following this strategy is given in Table S1.

Lattice constants (Å):			
a = 7.028	b = 7.028	c = 7.220	
Lattice angles (degrees):			
alpha = 80.14	beta = 88.86	gamma = 145.50	
Fractional atomic coordinates:			
Ag	0.00000	0.00000	0.00000
Bi	0.50000	0.50000	0.50000
I	0.63580	0.36420	0.88645
I	0.36420	-0.36420	0.11355
I	0.14486	-0.14486	0.37397
I	0.85514	0.14486	0.62603

Table S1. Lattice parameters and atomic coordinates of $AgBiI_4$ obtained from DFT/PBE calculations.

A3 Model for atomic structure of nanoplatelets

Experimentally investigated nanoplatelets have much larger lateral dimensions than thickness. For this reason, we modeled them as quantum wells that are infinite in *xy*-plane with the thickness L in the z-direction. To construct the atomic structure of such quantum wells, we performed the following procedure: we first noted that the atomic structure of the rhombohedral $AgBiI_4$ that we investigated can be constructed by putting together different atomic planes spanned by the vectors $\boldsymbol{a} + \boldsymbol{b}$ and $\boldsymbol{c}$**.** One such plane that contains Ag and Bi atoms is sandwiched between two planes that contain I atoms. These three planes form one monolayer of the material. We constructed a quantum well consisting of n monolayers by translating one monolayer n times by vector $\boldsymbol{a}$. The example of atomic structure of 8 monolayer quantum well is presented in Figure S9.

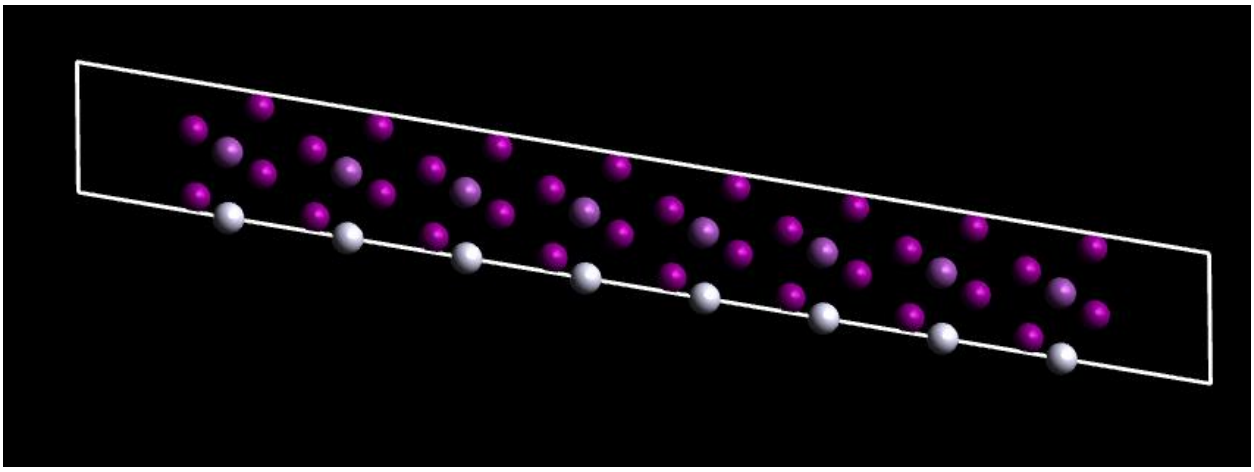

Figure S9. Atomic structure of a quantum well consisting of 8 monolayers. White lines denote the supercell used in the calculation of the electronic structure. Ag atoms are shown in white, Bi atoms are shown in violet, while I atoms are shown in magenta.

To calculate the electronic structure of a quantum well, we applied periodic boundary conditions in the *xy*-plane, while included a sufficiently thick vacuum layer in the *z*-direction (see Figure S9) to avoid electronic coupling in the *z*-direction between atoms from neighboring supercells.

A4 Determination of absolute positions of bulk energy levels with respect to vacuum

Density functional theory calculations with plane-wave basis and periodic boundary conditions do not yield the absolute value of the position of the energy levels with respect to vacuum. To align these levels with vacuum, we calculated the dependence of the averaged potential (the sum of the Hartree potential and the local part of the ionic pseudopotential averaged over the *xy*-plane) on *z*-coordinate. The dependence for 8 monolayer quantum well and for bulk is presented in Figure S10. It can be noted that the potential outside the well is flat, but it is different from zero. Therefore, the value of the potential outside the well gives us the shift that is necessary to align all the energy levels in the quantum well calculation with vacuum level. Next, we noticed that the shape of the bulk potential matches the potential in the middle of the well apart from a constant energy shift. By shifting the bulk potential by this energy shift, the bulk potential is then aligned with the quantum well potential. Hence, by aligning the bulk potential with quantum well potential and the quantum well potential with the vacuum level, we eventually aligned the bulk potential with the vacuum level, see Figure S11. Using the mentioned procedure and DFT/PBE calculation method, we found the valence band maximum (VBM) energy to be -5.1 eV.

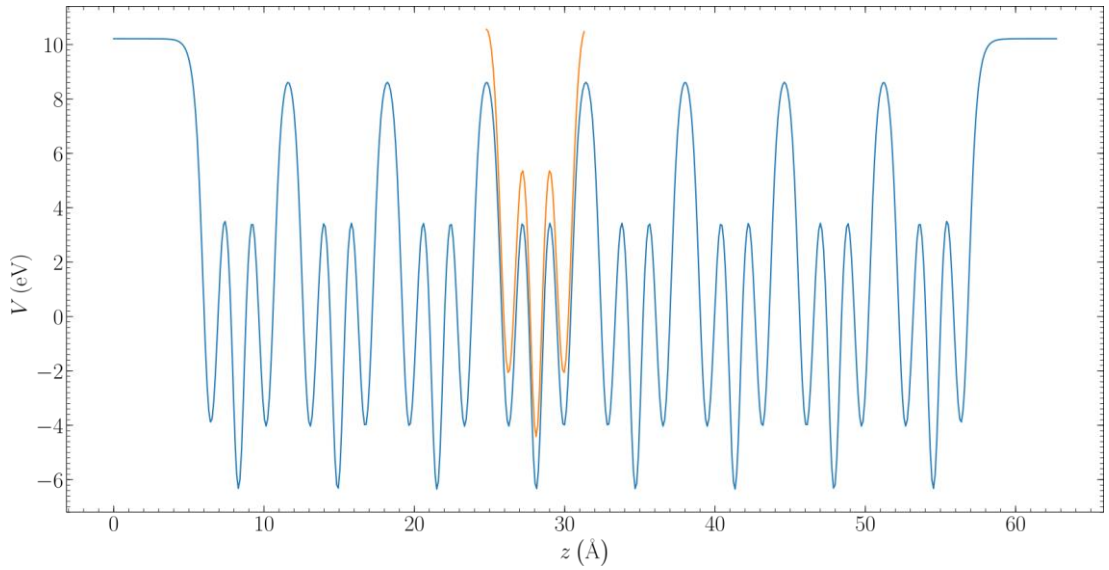

Figure S10. Averaged potential profile as obtained from DFT/PBE calculation of the 8 monolayer quantum well (blue line) and the bulk material (orange line).

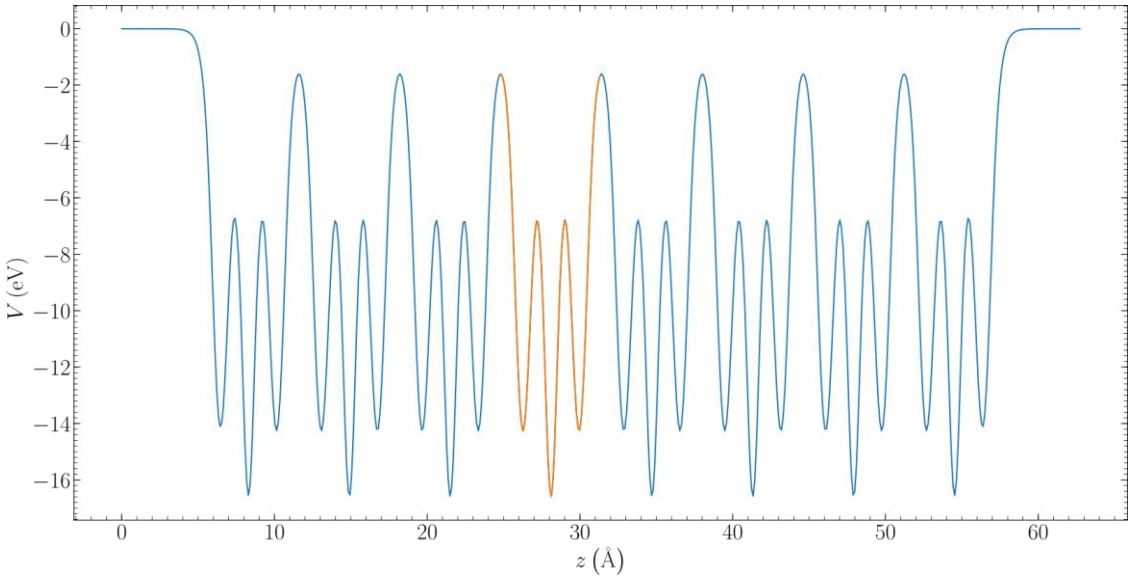

Figure S11. Averaged potential profile of the 8 monolayer quantum well (blue line) and the bulk material (orange line). The potentials obtained from DFT/PBE calculation were shifted to align the quantum well potential with vacuum and the bulk potential with the potential in the middle of the quantum well.

Still, the DFT/PBE calculation method gave slightly lower value for the position of the bulk VBM energy with respect to vacuum level. To improve the calculation procedure, we used the result obtained in hybrid PBE0 functional calculation. The VBM energy value obtained by DFT/PBE method is corrected by taking into account the differences in bulk VBM energies calculated using DFT/PBE0 and DFT/PBE methods. Such an approach is justified, because both PBE and PBE0 calculation methods when applied to the identical bulk material, using the same plane wave

computational code, have a common energy reference. Using this procedure we found VBM energy of the bulk material to be -5.95 eV.

A5 Electronic band structure of quantum wells calculated using DFT/PBE

Electronic structure calculations within DFT/PBE approach were performed for quantum wells that have from one to 8 monolayers. The dependence of quantum well band gap on width is presented in Figure S12. We found that this dependence is rather weak. For example, in the range from 2 to 5 nm the gap changes by about 50 meV indicating that the effects that come from quantum confinement are not particulary significant.

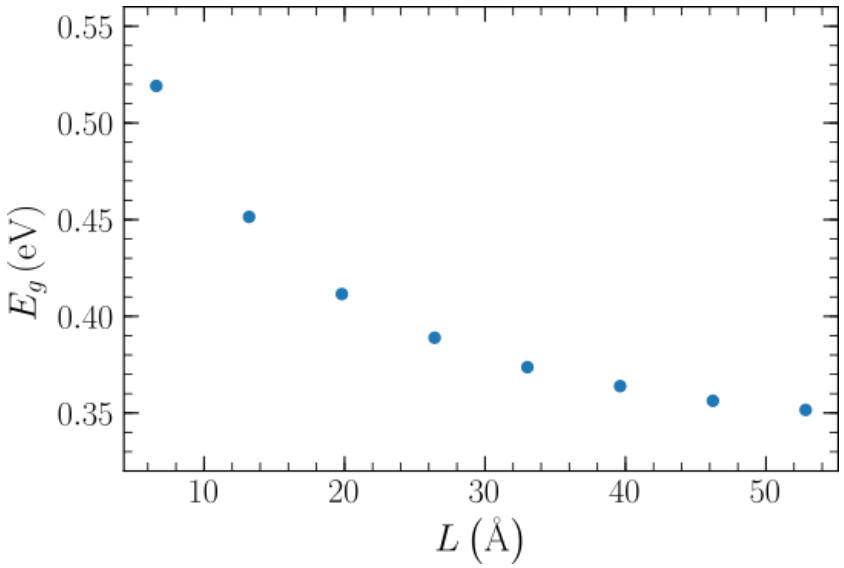

Figure S12. The dependence of quantum well band gap (E_g) on its width(L) calculated by DFT/PBE.

In Figures S13 and S14 we show the electronic band structure of the quantum well along several characteristic directions of the two-dimensional Brillouin zone. The results suggest that the band structure of multilayered quantum wells is rather similar to the band structure of one monolayer quantum well. It can be seen in Figure S14 that each band in Figure S13 is transformed into six similar and closely spaced bands. This also implies that the coupling between different monolayers of the material is rather weak. Consequently, the electronic structure of a single monolayer represents fairly well the electronic structure of the multilayered or even the bulk material. For this reason, the band gap should not be affected by the change in the thickness of the particles (number of quantum wells in the stack), which the results in Figure S12 indeed show.

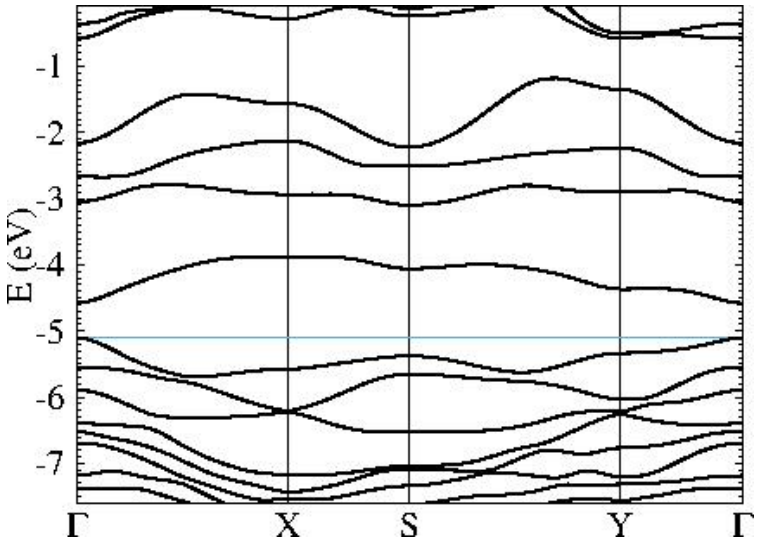

Figure S13. Electronic structure of single monolayer quantum well calculated using DFT/PBE. The blue horizontal line represents the valence band maximum energy. The energies are given with respect to the vacuum level.

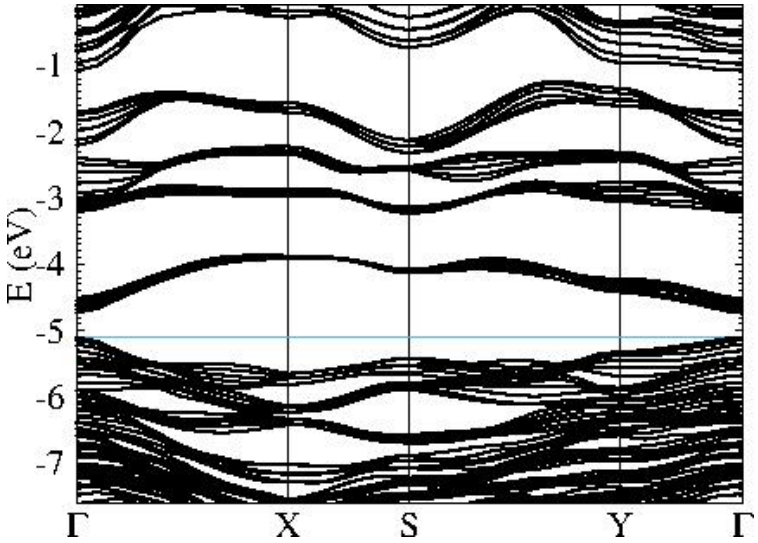

Figure S14. Electronic structure of six-layer stack of quantum wells calculated using DFT/PBE. The blue horizontal line represents the valence band maximum energy. The energies are given with respect to the vacuum level.

A6 Electronic states of quantum wells calculated using the $\mathbf{k} \cdot \mathbf{p}$ method parameterized by using results from DFT/PBE calculations

We calculated the electronic states at the top of the valence band and the bottom of the conduction band of the quantum wells using a 4-band $\mathbf{k} \cdot \mathbf{p}$ Hamiltonian. The Hamiltonian was derived from two highest (degenerate) states in the bulk valence band and two lowest (degenerate) states in the bulk conduction band at the Y_2 point where these bulk bands exhibit their maximum and minimum.

To check the accuracy of the $\mathbf{k}\cdot\mathbf{p}$ method, the calculation was first performed using the Hamiltonian derived from energies and wave functions obtained from DFT/PBE calculation. In this case, the $\mathbf{k}\cdot\mathbf{p}$ results can be compared to the results obtained from full DFT/PBE calculation of quantum wells. This comparison is presented in Figure S15. An excellent agreement between DFT/PBE and $\mathbf{k}\cdot\mathbf{p}$ results was found except for thinnest wells where $\mathbf{k}\cdot\mathbf{p}$ is not expected to perform well.

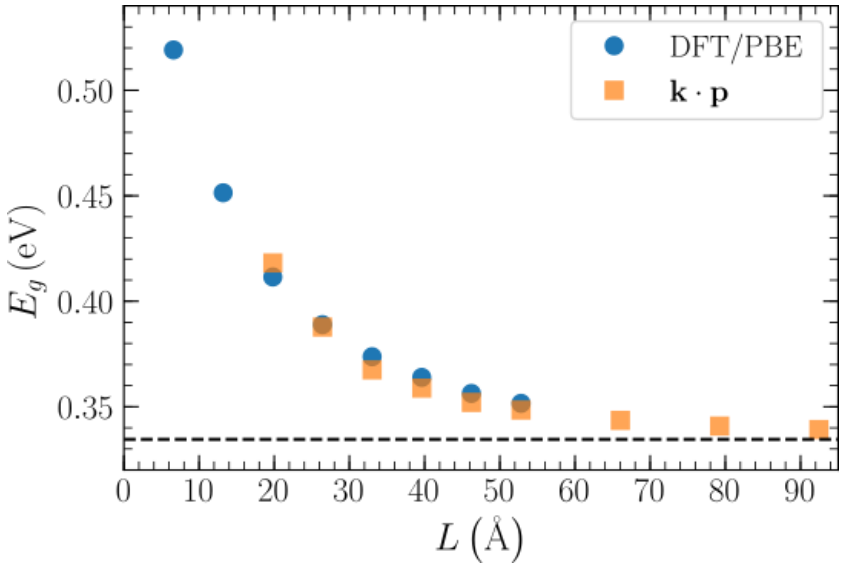

Figure S15. Dependence of quantum well band gap on its width calculated using DFT/PBE and using the $\mathbf{k}\cdot\mathbf{p}$ method with Hamiltonian parameterized with data from DFT/PBE calculations.

A7 Dielectric contrast effect

We also estimated the effect of dielectric contrast between the well and the surroundings. Self-energy arising from this effect was calculated using Eq. (4) from Ref. [3]. Assuming the high frequency dielectric constants of 2.1 for $AgBiI_4$ [4] and 1.8 for acetonitrile, we obtained that the change of energy levels is of the order of 25 meV for 2 nm wide quantum wells and decreases as the well width increases.

A8 Absorption spectrum of bulk $AgBiI_4$ material

To understand the measured absorption spectrum, we performed the calculation of the absorption of bulk $AgBiI_4$ material. We have previously observed (Figure 7 in the main part of the paper) that the quantum confinement effects are weak. Therefore, it is expected that the absorption spectrum of quantum well and the absorption spectrum of bulk should be similar.
The absorption coefficient is proportional to the quantity

$$A(E) = \frac{1}{N_k}\sum_{\mathbf{k}}\sum_{v,c}\frac{1}{3}\left[|p_x^{vc}(\mathbf{k})|^2 + \left|p_y^{vc}(\mathbf{k})\right|^2 + |p_z^{vc}(\mathbf{k})|^2\right]\frac{\delta[E_c(\mathbf{k}) - E_v(\mathbf{k}) - E]}{E_c(\mathbf{k}) - E_v(\mathbf{k})}.$$

In this equation, the sum is performed over N_k points from the first Brillouin zone and over all valence bands v and conduction bands, c. $E_c(\mathbf{k})$ and $E_v(\mathbf{k})$ denote the energies of states involved in the transition, while $\boldsymbol{p}^{vc}(\mathbf{k}) = \langle\Psi_{v\mathbf{k}}|\mathbf{p}|\Psi_{c\mathbf{k}}\rangle$ are the momentum matrix elements

between these states. In actual calculation procedure, the delta function was replaced by a Gaussian with standard deviation of 100 meV.
To perform the calculation on a sufficiently dense grid of $\mathbf{k}$ points, we performed $\mathbf{k}\cdot\mathbf{p}$ interpolation of energies and wave functions. First, we carried out a hybrid PBE0 functional calculation on a $4\times4\times4$ grid of points in reciprocal space. Then, for each $\mathbf{k}$ point which is not on that grid, we found the point $\mathbf{k_0}$ from the grid closest to that point and construct the $\mathbf{k}\cdot\mathbf{p}$ Hamiltonian with $\mathbf{k_0}$ as the reference point. By solving the eigenvalue problem of that Hamiltonian, we obtained the energies, wave functions, and momentum matrix elements at $\mathbf{k}$.

The absorption spectra calculated by mentioned procedure is shown in Figure S16. Each of the absorption curves is calculated using different sizes of the $\mathbf{k}$ point grid. As can be seen, the curves converge starting from 8 × 8 × 8 grid. The calculated spectrum clearly shows a rise in absorbance as energy increases, the trend that is observed experimentally. Also, the spectrum calculated on a $8\times8\times8$ grid exhibits a peak at 4.4 eV which matches well the experimental peak at 4.3 eV. The experimental absorption onset at 2.2 eV is larger than the energy onset obtained by calculations. Also, the experimental absorption peaks at 2.71 and 3.44 eV cannot be clearly distinguished in the calculated spectrum.

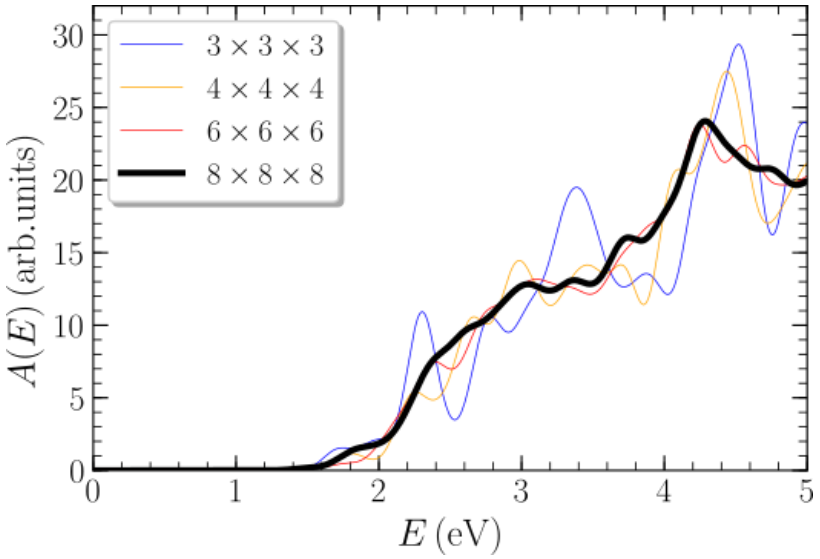

Figure S16. Absorption spectra of bulk $AgBiI_4$ material. The presented results correspond to different sizes of the $\mathbf{k}$ point grid.

References

(1) Jocić, M.; Vukmirović, N. Ab Initio Construction of Symmetry-Adapted k · p Hamiltonians for the Electronic Structure of Semiconductors. *Phys. Rev. B* **2020**, *102*, 085121.

(2) Koedtruad, A.; Goto, M.; Amano Patino, M.; Tan, Z.; Guo, H.; Nakamura, T.; Handa, T.; Chen, W. T.; Chuang, Y. C.; Sheu, H. S.; et al. Structure-Property Relations in Ag-Bi-I Compounds: Potential Pb-Free Absorbers in Solar Cells. *J. Mater. Chem. A* **2019**, *7*, 5583–5588.

(3) Cho, Y.; Berkelbach, T. C. Environmentally Sensitive Theory of Electronic and Optical Transitions in Atomically Thin Semiconductors. *Phys. Rev. B* **2018**, *97*, 041409.

(4) Hosseini, S. S.; Adelifard, M.; Ataei, M. An Investigation on Physical Properties of Ag_2BiI_5 Absorber Layers Synthesized by Microwave Assisted Spin Coating Technique. *J. Mater. Sci.: Mater. Electron.* **2019**, *30*, 5021–5029.

PCCP

ROYAL SOCIETY OF CHEMISTRY

PAPER

View Article Online
View Journal | View Issue

Cite this: *Phys. Chem. Chem. Phys.*, 2023, **25**, 29017

Ab-initio calculations of temperature dependent electronic structures of inorganic halide perovskite materials†

Milan Jocić and Nenad Vukmirović *

Despite wide interest in halide perovskite materials, it is still challenging to accurately calculate their electronic structure and its temperature dependence. In this work, we present *ab-initio* calculations of the temperature dependence of the electronic structure of $CsPbX_3$ materials (X = Cl, Br or I) in the cubic form and of the zero temperature electronic structure of the orthorhombic phase of these materials. Phonon-induced temperature dependent band energy renormalization was calculated within the framework of Allen–Heine–Cardona theory, where we exploited the self-consistent procedure to determine both the energy level shifts and their broadenings. The phonon spectrum of the materials was obtained using the self-consistent phonon method since standard density functional perturbation theory calculations in harmonic approximation yield phonon modes with imaginary frequencies due to the fact that the cubic structure is not stable at zero temperature. Our results suggest that low energy phonon modes mostly contribute to phonon-induced band energy renormalization. The calculated values of the band gaps at lowest temperature where the material exhibits a cubic structure are in good agreement with experimental results from the literature. The same is the case for the slope of the temperature dependence of the band gap for the $CsPbI_3$ material where reliable experimental data are available in the literature. We also found that phonon-induced temperature dependence of the band gap is most pronounced for the conduction band minimum and valence band maximum, while other bands exhibit a weaker dependence.

Received 4th May 2023,
Accepted 26th September 2023

DOI: 10.1039/d3cp02054a

rsc.li/pccp

1 Introduction

Halide perovskite materials emerged in the last decade as revolutionary materials for applications in solar cells,[1–4] lasers,[5] light-emitting diodes,[6,7] photodetectors,[8,9] detectors of ionizing radiation,[10,11] thermoelectric[12] and other devices.[13] To understand the characteristics of these devices and to design improved materials and devices, it is essential to be able to predict the electronic structure of the material. Despite great interest in understanding the electronic structure of halide perovskites and numerous developments of the methods for electronic structure calculations and the software for performing such calculations, it is still rather challenging to accurately determine the electronic structure of halide perovskites.

It is currently well understood that in electronic structure calculations of halide perovskites one has to take into account the effects of spin–orbit interactions due to the presence of heavy atoms such as lead.[14–16] As in the case for many other semiconductors, standard local or semilocal approximations to density functional theory (DFT) underestimate the material band gap[14–16] and more sophisticated approaches, such as the use of GW approximation[17–19] or hybrid functionals,[20,21] are necessary.

A group of challenges arises when it comes to predicting the electronic structures of halide perovskites at room or higher temperatures which are relevant for application in the mentioned devices. Temperature effects on the band gap and the overall electronic structure of perovskites are rather pronounced[22–28] and one cannot simply consider the electronic structure calculated for fixed atoms in a crystal lattice as the electronic structure at higher temperatures.

The most successful theory for determining the temperature effects on the electronic structure of semiconductors is the Allen–Heine–Cardona theory.[29–31] Within this theory, one expands the Hamiltonian up to second order terms in atomic displacements from the equilibrium position and perturbatively evaluates the change in band energies. In conjunction with the methods for the electronic structure calculation for fixed atomic positions, this theory was used to study the temperature dependence of the band gap and zero temperature band gap renormalization in a variety of semiconductors.[31–36] However, this theory can be

Institute of Physics Belgrade, University of Belgrade, Pregrevica 118, 11080 Belgrade, Serbia. E-mail: milan.jocic@ipb.ac.rs, nenad.vukmirovic@ipb.ac.rs

† Electronic supplementary information (ESI) available: Supplementary figures and cif files with initial and relaxed coordinates of the orthorhombic structure of $CsPbX_3$ materials. See DOI: https://doi.org/10.1039/d3cp02054a

straightforwardly applied to a particular material only if its crystal structure at a given temperature is the same as at zero temperature.

The last condition is not fulfilled in halide perovskite materials. Inorganic halide perovskite materials $CsPbX_3$ (X = Cl, Br or I) that are of main interest in this work exhibit a cubic structure at high temperatures only.[37–42] As the temperature is lowered, they transform into a tetragonal structure and finally to an orthorhombic structure.[37–40] Therefore, the cubic structure is not a stable structure at zero temperature. When one attempts to calculate the phonon dispersion in the material by assuming a cubic structure at zero temperature, phonon modes of imaginary frequencies are obtained[40,43–45] and it is not clear how to treat such phonons within the Allen–Heine–Cardona theory.

Previous studies on the effects of temperature on halide perovskite semiconductors have not addressed other bands than the conduction band minimum (CBM) and the valence band maximum (VBM). While these two bands are most relevant for the determination of the band gap of the material, there is significant interest in knowing the energies of the other bands. These are important, for example, to understand the optical response of the material in the ultraviolet spectral range relevant for ultraviolet detectors.[9] On the theoretical side, the knowledge of band energies at characteristic points in the Brillouin zone is necessary to construct multiband Hamiltonians[46–49] that can further be used to predict the electronic states in halide perovskite nanostructures. While the renormalization of energies of the other bands can in principle be obtained in the same way as for CBM and VBM within Allen–Heine–Cardona theory, certain issues, related to the energy level broadening parameter δ, arise. On the one hand, band renormalization for other bands converges linearly with respect to δ when $\delta \to 0$ in contrast to Lorentzian convergence of CBM and VBM,[32] which makes it more challenging to obtain the convergence of other bands. On the other hand, other bands typically exhibit larger broadening of energy levels compared with the CBM and VBM. Consequently, it is questionable if one should evaluate the $\delta \to 0$ limit for other bands at all. Preferably, the broadening of the energy levels should be evaluated simultaneously with the band energy renormalization.

In this work, we perform electronic structure calculations of the temperature dependence of the band gap and band energies for halide perovskite materials $CsPbX_3$ (X = Cl, Br or I) in a cubic crystal structure. Electronic structure calculations (without the effects of phonon-induced band renormalization) are performed using a hybrid functional that satisfies the Koopmans condition. The challenge of treating phonons within the Allen–Heine–Cardona theory is overcome by performing phonon band structure calculations at a finite temperature within the framework of self-consistent phonon (SCPH) theory, where all phonon modes remain stable. The challenge of the choice of energy level broadening is overcome by performing the calculation in which energy levels and their broadening are determined self-consistently. We compare the obtained temperature dependence of the band gap for the cubic structure to experimental results from the literature. We also perform calculations of the orthorhombic structure at zero temperature and comment on the overall temperature dependence of the band gap of $CsPbX_3$ materials from zero to high temperatures.

This paper is organized as follows. In Section 2, we present the main methods that were used in this work. Allen–Heine–Cardona theory is briefly reviewed in Section 2.1 along with the description of the two approaches that were used to calculate phonon-induced band energy renormalization within this theory. The SCPH method is reviewed in Section 2.2. In Section 3 we present the results obtained and the details of the calculations. We start with the results obtained using standard density functional theory (DFT) calculations with semilocal functionals that are presented in Section 3.1. In Section 3.2 we present the results obtained using a hybrid functional that gives improved values of the material band gap. Density functional perturbation theory (DFPT) based calculations of the phonon spectrum are reported in Section 3.3, while SCPH calculations of the phonon spectrum are presented in Section 3.4. In Sections 3.5 and 3.6 we present the main results of this work for the temperature dependence of renormalization of band energies, while we compare the results obtained with experiments in Section 3.7. We close the paper with a discussion and conclusions in Section 4.

2 Methods

2.1. Allen–Heine–Cardona theory

In this section, we briefly review the Allen–Heine–Cardona theory that describes phonon-induced band gap renormalization in semiconductor materials and present the procedure for self-consistent calculation of phonon-induced renormalization of band energies and their broadenings. The Hamiltonian of the system is given as

$$H = H_{\mathrm{el}} + H_{\mathrm{ph}} + H_{\mathrm{el\text{-}ph}}. \tag{1}$$

The first term

$$H_{\mathrm{el}} = \sum_{\boldsymbol{k}n} \varepsilon_{\boldsymbol{k}n} \hat{c}^{\dagger}_{\boldsymbol{k}n} \hat{c}_{\boldsymbol{k}n}, \tag{2}$$

describes the electrons, where $\hat{c}^{\dagger}_{\boldsymbol{k}n}$ and $\hat{c}_{\boldsymbol{k}n}$ are creation and annihilation operators, respectively, of an electron with wave vector $\boldsymbol{k}$ and electronic band n whose energy is $\varepsilon_{\boldsymbol{k}n}$. The second term

$$H_{\mathrm{ph}} = \sum_{\boldsymbol{q}\nu} \hbar\omega_{\boldsymbol{q}\nu} \left(\hat{a}^{\dagger}_{\boldsymbol{q}\nu} \hat{a}_{\boldsymbol{q}\nu} + \frac{1}{2} \right) \tag{3}$$

describes the phonons, where $\hat{a}^{\dagger}_{\boldsymbol{q}\nu}$ and $\hat{a}_{\boldsymbol{q}\nu}$ are phonon creation and annihilation operators, respectively, of a phonon with wave vector $\boldsymbol{q}$ and phonon mode ν whose angular frequency is $\omega_{\boldsymbol{q}\nu}$. The third term $H_{\mathrm{el\text{-}ph}}$ is the Hamiltonian of the electron–phonon interaction. By including the terms up to second order with respect to atomic displacements, it takes the form

$$\begin{aligned} H_{\mathrm{el\text{-}ph}} = {} & \frac{1}{N_q^{1/2}} \sum_{\boldsymbol{k}nm} \sum_{\boldsymbol{q}\nu} g^{\mathrm{Fan}}_{nm,\nu}(\boldsymbol{k},\boldsymbol{q}) \hat{c}^{\dagger}_{\mathbf{k}+\mathbf{q}m} \hat{c}_{\mathbf{k}n} (\hat{a}^{\dagger}_{-\mathbf{q}\nu} + \hat{a}_{\mathbf{q}\nu}) \\ & + \frac{1}{N_q} \sum_{\boldsymbol{k}nm} \sum_{\boldsymbol{q}\boldsymbol{q}'\nu\nu'} g^{\mathrm{DW}}_{nm,\nu\nu'}(\boldsymbol{k},\boldsymbol{q},\boldsymbol{q}') \hat{c}^{\dagger}_{\boldsymbol{k}+\boldsymbol{q}+\boldsymbol{q}'m} \hat{c}_{\mathbf{k}n} \\ & \times (\hat{a}^{\dagger}_{-\boldsymbol{q}\nu} + \hat{a}_{\boldsymbol{q}\nu})(\hat{a}^{\dagger}_{-\boldsymbol{q}'\nu'} + \hat{a}_{\boldsymbol{q}'\nu'}), \end{aligned} \tag{4}$$

where $g^{\mathrm{Fan}}_{\mathrm{nm},\nu}(\boldsymbol{k},\boldsymbol{q})$ and $g^{\mathrm{DW}}_{nm,\nu\nu'}(\boldsymbol{k},\boldsymbol{q},\boldsymbol{q}')$ are first order Fan and second order Debye–Waller matrix elements of electron–phonon interactions and N_q is the number of points in reciprocal space. The first order Fan matrix element is given as:

$$g^{\mathrm{Fan}}_{nm,\nu}(\boldsymbol{k},\boldsymbol{q}) = \sum_{\kappa\alpha}\left(\frac{\hbar}{2M_\kappa\omega_{\boldsymbol{q}\nu}}\right)^{1/2} \times \langle \boldsymbol{k}+\boldsymbol{q}n|\frac{\partial V_{\mathrm{SCF}}}{\partial R_{\kappa\alpha}(\boldsymbol{q})}|\boldsymbol{k}m\rangle \xi_{\kappa\alpha,\nu}(\boldsymbol{q}) e^{i\boldsymbol{q}\cdot\boldsymbol{R}_\kappa} \tag{5}$$

where $\frac{\partial V_{\mathrm{SCF}}}{\partial R_{\kappa\alpha}(\boldsymbol{q})}$ and $\xi_{\kappa\alpha,\nu}(\boldsymbol{q})$ are the perturbation of the Kohn–Sham potential due to nuclear displacement and the phonon eigenvector, respectively, describing the displacement of atom κ with mass M_κ at position $\boldsymbol{R}_\kappa$ in Cartesian direction α corresponding to phonon vector (mode) $\boldsymbol{q}$ (ν). The self-energy stemming from the first term in eqn (4) reads

$$\Sigma^{\mathrm{Fan}}_{\boldsymbol{k}n}(\omega,T) = \frac{1}{N_q}\sum_{m,\boldsymbol{q}\nu}\left|g^{\mathrm{Fan}}_{nm,\nu}(\boldsymbol{k},\boldsymbol{q})\right|^2 \times \left(\frac{n_{\boldsymbol{q}\nu}(T)+1-f_{\boldsymbol{k}+\boldsymbol{q}m}}{\omega-\varepsilon_{\boldsymbol{k}+\boldsymbol{q}m}-\omega_{\boldsymbol{q}\nu}+i\delta}+\frac{n_{\boldsymbol{q}\nu}(T)+f_{\boldsymbol{k}+\boldsymbol{q}m}}{\omega-\varepsilon_{\boldsymbol{k}+\boldsymbol{q}m}+\omega_{\boldsymbol{q}\nu}+i\delta}\right) \tag{6}$$

where $n_{\boldsymbol{q}\nu}(T)$ is the Bose–Einstein occupation factor at a temperature T, $f_{\boldsymbol{k}+\boldsymbol{q}m}$ is the Fermi–Dirac occupation factor and δ is a positive infinitesimal. The self-energy from the second term in eqn (4) takes the form

$$\Sigma^{\mathrm{DW}}_{\boldsymbol{k}nm}(T) = \frac{1}{N_q}\sum_{\mathbf{q}\nu} g^{\mathrm{DW}}_{nm,\nu\nu}(\boldsymbol{k},\boldsymbol{q},-\boldsymbol{q})(2n_{\boldsymbol{q}\nu}(T)+1), \tag{7}$$

where the second order electron–phonon matrix elements $g^{\mathrm{DW}}_{nm,\nu\nu}(\boldsymbol{k},\boldsymbol{q},-\boldsymbol{q})$ from eqn (7) can be expressed in terms of first order electron–phonon matrix elements by making use of translational invariance and rigid-ion approximation.[29,50]

The renormalization of energy levels can be calculated from the self-energies. Within the so-called on-the-mass-shell (OTMS) approximation,[51] the renormalized energy of band n at point $\boldsymbol{k}$ in the Brillouin zone is

$$E_{\boldsymbol{k}n}(T) = \varepsilon_{\boldsymbol{k}n} + \mathrm{Re}\Sigma^{\mathrm{Fan}}_{\boldsymbol{k}n}(\varepsilon_{\boldsymbol{k}n},T) + \mathrm{Re}\Sigma^{\mathrm{DW}}_{\boldsymbol{k}n}(T). \tag{8}$$

As discussed in the Introduction, there are challenges in obtaining converged results for band energy renormalization for bands other than VBM and CBM using eqn (6), (7) and (8). The convergence with respect to energy level broadening parameter δ as $\delta \to 0$ is a slow linear convergence[32] and hence one needs to use rather small δ, which in turn requires a large number of q-points in the summation. The broadening of the energy levels obtained from the imaginary part of the self-energy is on the order of 100 meV or more. It is therefore questionable if the $\delta \to 0$ limit is relevant at all. It is certainly more appropriate to self-consistently determine the renormalization and broadening of the energy levels. This can be achieved as follows. We note first that the terms $\frac{1}{\omega-\varepsilon_{\boldsymbol{k}+\boldsymbol{q}m}\pm\omega_{\boldsymbol{q}\nu}+i\delta}$ in eqn (6) represent the retarded Green's function of a bare electron $G^{(0)}_{\boldsymbol{k}+\boldsymbol{q}m}(\omega\pm\omega_{\boldsymbol{q}\nu})$, while eqn (6) is the self-energy in the so-called Migdal approximation. A more accurate approximation is the self-consistent Migdal approximation where the bare Green's function $G^{(0)}$ is replaced with the dressed Green's function G. Eqn (6) then takes the form

$$\Sigma^{\mathrm{Fan}}_{\boldsymbol{k}n}(\omega) = \frac{1}{N_q}\sum_{m,\boldsymbol{q}\nu}\left|g^{\mathrm{Fan}}_{nm,\nu}(\boldsymbol{k},\boldsymbol{q})\right|^2 \times \left[(n_{\boldsymbol{q}\nu}(T)+1-f_{\boldsymbol{k}+\boldsymbol{q}m})G_{\boldsymbol{k}+\boldsymbol{q}m}(\omega-\omega_{\boldsymbol{q}\nu}) + (n_{\boldsymbol{q}\nu}(T)+f_{\boldsymbol{k}+\boldsymbol{q}m})G_{\boldsymbol{k}+\boldsymbol{q}m}(\omega+\omega_{\boldsymbol{q}\nu})\right]. \tag{9}$$

One can in principle determine the Green's function, the self-energy, the spectral function and hence the energy level renormalization and broadening by self-consistently solving eqn (9) and the Dyson equation. However, this requires evaluation of all these quantities at wave vectors throughout the whole Brillouin zone in each step of the self-consistent procedure, which is a highly demanding computational task. A significant simplification that decouples different $\boldsymbol{k}n$ states can be made as follows. We first note that the Green's function in eqn (9) is given as

$$G_{\boldsymbol{k}+\boldsymbol{q}m}(\omega) = \frac{1}{\omega-\varepsilon_{\boldsymbol{k}+\boldsymbol{q}m}-\Sigma_{\boldsymbol{k}+\boldsymbol{q}m}(\omega)}. \tag{10}$$

We then make a replacement $\Sigma_{\boldsymbol{k}+\boldsymbol{q}m}(\omega) \to \Sigma_{\boldsymbol{k}n}(\omega)$ in the previous equation (where $\Sigma_{\boldsymbol{k}n}(\omega) = \Sigma^{\mathrm{Fan}}_{\boldsymbol{k}n}(\omega) + \Sigma^{\mathrm{DW}}_{\boldsymbol{k}n}$). This replacement is justified by the fact that the dominant contribution to the sum in eqn (9) comes from the terms in the sum that have $m = n$ and a small value of $\boldsymbol{q}$. For such terms $\Sigma_{\boldsymbol{k}+\boldsymbol{q}m}(\omega) \approx \Sigma_{\boldsymbol{k}n}(\omega)$. It is therefore appropriate to replace the self-energy for all terms in the sum with the self-energy of the dominant terms. The expression for $\Sigma^{\mathrm{Fan}}_{\boldsymbol{k}n}$ then reads

$$\Sigma^{\mathrm{Fan}}_{\boldsymbol{k}n}(\omega) = \frac{1}{N_q}\sum_{m,\boldsymbol{q}\nu}\left|g^{\mathrm{Fan}}_{nm,\nu}(\boldsymbol{k},\boldsymbol{q})\right|^2 \times \left(\frac{n_{\boldsymbol{q}\nu}(T)+1-f_{\boldsymbol{k}+\boldsymbol{q}m}}{\omega-\varepsilon_{\boldsymbol{k}+\boldsymbol{q}m}-\omega_{\boldsymbol{q}\nu}-\Sigma_{\boldsymbol{k}n}(\omega-\omega_{\boldsymbol{q}\nu})} + \frac{n_{\boldsymbol{q}\nu}(T)+f_{\boldsymbol{k}+\boldsymbol{q}m}}{\omega-\varepsilon_{\boldsymbol{k}+\boldsymbol{q}m}+\omega_{\boldsymbol{q}\nu}-\Sigma_{\boldsymbol{k}n}(\omega+\omega_{\boldsymbol{q}\nu})}\right). \tag{11}$$

It is important to note that eqn (11) does not contain the self-energies of the states other than $\boldsymbol{k}n$, which is a consequence of the approximation used for $\Sigma_{\boldsymbol{k}+\boldsymbol{q}m}(\omega)$. The self-energy $\Sigma^{\mathrm{Fan}}_{\boldsymbol{k}n}(\omega)$ can now be obtained using a self-consistent procedure as follows. One starts with an initial guess for $\Sigma_{\boldsymbol{k}n}(\omega)$ and evaluates $\Sigma^{\mathrm{Fan}}_{\boldsymbol{k}n}(\omega)$ using eqn (11) and the total self-energy as the sum of the Fan and the Debye–Waller term. A new value of $\Sigma^{\mathrm{Fan}}_{\boldsymbol{k}n}(\omega)$ is then calculated again using eqn (11) and the procedure is repeated until the convergence of $\Sigma^{\mathrm{Fan}}_{\boldsymbol{k}n}(\omega)$ is reached. The spectral function is then obtained as

$$A_{\boldsymbol{k}n}(\omega) = -\frac{1}{\pi}\mathrm{Im}\frac{1}{\omega-\varepsilon_{\boldsymbol{k}n}-\Sigma_{\boldsymbol{k}n}(\omega)} \tag{12}$$

and the renormalized energy $E_{\boldsymbol{k}n}$ is obtained as the energy $\omega_{\max}$ at which the spectral function reaches a maximum. The spectral function $A_{\boldsymbol{k}n}(\omega)$ represents the probability density that an

electron of momentum $\boldsymbol{k}$ in band n has the energy ω. We note that our procedure for evaluation of renormalized energies is similar in spirit to the procedure suggested in ref. 50 (Eq. 166 therein), where approximations that also lead to decoupling of different $\boldsymbol{kn}$ states were used. The difference between these procedures is that we consider the full frequency dependence of self-energies rather than the energy of the renormalized state and its broadening only.

In Section 3, we will present the results obtained using both of the mentioned approaches. The results obtained from eqn (8) with self-energies given by eqn (6) and (7) will be referred to as OTMS results, while the results obtained using eqn (12) and self-consistent solution of eqn (11) will be referred to as the self-consistent procedure (SCP) results.

We note that it is rather challenging to treat the electron–phonon interaction in real materials beyond the approximations mentioned. These approximations all contain the assumption that the electron–phonon interaction is not too strong. Full nonperturbative treatment of electron–phonon interactions has so far only been performed for model Hamiltonians, such as the Holstein or Fröhlich model. In a recent study of the Holstein model[52] it was shown that for relatively weak electron–phonon coupling the spectral functions in the Migdal and self-consistent Migdal approximation are similar to the spectral functions obtained using more advanced approaches, such as the cumulant expansion method and the dynamical mean field theory. Moreover, self-consistent Migdal approximation performs overall only somewhat worse than the cumulant expansion method, which is not the case for the Migdal approximation that gives inaccurate results starting from moderate values of electron–phonon coupling. Based on the knowledge gained from the Holstein model, we can infer about the accuracy of the OTMS and SCP results for real perovskite materials. It is expected that the SCP results which are based on the self-consistent Migdal approximation should in principle be more accurate than the OTMS results which are based on the Migdal approximation. On the other hand, it will be shown in Section 3 that OTMS and SCP results are not too different. This suggests that we are in the regime where electron–phonon coupling is relatively weak, where it is appropriate to apply either the Migdal or the self-consistent Migdal approximation.

We also note that in both the OTMS and SCP approach, as typically done in the literature,[50] we were evaluating only the diagonal (intraband) self-energies $\Sigma_{\boldsymbol{kn}}(\omega)$ and not the off-diagonal (interband) self-energies $\Sigma_{\boldsymbol{knm}}(\omega)$ (with $n \neq m$). In the case of the OTMS approach one is actually interested in diagonal self-energies only because they directly determine the band energy renormalization, see eqn (8). On the other hand, introduction of off-diagonal self-energies in the SCP approach would strongly increase the computational burden of the whole procedure. On physical grounds, it should be noted that band energy renormalization due to interband electron–phonon scattering processes is already described by the diagonal self-energies [*via* the $m \neq n$ terms in the sum in eqn (6)]. Hence, inclusion of non-diagonal self-energies would represent only a higher order effect.

2.2. The self-consistent phonon method

Since the standard approach based on the use of harmonic approximation and DFPT is not sufficient to describe phonons in cubic $CsPbX_3$ materials, a more sophisticated approach is needed. We therefore use the self-consistent phonon method following the methodology and the implementation of ref. 53. In this section, we briefly review the main ideas of the method and its implementation.

In the Born–Oppenheimer approximation, the dynamics of lattice ions is described by the Hamiltonian $H = T + U$, where T is their kinetic energy, while U is the potential energy which is a function of the displacements from the equilibrium position. The potential energy can be expanded as $U = U_0 + U_2 + U_3 + U_4 + \ldots$, where the term U_n is of n-th order with respect to atomic displacements and the term U_1 is missing because it contains forces which are zero in equilibrium. Keeping the terms U_0 and U_2 only is the standard harmonic approximation. In this case, phonon frequencies are obtained from diagonalization of the corresponding dynamical matrix.

To obtain the phonon frequencies in a general case when the terms beyond U_2 are included, one can make use of many body Green's function theory. The Hamiltonian is divided into $H = H_0 + H_1$ where $H_0 = T + U_0 + U_2$ is the harmonic part of the Hamiltonian whose solution is known, while the anharmonic terms $H_1 = U_3 + U_4 + \ldots$ constitute the interaction part. The phonon Green's function G_0 for the Hamiltonian H_0 is known, while the Dyson equation relates G_0, the phonon Green's function G of the Hamiltonian H and the self-energy Σ. The Dyson equation has to be complemented with the equation for self-energy. The self-energy is in principle given by a diagrammatic expansion involving an infinite number of Feynman diagrams.

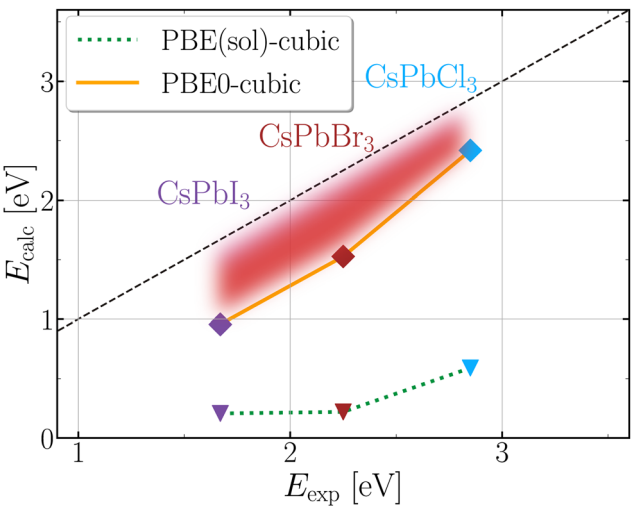

Fig. 1 Comparison of experimental and theoretical results for the electronic gap for $CsPbX_3$ (X = Cl, Br or I) calculated without taking temperature effects into account. The line $x = y$ represents the experimental results for the lowest temperature of the cubic structure. The symbols denote calculated values for the cubic structure using the PBE (PBEsol) functional for $CsPbI_3$ ($CsPbCl_3$ and $CsPbBr_3$) (inverted triangles) and PBE0 functional modified to satisfy the Koopmans condition (diamonds).

In practice one selects only the most relevant diagrams for the problem at hand. To obtain the renormalized phonon frequencies, it turns out that the most relevant diagram is the loop diagram originating from the quartic term U_4 (shown in Fig. 1(a) in ref. 53). The Green's function and the self-energy can then be found self-consistently and the renormalized phonon frequency is determined from the pole of the Green's function.

To perform the calculation within the SCPH method, one also has to obtain all relevant force constants that appear in the U_n terms in the expansion of U. The second order force constants are obtained from supercell density functional theory calculations and the finite displacement method. While the finite displacement method can in principle be used to obtain higher order force constants, a different strategy yields more stable results for the force constants. Namely, finite-temperature *ab-initio* molecular dynamics calculations are performed to obtain various atomic configurations and the corresponding total energy and forces in these configurations. The force constants that appear in anharmonic terms in U are then fitted to the data obtained, where great care has to be taken to avoid overfitting the data. Details of the full calculation protocol are reported in Section 3.4.

3. Results and calculation details

3.1. Density functional theory calculations with semilocal functionals

As a first step, we performed density functional theory calculations of the electronic structure of the $CsPbX_3$ materials using the semilocal PBEsol[54] functional in the case of $CsPbCl_3$ and $CsPbBr_3$, while the PBE functional[55] was used in the case of $CsPbI_3$. Calculations were performed using the plane-wave code Quantum Espresso.[56,57] Norm-conserving fully relativistic pseudopotentials[58,59] were used to treat the effect of core electrons. The effects of spin–orbit interaction were included. The wave functions were represented on a $4 \times 4 \times 4$ reciprocal space k- point grid with a kinetic energy cutoff of 50 Ry for $CsPbCl_3$ and $CsPbBr_3$ and a cutoff of 40 Ry for $CsPbI_3$. We note that a different functional was used for $CsPbI_3$ because the gap obtained using the PBEsol functional at the optimized lattice constant obtained from this functional is nearly zero, which prevents the use of this functional in further DFPT calculations.

The optimized lattice constants for the cubic structure obtained from the calculations are respectively 10.6 a_0, 11.1 a_0 and 12.1 a_0 (in units of first Bohr radius a_0 for $CsPbCl_3$, $CsPbBr_3$ and $CsPbI_3$). We note that the lattice constants obtained for $CsPbCl_3$ and $CsPbBr_3$ are in excellent agreement with the experimental lattice constant at the lowest temperature where the material exhibits a cubic structure (which are 10.59 a_0 at 320 K for $CsPbCl_3$ and 11.10 a_0 at 403 K for $CsPbBr_3$, see ref. 42). This agreement is reasonable in the case of $CsPbI_3$ (experimental lattice constant is 11.67 a_0 at 300 K, see ref. 60) and would be better if the PBEsol functional, which gives the lattice constant of 11.8 a_0, was used. However, as noted before, the use of PBEsol functional for $CsPbI_3$ closes the gap of the material and hence this functional was not used for $CsPbI_3$. While the agreements obtained are somewhat fortuitous because standard DFT calculations are performed at zero temperature, the lattice constants obtained were used in further calculations because they are in good agreement with experimental lattice constants. The direct band gaps at the R-point obtained for $CsPbCl_3$, $CsPbBr_3$ and $CsPbI_3$ are respectively 0.59 eV, 0.22 eV and 0.21 eV. These gaps are well below the experimental band gaps, see Fig. 1. This is expected because it is well known that semilocal functionals underestimate the band gap.[61]

We also performed calculations for the orthorhombic structure of the $CsPbX_3$ material that is stable at zero temperature. The coordinates of the initial structure were taken from The Materials Project website[62] as structures numbered 675 524, 567 629, and 1 120 768 for $CsPbCl_3$, $CsPbBr_3$ and $CsPbI_3$, respectively, and were further relaxed (cif files for the initial and relaxed structures are included in the ESI†). The $CsPbCl_3$ orthorhombic structure corresponds to space group number 38 (*Amm*2) with 10 atoms per primitive cell, while $CsPbBr_3$ and $CsPbI_3$ orthorhombic structures both correspond to space group number 62 (*Pmna*) with 20 atoms per primitive cell. The same density functionals, k-point grid dimension, and the plane wave kinetic energy cutoff were used as in the case of the cubic structure. We used the PBEsol functional for optimization of atomic coordinates and dimensions of the unit cell for all three materials (since the gap of orthorhombic $CsPbI_3$ does not close when the PBEsol functional is used in the calculation). The calculations were performed using the Quantum Espresso code[56,57] with variable cell relaxation option. The band gaps obtained for orthorhombic $CsPbCl_3$, $CsPbBr_3$ and $CsPbI_3$ are respectively 1.1 eV, 0.83 eV and 0.62 eV.

3.2. Hybrid functional calculations

To overcome the band gap problem of semilocal functionals, we performed the electronic structure calculation using a hybrid functional. In particular, we make use of the PBE0 functional[63,64] whose parameter α is chosen to satisfy the Koopmans condition. We used the values of α for $CsPbX_3$ materials that were calculated in ref. 65. Hybrid functional calculations were also performed using the Quantum Espresso code.[56,57,66] The calculation parameters common to standard semilocal DFT calculation were set to the same values. In addition, for cubic structures a $4 \times 4 \times 4$ reciprocal q- points grid was used to sample the Fock operator and the Gygi-Baldereschi method[67] was used to treat the singularity at $q \rightarrow 0$. For orthorhombic structures that have a larger unit cell than cubic structures, $3 \times 3 \times 2$ k- and q-points grids were used in the case of $CsPbBr_3$ and $CsPbI_3$, while we used $4 \times 4 \times 4$ k- and q-points grids for $CsPbCl_3$.

In hybrid functional calculations, we obtain the values of 2.4 eV, 1.5 eV and 0.96 eV for the band gap of cubic $CsPbCl_3$, $CsPbBr_3$ and $CsPbI_3$. These values are closer to experimental values than the values obtained from semilocal functionals. However, these values are still smaller than the experimental band gaps, see Fig. 1. This result indicates that temperature effects might play a significant role and that it is important to investigate them.

In the case of orthorhombic structures, we obtain band gaps of 3.0 eV, 2.4 eV and 1.5 eV, respectively for $CsPbCl_3$, $CsPbBr_3$

and $CsPbI_3$. These results are in good agreement with experimental gaps of the low-temperature orthorhombic structures, which are 3.056 eV for $CsPbCl_3$ (ref. 68), 2.25 eV for $CsPbBr_3$ (ref. 69) and 1.72 eV for $CsPbI_3$ (ref. 70).

3.3. Density functional perturbation theory calculations of the phonon band structure

To take into account the effect of temperature on the electronic band structure, it is necessary to calculate the phonon frequencies and eigenvectors and the electron–phonon coupling constants. For this reason, we perform DFPT calculations of phonons in harmonic approximation. The same density functional, kinetic energy cutoff and the reciprocal space k-point grid were used as in DFT calculations. The calculations were performed using the ABINIT code.[71–74]

The phonon band structures obtained from calculations for cubic $CsPbX_3$ materials are presented in Fig. 2 (dashed line), where phonons with imaginary frequencies are presented using negative values. Since the cubic structure is not stable at zero temperature, there is a significant number of phonon modes with imaginary frequencies. It is therefore a challenge to include such modes in the calculation of phonon-induced band renormalization.

3.4. Calculation of phonon band structure within the self-consistent phonon method

Standard DFPT calculations of the phonon band structure assume zero temperature and the harmonic approximation. As discussed in Section 3.3, this leads to phonon modes with imaginary frequencies for the cubic structure. To overcome this issue, one has to take into account the anharmonic effects and the effects of temperature. This can be naturally accomplished using the self-consistent phonon method.[53,75]

The calculations based on the SCPH method were performed using the following protocol. The calculations were performed using the ALAMODE code,[53,76] while DFT calculations and *ab-initio* molecular dynamics simulations were performed using the Quantum Espresso code.[56,57] One first has to obtain all relevant force constants. (i) Harmonic force constants were obtained by performing the DFT calculation of $2 \times 2 \times 2$ cubic supercells, where a shifted $4 \times 4 \times 4$ k-point grid was employed. Other parameters of the DFT calculation are the same as in Section 3.1. An atom is displaced by 0.01 Å in a certain direction and new atomic forces are calculated. The harmonic force constants are then obtained from these forces using a least squares fit implemented in the ALAMODE code. (ii) To obtain anharmonic force constants, we first generate representative atomic structures which will be used for evaluation of forces and subsequent force constant fitting. We perform 2000 steps of *NVT ab-initio* molecular dynamics at a temperature of 500 K with a timestep of 2 fs for a $2 \times 2 \times 2$ cubic supercell. To gain computational speed in this calculation we reduce the kinetic energy cut-off to 30 Ry and we use the k-point grid consisting of the Γ point only. This is justified in this place, since the goal is only to obtain configurations where atoms are displaced from their equilibrium positions, rather than to extract physical quantities from the molecular dynamics simulation. We then select 30 snapshots from the simulation which are equally spaced from timestep 500 to timestep 2000. (iii) For the snapshots obtained, we additionally displace each atom by up to 0.1 Å in each direction. For these 30 snapshots, we accurately compute the atomic forces from DFT by using 50 Ry kinetic energy cutoff and a shifted $4 \times 4 \times 4$ k-point grid. (iv) With the forces obtained we perform fitting of the force constants using the adaptive LASSO method, following ref. 53 and 77. In the fitting, we put a restriction that fourth order force constants are zero beyond third neighbor atoms, that the fifth and sixth order constants are nonzero for nearest neighbors only and that higher order constants are equal to zero. (v) The force constants obtained in the previous step are used as an input for the SCPH method calculation. In the SCPH method calculation, we neglect the off-diagonal elements of the self-energy and use a $4 \times 4 \times 4$ grid to represent the self-energy in reciprocal space.

The phonon band structure obtained from the SCPH method is presented in Fig. 2. We obtain phonon frequencies that are non-negative throughout the whole Brillouin zone. We also find that with an increase of temperature, a small but non negligible shift in frequencies is present. These shifts are negative for the three highest bands and positive for the rest. We will see in Section 3.5 that these shifts are large enough to have a significant contribution to the renormalization of electronic bands.

3.5. Band energy renormalization calculations using the OTMS approach

In this section, we present the results for band energy renormalization calculations of cubic $CsPbX_3$ materials obtained using the OTMS approach. The calculations, in this and in the following section, were performed using our own code which takes DFPT results from the ABINIT code.[71] These results include variations of the Kohn–Sham potential with respect to ionic displacements and the interatomic force constants, that are then used to calculate first and second order matrix elements of electron–phonon interaction. In all band energy renormalization calculations bare band energies that appear in eqn (6) and (7) were taken from DFT calculations reported in Section 3.1.

To make sure that the results obtained are reliable one has to take enough q-points in the summations in eqn (6) and (7) and one has to check the sensitivity of the results to the value of the parameter δ in eqn (6). It has been shown in ref. 32 that the band energy renormalization for polar materials converges as $\frac{1}{N_q}$ with the number of points N_q and that a Lorentzian type convergence for CBM and VBM energies of polar materials is obtained while decreasing δ.

In ref. 22 phonon modes obtained within the harmonic approximation were used, however, the phonon modes with imaginary frequencies were simply disregarded. In this approach it remains unclear whether one should disregard only the phonons at certain q-points where their frequency becomes imaginary or one should disregard the whole phonon mode that produces an imaginary frequency in at least one

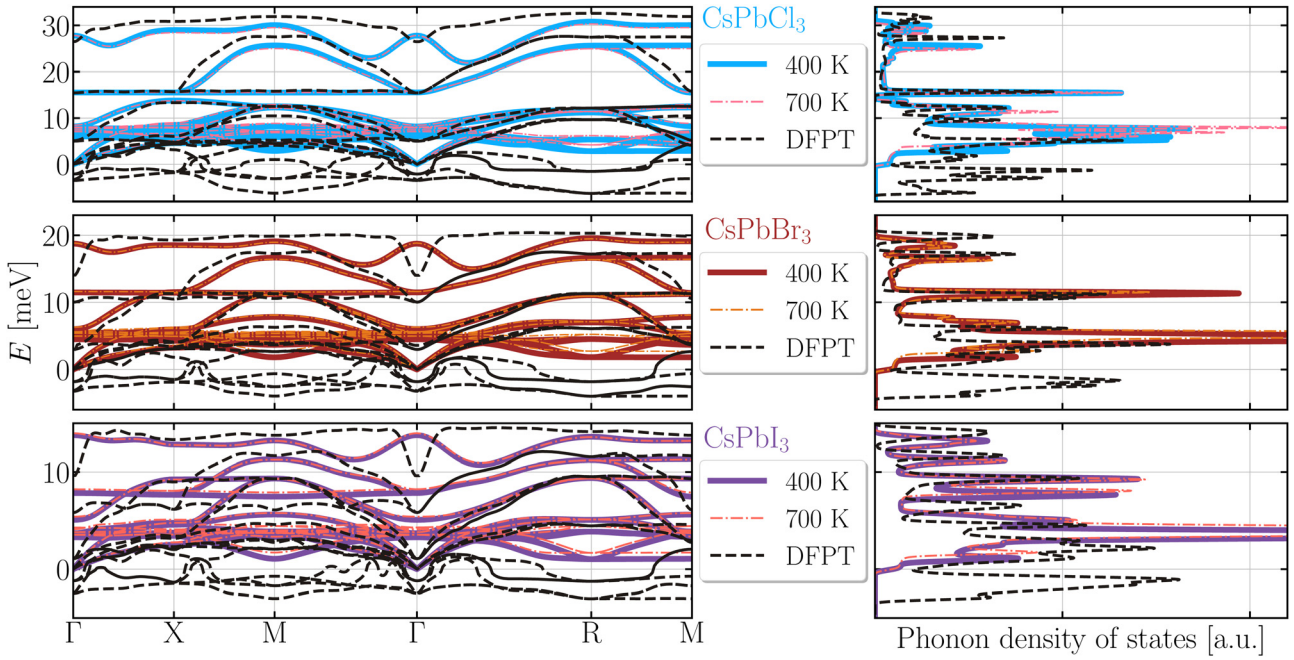

Fig. 2 Phonon dispersion (left column) and phonon density of states (in arbitrary units) for $CsPbX_3$ (X = Cl, Br or I, in rows from top to bottom) obtained using the SCPH method at T = 400 K (solid line) and T = 700 K (dot-dashed line), as well as using DFPT with harmonic approximation (dashed line).

point in the Brillouin zone. To understand whether the approach where imaginary phonon frequencies are discarded can provide reasonably good results, we performed the convergence tests with respect to N_q and δ in three cases: (i) assuming phonon frequencies from DFPT and disregarding the contribution from phonons with imaginary frequencies; (ii) assuming phonon frequencies from DFPT and disregarding the contribution from the whole phonon bands that exhibit imaginary frequencies at any q-point; (iii) assuming phonon frequencies obtained from the SCPH method. These three cases will be referred to as cases (i), (ii) and (iii) in what follows.

In Fig. 3 we present the results for band gap renormalization obtained using the OTMS approach in each of these cases. We see that in case (i) the behavior with respect to N_q is not convergent and one obtains unphysically large band gap renormalizations. In this case several phonon bands cross zero energy at several different points in the Brillouin zone (see the left column in Fig. 2), which leads to divergence of Fan matrix elements due to the $\omega_{q\nu}$ term in the denominator, see eqn (5). The convergence is better in case (ii) when such phonon bands are simply disregarded, however one obtains band gap renormalization which is underestimated with respect to case (iii). In case (iii), we obtain convergence with respect to δ and N_q.

In Fig. 4 we decompose the CBM and VBM renormalization into contributions from phonons of different energies. Most of the contributions come from the region where the density of phonon states is the highest and these contributions come mostly from lower bands. Lower energy phonons also tend to have larger electron–phonon coupling matrix elements due to the $\omega_{q\nu}$ term in the denominator in eqn (5). This fact also contributes to prevalent contribution of lower energy phonons to band energy renormalization. Since most of these lower energy phonons turn into imaginary frequency phonons within the DFPT calculation, the results obtained in case (ii) are underestimated in comparison to the results in case (iii). We also analyzed the contributions of the first order Fan and second order Debye–Waller terms in eqn (8) to band energy renormalization. In line with previous literature results for other materials,[29,78] we find that these two terms have opposite signs and that both of these terms have significant absolute values, see Fig. S22 in the ESI.† For these reasons, accurate calculation of each of these terms is necessary to obtain reliable final results for band energy renormalization.

Next, we discuss the linearity of the temperature dependence of the band gap renormalization. One can notice from eqn (8) [with self-energies given by eqn (6) and (7)] that the temperature dependence originates only from the Bose term in these equations. When phonon energies are small the temperature dependence of the Bose term is linear. As a consequence, the temperature dependence of band energy renormalization is also linear in case (ii), as can be seen in Fig. 4. On the other hand, in case (iii) the phonon frequencies also depend on temperature and the temperature dependence of the band gap is determined by the ratio of the Bose term (which contains temperature dependent phonon frequency) and the phonon frequency [which comes from the Fan matrix element, see eqn (5) and (6)]. The Bose term increases the gap with temperature as in case (ii), however, most of the temperature dependent frequencies (especially the ones where the density of phonon states is the largest) increase with temperature. They then tend to decrease the renormalization, which leads to nonlinear dependence in case (iii), as seen in Fig. 4.

Our final result for temperature dependence of the band gap of the investigated materials using the OTMS approach is among the results presented in Fig. 5. For the reasons

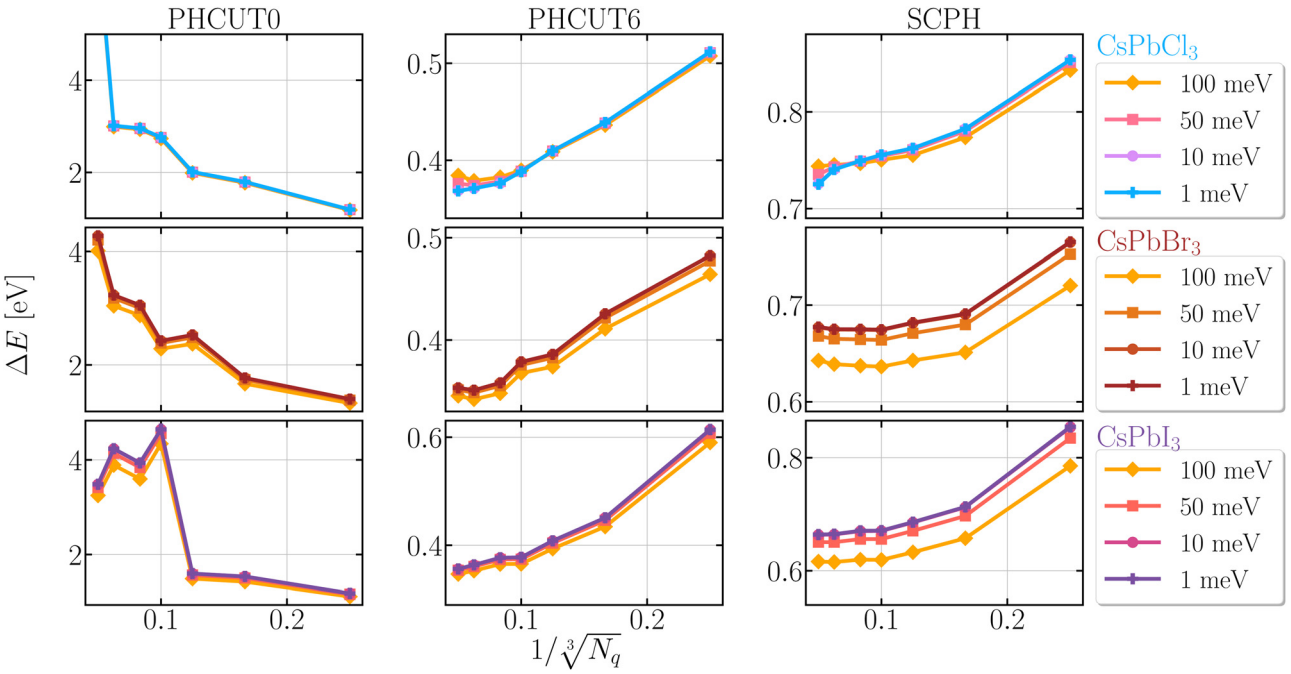

Fig. 3 Dependence of band gap renormalization obtained using the OTMS approach on the number of q-points N_q and on the small parameter δ (whose value is specified in the legend) for $CsPbX_3$ (X = Cl, Br or I, in rows from top to bottom) materials at T = 400 K. The column labeled as PHCUT0 denotes the result obtained assuming phonon frequencies from DFPT and disregarding the contribution from phonons with imaginary frequencies [case (i) discussed in the text], while the column labeled as PHCUT6 denotes the results obtained assuming phonon frequencies from DFPT and disregarding the contribution from the whole bands that exhibit imaginary frequencies at any q-point [case (ii) in the text]. The column labeled as SCPH denotes the result obtained by taking phonon frequencies from the SCPH method [case (iii) in the text].

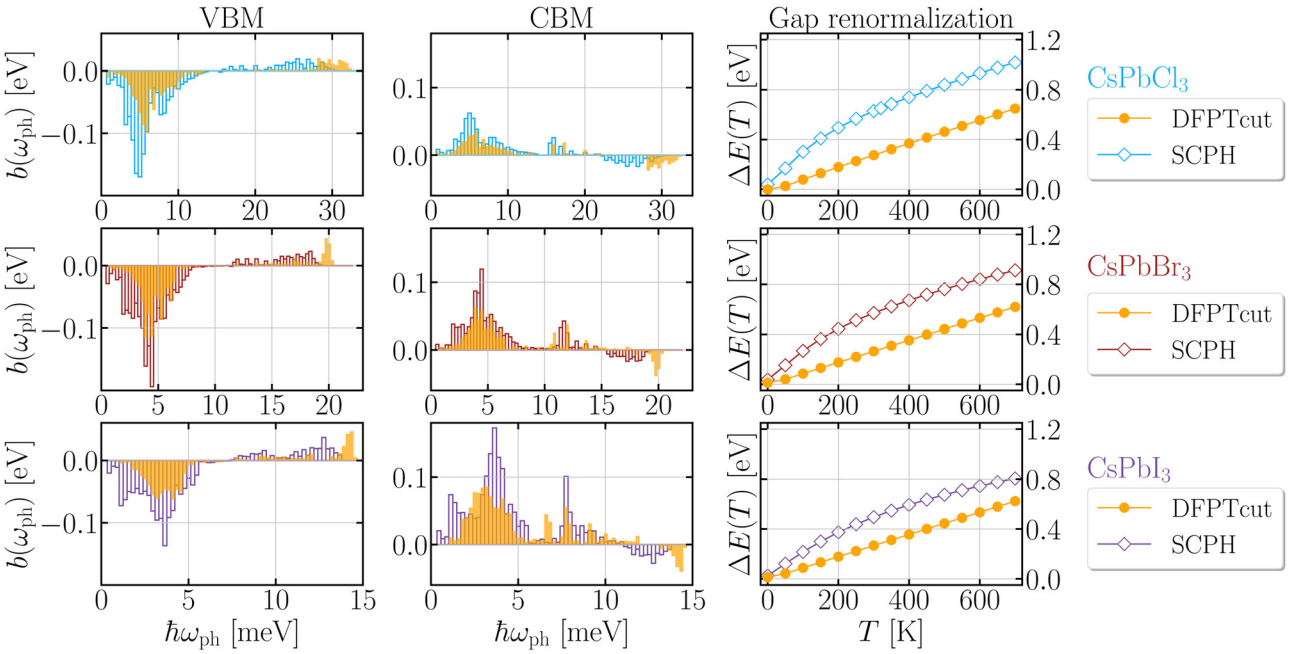

Fig. 4 Contributions from phonons of different frequencies to VBM (left column) and CBM (middle column) renormalization at T = 400 K and temperature dependent gap renormalization (right column) for $CsPbX_3$ (X = Cl, Br or I, in rows from top to bottom) obtained using the OTMS approach. The results in case (ii) are shown as filled bins, while the results in case (iii) are shown as transparent bins. The value of each bin $b(\omega_i)$ represents the contribution of all phonons with frequencies from the range $(\omega_i - \Delta\omega/2, \omega_i + \Delta\omega/2)$ to band energy renormalization, so that $\Delta E_{\boldsymbol{k}n} = \Sigma_i b(\omega_i)$. Filled circles in the right column correspond to case (ii), while empty deltoids correspond to case (iii).

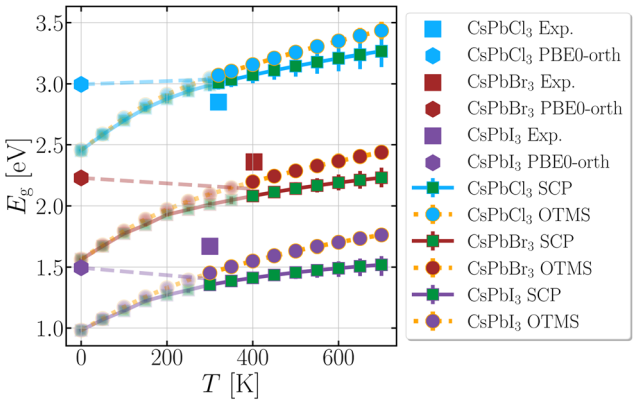

Fig. 5 Temperature dependence of the calculated band gap of $CsPbX_3$ materials (X = Cl, Br or I, from top to bottom). The calculated band gap of orthorhombic structures at zero temperature is represented by hexagons, while the band gaps of the cubic structure calculated using the SCP (OTMS) approach are represented by full (dotted) lines and two color squares (circles). Experimental results are represented by single color squares with the values of 2.85 eV (ref. 79), 2.36 eV (ref. 80), and 1.67 eV (ref. 81) respectively, at temperatures of 320 K, 403 K and 300 K, respectively, for $CsPbCl_3$, $CsPbBr_3$ and $CsPbI_3$, respectively. Dashed lines are used as a guide to the eye to connect the zero temperature result for the band gap of the orthorhombic structure with the result at the lowest temperature where the material exhibits a cubic structure.

previously discussed, these results and all subsequent results were obtained by taking the phonon frequencies obtained from the calculation based on the SCPH method. In all calculations reported in this and the next section renormalized band energies were obtained by adding the phonon-induced renormalization to the band energies calculated using the hybrid functional as described in Section 3.2. The results at temperatures lower than the temperatures where the cubic structure exists are blurred.

The OTMS approach can be used in principle to determine the renormalization of bands other than the CBM and the VBM. As discussed in the introduction and Section 2.1, band renormalization for other bands exhibits a slow linear convergence with respect to δ when $\delta \to 0$ in contrast to Lorentzian convergence of CBM and VBM. As a consequence, one has to go to rather small values of δ to reach convergence. However, for small values of δ, large values of N_q are needed, which introduces a large computational burden. We illustrate this behavior in Fig. S1, Fig. S9 and Fig. S14 in the ESI,† for the cases of $CsPbCl_3$, $CsPbBr_3$, and $CsPbI_3$, respectively. For larger values of δ (100 meV and 50 meV in the figure) good convergence with respect to N_q is achieved but the result still depends on δ and one therefore needs to go to smaller δ to achieve convergence with respect to δ. However, for smaller values of δ (10 meV and 1 meV), convergence with respect to N_q could not be achieved with grids up to $20 \times 20 \times 20$. As also discussed in the introduction and Section 2.1, it is questionable whether the limit $\delta \to 0$ of the energy level broadening parameter gives accurate results given the fact that the energy levels of higher bands can exhibit significant broadening. For all these reasons, it is more desirable to self-consistently determine the energy level broadening. These results are the subject of Section 3.6.

3.6. Band energy renormalization calculations using the SCP approach

We now present the results for band energy renormalization obtained using the SCP approach. The frequency dependence of the self-energy and the spectral function for several bands at the R point in the case of the $CsPbBr_3$ material at $T = 400$ K is presented in Fig. 6 (the same results for $CsPbCl_3$ and $CsPbI_3$ are presented respectively in Fig. S4 and S17 in the ESI†). We denote the bands in ascending order of energies at the R point as VBM4 (2×), VBM3 (4×), VBM2 (2×), VBM1 (4×), VBM (2×), CBM (2×), CBM1 (4×), CBM2 (2×), CBM3 (2×), and CBM4 (4×), where the numbers in brackets denote their degeneracy. The spectral functions of the CBM and VBM are relatively narrow and symmetric, while the spectral functions of other bands (CBM1 and VBM1 in Fig. 6 and CBM2-4 and VBM2-4 in Fig. S10 and S12 in the ESI† in the case of $CsPbBr_3$, see also Fig. S2, S4 and S6 (ESI†) for $CsPbCl_3$, as well as Fig. S15, S17 and S19 (ESI†) for the $CsPbI_3$ material) are wider and somewhat asymmetric. This result confirms that it was necessary to go beyond the OTMS approach in the $\delta \to 0$ limit to obtain accurate results for bands other than the CBM and VBM. There is even a difference between the OTMS and SCP result for CBM and VBM which leads to a band gap difference between the two approaches on the order of 100 meV at $T = 400$ K (see Section 3.7 for more details).

In Fig. 7 we demonstrate that convergence with respect to N_q was achieved with a $20 \times 20 \times 20$ grid. Convergence is achieved both for the real part of self-energy that corresponds to band energy renormalization and for the imaginary part of the self-energy that is related to energy level broadening. As expected, it is easier to reach convergence for energy levels that exhibit larger broadening, that is, for states other than the CBM and VBM (Fig. 7 and Fig. S11 and S13 in the ESI,† see also Fig. S3, S5 and S7 (ESI†) for the $CsPbCl_3$ material, as well as Fig. S16, S18 and S20 (ESI†) for the $CsPbI_3$ material). The CBM and VBM states exhibit the lowest broadening due to the fact that single phonon emission processes from these states are not possible. Hence the total scattering rate from these states, which is related to energy level broadening, is determined by phonon absorption processes only. On the other hand, for bands higher than the CBM (lower than the VBM), there is always a nearby other band below (above) it to which phonon emission is also possible. Hence, these states exhibit higher electron–phonon scattering rates than the CBM and VBM, which leads to larger broadening of these states.

The final results for temperature dependence of band energies and the imaginary part of self-energies (that are related to energy level broadening) at the R point for the $CsPbBr_3$ material are presented in Fig. 8. The same results for $CsPbCl_3$ and $CsPbI_3$ are presented in Fig. S8 and S21, respectively, in the ESI.† The results indicate that the temperature dependence of band energies is most pronounced for the CBM and the VBM and that it is much weaker for the other bands. The energy level broadenings increase as the temperature increases and this dependence is nearly linear for most bands.

The temperature dependence of the band gap calculated within the SCP approach is presented in Fig. 5. The results

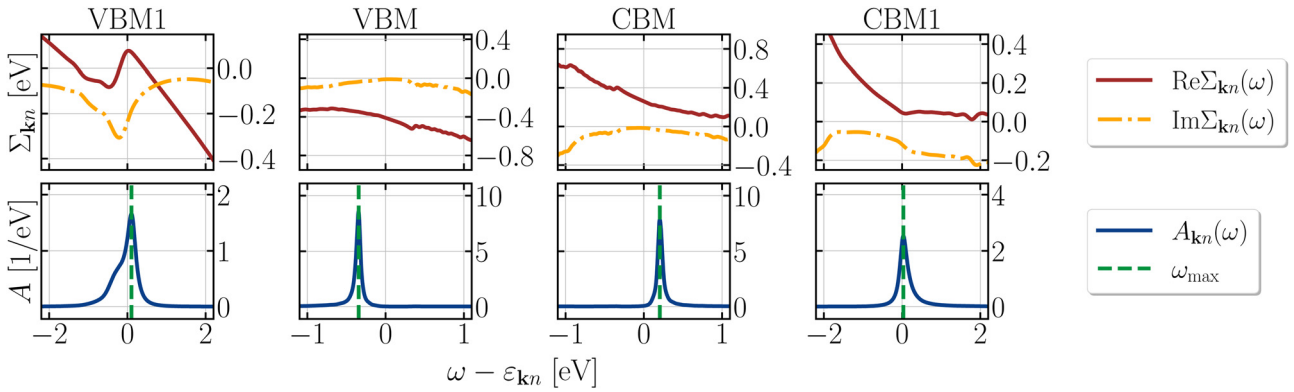

Fig. 6 The frequency dependence of the self-energy and the spectral function for bands VBM1, VBM, CBM and CBM1 at the R point in the case of the $CsPbBr_3$ material at T = 400 K.

suggest that the gap renormalization and the band gap are somewhat smaller in the SCP approach than in the case of the OTMS approach. The largest difference between the two approaches is at the highest temperatures. This difference originates from the fact that the spectral function within the SCP approach takes a relatively broad asymmetric shape at these temperatures, while the OTMS approach inherently assumes a narrow symmetric Lorentzian spectral function. A comparison of the temperature dependence of the band gap within the SCP approach with experiments will be discussed in Section 3.7.

To gain insight into the effect of temperature on band energies throughout the Brillouin zone, we also performed SCP calculations of the spectral function and band energy renormalization at points Γ, X and M in the Brillouin zone for the three investigated materials. The results are presented in Fig. S23–S85 in the ESI.† All energy levels at X and M points are twofold degenerate, while the degeneracy of the bands at Γ is as follows: VBM4 (4×), VBM3 (2×), VBM2 (4×), VBM1 (2×), VBM (4×), CBM (2×), CBM1 (4×), CBM2 (2×), CBM3 (2×), and CBM4 (4×). We can see (Fig. S29, S36, S43, S50, S57, S64, S71, S78, and S85 in the ESI†) that in most cases the real and the imaginary part of the self-energy are smooth and continuous when the temperature changes. The exceptions are VBM2 for $CsPbCl_3$ between T = 50 K and T = 100 K, and VBM1 for $CsPbBr_3$ and $CsPbI_3$ between T = 550 K and T = 600 K, all three at the X point (Fig. S50, S57, and S64 in the ESI,† respectively). In these cases, the spectral function has two competing maxima (see Fig. S87–S89 in the ESI†) that are well inside the range of its half-width and the change in temperature changes the dominant maximum. It should be noted that for all of the examined points, the changes in state energies are such that the band gap remains determined by the R point VBM and CBM. However, an increase in the temperature can change the ordering of the bands: at certain points in the Brillouin zone some neighbouring bands below (above) the VBM1 (CBM1) will swap places with respect to their order obtained from the PBE0 functional calculations. Nevertheless, for simplicity, we label the bands based on their ordering obtained from zero temperature PBE0 functional calculations. When it comes to energy level broadening, it turns out that it is lowest for the VBM and CBM bands (with the imaginary part of the self-energy well below 100 meV for these states and significantly above 100 meV for the other states), as in the case of the R point. The CBM and VBM states at these points are well separated in energy from the other bands (see the material band structures in Fig. S86 in the ESI†) which restricts the phase space for electron scattering. The exception to this behaviour is the VBM state at the Γ point which is rather broad. In this case, there are several bands that

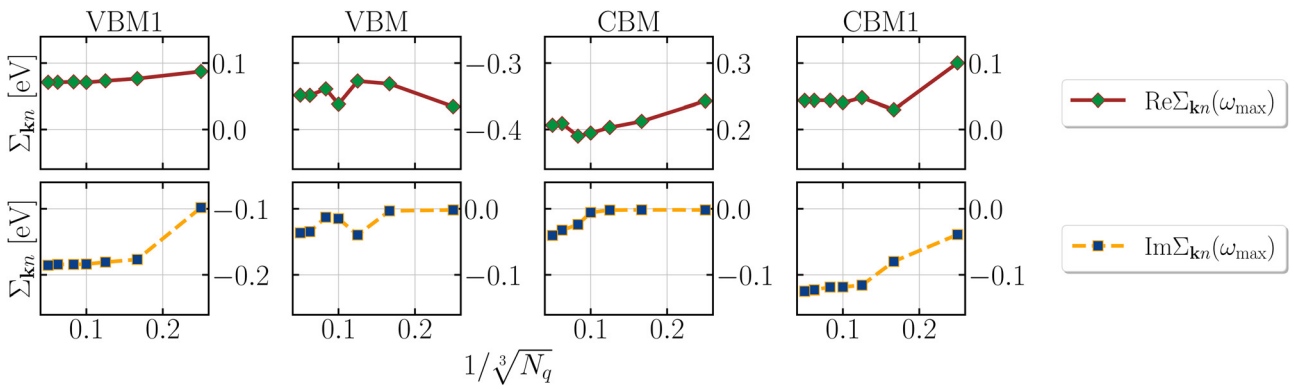

Fig. 7 The dependence of the real and imaginary part of self-energy at the renormalized energy on the size of the q-points grid. The results are presented for the $CsPbBr_3$ material at T = 400 K for bands VBM1, VBM, CBM and CBM1 at the R point.

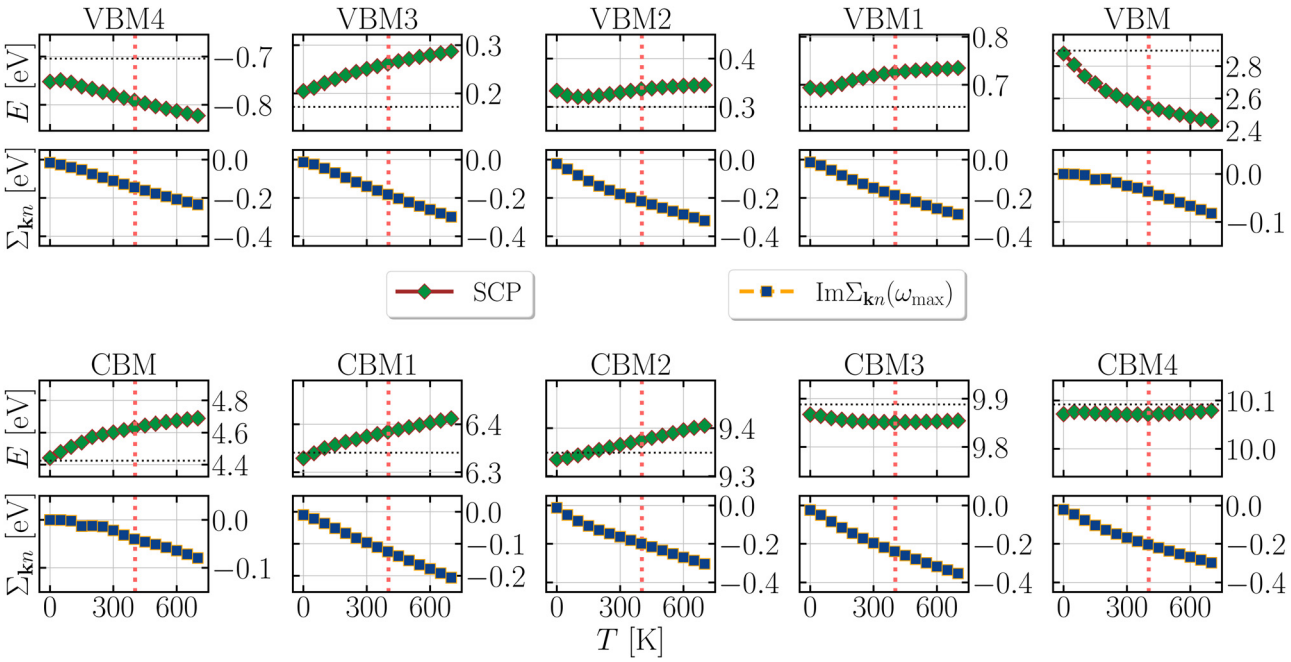

Fig. 8 Temperature dependence of the band energy and the imaginary part of the self-energy for VBM and VBMx (CBM and CBMx) bands (where x = 1, 2, 3, 4) calculated using the SCP approach. The results are shown for $CsPbBr_3$ at the R point. Vertical and horizontal dotted lines represent the temperature of the phase transition to cubic structure T_c = 403 K and band energy from PBE0 calculations, respectively.

are close in energy to the VBM state at Γ. The hole can scatter to these bands which contributes to the increase of energy level broadening.

3.7. Comparison of temperature dependence of the band gap with experiments

In this section, we compare the results for the band gap and its temperature dependence with available experimental results from the literature.

In the case of $CsPbBr_3$ we obtain the band gap of 2.08 eV and 2.20 eV from SCP and OTMS, respectively, at a temperature of 400 K. This result is close to the experimental value of 2.36 eV from ref. 80, obtained at 403 K. Our calculation gives the band gap of $CsPbCl_3$ of 3.01 eV and 3.07 eV from SCP and OTMS, respectively, at a temperature of 320 K. This result is in good agreement with experimental value of 2.85 eV from ref. 79. For the $CsPbI_3$ material we obtain the band gaps of 1.35 eV and 1.45 eV from SCP and OTMS, respectively, at a temperature of 300 K, which is in reasonable agreement with experimental values of 1.67 eV (ref. 81) and 1.73 eV (ref. 82).

Next, we discuss the slope of the temperature dependence of the band gap. In the range of temperatures where the material is in the cubic form, the calculated temperature dependence is nearly linear. Therefore, for the purpose of comparison with experiments, it is sufficient to discuss its slope. In the case of $CsPbBr_3$, we obtain the slope $\left(\frac{dE_g}{dT}\right)_{ph}$ of 0.50 meV K^{-1} and 0.80 meV K^{-1} from SCP and OTMS, respectively, in the temperature range from 400 K to 700 K. For $CsPbCl_3$, the calculation yields the slope of 0.68 meV K^{-1} and 0.96 meV K^{-1} from SCP and OTMS, respectively, in the temperature range from 320 K to 700 K. Finally, for $CsPbI_3$ we obtain the slope $\left(\frac{dE_g}{dT}\right)_{ph}$ of 0.41 meV K^{-1} and 0.77 meV K^{-1} from SCP and OTMS, respectively, in the temperature range from 300 K to 700 K.

To compare the slope of the temperature dependence to experiments, one also has to take into account the effect of thermal expansion, which is not included in the calculation with a fixed lattice constant. The slope of the temperature dependence of the band gap from the effect of thermal expansion is given as

$$\left(\frac{dE_g}{dT}\right)_{TE} = \left(\frac{dE_g}{da}\right)\left(\frac{da}{dT}\right), \quad (13)$$

where $\frac{dE_g}{da}$ is the slope of the dependence of the band gap on the lattice constant and $\frac{da}{dT}$ is the slope of the temperature dependence of the lattice constant, which is related to linear thermal expansion coefficient as

$$\alpha = \frac{1}{a}\frac{da}{dT}. \quad (14)$$

We estimate $\frac{dE_g}{da}$ by calculating the gap dependence of the lattice constant using DFT with the same semilocal functional used in Section 3.1. We obtain respectively the values of 2.1, 2.4 and 1.1 eV $Å^{-1}$ for $CsPbBr_3$, $CsPbCl_3$ and $CsPbI_3$. Literature values of linear thermal expansion coefficients are respectively 0.26 × 10^{-4} K^{-1}, (0.22–0.30) × 10^{-4} K^{-1} and (0.39–0.40) × 10^{-4} K^{-1} for $CsPbBr_3$, $CsPbCl_3$ and $CsPbI_3$ (ref. 83). From eqn (13) and (14) we then obtain that $(dE_g/dT)_{TE}$ is respectively

equal to 0.32 meV K^{-1}, 0.35 meV K^{-1} and 0.29 meV K^{-1} for $CsPbBr_3$, $CsPbCl_3$ and $CsPbI_3$. The results suggest that the contribution from thermal expansion is smaller than the contribution from phonon-induced band gap renormalization for all the materials studied.

The total slope of the temperature dependence of the band gap can be estimated by adding contributions from phonon-induced band gap renormalization and from thermal expansion

$$\frac{dE_g}{dT} = \left(\frac{dE_g}{dT}\right)_{TE} + \left(\frac{dE_g}{dT}\right)_{ph}. \quad (15)$$

We then obtain $\frac{dE_g}{dT}$ of 0.81 meV K^{-1} (1.12 meV K^{-1}), 1.02 meV K^{-1} (1.31 meV K^{-1}), and 0.70 meV K^{-1} (1.06 meV K^{-1}) from SCP (OTMS) results, respectively, for $CsPbBr_3$, $CsPbCl_3$ and $CsPbI_3$.

Experimental data for the temperature dependence of the band gap of the cubic structure and its slope are relatively scarce. In ref. 84 the slope of (0.85 ± 0.05) meV K^{-1} was reported for $CsPbI_3$ based on the measurements in the temperature range from 570 K to 620 K. This value is in the range between our results from SCP and OTMS for the same material. The slope of 0.341 meV K^{-1} was reported for $CsPbBr_3$ in ref. 27 in the temperature range from 380 K to 435 K where the material exhibits a phase transition from tetragonal to cubic structure. This slope is significantly smaller than our estimated slope. It is however questionable if the comparison of these slopes is meaningful given the fact that experimental data cover only a very small initial part of the temperature range where the material is cubic. For the $CsPbCl_3$ material, we are not aware of any literature data with temperature dependence of the band gap in the cubic phase. Overall, further experimental measurements of the temperature dependence of the band gap in a broader temperature range in the cubic phase are certainly desirable.

Finally, we briefly discuss the temperature dependence of the band gap at lower temperatures when the materials exhibit an orthorhombic or a tetragonal structure. Experimental results at these temperatures generally indicate that temperature dependence of the band gap is rather weak. For example, it was reported in ref. 70 that the band gap of $CsPbBr_3$ ($CsPbI_3$) increases by about 60 meV (80 meV) from 0 K to 300 K. In ref. 79 a similar result was obtained for $CsPbBr_3$, while in the case of $CsPbCl_3$ the changes in the band gap in this temperature range were smaller than 20 meV. In ref. 85–87, a comparably weak temperature dependence of the gap was observed for nanocrystals based on $CsPbX_3$ materials in the same temperature range. For all three materials, the band gap at zero temperature is only slightly (by less than 100 meV) lower or even slightly larger than at the lowest temperature where the materials exhibit a cubic structure, see the reference to the values of experimental band gaps at the end of Section 3.2 for the orthorhombic structure and the beginning of this section for the cubic structure. Our calculations of the band gap of the orthorhombic structure at zero temperature and of the cubic structure are in line with such behavior (see the dashed lines in Fig. 5). Since the orthorhombic and tetragonal structure have a larger unit cell than the cubic structure, we did not perform temperature dependent electronic structure calculations of these structures due to larger computational cost and the fact that experimental results indicate a rather weak temperature dependence in this range of temperatures.

4 Discussion and conclusions

Next, we discuss previous computational studies where the effects of temperature on the electronic structure of halide perovskites were investigated. In ref. 23, the effects of temperature were included by performing finite temperature *ab-initio* molecular dynamics with a sufficiently large supercell and by calculating the average band gap change from many molecular dynamics snapshots. Excellent agreement with experimental band gaps of cubic inorganic halide perovskites at the lowest temperature where the material exhibits a cubic structure was obtained. On the computational side, this approach is rather demanding as it would require a separate molecular dynamics simulation at each temperature to obtain the temperature dependence of the band gap. This approach inherently assumes classical phonons which is likely good approximation at room temperature because the dominant phonon modes that determine electronic structure renormalization have energies which are significantly smaller than thermal energy k_BT at room temperature. In ref. 45 and 88 the effects of temperature were also included by taking an average over many different configurations with atoms displaced from their equilibrium positions. In ref. 24 and 25 the authors exploited the special displacements method[89,90] which enables calculation of the band gap at a given temperature from a single calculation of a large supercell with atoms displaced from their equilibrium positions in accordance with a particular pattern. In ref. 22, Allen–Heine–Cardona theory, the finite difference approach, as well as the approach with an average over many different atomic configurations sampled using a Monte Carlo approach were used to study the temperature dependence of the band gap of cubic methylammonium lead iodide perovskite. However, the Allen–Heine–Cardona theory was applied by simply excluding imaginary phonon modes, while we find that this procedure does not give reliable results in the case of the inorganic halide perovskites that we investigated.

We finally note several advantages, as well as shortcomings, of the approach based on the Allen–Heine–Cardona theory over other approaches. To obtain temperature dependence of the electronic structure, the most demanding steps of the procedure – DFPT calculations and extraction of force constants for application of the SCPH method – need to be performed only once, that is, they do not have to be repeated for each temperature. On the other hand, in all approaches based on atomic displacements (sampled either from molecular dynamics, Monte Carlo or using the special displacements) the whole computational procedure has to be repeated at each temperature. Within the Allen–Heine–Cardona approach it is straightforward to obtain

renormalization of states other than the CBM or VBM, while in the methods based on supercell calculations this is either impossible or one has to exploit a certain type of unfolding procedure, such as the one used in ref. 89. It should be mentioned that the approach based on the Allen–Heine–Cardona theory certainly has its limitations. Being based on expansion up to second order terms with respect to atomic displacements, it is not expected to be highly accurate in conditions when this expansion is not sufficient. On the other hand, the approaches based on atomic displacements usually do not have such a limitation.

In conclusion, we performed *ab-initio* calculations of the temperature dependent electronic structure of inorganic halide perovskite materials $CsPbX_3$. The challenge that comes from the fact that cubic structure is not stable at zero temperature and that one obtains phonon modes with imaginary frequencies in a standard DFPT calculation was overcome by using the SCPH method that gives the phonon spectrum with real non-negative frequencies. The challenge of obtaining the energies of bands other than the CBM and the VBM in the calculations based on the Allen–Heine–Cardona theory was addressed by exploiting a self-consistent procedure for evaluation of relevant self-energies and spectral functions. We obtain the band gaps at the lowest temperature where the materials exhibit a cubic structure in good agreement with experiments. We also find good agreement of calculated and experimental temperature dependence of the band gap for the $CsPbI_3$ material where reliable experimental data are available in the literature. Our results also suggest that the band gaps at the lowest temperature where the materials exhibit a cubic structure are similar to the band gaps at zero temperature where the materials exhibit an orthorhombic structure. This finding is consistent with experimental data that suggest a rather weak temperature dependence at lower temperatures where the materials exhibit an orthorhombic or a tetragonal structure. Finally, we find that the temperature dependence of band energies at the *R* point is most pronounced for the CBM and the VBM, while it is less pronounced for higher and lower bands.

Conflicts of interest

There are no conflicts of interest to declare.

Acknowledgements

We acknowledge funding provided by the Institute of Physics Belgrade, through the grant by the Ministry of Science, Technological Development and Innovation of the Republic of Serbia. Numerical computations were performed on the PARADOX-IV supercomputing facility at the Scientific Computing Laboratory, National Center of Excellence for the Study of Complex Systems, Institute of Physics Belgrade.

References

1 M. M. Lee, J. Teuscher, T. Miyasaka, T. N. Murakami and H. J. Snaith, *Science*, 2012, **338**, 643–647.
2 M. Liu, M. B. Johnston and H. J. Snaith, *Nature*, 2013, **501**, 395–398.
3 A. K. Jena, A. Kulkarni and T. Miyasaka, *Chem. Rev.*, 2019, **119**, 3036–3103.
4 M. Aldamasy, Z. Iqbal, G. Li, J. Pascual, F. Alharthi, A. Abate and M. Li, *Phys. Chem. Chem. Phys.*, 2021, **23**, 23413–23427.
5 L. Lei, Q. Dong, K. Gundogdu and F. So, *Adv. Funct. Mater.*, 2021, **31**, 2010144.
6 X.-K. Liu, W. Xu, S. Bai, Y. Jin, J. Wang, R. H. Friend and F. Gao, *Nat. Mater.*, 2021, **20**, 10–21.
7 K. Xing, S. Cao, X. Yuan, R. Zeng, H. Li, B. Zou and J. Zhao, *Phys. Chem. Chem. Phys.*, 2021, **23**, 17113–17128.
8 M. Ahmadi, T. Wu and B. Hu, *Adv. Mater.*, 2017, **29**, 1605242.
9 T. M. H. Nguyen, S. Kim and C. W. Bark, *J. Mater. Chem. A*, 2021, **9**, 1269–1276.
10 H. Wei and J. Huang, *Nat. Commun.*, 2019, **10**, 1066.
11 S. Svanström, A. García Fernández, T. Sloboda, T. J. Jacobsson, H. Rensmo and U. B. Cappel, *Phys. Chem. Chem. Phys.*, 2021, **23**, 12479–12489.
12 H. Xie, S. Hao, J. Bao, T. J. Slade, G. J. Snyder, C. Wolverton and M. G. Kanatzidis, *J. Am. Chem. Soc.*, 2020, **142**, 9553–9563.
13 X. Liu, J. Qiu, Q. Huang, X. Chen, J. Yu and J. Bao, *Phys. Chem. Chem. Phys.*, 2023, **25**, 11620–11629.
14 L. D. Whalley, J. M. Frost, Y.-K. Jung and A. Walsh, *J. Chem. Phys.*, 2017, **146**, 220901.
15 W.-J. Yin, J.-H. Yang, J. Kand, Y. Yan and S.-H. Wei, *J. Mater. Chem. A*, 2015, **3**, 8926–8942.
16 J. Even, L. Pedesseau, C. Katan, M. Kepenekian, J.-S. Lauret, D. Sapori and E. Deleporte, *J. Phys. Chem. C*, 2015, **119**, 10161–10177.
17 F. Brivio, K. T. Butler, A. Walsh and M. van Schilfgaarde, *Phys. Rev. B: Condens. Matter Mater. Phys.*, 2014, **89**, 155204.
18 A. Amat, E. Mosconi, E. Ronca, C. Quarti, P. Umari, M. K. Nazeeruddin, M. Grätzel and F. De Angelis, *Nano Lett.*, 2014, **14**, 3608–3616.
19 P. Umari, E. Mosconi and F. De Angelis, *Sci. Rep.*, 2014, **4**, 4467.
20 M. H. Du, *J. Mater. Chem. A*, 2014, **2**, 9091–9098.
21 J. Feng and B. Xiao, *J. Phys. Chem. Lett.*, 2014, **5**, 1278–1282.
22 W. A. Saidi, S. Poncé and B. Monserrat, *J. Phys. Chem. Lett.*, 2016, **7**, 5247–5252.
23 J. Wiktor, U. Rothlisberger and A. Pasquarello, *J. Phys. Chem. Lett.*, 2017, **8**, 5507–5512.
24 H. Wang, A. Tal, T. Bischoff, P. Gono and A. Pasquarello, *npj Comput. Mater.*, 2022, **8**, 237.
25 J. Ning, L. Zheng, W. Lei, S. Wang, J. Xi and J. Yang, *Phys. Chem. Chem. Phys.*, 2022, **24**, 16003–16010.
26 A. Francisco-López, B. Charles, O. J. Weber, M. I. Alonso, M. Garriga, M. Campoy-Quiles, M. T. Weller and A. R. Goñi, *J. Phys. Chem. Lett.*, 2019, **10**, 2971–2977.
27 G. Mannino, I. Deretzis, E. Smecca, A. La Magna, A. Alberti, D. Ceratti and D. Cahen, *J. Phys. Chem. Lett.*, 2020, **11**, 2490–2496.
28 M. Mladenovic and N. Vukmirovic, *Phys. Chem. Chem. Phys.*, 2018, **20**, 25693–25700.

29 P. B. Allen and V. Heine, *J. Phys. C: Solid State Phys.*, 1976, **9**, 2305–2312.
30 P. B. Allen and M. Cardona, *Phys. Rev. B: Condens. Matter Mater. Phys.*, 1981, **23**, 1495–1505.
31 P. B. Allen and M. Cardona, *Phys. Rev. B: Condens. Matter Mater. Phys.*, 1983, **27**, 4760–4769.
32 S. Poncé, Y. Gillet, J. Laflamme Janssen, A. Marini, M. Verstraete and X. Gonze, *J. Chem. Phys.*, 2015, **143**, 102813.
33 J. Park, W. A. Saidi, B. Chorpening and Y. Duan, *J. Phys. Chem. C*, 2021, **125**, 22231–22238.
34 F. Giustino, S. G. Louie and M. L. Cohen, *Phys. Rev. Lett.*, 2010, **105**, 265501.
35 A. Miglio, V. Brousseau-Couture, E. Godbout, G. Antonius, Y.-H. Chan, S. G. Louie, M. Côté, M. Giantomassi and X. Gonze, *npj Comput. Mater.*, 2020, **6**, 167.
36 R. D. King-Smith, R. J. Needs, V. Heine and M. J. Hodgson, *EPL*, 1989, **10**, 569–574.
37 S. Hirotsu, J. Harada, M. Iizumi and K. Gesi, *J. Phys. Soc. Jpn.*, 1974, **37**, 1393–1398.
38 S. Plesko, R. Kind and J. Roos, *J. Phys. Soc. Jpn.*, 1978, **45**, 553–557.
39 A. Marronnier, G. Roma, S. Boyer-Richard, L. Pedesseau, J.-M. Jancu, Y. Bonnassieux, C. Katan, C. C. Stoumpos, M. G. Kanatzidis and J. Even, *ACS Nano*, 2018, **12**, 3477–3486.
40 R. X. Yang, J. M. Skelton, E. L. da Silva, J. M. Frost and A. Walsh, *J. Phys. Chem. Lett.*, 2017, **8**, 4720–4726.
41 D. Trots and S. Myagkota, *J. Phys. Chem. Solids*, 2008, **69**, 2520–2526.
42 C. K. Møller, *Nature*, 1958, **182**, 1436.
43 X. Zhou and Z. Zhang, *AIP Adv.*, 2020, **10**, 125015.
44 T. Tadano and W. A. Saidi, *Phys. Rev. Lett.*, 2022, **129**, 185901.
45 C. E. Patrick, K. W. Jacobsen and K. S. Thygesen, *Phys. Rev. B: Condens. Matter Mater. Phys.*, 2015, **92**, 201205.
46 M. El Kurdi, G. Fishman, S. Sauvage and P. Boucaud, *J. Appl. Phys.*, 2010, **107**, 013710.
47 S. Boyer-Richard, F. Raouafi, A. Bondi, L. Pédesseau, C. Katan, J.-M. Jancu and J. Even, *Appl. Phys. Lett.*, 2011, **98**, 251913.
48 Z. Song, W. Fan, C. S. Tan, Q. Wang, D. Nam, D. H. Zhang and G. Sun, *New J. Phys.*, 2019, **21**, 073037.
49 M. Jocic and N. Vukmirovic, *Phys. Rev. B*, 2020, **102**, 085121.
50 F. Giustino, *Rev. Mod. Phys.*, 2017, **89**, 015003.
51 E. Cannuccia and A. Marini, *Eur. Phys. J. B*, 2012, **85**, 320.
52 P. Mitric, V. Jankovic, N. Vukmirovic and D. Tanaskovic, *Phys. Rev. B*, 2023, **107**, 125165.
53 T. Tadano and S. Tsuneyuki, *Phys. Rev. B: Condens. Matter Mater. Phys.*, 2015, **92**, 054301.
54 J. P. Perdew, A. Ruzsinszky, G. I. Csonka, O. A. Vydrov, G. E. Scuseria, L. A. Constantin, X. Zhou and K. Burke, *Phys. Rev. Lett.*, 2008, **100**, 136406.
55 J. P. Perdew, K. Burke and M. Ernzerhof, *Phys. Rev. Lett.*, 1996, **77**, 3865–3868.
56 P. Giannozzi, S. Baroni, N. Bonini, M. Calandra, R. Car, C. Cavazzoni, D. Ceresoli, G. L. Chiarotti, M. Cococcioni, I. Dabo, A. D. Corso, S. de Gironcoli, S. Fabris, G. Fratesi, R. Gebauer, U. Gerstmann, C. Gougoussis, A. Kokalj, M. Lazzeri, L. Martin-Samos, N. Marzari, F. Mauri, R. Mazzarello, S. Paolini, A. Pasquarello, L. Paulatto, C. Sbraccia, S. Scandolo, G. Sclauzero, A. P. Seitsonen, A. Smogunov, P. Umari and R. M. Wentzcovitch, *J. Phys.: Condens.Matter*, 2009, **21**, 395502.
57 P. Giannozzi, O. Andreussi, T. Brumme, O. Bunau, M. B. Nardelli, M. Calandra, R. Car, C. Cavazzoni, D. Ceresoli, M. Cococcioni, N. Colonna, I. Carnimeo, A. D. Corso, S. de Gironcoli, P. Delugas, R. A. DiStasio, A. Ferretti, A. Floris, G. Fratesi, G. Fugallo, R. Gebauer, U. Gerstmann, F. Giustino, T. Gorni, J. Jia, M. Kawamura, H.-Y. Ko, A. Kokalj, E. Küçükbenli, M. Lazzeri, M. Marsili, N. Marzari, F. Mauri, N. L. Nguyen, H.-V. Nguyen, A. O. De-la Roza, L. Paulatto, S. Poncé, D. Rocca, R. Sabatini, B. Santra, M. Schlipf, A. P. Seitsonen, A. Smogunov, I. Timrov, T. Thonhauser, P. Umari, N. Vast, X. Wu and S. Baroni, *J. Phys.: Condens.Matter*, 2017, **29**, 465901.
58 M. van Setten, M. Giantomassi, E. Bousquet, M. Verstraete, D. Hamann, X. Gonze and G.-M. Rignanese, *Comput. Phys. Commun.*, 2018, **226**, 39–54.
59 D. R. Hamann, *Phys. Rev. B: Condens. Matter Mater. Phys.*, 2013, **88**, 085117.
60 G. E. Eperon, G. M. Paternò, R. J. Sutton, A. Zampetti, A. A. Haghighirad, F. Cacialli and H. J. Snaith, *J. Mater. Chem. A*, 2015, **3**, 19688–19695.
61 J. P. Perdew, *Int. J. Quantum Chem.*, 1985, **28**, 497–523.
62 A. Jain, S. P. Ong, G. Hautier, W. Chen, W. D. Richards, S. Dacek, S. Cholia, D. Gunter, D. Skinner, G. Ceder and K. A. Persson, *APL Mater.*, 2013, **1**, 011002.
63 J. P. Perdew, M. Ernzerhof and K. Burke, *J. Chem. Phys.*, 1996, **105**, 9982–9985.
64 C. Adamo and V. Barone, *J. Chem. Phys.*, 1999, **110**, 6158–6170.
65 T. Bischoff, J. Wiktor, W. Chen and A. Pasquarello, *Phys. Rev. Mater.*, 2019, **3**, 123802.
66 L. Lin, *J. Chem. Theory Comput.*, 2016, **12**, 2242–2249.
67 F. Gygi and A. Baldereschi, *Phys. Rev. B: Condens. Matter Mater. Phys.*, 1986, **34**, 4405–4408.
68 M. Baranowski, P. Plochocka, R. Su, L. Legrand, T. Barisien, F. Bernardot, Q. Xiong, C. Testelin and M. Chamarro, *Photonics Res.*, 2020, **8**, A50–A55.
69 Z. Liu, J. A. Peters, C. C. Stoumpos, M. Sebastian, B. W. Wessels, J. Im, A. J. Freeman and M. G. Kanatzidis, Hard X-Ray, Gamma-Ray, and Neutron Detector Physics XV, 2013, 88520A.
70 Z. Yang, A. Surrente, K. Galkowski, A. Miyata, O. Portugall, R. J. Sutton, A. A. Haghighirad, H. J. Snaith, D. K. Maude, P. Plochocka and R. J. Nicholas, *ACS Energy Lett.*, 2017, **2**, 1621–1627.
71 X. Gonze, B. Amadon, P.-M. Anglade, J.-M. Beuken, F. Bottin, P. Boulanger, F. Bruneval, D. Caliste, R. Caracas, M. Côté, T. Deutsch, L. Genovese, P. Ghosez, M. Giantomassi, S. Goedecker, D. Hamann, P. Hermet, F. Jollet, G. Jomard, S. Leroux, M. Mancini, S. Mazevet,

M. Oliveira, G. Onida, Y. Pouillon, T. Rangel, G.-M. Rignanese, D. Sangalli, R. Shaltaf, M. Torrent, M. Verstraete, G. Zerah and J. Zwanziger, *Comput. Phys. Commun.*, 2009, **180**, 2582–2615.

72 X. Gonze, F. Jollet, F. Abreu Araujo, D. Adams, B. Amadon, T. Applencourt, C. Audouze, J.-M. Beuken, J. Bieder, A. Bokhanchuk, E. Bousquet, F. Bruneval, D. Caliste, M. Côté, F. Dahm, F. Da Pieve, M. Delaveau, M. Di Gennaro, B. Dorado, C. Espejo, G. Geneste, L. Genovese, A. Gerossier, M. Giantomassi, Y. Gillet, D. Hamann, L. He, G. Jomard, J. Laflamme Janssen, S. Le Roux, A. Levitt, A. Lherbier, F. Liu, I. Lukacevic, A. Martin, C. Martins, M. Oliveira, S. Poncé, Y. Pouillon, T. Rangel, G.-M. Rignanese, A. Romero, B. Rousseau, O. Rubel, A. Shukri, M. Stankovski, M. Torrent, M. Van Setten, B. Van Troeye, M. Verstraete, D. Waroquiers, J. Wiktor, B. Xu, A. Zhou and J. Zwanziger, *Comput. Phys. Commun.*, 2016, **205**, 106–131.

73 X. Gonze, B. Amadon, G. Antonius, F. Arnardi, L. Baguet, J.-M. Beuken, J. Bieder, F. Bottin, J. Bouchet and E. Bousquet, *et al.*, *Comput. Phys. Commun.*, 2019, **248**, 107042.

74 X. Gonze, B. Amadon, G. Antonius, F. Arnardi, L. Baguet, J.-M. Beuken, J. Bieder, F. Bottin, J. Bouchet, E. Bousquet, N. Brouwer, F. Bruneval, G. Brunin, T. Cavignac, J.-B. Charraud, W. Chen, M. Côté, S. Cottenier, J. Denier, G. Geneste, P. Ghosez, M. Giantomassi, Y. Gillet, O. Gingras, D. R. Hamann, G. Hautier, X. He, N. Helbig, N. Holzwarth, Y. Jia, F. Jollet, W. Lafargue-Dit-Hauret, K. Lejaeghere, M. A. L. Marques, A. Martin, C. Martins, H. P. C. Miranda, F. Naccarato, K. Persson, G. Petretto, V. Planes, Y. Pouillon, S. Prokhorenko, F. Ricci, G.-M. Rignanese, A. H. Romero, M. M. Schmitt, M. Torrent, M. J. van Setten, B. V. Troeye, M. J. Verstraete, G. Zérah and J. W. Zwanziger, *Comput. Phys. Commun.*, 2020, **248**, 107042.

75 N. R. Werthamer, *Phys. Rev. B: Solid State*, 1970, **1**, 572–581.

76 T. Tadano, Y. Gohda and S. Tsuneyuki, *J. Phys.: Condens.-Matter*, 2014, **26**, 225402.

77 F. Zhou, W. Nielson, Y. Xia and V. Ozolins, *Phys. Rev. Lett.*, 2014, **113**, 185501.

78 S. Poncé, G. Antonius, Y. Gillet, P. Boulanger, J. Laflamme Janssen, A. Marini, M. Côté and X. Gonze, *Phys. Rev. B: Condens. Matter Mater. Phys.*, 2014, **90**, 214304.

79 M. Sebastian, J. A. Peters, C. C. Stoumpos, J. Im, S. S. Kostina, Z. Liu, M. G. Kanatzidis, A. J. Freeman and B. W. Wessels, *Phys. Rev. B: Condens. Matter Mater. Phys.*, 2015, **92**, 235210.

80 J. B. Hoffman, A. L. Schleper and P. V. Kamat, *J. Am. Chem. Soc.*, 2016, **138**, 8603–8611.

81 C. C. Stoumpos, C. D. Malliakas and M. G. Kanatzidis, *Inorg. Chem.*, 2013, **52**, 9019–9038.

82 G. E. Eperon, S. D. Stranks, C. Menelaou, M. B. Johnston, L. M. Herz and H. J. Snaith, *Energy Environ. Sci.*, 2014, **7**, 982–988.

83 T. Haeger, R. Heiderhoff and T. Riedl, *J. Mater. Chem. C*, 2020, **8**, 14289–14311.

84 R. J. Sutton, M. R. Filip, A. A. Haghighirad, N. Sakai, B. Wenger, F. Giustino and H. J. Snaith, *ACS Energy Lett.*, 2018, **3**, 1787–1794.

85 B. T. Diroll, H. Zhou and R. D. Schaller, *Adv. Funct. Mater.*, 2018, **28**, 1800945.

86 R. Saran, A. Heuer-Jungemann, A. G. Kanaras and R. J. Curry, *Adv. Opt. Mater.*, 2017, **5**, 1700231.

87 J. Yi, X. Ge, E. Liu, T. Cai, C. Zhao, S. Wen, H. Sanabria, O. Chen, A. M. Rao and J. Gao, *Nanoscale Adv.*, 2020, **2**, 4390–4394.

88 T. Lanigan-Atkins, X. He, M. J. Krogstad, D. M. Pajerowski, D. L. Abernathy, G. N. M. N. Xu, Z. Xu, D.-Y. Chung, M. G. Kanatzidis, S. Rosenkranz, R. Osborn and O. Delaire, *Nat. Mater.*, 2021, **20**, 977–983.

89 M. Zacharias and F. Giustino, *Phys. Rev. Res.*, 2020, **2**, 013357.

90 M. Zacharias and F. Giustino, *Phys. Rev. B*, 2016, **94**, 075125.

FACTA UNIVERSITATIS
Series: **Physics, Chemistry and Technology** Vol. 22, N° 1, 2024, pp. 1 - 11
https://doi.org/10.2298/FUPCT2401001J

Original scientific paper

TEMPERATURE DEPENDENCE OF THE ELECTRONIC BAND GAP OF $CsPbBr_3$ QUANTUM WELLS OBTAINED USING K•P METHOD

Milan Jocić[1], Nenad Vukmirović[2]

[1]Department of Physics, Faculty of Sciences and Mathematics,
University of Niš, Niš, Serbia
[2]Institute of Physics Belgrade, University of Belgrade, Belgrade, Serbia

ORCID iDs: Milan Jocić https://orcid.org/0000-0003-4929-9907
Nenad Vukmirović https://orcid.org/0000-0002-4101-1713

Abstract. *We calculated the electronic structure of $CsPbBr_3$ quantum wells using the **k•p** model with parameters extracted from hybrid functional based DFT calculations supplemented with self-energy corrections arising from the electron-phonon interaction. We obtained the temperature dependence of the band gap for different sizes of the quantum well. The results show that the temperature dependence in quantum wells is similar to the one found in bulk phase for all sizes of the well that were considered.*

Key words: *nanostructure, temperature dependence, quantum well, **k•p** method*.

1. INTRODUCTION

Since most electronic and optical devices consist of semiconductor materials, there is a great significance in knowing the properties of these materials. Over the years, general improvements of these devices made them smaller in size and more power efficient. Reducing the size from a bulk phase, that can be as small as few micrometers, down to a nanostructure that has a scale of a few dozen nanometers or less introduces a change in electronic properties of the material. This makes it possible to tune the electronic properties, like the band gap of a material, to desired values, allowing us to replicate the electronic properties of a much more expensive or less durable material with a material that is cheaper to produce or more durable. Working with nanostructures whose electronic properties change with their size introduces new challenges for investigating and modeling semiconductor materials.

For the past few decades, density functional theory (DFT) has been routinely used for modeling the properties of the bulk phase of semiconductors with much success, while their nanostructures would prove to be challenging since the required computational

Received: January 15th, 2024; accepted: December 10th, 2024
Corresponding author: Milan Jocić
Department of Physics, Faculty of Sciences and Mathematics, Višegradska 33, 18000 Niš, Serbia
E-mail: milan.jocic@pmf.ni.ac.rs

resources are increasing with the size of the nanostructure, and in some cases they become infeasible. Relying on the **k•p** method, alongside DFT, the computational resources required to obtain the electronic structure can be significantly reduced. One disadvantage of the **k•p** is that it considers only several selected bands of interest, while the rest of them are treated perturbatively (like in Löwdin, 1951.). The energy of these bands and their wave-functions have to be extracted from DFT calculation. Another disadvantage is that it can be a good approximation only in a relatively small vicinity around the point in the Brillouin zone from which DFT results are extracted. Since our main interest is the band gap of a nanostructure device, these disadvantages come at an acceptable cost. On the other hand, DFT provides information about all bands in the whole Brillouin zone which is more than sufficient in this case.

Once we determine the size dependent electronic properties of the nanostructure for the desired device, we have to take into account various external conditions that such device would operate under like the surrounding temperature. Both **k•p** and DFT, however, by themselves do not take into account any temperature effects that such devices might be exposed to, and since in practice they are expected to perform at a wide range of outside temperature conditions, these effects should be taken into account as well.

Regarding ab initio modeling of nanostructures, in our previous work (Jocić and Vukmirović 2020.) we provided, among other, a detailed explanation and comparison of DFT and k•p methods for bulk and quantum well (QW) nanostructures of CdSe. We have shown that the k•p method is in excellent agreement with DFT, even for rather thin QWs, using standard 8×8 (H8) and extended 26×26 (H26) **k•p** Hamiltonians which take into account the effects of spin-orbit coupling (SOC), which is necessary in the case of heavy ions such as lead.

To determine the effects of temperature on the electronic structure, in our recent paper (Jocic and Vukmirovic 2023.) we proposed a method that combines hybrid PBE0 functional based calculation in DFT with the Allen-Heine-Cardona (AHC) theory that provides temperature dependent self-energy correction of electronic bands. Because this self-energy has its origin in electron-phonon interactions it was necessary to obtain proper phonon frequencies, which are also temperature dependent and were obtained using the self-consistent phonon (SCPH) method. Self-energies are then obtained within the AHC theory using the on-the-mass-shell (OTMS) approximation. We also introduced a self-consistent procedure (SCP), which improves upon OTMS approximation, which evaluates these self-energies using interacting Green's functions and extracts the results from the corresponding spectral function. We performed this for several bands below and above the band gap at key points in the first Brillouin zone (1BZ). These methods allowed us to obtain good agreement of the band gap with the available experimental data for $CsPbCl_3$, $CsPbBr_3$ and $CsPbI_3$ at zero temperature and the temperature at which transition to cubic phase takes place.

In this work, we turn our attention to perovskite crystal $CsPbBr_3$, and calculate the temperature dependent gap of quantum wells (QW) made from this material. It was observed that $CsPbBr_3$ has two phase transitions as temperature increases. At low temperatures it forms an orthorhombic crystal structure that transforms to a tetragonal structure for a narrow range of temperatures, and then transforms to a cubic structure at a temperature of $T = 403$ K. Since $CsPbBr_3$ has recently found application in solar cells, the most interesting region would be the one of high temperatures of the cubic structure at which these solar cells would operate.

In this paper, we combine the method from our previous (Jocić and Vukmirović 2020.) and results from our recent (Jocić and Vukmirović 2023.) work in order to obtain the temperature dependence of band gaps for $CsPbBr_3$ QW nanostructures. The structure of the paper is as follows: In Theory section, we first provide a brief theoretical overview of the **k•p** method for QW nanostructures using a plane wave (PW) basis and discuss the ordering of the bands that go into H8 and H26 Hamiltonians for the cubic structure of $CsPbBr_3$. In the Results section, we first demonstrate the procedure for obtaining the convergence of the results with respect to necessary numerical parameters used in **k•p** method for QWs. We then present band structure with a more accurate band gap that is obtained from **k•p**, using hybrid DFT and temperature corrections for bulk, and a band structure for QW of fixed size using the same parameters. Finally, we show the temperature dependence of the electronic bands and band gaps for QW sizes ranging from around 2 nm to around 18 nm for temperature range from 400 to 700 K.

2. THEORY

Constructing a **k•p** Hamiltonian for nanostructures requires rewriting equations for bulk in a new form that is suitable for that case. Since the periodicity of the crystal is violated, in the general case, the electron momentum **k** is not a good quantum number anymore and we have to introduce envelope functions ψ_m alongside Bloch unit cell functions u_m in the expression for the wave-function Ψ:

$$\Psi = \sum_m \psi_m u_m. \tag{1}$$

In the case of a cubic $CsPbBr_3$ lattice, the QW is periodic in the (x, y) plane, and its size can be determined by counting the number of bulk unit cells along the z-direction. We choose the coordinate system in such a way that the QW is located in the region from l_1 to l_2 ($0 < l_1 < l_2 < L$) and the surrounding material is in the region from 0 to L.

We expand envelopes in PW basis as $\psi_m(z) = \sum_q W_{mq}\, a_q$, where $a_q(z) = L^{-1/2} \exp(ik_q z)$ are a set of basis functions, and $k_q = 2\pi q/L$, with $q = 0, \pm 1, \pm 2, \pm 3, \ldots \pm N_{\mathrm{PW}}$, where $2N_{\mathrm{PW}} + 1$ is the number of plane waves. This makes the envelope function periodic in space as $\psi_m(z) = \psi_m(z + L)$. Using the condition that $\psi_m(r)$ are smooth, continuous, infinitely differentiable and slowly varying functions, whose plane-wave expansion is restricted to the 1BZ and $u_m(r)$ are a complete set of orthogonal Bloch functions at $\mathbf{k}_0$, periodic over the whole structure, with the periodicity of Bravais lattice (Lew Yan Voon and Willatzen, 2009.), we arrive at **k•p** equations for QWs:

$$\begin{aligned}\sum_{m,q} \left[\frac{\hbar^2}{2m_0} (\mathbf{k} - \mathbf{k}_0)^2_{(x,y)}\, \delta_{sq} + \frac{\hbar^2}{2m_0} k_q^2\, \delta_{sq} + I^{sq}(E_m) \right] \delta_{nm}\, W_{mq} \\ + \sum_{m,q} \left[\frac{\hbar}{m_0} (\mathbf{k} - \mathbf{k}_0)_{(x,y)} \cdot \mathbf{p}_{nm}\, \delta_{sq} + \frac{\hbar}{m_0} k_q \mathbf{e}_z \cdot \mathbf{p}_{nm} \right] W_{mq} \\ + \sum_{m,q} H^{(2)}_{nm}(s,q)\, W_{mq} = E\, W_{ns}\ ,\end{aligned} \tag{2}$$

where $\mathbf{p}_{nm}$ and E_m are momentum matrix elements and band energies obtained as **k•p** parameters in bulk for $\mathbf{k}_0$, m_0 is the electron mass, and:

$$\Delta k_{sq} = 2\pi(s-q)/L\,,$$
$$I^{sq}(E) = (E - E_B) I^{sq}(E)\,|_{l_2}^{l_1}\ ,\ \ E_B = E \pm \Delta E_B,$$
$$I^{sq}(E)\,|_{l_2}^{l_1} = \frac{1}{L}\int_{l_1}^{l_2} e^{-i\Delta k_{sq} z}\, dz \qquad (3)$$
$$= \frac{l_1 - l_2}{L}\ \delta_{sq} + \frac{\delta_{sq} - 1}{iL\Delta k_{sq}}\left(e^{-i\Delta k_{sq} l_1} - e^{-i\Delta k_{wq} l_2}\right).$$

The second-order perturbation band term $H_{nm}^{(2)}(s,q)$, which accounts for remote bands *r* that are not present in the first-order Hamiltonian are:

$$H_{nm}^{(2)}(s,q) = \sum_r \frac{1}{L}\int dz\ e^{-ik_s z}\frac{(\hbar\mathbf{K}\cdot\mathbf{p}_{nr})(\mathbf{p}_{rn}\cdot\hbar\mathbf{K})}{m_0^2[(E_n+E_m)/2 - E_r]}\ e^{ik_q z}$$
$$= \sum_{\alpha,\beta}\frac{1}{L}\int dz\ e^{-ik_s z}\ \frac{\hbar K_\alpha}{m_0} P_{nm,\alpha\beta}\frac{\hbar K_\beta}{m_0}\ e^{ik_q z} \qquad (4)$$

where $\hbar\mathbf{K} = (\hbar\mathbf{k} - \hbar\mathbf{k}_0)_{(x,y)} + p_z\,\mathbf{e}_z$, $p_z = -i\hbar\partial_z$ is the momentum operator, and $P_{nm,\alpha\beta}$ is the second-order **k•p** momentum tensor. We used *n,m* for band indices in bulk and *α, β* indices for directions *x, y, z* .

We assume that the surrounding material has the same parameters as the QW, except for the valence and conduction band energies, that are respectively shifted by $-\Delta E_B$ and $+\Delta E_B$ with respect to the QW parameters, where ΔE_B is the absolute shift of the bands. This shift is chosen to be large enough to ensure that the wave functions are located in the QW and was set to 10 eV for all our calculations.

Size of the well (surrounding material) is a product of the size of the unit cell in *z*-direction *a* and some integer *N* (N_B), *l* = *Na* ($L = N_B a$). N_{PW} and *L/l* are the parameters that need to be studied in more detail, and we will show how to determine them in the next section.

In the limit where **k** is a good quantum number, eqn. (2) transforms to the case of bulk by removing every integration over *z*-components and PWs from envelope function expansion, reducing to:

$$\sum_m \left[\frac{\hbar^2}{2m_0}(\mathbf{k}-\mathbf{k}_0)^2 + E_m\right]\delta_{nm}\, W_m$$
$$+ \sum_m \left[\frac{\hbar}{m_0}(\mathbf{k}-\mathbf{k}_0)\cdot\mathbf{p}_{nm} + H_{nm}^{(2)}\right] W_m = E\, W_m\,, \qquad (5)$$
$$H_{nm}^{(2)} = \sum_{\alpha,\beta}\frac{\hbar\,(\mathbf{k}-\mathbf{k}_0)_\alpha}{m_0} P_{nm,\alpha\beta}\frac{\hbar(\mathbf{k}-\mathbf{k}_0)_\beta}{m_0}\ .$$

Eqn. (2) and eqn. (5) show us how to construct the Hamiltonian, but not which bands and which **k**-point should be used for unperturbed results from DFT. Most of the electronic properties are governed by the symmetry of the crystal and most of the information about the current carriers can be obtained by considering points with the greatest probability for their detection. Extremal states in the electron structure are most likely to have current carriers: holes in the valence band maximum (VBM), and electrons in the conduction band minimum (CBM). Historically, these points and their symmetry have been the center of interest when DFT calculations were not yet computationally feasible, so the electronic

structure was mostly studied by analytical methods in combination with available experimental data. A good overview of these analytical methods can be found in a book by Bir and Pikus, 1974.

The point group of the bulk cubic $CsPbBr_3$ crystal is O_h, and the band gap is located at the R-point in the 1BZ. Point group O_h transforms to a double group, that describes bands when SOC in included, by multiplying all irreducible representations by a spinor representation Γ^+_6. **Fig.** 1 illustrates this for bands around the gap in the bulk $CsPbBr_3$. When SOC is not included, VBM at R-point is non-degenerate band corresponding to Γ^-_2 irreducible representation that transforms to 2-fold degenerate band Γ^-_7 when SOC is included. CBM is 3-fold degenerate band at R-point, corresponding to Γ^+_5 when SOC is omitted, and transforms by splitting into a 2-fold Γ^+_7 with lower energy, now CBM, and 4-fold Γ^+_8 band with higher energy, now CBM1. These 8 bands in total make the H8 Hamiltonian.

The larger H26 Hamiltonian is formed when along these 8, we include 3 more valence bands, counting with decreasing energies from VBM: 4-fold Γ^-_8, 2-fold Γ^-_7, and 4-fold Γ^-_8, respectively, and 3 more conduction bands, counting with increasing energies from CBM1: 2-fold Γ^+_6, 2-fold Γ^+_7, and 4-fold Γ^+_8, respectively.

Both H8 and H26 have a unique set of **k•p** parameters that consist of energies E_m, momentum matrix elements $\mathbf{p}_{nm}$ and second-order momentum tensors $P_{nm,\alpha\beta}$. Using the same parameters for bulk, we construct the H26 Hamiltonian for QW from eqn. (2), taking note that the periodicity is now valid only in the (*x, y*) plane.

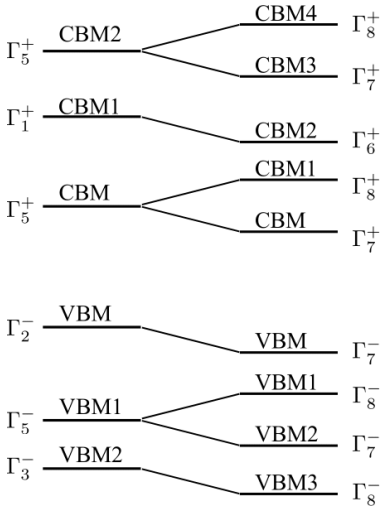

Fig. 1 Ordering of the bands around the gap and their transformation when SOC is included. Distance between the bands does not scale with energy distance between them. Notation for the irreducible representations that was used here follows the one found in Bradley and Cracknell, 2010.

3. Results and Discussions

Depending on the size of the **k•p** Hamiltonian, a small change of numerical parameters L/l and N_{PW} can have a significant effect on the result. This is especially true for smaller wells, while large wells that approach bulk in terms of size are less sensitive to those changes. For this reason, we inspect the convergence with respect to those parameters as follows. First, we fix some l, and gradually increase the size of the surrounding material L and number of plane waves N_{PW} until we achieve convergence. This process is repeated for every l.

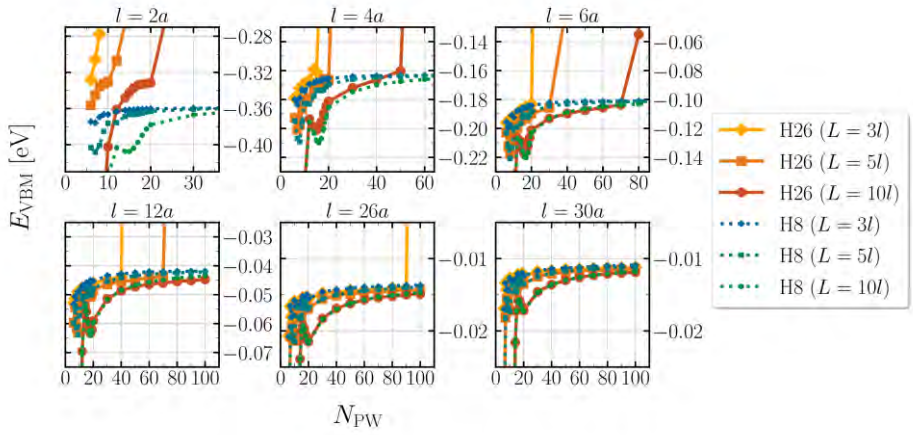

Fig. 2 Energy of VBM as a function of N_{PW}, in QWs. The results were obtained using H26 (solid lines) and H8 (dotted lines) Hamiltonians, respectively, for QWs of the size *l=2a*, *l=4a*, *l=6a*, *l=12a*, *l=26a*, *l=30a* in units of the lattice constant *a*. The size of the surrounding material is *L =3l* (diamonds), *L=5l* (squares), and *L=10l* (circles).

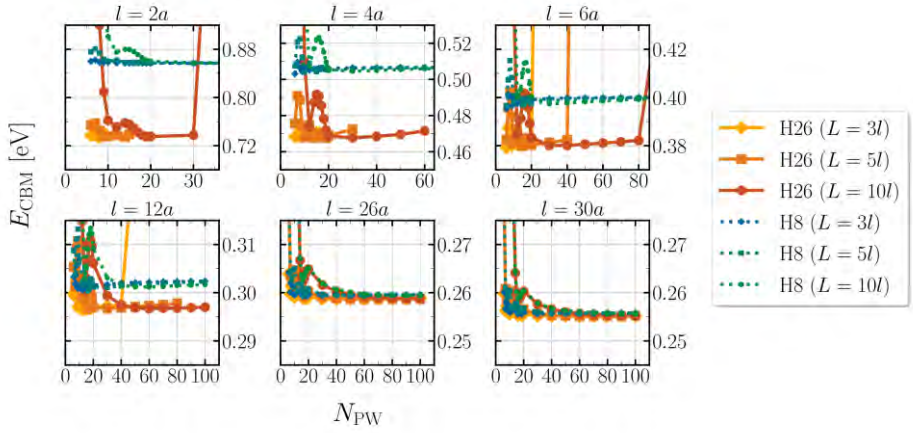

Fig. 3 Energy of CBM as a function of N_{PW}, in QWs. The results were obtained using H26 (solid lines) and H8 (dotted lines) Hamiltonians, respectively, for QWs of the size *l=2a*, *l=4a*, *l=6a*, *l=12a*, *l=26a*, *l=30a* in units of the lattice constant *a*. The size of the surrounding material is *L =3l* (diamonds), *L=5l* (squares), and *L=10l* (circles).

We will focus on H8 and H26 **k•p** Hamiltonians, both of which we first construct for bulk from DFT results using PBEsol functional as described in Jocić and Vukmirović 2020. and eqn.(2). For DFT calculation we used a 4×4×4 **k**-grid for electron states, electron kinetic energy cutoff of 50 Ry, and a total of 240 bands for cubic phase of $CsPbBr_3$ with a lattice constant of a = 11.1 a_0 (where a_0 is the first Bohr radius). DFT calculations were performed with included SOC. Since we are most interested in the position of VBM and CBM, and therefore the band gap, we will focus our convergence tests on these bands.

In Fig. 2 (Fig. 3) we present the energy of the VBM (CBM), as a function of N_{PW}, respectively. The resulting band gap is presented in Fig. 4. All three figures show results for small ($l = 2a$ and $l = 4a$), intermediate ($l = 6a$ and $l = 12a$) and large ($l = 26a$ and $l = 30a$) QWs, respectively.

Although the **k•p** method for QWs itself does not require much computational resources and it can be done, on a single-core desktop computer, it is important to estimate, for every l, at which point increasing L/l and N_{PW} does not change the results of the band gap by more than 10 meV. For H8 one usually needs a smaller ratio of L/l, and for $L/l = 3$, the N_{PW} of 10, 20, 30, 40 and 40, for $l = 2a$, $l = 4a$, $l = 12a$, $l = 26a$, and $l = 30a$, respectively, was sufficient. For H26 one usually needs a larger L/l ratio for smaller wells, while larger wells that approach bulk can have acceptable results for a smaller size of the surrounding material. For $l = 2a$ and $l = 4a$, it was sufficient to use $N_{PW} = 16$ and $N_{PW} = 30$, respectively with $L/l = 10$. For $l = 6a$ and $l = 12a$, it was sufficient to use $N_{PW} = 20$ and $N_{PW} = 40$, respectively with $L/l = 5$. For $l = 26a$ and $l = 30a$, it was sufficient to use $N_{PW} = 30$ and $L/l = 3$.

For small QWs, the results for band gaps obtained from H8 and H26 can differ as much as 150 meV (see Fig. 4), with H8 overestimating the band gap with respect to H26. For intermediate and large QWs, difference in band gaps between H8 and H26 is still present, although it is much smaller and does not exceed 15 meV and 2 meV, respectively.

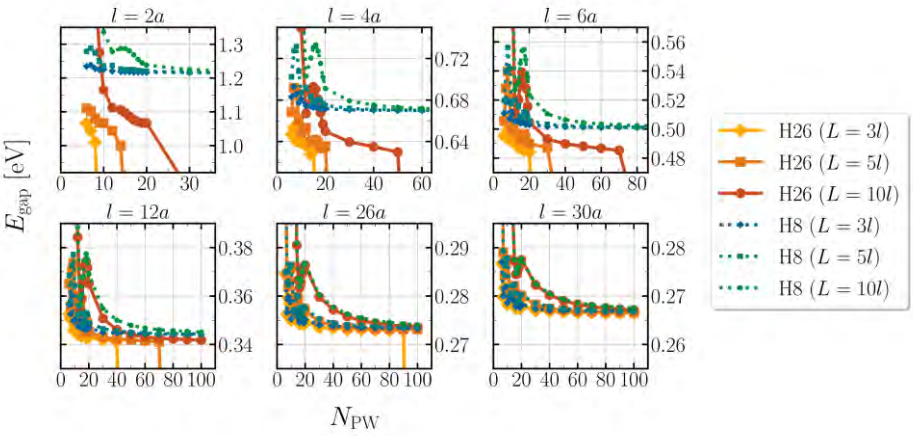

Fig. 4 Energy of the band gap as a function of N_{PW}, in QWs. The results were obtained using H26 (solid lines) and H8 (dotted lines) Hamiltonians, respectively, for QWs of the size l=2a, l=4a, l=6a, l=12a, l=26a, l=30a in units of the lattice constant a. The size of the surrounding material is L =3l (diamonds), L=5l (squares), and L=10l (circles).

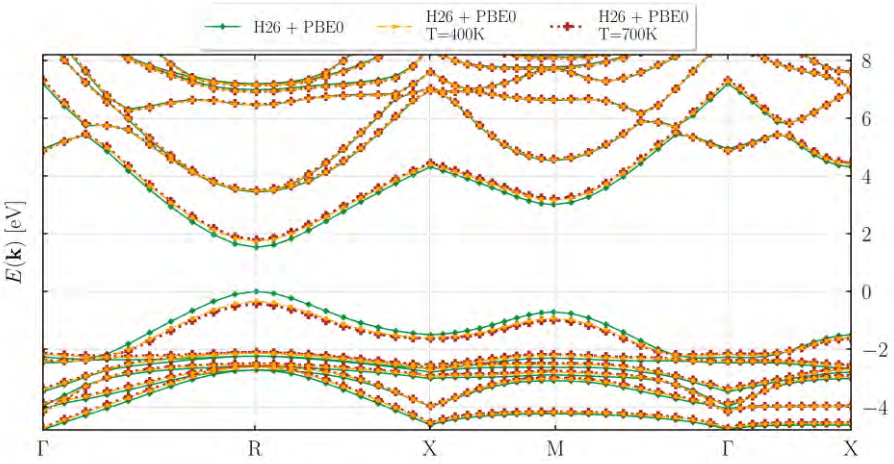

Fig. 5 The band structure of bulk $CsPbBr_3$ obtained using H26 Hamiltonians, replacing E_m with E_m^{PBE0} (solid line with diamonds) and with $E_m^{PBE0} + \Sigma_m(T)$ correction from SCP calculations at T = 400 K (dash-dot line with circles) and T = 700 K (dotted line with crosses), respectively.

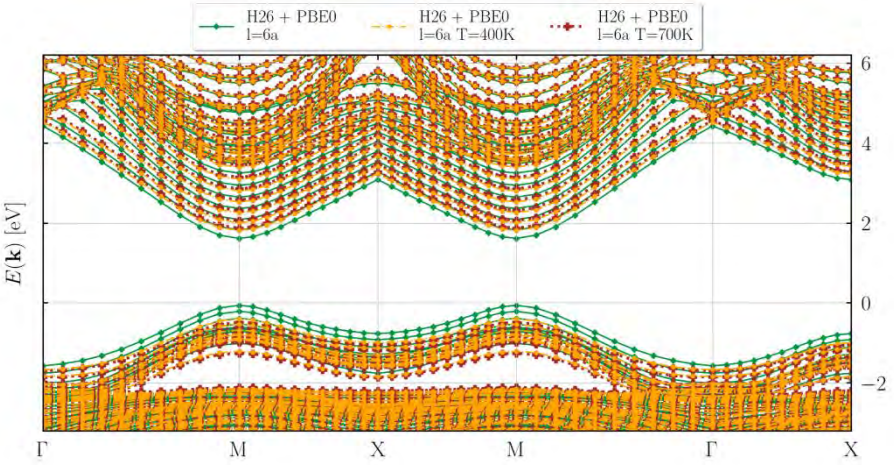

Fig. 6 The band structure of $CsPbBr_3$ QW of size $l = 6a$ obtained using H26 Hamiltonians replacing E_m with E_m^{PBE0} (solid line with diamonds) and with $E_m^{PBE0} + \Sigma_m(T)$ correction from SCP calculations at T = 400 K (dash-dotted line with circles) and T = 700 K (dotted line with crosses), respectively.

In eqn. (2), we restrict envelope functions to the expansion on plane-waves only in the 1BZ. Therefore, in the general case, one would expect some kind of divergence for both H8 and H26, when $N_{PW} > L/a$ or equivalently when $N_{PW} > N_B$. However, due to having much less parameters than H26, H8 seems to be stable even when $N_{PW} > N_B$ unlike H26

which shows divergence in this case, as seen in Fig. 2, Fig. 3 and Fig. 4. We also note that H8 always converges before N_{PW} exceeds the limits of the 1BZ. However, for large wells, both H8 and H26 require less plane-waves than are needed to fill the whole 1BZ, in order to calculate the band gap. For these reasons, we can also check the convergence, by fixing the $N_{PW} = N_B$ to always include all plane-waves in the 1BZ, while only increasing the size ratio of the surrounding material and the QW L/l, and then checking if the resulting band gap changes with reduction of N_{PW}.

Since DFT has a well-documented problem that it typically underestimates the band gaps (Perdew, 1985.), we can improve our **k•p** results by replacing DFT bulk PBEsol energies with the ones obtained using PBE0 (Perdew, 1996.) to obtain a more accurate gap. To include the temperature correction, we add the electron self-energy correction $\Sigma_m(T)$ that comes from the electron-phonon interaction. When calculating PBE0 energies E_m^{PBE0}, we used the same numerical parameters as previously mentioned for PBEsol, with the addition of 4×4×4 q-grid for sampling the required Fock operator and we used the Gygi-Baldereschi method to treat the singularity at $q \to 0$. Results for $\Sigma_m(T)$ were used from our recent paper (Jocić and Vukmirović 2023.), where we used the maxima of the spectral function from SCP method to obtain band energy corrections. The results are available for temperatures from $T = 400$ K to $T = 700$ K.

In eqn. (5), we replace all E_m with E_m^{PBE0}, for H26 without temperature correction, and with $E_m^{PBE0} + \Sigma_m(T)$ for $T = 400$ K and $T = 700$ K, respectively, to include temperature effects in bulk. The resulting band dispersion plot is presented in Fig. 5. As expected from our recent work the biggest shift in energies is observed for VBM and CBM (when comparing against other bands that form H26), which effectively gives the band gap of 2.08 eV and 2.23 eV at $T = 400$K and $T = 700$K, respectively, and 1.5 eV without the $\Sigma_m(T)$. Inserting the same parameters in eqn. (2), we obtained the band gaps of 1.67 eV, 2.21 eV and 2.35 eV, respectively for QW of size $l = 6a$ with its band dispersion shown in Fig. 6.

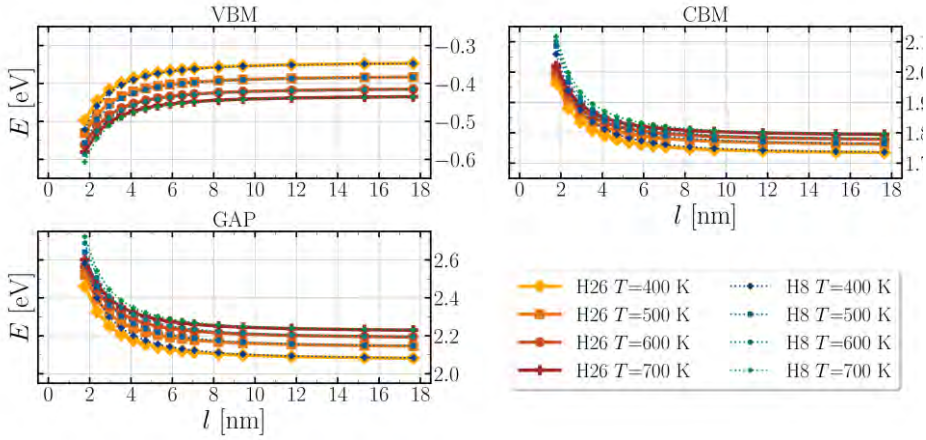

Fig. 7 Energies of VBM, CBM and band gaps for $CsPbBr_3$ QW as a function of the size of the QW l, obtained using H26 Hamiltonian (solid lines) and H8 (dotted lines) when E_m is replaced by $E_m^{PBE0} + \Sigma_m(T)$, at temperatures of $T = 400$ K (diamonds), $T = 500$ K (squares), $T = 600$ K (circles), $T = 700$ K (crosses).

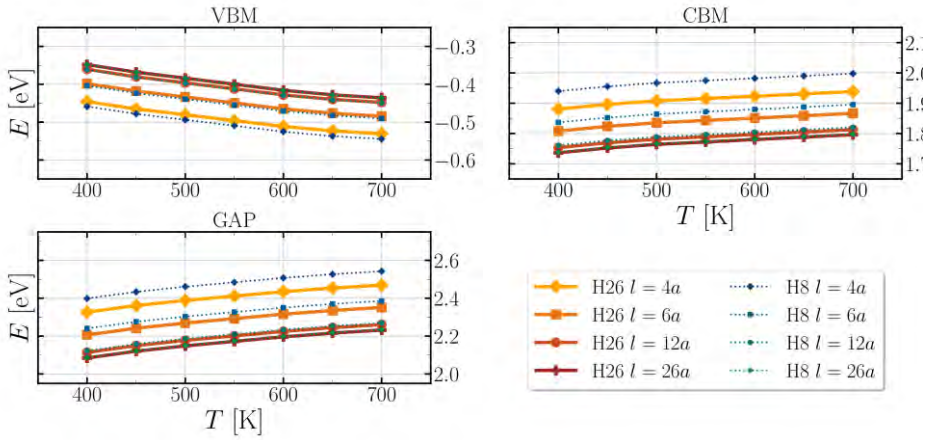

Fig. 8 Energies of VBM, CBM and band gaps for $CsPbBr_3$ QW as a function of temperature T, obtained using H26 Hamiltonian (solid lines) and H8 (dotted lines) when E_m is replaced by $E_m^{PBE0} + \Sigma_m(T)$, respectively for several sizes of QWs $l = 4a$ (diamonds), $l = 6a$ (squares), $l = 12a$ (circles), $l = 26a$ (crosses) in units of lattice constant a.

Finally, we present the temperature dependence of QW band gaps using H26 and H8 Hamiltonians. We calculated how energies of VBM, CBM, and the band gap change with the size of the QW and temperature, respectively. The $E = 0$ level is the one VBM takes for the bulk phase with E_m^{PBE0} energy set. Consistent with the previous figures, H26 and H8 give almost identical results for intermediate and large QWs, while they show a slight discrepancy for small QWs.

Fig. 7 shows energies of VBM, CBM, and band gaps, respectively, as a function of QW size l, starting from $l = 2a$ and going to $l = 30a$ for several temperatures that range from 400 to 700 K. From this figure we can conclude that the energies of the bands and therefore the gap change significantly with the increase of the QW size until certain point (around 8 nm), after which the results very slowly approach the same ones found in the bulk phase.

Fig. 8 shows energies of VBM, CBM, and band gaps, respectively, for temperatures from $T = 400$ K to $T = 700$ K for several QW sizes of $l = 4a$, $l = 6a$, $l = 12a$, and $l = 26a$. From this figure we can see that the relative change of energies with temperature is similar for all sizes of QWs and again similar for bulk when compared to results from Jocić and Vukmirović 2023.

4. CONCLUSION

In this work, we demonstrated a procedure for obtaining convergence with respect to numerical parameters used for H8 and H26 **k•p** Hamiltonians for QWs like the size ratio of the surrounding material and the QW of width L/l and the number of plane waves in the envelope function expansion N_{PW}, relying on the procedure used in Jocić and Vukmirović 2020. We demonstrated that even when H8 shows no divergence for $N_{PW} > N_B$, the results do not change from the ones that take all plane-waves in the 1BZ. The H26 produces

diverging results whenever $N_{PW} > N_B$, but for large QWs a good result can be obtained when $N_{PW} < N_B$. We obtained a band dispersion with improved value for the band gap for bulk and QW, using H26 and replacing PBEsol energies E_m with PBE0 energies E_m^{PBE0} and then introducing the temperature effects from electron self-energy corrections $\Sigma_m(T)$, obtained from spectral function maxima, as in Jocić and Vukmirović 2023. Finally, we obtained results for the temperature dependence of band gaps for QWs using the **k•p** method. Band gap results were obtained for wells in the range from $l = 2a$ to $l = 30a$, and for the temperatures from 400 K to 700 K. This way, we showed how the band gap of the QWs changes with size and temperature in the case of perovskite $CsPbBr_3$ in cubic form.

Acknowledgments. We acknowledge funding provided by the Institute of Physics Belgrade, through the grant by the Ministry of Science, Technological Development and Innovation of the Republic of Serbia. Numerical computations were performed on the PARADOX-IV supercomputing facility at the Scientific Computing Laboratory, National Center of Excellence for the Study of Complex Systems, Institute of Physics Belgrade.

REFERENCES

Bir, G., Pikus, G., *Symmetry and Strain-induced Effects in Semiconductors,* Wiley, New York, 1974.

Bradley, C., Cracknell, A., *The Mathematical Theory of Symmetry in Solids: Representation Theory for Point Groups and Space Groups,* Oxford University Press, Oxford **2010**.

Jocić, M., Vukmirović, N., 2020. Phys. Rev. B, 102, 085121. doi: 10.1103/PhysRevB.102.085121

Jocić, M., Vukmirović, N., 2023. Phys. Chem. Chem. Phys., 25, 29017–29031, doi: 10.1039/D3CP02054A

Lew Yan Voon, L. C., Willatzen, M., *The* **k•p** *Method: Electronic Properties of Semiconductors,* Springer-Verlag, Berlin Heidelberg, **2009**.

Löwdin, P., 1951. J. Chem.Phys., 19, 1396–1401, doi: 10.1063/1.1748067

Perdew, J. P., 1985. Int. J. Quantum Chem., 28, 497–523, doi: 10.1002/qua.560280846

Perdew, J. P., Burke, K., Ernzerhof, M., 1996. Phys. Rev. Lett., 77, 3865–3868, doi: 10.1103/PhysRevLett.77.3865

TEMPERATURSKA ZAVISNOST ELEKTRONSKOG ENERGETSKOG PROCEPA KVANTNIH JAMA $CsPbBr_3$ DOBIJENIH POMOĆU k•p METODA

Izračunali smo elektronsku strukturu $CsPbBr_3$ kvantne jame pomoću **k•p** *modela korišćenjem parametara iz DFT proračuna na bazi hibridnih funkcionala sa dodatkom korekcija za self-energije koje potiču od elektron-fonon interakcije. Dobili smo temperatursku zavisnost procepa za različite veličine kvantne jame. Rezultati pokazuju da je temperaturska zavisnost u kvantnim jamama, za sve veličine jama koje su uzete u obzir, slična onoj koja se dobija za balk fazu.*

Ključne reči: *nanostrukture, temperaturska zavisnost, kvantne jame,* ***k•p*** *metod.*

УНИВЕРЗИТЕТ У НИШУ
ПРИРОДНО-МАТЕМАТИЧКИ ФАКУЛТЕТ У НИШУ

Милан М. Јоцић

Електронска својства перовскитних нанокристала

ДОКТОРСКА ДИСЕРТАЦИЈА

Ниш, 2025.

UNIVERSITY OF NIŠ
FACULTY OF SCIENCES AND MATHEMATICS

Milan M. Jocić

Electronic properties of perovskite nanocrystals

DOCTORAL DISSERTATION

Niš, 2025.

Подаци о докторској дисертацији

Ментор:	др, Ненад Вукмировић, научни саветник, Институт за физику у Београду, Универзитет у Београду. др, Ненад Милојевић, редовни професор, Природно-математички факултет, Универзитет у Нишу.
Наслов:	Електронска својства перовскитних нанокристала
Резиме:	Халидни перовскитни материјали су током година детаљно испитивани експериментално захваљујући својим изузетним оптоелектронским особинама. Међутим, многа питања су остала отворена и захтевају одговарајућа теоријска истраживања. Теоријска истраживања су се углавном фокусирала на кристалне перовскитне материјале и била су заснована на примени ab initio метода за прорачун електронске структуре материјала. Ове методе се не могу практично применити на нанокристале који садрже велики број атома, па се прорачун не може извршити у разумном временском оквиру. Методе које омогућавају проучавање електронских стања у перовскитним нанокристалима развијене су у овој дисертацији. Прва тема овог рада је развој методе која користи резултате ab initio прорачуна кристалног материјала у балк фази за конструкцију симтетријски адаптираног Хамилтонијана. Параметри таквог Хамилтонијана могу се користити за конструкцију Хамилтонијана у репрезентацији анвелопних функција, који се даље може применити на нанокристале. Друго, електронска структура халидних перовскитних материјала се детаљно истражује, узимајући у обзир све релевантне ефекте. То укључује ефекте измене и корелације електрона, као и температурне ефекте који потичу од интеракције електрона и фонона. Ефекти измене и корелације укључени су коришћењем хибридног PBE0 функционала модификованог да задовољи Копмансов услов у оквиру теорије функционала густине (DFT). Температурни ефекти су добијени коришћењем модификоване Ален-Хајне-Кардона методе: елементи матрице прелаза услед фононске пертурбације добијени су коришћењем пертурбационе теорије функционала густине, док су фреквенције фонона добијене самоконзистентним фононским методом који узима у обзир анхармонијске ефекте, при чему се истовремено третира и ширење и ренормализација енергетских зона помоћу самоконзистентне процедуре засноване на Мигдаловој апроксимацији. На крају, температурно зависна електронска стања у перовскитним нанокристалима су израчуната за квантне јаме, жице и тачке различитих димензија.
Научна област:	Физика
Научна дисциплина:	Електронске особине наноструктура

Кључне речи:	Електронска својства, електронска структура, халидни перовскити, нанокристали, ab initio, теорија функционала густине (DFT), k·p метод, електрон-фонон интеракција, симетријска адаптација, групе симетрија, квантна јама, квантна жица, квантна тачка.
УДК:	621.38:621.383.51(043.3)
CERIF класификација:	P 260 Кондензоване материје: електронска структура, електричне, магнетне и оптичке карактеристике, суперпроводници, магнетна резонанца, релаксација, спектроскопија P 265 Физика полупроводника
Тип лиценце Креативне заједнице:	**CC BY-NC-ND**

Data on Doctoral Dissertation

Doctoral Supervisor:	Dr. Nenad Vukmirović, Research Professor, Institute of Physics Belgrade, University of Belgrade. Dr. Nenad Milojević, Professor, Faculty of Sciences and Mathematics, University of Niš
Title:	Electronic properties of perovskite nanocrystals
Abstract:	Halide perovskite materials have been investigated in detail experimentally over the years due to their exceptional optoelectronic properties. However, many questions remained open which call for appropriate theoretical research. Theoretical investigations were mainly focused on crystalline perovskite materials and were based on the application of ab initio methods for calculation of electronic structure of materials. These methods cannot be applied in practice to nanocrystals which contain a large number of atoms and hence the calculation cannot be performed in reasonable timeframe. The methods that enable investigation of electronic states in perovskite nanocrystals are developed in this thesis. The first subject of this work is the development of method that uses the result of ab initio calculation of crystalline material in bulk phase to construct the symmetry-adapted Hamiltonian. The parameters from such Hamiltonian can be used to construct a Hamiltonian in the envelope function representation, which can be applied to nanocrystals. Second, the electronic structure of halide perovskite materials is investigated in detail, taking into account all relevant effects. This includes the electron exchange and correlation effects, as well as temperature effects that stem from electron-phonon interaction. The exchange and correlation is included using hybrid PBE0 functional modified to meet the Koopmans' condition within DFT framework. The temperature effects are obtained using modified Allen-Heine-Cardona method: transition matrix elements due to phononic perturbation are obtained using density functional perturbation theory, phonon frequencies are obtained from self-consistent phonon method that takes anharmonic effects into account, while broadening and renormalization of the bands is treated simultaneously using self-consistent procedure based on Migdal approximation. Finally, the temperature dependent electronic states in perovskite nanocrystals are computed for quantum wells, wires and dots of various sizes.
Scientific Field:	Physics
Scientific Discipline:	Electronic properties of nanostructures
Key Words:	Electronic properties, electronic structure, halide perovskites, nanocrystals, ab initio, density functional theory (DFT), k·p method, electron-phonon interaction, symmetry adaptation, symmetry groups, quantum well, quantum wire, quantum dot.

UDC:	621.38:621.383.51(043.3)
CERIF Classification:	P 260 Condensed matter: electronic structure, electrical, magnetic and optical properties, superconductors, magnetic resonance, relaxation, spectroscopy P265 Semiconductor physics

ПРИРОДНО - МАТЕМАТИЧКИ ФАКУЛТЕТ
НИШ

КЉУЧНА ДОКУМЕНТАЦИЈСКА ИНФОРМАЦИЈА

Редни број, **РБР**:	
Идентификациони број, **ИБР**:	
Тип документације, **ТД**:	монографска
Тип записа, **ТЗ**:	текстуални / графички
Врста рада, **ВР**:	докторска дисертација
Аутор, **АУ**:	Милан М. Јоцић
Ментор, **МН**:	Ненад Вукмировић, Ненад Милојевић
Наслов рада, **НР**:	Електронска својства перовскитних нанокристала
Језик публикације, **ЈП**:	енглески
Језик извода, **ЈИ**:	енглески
Земља публиковања, **ЗП**:	Србија
Уже географско подручје, **УГП**:	Србија
Година, **ГО**:	2025.
Издавач, **ИЗ**:	ауторски репринт
Место и адреса, **МА**:	Ниш, Вишеградска 33.
Физички опис рада, **ФО**: (поглавља/страна/ цитата/табела/слика/графика/прилога)	6 поглавља; 214 страна; 211 цитата; 59 слика; 4 табела; 4 прилога;
Научна област, **НО**:	Физика
Научна дисциплина, **НД**:	Електронске особине наноструктура
Предметна одредница/Кључне речи, **ПО**:	Електронска својства, електронска структура, халидни перовскити, нанокристали, ab initio, теорија функционала густине (DFT), k·p метод, електрон-фонон интеракција, симетријска адаптација, групе симетрија, квантна јама, квантна жица, квантна тачка.
УДК	**621.38:621.383.51(043.3)**
Чува се, **ЧУ**:	библиотека
Важна напомена, **ВН**:	Дисертација израђена у Лабораторији за примену рачунара у науци, Институт за физику у Београду.

Извод, **ИЗ**:		Халидни перовскитни материјали су током година детаљно испитивани експериментално захваљујући својим изузетним оптоелектронским особинама. Међутим, многа питања су остала отворена и захтевају одговарајућа теоријска истраживања. Теоријска истраживања су се углавном фокусирала на кристалне перовскитне материјале и била су заснована на примени ab initio метода за прорачун електронске структуре материјала. Ове методе се не могу практично применити на нанокристале који садрже велики број атома, па се прорачун не може извршити у разумном временском оквиру. Методе које омогућавају проучавање електронских стања у перовскитним нанокристалима развијене су у овој дисертацији. Прва тема овог рада је развој методе која користи резултате ab initio прорачуна кристалног материјала у балк фази за конструкцију симтетријски адаптираног Хамилтонијана. Параметри таквог Хамилтонијана могу се користити за конструкцију Хамилтонијана у репрезентацији анвелопних функција, који се даље може применити на нанокристале. Друго, електронска структура халидних перовскитних материјала се детаљно истражује, узимајући у обзир све релевантне ефекте. То укључује ефекте измене и корелације електрона, као и температурне ефекте који потичу од интеракције електрона и фонона. Ефекти измене и корелације укључени су коришћењем хибридног PBE0 функционала модификованог да задовољи Копмансов услов у оквиру теорије функционала густине (DFT). Температурни ефекти су добијени коришћењем модификоване Ален-Хајне-Кардона методе: елементи матрице прелаза услед фононске пертурбације добијени су коришћењем пертурбационе теорије функционала густине, док су фреквенције фонона добијене самоконзистентним фононским методом који узима у обзир анхармонијске ефекте, при чему се истовремено третира и ширење и ренормализација енергетских зона помоћу самоконзистентне процедуре засноване на Мигдаловој апроксимацији. На крају, температурно зависна електронска стања у перовскитним нанокристалима су израчуната за квантне јаме, жице и тачке различитих димензија.
Датум прихватања теме, **ДП**:		06.04.2022.
Датум одбране, **ДО**:		
Чланови комисије, **КО**:	Председник:	
	Члан:	
	Члан, ментор:	

ПРИРОДНО - МАТЕМАТИЧКИ ФАКУЛТЕТ
НИШ

KEY WORDS DOCUMENTATION

Accession number, **ANO**:	
Identification number, **INO**:	
Document type, **DT**:	monograph
Type of record, **TR**:	textual / graphic
Contents code, **CC**:	doctoral dissertation
Author, **AU**:	Milan M. Jocić
Mentor, **MN**:	Nenad Vukmirović, Nenad Milojević
Title, **TI**:	Electronic properties of perovskite nanocrystals
Language of text, **LT**:	English
Language of abstract, **LA**:	English
Country of publication, **CP**:	Serbia
Locality of publication, **LP**:	Serbia
Publication year, **PY**:	2025
Publisher, **PB**:	author's reprint
Publication place, **PP**:	Niš, Višegradska 33.
Physical description, **PD**: (chapters/pages/ref./tables/pictures/graphs/appendixes)	6 chapters; 214 pages; 211 references; 59 figures; 4 tables; 4 appendices;
Scientific field, **SF**:	physics
Scientific discipline, **SD**:	electronic properties of nanostructures
Subject/Key words, **S/KW**:	Electronic properties, electronic structure, halide perovskites, nanocrystals, ab initio, density functional theory (DFT), k·p method, electron-phonon interaction, symmetry adaptation, symmetry groups, quantum well, quantum wire, quantum dot.
UC	621.38:621.383.51(043.3)
Holding data, **HD**:	library
Note, **N**:	Work on this thesis was done at the Scientific Comptuing Laboratory, Institute of Physics Belgrade.

Abstract, **AB**:		Halide perovskite materials have been investigated in detail experimentally over the years due to their exceptional optoelectronic properties. However, many questions remained open which call for appropriate theoretical research. Theoretical investigations were mainly focused on crystalline perovskite materials and were based on the application of ab initio methods for calculation of electronic structure of materials. These methods cannot be applied in practice to nanocrystals which contain a large number of atoms and hence the calculation cannot be performed in reasonable timeframe. The methods that enable investigation of electronic states in perovskite nanocrystals are developed in this thesis. The first subject of this work is the development of method that uses the result of ab initio calculation of crystalline material in bulk phase to construct the symmetry-adapted Hamiltonian. The parameters from such Hamiltonian can be used to construct a Hamiltonian in the envelope function representation, which can be applied to nanocrystals. Second, the electronic structure of halide perovskite materials is investigated in detail, taking into account all relevant effects. This includes the electron exchange and correlation effects, as well as temperature effects that stem from electron-phonon interaction. The exchange and correlation is included using hybrid PBE0 functional modified to meet the Koopmans' condition within DFT framework. The temperature effects are obtained using modified Allen-Heine-Cardona method: transition matrix elements due to phononic perturbation are obtained using density functional perturbation theory, phonon frequencies are obtained from self-consistent phonon method that takes anharmonic effects into account, while broadening and renormalization of the bands is treated simultaneously using self-consistent procedure based on Migdal approximation. Finally, the temperature dependent electronic states in perovskite nanocrystals are computed for quantum wells, wires and dots of various sizes.
Accepted by the Scientific Board on, **ASB**:		06.04.2022.
Defended on, **DE**:		
Defended Board, **DB**:	President:	
	Member:	
	Member, Mentor:	

Acknowledgements

The research presented in this thesis was carried out at the Scientific Computing Laboratory (SCL) of the Institute of Physics in Belgrade (IPB), where I was employed during my PhD studies.

First and foremost, I would like to express my deepest gratitude to my thesis supervisor, Dr. Nenad Vukmirović, for his patience and guidance throughout our years of collaboration. His exemplary work ethic and profound understanding of various areas in physics made it possible for me to discover true joy in the field of solid-state and semiconductor physics. Through his mentorship, I have learned not only about science, but also about life.

I would also like to thank the head of SCL, Dr. Antun Balaž, for giving me the opportunity to work in such a supportive and inspiring environment. Coming from the University of Niš, without any prior connections to IPB, the University of Belgrade, or even the city of Belgrade, I will always be grateful for the trust placed in me from the very beginning. In this regard, I sincerely thank Dr. Ivan Mančev, whose recommendation was instrumental, and Dr. Darko Tanasković, who first introduced me to Dr. Balaž.

My heartfelt thanks go to my dear friend, MSc thesis mentor, and PhD comentor, Dr. Nenad Milojević. Without his guidance, my interest in physics might never have extended beyond undergraduate studies. His lectures, practical classes, and personal support played a key role in my decision to pursue both MSc and PhD studies.

Last but not least, I want to thank my family, friends, and colleagues, who have endured me throughout all the years of my life, schooling, and studies—including my ever-present inappropriate humor (or at least, attempts at it). Your patience, support, and laughter have meant the world to me.

The funding for this research was provided by IPB, through the grant from the Ministry of Science, Technological Development, and Innovation of the Republic of Serbia. From January 2024, this research was also supported by the Science Fund of the Republic of Serbia, Grant No. 5468, Polaron Mobility in Model Systems and Real Materials - PolMoReMa. Numerical computations were performed on the PARADOX-IV supercomputing facility at the SCL, National Center of Excellence for the Study of Complex Systems, IPB.

Abstract

Halide perovskite materials have been investigated in detail experimentally over the years due to their exceptional optoelectronic properties. However, many questions remained open which call for appropriate theoretical research. Theoretical investigations were mainly focused on crystalline perovskite materials and were based on the application of ab initio methods for calculation of electronic structure of materials. These methods cannot be applied in practice to nanocrystals which contain a large number of atoms and hence the calculation cannot be performed in reasonable timeframe. The methods that enable investigation of electronic states in perovskite nanocrystals are developed in this thesis.

The first subject of this work is the development of method that uses the result of ab initio calculation of crystalline material in bulk phase to construct the symmetry-adapted Hamiltonian. The parameters from such Hamiltonian can be used to construct a Hamiltonian in the envelope function representation, which can be applied to nanocrystals. Second, the electronic structure of halide perovskite materials is investigated in detail, taking into account all relevant effects. This includes the electron exchange and correlation effects, as well as temperature effects that stem from electron-phonon interaction. The exchange and correlation is included using hybrid PBE0 functional modified to meet the Koopmans' condition within DFT framework. The temperature effects are obtained using modified Allen-Heine-Cardona method: transition matrix elements due to phononic perturbation are obtained using density functional perturbation theory, phonon frequencies are obtained from self-consistent phonon method that takes anharmonic effects into account, while broadening and renormalization of the bands is treated simultaneously using self-consistent procedure based on Migdal approximation. Finally, the temperature dependent electronic states in perovskite nanocrystals are computed for quantum wells, wires and dots of various sizes.

Contents

List of Figures

List of Tables

Chapter 1

Introduction

Halide perovskite materials, in both inorganic and organic-inorganic forms, have garnered much attention. Significant advancements have been made in recent years, with ongoing progress in the field. This introduction provides an overview of solid-state perovskite materials, their applications, and challenges in theoretical modeling, focusing on both inorganic and organic-inorganic variants. While the primary focus of this thesis is on inorganic halide perovskites, many of the concepts discussed here can be applied, or at least adapted, to organic-inorganic halide perovskites. The main property addressed in this thesis is the electronic structure, beginning with the bulk phase and later extending to nanostructures. In the following sections, we will review some basic facts and applications of halide perovskites, as well as the open questions that remain relevant in the field.

Before delving into a brief history of halide perovskites, it's important to first address why these materials are so significant and why they have become a highly active area of research.

The ever-growing global population is driving an increasing demand for energy. This includes powering consumer electronics, as well as food production and industrial expansion. Meeting these demands presents a significant challenge, given that current energy resources for generation and storage are finite. Traditional energy sources, such as fossil fuels, are not only limited but also generate pollution and environmental concerns, including air pollution and greenhouse gas emissions. Nuclear energy raises issues with waste disposal, while some renewable sources, such as hydroelectric plants, can disrupt local ecosystems, including aquatic habitats. Wind turbines, though less harmful, can affect local wildlife, such as birds and bats.

Solar power presents a promising alternative, with photovoltaic (PV) cells directly converting solar radiation into electricity, while concentrated solar power (CSP) uses mirrors to focus sunlight and generate heat for conversion into electricity. While CSP is effective in regions with abundant sunlight, such as deserts, it is less commonly used due to its specific geographical requirements and higher initial installation costs. They can be deployed on rooftops in urban areas without the need for large, dedicated installations and require minimal maintenance.

Beyond terrestrial applications, PVs are also essential in space, where they are used to power satellites, the International Space Station, and various lunar and

Martian exploration missions.

The widespread application of PVs in both terrestrial and space environments underscores the importance of developing efficient, cost-effective, and sustainable materials for solar energy devices. One of the most promising materials to meet these demands are halide perovskites.

In addition to large-scale industrial applications, the benefits of energy efficiency can be scaled down to the household level. In the 21st century, much of the technological progress has been driven by advancements in semiconductors, either through miniaturization or by increasing their performance. For example, what was considered a cutting-edge desktop computer in 2000 is now outpaced in processing power, screen resolution, and refresh rate by handheld mid-range consumer devices of 2025, such as tablets and smartphones.

With this increased processing power, however, comes a trade-off: higher power consumption. As a result, frequent device charging has become the norm, with many users recharging their devices daily or multiple times per day. Fortunately, devices have also become more power-efficient and charge more quickly. This is where innovations like solar-powered charging stations—already found in many public places, such as parks—become highly beneficial to society.

On an even smaller scale, semiconductor-based wristwatches have evolved far beyond their initial function of simply telling time. Modern smartwatches now allow users to make calls, check emails, monitor heart rate, track steps, and even measure respiration. These devices run operating systems that support a variety of applications. Some can even replace credit cards and offer navigation features through sophisticated GPS systems.

As the demand for smaller, more efficient devices grows, design choices have evolved as well. Most smartwatches now include touch, heat, and light sensors that automatically adjust screen brightness based on ambient lighting to conserve power. Furthermore, an increasing number of devices, such as sport watches and cycling computers, are integrating solar cells to provide solar-assisted charging. This integration has been shown to significantly extend battery life, with some manufacturers claiming that solar-assisted charging can boost battery life several times compared to models without solar charging. While these solar-powered features are typically found on flagship models, as with most technology, they tend to trickle down to more affordable models in subsequent generations, or even trickle up to more sophisticated devices like smartphones and tablets.

This trend highlights the importance of continuing to improve device efficiency, durability, and cost-effectiveness, as these innovations are crucial for both individual consumers and society as a whole.

This thesis on perovskite nanostructures is structured as follows. The present chapter, Chapter 1, serves as an introduction to perovskite materials, their crystal structure, previously performed computations, and their applications. Chapter 2 provides the theoretical background required to follow the subsequent chapters, as well as an introduction to notations, abbreviations, and terminology. Readers already familiar with the subject can skip this chapter and refer back to it for clarification when needed. Chapters 3, 4, and 5 present the results obtained during

this research. Chapter 3 introduces a streamlined method for deriving a symmetry-adapted $\mathbf{k} \cdot \mathbf{p}$ Hamiltonian directly from ab initio DFT calculations, applying this method to the cases of CdSe and $CsPbX_3$ (X=Cl, Br, I) halide perovskites. Chapter 4 focuses on obtaining an accurate, temperature-dependent band gap for $CsPbX_3$ (X=Cl, Br, I) in its bulk phase. Chapter 5 combines the methods and results from Chapters 3 and 4 to derive the electronic structure of $CsPbX_3$ (X=Cl, Br, I) halide perovskite nanostructures, including quantum wells, wires, and dots. Chapter 6 provides the conclusion to the thesis. Additionally, supporting information is provided in the Appendix, which the main text will reference at appropriate points.

1.1 Perovskite crystal structure

The study of perovskite crystal structures dates back to 1839 when the first calcium titanate compounds ($CaTiO_3$) mineral was discovered. This structure was named 'perovskite' in honor of the Russian mineralogist Lev Perovski, and today it is the designation for materials that share their crystal structure with $CaTiO_3$. Today, the term 'perovskite' is commonly used in the field of optoelectronics as an umbrella term for any metal halide perovskite.The general formula of metal halide perovskites is ABX_3, where A can either be monovalent organic cation like metylammonium $CH_3NH_3^+$ (MA^+) or formamidinium $CH_3(NH_2)_2^+$ (FA^+), or monovalent inorganic cation like Cs^+; B is a divalent metal cation like Pb^{2+}, Sn^{2+}, Ge^{2+}; and X sites contain a monovalent halide anion like Cl^-, Br^-, or I^-. Halide perovskites $CsBX_3$ crystallize in orthorhombic, tetragonal, or cubic polymorphs depending on external pressure and temperature [1]. Figure 1.1 shows all three of these structures and spatial distortions that differentiate them. In inorganic (and organic) cubic crystals, B^{2+} cations and X^- anions form a 3D network of corner sharing octahedra with X^- positioned at the corners and B^{2+} at the center of the octahedron, and A^+ cations centered at the voids between octahedra [as seen in Figure 1.1(a) from direction that is perpendicular to one of the octahedral planes]. Cubic structure is the most symmetric of the 3, and its primitive cell contains 5 atoms [dashed pink square in Figure 1.1(a)]. Tetragonal structure is obtained from cubic by tilting the octahedra, as the void between them appears to be pinched-in and pinched out along perpendicular directions with all neighboring voids having the opposite pinch direction [Figure 1.1(b)]. The resulting structure has lower symmetry than cubic, and the primitive cell now contains 10 atoms (dashed pink square in [Figure 1.1(b). Orthorhombic structure is obtained from tetragonal by distorting the A^+ sites from the void centers between octahedra [Figure 1.1(c)]. As the distortion between sites follows the pinch direction of the voids, no two neighboring distortions are the same. The resulting orthorhombic structure has the lowest symmetry out of all 3, and its primitive cell is made from two neighboring tetragonal primitive cells due to A^+ distortion and contains 20 atoms in total [dashed pink square in Figure 1.1(c)].

The formation and stability of perovskite structures is evaluated by two param-

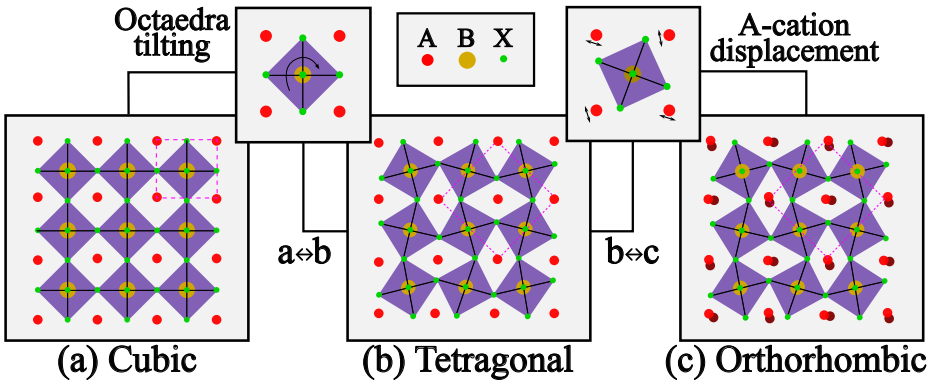

Figure 1.1. Cubic (a), tetragonal (b) and orthorhombic phases (c) of perovskite structure with their primitive cells (pink dashed squares) and spatial distortions that connect them.

eters: the tolerance t and the octahedral μ factor:

$$t = \frac{r_{\mathrm{A}} + r_{\mathrm{X}}}{\sqrt{2}(r_{\mathrm{B}} + r_{\mathrm{X}})}, \quad \mu = \frac{r_{\mathrm{B}}}{r_{\mathrm{X}}}, \tag{1.1}$$

where r_I, I = A, B, X, is the ionic radius of A, B, X ions, respectively. Typically, when $0.8 < t < 1.0$ the crystal shows a 3D perovskite structure, and a value of $0.4 < \mu < 0.9$ favors a stable BX_6 octahedra [1].

Besides ABX_3 formula, halide perovskites can be also formed by partial replacing atoms on X sites with another halide X′ to form $AB(X_\alpha X'_{(1-\alpha)})_3$, where α is a rational number, in order to tune the performance. Besides X sites, the same can be done for B sites with either another B′ atom or B^0 vacancy. Formula in the case when B site is substituted is usually written as $A_2BB'X_6$ which is sometimes referred to as a double perovskite or $A_2BB^0X_6$ or $A_3BB^0X_9$ depending on the vacant sites. If there is a plane where all B sites are replaced with B′ then this structure is sometimes referred as a layered perovskite structure, and in the case where B^0 vacancies disconnect the bonds between layers or unit cells, a non-perovskite dimer phase appears.

1.2 Applications of perovskites

Over the years, halide perovskite materials have demonstrated superior capabilities suited for optoelectronic devices, which is due to their excellent optical and electronic capabilities such as: high light harvesting ability, long and balanced carrier diffusion length, high defect tolerance, high photoluminescence quantum yield and readily tunable band gap. Production-vise, these materials hove proven to be solution processible, flexible and contain great cost-effective potential which is ideal for industrial applications [2]. They emerged in the last decade as revolutionary materials for applications in solar cells [3, 4, 5, 6], light-emitting diodes (LEDs) [7, 8], photodetectors [9, 10], lasers [11], detectors of ionizing radiation [12, 13], thermoelectric [14] and other devices [15]. To understand the characteristics of these devices and to design improved materials and devices, it is essential to be able to predict

the electronic structure of the material. Despite a great interest in understanding the electronic structure of halide perovskites and numerous developments of the methods for electronic structure calculations and the software for performing such calculations, it is still rather challenging to obtain accurate electronic structure of halide perovskites.

The great interest in halide perovskites started in 2009, with the pioneering work of Miyasaka et al. which synthesized $MAPbI_3$ perovskite solar cell (PSC) and achieved a power conversion efficiency (PCE) of 3.8% [16] and later with Lee and Snaith [3] with PCE of 10.9%. The efficiency of PSCs has recently reached 26.0% [17] , which proves to be stepping stone into commercialization. The idea of perovskite LEDs goes back at least as far as PSCs, however it wasn't unit Friend et al. in 2014 prepared $MAPbX_3$ thin-film based LEDs with about 1% external quantum efficiency (EQE) [18]. Nearly 10 years later, green, red, and near-infrared (NIR) perovskite LEDs have all surpassed 20% EQE, with green variant reaching up to 28.9%. Thanks to their high color purity and tunability, luminescence efficiencies, and wide color gamut, perovskites LEDs have the potential to become common in high quality color displays. Meanwhile, perovskites have also shown promise as a good choice for photodetectors and imaging array materials, with a very broad detection region that spans from UV, visible, and NIR to X-ray and γ-ray beams. Perovskite films can also be prepared with amplified spontaneous emission in mind, able to produce coherent beam of light making them capable for laser devices with their performance improving over the years [2].

Another important factor, that can be connected both to the stability and efficiency of the material, is the environmental and health concern. This is an important issue for devices that may contain toxic materials that can degrade, or need special disposal methods, which also raises a sustainability concern. Namely, when dealing with halide perovskites, great performance and stability is achieved with inorganic and organic variants that unfortunately contain the toxic Pb. Efforts are made towards Pb-free perovskites, however for now Pb-based perovskites show superior photovoltaic properties compared to Pb-free ones. The consequences of replacing Pb atoms on performance of and stability of perovskites can be found in more detail in a recent review in Refs. [19, 20, 1, 2].

1.2.1 Solar cells

Solar cell devices can be simply considered as a PIN heterojunction, that consists of P-type and N-type semiconductors with I as an intrinsic layer sandwiched between them, where P-type serves as hole transport layer (HTL), and N-type as electron transport layer (HTL). P and N semiconductors generate a built-in electric field E_{bi} in I layer. Photocarrier dynamics is realized in the following steps: (1) charge-generation, (2) charge-separation, (3) transport of charges, (4) recombination and (5) collection. The intrinsic layer I is where perovskite material would be placed in PSCs.

First, charges are generated (1) as incident photons enter the I material and excite hole and electrons together that must dissociate and overcome the exciton

binding energy (E_B). Perovskites with narrow gaps have an absorption spectrum that covers a wide range, leading to higher usage of incident photons at lower voltage, while having small binding energy E_B that is less than 50 meV [21]. After exciton dissociation, charges are separated (2) toward N(P) type ETL(HTL), which is followed by charge extraction and transport (3) by ETL(HTL) to the electrode. Unfortunately, radiative charge recombination (4) is inevitable which leads to losses. Further losses can be caused by non-radiative recombination from defects and interface imperfections. Finally, charges (electrons and holes) are collected (5) at their respective electrodes.

Efficiency and stability of solar cells

The maximum power conversion efficiency (PCE) of solar cells can be estimated by the Shockley-Queisser (SQ) limit, taking into account that photonic energy of the Sun can be lost in one absorption layer due to multiple factors, some of which are thermalization, transmision and recombination losses. Thermalization losses account for photons that have a higher energy than the band gap of the material and therefore the excess energy is lost to generating heat. On the other hand, transmission losses account for photons with energy lower than the band gap that are transmitted through the material. Finally, recombination losses account for absorbed photons which excited electrons that recombine without generating electricity. The first result obtained by William Shockley and Hans-Joachim Queisser at Shockley Semiconductor in 1961, gave a maximum efficiency of 30% at 1.1 eV [22], while subsequent calculations obtained a value of 33.16% at 1.34 eV [23]. Today, most solar cells are based on Si which dominates the market with its high PCE (reaching 26.7%), great stability and mature fabrication technology [1]. However, the efficiency of Si based solar cells is held back by significant thermal losses due to the narrow band gap of Si, which cannot be widened because of poor tunability of the material.

The PCE over SQ limit can be achieved with multi-junction solar cells using band gap complementary strategy, which can simultaneously absorb more photons and reduce thermalization losses. This strategy involves stacking layers with decreasing band gap, starting from the layer that absorbs incident photon, so that subsequent layers can absorb lower energy photons that were transmitted through the previous layer with a wider gap. This way, high PCE was obtained from III–V semiconductors using multi-junction solar cells, breaking the SQ limit for single-junction cells [24, 25, 26, 27]. Ideally, these layers can be made from material whose band gap can easily be tuned for the required purpose. Fortunately, halide perovskites have a very tunable gap which makes them ideal candidates for this application. For example, tandem solar cells that have perovskite top layer and Si bottom layer have recently achieved PCE of 34.6% [28].

This breakthrough in efficiency can be attributed to greater understanding of the material, precise control of the crystallization process, better device engineering and fabrication techniques. To go beyond current efficiency, it is necessary to minimize losses that stem from non-radiative recombination in the perovskite layer and

develop more efficient charge extraction layers while reducing defects and improving the interface at the contacts with transport layers and electrodes [2].

Besides PCE, another important parameter to take into consideration for solar cells and other devices is the stability of materials. Degradations can occur after prolonged exposure to atmospheric conditions (due to moisture or high temperature) and Sun's UV radiation. Other issues include mechanical instabilities (like cracking or delamination due to wind or vibrations), chemical instabilities (like oxidation), photodegradation (organic molecules can be broken by UV light, reducing the efficiency over time), ion migration (electrical or thermal stress can cause defects in the material), electrochemical instabilities (unwanted chemical reactions can occur on contact points with electrodes) and many more. Even though some materials may show excellent performance and stability, over time they can significantly lose their efficiency for one or more before mentioned reasons.

Pb-based perovskite solar cells

High optical absorption is very desirable for efficient and low-cost thin-film solar cells. $APbX_3$ exhibits extremely high optical absorption coefficients. The record efficiency Pb perovskite solar cell has an absorber layer thickness of around 500 nm, which is much thinner than the absorber layers used in the mainstream inorganic thin-film solar cell technologies with similar PCEs such as GaAs, $Cu(In,Ga)Se_2$ (CIGS), and CdTe.

First, the excellent performance of Pb-based perovskites is due to the combination of high symmetry (O_h point group) which results in high electronic dimensionality, the band gap made from lone-pair Pb $6s$ and the inactive Pb $6p$ orbitals combined with the strong spin-orbit coupling (SOC) results in small effective masses of electrons and holes. For organic perovskites there is also the case for arrangement of polar organic cations, and the ionic nature of halides (lone pair Pb $6s$ and X halide p orbital have strong antibonding coupling) which leads to superior defect tolerance. Removing any of these elements can degrade the performance and/or stability of the solar cell [19].

Starting from the electronic structure, a desirable parameter for any solar cell are small effective masses for both electrons and holes, which then give higher carrier mobilities, longer carrier diffusion lengths, and less nonradiative recombination. In $APbX_3$, band edge of valence band maximum (VBM) originates from Pb $6s$ bands, while conduction band minimum (CBM) comes from Pb $6p$ electrons. Even though band edges from p orbitals give larger effective masses than those coming from more localized s orbitals, $APbX_3$ shows relatively small electron effective masses since CBM originates from $6p$ orbital, that shows strong SOC. Indeed, a strong SOC produces higher band dispersion, large splitting of $6p$ CBM and lower effective masses. Thus elements with strong SOC like Pb provide beneficial parameters for current carriers in perovskite structures[19].

Besides small effective masses, Pb-based perovskites have excellent defect tolerance. For solar cells, the formation of shallow (deep)-level point defects is desirable (undesirable) since they present traps for free carriers (can cause nonradiative recom-

bination). The most important features that contribute to domination of shallow over deep defects in $APbX_3$, is the inactive Pb $6p$ orbital and Pb $6s$ lone-pair states, along with strong antibonding coupling between Pb $6s$ and halide X p orbitals and their high ionicity, high crystal symmetry and large atomic size [20, 19].

The electronic dimensionality can in many cases be connected with structural dimensionality. Namely, under electronic dimensionality one defines in how many directions the atoms that contribute to band edges are spatially connected. For example, pure ABX_3 perovskite structure has 3D dimensionality since B and X atoms that make up band edges are connected the same in all 3 directions. However, some double perovskites $A_2BB'X_6$ like Cs_2SrPbI_6 have 3D perovskite structure but have 0D electronic structure, since Sr-I octahedra doesn't contribute orbitals to band edges. Other examples are Cs_2PbI_4 and Cs_3PbI_5, which are 3D perovskites, but have 2D and 1D electric dimesionality, respectively, due to the Pb vacancies in the structure which break the spatial continuity of Pb-I octahedra that contributes orbitals to band edges. In the direction that Pb-I octahedra are vacant, the band edges are almost flat making the effective masses of electrons and holes too heavy to move in that direction, which is undesirable for current transport, therefore such localized band edges are not suitable for single-junction photovoltaic applications. Therefore, in general, as the electronic dimensionality generally decreases, the associated photovoltaic properties deteriorate. Exception is the case of 2D absorber materials where the film growth is parallel with the layer that has small effective electron and hole masses.

Pb-free perovskite solar cells

There are several ways to produce Pb-free perovskites. One is to replace Pb atoms with another homovalent equivalent like Sn or Ge or heterovalent elements like Bi and Sb. Another is to use heterovalent atoms either by ordered replacement or ordered vacancy. This can be done for halide X atoms to obtain perovskites with formula $AB(X_xX'_{(1-x)})_3$, in order to tune the gap and improve performance[1]. Besides X halides, B sites can be also modified to obtain perovskites with formula $A_2BB'X_6$, sometimes referred as double perovskite. Besides double perovskites, Pb can be replaced with tetravalent Sn^{4+} or trivalent Bi^{3+} atoms, with modified perovskite formulas A_2SnX_6 and $A_3Bi_2X_9$, respectively, in order to keep charge neutrality.

Homovalent replacement is straightforward, as the structure and formula ABX_3 of the perovskite is preserved. Replacing Pb with Sn has its benefits and drawbacks. For example $MASnI_3$ shows a reduced band gap and higher absorption coefficients in the visible light region compared to $MAPbI_3$, which is suitable for single-junction solar cells, but has proven to be much less stable. Namely, Sn atoms have a higher energy $5s^2$ states (compared to $6s^2$ Pb states) that make Sn-X bonds less stable which can lead to Sn vacancies. Furthermore Sn^{2+} can easily oxidize to Sn^{4+}, making the solar cell much more unstable when in contact with air and moisture compared to its Pb counterpart. Using Ge as a replacement doesn't produce desired effect either, since it has a larger band gap compared to Sn (and even some Pb) counterparts,

[1]This was done for both Pb-based and Pb-free perovskites.

even though one would expect the band gap to decrease from Pb to Sn to Ge. One reason for this anomaly is that Ge has $4s^2$ states that are even deeper than $5s^2$ states, the hybridization with halide p states is weaker which results in lower VBM than for Sn analogs. Another reason the small radius of Ge^{2+} atom which leads to structural distortion of the Ge-X_6 octahedra, forming 3 shorter and 3 longer Ge-X bonds. Combining large band gap with instability and likely oxidation from Ge^{2+} to Ge^{4+}, and poor performance is the reason why Ge is not a good substitute for Pb.

1.2.2 LEDs

LEDs with their high color purity and narrow light emission wavelengths are ideal for displays, ambient and signal lighting, consumer electronics and other gadgets. Compared to traditional incandescent light sources, LEDs are more efficient as they can be switched on and off with periodicity too fast for the human eye to notice but this enables less heat losses during operation and have high chromaticity [18].

Perovskite LEDs (PeLEDs) are shown to be a promising candidate as light emitters due to their excellent color purity, spectral tunability, high luminescence efficiencies and low production costs [18]. Despite the rapid advancements in PeLEDs there are still some performance and stability concerns that prevent them to enter commercial use. For now, the key focus is on improving device stability, and realizing high-performance for blue and white color PeLEDs while suppressing efficiency roll-off and minimizing toxicity in the materials. First report of room-temperature electroluminescence from halide perovskites was in 2014 and the field has been advancing ever since. The external quantum efficiency (EQE) of PeLEDs has exceeded the 20% threshold in 2018, followed by more recent improvement to over 28% [2]. This rapid development is related to advances in material synthesis and device design. Thanks to the popularity of PSC, early PeLEDs inherited many designs from them as well as solution processed organic LEDs (OLEDs). PeLEDs show comparable optoelectronic properties of conventional III-V semiconductors while having much simpler manufacturing process. The performance of PeLEDs can further be improved by compositional engineering, passivization of defects and improving morphology, control of dimensionality and more. Regardless of the dominant emission mechanism for particular perovskite material, the main focus is on improving the internal quantum efficiency (IQE) of electroluminescence towards unity. This is rather challenging, since radiative emissions need to be enhanced, while at the same time, non-radiative recombination losses need to be suppressed. While many advancements have been made regarding the efficiency, many challenges still remain, like the device stability. Even though recently near infra red (NIR) PeLEDs have reached commercially stable lifetimes, visible light variants are still unsatisfactory. Efficient blue and white emitters are yet to be produced, with ion migration, efficiency roll-off and device stability being the biggest concerns.

Using material engineering the optoelectronic properties of PeLEDs can be modulated. This consists of dimensional engineering and compositional engineering. Dimensional engineering can be performed by preparing the material in various forms

like 3D bulk crystals, 2D/quasi-2D layers or nanosheets, 1D nanowires or 0D quantum dots. Modulation of dimensionality can be effective method in modulating the perovskite emission color, radiative efficiency, excitonic/non-excitonic nature, charge/energy transfer routes and anisotropic emission. Like in PCE, compositional engineering consists of mixing halide anions at X site. Various colors can be produced: from violet to blue using $ABCl_3$ to $AB(Cl_xBr_{1-x})_3$, green to red using $ABBr_3$ to $AB(Br_xI_{1-x})_3$, and to NIR using ABI_3. Besides X sites, A and B sites can be modulated as well to improve device stability, crystal quality or reduce Pb toxicity [2].

Stability concerns for PeLEDs are similar to PSCs as it currently presents the biggest obstacle towards commercial use. Halide perovskites were considered intrinsically unstable under electric fields due to their soft and ionic crystal lattice. Typical device lifetimes of PeLED are from 1 to 100 hours, which is far from $> 10^4$ hours required for commercial use. Exception are NIR PeLEDs, which EQE of 28% and ultra long lifespan which are about 1.2×10^4 and 3.3×10^4 hours for $5\,\mathrm{mA\,cm^{-2}}$ and $3.2\,\mathrm{mA\,cm^{-2}}$, while lifetimes of about 2.4×10^6 were estimated at lower current densities. However, similar performance and stability for visible light PeLEDs is yet to be achieved. The primary factor for poor lifetimes is the ion migration which occurs under external factors like electric fields, heat and light, due to the low ion migration activation energies and hybrid electronic-ionic conduction properties of perovskites. Several strategies like molecular passivation, changing the dimensionality and thermal management have been explored in order to suppress ion migration to which halide ions mostly contribute [2].

Another concern is the efficiency roll-off, which happens when EQE decreases with the increase of current density. This is a general issue for PeLEDs, which prevents the progress of efficient high-brightness devices and lasers. The main contributing process is the dominant Auger recombination at regions with high carrier density. In general the decay rate of Auger recombination w.r.t. carrier density can be quadratic or linear, depending on the dimensionality, for 3D and 2D/1D perovskites, respectively. In general, small 3D and 2D/1D perovskites have greater confinement of carriers in limited space, which results in higher local carrier density and greater Auger recombination. One solution is to increase the physical volume and reduce carrier density in order to suppress the Auger recombination. Another is to reduce wave-function overlapping in order to minimize the possibility of inter- and intra-band transitions between states, after which Auger recombination occurs. Besides the Auger recombination, other factors that contribute to efficiency roll-off at high density carrier regions are Joule heat generation that degrades the perovskite, ion migration which can encourage phase segregation and defect formation under high applied voltage, and carrier leakage that stems from imbalance of injected electrons and holes [2].

1.2.3 Perovskite nanocrystals

Conventional colloidal semiconductor nanostructures are usually made from binary compounds with simple crystal structure such as zinc-blende (ZnS, ZnSe, CdS, CdSe,

HgTe, InP, InAs) or wurtzite (ZnS, ZnSe, CdS, CdSe) structure or face-centered rock-salt-type compounds (PbS, PbSe) [29]. The synthesis of these nanostructures is performed by costly and elaborate methods that require molecular precursors that are highly air, moisture, or heat sensitive, or difficult to make, or require a sophisticated synthesis in a core-shell structure (for example CdSe-CdZnS) in order to meet the desired performance. These nanostructures also require electronic surface passivation, are likely to form deep trap states due to their covalent nature and band edges consisting of bonding orbitals [29]. In contrast, bonding in perovskite nanocrystals is ionic in nature, which helps them form at room temperature and standard pressure, using a vast selection of molecular precursors. The antibonding character of their band edges contribute to the benign shallow state over the deep trap state defects. The surface defects mostly consist of vacancies due to their low formation energy, and deep trap defects are almost absent due to high energies required to displace ions in the perovskite lattice. This excellent defect tolerance that favors shallow state vacancies removes the need for passivation layers in perovskite nanostructures [29].

Conventional colloidal semiconductors require core-shell strucure and passivation of surface layers obtained from costly synthesis methods, in order to achieve high-photoluminescence (PL) quantum yields (QY) for photoemission devices like LEDs. The same can be obtained using perovskite nanocrystals, from using homogeneous nanocrystals without passivation of the surface layer, with synthesis that is performed under ambient conditions and/or without pre-purified chemicals [29].In both cases, high PL QY of 95-100% with narrow emission lines are observed. However, the spectral range for conventional core-shell nanostructures is limited to wavelengths from 510 nm to 650 nm, while thanks to their highly modular composition (and therefore their band gap), halide perovskite nanocrystals can reproduce the entire visible spectrum from 400 nm to 700 nm. Unfortunately, this excellent performance of PeLED nanocrystals is hindered by their instability and low EQEs. While NIR, red and green PeLEDs have seen improvements in their EQEs, the progress for blue PeLEDs is still desired [29].

1.3 Theoretical modeling performed on perovskite structure

The perovskite electronic structure has been studied extensively using theory with density functional theory (DFT) [30, 31, 32], frozen phonon (FP) method [33, 34, 35], Monte Carlo (MC) [36, 37, 38], molecular dynamics (MD) [39, 37, 35, 40] and many more.

The crystal structure and lattice dynamics have been extensively studied in order to explain: (1) phase diversity, (2) local and average crystal environment, (3) thermodynamic and kinetic stability, and (4) anharmonic lattice vibration and conductivity [41]. Under (1) phase diversity; ab initio MD calculations have been performed in order to confirm x-ray diffraction (XRD) measurements that follow phase transitions upon changing the temperature of the perovskite. For (2) local and aver-

age crystal environment; ab initio MD, neutron scattering [36, 42] and time resolved infra-red [43] data all indicate a 1-10 ps reorientation process at room tempearture for organic perovskite variant, which is the result of anharmonic molecular rotation and large-scale dynamic distortions along imaginary vibration modes which results in considerable deviation of the local structure. DFPT calculations show that the acoustic phonon modes become imaginary (ω^2 is negative) as they approach M and R points in Brillouin zone (see for example Figure 4.2). Within the FP approximation, potential energy surface along M and R points has a double well with an energy barrier of $k_{\mathrm{B}}T$ at the saddle point [35], while MD simulations show continuous tilting of the octahedra at room temperature [39, 35]. With decrease in temperature, this structural instability is reinforced by soft mode at R and cubic lattice transitions into lower symmetry of the tetragonal, followed by the instability contributions from the M point and lowers the symmetry again into orthorhombic phase [35]. Some calculations regarding (3) thermodynamic and kinetic stability have been performed. Using DFT and ab initio thermodynamics (TD), the total energy of the system, Gibbs free energy and other thermodynamic derivatives can be evaluated. For halide perovskites, calorimetric experiments have shown that they are metastable, and it's likely that they are formed due to entropic (configurational, vibrational and rotational) contributions to free energy. Although kinetic factors can be calculated using ab initio techniques, they are considerably more cumbersome and computationally expensive than equilibrium bulk thermodynamics and there have been no rigorous attempts to use them on halide perovskites.Finally, (4) anharmonic lattice vibrations and thermal conductivity have been calculated using quasi-harmonic (QH) approximation as well as perturbative many-body expansions and MD simulations. While QH approximation can calculate anharmonic effects, it still considers that phonons have infinite lifetimes and do not scatter, so the thermal conductivity is ill-defined in this case. Thermal conductivity can be calculated from anharmonic lattice dynamics using perturbation theory that calculates third order force constants or MD that considers contribution to all orders [41].

The electronic structure of halide perovskites resembles the characteristics of traditional semiconductors with a well defined electronic structure and band gap, however some peculiarities have been confirmed over the years, like the strong spin-orbit coupling (SOC) effects and electron-phonon interaction.

In the case of halide perovskites, non-SOC calculation can provide an accurate band gap due to cancellation of errors from local and semi-local functionals and non-SOC treatment. For Pb-based perovskites, the $6s$ electrons contribute mostly to the valence band maximum (VBM), so structural properties are not too influenced by SOC. However, the conduction band minium (CBM) displays mostly Pb $6p$ characteristics, where SOC treatment can result in gap closure of about 1 eV compared to no-SOC calculation. Besides DFT, there were many many-body theory based calculations for perovskites, like the quasi-particle GW approximation, that shows that the band dispersion, as well as density of states, optical character and effective mass, have considerable contributions from electron-electron interaction and SOC. For inorganic halide perovskites, the SOC effects affect mostly the splitting of Pb $6p$ band into $p_{1/2}$ and $p_{3/2}$ two and four degenerate states at R point maintaining

the direct gap. The same happens for organic variants, plus the VBM and CBM split into two valleys symmetrically around R point in momentum space. This kind of splitting occurs when crystals lack the center of inversion symmetry which can generate a local electric field. Inorganic cubic perovskites have center of inversion while organic do not.

Electron-phonon coupling can perturb the band structure and introduce temperature dependence and couple electronic excitations (quasi-electrons and quasi-holes) with vibrational excitations (phonon quasi-particles). In semiconductors, charge carrier scattering is mostly due to this electron-phonon interaction which can set a limit on their mobility. Electron-phonon calculations are usually performed for a static (rigid-ion) structure to the second-order using DFPT. However, electron-phonon calculations of physical properties can be difficult to converge since the required integration is over electronic and vibrational reciprocal space while electron-phonon interaction is rarely a smooth function for real materials [44].

This thesis contributes to better understanding of halide perovskite nanocrystals by exploring two important points.

First point focuses on developing a reliable way for obtaining accurate electronic structure in bulk halide perovskites for $CsPbX_3$ (X=Cl, Br, I) at various temperatures. This result is presented in this thesis as well as Ref. [45]. Therein, the electronic structure of inorganic halide perovskites has been calculated using DFT with hybrid functionals along with anharmonic phonon calculations in order to obtain a temperature dependent self-energy. Using this self-energy, one can calculate band renormalization and width due to electron-phonon coupling, both statically and dynamically. Dynamic calculation is performed using Migdal approximation and a self-consistent procedure was developed. This is one of the main focus of this thesis and can be found in Chapter 4.

Second point expands on the first point by using the results for bulk in order to produce the electronic structure of nanocrystals. The method that is used for extracting bulk structure results directly from DFT and performing symmetry-adaptation when used on Kane model is described in Chapter 3 and published in Ref. [46]. This method is then tested and applied to nanostructures as well [46, 47], however instead of Kane model used for bulk, nanostructures require adopting the Burt-Foreman envelope model that makes use of the same symmetry-adaptation procedure. Chapter 5 is dedicated to testing Burt-Foreman model against DFT for CdSe quantum wells [46] and proceeds with obtaining temperature dependent electronic structure for $CsPbX_3$ (X=Cl, Br, I) nanocrystals in the shape of quantum wells, wires and dots. The later results, concerning the temperature dependent electronic structure of $CsPbX_3$ (X=Cl, Br, I) perovskite nanocrystals, presents original work, published first in this thesis.

Chapter 2

Theory

2.1 Introduction

This chapter serves as an overview of theoretical methods that were used in obtaining the results in subsequent Chapters and will be structured as follows. First, some general information about crystal structure is given in Sec. 2.2. Next, the full electron Hamiltonian and approximations that are routinely used like the Born-Oppenheimer, perfect crystal, mean-field, nearly-free electron, adiabatic and harmonic approximations are expanded upon in Sec. 2.3. Once these approximations are set, some general notions and solutions for an electron in periodic potential are presented in Sec. 2.4 and Sec. 2.5, respectively. Next, the basis of the Kane model, which is used throughout the thesis, is presented in Sec. 2.6. The rest of the chapter takes a more general approach, by splitting calculations for electronic and phononic structure and presenting them in Sections 2.7 and Sec. 2.8, before combining these two into electron-phonon interaction explained is Sec. 2.9. Finally, the chapter finishes with Sec. 2.10 where basic elements of Group theory, required to follow basic concepts present in Chapter 3, are presented.

2.2 Crystal structure

Perfect crystal

Understanding the electronic structure is one of the key components of solid-state physics and material science both in theoretical and experimental terms. Crystalline materials consist of atoms that are connected by bonds and form a periodic lattice in real space. In theory, the *perfect crystal* approximation is often used. Under this approximation, the crystal is made up from orderly spaced atoms of the material without any local impurities, disorder or deformations in the structure. In practice, this is rarely true, however, the number of impurities and imperfections can be reduced enough for their effects on the crystal structure to become negligible. Within the perfect crystal approximation, group theory is a powerful tool which can be used to deduce many properties of the crystal structure. Symmetry operators of a crystal form a group, and they commute with the corresponding Hamiltonian, which

means that the symmetry operators and the Hamiltonian have a common basis of eigenfunctions.

Symmetries that are present in the system define what kind of eigenfunctions can be used to describe it. For example, a sphere will be symmetric for rotations by a continuum set of angles around any axis that contains its center symmetry. In this case there in an infinite number of symmetry operations. However, a cube will be symmetric only for discrete set of angles around a finite number of axes. In group theory language it can be said that, a sphere contains *full rotation group* of symmetries, while a cube contains finite number of rotations contained in the full rotation group.

Symmetry operations

Symmetry operation that is simply defined only by an axis, direction and an angle of rotation is referred to as a *proper rotation* or just a *rotation*, where all points on the axis are fixed. All rotations around one axis belong to the full group of rotations, which is a continuous group with infinitely many elements. In atom, there are infinitely many rotations around infinitely many axes that pass through the center of the nucleus (central axis). Once atoms are brought together, they can form bonds, and organize into a crystal lattice structure, the number of rotations and axes that preserve the symmetry is reduced to a finite number. These rotations also form a group of symmetry operations, which will be a subgroup of the full group of rotations.

Another symmetry operation is *reflection*, which is defined by a plane upon the space is mirrored, where all points on that plane are fixed.

If there exists a symmetry operation that contains a rotation around an axis and a reflection on a plane perpendicular to that axis, it is referred as an *improper rotation*.

If there is at least one shared fixed point for all rotations and reflections in a system, then all these operations will form a *point group*.

There are 14 types of point groups: C_n, S_{2n}, C_{nh}, C_{nv}, D_n, D_{nh}, D_{nd}, T, T_d, T_h, O, O_h, Y, Y_h, where n is an integer, and they yield 32 crystallographic point groups.

Translations translate all points in crystal space to an equivalent point in that same space by some vector, and they do not contain any fixed points.

If translations are added to a point group, then such symmetry group is called a *space group*.

Symmetry group can also contain a compound symmetry operation that consists of a translation followed by a rotation. Individually, this translation and rotation may not even be a symmetry operation of the crystal, but together form a symmetry in the space group. If the rotation is proper, the direction of translation is called a *screw axis*. If the rotation is improper, the corresponding plane of reflection is called a *glide plane*. Groups that have only rotations (proper and improper) and translations, which in themselves can form subgroups of the full symmetry group of a crystal, are called *symmorphic*. Groups that contain a screw axis or a glide plane, are called *nonsymmorhpic*.

The symmetry group (point or space) will govern which eigenvalues and eigenvectors can describe the system. For example, any set of eigenvectors of a Hamiltonian can be transformed by symmetry operations to produce degenerate eigenvalues. The symmetry of a system and its Hamiltonian, is directly responsible for the degeneracy of states. The higher the symmetry, the greater is the possible degeneracy of states.

Certain rules, limit the number of possible rotations and screw axes, as well as reflection and glide planes. It can be mathematically shown (it was first done by Fedorov and then independently by Schoenfiels [48]), that there is a finite number of possible space and point groups. There are 230 possible space groups, and only 73 of them are symmorphic. This means that there are 230 ways to form a crystal structure, however not all 230 ways have been discovered.

More details on symmetry operations can be found in Refs. [48, 49].

Consequences of symmetry in a system

In free hydrogen-like atom, the full group of rotations allows for electrons to have degenerate levels. Angular orbital momentum l and spin angular momentum $s = 1/2$ of an electron, are dictating the degeneracy of each energy level. As an infinite group, full group of rotations does not limit the number of degeneracy, so the principal quantum number n, and therefore $l \leq n-1$ can take any number provided that the atom can have electrons with such quantum number. The degeneracy for each n is d_n, and is equal to $d_n = \sum_{l=0}^{l=n-1}(2l+1)(2s+1) = 2n^2$. Each degenerate level, will have d wave functions that correspond to some irreducible representation of the full rotation group. These wave functions are also called the *partners of the irreducible representation*, and any symmetry operation can be expressed in matrix form with these wave functions as basis functions.

When such atom is placed in a crystal structure, many of these degeneracies are lifted as a result of lowered symmetry and these levels will split according to decomposition of irreducible representations between infinite full rotation group and finite point group of the crystal. Just like for hydrogen-like atom, every energy level in crystal, degenerate or non-degenerate, corresponds to some irreducible representation of the crystal point group, where the number of degeneracy d is equal to the dimension of that irreducible representation [50].

Even though full rotation symmetry is lost in a crystal, another class of symmetry operations becomes present as a consequence of the crystal structure. In the perfect crystal approximation, the crystal is not bounded and its structure spawns to infinity in space. Rotations and reflections, rotate and reflect all points in crystal space, respectively, to equivalent points in that space. Translations translate all points in crystal space to an equivalent point in that same space, and for infinite crystal approximation, there are infinitely many possible translations. Translational symmetry allows for a whole crystal structure to be represented by finite volume in crystal space, called *unit cell*. Translating a copy of a unit cell in three directions, infinitely many times, reproduces the crystal structure in perfect crystal approximation.

Bravais lattice and unit cells

Translations that form a group of translations in a crystal can be expressed by these lattice vectors as:

$$\mathbf{T} = n_1\mathbf{A}_1 + n_2\mathbf{A}_2 + n_3\mathbf{A}_3 \tag{2.1}$$

where $i = 1, 2, 3$, and three non-planar vectors $\mathbf{A}_i$ are multiplied by integer values n_i. Each translation $\mathbf{T}$ points to one point in space and all these points form a *Bravais lattice*.

All points on the Bravais lattice are equivalent, and every such point has a finite number of closest neighbors, which is called the *coordination number* of the lattice.

The whole space of Bravais lattice can be divided on finite volumes that do not overlap or leave voids in space between them, and contain only one point of the Bravais lattice. Such volume is called the *primitive cell* or *primitive unit cell*. Space inside the primitive cell can be determined by vector $\mathbf{t}$ as:

$$\mathbf{t} = x_1\mathbf{a}_1 + x_2\mathbf{a}_2 + x_3\mathbf{a}_3, \tag{2.2}$$

where $i = 1, 2, 3$, and a set of three non-planar vectors $\mathbf{a}_i$ are multiplied by x_i, which are real number between 0 and 1. Vectors $\mathbf{a}_i$ are called vectors of the primitive cell, or *primitive vectors*. In general, $\mathbf{A}_i$ and $\mathbf{a}_i$ do not have to be parallel to each other, since the choice for the shape of primitive cell is not unique. However, some choices for a primitive cell can have a lower symmetry than the underlying Bravais lattice.

In order to keep the symmetry of the Bravais lattice, one can choose to work with a non-primitive or *conventional unit cell* (sometimes simply referred to as a *unit cell*). The conventional unit cell fills the whole space without overlap or voids by translation using a subspace of the Bravais lattice vectors $\mathbf{T}$. It is usually bigger in volume than the primitive cell and can contain more than one lattice point, but has the same symmetry as the underlying Bravais lattice. Numbers that specify the size of the (conventional) unit cell are called lattice constants.

Another choice for a unit cell is the *Wigner-Seitz unit cell*. Wigner-Seitz cell contains one lattice point and the smallest polyhedron bounded by planes that bisect and are perpendicular to lines connecting all neighboring points. This way, the Wigner-Seitz unit cell is also a primitive unit cell: it contains one lattice point but has the same symmetry as the underlying Bravais lattice.

While Bravais lattice is a mathematical order of points in space, crystal itself can be viewed as a physical structure that contains physical objects of finite size (like atoms or molecules) located at points of the Bravais lattice. In order to differentiate the physical crystal from the Bravais lattice the term *crystal structure* is used. Crystal structure consists of a physical unit (made out of atoms or molecules) called *basis*, and its copies which are translated by all Bravais lattice vectors. Equivalently, each point on Bravais lattice contains a copy of the basis, hence sometimes this is referred as a *lattice with a basis*. Crystal structure that has only one atom as its basis is called monoatomic Bravais lattice.

Bravais latices can be divided into seven systems (and their corresponding point group): triclinic T (group S_2), monoclinic M (group C_{2h}), orthorhombic O (group D_{2h}), rhombohedral or trigonal R (group D_{3d}), tetragonal or quadratic Q (group

D_{4h}), hexagonal H (group D_{6h}) and cubic K (group O_h). Several of these systems can have be further divided into different types of the same system: monoclinic into two, orthorhombic into four, tetragonal into two, and cubic into three, to give a total of 14 types of Bravais lattices.

More detail on Bravais lattices, systems and types, as well as unit cells can be found in Refs.[48, 49].

Reciprocal lattice and Brillouin zones

Consider a general plane wave $e^{i\mathbf{k}\cdot\mathbf{r}}$, where $\mathbf{r}$ and $\mathbf{k}$ are arbitrary vectors in direct and reciprocal space, respectively. In order to express periodicity of a lattice using plane waves the following must be true:

$$e^{i\mathbf{T}\cdot\mathbf{G}} = 1, \tag{2.3}$$

where $\mathbf{T}$ are the Bravais lattice vectors in direct space, and $\mathbf{G}$ are lattice vectors in reciprocal space or *reciprocal lattice vectors* for that Bravais lattice defined by vectors $\mathbf{T}$. Reciprocal lattice vectors $\mathbf{G}$ can be expressed as:

$$\mathbf{G} = m_1\mathbf{B}_1 + m_2\mathbf{B}_2 + m_3\mathbf{B}_3, \tag{2.4}$$

where $i = 1, 2, 3$, $\mathbf{B}_i$ are three non-planar vectors in reciprocal space and m_i is an integer.

Reciprocal lattice vectors form a Bravais lattice in reciprocal space that inherits symmetry properties from the direct Bravais lattice however, they do not have to share the same lattice type (and usually do not). Using the condition $\mathbf{A}_i\cdot\mathbf{B}_j = 2\pi\delta_{ij}$, the vectors $\mathbf{B}_j$, $j = 1, 2, 3$, in reciprocal space are:

$$\mathbf{B}_j = \epsilon_{jpq} 2\pi \frac{\mathbf{A}_p \times \mathbf{A}_q}{\mathbf{A}_1 \cdot (\mathbf{A}_2 \times \mathbf{A}_3)}. \tag{2.5}$$

For arbitrary $\mathbf{r}$ and $\mathbf{k}$ the periodicity of Bravais lattice will lead to:

$$\begin{aligned} e^{i\mathbf{G}\cdot(\mathbf{r}+\mathbf{T})} &= e^{i\mathbf{G}\cdot\mathbf{r}}, \\ e^{i(\mathbf{k}+\mathbf{G})\cdot\mathbf{T}} &= e^{i\mathbf{k}\cdot\mathbf{T}}. \end{aligned} \tag{2.6}$$

Same as unit cell in direct space, the reciprocal space can be filled by primitive unit cells that contain one lattice point. The Wigner-Seitz primitive cell in reciprocal space is called the *First Brillouin zone* (1BZ). If $\mathbf{a}_i$, $i = 1, 2, 3$, are primitive vectors of the unit cell in direct space, then the primitive vectors in reciprocal space $\mathbf{b}_j$, $j = 1, 2, 3$, will obey the relation $\mathbf{a}_i \cdot \mathbf{b}_j = 2\pi\delta_{ij}$. The point at the center of 1BZ is called the Γ point. If one were to construct the Wigner-Seitz cell in reciprocal space around Γ point, but instead of bisecting the lines that connect the first closest neighbors with perpendicular planes, repeats the process for second closest neighboring points, the intersection of these planes would be called the Second Brillouin zone. The same can be repeated for third or n-th closest neighboring points to construct third or n-th Brillouin zone.

Possible lattice formations

Certain rules, limit the number of possible rotations and screw axes, as well as reflection and glide planes. It can be mathematically shown (Fedorov and Schoenfiels), that there is a finite number of possible space and point groups. There are 14 types of point groups, and 32 point groups in total. These 32 point groups are also referred to as *crystallographic point groups*. There are 7 systems of Bravais latices and 14 types of Bravais lattices in total. All these combine for 230 possible space groups, and only 73 of them are symmporphic. This means that there 230 ways for a crystal structure to form, however not all 230 ways have been discovered.

Further reading

More detailed description of group theory and its application to crystal structure can be found in Refs. [48, 50] and effective-mass method and $\mathbf{k}\cdot\mathbf{p}$ can be found in Refs. [48, 51]. Since knowledge basic of group theory and point groups is essential when reading this thesis, a short reminder about particular point groups and irreducible representations used in this thesis will be presented in Sec. 2.10.

2.3 Approximations to the full electronic Hamiltonian

In Sec. 2.2, general considerations were made about the crystal structure, possible symmetry operations and their connection to the group theory, or more precisely point groups and space groups.

In this section, an introduction to the electronic structure problem is given: what kind of Hamiltonian describes system of electrons in a crystal and what approximations can be used to simplify the problem but still maintain a good physical description of the emerging phenomena?

One can start from the total Hamiltonian $\mathcal{H}^{\mathrm{TOT}}$, that considers positions and momentum of all nuclei and electrons, and Coulomb interaction between them (while at this point neglecting spin-orbit interactions for simplicity):

$$\begin{aligned}\mathcal{H}^{\mathrm{TOT}} = &\sum_I \frac{\mathbf{P}_I^2}{2M_I} + \sum_{I>J} \frac{Z_I Z_J}{4\pi\epsilon_0} \frac{e^2}{|\mathbf{R}_I - \mathbf{R}_J|} \\ &- \sum_{I,i} \frac{Z_I}{4\pi\epsilon_0} \frac{e^2}{|\mathbf{R}_I - \mathbf{r}_i|} \\ &+ \sum_i \frac{\mathbf{p}_i^2}{2m_e} + \sum_{i>j} \frac{1}{4\pi\epsilon_0} \frac{e^2}{|\mathbf{r}_i - \mathbf{r}_j|},\end{aligned} \tag{2.7}$$

where nuclei have mass M_I, atomic number Z_I, momentum P_I, and position $\mathbf{R}_I$ and electrons have mass m_e, elementary charge e, momentum p_i, and position $\mathbf{r}_i$. The first two terms are the kinetic energy of nuclei and Coulomb interaction between them, the third is the Coulomb interaction between nuclei and electrons, and the

fourth and the fifth term are the kinetic energy of electrons and the electron-electron Coulomb interaction. The total Hamiltonian $\mathcal{H}^{\mathrm{TOT}}$ is inserted into a Schrödinger equation:

$$\mathcal{H}^{\mathrm{TOT}}\Psi^{\mathrm{TOT}} = E^{\mathrm{TOT}}\Psi^{\mathrm{TOT}}, \tag{2.8}$$

where Ψ^{TOT}, E^{TOT} are the total wave-function and energy of the system accounting for all electrons and ions. In order to find a solution one first has to simplify the problem and introduce several approximations.

Born-Oppenheimer approximation

The first one is the *Born-Oppenheimer* approximation which decouples nuclei kinetic energy and Coulomb interaction between them from the rest of the terms that contain some information about electrons. The justification for this is as follows: the mass of a proton m_p is about 1.8×10^3 times greater than the mass of electron m_e ($m_p/m_e = 1836.15267343$). The frequencies at which nucleus moves in a crystal are around 10^{13} s^{-1}, and if we assume that in typical semiconductors band gap is around 1 eV, which is the least energy required to excite the electron, that makes the frequency of electronic motion to be around 10^{15} s^{-1}, which means that response of electrons to the movement of the nuclei in the atom is instantaneous, or from the electron's point of view - nuclei appear to be stationary. This approximation allows a separation of two problems: ionic movement and Coulomb interactions between the charges. When decoupled, ionic and electronic part of the Hamiltonian $\mathcal{H}^{\mathrm{TOT}}$ can be solved separately and the total wave-function and energy can be decoupled:

$$\begin{aligned}
\Psi^{\mathrm{TOT}} &= \Phi(\{\mathbf{R}\})\Psi(\{\mathbf{R}\},\{\mathbf{r}\}),\\
\mathcal{H}^{\mathrm{TOT}} &= \mathcal{H}_{\mathrm{ion}} + \mathcal{H}_{\mathrm{el}}\\
\mathcal{H}_{\mathrm{ion}}\Phi(\{\mathbf{R}\}) &= E^{\mathrm{ion}}\Phi(\{\mathbf{R}\}),\\
\mathcal{H}_{\mathrm{el}}\Psi(\{\mathbf{R}\},\{\mathbf{r}\}) &= E^{\mathrm{el}}\Psi(\{\mathbf{R}\},\{\mathbf{r}\}),
\end{aligned} \tag{2.9}$$

where $\Phi(\{\mathbf{R}\})$ and $\Psi(\{\mathbf{R}\},\{\mathbf{r}\})$ are separated ionic and electronic wave functions, respectively, with $\{\mathbf{R}\}$, and $\{\mathbf{r}\}$ as a short-hand notation for collection of all ionic and electronic coordinates, respectively. This approximation is assumed in Sections 2.7 and 2.8, that deal with the electronic and phononic structure, respectively, as well as in Sec. 2.9, that considers the electron-phonon interaction.

Perfect crystal approximation

After decoupling nuclear and electronic parts of the Hamiltonian, one is still left with two many-body problems that describe a crystal system with a very large number of atoms (at the order of 10^{23}). The second approximation is the *perfect crystal* approximation, mentioned in the previous section when discussing the crystal structure. In perfect crystal, translational invariance and periodic conditions, allow one to reduce computations in the irreducible *unit cell* that generates the whole structure when translated along 3 axes. For most systems considered here it also assumes that a crystal has no boundaries (edges) or interfaces with other materials. Such

approximation is true for large systems, which are referred here as *bulk* crystals. Crystal structures that are confined in one, two, or all three dimensions are collectively referred to as *nanostructures* or *nanocrystals*. In the case of nanostructures, periodic conditions are valid only in directions where there is no confinement: the irreducible cell now has to include all atoms in the confined space and take into account the boundaries of the crystal in confined directions. Depending on the confinement, there are 3 types of nanostructures: quantum wells, quantum wires, and quantum dots, which correspond to 1- ,2- ,and 3- dimensional confinement. The effects of the confinement on electronic properties when compared to bulk phases varies over different shapes and sizes of the nanostructure as well as type of material that is considered.

Even though infinite crystals don't really exist, in theory this is usually a good approximation. Since the number of atoms in a real crystal is of the order of 10^{23}, the approximation of an infinite crystal structure is good as long as the number of atoms in the unit cell is much smaller. For bulk crystals this is always the case. However, in the cases where crystal is confined to a much smaller space, like in a nanostructure, this approximation is not valid. Instead of boundary conditions, the infinite crystal approximation and translation symmetry allow for the use of periodic conditions, since all points in the unit cell have their equivalence in another unit cell under certain rules, which simplifies many aspects of the calculation for bulk crystals. These periodic conditions will be the basis for *Bloch theorem* that solves the problem of electron in a periodic potential.

Mean-field approximation

With the electronic part decoupled and computational cell reduced, one is still faced with a fermion many-body problem that is still impossible to solve even with modern supercomputers. One electron interacts with the collective charge distribution of all the other electrons and ions, and, they in turn respond and redistribute their charge to again interact with that electron and so on. Since all electrons are indistinguishable, they should all respond the same.

One way to approximate this behavior is to introduce the *mean-field* approximation which replaces Coulomb terms with an averaged potential $V(\mathbf{r})$ that is the same for all electrons. This allows one to further reduce the problem from many-interacting electrons to a one-electron in periodic potential $V(\mathbf{r})$. It is clear that the many-body interactions make this kind of approximation not so obviously valid, however, this approximation has proven quite useful. In some cases, it can produce both qualitatively and quantitatively decent results, and in some it can fail completely. In many cases however, it produces decent qualitative results, with some discrepancy from experimental results. If a good quantitative estimate is required in these cases, mean-field results can be a starting point for a more refined method that introduces some many-body effects.

For example, *Density Functional Theory* (DFT), that relies on self-consistent mean-field $V^{\mathrm{SCF}}(\mathbf{r})$ that takes into account the Hartree potential and exchange-correlation energy that accounts for many-body interactions has proved to be a very

useful method, whose advantages and disadvantages have been studied intensively. A more refined method would be the GW method that relies on electronic Green's function G to include many-body effects like the electron self-energy, and replaces the electronic mean-field Coulomb interaction with a screened Coulomb term W. More details on both the DFT and GW can be found in Sections 2.7.1 and 2.7.5, respectively.

Nearly-free and tight-binding approximation for electrons

In solids, the bonds between the neighboring atoms are formed from *valence* electrons while all other electrons that occupy the filled orbitals are referred as *core* electrons. Since most of the information about the electronic structure of a crystal can be deduced from valence electrons one can make a convenient (but not necessary) approximation to group nuclei and their respected core electrons together, into ions. The valence electrons see the effective potential made from core electrons and the nucleus as a *pseudopotential*[1]. However, valence (or all) electrons can be considered as nearly-free or tightly-bounded to their core atoms.

The *nearly-free electron* approximation assumes that electrons are not strongly bounded to their core atoms(ions) and behave similarly to free electrons, which makes plane waves a convenient basis for nearly-free electrons. A different approach would be the *tight-binding* approximation which assumes that electrons are tightly bounded to their atoms. In this case, convenient basis for bound electrons are atomic orbitals, so the wave functions are usually represented as a *linear combination of atomic orbitals* (LCAO).

Both the plane wave basis and LCAO are routinely used in DFT with and without the use of pseudopotentials. There are also other ways to solve the electron problem using a different basis from the ones mentioned but they are outside of the scope of this work, and will be briefly mentioned in Sec. 2.7.1 that deals with DFT in more detail. For all DFT results that are presented in Chapters 3, 4, and 5, the plane wave basis with pseudopotentials is used.

Adiabatic and harmonic approximation

When computing the movement of nuclei, nuclear interactions are neglected and they are considered as a system of bosons with different masses, that have classical trajectories and interact like point charges. In the Born-Oppenheimer approximation, it is considered that electrons remain in their ground state as nuclei vibrate. This is also an *adiabatic* approximation, which allows for nuclei to only see the timed-average of electronic potential of all electrons. The sum of all averaged potentials and averaged kinetic energy of electrons in the crystal is called the Born-Oppenheimer energy E^{BO}. All possible configurations of ions make up the Born-Oppenheimer energy surface $E^{\mathrm{BO}}(\{\mathbf{R}\})$ that depends on collective positional coordinates of nuclei

[1] In practical calculations however, this is not straightforward, since sometimes it's not clear if all core electrons should be grouped into ions or should some electrons from filled orbitals also be considered as 'valence', therefore careful tests are necessary.

$\{\mathbf{R}\}$. The Born-Oppenheimer energy, acts as a potential and causes a restitution force that nuclei see while moving.

The Born-Oppenheimer energy $E^{\mathrm{BO}}(\{\mathbf{R}\})$ can be expanded into a Taylor series, by displacing atoms from their equilibrium positions up to some order. In the *harmonic approximation*, the atomic displacements are only to second-order. This way, phononic frequencies are obtained as a solution to the Hessian problem, that includes second-order derivatives of the Born-Oppenheimer surface with respect to positions of atoms.

One method that takes advantage of the harmonic approximation is the *Density Functional Perturbation Theory* (DFPT) which combines DFT with perturbation theory and linear response to obtain solutions for the collective nuclear motion: interatomic force constants, vibrational (phonon) frequencies and vibrational (phonon) modes.

Harmonic approximation is valid in many semiconductors that are stable at both low and high temperatures. However it fails in some cases where material shows a phase transition at a high temperature when anharmonic terms are necessary (e.g. cubic ABX_3 perovskites at high-T, like the $CsPbX_3$ (X=Cl, Br, I), which is the material investigated in this thesis, and its anharmonic phonon structure was necessary to obtain the important results in Chapter 4).

For anharmonic vibrations, one of the methods that can be used is the *Self-Consistent Phonon* (SCPH) theory. SCPH employs many-body formalism with phonon Green functions and phonon self-energy.

More details on DFPT and SCPH can be found in Sections 2.8.3 and 2.8.4, respectively.

2.4 Electron in periodic potential

In order to simplify the problem, one can apply the Born-Oppenheimer, mean-field and perfect crystal approximations mentioned in Sec. 2.3 and imagine that there is only one nearly-free electron in the whole crystal. This electron interacts with a periodic mean-field potential $V(\mathbf{r})$:

$$T(\mathbf{T})V(\mathbf{r}) = V(\mathbf{r}+\mathbf{T}) = V(\mathbf{r}), \tag{2.10}$$

where $T(\mathbf{T})$ is an operator that translates $\mathbf{r}$ by $\mathbf{T}$: $\mathbf{r} \to \mathbf{r}+\mathbf{T}$, and $\mathbf{T}$ is a lattice vector $\mathbf{T} = n_1\mathbf{A}_1 + n_2\mathbf{A}_2 + n_3\mathbf{A}_3$.

The equation that describes a one-electron Hamiltonian $\mathcal{H}^{(1e)}$ in a crystal:

$$\mathcal{H}^{(1e)}\Psi^{(1e)}(\mathbf{r}) = \left[\frac{p^2}{2m_e} + V(\mathbf{r})\right]\Psi^{(1e)} = E^{(1e)}\Psi^{(1e)}(\mathbf{r}). \tag{2.11}$$

where $E^{(1e)}$ is the energy of an electron corresponding to an eigenfunction $\Psi^{(1e)}(\mathbf{r})$. Kinetic energy operator $p^2/(2m_e)$ commutes with $T(\mathbf{T})$ for any system of independent electrons, which means that if $V(\mathbf{r})$ commutes with $T(\mathbf{T})$ then $\mathcal{H}^{(1e)}$ will also commute with $T(\mathbf{T})$. From Eq. (2.10), one can see that $[V(\mathbf{r}), T(\mathbf{T})]\Psi^{(1e)}(\mathbf{r}) = 0$ is true, therefore $[\mathcal{H}^{(1e)}, T(\mathbf{T})]\Psi^{(1e)}(\mathbf{r}) = 0$ must also also true.

Bloch functions and Bloch theorem

Bloch theorem[2] states that solution for Schrodinger equation for an electron in a periodic potential can be expressed as plane waves modulated by periodic functions. These solutions are expressed using *Bloch functions* $\Psi_{\mathbf{k}}^{(1e)}(\mathbf{r})$ as:

$$\Psi_{\mathbf{k}}^{(1e)}(\mathbf{r}) = e^{i\mathbf{k}\cdot\mathbf{r}} u_{\mathbf{k}}(\mathbf{r}), \tag{2.12}$$

where $\mathbf{k}$ is a continuous vector in reciprocal space. Periodic functions $u_{\mathbf{k}}(\mathbf{r})$ are sometimes called *Bloch factors* or modulating factors [48] since they modulate the plane wave $e^{i\mathbf{k}\cdot\mathbf{r}}$. The wavefunction in Eq. (2.12) can be interpreted as describing a free electron described by the plane wave $e^{i\mathbf{k}\cdot\mathbf{r}}$, that is modulated by some periodic potential described with $u_{\mathbf{k}n}(\mathbf{r})$. This makes a clear connection of Bloch theorem and the *nearly-free electron* approach, since free electrons can be expressed using plane waves $e^{i\mathbf{k}\cdot\mathbf{r}}$.

Translation symmetry

Translation symmetry introduces a new quantum number $\mathbf{k}$, which is a position vector in the reciprocal crystal space, and when multiplied by $\hbar$ it is sometimes called the *crystal momentum* of an electron. In crystal, energy levels of electron form bands since they now change with the continuous quantum number $\mathbf{k}$. Full set of electron energy levels for all $\mathbf{k}$ forms a dispersion relation which is also called the *electronic crystal structure*. The shape of the unit cell in reciprocal space determines the *the first Brillouin zone*, so all points on the reciprocal lattice can be reduced points inside that cell. When switching from real to reciprocal space of the crystal, primitive vectors and shape of the unit cell also change, but all symmetry properties from the real space are conserved. For arbitrary $\mathbf{k}$ in the reciprocal space, a point group $G_{\mathbf{k}}$ can be assigned which is a subgroup of the point group of the whole crystal symmetry G_Γ, where Γ corresponds to the origin in reciprocal space $\mathbf{k}_\Gamma = \vec{0}$. Using decomposition of irreducible representations from G_Γ to $G_{\mathbf{k}}$, it is possible to deduce which degeneracies will be allowed at point $\mathbf{k}$.

If the electronic crystal structure can be obtained at some point $\mathbf{k}_0$ for some or all bands, then the splitting of these bands can be deduced when moving away from $\mathbf{k}_0$ using group theory. Band at $\mathbf{k}_0$ which corresponds to an irreducible representation within $G_{\mathbf{k}_0}$, can at $\mathbf{k}_0 + \Delta\mathbf{k}$ become either reducible (if the band is degenerate and the symmetry is lowered) or it can compose a larger irreducible representation with another band (and increase degeneracy if the symmetry is raised). Even though group theory provides information about composition and decomposition of the irreducible representations and therefore the composition and decomposition of the band structure in $\mathbf{k}$-space it cannot predict the order of magnitude at which the energy of the band is raised, lowered or split. In other words, group theory can provide possible degeneracies of bands at any $\mathbf{k}$ (and their corresponding irreducible representations) but not their ordering with respect to the energy. Magnitudes at which

[2]Discovered by Felix Boch in 1929. In mathematics, this is also known as *Floquet's theorem*, discovered by Gaston Floquet in 1883.

band structure changes when moving away from a $\mathbf{k}_0$ point for which band energies and their wave functions are known, can be obtained with perturbation method using effective-mass method for a non-degenerate or degenerate band, included in Sec. 2.5, as well as $\mathbf{k}\cdot\mathbf{p}$ theory which can include several bands (non-degenerate and degenerate) at once, included in Sec. 2.6. However, both of these perturbation methods are usually limited to a small area around $\mathbf{k}_0$.

2.5 The effective-mass model

From translational properties, Bloch functions $\Psi^{(1e)}_{\mathbf{k}n}$ were introduced as a general solution for an electron in periodic potential with two quantum numbers: n - which refers to the state of an electron, and $\mathbf{k}$ which is a continuous vector restricted to the 1BZ. Energy of an electron in a mean-field periodic potential $E^{(1e)}_{\mathbf{k}n}$, corresponding to n and $\mathbf{k}$, is the solution to equation:

$$\mathcal{H}^{(1e)}\Psi^{(1e)}_{\mathbf{k}n}(\mathbf{r}) = E^{(1e)}_{\mathbf{k}n}\Psi^{(1e)}_{\mathbf{k}n}(\mathbf{r}), \tag{2.13}$$

which can also be expressed as:

$$\left[\frac{p^2}{2m_e} + V(\mathbf{r})\right] e^{i\mathbf{k}\cdot\mathbf{r}}u_{\mathbf{k}n}(\mathbf{r}) = E^{(1e)}_{\mathbf{k}n}e^{i\mathbf{k}\cdot\mathbf{r}}u_{\mathbf{k}n}(\mathbf{r}), \tag{2.14}$$

and after acting with operator $\mathbf{p} = (-i\hbar\nabla)$ on $e^{i\mathbf{k}\cdot\mathbf{r}}$, and then multiplying by $e^{-i\mathbf{k}\cdot\mathbf{r}}$ from the left one obtains:

$$\left[\frac{1}{2m_e}\left(p^2 + 2\hbar\mathbf{k}\cdot\mathbf{p} + \hbar^2k^2\right) + V(\mathbf{r})\right] u_{\mathbf{k}n}(\mathbf{r}) = E^{(1e)}_{\mathbf{k}n}u_{\mathbf{k}n}(\mathbf{r}), \tag{2.15}$$

or simply

$$\mathcal{H}^{(1e)}_{\mathbf{k}}u_{\mathbf{k}n}(\mathbf{r}) = E^{(1e)}_{\mathbf{k}n}u_{\mathbf{k}n}(\mathbf{r}), \tag{2.16}$$

where $\mathcal{H}^{(1e)}_{\mathbf{k}}$ is the term in the large bracket on the left-hand side of Eq. (2.15). The $\hbar\mathbf{k}$ in $\mathcal{H}^{(1e)}_{\mathbf{k}}$, which is a consequence of the periodicity of the crystal, is sometimes also called the *crystal momentum* of an electron[3].

Bloch functions $\Psi_{\mathbf{k}n}$ and Bloch factors $u_{\mathbf{k}n}$ now obey the following relations:

$$\begin{aligned}\langle\Psi_{\mathbf{k}n}|\Psi_{\mathbf{k}'m}\rangle &= \frac{1}{NV_{\mathrm{uc}}}\int_{\mathrm{sc}}\mathrm{d}\mathbf{r}\,\Psi^*_{\mathbf{k}n}(\mathbf{r})\Psi_{\mathbf{k}'m}(\mathbf{r}) = \delta_{nm}\delta_{\mathbf{k},\mathbf{k}'},\\ \langle u_{\mathbf{k}n}|u_{\mathbf{k}m}\rangle &= \frac{1}{V_{\mathrm{uc}}}\int_{\mathrm{uc}}\mathrm{d}\mathbf{r}\,u^*_{\mathbf{k}n}(\mathbf{r})u_{\mathbf{k}'m}(\mathbf{r}) = \delta_{nm},\end{aligned} \tag{2.17}$$

[3]Like the genuine momentum $\mathbf{p}$, whose conservation law is a consequence of continuous invariance of space, the crystal momentum is also conserved, but only up to a translation by a discrete reciprocal lattice vector $\mathbf{G}$: $\hbar\mathbf{k}' = \hbar\mathbf{k} + \hbar\mathbf{G}$, as a consequence of discrete translational symmetry of the crystal (another reason for confining $\mathbf{k}$ to 1BZ). Because the symmetry of the crystal is discrete and not continuous, conservation of $\hbar\mathbf{k}$ cannot be proved using Noether's theorem. Bloch functions are not eigenstates of the momentum $\mathbf{p} = -i\hbar\nabla$, since: $-i\hbar\nabla\Psi^{(1e)}_{\mathbf{k}n}(\mathbf{r}) = e^{i\mathbf{k}\cdot\mathbf{r}}\left(\hbar\mathbf{k} - i\hbar\nabla\right)u_{\mathbf{k}n}(\mathbf{r})$.

where $\mathcal{V} = NV_{\text{uc}}$ is the full crystal volume, V_{uc} is the volume of the unit cell, number $N \to \infty$ is the total number of unit cells in the crystal, and δ_{nm} and $\delta_{\mathbf{k},\mathbf{k}'}$ are Kronecker delta function, respectively. In the reciprocal space, volume of the crystal and unit cell (1BZ) are $(2\pi)^3/\mathcal{V}$ and $(2\pi)^3/V_{\text{uc}}$, respectively. The '$(1e)$' label from superscripts is from this point forward, always assumed and dropped for simplicity.

If Bloch factors $|u_{\mathbf{k}n}\rangle$ form a complete set of periodic functions, where n goes through all possible states: occupied and unoccupied, then the representation of $\mathcal{H}_{\mathbf{k}}$ in $|u_{\mathbf{k}n}\rangle$ basis is exact. In the case when n goes to all possible states $n \in [1, \infty)$, diagonalizing an infinite matrix $\langle u_{\mathbf{k}m}| \mathcal{H}_{\mathbf{k}} |u_{\mathbf{k}n}\rangle$ leads to dispersion relation in the 1BZ. However, in practice, one can only work with a finite subset of $|u_{\mathbf{k}n}\rangle$. In case when $n \in [1, N]$, where N is some finite number, the dispersion relation is not exact and gives only an approximate solution.

In most III-V and II-VI semiconductors highest valence and lowest conduction bands are fairly isolated and contain most of the current carriers around small regions of $\mathbf{k}$ that lie at extreme values of these bands where the gap is found, making this approximation somewhat justified. In the case of a direct gap, one can consider only one $\mathbf{k}_0$ for an exact solution and then perform a perturbative expansion around $\mathbf{k} - \mathbf{k}_0$.

Non-degenerate effective-mass model

If one considers an example of spinless GaAs, which is a III-V semiconductor with zincblende structure. The direct gap is at $\mathbf{k}_0 = \Gamma$, where $E_{\mathbf{k}0c}$ is the energy of the non-degenerate lowest conduction state $\mathbf{k}_0 c$. Using the second-order non-degenerate perturbation theory, one can expand the conduction band energy $E_{\mathbf{k}c}$ around gap point $\mathbf{k}_0$ to a small area in $\mathbf{k}$-space:

$$E_{\mathbf{k}c} = E_{\mathbf{k}0c} + \frac{\hbar^2}{2m_e}(\mathbf{k} - \mathbf{k}_0)^2 + E^{(1)}_{\mathbf{k}c} + E^{(2)}_{\mathbf{k}c}, \tag{2.18}$$

where

$$\begin{aligned} E^{(1)}_{\mathbf{k}c} &= \frac{\hbar}{m_e}(\mathbf{k} - \mathbf{k}_0) \cdot \mathbf{p}_{cc}, \\ E^{(2)}_{\mathbf{k}c} &= \sum_{r \neq c} \frac{\hbar^2}{m_e^2} \frac{|(\mathbf{k} - \mathbf{k}_0) \cdot \mathbf{p}_{cr}|^2}{E_{\mathbf{k}_0 c} - E_{\mathbf{k}_0 r}}, \\ \mathbf{p}_{cr} &= \langle \Psi_{\mathbf{k}_0 c}| \mathbf{p} |\Psi_{\mathbf{k}_0 r}\rangle, \end{aligned} \tag{2.19}$$

and the case of GaAs, $E^{(1)}_{\mathbf{k}c} = 0$ since $\mathbf{p}_{cc} = 0$. The Eq. (2.18) is the so-called effective-mass equation and it is limited to a small area around $\mathbf{k}_0$ and relatively isolated bands. The derivation of Eq. (2.18) can be done by using time-independent perturbation theory as seen in A.2 of the Appendix.

Degenerate effective-mass model

For spinless zincblende GaAs, the valence band maximum is a 3-fold degenerate state with energy $E_{\mathbf{k}_0 v}$. Degenerate eigenstate $\Psi_{\mathbf{k}_0 v} = \sum_i C_i |\mathbf{k}_0 v(i)\rangle$, can be expressed

using basis $|\mathbf{k}_0 v(i)\rangle$ and coefficients C_i where $i = 1, 2, 3$. When moving away from $\mathbf{k}_0$ these 3 states are no longer degenerate. Using the degenerate perturbation theory, and assuming that $|\mathbf{k}_0 v(i)\rangle$ and $E_{\mathbf{k}_0 v}$ are known, one has to solve for system of 3 equations in order to obtain C_i coefficients and energies $E_{\mathbf{k}v}$ away from $\mathbf{k}_0$:

$$\sum_j \left[H_{ij}^{(0)} \delta_{ij} + H_{ij}^{(1)} + H_{ij}^{(2)} \right] C_j = E_{\mathbf{k}v} C_i, \quad i, j = 1, 2, 3, \tag{2.20}$$

where:

$$\begin{aligned} H_{ij}^{(0)} &= E_{\mathbf{k}_0 v} + \frac{\hbar^2}{2m_e} (\mathbf{k} - \mathbf{k}_0)^2, \\ H_{ij}^{(1)} &= \frac{\hbar}{m_e} (\mathbf{k} - \mathbf{k}_0) \cdot \mathbf{p}_{ij}, \\ H_{ij}^{(2)} &= \sum_{r \neq v} \frac{\hbar^2}{m_e^2} \frac{(\mathbf{k} - \mathbf{k}_0) \cdot \mathbf{p}_{ir} \mathbf{p}_{rj} \cdot (\mathbf{k} - \mathbf{k}_0)}{E_{\mathbf{k}_0 v} - E_{\mathbf{k}_0 r}}. \end{aligned} \tag{2.21}$$

Perturbative terms $H_{ij}^{(1)}$ and $H_{ij}^{(2)}$ can conveniently be expressed by a 3×3 matrix, which is sometimes referred as Dresselhaus-Kip-Kittel (DKK) model[52].

The derivation of Eq. (2.21) can be done by using time-independent perturbation theory as seen in A.2 of the Appendix. In practice, one can first obtain the crystal structure experimentally using X-ray crystallography with great degree of accuracy. Next step would be to identify the type of lattice and obtain all possible symmetries present in the crystal. After that, one can attempt to calculate the electronic crystal structure.

Another method similar to DDK was developed by Luttinger and Kohn[53], and later Luttinger[54]. This method can determine the analytical form of Hamiltonian using theory of invariants.

If the semiconductor had a relatively small gap (around 0.5 eV), these methods would not hold well, and Kane developed a quasi-degenerate theory using a multi-band model [55, 56, 57] which is used throughout Chapter 3.

2.6 Kane model: The $\mathbf{k} \cdot \mathbf{p}$ equation

Kane's solution to narrow band semiconductors was to include both the conduction band and 3-fold degenerate valence band into one $\mathbf{k} \cdot \mathbf{p}$ model[55, 56, 57]. The model uses $\mathbf{k} \cdot \mathbf{p}$ term as a perturbation and includes contribution from the rest of the bands in the second-order terms using Löwdin's perturbation method[58]. For simplicity, the spin-orbit coupling (SOC) was omitted in the previous section, but here it will be included. Starting equation is the one-electron equation for periodic potential:

$$\left[\frac{p^2}{2m_e} + V(\mathbf{r}) + \frac{\hbar}{4m_e^2 c^2} (\sigma \times \nabla V) \cdot \mathbf{p} \right] |\Psi_{\mathbf{k}n}\rangle = E_{\mathbf{k}n} |\Psi_{\mathbf{k}n}\rangle , \tag{2.22}$$

where $\hbar(\sigma \times \nabla V) \cdot \mathbf{p}/(4m_e^2c^2)$ term takes SOC into account and $\sigma = (\sigma_x, \sigma_y, \sigma_z)$ is a vector whose components are Pauli matrices:

$$\sigma_x = \begin{bmatrix} 0 & 1 \\ 1 & 0 \end{bmatrix}, \quad \sigma_y = \begin{bmatrix} 0 & -i \\ i & 0 \end{bmatrix}, \quad \sigma_z = \begin{bmatrix} 1 & 0 \\ 0 & -1 \end{bmatrix}. \tag{2.23}$$

With SOC included $|\Psi_{\mathbf{k}n}\rangle$ is now a two-component spinor:

$$\begin{aligned} |\Psi_{\mathbf{k}n}\rangle &= e^{i\mathbf{k}\cdot\mathbf{r}} |u_{\mathbf{k}n}\rangle , \\ |u_{\mathbf{k}n}\rangle &= u^{\alpha}_{\mathbf{k}n} |\alpha\rangle + u^{\beta}_{\mathbf{k}n} |\beta\rangle , \end{aligned} \tag{2.24}$$

accounting for spin up($|\alpha\rangle$) and spin-down($|\beta\rangle$) states:

$$|\alpha\rangle = \begin{bmatrix} 1 \\ 0 \end{bmatrix}, \quad |\beta\rangle = \begin{bmatrix} 0 \\ 1 \end{bmatrix}, \quad \langle\alpha|\beta\rangle = \langle\beta|\alpha\rangle = \delta_{\alpha\beta}. \tag{2.25}$$

Inserting Eq. (2.24) in Eq. (2.22) gives:

$$\begin{aligned} &\left[H + \frac{\hbar^2 k^2}{2m_e} + \frac{\hbar}{m_e}\ \mathbf{k}\cdot\mathbf{p}_{\text{soc}}\right] |u_{\mathbf{k}n}\rangle = E_{\mathbf{k}n} |u_{\mathbf{k}n}\rangle , \\ &H = \frac{p^2}{2m_e} + V(\mathbf{r}) + \frac{\hbar}{4m_e^2c^2}(\sigma \times \nabla V)\cdot\mathbf{p}, \\ &\mathbf{p}_{\text{soc}} = \mathbf{p} + \frac{\hbar}{4m_ec^2}(\sigma \times \nabla V) \qquad . \end{aligned} \tag{2.26}$$

For any $\mathbf{k}$, Bloch factors $|u_{\mathbf{k}n}\rangle$ form a complete set ($n = 1, \ldots N$) . Assuming that for some $\mathbf{k}_0$, all Bloch factors $|u_{\mathbf{k}_0 m}\rangle$ can be obtained and energies $E_{\mathbf{k}_0 m}$ can be computed, Bloch factors for any vector $\mathbf{k}$ and band a can be expressed in the basis of $\mathbf{k}_0$ as:

$$|u_{\mathbf{k}a}\rangle = \sum_m B^{(a)}_m |u_{\mathbf{k}_0 m}\rangle . \tag{2.27}$$

Inserting Eq. (2.27) in Eq. (2.26) and multiplying by $\langle u_{\mathbf{k}_0 n}|$ from the left remembering that $\langle u_{\mathbf{k}_0 n}|u_{\mathbf{k}_0 m}\rangle = \delta_{nm}$, the $\mathbf{k}\cdot\mathbf{p}$ problem is reduced to:

$$\begin{aligned} &\sum_m \left[E_{\mathbf{k}_0 m} + \frac{\hbar^2}{2m_e}(k^2 - k_0^2)\right] \delta_{nm} B^{(a)}_m \\ &+ \sum_m \left[\frac{\hbar}{m_e}\ (\mathbf{k} - \mathbf{k}_0)\cdot\langle u_{\mathbf{k}_0 n}| \mathbf{p}_{\text{soc}} |u_{\mathbf{k}_0 m}\rangle\right] B^{(a)}_m = E^{(a)}_{\mathbf{k}} B^{(a)}_n, \end{aligned} \tag{2.28}$$

which can be written as a matrix eigenvalue problem $\sum_m H_{nm}(\mathbf{k}) B^{(a)}_m = E^{(a)}_{\mathbf{k}} B^{(a)}_n$. Eq. (2.28) is expressed in the basis of Bloch factors, so reverting back to basis of Bloch functions $|\Psi_{\mathbf{k}n}\rangle$ is straightforward using the relation that connects matrix elements of $\mathbf{p}_{\text{soc}}$ between the two:

$$\mathbf{p}_{nm} \equiv \langle\Psi_{\mathbf{k}_0 n}| \mathbf{p}_{\text{soc}} |\Psi_{\mathbf{k}_0 m}\rangle = \hbar\mathbf{k}_0\delta_{nm} + \langle u_{\mathbf{k}_0 n}| \mathbf{p}_{\text{soc}} |u_{\mathbf{k}_0 m}\rangle , \tag{2.29}$$

so that Eq. (2.28) can be also written as:

$$\begin{aligned}\sum_m \left[E_{\mathbf{k}_0 m} + \frac{\hbar^2}{2m_e}(\mathbf{k}-\mathbf{k}_0)^2\right]\delta_{nm}B_m^{(a)} \\ +\sum_m \left[\frac{\hbar}{m_e}\,(\mathbf{k}-\mathbf{k}_0)\cdot\mathbf{p}_{nm}\right]B_m^{(a)} = E_{\mathbf{k}}^{(a)}B_n^{(a)}.\end{aligned} \tag{2.30}$$

The Eq. (2.30) is the first-order $\mathbf{k}\cdot\mathbf{p}$ equation for Kane model.

The size of the square matrix H_{nm} depends on how many bands are included. If infinite amount of bands were included in the H_{nm}, this problem would be exactly solved, for any $\mathbf{k}$ in the 1BZ, to an accuracy of obtained $|u_{\mathbf{k}_0 m}\rangle$ and $E_{\mathbf{k}_0 m}$. However, this would obviously not be computationally feasible, so the size of H_{nm} has to be finite. To include contributions from other bands which are not contained in the first-order of H_{mn}, Kane used Löwdin's perturbation method which produces second-order terms $H_{nm}^{(2)}$:

$$\begin{aligned}H_{nm}^{(2)} &= \sum_{ij}\frac{\hbar(\mathbf{k}-\mathbf{k}_0)_i}{m_e}P_{nm,ij}\frac{\hbar(\mathbf{k}-\mathbf{k}_0)_j}{m_e}, \\ P_{nm,ij} &= \sum_{r\neq[m,n]}\frac{(\mathbf{p}_{nm})_i(\mathbf{p}_{nm})_j}{(E_{\mathbf{k}_0 n}+E_{\mathbf{k}_0 m})/2 - E_{\mathbf{k}_0 r}}, \qquad i,j=x,y,z \quad ,\end{aligned} \tag{2.31}$$

where bands labeled r are called *remote bands* in order to distinguish them from the *main bands*, labeled with n and m, that enter the Hamiltonian through the zeroth ($E_{\mathbf{k}_0 m}$) and the first-order perturbation ($\mathbf{p}_{nm}$)[4]. The second-order $\mathbf{k}\cdot\mathbf{p}$ equation in Kane model for bulk crystal is:

$$\begin{aligned}\sum_m \left[E_{\mathbf{k}_0 m} + \frac{\hbar^2}{2m_e}(\mathbf{k}-\mathbf{k}_0)^2\right]\delta_{nm}B_m^{(a)} \\ +\sum_m \left[\frac{\hbar}{m_e}\,(\mathbf{k}-\mathbf{k}_0)\cdot\mathbf{p}_{nm} + H_{nm}^{(2)}\right]B_m^{(a)} = E_{\mathbf{k}}^{(a)}B_n^{(a)}.\end{aligned} \tag{2.32}$$

The set of parameters which must be obtained before solving for $E_{\mathbf{k}n}$ in Eq. (2.32) can be distinguished as ones of the: zeroth order $E_{\mathbf{k}_0 m}$, first-order $\mathbf{p}_{nm}$, and second-order $P_{nm,ij}$ in terms of perturbation, and will be referred as *the* $\mathbf{k}\cdot\mathbf{p}$ *parameters* for H_{nm}. However, Kane model doesn't provide any method of obtaining these parameters and they have to be obtained by some other means.

Obtaining $\mathbf{k}\cdot\mathbf{p}$ parameters using fitting methods

One way to obtain $\mathbf{k}\cdot\mathbf{p}$ parameters of H_{nm} is to perform a fit using experimentally obtained energy levels $E_{\mathbf{k}n}$ for some $\mathbf{k}$ points in 1BZ. Using only this method however, it is impossible to know how many independent parameters there should be,

[4]Originally, Löwdin's perturbation method would contain $E_{\mathbf{k}n}$ instead of $(E_{\mathbf{k}_0 n}+E_{\mathbf{k}_0 m})/2$ in the denominator of Eq. (2.31), which would require a self-consistent method of solution. Kane opted for this geometric average in his method [57]

since when fitting the data there isn't a unique way to do it. It would be most useful to know how many independent parameters there should be just by considering the symmetries of the crystal structure.

This was solved by Luttinger [53, 54] and later generalized by Pikus and coworkers [48], by using the *theory of invariants* to obtain the number of $\mathbf{k} \cdot \mathbf{p}$ parameters by taking advantage of the group theory and symmetry of the crystal. The advantage of this method is that it produces the exact (and the least) number of parameters that are required according to the crystal symmetry. However, the disadvantage is that it can not determine the numerical values of these parameters and that some input from experimental results is required. This way, $\mathbf{k} \cdot \mathbf{p}$ parameters can be uniquely fitted to experimental results.

Obtaining $\mathbf{k} \cdot \mathbf{p}$ parameters using ab initio methods

Another way to obtain $\mathbf{k} \cdot \mathbf{p}$ parameters of H_{nm} is to perform an *ab initio* calculation using DFT or some other available method to obtain numerical values for $E_{\mathbf{k}_0 m}$ and $|\Psi_{\mathbf{k}_0 n}\rangle$ in order to calculate $\mathbf{p}_{nm}$ and $P_{nm,ij}$. This method produces all numerical parameters without the need for any experimental results however, it does not initially give the same analytical form like the theory of invariants does and can appear to have more parameters than the crystal symmetry would suggest.

This shortcoming can be overcome by finding a unitary transformation that transforms initial 'symmetry non-adapted'[5] analytical form into the 'symmetry-adapted' form that theory of invariants produces, thus reducing the initial number of parameters to the one that is required by the crystal symmetry. Even though the exact number of parameters is unique to the crystal symmetry and size of H_{nm}, the analytical forms are not unique.

Using unitary transform to adapt parameters from one analytical form to another is called *symmetry-adaptation of the* $\mathbf{k} \cdot \mathbf{p}$ *Hamiltonian*. Procedure which performs this symmetry-adaptation relying only on ab initio methods was developed for the purpose of this thesis. The whole procedure that starts with obtaining initial $\mathbf{k} \cdot \mathbf{p}$ parameters from DFT, then obtaining the unitary transformation that rotates the basis to a symmetry-adapted form as published in Ref. [46], and described in Chapter 3.

[5]This analytical from actually has all symmetry properties that are required by the crystal symmetry however, it is not that obvious until some unitary transformation is performed.

2.7 Electronic structure

This section is dedicated to computational techniques for obtaining the electronic structure, namely the density functional theory (DFT) and the many-body GW method. In all subsequent subsections, the Born-Oppenheimer approximation is assumed and the calculations are considering only the electronic subsystem neglecting all influence of the ionic vibrations. The ionic movement in the crystal is studied in Sec. 2.8, while Sec. 2.9 studies the influence of this ionic movement on the electronic structure.

Both DFT and GW are considered ab initio methods, in a sense that they do not require any experimental parameters as inputs. In practical calculations, one can consider the lattice structure itself as an experimental input, to some degree. Atomic positions can be declared in coordinates that are relative to the lattice constant, which can be determined by minimization of the total energy of the unit cell. Modern DFT codes can also start from an approximate lattice structure and relax both atomic positions and lattice constant until forces on all atoms vanish.

DFT has proven to be a very powerful and universal tool. In practice, it relies on the ansatz that the electronic density of an interacting system can be determined by an electronic density of an auxiliary non-interacting system that is easier to solve mathematically. In DFT, the total energy of the ground state of a system is a functional of the ground state electron density only. This density is obtained self-consistently through an auxiliary problem described by the Kohn-Sham equations. These equations provide one-electron energies and wave functions of this auxiliary Kohn-Sham system, which can be used to estimate the electronic structure. In some cases, the Kohn-Sham electronic structure gives a very good estimate, while in others it fails to reproduce even the most basic features like the electronic gap. This problem has several solutions and one of them is to explicitly include many-body effects using Hedin's equations and the appropriate GW approximation in order to make the computation feasible.

Although GW provides a more accurate picture of the electronic structure as a more refined, many-body model [6], it still relies on DFT to provide that initial step to obtain the starting electronic density, energies and wave functions. Using DFT states as an input, GW computes self-consistently the electronic self-energy using interacting or non-interacting Green function G and the screened Coulomb interaction W. This way, the electronic properties obtained from the Kohn-Sham equation can be improved to better resemble experimental results.

Interested readers can find more information about DFT, GW and other techniques in obtaining electronic structure across the literature, for example in Ref. [59, 60, 61].

[6] One can recognize that a similar many-body treatment which dealt with electron-electron many-body interactions is applied for electron-phonon interactions in Sec. 2.9.

2.7.1 Density Functional Theory - DFT

One of the many challenges of the problem of many interacting electrons is that the solution for $\mathcal{H}_{\text{el}}$ inherits dependence on the position $\mathbf{r}$ for all N electrons described by the many-body function $\Psi(\mathbf{r}_1, \mathbf{r}_2, \dots \mathbf{r}_N)$. Hohenberg and Kohn [62] approached the problem for systems with many electrons with the idea to simplify the search for its solution by suggesting that all properties of such systems can be determined by the electronic density $n(\mathbf{r})$ of the ground state, which is a scalar function that depends on one vector coordinate $\mathbf{r}$ only:

$$n(\mathbf{r}) = \int \mathrm{d}\mathbf{r}_2 \dots \mathbf{r}_N \, |\Psi(\mathbf{r}, \mathbf{r}_2, \dots \mathbf{r}_N)|^2. \tag{2.33}$$

The result was an exact theory for many-body electron systems.

The Hamiltonian operator H of such many-body system can be expressed as:

$$H = T_{\text{el}} + V_{\text{el-el}} + V_{\text{ext}}, \tag{2.34}$$

where T_{el} and $V_{\text{el-el}}$, are the kinetic energy operator and operator for electron-electron interaction, respectively, accounting for all electrons in the system. The external potential operator $V_{\text{ext}}(\mathbf{r})$ contains all electron-ion interaction in the system and the background potential created by all ions. Ions are considered static by the BA approximation.

Hohenberg-Kohn theorems

Hohenberg and Kohn provided and proved two theorems which are the basis of the *density functional theory* (DFT):

- **Theorem 1**: For any system of interacting particles in an external potential $V_{\text{ext}}(\mathbf{r})$, the potential $V_{\text{ext}}(\mathbf{r})$ is determined uniquely, up to a constant, by the ground state particle density $n_0(\mathbf{r})$.
  Corollary: Since the Hamiltonian is fully determined, except to a constant shift of the energy, it follows that the many-body wave functions for all states (ground and excited) are determined. Therefore all the properties of the system are completely determined by the ground state density $n_0(\mathbf{r})$.

- **Theorem 2**: A universal functional $F[n]$ for the energy $E[n]$ in terms of the density $n(\mathbf{r})$ can be defined, valid for any potential $V_{\text{ext}}(\mathbf{r})$. For any particular $V_{\text{ext}}(\mathbf{r})$, the exact ground state energy of the system is the global minimum value of this functional, and the density $n(\mathbf{r})$ that minimizes this functional is the exact ground state density $n_0(\mathbf{r})$.
  Corollary: The functional $E[n]$ alone is sufficient to determine the exact ground state energy and density. In general, the excited sates of the electrons must be determined by other means.

The functional $F[n]$ is universal in a sense that it doesn't depend on $V_{\text{ext}}(\mathbf{r})$. In other words, the mathematical form of $F[n]$ will be the same for any kind of system: semiconductor, metal, superconductor, molecule etc.[7]

Theorem 1 can be easily proved by *reductio ad apsurdum* as shown in Ref. [62]. Assume that two external potentials for the same system, that differ more than just by a constant $V_{\text{ext}}^{(1)}$ and $V_{\text{ext}}^{(2)}$ and lead to two different Hamiltonians $H^{(1)}$ and $H^{(2)}$, respectively. Assume that both $V_{\text{ext}}^{(1)}$ and $V_{\text{ext}}^{(2)}$ produce the same electron density $n_0(\mathbf{r})$. This density n_0, should return two different ground states $\Psi^{(1)}$ and $\Psi^{(2)}$, for Hamiltonians $H^{(1)}$ and $H^{(2)}$, respectively, with energies $E^{(1)}[n]$ and $E^{(2)}[n]$, respectively:

$$E^{(i)}[n] = \left\langle \Psi^{(i)} \right| H^{(i)} \left| \Psi^{(i)} \right\rangle, \quad i = 1, 2. \tag{2.35}$$

Because $E^{(1)} = \left\langle \Psi^{(1)} \right| H^{(1)} \left| \Psi^{(1)} \right\rangle$ is not a ground state of $\Psi^{(2)}$, then:

$$E^{(1)} = \left\langle \Psi^{(1)} \right| H^{(1)} \left| \Psi^{(1)} \right\rangle < \left\langle \Psi^{(2)} \right| H^{(1)} \left| \Psi^{(2)} \right\rangle, \tag{2.36}$$

so adding and subtracting $H^{(2)}$ from the right-hand side leads to:

$$\begin{aligned} E^{(1)} &< \left\langle \Psi^{(2)} \right| H^{(1)} + H^{(2)} - H^{(2)} \left| \Psi^{(2)} \right\rangle, \\ E^{(1)} &< E^{(2)} + \int \mathrm{d}\mathbf{r} \left[V_{\text{ext}}^{(1)}(\mathbf{r}) - V_{\text{ext}}^{(2)}(\mathbf{r}) \right] n_0(\mathbf{r}). \end{aligned} \tag{2.37}$$

The same argument from Eq. (2.36) can used in the case for $E^{(2)}$ and $\Psi^{(1)}$ with manipulation from Eq. (2.37) to obtain:

$$E^{(2)} < E^{(1)} + \int \mathrm{d}\mathbf{r} \left[V_{\text{ext}}^{(2)}(\mathbf{r}) - V_{\text{ext}}^{(1)}(\mathbf{r}) \right] n_0(\mathbf{r}), . \tag{2.38}$$

Together, Eq. (2.37) and Eq. (2.38), produce a contradiction:

$$E^{(1)} + E^{(2)} < E^{(2)} + E^{(1)}. \tag{2.39}$$

The strict inequality in Eq. (2.39) is due to assumption that the ground state is not degenerate. This leads to a conclusion of *uniqueness* of ground state density $n_0(\mathbf{r})$ which can be attributed to only one possible external potential V_{ext}.

Theorem 2 is sometimes split into two points. The first point implies is that for *any* potential V_{ext} some functional $F[n]$ can be defined with *a* density $n(\mathbf{r})$. This defines a set of all possible densities $n(\mathbf{r})$ that V_{ext} can produce. The second point, is that not *every* such density $n(\mathbf{r})$ in the space of densities that V_{ext} defines, can be the density of the ground state $n_0(\mathbf{r})$ for that particular V_{ext}. In degenerate case, ground state densities will be a subset of all possible densities, while in non-degenerate case, only one density will return a ground state, and any other That means, that only densities that return a ground state for some V_{ext} can be, in reverse, obtained from that same V_{ext}. These unique densities are called 'V-representable'

[7] Of course, this functional will differ in terms of the number of electrons and ions, ionic masses and distance between ions etc. but the mathematical form is conserved.

densities. This limits the number of possible densities that are possible within DFT. These densities are usually limited to smooth potentials without delta functions or singularities. One can write the energy functional $E_{\mathrm{HK}}[n]$ as a sum of individual functionals of density:

$$\begin{aligned} E_{\mathrm{HK}}[n] &= F[n] + \int \mathrm{d}\mathbf{r}\, V_{\mathrm{ext}}(\mathbf{r}) n_0(\mathbf{r}) \\ &= T_{\mathrm{el}}[n] + E_{\mathrm{el-el}}[n] + \int \mathrm{d}\mathbf{r}\, V_{\mathrm{ext}}(\mathbf{r}) n(\mathbf{r}) + E_{\mathrm{ion-ion}} \\ &= F_{\mathrm{HK}}[n] + \int \mathrm{d}\mathbf{r}\, V_{\mathrm{ext}}(\mathbf{r}) n(\mathbf{r}) + E_{\mathrm{ion-ion}}, \end{aligned} \tag{2.40}$$

where $T_{\mathrm{el}}[n]$ and $E_{\mathrm{el-el}}$ are functionals of many-body kinetic and potential energy of electrons, respectively. The classical potential energy between ions $E_{\mathrm{ion-ion}}$ doesn't depend on electron density, and it is the before mentioned constant part extracted from the external potential. The functional $F_{\mathrm{HK}}[n]$ is the universal functional that contains all internal energies (kinetic and potential) for the system of interacting electrons:

$$F_{\mathrm{HK}}[n] = T_{\mathrm{el}}[n] + E_{\mathrm{el-el}}[n]. \tag{2.41}$$

Functional $F_{\mathrm{HK}}[n]$ does not depend on V_{ext} and is mathematically universal for all systems. The label 'HK' is used here to emphasize that it refers to Hohenberg-Kohn formulation of $F[n]$, which is limited to non-degenerate ground states.

Consider a system with a ground state density $n^{(1)}(\mathbf{r})$ is produced by V_{ext}, and corresponds to a non-degenerate state $\Psi^{(1)}$ with energy $E^{(1)}$:

$$E^{(1)} = E_{\mathrm{HK}}[n^{(1)}] = \left\langle \Psi^{(1)} \right| H \left| \Psi^{(1)} \right\rangle. \tag{2.42}$$

Consider another density $n^{(2)}(\mathbf{r})$ that corresponds to a state $\Psi^{(2)}$, which is not a ground sate but a possible density for V_{ext}, with energy $E^{(2)}$:

$$E^{(2)} = E_{\mathrm{HK}}[n^{(2)}] = \left\langle \Psi^{(2)} \right| H \left| \Psi^{(2)} \right\rangle. \tag{2.43}$$

If $n^{(1)}$ is the density obtained from the ground state $\Psi^{(1)}$ then any other density $n^{(2)}$ obtained from state $\Psi^{(2)}$ will have higher energy than $E^{(1)}$:

$$\left\langle \Psi^{(1)} \right| H \left| \Psi^{(1)} \right\rangle < \left\langle \Psi^{(2)} \right| H \left| \Psi^{(2)} \right\rangle. \tag{2.44}$$

This means that if the exact functional $F_{\mathrm{HK}}[n]$ is known, then one can search for the ground state by trial densities n until the minium of $E_{\mathrm{HK}}[n]$ is found. Once the minimum of $E_{\mathrm{HK}}[n]$ is obtained by varying the density, the ground state density is also obtained. Note that this functional F_{HK} can be used to find the ground state only and for any other excited state of the system with the same V_{ext} has to be determined in another way. In other words, if one knew a density n' of some excited state Ψ', then $E_{\mathrm{HK}}[n']$ doesn't have to be the energy of that excited state. Excited states can in a way be connected to some local minimum or a saddle point of some functional, but Hohenberg-Kohn theorem is explicitly restricted to a global minimum, which corresponds to the ground state.

One issue with this formulation of DFT by Hohenberg and Kohn is that it does not provide any insight on how to construct the functional F_{HK}, it just states that it should exist. The other is that it is limited to 'V-representable' densities, cases where the ground state is non-degenerate, and does not consider the case when different states Ψ produce the same density $n(\mathbf{r})$.

Universal functional $F[n]$ can also be expressed in another formulation of by Lieb and Levy $F_{\mathrm{LL}}[n]$ to extend Hohengerg-Kohn theorems to degenerate cases. One such example for a case of degenerate ground state density is the homogeneous electron gas: wave functions are plane waves which all correspond to the same uniform density however, the ground state is determined by the lowest kinetic energy in the case of non-interacting electrons. In the case of interacting electrons, the density is also uniform, however the wave functions are correlated and cannot be expressed by a simple determinant. The same logic can be applied for inhomogeneous cases.

Levy-Lieb formulation of $F[n]$

Formulation of DFT by Levy[63] and Lieb[64] extends the range of the definition of the energy functional giving it a more physical meaning, provides some insight on how the functional should be constructed, and leads to the same ground state density as Hohenberg-Kohn formulation, but also applies for degenerate ground states. The idea is to define a functional $E_{\mathrm{LL}}[n]$ and perform minimization in two steps. In the first step of minimization, the purely electron part of Hamiltonian is minimized by varying Ψ over all variables to define functional $F_{\mathrm{LL}}[n]$:

$$\begin{aligned} E_{\mathrm{LL}}[n] &= \min_{\Psi \to n(\mathbf{r})} \langle \Psi | \, T_{\mathrm{el}} + V_{\mathrm{el-el}} \, | \Psi \rangle + \int \mathrm{d}\mathbf{r} \, V_{\mathrm{ext}}(\mathbf{r}) n(\mathbf{r}) \\ &= F_{\mathrm{LL}}[n] + \int \mathrm{d}\mathbf{r} \, V_{\mathrm{ext}}(\mathbf{r}) n(\mathbf{r}), \end{aligned} \tag{2.45}$$

where $F_{\mathrm{LL}}[n]$ is the universal functional minimized for a set of Ψ that produce the same density $n(\mathbf{r})$:

$$F_{\mathrm{LL}}[n] = \min_{\Psi \to n(\mathbf{r})} \langle \Psi | \, T_{\mathrm{el}} + V_{\mathrm{el-el}} \, | \Psi \rangle \, . \tag{2.46}$$

The difference between F_{HK} and F_{LL} can be demonstrated on the homogeneous electron gas of non-interacting electrons. In such case, the many-body wavefunction is constructed from a Slater determinant where individual electrons are represented as plane waves. All states correspond to one uniform density which is generated uniquely by a uniform V_{ext}. Since there is no interactions between the electrons, only the functional of the kinetic energy is present. In F_{HK} formulation, there is no use to vary over density to obtain the ground state however, in F_{LL} formulation, the ground state is defined by minimizing the kinetic energy over different Ψ to obtain the lowest value and therefore the ground state.

The formulation of F_{LL} in Eq. (2.46) provides a practical meaning for the functional as the minimum of the sum of kinetic and potential parts for all possible many-electron wave functions Ψ that have the given density $n(\mathbf{r})$.

In the second step of the minimization, same as for $E_{\mathrm{HK}}[n]$, the functional $E_{\mathrm{LL}}[n]$ is minimized by varying over the density $n(\mathbf{r})$. In order for density $n(\mathbf{r})$ to be 'N-representable' it needs to be positive for all $\mathbf{r}$ and integrate to N electrons present in the system, there is no requirement to be a ground state density of any potential V^{ext}. If a density isn't 'N-representable', automatically it will not be 'V-representable', therefore it cannot minimize $E_{\mathrm{LL}}[n]$. This way Levy-Lieb formulation provides some insight of possible trial densities in the minimizing procedure.

In order for a trial density to describe the exact ground state for some external potential V_{ext} and be 'V-representable' it must be checked first if it is 'N-representable'. In other words, all 'V-representable' densities from Hohenberg-Kohn formulation are also 'N-representable". Because the condition for minimization of the functional $E[n]$ by varying over density is fulfilled in both Hohenberg-Kohn E_{HK} and Levy-Lieb E_{LL} formulations, they must lead to the same ground state density.

In summary, in Hohenberg-Kohn formulation, functional F_{HK} is defined *only* for densities that can be generated by some external potential V_{ext} which minimize E_{HK}(i.e. the 'V-representable' densities that lead to ground state). In Levy-Lieb formulation the functional $F_{\mathrm{LL}}[n]$ can be defined for *any* density $n(\mathbf{r})$ that is formed from many-body electron wavefunction Ψ_N, with the condition that it integrates to finite number of N electrons over the whole space $\int \mathrm{d}\mathbf{r}\, n(\mathbf{r}) = \int \mathrm{d}\mathbf{r}\, \Psi_N^* \Psi_N = N$. Densities that minimize $F_{\mathrm{HK}}[n]$ for some Ψ_N are called 'N-representable' densities. If they can also be obtained from some V_{ext}, they are 'V-representable' and they must lead to the same ground state in $E_{\mathrm{HK}}[n]$ and $E_{\mathrm{LL}}[n]$.

2.7.2 Kohn-Sham scheme

Until this point, all discussion was on the exact DFT, that is, on the assumption that the functional $F[n]$ can be exactly defined, ground state density obtained by minimizing $E_{[}n]$ and determining the many body Hamiltonian for all states (ground and excited) Ψ. Unfortunately, to this day, no one knows how $F[n]$ should look like. This problem is further complicated by the fact that one is dealing with many-body functions Ψ and some simplification has to be performed in order to make this problem solvable.

One such, simplification is the Kohn-Sham scheme which asserts the following: For any interacting system, there is a local single-particle potential $V_{\mathrm{KS}}(\mathbf{r})$ which corresponds to an auxiliary non-interacting system, and this auxiliary system produces the ground state density $n_{\mathrm{KS}}(\mathbf{r})$ which is equal to the ground state density of that interacting system $n_0(\mathbf{r})$.

This also asserts that 'V-representable' densities of an interacting system for can also be 'V-representable' densities of the auxiliary non-interacting system.

This way, the electrons density is still connected to an interacting system but the kinetic part acts on individual electrons the same as in the non-interacting case. Unlike in the case of homogeneous gas of non-interacting electrons, where all electron-electron interactions are omitted, here the electrons are only independent in a sense that one electron interacts with the Coulomb field generated of all the other electrons, which is described by the Hartree energy, and all many body effects

are described by the exchange-correlation energy. This allows one to write a system of one-electron Schrödinger equations, called Kohn-Sham equations, whose solutions are eigenstates of the auxiliary system, called the Kohn-Sham states.

The idea is to start from the energy functional $E[n]$ and add and subtract the kinetic energy operator of non-interacting electrons $T_\mathrm{s}[n]$ and Hartree energy E_H:

$$E[n] = F[n] + T_\mathrm{s}[n] - T_\mathrm{s}[n] + E_\mathrm{H}[n] - E_\mathrm{H}[n] + \int \mathrm{d}\mathbf{r}\, V_\mathrm{ext}(\mathbf{r}) n(\mathbf{r}), \tag{2.47}$$

and rewrite the energy functional $E[n]$ as:

$$E[n] = T_\mathrm{s}[n] + E_\mathrm{H}[n] + \int \mathrm{d}\mathbf{r}\, V_\mathrm{ext}(\mathbf{r}) n(\mathbf{r}) + E_\mathrm{xc}, \tag{2.48}$$

where E_xc is the so-called *exchange-correlation energy* which contains all many-body effects of exchange (due to Pauli principle) and correlation (from many-body effects) in $F[n]$ (either in HK or LL formulation) reduced by the kinetic energy of non-interacting electrons and Hartree energy:

$$E_\mathrm{xc} = F[n] - T_\mathrm{s}[n] - E_\mathrm{H}[n]. \tag{2.49}$$

To emphasize that the Kohn-Sham scheme was applied, the energy functional $E[n]$ can simply be renamed to $E_\mathrm{KS}[n]$ and written as:

$$E_\mathrm{KS}[n] = F_\mathrm{KS}[n] + \int \mathrm{d}\mathbf{r}\, V_\mathrm{ext}(\mathbf{r}) n(\mathbf{r}) + E_\mathrm{xc}, \tag{2.50}$$

where the Kohn-Sham functional $F_\mathrm{KS}[n]$ is:

$$F_\mathrm{KS}[n] = T_\mathrm{s}[n] + E_\mathrm{H}[n]. \tag{2.51}$$

The kinetic energy of non-interacting electrons $T_\mathrm{s}[n]$ is explicitly:

$$T_\mathrm{s}[n] = \sum_i \int \mathrm{d}\mathbf{r}\, \psi_i^* \frac{(-i\hbar\nabla)^2}{2m_e} \psi_i, \tag{2.52}$$

while Hartree energy E_H is:

$$E_\mathrm{H} = \frac{1}{2} \int \mathrm{d}\mathbf{r} \int \mathrm{d}\mathbf{r}'\, \frac{e^2 n(\mathbf{r}) n(\mathbf{r}')}{4\pi\varepsilon_0 |\mathbf{r} - \mathbf{r}'|}. \tag{2.53}$$

The Kohn-Sham approach asserts that the exact ground state density of the auxiliary system and the ground state density of the many body system are the same. This means that the same ground state density $n_0(\mathbf{r})$ can be expressed either by many-body functions Ψ or a sum of wave functions of the auxiliary system:

$$n(\mathbf{r}) = \int \mathrm{d}\mathbf{r}_2 \ldots \mathbf{r}_N\, |\Psi(\mathbf{r}, \mathbf{r}_2, \ldots \mathbf{r}_N)|^2 = \sum_i^N |\psi_i(\mathbf{r})|^2, \tag{2.54}$$

where N is the number of electrons is the system and $\psi_i(\mathbf{r})$ are wave functions of the independent electrons of the auxiliary system that are also orthonormal:

$$\langle\psi_i|\psi_j\rangle = \delta_{ij}. \tag{2.55}$$

From **Theorem 2** of Hohenberg and Kohn, varying over density will produce the ground state of functional $E_{\mathrm{KS}}[n]$ and the chain rule:

$$\frac{\delta E_{\mathrm{KS}}}{\delta n} = 0, \quad \frac{\delta E_{\mathrm{KS}}}{\delta \psi_i^*} = \frac{\delta E_{\mathrm{KS}}}{\delta n}\frac{\delta n}{\delta \psi_i^*} = \frac{\delta E_{\mathrm{KS}}}{\delta n}\psi_i \quad \Rightarrow \quad \frac{\delta E_{\mathrm{KS}}}{\delta \psi_i^*} = 0. \tag{2.56}$$

This minimization procedure can be solved by using Lagrange optimization which states that extreme values for some function $f(x)$ can be obtained by differentiating the Lagrange function $\mathcal{L}(x,\lambda) = f(x) - \lambda g(x)$, under the condition that $g(x) = 0$, where λ is the Lagrange multiplier. In this case, $f(x) \to E_{\mathrm{KS}}$ and $g(x) \to \langle\psi_i|\psi_j\rangle - \delta_{ij}$. The Lagrange function is:

$$\mathcal{L} = E_{\mathrm{KS}}[n] - \sum_{ij}\lambda_{ij}\left[\langle\psi_i|\psi_j\rangle - \delta_{ij}\right]. \tag{2.57}$$

Varying $\mathcal{L}$ over all ψ_i^*:

$$\frac{\delta \mathcal{L}}{\delta \psi_i^*} = 0 \quad \Rightarrow \quad \frac{\delta E_{\mathrm{KS}}}{\delta \psi_i^*} = \sum_j \lambda_{ij}\psi_j, \tag{2.58}$$

one arrives at:

$$\left[-\frac{\hbar^2\nabla^2}{2m_e} + V_{\mathrm{KS}}(\mathbf{r})\right]\psi_i(\mathbf{r}) = \sum_j \lambda_{ij}\psi_j(\mathbf{r}), \tag{2.59}$$

where $V_{\mathrm{KS}}(\mathbf{r})$ is the Kohn-Sham effective potential obtained after Lagrange optimization:

$$V_{\mathrm{KS}}(\mathbf{r}) = V_{\mathrm{ext}}(\mathbf{r}) + V_{\mathrm{H}}(\mathbf{r}) + V_{\mathrm{xc}}(\mathbf{r}), \tag{2.60}$$

V_{H} is related to the Hartree potential:

$$V_{\mathrm{H}}(\mathbf{r}) = \left.\frac{\delta E_{\mathrm{H}}}{\delta n}\right|_{n(\mathbf{r})} = \int \mathrm{d}\mathbf{r}'\,\frac{e^2 n(\mathbf{r}')}{4\pi\varepsilon_0|\mathbf{r}-\mathbf{r}'|}, \tag{2.61}$$

and V_{xc} is related to exchange-correlation:

$$V_{\mathrm{xc}}(\mathbf{r}) = \left.\frac{\delta E_{\mathrm{xc}}}{\delta n}\right|_{n(\mathbf{r})}. \tag{2.62}$$

Potential V_{xc} is in this simplest (pedagogical) case a local function of $\mathbf{r}$ however, that isn't always true. Because the terms on the left of Eq. (2.59) are hermitian, the Lagrange multipliers λ_{ij} will also be hermitian and there should always exist a unitary transformation U that transforms basis functions ψ to ψ^{KS} which make λ_{ij} diagonal, while retaining orthonormal relations and keeping the density same:

$$\begin{aligned} \psi^{\mathrm{KS}} = U\psi \quad &\Rightarrow \quad U\lambda_{ij}U^\dagger = \delta_{ij}\varepsilon_j^{\mathrm{KS}}, \\ \left\langle\psi_i^{\mathrm{KS}}\middle|\psi_j^{\mathrm{KS}}\right\rangle = \delta_{ij}, \quad &\Rightarrow \quad n(\mathbf{r}) = \sum_i |\psi_i^{\mathrm{KS}}(\mathbf{r})|^2. \end{aligned} \tag{2.63}$$

In the new basis, Eq. 2.59 becomes:

$$\left[-\frac{\hbar^2\nabla^2}{2m_e} + V_{\mathrm{KS}}(\mathbf{r})\right]\psi_i^{\mathrm{KS}}(\mathbf{r}) = \varepsilon_i^{\mathrm{KS}}\psi_i^{\mathrm{KS}}(\mathbf{r}), \tag{2.64}$$

Finally, one can see that the Kohn-Sham eigenvalues are just unitary transform of Lagrange multipliers from Eq. (2.59) which raises the ambiguity of their physical meaning.

Density of the auxiliary system $n(\mathbf{r}) = \sum_i^N |\psi_i^{\mathrm{KS}}(\mathbf{r})|^2$ that appears in the Hartree part of V_{KS} must be the same one that minimizes $E_{\mathrm{KS}}[n]$ and the same as a ground state density for a many body system. The Kohn-Sham equation must be solved self-consistently until the input density $n_{\mathrm{in}}(\mathbf{r})$ obtained from the previous step[8] and and the one constructed in the current step $n_{\mathrm{out}}(\mathbf{r}) = \sum_i^N |\psi_i^{\mathrm{KS}}(\mathbf{r})|^2$ are numerically same up to an arbitrary small parameter ε:

$$|n_{\mathrm{in}}(\mathbf{r}) - n_{\mathrm{out}}(\mathbf{r})| < \varepsilon, \quad \forall\ \mathbf{r} \in V. \tag{2.66}$$

Other conditions for self-consistency can also include the total energy:

$$\left|E^{\mathrm{step}+1}[n] - E^{\mathrm{step}}[n]\right| < \varepsilon_E, \quad \forall\ \mathbf{r} \in V, \tag{2.67}$$

the Kohn-Sham effective potential:

$$\left|V_{\mathrm{KS}}^{\mathrm{step}+1}(\mathbf{r}) - V_{\mathrm{KS}}^{\mathrm{step}}(\mathbf{r})\right| < \varepsilon_V, \quad \forall\ \mathbf{r} \in V, \tag{2.68}$$

or Kohn-Sham wave functions:

$$\left|\psi_i^{\mathrm{KS\ step}+1}(\mathbf{r}) - \psi_i^{\mathrm{KS\ step}}(\mathbf{r})\right| < \varepsilon_\psi, \quad \forall\ \mathbf{r} \in V. \tag{2.69}$$

Because it is used in self-consistent calculations, the Kohn-Sham effective potential V_{KS} is sometimes also referred to as the *self-consistent field potential*[9].

Once Kohn-Sham eigenvalues $\varepsilon_i^{\mathrm{KS}}$ and ground state density $n_0(\mathbf{r})$ are found, the kinetic energy functional $T_{\mathrm{s}}[n]$ can be determined as:

$$T_{\mathrm{s}}[n] = \sum_i^N \varepsilon_i^{\mathrm{KS}} - \int \mathrm{d}\mathbf{r}\, V_{\mathrm{KS}}(\mathbf{r})n(\mathbf{r}), \tag{2.70}$$

[8] In practice, the input density for the next step is usually constructed as a mixture of input and output density of the current step:

$$n_{\mathrm{in}}^{\mathrm{step}+1} = (1-\alpha_{\mathrm{mix}})n_{\mathrm{in}}^{\mathrm{step}} + \alpha_{\mathrm{mix}}n_{\mathrm{out}}^{\mathrm{step}}, \tag{2.65}$$

where α_{m} is the mixing parameter. The input density for the first step can be guessed in many different ways, one example is to start with a density of isolated atoms. The mixing parameter $0 \leq \alpha_{\mathrm{m}} \leq 1$ should be chosen to speed up the convergence however, if it's too large, then there is the risk of oscillations in total energy and the charge density in each step which makes convergence impossible, if it is too small then the convergence can be very slow w.r.t. number of cycles required for self-consistency.

[9] Although, this is a broader term and could be applied to cases other than Kohn-Sham DFT, like the Hartree-Fock method for example.

and from Eq. (2.61), the Hartree energy E_{H} is:

$$E_{\mathrm{H}} = \frac{1}{2}\int \mathrm{d}\mathbf{r}\, V_{\mathrm{H}}(\mathbf{r}) n_0(\mathbf{r}). \tag{2.71}$$

Using Eq. (2.50) (or Eq. (2.48)) with Eq. (2.70) and Eq. (2.71) the energy functional $E_{\mathrm{KS}}[n]$ for ground state density becomes:

$$\begin{aligned} E_{\mathrm{KS}}[n_0] &= T_{\mathrm{s}}[n_0] + E_{\mathrm{H}}[n_0] + \int \mathrm{d}\mathbf{r}\, V_{\mathrm{ext}}(\mathbf{r}) n_0(\mathbf{r}) + E_{\mathrm{xc}}[n_0] \\ &= \sum_i^N \varepsilon_i^{\mathrm{KS}}[n_0] - \int \mathrm{d}\mathbf{r}\, V_{\mathrm{KS}}(\mathbf{r}) n_0(\mathbf{r}) + \frac{1}{2}\int \mathrm{d}\mathbf{r}\, V_{\mathrm{H}}(\mathbf{r}) n_0(\mathbf{r}) + E_{\mathrm{xc}}[n_0] \\ &= \sum_i^N \varepsilon_i^{\mathrm{KS}}[n_0] - \frac{1}{2}\int \mathrm{d}\mathbf{r}\, V_{\mathrm{H}}(\mathbf{r}) n_0(\mathbf{r}) - \int \mathrm{d}\mathbf{r}\, V_{\mathrm{xc}}(\mathbf{r}) n_0(\mathbf{r}) + E_{\mathrm{xc}}[n_0]. \end{aligned} \tag{2.72}$$

With Eq. (2.72), the DFT cycle in Kohn-Sham formulation is complete - the total energy of the ground state is a functional of the ground state density $E_{\mathrm{KS}}[n_0]$, which is represented as a sum of:

- Kohn-Sham energies for N electrons $\varepsilon_i^{\mathrm{KS}}$ obtained from an auxiliary system which was used to obtain the ground state density $n_0(\mathbf{r})$, minus two terms which are a byproduct of using functional derivatives $\delta E_{\mathrm{H}}/\delta n$ and $\delta E_{\mathrm{xc}}/\delta n$ in Lagrange optimization procedure, but also a functional of the same ground state density n_0,
- Exchange-correlation energy as a functional of the ground state density $E_{\mathrm{xc}}[n_0]$, and

Energy of Coulomb interaction between the ions[10] $E_{\mathrm{ion-ion}}$ which is a constant term in the BA approximation is included in the external potential V_{ext}. A more detailed discussion about formulation of DFT can be found in paper by Hohenberg and Kohn[62] and many DFT related literature like Refs. [65, 59, 61] and more.

2.7.3 Kohn-Sham scheme in practice

The Kohn-Sham scheme is a straightforward procedure that generates electronic density of the ground state of an interacting electronic system using an auxiliary system of non-interacting electrons. The process is repeated until the input and output density produced using Kohn-Sham states differ less than a preset arbitrary value as in Eq. (2.66), and/or if some of the other self-consistency conditions are met, like for example from Eq. (2.67), Eq. (2.68), or Eq. (2.69).

In practical implementations, there are several ways the scheme can be implemented. Namely, Kohn-Sham states $\psi_i^{\mathrm{KS}}(\mathbf{r})$ can be represented in several ways

[10] Why they are more often referred as ions rather than nuclei will be clear in on of the subsequent paragraphs.

considering basis functions (like plane waves or molecular orbitals). Because the exact form of the exchange-correlation functional V_{xc} is still unknown, there are several ways this functional can be approximated.

Besides the choice of basis and exchange-correlation approximation, there is also a choice of working with all electron calculations or employing the pseudopotential method to reduce calculations to valence electrons only.

Pseudopotentials and plane wave basis

In order to solve Eq. (2.64) to obtain the electron density $n(\mathbf{r})$, one must solve a system of N equations, where N is the number of all electrons - both core and valence. Without going into much detail, one can justify that in order to model electronic structure of solids and molecules, only valence atoms are of interest, since it is the valence atoms that form chemical bonds and are responsible for many chemical properties of the material. Solving for just valence electrons rather than for all electrons would significantly reduce the computational burden. Core electrons are localized close to the nucleus and do not participate in forming chemical bonds, they can be considered as a fixed cloud of negative charge around the nucleus. Valence electrons on the other hand, localize much further from the nucleus, so it is possible to treat them separately, as if they are interacting with a positive ion consisting of nucleus and the cloud of core electrons. This is the basic idea of *pseudopotentials*. Pseudopotentials are constructed by first performing an all electron atomic calculation and then designing a (pseudo)potential that would replicate the same properties by acting only on valence electrons.

The pseudopotentials have been implemented for several basis functions for ψ_i^{KS}. Depending on the system that is in question, each implementation has its own strengths and weaknesses. One of the more popular choices is the plane wave method where ψ_i^{KS} are represented as regular plane waves. This is a very common method for crystals. In most codes that use this method, the number of plane waves is controlled by the kinetic energy cutoff E_{cutt}. Plane waves with increasing energy are added to the basis until their energy exceeds E_{cutt}. There are two most popular types of plane wave pseudopotential implementations: norm-conserving and ultra-soft.

The norm-conserving (NC) pseudopotentials [66, 67], ensure that the integral over squared electron wave functions is conserved when compared to the all electron calculation:

$$\int \mathrm{d}\mathbf{r}\, |\psi_i^{\text{KS}-\text{pseudo}-\text{nc}}(\mathbf{r})|^2 = \int \mathrm{d}\mathbf{r}\, |\psi_i^{\text{KS}-\text{all}-\text{elec.}}(\mathbf{r})|^2. \tag{2.73}$$

They are able to model various systems with quite formidable accuracy, and the easiest to implement which is reason why most DFT codes develop bleeding edge capabilities for NC and plane waves first. However, they can require a large basis which in turn requires more computational resources.

Ultra soft (US) pseudopotentials [68], which are able to better produce states closer to the core using a smaller basis thus requiring less computational resources than NC pseudopotentials however, they are more difficult to construct and depending on the system their accuracy is not always consistent.

Another popular implementation is the projector augmented wave (PAW) [69]. PAW combines plane waves for the valence regions to ensure computational efficiency and localized projectors for core regions in order to improve accuracy and reproduce the all electron states in the core and valence region. This way PAW produces more detailed and accurate results than the simpler plane wave method, while using approximately the same computational resources. However, PAW pseudopotentials are much more difficult to construct and implement, resulting in a much more complex code. For this reason, they are usually the last method to be implemented for bleeding edge capabilities in most DFT codes.

All electron calculation

The all electron calculation can be implemented using plane waves and Gaussian basis. Other popular implementations include some form of modified plane waves in order to increase accuracy of the description for electronic states near nuclei. Most notable ones that are worth mentioning are: augmented plane waves (APW) which combine atomic functions with plane waves, linearized augmented plane waves (LAPW) which are an extension of APW that linearize the energy dependence of atomic spheres to increase accuracy.

Exchange-correlation functionals

As mentioned, the exchange-correlation part of the self-consistent potential V_{xc}, is still unknown. Whether using pseudopotentials or all electron models, there are several ways to model them in regards on whether it is expressed as a local $V_{\text{xc}}^{\text{LDA}}[n(\mathbf{r})]$, semi-local $V_{\text{xc}}^{\text{GGA}}[n(\mathbf{r}), \nabla n(\mathbf{r})]$, or non-local potential $V_{\text{non-loc}}$.

The simplest one is the *local density approximation* (LDA) [70, 71, 72] which approximates V_{xc} at $\mathbf{r}$ with the exchange-correlation energy that a homogeneous electron gas $E_{\text{xc}}^{\text{heg}}[n(\mathbf{r})]$ with density $n(\mathbf{r})$ would have at point $\mathbf{r}$. The total exchange-correlation energy of LDA is then an integral sum over whole volume:

$$E_{\text{xc}}^{\text{LDA}} = \int \mathrm{d}\mathbf{r}\, V_{\text{xc}}^{\text{LDA}}(\mathbf{r}) n(\mathbf{r}) = \int \mathrm{d}\mathbf{r}\, E_{\text{xc}}^{\text{heg}}[n(\mathbf{r})] n(\mathbf{r}). \tag{2.74}$$

LDA relies on the assumption that electron density of an inhomogeneous system $n(\mathbf{r})$ is an overall smooth function over $\mathbf{r}$ and that the change of density $\nabla_{\mathbf{r}} n(\mathbf{r})$ doesn't affect the exchange-correlation energy.

Semi-local potential $V_{\text{GGA}}[n, \nabla n]$ makes use of a *generalized gradient approximation* (GGA) in order to make V_{xc} dependent on density $n(\mathbf{r})$ and the gradient of the density $\nabla_{\mathbf{r}} n(\mathbf{r})$. The total exchange-correlation energy $E_{\text{xc}}^{\text{GGA}}$ is obtained as:

$$E_{\text{xc}}^{\text{GGA}} = \int \mathrm{d}\mathbf{r}\, V_{\text{xc}}^{\text{GGA}}(\mathbf{r}, \nabla_{\mathbf{r}} n) n(\mathbf{r}). \tag{2.75}$$

Most popular GGA functionals are the ones by PBE Perdew-Burke-Ernzerhof (PBE) [73] and Becke-Lee-Yang-Parr (BLYP) [74, 75]. For solids, a modified PBE functional called PBEsol is usually preferred over regular PBE since it is optimized to produce more accurate lattice constants [76].

In order to increase accuracy, dependence on the second derivative of the density, which is supposed to improve description for densities that vary rapidly, and kinetic energy density $\tau(\mathbf{r})$ which is supposed to improve description of correlation effects can be included:

$$E_{\mathrm{xc}}^{\mathrm{meta-GGA}} = \int \mathrm{d}\mathbf{r}\, V_{\mathrm{xc}}^{\mathrm{meta-GGA}}(\mathbf{r}, \nabla_{\mathbf{r}} n, \nabla_{\mathbf{r}}^2 n, \tau(\mathbf{r})) n(\mathbf{r}). \tag{2.76}$$

These functionals are called Meta generalized gradient approximation (meta-GGA), and one example is Tao-Perdew-Staroverov-Scuseria (TPSS) [77].

When it comes non-local potentials, most famous are the class of *hybrid potentials*. In general, they are usually constructed as a mixture of exchange-correlation in local or semi-local functional and the exact exchange energy from Hartree-Fock theory $E_{\mathrm{x}}^{\mathrm{HF}}$ in some ratio α:

$$E_{\mathrm{xc}}^{\mathrm{hyb.}} = (1-\alpha) E_{\mathrm{xc}}^{\beta} + \alpha E_{\mathrm{xc}}^{\mathrm{HF}}, \tag{2.77}$$

where β is a type of functional (e.g. LDA, PBE, etc.) and $0 < \alpha < 1$ is the mixing parameter, although there can be multiple α_i parameters. The exact Hartree-Fock (HF) exchange energy:

$$E_{\mathrm{x}}^{\mathrm{HF}} = -\sum_{i>j} \int\int \mathrm{d}\mathbf{r}_1 \mathbf{r}_2 \, \frac{\psi_i^{\mathrm{KS}*}(\mathbf{r}_1)\psi_j^{\mathrm{KS}*}(\mathbf{r}_2)\psi_i^{\mathrm{KS}}(\mathbf{r}_1)\psi_i^{\mathrm{KS}}(\mathbf{r}_2)}{|\mathbf{r}_1 - \mathbf{r}_2|}, \tag{2.78}$$

is obviously non-local since it accounts for exchange of two electrons at $\mathbf{r}_1$ and $\mathbf{r}_2$, respectively. One popular choice is the mixture of PBE functional with HF exchange known as PBE0 [78]:

$$E_{\mathrm{xc}}^{\mathrm{PBE0}} = \alpha E_{\mathrm{x}}^{\mathrm{HF}} + (1-\alpha) E_{\mathrm{x}}^{\mathrm{PBE}} + E_{\mathrm{c}}^{\mathrm{PBE}}, \tag{2.79}$$

where $E_{\mathrm{x}}^{\mathrm{PBE}}$ and $E_{\mathrm{c}}^{\mathrm{PBE}}$ are separate exchange and correlation parts from PBE functional, repsectively. The mixing parameter is usually $\alpha = 0.25$ however, for certain purposes this parameter can be determined in order to meet certain conditions in order to increase the accuracy of the calculation as seen in Ref. [79].

Using periodic conditions, Eq. (2.64) is solved for states $i \to \mathbf{k}n$, where $\mathbf{k}$ is a point on the grid in reciprocal space and n is the Kohn-Sham state at $\mathbf{k}$. In order to have a converged self-consistent calculation one should check the convergence parameters for E_{cut} (in plane wave basis) and the size of the k-grid. Specially, for hybrid functionals, the non-local nature of HF exchange requires additional Fourier transform for the other electron, which introduces another grid in reciprocal space, called q-grid. This is one of the reasons why hybrid functionals are not as practical since their computational resources increase as square compared to local or semi-local counterparts.

Non-self-consistent calculation

After the self-consistent calculation is completed, and ground state density is obtained $n_0(\mathbf{r})$ one can perform a non-self-consistent calculation which can interpolate Kohn-Sham states on a more dense k-grid or for higher states n. Specially if

the dispersion relation of Kohn-Sham states is desired, one can perform a non-self-consistent calculation on a k-path in reciprocal space. One of the ways interpolation is routinely done in DFT is by $\mathbf{k} \cdot \mathbf{p}$ perturbation theory, which is explained in detail in Sec. 2.6.

DFT with many-body techniques

The only observable that DFT can provide exact information on are the total energy of the ground state and the ground state density. Therefore, the Kohn-Sham band structure can be considered just an approximation, without the full many-body treatment, to the real electronic band structure. However, this has proved to be a good approximation, the main reason lies in the fact that Kohn-Sham equation relies on ground state density that is considered exact in DFT. In most cases Kohn-Sham electronic structure provides decent results when compared to experiment. While the simpler LDA can predict some small gap insulators as metals (like for e.g. Ge), most functionals based on GGA correct these mistakes [60]. The main downside is that many-body effects which lead to broadening of the bands are neglected. In the absence of a more reliable and computationally cheaper method, this is the best first estimate for the electronic structure for most metals, insulators and semiconductors.

Around the same time that Kohn-Sham DFT was formulated, in 1965, Hedin [80] developed a full many-body theory for obtaining ground and excited states in electron systems. This theory accounts for all many-body effects using self-energy of the Dyson equation, which can be solved self-consistently. Unfortunately, this requires computational resources not available even to modern computer clusters. Using many approximations, and keeping only the simplest diagrams of self energy, Hedin equations reduce to computationally solvable GW equations [80, 81],where G stands for Green's function and W for the screened Coulomb interaction. The GW is routinely used with Kohn-Sham states as a starting point for Green's function, which after self-consistent calculations leads to many-body corrections to Kohn-Sham energies for band structure and band gap. However, since screened potential is non-local, the computational resources needed for GW greatly surpass the ones for DFT, so it is limited to systems with fewer electrons. The GW method is further explained in Sec. 2.7.5.

2.7.4 Band gap in electronic structure

In electronic structure, the difference between the extremum of energy levels of the highest occupied valence band and the lowest occupied conduction band is called the electronic band gap or just *band gap* of the material. It is an essential property of materials that determines their electrical conductivity. Based on the width of the gap, and the possible conductivity of current, materials can be classified as metals (in the case when there is no band gap, i.e. conduction and valence bands overlap), insulators (in the case of wide band gaps) and semiconductors (in the case of small or moderate band gap).

In spectroscopic experiments, these band gaps are usually determined by pho-

toemission. In these experiments an electron is either ejected out of, or, added into the material sample, by direct and inverse photoemission, respectively.

In absorption experiments, where an incident photon excites an electron to another state but doesn't eject it out of the material, a different type of band gap is observed. This is the so-called optical gap. In this process an excited electron is still bound to the material and in its place a hole is created. In theory, this process is very difficult to compute numerically. Because excited electron and hole form a pair, all theoretical aspects must consider them together, which means that two-particle Green's functions must be involved which leads to significant numerical burden.

Unlike the optical gap, electrical band gap can be theoretically obtained much easier. There are several ways, some of which are: using DFT Kohn-Sham states, using Hartree-Fock, or using Δ SCF method, which are explained below in this section. An improvement to DFT Kohn-Sham gap, can be obtained using the GW method, to which Sec. 2.7.5 is dedicated.

Electronic gap: photoemission experiments

Direct photoemission uses ultraviolet of X-ray photons to eject electron from a neutral sample. Incidental photon with energy $h\nu$ ejects an electron from its initial valence state s, which is below and separated from the Fermi level E_{Fermi} by energy E_{s}, to the surface of the material. The electron then hits the detector with kinetic energy E_{kin}. The *ionization potential* E_s^{IP} for state s, is defined as energy required to remove the bound electron from the state s:

$$E_s^{\text{IP}} = -E_s = h\nu - E_{\text{kin}} - F_{\text{work}}, \quad E_s < E_{\text{Fermi}}, \tag{2.80}$$

where F_{work} is the work function, or rather, energy distance from the Fermi level to vacuum (surface of the material). Using direct photoemission valence states can be probed. Ionization potential E_s^{IP} is a positive number.

Inverse photoemission is used to probe conduction and valence states. In inverse photoemission incidental electron of kinetic energy E_{kin} is scattered into the sample and it goes into radiative transmission to conduction state s, which is above and separated from the Fermi level E_{Fermi} by energy E_{s}, emitting a photon of energy $h\nu$ in the process. The *electron affinity* E_s^{EA} for state s, is defined as:

$$-E_{\text{EA}} = E_{\text{s}} = E_{\text{kin}} - h\nu + F_{\text{work}}, \quad E_{\text{s}} \geq E_{\text{Fermi}}. \tag{2.81}$$

Electron affinity E_{EA} is positive when s is a valence state and negative when s is conduction state.

Theoretically, the band gap can be determined using several methods, some of which are described below.

DFT Kohn-Sham gap

The electron density $n(\mathbf{r})$ is made from N electrons, which in the ground state account for all occupied states in the case of insulators and semiconductors. However, Kohn-Sham equations Eq. (2.59) and Eq. (2.64) do not impose any kind of limit

on the number of states. This means that one could solve for arbitrary number of Kohn-Sham states $N_{\mathrm{KS}} \geq N$ and thus obtain Kohn-Sham energies for unoccupied states. The difference between the highest occupied and lowest unoccupied states is the *Kohn-Sham band gap* $E_{\mathrm{gap}}^{\mathrm{KS}}$ in insulators and semiconductors:

$$E_{\mathrm{gap}}^{\mathrm{KS}} = \varepsilon_{N+1}^{\mathrm{KS}} - \varepsilon_{N}^{\mathrm{KS}}. \tag{2.82}$$

If $E_{\mathrm{KS}}[n_0]$ were simply equal to just the sum of Kohn-Sham states $\sum_i^{N_{\mathrm{KS}}} \varepsilon_i^{\mathrm{KS}}$ (plus constant $E_{\mathrm{ion-ion}}$), then Kohn-Sham energies would represent the energies of adding or removing an electron at state i from the system, thus the Kohn-Sham band gap would represent the DFT gap in semiconductors and insulators. However, since there is no way to obtain any excited states in DFT using Eq. (2.72), and the simplest estimate about the band gap is the one obtained from Kohn-Sham states, the DFT band gap usually refers to the simple Kohn-Sham band gap.

Hartree-Fock

In the Hartree-Fock method, the many-electron function Φ_{HF} is represented as a Slater determinant. This determinant is filled with single particle electron orbitals $\phi_i(\mathbf{r}_j)$, where i and j represent the indices for columns and rows, respectively:

$$\Phi_{\mathrm{HF}}(\mathbf{r}_1, \mathbf{r}_2, \ldots) = \frac{1}{\sqrt{N!}} \begin{vmatrix} \phi_1(\mathbf{r}_1) & \phi_1(\mathbf{r}_2) & \ldots & \phi_1(\mathbf{r}_N) \\ \phi_2(\mathbf{r}_1) & \phi_2(\mathbf{r}_2) & \ldots & \phi_2(\mathbf{r}_N) \\ \vdots & \vdots & \ddots & \vdots \\ \phi_N(\mathbf{r}_1) & \phi_N(\mathbf{r}_2) & \ldots & \phi_N(\mathbf{r}_N) \end{vmatrix}. \tag{2.83}$$

where N is the number of electrons in the system and the only condition for Φ_{HF} is to be antisymmetric when two electrons are exchanged, as per Fermi-Dirac statistics.

This property can account for the exchange effects due to Pauli principle, however the correlation is not included since this determinant produces a simple sum of all possible exchanges of products of wave functions of individual electron orbitals $\phi_i(\mathbf{r}_j)$ so the operator $\nabla_{\mathbf{r}_k}^2$ simply commutes with all $\phi_i(\mathbf{r}_j)$ for which $k \neq j$, thus making individual electron orbitals uncorrelated to one another in terms of their individual kinetic energy.

The expectation value of Hamiltonian H returns the total energy of the system in HF approximation E^{HF}. For spinless system E^{HF} is:

$$\begin{aligned} E_N^{\mathrm{HF}} = \langle \Phi_{\mathrm{HF}} | \, H \, | \Phi_{\mathrm{HF}} \rangle = & \sum_i^N \int \mathrm{d}\mathbf{r} \, \phi_i^*(\mathbf{r}) \left[-\frac{\hbar^2 \nabla_i^2}{2m_e} + V_{\mathrm{ext}}(\mathbf{r}) \right] \phi_i(\mathbf{r}) \\ & + \sum_{i>j}^N \int \mathrm{d}\mathbf{r} \, \mathrm{d}\mathbf{r}' \, \phi_i^*(\mathbf{r}) \phi_j^*(\mathbf{r}') v_{\mathrm{c}}(\mathbf{r}_i - \mathbf{r}_j) \phi_i(\mathbf{r}) \phi_j(\mathbf{r}') \\ & - \sum_{i>j}^N \int \mathrm{d}\mathbf{r} \, \mathrm{d}\mathbf{r}' \, \phi_i^*(\mathbf{r}) \phi_j^*(\mathbf{r}') v_{\mathrm{c}}(\mathbf{r}_i - \mathbf{r}_j) \phi_j(\mathbf{r}) \phi_i(\mathbf{r}') \end{aligned} \tag{2.84}$$

where $v_c(\mathbf{r}) = 1/(4\pi\epsilon_0|\mathbf{r}|)$ is the Coulomb potential.

Following a similar procedure to the one used to derive the Kohn-Sham equations, from Eq. (2.56) to Eq. (2.64), one arrives at Hartree-Fock equations for electron orbitals:

$$\left[-\frac{\hbar^2\nabla_i^2}{2m_e} + V_{\text{ext}}(\mathbf{r}) + V_{\text{H}}(\mathbf{r})\right]\psi_i^{\text{HF}}(\mathbf{r}) + \int \mathrm{d}\mathbf{r}'\, V_{\text{x}}(\mathbf{r},\mathbf{r}')\psi_i^{\text{HF}}(\mathbf{r}') = \varepsilon_i^{HF}\psi_i^{\text{HF}}(\mathbf{r}), \quad (2.85)$$

where ψ_i^{HF} and $\varepsilon_i^{\text{HF}}$ are obtained after unitary transform similar to Eq. (2.63), $V_{\text{H}}(\mathbf{r})$ and $V\text{x}(\mathbf{r})$ are Hartree and exchange terms, respectively:

$$\begin{aligned} V_{\text{H}}(\mathbf{r}) &= \sum_j \int \mathrm{d}\mathbf{r}'\, |\psi_j^{\text{HF}}(\mathbf{r}')|^2 v_c(\mathbf{r}-\mathbf{r}'), \\ V_{\text{x}}(\mathbf{r},\mathbf{r}') &= -\sum_j \int \mathrm{d}\mathbf{r}'\, \psi_j^{\text{HF}*}(\mathbf{r}')(\mathbf{r}) v_c(\mathbf{r}-\mathbf{r}')\psi_j^{\text{HF}}(\mathbf{r}). \end{aligned} \quad (2.86)$$

Unlike for Kohn-Sham wave functions and energies ψ_i^{KS} and $\varepsilon_i^{\text{KS}}$, for which it was established previously that they posses no physical meaning, in the Hartree-Fock case ψ_i^{HF} and $\varepsilon_i^{\text{HF}}$ have a physical meaning, they represent eigenfunction and eigenvalue of i-th orbital, respectively. This interpretation is stated using *Koopmans' theorem*[11] [59].

Koopmans' theorem: The eigenvalue of the filled (empty) orbital $\varepsilon_i^{\text{HF}}$ is equal to the change in the total energy from Eq. (2.84), if an electron is subtracted from (added to) the system i.e. decreasing (increasing) the size of the determinant by omitting (adding) a row and a column in Eq. (2.83) involving a particular orbital $\phi_j(\mathbf{r}_i)$, keeping all the other orbitals same.

This means that the first ionization energy is equal to $E_{\text{io}} = E_{N-1}^{\text{HF}} - E_N^{\text{HF}} = -\varepsilon_N^{\text{HF}}$ and first energy of electron affinity is $E_{\text{ea}} = E_N^{\text{HF}} - E_{N+1}^{\text{HF}} = -\varepsilon_{N+1}^{\text{HF}}$. Using this interpretation, the band gap in Hartree-Fock approximation can be computed by performing one calculation with N electrons, and using $N+n$, $n \geq 1$, orbitals and simply subtracting the energies of $\varepsilon_{N+1}^{\text{HF}}$ and $\varepsilon_N^{\text{HF}}$ orbitals as $E_{\text{gap}}^{\text{HF}} = \varepsilon_{N+1}^{\text{HF}} - \varepsilon_N^{\text{HF}}$. In Eq. (2.85), the eigenvalue of occupied orbitals $\varepsilon_i^{\text{HF}}$ is lowered by the exchange part V_{x}, which reduces the self-interaction of Hartree term V_{H} by some degree. However, for empty orbitals, this is not the case since V_{x} this term is omitted in Eq. (2.85). This the reason why Hartree-Fock approximation overestimates band gaps in most cases. Significant improvements can be made by allowing orbitals to relax and taking into account the exchange of an added electron with all the others, which is routinely done for finite systems and knows as Δ SCF approximation [59].

[11] Besides that density must be constructed from N occupied states only, Kohn-Sham equations pose no limit on the number of states $N_{\text{KS}} \geq N$ that are calculated or requires any antisymmetric condition on the total wavefunction, the Koopmans' theorem doesn't apply in their case. Koopmans' theorem can be reinstated for DFT, in a sense that highest occupied Kohn-Sham state would correspond to ionization energy if the exact effective potential was known.

Δ SCF

In experiments, removing or adding an electron to the system corresponds to direct and inverse photoemission, after which the system, with changed number of electrons, has to relax to its ground state. One should also consider these relaxation effects. For finite systems like isolated atoms and small molecules, the so-called 'Δ SCF' approximation is reasonably successful [82, 61] and consists of calculating ground state densities and energies for three systems: cation - with one electron removed E_{N-1} (direct photoemission), neutral - with all electrons present E_N, and anion - with one electron added E_{N+1} (inverse photoemission), to produce the quasi-particle gap $E^{\mathrm{qp}}_{\Delta\mathrm{SCF}}$:

$$E^{\mathrm{qp}}_{\Delta\mathrm{SCF}} = (E_{N+1} - E_N) - (E_N - E_{N-1}). \tag{2.87}$$

When 'Δ SCF' is applied with Hartree-Fock it can improve results when compared to $E^{\mathrm{HF}}_{\mathrm{gap}}$ that doesn't allow for orbitals to relax, which usually leads to overestimation of ionization and excitation energies. By performing 3 separate self-consistent calculations for E_N, E_{N-1}, and E_{N+1}, with N, $N-1$ and $N+1$ electrons, respectively, orbitals are relaxed in each, and some correlation effects are included.

Unfortunately, for infinite systems like solids where the number of electrons is at the order of 10^{23}, Δ SCF approximation does not hold because the removal or addition of one electron is negligible on the total density. Furthermore, the exact exchange-correlation energy and potential is not known, and most approximations rely on assumption that it is a smooth function of density, so removal or addition of one electron wouldn't introduce a discontinuity in the density and exchange-correlation energy. Without such discontinuity, the quasi-particle gap of Eq. (2.87) reduces to Kohn-Sham gap since:

$$n_0 + \Delta n \simeq n_0, \quad \Rightarrow \quad V_{\mathrm{xc}}[n_0 + \Delta n] \simeq V_{\mathrm{xc}}[n_0]. \tag{2.88}$$

Optical gap: absorption experiments

As previously mentioned, besides electronic band gap, materials also have an *optical gap*. Experimentally, optical gaps occur in the process of *absorption*, where electron is excited to a conduction state by the absorbed photon, but unlike in the process of emission, the electron doesn't leave the system. For photoemission the system relaxes to a static ground state, whereas in absorption the system is in a dynamic excited state, thus it cannot be described by any direct DFT approach. Another problem with optical gaps, is that excited electron creates a hole, which interacts with that excited electron. Therefore any such excitation must consider excited electron and hole as a pair or an exciton. This makes it impossible to impose any local approximation.

This is a very complex many body problem which has to capture non-locality and dynamics. In order to do so, it has to take into account some higher order interaction terms, which are usually solved by the Bethe-Salpeter equation [83].Solving this equation is rather complex and requires significant computational resources that far surpass any DFT method.

These are just several most relevant aspects of the DFT *band gap problem*, which is explored in great detail in literature [84], and is out of scope of this work.

2.7.5 GW method

Kohn-Sham formulation of DFT assumes that the mean field, with which one electron interacts, and consists of external potential generated by ions, the Hartree potential of all other electrons and the exchange-correlation potential is static. All Coulomb-like interactions are considered long range.Being only able to describe the ground state energy and density, DFT itself is unable to give any information about excited states or band structure. In absence of such information of the electronic structure, Kohn-Sham energies and wave functions are often considered as DFT electronic structure. Even though Kohn-Sham eigenvalues and eigenstates are just solutions for an auxiliary problem that leads to the same density as the ground state of the system, they have proven to be an excellent starting point in more sophisticated calculations.

Precisely, the GW approximation, which relies on one electron Green function G and the dynamical screened Coulomb interaction W is one such example where Kohn-Sham solutions can be used as components for many-body approach. Using Dyson's equation, any Green function G can be expressed in series of Feynman diagrams of simpler *bare* Green functions G^0. Collection of all diagrams is represented as the self-energy Σ which is analogous to exchange-correlation energy in DFT.

This section serves as an overview of the main concepts of GW method, and keen readers can find more insightful information in Refs. [80, 85, 86, 81, 87, 82, 88].

From Hedin's equations to GW approximation

Using functional derivatives, in 1965, Hedin [80] derived a system of equations that describe all many-body physics of an electron system[12]:

$$\Sigma^{\mathrm{xc}}(1,2) = iG(1,\overline{4})W(1^+,\overline{3})\tilde{\Gamma}(\overline{4},2;\overline{3}) \tag{2.89}$$

$$G(1,2) = G^0(1,2) + G^0(1,\overline{3})\Sigma^{\mathrm{xc}}(\overline{3},\overline{4})G(\overline{4},2) \tag{2.90}$$

$$\tilde{\Gamma}(1,2;3) = \delta(1,2)\delta(1,3) + \frac{\delta\Sigma_{\mathrm{xc}}(1,2)}{\delta G(\overline{4},\overline{5})}G(\overline{4},\overline{6})G(\overline{7},\overline{5})\tilde{\Gamma}(\overline{6},\overline{7};3) \tag{2.91}$$

$$\tilde{\chi}(1,2) = -iG(1,\overline{3})G(\overline{4},1)\tilde{\Gamma}(\overline{3},\overline{4};2) \tag{2.92}$$

$$W(1,2) = v_{\mathrm{c}}(1,2) + v_{\mathrm{c}}(1,\overline{3})\tilde{\chi}(\overline{3},\overline{4})W(\overline{4},2) \tag{2.93}$$

where integer numbers $1, 2, 3 \ldots 7$ are used instead of space, time and spin coordinates, e.g. $\mathbf{r}_1, t_1, \sigma_1 \to 1$, and integration over these coordinates is noted by an overline, e.g. $\int \mathrm{d}\mathbf{r}_1 \int \mathrm{d}t_1 \to \overline{1}$. The exchange-correlation is expressed through self-energy Σ_{xc}, W and v_{c} are screened and bare Coulomb interaction, respectively, G and G^0 are dressed and bare Green's function (or dressed and bare propagator), respectively. Irreducible polarization $\tilde{\chi}$ represents a response of electron density to

[12] Presented equations are taken directly from Ref [60].

an external potential, $\tilde{\Gamma}$ is a irreducible version of a three point vertex Γ which represents a response of inverse dressed propagator to perturbation potential u:

$$\Gamma(1,2;3) = -\frac{\delta G^{-1}(1,2)}{\delta u(3)} \tag{2.94}$$

Perturbation potential u is introduced as a probing potential when deriving Hedins equations using functional derivatives. The total effective potential that electrons v_{eff} see is their internal Hartree potential v_{H} plus the perturbation potential u : $v_{\text{eff}} = v_{\text{H}} + u$. Finally, $\delta\Sigma_{\text{xc}}/\delta G$ is a four-point kernel. These equations are rather involved and impossible to solve even for simplest systems.

First approximation is to neglect three point vertex corrections Γ and $\tilde{\Gamma}$, i.e. to assume that these vertices are diagonal in space and time coordinates:

$$\Gamma(1,2,3) = \tilde{\Gamma}(1,2;3) = \delta(1,2)\delta(1,3), \tag{2.95}$$

which makes the polarization $\tilde{\chi}$:

$$\tilde{\chi}(1,2) = -iG(1,2)G(2,1^+) \tag{2.96}$$

where $\tilde{\chi}$ is the polarization in the so-called bubble approximation, because it corresponds to a closed bubble diagram formed from electron and hole pair: $G(1,2)$ and $G(2,1^+)$, respectively. Another name for bubble approximation is the *random-phase approximation* (RPA), which originates from calculations on homogeneous electron gas, where wave functions are plane waves so the response function $\tilde{\chi}$ would contain sums of exponents with dominant phases entering the sum, and 'random-phase' terms would average to zero. The self-energy Σ_{xc} becomes:

$$\Sigma_{\text{xc}}(1,2) = iG(1,2)W(1^+,2). \tag{2.97}$$

The new system of equations is now:

$$\begin{aligned}
\Sigma^{\text{xc}}(1,2) &= iG(1,\overline{4})W(1^+,2) && (2.98)\\
G(1,2) &= G^0(1,2) + G^0(1,\overline{3})\Sigma^{\text{xc}}(\overline{3},\overline{4})G(\overline{4},2) && (2.99)\\
\tilde{\Gamma}(1,2;3) &= \delta(1,2)\delta(1,3) && (2.100)\\
\tilde{\chi}(1,2) &= -iG(1,2)G(2,1^+) && (2.101)\\
W(1,2) &= v_{\text{c}}(1,2) + v_{\text{c}}(1,\overline{3})\tilde{\chi}(\overline{3},\overline{4})W(\overline{4},2) && (2.102)\\
& && (2.103)
\end{aligned}$$

GW using Kohn-Sham states

The basic components of many-body perturbative approach is the reference non-interacting system which can be represented using solution from DFT Kohn-Sham equations[87]. In order to construct bare Green functions $G^0_{\mathbf{k}n}$, one would usually start using single particle Kohn-Sham states $|\mathbf{k}n\rangle$ with energy $\varepsilon_{\mathbf{k}n}$:

$$G^0_{\mathbf{k}n}(\omega) = \frac{f_{\mathbf{k}n}}{\omega - \varepsilon_{\mathbf{k}n} - i\eta} + \frac{1 - f_{\mathbf{k}n}}{\omega - \varepsilon_{\mathbf{k}n} + i\eta} \tag{2.104}$$

where $f_{\mathbf{k}n}$ are electron occupation numbers (1 or 0 for semiconductors and insulators at zero temperature) and $\eta \to 0^+$ is a positive real infinitesimal which shifts poles above and below the real axis for occupied and empty states, respectively. The dressed Green functions $G_{\mathbf{k}n}(\omega)$ obey the Dyson equation:

$$[G_{\mathbf{k}n}(\omega)]^{-1} = \left[G^0_{\mathbf{k}n}(\omega)\right]^{-1} - [\Sigma^{\mathrm{xc}}_{\mathbf{k}n}(\omega) - V^{\mathrm{xc}}_{\mathbf{k}n}]\,. \tag{2.105}$$

The static term $V^{\mathrm{xc}}_{\mathbf{k}n}$ is subtracted from the dynamic self-energy $\Sigma_{\mathrm{xc}}(\omega)$ to avoid double counting since the static exchange-correlation is included in Kohn-Sham eigenvalues $\varepsilon_{\mathbf{k}n}$.

Self-energy $\Sigma_{\mathrm{xc}}(\omega)$ can be separated into *static exchange* and *dynamic correlation* as $\Sigma^{\mathrm{xc}}_{\mathbf{k}n}(\omega) = \Sigma^{\mathrm{x}}_{\mathbf{k}n} + \Sigma^{\mathrm{c}}_{\mathbf{k}n}(\omega)$. The static exchange part $\Sigma^{\mathrm{x}}_{\mathbf{k}n}$ is simply the Fock term from Hartree-Fock self-energy:

$$\begin{aligned}\Sigma^{\mathrm{x}}_{\mathbf{k}n} &= \langle \mathbf{k}n |\, \Sigma^{\mathrm{x}}(\mathbf{r}_1, \mathbf{r}_2)\, | \mathbf{k}n \rangle \\ &= -\sum_m^{\mathrm{occ}} \int_{\mathrm{BZ1}} \frac{\mathrm{d}\mathbf{q}}{(2\pi)^3} \sum_{\mathbf{G}} v(\mathbf{q}+\mathbf{G})\, |\rho_{nm}(\mathbf{k},\mathbf{q},\mathbf{G})|^2\, f_{\mathbf{k}-\mathbf{q}m}.\end{aligned} \tag{2.106}$$

where the sum goes over occupied bands m only. The dynamic correlation part $\Sigma^{\mathrm{c}}_{\mathbf{k}n}$ is:

$$\begin{aligned}\Sigma^{\mathrm{c}}_{\mathbf{k}n}(\omega) &= \langle \mathbf{k}n |\, \Sigma^{\mathrm{c}}(\mathbf{r}_1, \mathbf{r}_2, \omega)\, | \mathbf{k}n \rangle \\ &= i \sum_m^{\mathrm{all}} \int_{\mathrm{BZ1}} \frac{\mathrm{d}\mathbf{q}}{(2\pi)^3} \sum_{\mathbf{G}\mathbf{G}'} v(\mathbf{q}+\mathbf{G}) \rho_{nm}(\mathbf{k},\mathbf{q},\mathbf{G}) \rho^*_{nm}(\mathbf{k},\mathbf{q},\mathbf{G}') \\ &\times \int \mathrm{d}\omega'\, G^0_{\mathbf{k}-\mathbf{q}m}(\omega-\omega') \epsilon^{-1}_{\mathbf{G}\mathbf{G}'}(\mathbf{q},\omega').\end{aligned} \tag{2.107}$$

The sum in Eq. (2.107) goes over both occupied and unoccupied bands, $\mathbf{q}$,$\mathbf{G}$ and $\mathbf{G}'$ are vectors in reciprocal space, $v(\mathbf{q}+\mathbf{G}) = 4\pi/|\mathbf{q}+\mathbf{G}|^2$ is the Fourier transform of v_{c}, and $\rho_{nm}(\mathbf{k},\mathbf{g},\mathbf{G})$ [13] is expressed as:

$$\rho_{nm}(\mathbf{k},\mathbf{g},\mathbf{G}) = \langle \mathbf{k}n |\, e^{i(\mathbf{q}+\mathbf{G})\cdot\mathbf{r}}\, | \mathbf{k}-\mathbf{q}m \rangle = \int_\Omega \mathrm{d}\mathbf{r}\, \psi^*_{\mathbf{k}n}(\mathbf{r}) e^{i(\mathbf{q}+\mathbf{G})\cdot\mathbf{r}} \psi_{\mathbf{k}-\mathbf{q}m}(\mathbf{r}) \tag{2.108}$$

The inverse dielectric function $\epsilon^{-1}_{\mathbf{G}\mathbf{G}'}(\mathbf{q},\omega')$ is connected to reducible polarization χ as:

$$\epsilon^{-1}_{\mathbf{G}\mathbf{G}'}(\mathbf{q},\omega) = \delta_{\mathbf{G}\mathbf{G}'} + v(\mathbf{q}+\mathbf{G}) \chi_{\mathbf{G}\mathbf{G}'}(\mathbf{q},\omega), \tag{2.109}$$

and reducible polarization χ is connected to irreducible polarization $\tilde{\chi}$ by a Dyson equation:

$$\chi(1,2) = \tilde{\chi}(1,2) + \tilde{\chi}(1,\overline{3}) v_{\mathrm{c}}(\overline{3},\overline{4}) \chi(\overline{4},2), \tag{2.110}$$

[13] In Yambo code documentation and Ref. [87], $\rho_{nm}(\mathbf{k},\mathbf{g},\mathbf{G})$ is referred as 'oscillator'. This quantity and its Fourier transform appear frequently so within Yambo there are procedures that take advantage of symmetry operations to reduce the number of calculations for $\mathbf{k}$ and $\mathbf{k}-\mathbf{q}$ pairs, and fast Fourier transform numerical techniques to speed up the computations.

which leads to a practical expression:

$$\chi_{\mathbf{G}\mathbf{G}'}(\mathbf{q},\omega) = \left[\delta_{\mathbf{G}\mathbf{G}''} - v(\mathbf{q}+\mathbf{G}'')\tilde{\chi}_{\mathbf{G}\mathbf{G}''}(\mathbf{q},\omega)\right]^{-1}\tilde{\chi}_{\mathbf{G}''\mathbf{G}'}(\mathbf{q},\omega). \tag{2.111}$$

Irreducible polarization is often approximated with bare polarization $\tilde{\chi}^0 = -iG^0G^0$ that is constructed from bare Green functions G^0 :

$$\begin{aligned}\tilde{\chi}_{\mathbf{G}\mathbf{G}'}(\mathbf{q},\omega) &\approx \tilde{\chi}^0_{\mathbf{G}\mathbf{G}'}(\mathbf{q},\omega)\\ &= 2\sum_{nn'}\int_{\mathrm{BZ1}}\frac{\mathrm{d}\mathbf{q}}{(2\pi)^3}\rho^*_{\mathbf{k}n'n}(\mathbf{q},\mathbf{G})\rho_{\mathbf{k}n'n}(\mathbf{q},\mathbf{G}')(f_{\mathbf{k}-\mathbf{q}n})(1-f_{\mathbf{k}n'})\\ &\times\left[\frac{1}{\omega-\varepsilon_{\mathbf{k}-\mathbf{q}n}-\varepsilon_{\mathbf{k}n'}+i\eta}-\frac{1}{\omega-\varepsilon_{\mathbf{k}-\mathbf{q}n'}-\varepsilon_{\mathbf{k}n}-i\eta}\right].\end{aligned} \tag{2.112}$$

Once the diagonal terms for state $|\mathbf{k}n\rangle$ of static exchange Σ^{x} and dynamic correlation $\Sigma^{\mathrm{c}}(\omega)$ parts of self-energy are obtained they are inserted into Eq. (2.105). The GW quasi-particle energy $\omega^{\mathrm{QP}}_{\mathbf{k}n}$ are poles of $G_{\mathbf{k}n}(\omega)$ or obtained by solving for ω:

$$\omega - \varepsilon_{\mathbf{k}n} - \Sigma^{\mathrm{xc}}_{\mathbf{k}n}(\omega) + V^{\mathrm{xc}}_{\mathbf{k}n} = 0 \tag{2.113}$$

Another way of obtaining quasi-particle energies is by plotting the imaginary part of the dressed Green function on a dense ω grid, i.e. the spectral function $A_{\mathbf{k}n}(\omega) = -1/\pi|\operatorname{Im} G_{\mathbf{k}n}(\omega)|$ which should produce a quasi-particle peak at $\operatorname{Re}\omega^{\mathrm{QP}}_{\mathbf{k}n} = E^{\mathrm{QP}}_{\mathbf{k}n}$ which is a value relatively close to $\varepsilon_{\mathbf{k}n}$ and perhaps some satellites. The half-width of that peak is the imaginary part of the solution $\operatorname{Im}\omega^{\mathrm{QP}}_{\mathbf{k}n}$ which is closely related to the lifetime of that state. In practice however, calculating $\Sigma^{\mathrm{xc}}(\omega)$ on a dense set of ω is often avoided if the spectral function $A_{\mathbf{k}n}(\omega)$ is not required.

GW calculation in practice

Most codes perform a DFT calculation first and then GW on top of those results. Even though DFT calculation can converge for a set of numerical parameters like the $\mathbf{k}$-grid density, number of bands in KS equation m, or the kinetic energy cutoff determined by the number of $\mathbf{G}$ vectors, often GW calculations require careful study of convergence for every value separate. In that case it is often a good strategy for starting DFT calculation to have more ingredients than the convergence requires in order to insure a good convergence in GW as well.

Because $\Sigma^{\mathrm{x}}_{\mathbf{k}n}$ from Eq. (2.106), is static and doesn't require much computational resources it is calculated first to check the convergence and determine if starting DFT calculation provides enough ingredients. The convergence is checked for density of $\mathbf{k}$-grid where integration over $\mathbf{q}$ becomes a sum over all $\mathbf{k}$. If DFT is converged, a non-self-consistent calculation can be performed to increase the density of the $\mathbf{k}$ grid. The number of $\mathbf{G}$ vectors $N_{\mathbf{G}}$ in the sum is controlled by kinetic energy cutoff which cannot be increased by a non-self-consistent calculation and a new starting DFT calculation has to be performed. These convergence parameters should give a decent estimate on where one can look for convergence when calculating the dynamical part $\Sigma^{\mathrm{c}}_{\mathbf{k}n}(\omega)$.

The dynamical part of self-energy $\Sigma^{\mathrm{c}}_{\mathbf{k}n}(\omega)$ is the most involved part and requires careful study of convergence. The number of $\mathbf{G}$ vectors $N_{\mathbf{G}}$ determines the size of the inverse dielectric square matrix $\epsilon^{-1}(\mathbf{q},\omega)$. At the same time calculations of $\tilde{\chi}$ which make up ϵ^{-1} must contain enough empty bands for sums over n and n' in Eq. (2.112) to converge. If DFT calculation is well converged a non-self consistent calculation can be performed to obtain more empty KS states. There is also an integral over $\mathbf{q}$ which turns into a sum over the whole $\mathbf{k}$-grid from the DFT calculations. If DFT is well converged, a non-self consistent calculation can be used to obtain results for a denser $\mathbf{k}/\mathbf{q}$-grid. Convergence over the number of $\mathbf{G}$, n, and $\mathbf{q}$ must be checked carefully and independently of each other.

Simplifying the dielectric function $\epsilon^{-1}_{\mathbf{GG'}}$: RPA and PPA

The most involved term of the dynamic correlation part $\Sigma^{\mathrm{c}}_{\mathbf{k}n}$ in Eq. (2.107) is the inverse dielectric function $\epsilon^{-1}_{\mathbf{GG'}}(\mathbf{q},\omega)$. Within RPA, when polarization contains only bubble diagrams, and even when irreducible polarization is approximated with bare polarization $\tilde{\chi}_{\mathbf{GG'}}(\mathbf{q},\omega) \approx \tilde{\chi}^0_{\mathbf{GG'}}(\mathbf{q},\omega)$, dielectric function $\epsilon^{-1}_{\mathbf{GG'}}(\mathbf{q},\omega)$ and therefore $\tilde{\chi}^0_{\mathbf{GG'}}(\mathbf{q},\omega)$ will require a very dense set of ω values. In Eq. (2.111), in order to obtain reducible polarization $\chi_{\mathbf{GG'}}(\mathbf{q},\omega)$, one has to find an inverse matrix of $[\delta_{\mathbf{GG''}} + v(\mathbf{q}+\mathbf{G''})\tilde{\chi}_{\mathbf{GG''}}(\mathbf{q},\omega)]$, which is a $N_{\mathbf{G}}\times N_{\mathbf{G}}$ sized matrix, where $N_{\mathbf{G}}$ is the number of $\mathbf{G}$ vectors.

The number $N_{\mathbf{G}}$ is often huge, and finding an inverse to such large matrices is, by itself a significant computational burden making the calculation of $\tilde{\chi}^0_{\mathbf{GG'}}(\mathbf{q},\omega)$ a bottleneck of the whole computational procedure. Things become more cumbersome if this has to repeated for every ω and $\mathbf{q}$, which means that $N_\omega \times N_{\mathbf{q}}$ such matrices have to be inverted, where N_ω and $N_{\mathbf{q}}$ are the number of ω and $\mathbf{q}$ points, respectively. Such approach requires many computationally demanding (time consuming and often memory intensive) calculations that one wishes to avoid.

In order to avoid the inversion of $N_\omega \times N_{\mathbf{q}}$ matrices of size $N_{\mathbf{G}}\times N_{\mathbf{G}}$, one can use the plasmon-pole approximation (PPA) and determine $\epsilon^{-1}_{\mathbf{GG'}}(\mathbf{q},\omega)$ directly as:

$$\begin{aligned}\epsilon^{-1}_{\mathbf{GG'}}(\mathbf{q},\omega) &\approx \epsilon^{-1}_{\mathbf{GG'}}(\mathbf{q},\omega)_{\mathrm{PPA}} \\ &= \delta_{\mathbf{GG'}} \\ &+ R_{\mathbf{GG'}}(\mathbf{q})\left[(\omega - \Omega_{\mathbf{GG'}}(\mathbf{q}) + i\eta)^{-1} - (\omega - \Omega_{\mathbf{GG'}}(\mathbf{q}) - i\eta)^{-1}\right],\end{aligned} \tag{2.114}$$

where $R_{\mathbf{GG'}}(\mathbf{q})$ and $\Omega_{\mathbf{GG'}}(\mathbf{q})$ are parameters which are determined by fitting each component. Fitting is performed using the PPA condition which states that non-PPA $\epsilon^{-1}_{\mathbf{GG'}}(\mathbf{q},\omega)$ from Eq. (2.109) and from PPA Eq. (2.114) must give the same result for frequencies $\omega = 0$ and $\omega = iE_{\mathrm{PPA}}$, where E_{PPA} is an input parameter. This way, for non-PPA $\epsilon^{-1}_{\mathbf{GG'}}(\mathbf{q},\omega)$ from Eq. (2.109), the polarization $\tilde{\chi}^0_{\mathbf{GG'}}(\mathbf{q},\omega)$ is calculated only twice, namely for $\omega = 0$ and $\omega = iE_{\mathrm{PPA}}$, instead for a dense grid of ω. Although the inversion of $N_{\mathbf{G}}\times N_{\mathbf{G}}$ matrices is avoided, there are still $N_\omega \times N_{\mathbf{q}}$ matrices, which is often a very large number.

The number of calculations for different $\mathbf{q}$ points can also be reduced by deducing which points are equivalent due to symmetry rules to avoid repeated calculations.

Secant method and quasi-particle approximation (QPA) can reduce the number of ω points for which $\Sigma^{\mathrm{c}}_{\mathbf{k}n}(\omega)$ has to be calculated.

Avoiding calculation for a dense ω set: Secant method

To avoid N_ω calculations over dense set of ω, one can look for a solution for Eq. (2.113) by some method of optimization like the Secant method. In Secant method, $\Sigma^{\mathrm{xc}}_{\mathbf{k}n}(\omega)$ is calculated for initial guess of ω (for e.g. $\omega = \varepsilon_{\mathbf{k}n}$) and then in subsequent steps in search of the solution of Eq. (2.113) for ω.

Further reducing calculations over ω: QPA

Besides the Secant method, another useful approximation is the linear or quasi-particle approximation (QPA), which assumes that $\Sigma^{\mathrm{xc}}_{\mathbf{k}n}$ can be approximated by a smooth linear function i.e. a linear Taylor series around $\varepsilon_{\mathbf{k}n}$. In QPA, the energies are:

$$E^{\mathrm{QPA}}_{\mathbf{k}n} = \varepsilon_{\mathbf{k}n} + Z_{\mathbf{k}n}\left[\Sigma^{\mathrm{xc}}_{\mathbf{k}n}(\varepsilon_{\mathbf{k}n}) - V^{\mathrm{xc}}_{\mathbf{k}n}\right], \tag{2.115}$$

where

$$Z_{\mathbf{k}n} = \left[1 - \left.\frac{\partial \Sigma^{\mathrm{xc}}(\omega)}{\partial \omega}\right|_{\omega=\varepsilon_{\mathbf{k}n}}\right]^{-1} \tag{2.116}$$

is sometimes also called the quasi-particle strength or renormalization factor, it is usually $0.6 \leq Z \leq 1$. The dressed Green function $G_{\mathbf{k}n}(\omega)$ from Eq. (2.105) in QPA becomes:

$$G_{\mathbf{k}n}(\omega) \approx G^{\mathrm{QPA}}_{\mathbf{k}n}(\omega) = Z_{\mathbf{k}n}\left[\frac{f_{\mathbf{k}n}}{\omega - E^{\mathrm{QPA}}_{\mathbf{k}n} - i\eta} - \frac{1 - f_{\mathbf{k}n}}{\omega - E^{\mathrm{QPA}}_{\mathbf{k}n} + i\eta}\right]. \tag{2.117}$$

One-shot method: $\mathrm{G_0W_0}$

Performing the GW loop only once using the RPA approximation $\tilde{\chi} \approx \tilde{\chi}^0 = -iG^0G^0$ produces $W \approx W^0 = v_{\mathrm{c}} + v_{\mathrm{c}}\tilde{\chi}^0 W^0$ is often called the *one-shot* or $\mathrm{G_0W_0}$ approximation. To go further, one would calculate the polarization $\tilde{\chi}$ again with dressed G or G^{QPA} and continue the loop until self-consistency is achieved. Even though calculations that go beyond $\mathrm{G_0W_0}$ are possible, they are much more computationally demanding. All mention of GW results in this work will refer to the $\mathrm{G_0W_0}$ calculations.

Band gaps obtained within $\mathrm{G_0W_0}$ correspond to energies of adding or removing an electron like the ones measured using inverse and direct photoemission spectroscopy. Optical gaps, where electron is excited to an empty state by a photon, which is measured by absorption spectroscopy methods, cannot be obtained by any GW approximation. The reason for this is that absorbed photon creates an electron and hole pair, which in turn interact with the system, and such pair cannot be described when 3 and 4 point vertices are neglected ($\tilde{\Gamma}(1,2;3) = \delta(1,2)\delta(1,3)$ and $\delta\Sigma^{\mathrm{xc}}(1,2)/\delta G(\overline{4},\overline{5}) = 0$ in Eq. (2.91), respectively) like in the case of GW approximation. One has to return to Hedin's equations and include them to form a

Bethe-Salpeter equation [83] which solves the problem for electron-hole pair and produces absorption spectra. Such calculations are only mentioned here in passing, since they are not related to any results obtained in this thesis.

2.8 Phononic structure

In Sec. 2.3, the problem of total Hamiltonian $\mathcal{H}^{\mathrm{TOT}}$ was separated on electronic $\mathcal{H}_{\mathrm{el.}}$ and ionic parts $\mathcal{H}_{\mathrm{ion.}}$ using the Born-Oppenheimer approximation. Section 2.7 contained theoretical discussion and described computational methods for obtaining the electronic structure in crystals by solving for the electronic part $\mathcal{H}_{\mathrm{el.}}$ of $\mathcal{H}^{\mathrm{TOT}}$.

This section is dedicated to the ionic part $\mathcal{H}_{\mathrm{ion.}}$ of the total Hamiltonian $\mathcal{H}^{\mathrm{TOT}}$. In solids, ions move around their equilibrium positions producing quanta of vibration called *phonons*. Ionic movement directly depends on the ground state electronic structure, which is the reason why computation of the electronic structure was explained first, in the previous chapter, and is essential for following the computational techniques explained in the present chapter.

The section starts with a general theoretical discussion about ionic vibration assuming the harmonic approximation. Even though BO approximation separated the electronic and ionic problem, in practice the ionic problem is closely related to the atomic configuration and the ground state energy of the electronic system, so these two problems become again, in a way, non separable. Atomic configuration affects the electronic ground state and electronic ground state in turn affects the vibration of ions.

Similar to electronic structure, one is interested in the dispersion relation of phononic energies in the 1BZ, called the *phononic structure*. Periodic ionic movement can be described using phononic frequencies $\omega_{\mathbf{q}\nu}$ (energies $\hbar\omega_{\mathbf{q}\nu}$) which are distinguished by phonon bands ν ($N_\nu = 3 \times N_{\mathrm{at.}}$), and their reciprocal vector $\mathbf{q}$ (crystal momentum $\hbar\mathbf{q}$) in the 1BZ[14]. Naturally, all symmetry operations that were valid in the electronic case, hold here as well and can be used to reduce the number of calculations in same aspects.

When ionic vibrations are small and harmonic, they can be computed by distorting one-by-one atom from its equilibrium position, to obtain forces on the atoms and then interatomic force constants which lead to phonon frequencies. Interatomic force constants can then be Fourier transformed to reciprocal space and sorted to their respectable $\mathbf{q}$ vectors. This method is called the *frozen phonon* method. The phonon related to reciprocal vector $\mathbf{q}$ is calculated by moving atoms from separate unit cells that are connected by a lattice vector $\mathbf{T}$ from Sec. 2.4, which requires the usage of large supercells. Calculations can become untractable as $\mathbf{T}$ becomes larger in order for $\mathbf{q}$ to become smaller, i.e. in the case of $\mathbf{q} \to 0$. Another downside of this method is the fact that a chosen supercell defines the $\mathbf{q}$-grid: if one wishes use a new, denser $\mathbf{q}'$-grid, the whole procedure must be repeated, even for points that

[14]To distinguish electron- and phonon- related indices, the vectors for the crystal momentum for phonons (electrons) will be labeled $\mathbf{q}$ ($\mathbf{k}$) and phonon (electron) bands will be labeled with Greek letters ν, ν' (Latin letters n, n', m, etc.)

$\mathbf{q}'$- and $\mathbf{q}$-grid share. General theoretic discussion and basis of the frozen phonon method is presented in Sec. 2.8.1

To overcome this problem, a perturbation theory can be implemented directly into DFT, called the density functional perturbation theory (DFPT) which reduces all calculations to one unit cell and the 1BZ. Within DFPT, linear responses to electronic density, Kohn-Sham states, and self-consistent potential are obtained which are then used to generate interatomic force constants and phonon frequencies. DFPT method is explained in greater detail in Sec. 2.8.3

Finally, in the case when ionic movement is not harmonic, the self-consistent phonon (SCPH) method can be used to obtain phononic frequencies for anharmonic vibrations using many body Green's function theory. SCPH method is expanded in Sec. 2.8.4.

2.8.1 Ionic vibrations

When possible lattice structures were discussed in Sec. 2.2 and for the purpose of translational invariance within the lattice in Sec. 2.4, atoms were considered to have a fixed position in space. Even though atoms in the sense of a crystal structure are considered to be static, they are actually periodically moving around their equilibrium positions, and their crystal structure is then considered to be a time average of their individual positions. This movement however, is rather slow compared to the frequency of electrons since the mass of a proton is about 1.8×10^3 greater than the mass of an electron which means that for typical semiconductors with a band gap around 1 eV the frequency of the electrons will be around 10^3 times greater than the frequency of the ions. In other words, ions seem stationary from the electron's point of view and from ionic point of view, the movement of electrons is instantaneous i.e. ions can't excite electrons enough and they stay in their ground state while ions are moving. This is the basis of the adiabatic Born-Oppenheimer (BO) approximation first mentioned in Sec. 2.3.

In such adiabatic approximation, the total Hamiltonian $\mathcal{H}^{\mathrm{TOT}}$ can be decoupled into kinetic part of the ions T_{ion} and the total BO Hamiltonian that contains kinetic energy of all electrons T_{el} and Coulomb interaction between electrons and ions $V_{\mathrm{el-ion}}$, electrons and electrons $V_{\mathrm{el-el}}$ and between ions $V_{\mathrm{ion-ion}}$:

$$\begin{aligned} H_{\mathrm{el.+ions}} \equiv \mathcal{H}^{\mathrm{TOT}} &= T_{\mathrm{ion}} + H^{\mathrm{BO}}, \\ H^{\mathrm{BO}} &= T_{\mathrm{el}} + V_{\mathrm{ion-ion}} + V_{\mathrm{el-ion}} + V_{\mathrm{el-el}}. \end{aligned} \tag{2.118}$$

Suppose that it is possible to obtain a wavefunction $\Psi(\{\mathbf{R}\},\{\mathbf{r}\})$ which solves for H^{BO} where $\{\mathbf{R}\}$ and $\{\mathbf{r}\}$ are the collective coordinates af all ions and electrons, respectively. This solution results in the BO energy surface $E^{\mathrm{BO}}(\{\mathbf{R}\})$ which is defined on a manyfold of all possible positions of ions in the crystal $\{\mathbf{R}\}$. The configuration of ionic positions which produces the minimal value for E^{BO} on the manyfold of possible ion configuration $\{R\}$ is called the equilibrium configuration $\{\mathbf{R}^{\mathrm{eq}}\}$:

$$E^{\mathrm{BO}}(\{\mathbf{R}^{\mathrm{eq}}\}) = \min_{\{\mathbf{R}\}} \frac{\langle\Psi(\{\mathbf{R}\})|\, H_{\mathrm{BO}}(\{\mathbf{R}\})\,|\Psi(\{\mathbf{R}\})\rangle}{\langle\Psi(\{\mathbf{R}\})|\Psi(\{\mathbf{R}\})\rangle}. \tag{2.119}$$

In BO approximation, where E^{BO} is solved separately, the Schrödinger equation for ionic vibrational energy E^{vib} is:

$$\left(\sum_{\kappa,p}\frac{P_{\kappa,p}^2}{2M_\kappa}+E^{\mathrm{BO}}(\{\mathbf{R}\})\right)\Phi(\mathbf{R})=E^{\mathrm{vib}}\Phi(\mathbf{R}), \tag{2.120}$$

where $\kappa = 1,\ldots,N_{\mathrm{at.}}$ is used to distinguish individual atoms, out of N_{at} atoms contained in one unit cell, and p is used to distinguish individual unit cells in the crystal.

In order to make sum over p finite, a set of connected but not overlaping primitive unit cells is constructed in order to form a supercell. This supercell conmensurates with the underlying Bravais lattice [49].

The position of one unit cell from the origin is determined by a lattice vector $\mathbf{T}_p$, where p marks the index or a particular unit cell.

The position of individual ions can be determined relative to their unit cell $\mathbf{R}_{\kappa,p}=\mathbf{T}_p+\mathbf{R}_\kappa$, where κ is the index of an atom found in the unit cell p[15].

Since the movement of the atoms is much smaller than the distance between them, one can assume that the ionic configuration will change only in a small area around the minima of the BO energy surface E^{BO}, thus allowing one to expand it using Taylor series:

$$\begin{aligned}E^{\mathrm{BO}}(\{\mathbf{R}\}) =& E^{\mathrm{BO}}(\{\mathbf{R}^{\mathrm{eq}}\})+\sum_{\kappa,p}\left.\frac{\partial E^{\mathrm{BO}}(\{\mathbf{R}\})}{\partial\mathbf{R}_{\kappa,p}}\right|_{\mathbf{R}=\mathbf{R}^{\mathrm{eq}}}\Delta\mathbf{R}_{\kappa,p}\\ &+\frac{1}{2}\sum_{\substack{\kappa\ ,p\\ \kappa',p'}}\left.\frac{\partial^2 E^{\mathrm{BO}}(\{\mathbf{R}\})}{\partial\mathbf{R}_{\kappa,p}\partial\mathbf{R}_{\kappa',p'}}\right|_{\mathbf{R}=\mathbf{R}^{\mathrm{eq}}}\Delta\mathbf{R}_{\kappa,p}\Delta\mathbf{R}_{\kappa',p'}+\ldots\end{aligned} \tag{2.121}$$

where $\Delta\mathbf{R}_{\kappa,p}=\mathbf{R}^{\mathrm{eq}}_{\kappa,p}-\mathbf{R}_{\kappa,p}$. The zero-th term $E^{\mathrm{BO}}(\{\mathbf{R}^{\mathrm{eq}}\})$ can be normalized to zero. The first term, linear in $\Delta\mathbf{R}$, represents a force acting on ion κ in cell p:

$$\mathbf{F}_{\kappa,p}=-\frac{\partial E^{\mathrm{BO}}(\{\mathbf{R}\})}{\partial\mathbf{R}_{\kappa,p}}, \tag{2.122}$$

where all forces on ions is zero for $\mathbf{R}=\mathbf{R}^{\mathrm{eq}}$ since it is a derivative at the minima of the energy surface. The second term, quadratic in $\Delta\mathbf{R}$, describes harmonic oscillations around $\{\mathbf{R}^{\mathrm{eq}}\}$. These harmonic terms are also called *interatomic force constants* $C^{\kappa\alpha,p}_{\kappa'\alpha'p'}$:

$$C^{\kappa\alpha,p}_{\kappa'\alpha'p'}=\frac{\partial E^{BO}}{\partial R_{\kappa'\alpha',p'}\partial R_{\kappa\alpha,p}}, \tag{2.123}$$

and they provide information on how the force on ion κ,p along the direction α is affected by the movement of ion κ',p' along the direction α' and vice versa since derivatives in this case are symmetric w.r.t. exchange of indices $(\kappa\alpha,p)\leftrightarrow(\kappa'\alpha',p')$. In the

[15]The terms 'atom' and 'ion' are used interchangeably in most of this chapter. When atomic cores (with or without their core electrons) are approximated as point charges, with net positive charge, as in this case, the term ion is more accurate. It should be emphasized that these ions originate from atoms. However, there are cases where these ions originate from molecules, but that is out of the scope of this work.

harmonic approximation all terms of $\Delta\mathbf{R}$ that are beyond quadratic in Eq. (2.121) are neglected.

In the harmonic and adiabatic BO approximation, the equation for ionic vibrations is:

$$\left(\sum_{\kappa,p}\frac{P_{\kappa,p}^2}{2M_\kappa}+\frac{1}{2}\sum_{\substack{\kappa\ ,p\\ \kappa',p'}}C^{\kappa\alpha,p}_{\kappa'\alpha',p'}\Delta R_{\kappa\alpha,p}\Delta R_{\kappa'\alpha',p'}\right)\Phi(\mathbf{R})=E^{\text{vib}}\Phi(\mathbf{R}). \tag{2.124}$$

One can use Fourier transform on the interatomic force constants $C^{\kappa\alpha,p}_{\kappa'\alpha',p'}$ to obtain the *dynamical matrix* $D^{\kappa\alpha}_{\kappa'\alpha'}(\mathbf{q})$:

$$\begin{aligned}D^{\kappa\alpha}_{\kappa'\alpha'}(\mathbf{q})&=\frac{1}{N_{\text{uc}}}\sum_{p,p'}\frac{e^{-i\mathbf{q}\cdot\mathbf{T}_p}}{M_\kappa^{1/2}}C^{\kappa\alpha,p}_{\kappa'\alpha'p'}\frac{e^{i\mathbf{q}\cdot\mathbf{T}_{p'}}}{M_{\kappa'}^{1/2}}\\&=\sum_{p'}(M_\kappa M_{\kappa'})^{-1/2}C^{\kappa\alpha,0}_{\kappa'\alpha',p'}e^{i\mathbf{q}\cdot\mathbf{T}_{p'}}.\end{aligned} \tag{2.125}$$

The dynamical matrix can be made to depend only on the distance between unit cells $(\mathbf{T}_p-\mathbf{T}_{p'})$, and since the interatomic constants are symmetric when exchanging indices $p\leftrightarrow p'$ (as well as $\kappa\leftrightarrow\kappa'$ and $\alpha\leftrightarrow\alpha'$), one unit cell can be chosen as the origin to reduce the summation over p since $\sum_p e^{i\mathbf{q}\cdot\mathbf{0}}=N_{\text{uc}}$ in Eq. (2.125).

Conmensurable and inconmensurable perturbations

One can take a brief moment, to analyze the meaning of Eq. (2.125) for different values of $\mathbf{q}$. For phonons, same as for electrons, all reciprocal vectors $\mathbf{q}$ can be reduced to one unit cell in the reciprocal space, i.e. to the 1BZ.

If one were to imagine a 1 dimensional chain of unit cells with primitive vectors of real and reciprocal lattice $\mathbf{a}$ and $\mathbf{b}$, respectively, then the lattice vectors can be expressed as $\mathbf{T}_p=\mathbf{a}\times p$, $p\in\mathbb{Z}$ and generators of translations $\mathbf{q}=(2\pi/a)\mathbf{b}\times s$, $s\in\mathbb{R}$, and $\mathbf{a}\cdot\mathbf{b}=1$.

For $s\in\mathbb{Z}$, the exponent in Eq. (2.125) is $e^{i\frac{2\pi}{a}s\times ap'}=e^{i2\pi s\times p'}=1$, and the dynamical matrix

$$D^{\kappa\alpha}_{\kappa'\alpha'}(\mathbf{q})=\sum_{p'}(M_\kappa M_{\kappa'})^{-1/2}C^{\kappa\alpha,0}_{\kappa'\alpha',p'}, \tag{2.126}$$

describes a phonon for which displacement is periodic over all unit cells p' and $D^{\kappa\alpha}_{\kappa'\alpha'}(\mathbf{q})$ are purely real. This case is equivalent to $\mathbf{q}=\vec{0}\equiv\Gamma$, also known as the long-wavelength limit[16].

In the case where $s=1/m$, $m\in\mathbb{Z}/\{0,\pm1\}$, the exponent in Eq. (2.125) is $e^{i\frac{2\pi}{a}s\times ap'}=e^{i2\pi s\times p'}=e^{i2\pi\times\frac{p'}{m}}$, the dynamical matrix

$$D^{\kappa\alpha}_{\kappa'\alpha'}(\mathbf{q})=\sum_{p'}(M_\kappa M_{\kappa'})^{-1/2}C^{\kappa\alpha,0}_{\kappa'\alpha',p'}e^{i2\pi\times\frac{p'}{m}}, \tag{2.127}$$

[16]In the case of molecules, where there is no translational invariance, calculation for Γ point only is sufficient.

describes a phonon for which displacement is periodic at every m-th cell and $D^{\kappa\alpha}_{\kappa'\alpha'}(\mathbf{q})$ are complex numbers. This case is equivalent to $\mathbf{q} \neq \vec{0}$. For solids where translational invariance holds, calculation on $\mathbf{q}$-grid is required. Denser $\mathbf{q}$-grids require larger supercells as small $\mathbf{q}$ corresponds to an interatomic constant for large a distance between unit cells $\mathbf{T}_{p'}$ in the BvK cell.

When $s \in \mathbb{Z}/\{0\}$ and $s = 1/m$, $m \in \mathcal{Z}/\{0, \pm 1\}$ it is said that these perturbations are *conmensurable* with the BvK cell, since a 1-to-1 correspondence between lattice vectors $\mathbf{T}_{p'}$ and $\mathbf{q}$ grid can be established.

However, when $s = 1/m$, but $m \in \mathbb{R}/\mathbb{Q}$ (e.g. $s = 1/\sqrt{2}, 1/\sqrt{7}$), a 1-to-1 correspondence between $\mathbf{q}$ and $\mathbf{T}_{p'}$ is impossible. In this case the perturbation described by $\mathbf{q}$ is *inconmensurable* with the BvK cell[17].

In practice, only conmensurable perturbations can be calculated using methods that obtain dynamical matrices directly from BvK supercells like for e.g. the frozen phonon method. Inconmensurable (as well ass conmensurable) perturbations in harmonic approximation can be directly computed using DFPT (Sec. 2.8.3).

Properties of dynamical matrices

Even though interatomic force constants are real, the dynamical matrix will be purely real only when $\mathbf{q} = \vec{0} \equiv \Gamma$. Exchanging $p \leftrightarrow p'$ in Eq. (2.125) in interatomic force constant is equivalent to exchanging $\mathbf{q} \leftrightarrow -\mathbf{q}$, and which is equivalent to complex conjugation of dynamical matrices $D^{\kappa\alpha}_{\kappa'\alpha'}(-\mathbf{q}) = (D^{\kappa\alpha}_{\kappa'\alpha'})^*(\mathbf{q})$, which leads to relations:

$$\omega^2_{\mathbf{q}\nu} = \omega^2_{-\mathbf{q}\nu} \ , \qquad \xi_{\kappa\alpha,\nu}(-\mathbf{q}) = \xi^*_{\kappa\alpha,\nu}(\mathbf{q}), \tag{2.128}$$

where $\xi_{\kappa\alpha,\nu}(-\mathbf{q})$ are eigenvectors that diagonalize dynamical matrices and $\omega_{\mathbf{q}\nu}$ are their eigenvalues:

$$\sum_{\kappa'\alpha'} \mathcal{D}^{\kappa'\alpha'}_{\kappa\ \alpha}(\mathbf{q})\ \xi_{\kappa'\alpha',\nu}(\mathbf{q}) = \omega^2_{\mathbf{q}\nu}\ \xi_{\kappa\alpha,\nu}(\mathbf{q}). \tag{2.129}$$

The size of the dynamical matrix is $3\times N_{at}$, where N_{at} is the number of atoms in one unit cell. The number of possible solutions ν for each $\mathbf{q}$ will be $3\times N_{at}$.

Eigenvectors $\xi_{\kappa\alpha,\nu}(\mathbf{q})$ are orthogonal and normalized to unity:

$$\begin{aligned} \sum_{\nu} \xi^*_{\kappa'\alpha',\nu}(\mathbf{q})\xi_{\kappa\alpha,\nu}(\mathbf{q}) &= \delta_{\kappa\kappa'}\delta_{\alpha\alpha'}, \\ \sum_{\kappa\alpha} \xi^*_{\kappa\alpha,\nu'}(\mathbf{q})\xi_{\kappa\alpha,\nu}(\mathbf{q}) &= \delta_{\nu\nu'}, \end{aligned} \tag{2.130}$$

[17] As a remainder: $\mathbb{Z}$ and $\mathbb{Q}$ represent a set of integers and rational numbers, both of which are subsets or the set of real numbers $\mathbb{R}$.

Phonons in the classical treatment

The solutions for ionic displacements can also be obtained by following the classical route. The ionic Hamiltonian $H_{\text{ion.}}$ in the BO approximation from Eq. (2.124) is

$$H_{\text{ion.}} = \sum_{\kappa,p} \frac{P_{\kappa,p}^2}{2M_\kappa} + \frac{1}{2} \sum_{\substack{\kappa \ ,p \\ \kappa',p'}} C_{\kappa'\alpha',p'}^{\kappa\alpha,p} \Delta R_{\kappa\alpha,p} \Delta R_{\kappa'\alpha',p'}. \tag{2.131}$$

One can write down the equations of motion using the Hamiltonian equations:

$$\begin{aligned}
\dot{P}_{\rho\gamma,s} &= -\frac{\partial H_{\text{ion.}}}{\partial \Delta R_{\rho\gamma,s}} = -\frac{1}{2} \sum_{\substack{\kappa \ ,p \\ \kappa',p'}} C_{\kappa'\alpha'p'}^{\kappa\alpha,p} \left(\Delta R_{\kappa\alpha,p} \delta_{\rho\kappa'} \delta_{\gamma\alpha'} \delta_{sp'} + \Delta R_{\kappa'\alpha',p'} \delta_{\rho\kappa} \delta_{\gamma\alpha} \delta_{sp} \right) \\
\dot{R}_{\rho\gamma,s} &= \frac{\partial H_{\text{ion.}}}{\partial P_{\rho\gamma,s}} = \sum_{\kappa,p} \frac{P_{\kappa\alpha,p}}{M_\kappa} \delta_{\rho\kappa} \delta_{\gamma\alpha} \delta_{sp} \\
M_\rho \Delta \ddot{R}_{\rho\gamma,s} &= -\sum_{\kappa\alpha,p} C_{\rho\gamma,s}^{\kappa\alpha,p} \Delta R_{\kappa\alpha,p}
\end{aligned} \tag{2.132}$$

The solution in the harmonic approximation can be represented using plane waves that travel parallel to vector $\mathbf{q}$:

$$\Delta R_{\kappa\alpha,p} = M_\kappa^{-1/2} \sum_{\mathbf{q}} Q_{\kappa\alpha}(\mathbf{q}) e^{-i(\omega_{\mathbf{q}} t - \mathbf{q}\cdot\mathbf{T}_p)}, \tag{2.133}$$

where $Q_{\kappa\alpha}(\mathbf{q})$ contains the polarization and the amplitude of the wave. Inserting Eq. (2.133) into equation of motion Eq. (2.132):

$$\sum_{\mathbf{q}} \omega_{\mathbf{q}}^2 Q_{\rho\gamma}(\mathbf{q}) e^{i\mathbf{q}\cdot\mathbf{T}_s} = \sum_{\mathbf{q}} \sum_{\kappa\alpha,p} \frac{1}{M_\rho^{1/2}} C_{\rho\gamma,s}^{\kappa\alpha,p} \frac{1}{M_\kappa^{1/2}} Q_{\kappa\alpha}(\mathbf{q}) e^{i\mathbf{q}\cdot\mathbf{T}_p}, \tag{2.134}$$

and multiplying both sides by $N_{\text{uc}}^{-1} \sum_s e^{-i\mathbf{q}\cdot\mathbf{T}_s}$, where N_{uc} is the number of unit cells in BvK cell:

$$\begin{aligned}
\sum_{\mathbf{q}} \omega_{\mathbf{q}}^2 Q_{\rho\gamma}(\mathbf{q}) &= \sum_{\mathbf{q}} \sum_{\kappa\alpha} \frac{1}{N_{\text{uc}}} \sum_{p,s} \frac{e^{-i\mathbf{q}\cdot\mathbf{T}_s}}{M_\kappa^{1/2}} C_{\rho\gamma,s}^{\kappa\alpha,p} \frac{e^{i\mathbf{q}\cdot\mathbf{T}_p}}{M_\kappa^{1/2}} Q_{\kappa\alpha}(\mathbf{q}) \\
&= \sum_{\mathbf{q}} \sum_{\kappa\alpha} D_{\rho\gamma}^{\kappa\alpha}(\mathbf{q}) Q_{\kappa\alpha}(\mathbf{q}),
\end{aligned} \tag{2.135}$$

leads to:

$$\sum_{\mathbf{q}} \left[\sum_{\kappa\alpha} D_{\rho\gamma}^{\kappa\alpha}(\mathbf{q}) Q_{\kappa\alpha}(\mathbf{q}) - \omega_{\mathbf{q}}^2 Q_{\rho\gamma,\nu}(\mathbf{q}) \right] = 0. \tag{2.136}$$

Since all $\mathbf{q}$ terms are independent to each other, the last equation will be zero when all terms in the sum over $\mathbf{q}$ are zero, which essentially leads to Eq. (2.129):

$$D_{\rho\gamma}^{\kappa\alpha}(\mathbf{q}\nu) Q_{\kappa\alpha,\nu}(\mathbf{q}) - \omega_{\mathbf{q}\nu}^2 Q_{\rho\gamma,\nu}(\mathbf{q}) = 0. \tag{2.137}$$

The polarization $Q_{\kappa\alpha,\nu}(\mathbf{q})$ is equivalent to eigenvectors of $\xi_{\kappa\alpha,\nu}(\mathbf{q})$, and they obey the same relations. Because of this, vectors $\mathbf{e}_{\kappa,\nu}(\mathbf{q}) = \sum_\alpha \xi_{\kappa\alpha,\nu} \mathbf{e}_\alpha$ are also called polarization vectors of phonon mode $\mathbf{q}, \nu$ or just phonon polarization vectors.

Acoustic and optical phonon modes

If the unit cell would contain only one atom, all three frequencies should linearly approach zero in the long wavelength limit, i.e. when $|\mathbf{q}| \to 0$. Classically speaking, this case corresponds to whole unit cells with their center of mass moving together, the group velocity of this wave is non-zero, like a runaway wave. Since it resembles the acoustic sound waves, these 3 modes are called the *acoustic* modes. When $\mathbf{q} = 0$ the relative distance between unit cells (atoms) doesn't change, so the whole lattice is moving in phase (unison) so the restitution force acting on the atoms is zero, and the frequency is also zero: $\omega^2_{\mathbf{q}\nu} = 0$.

The *translational invariance* in the crystal, ensures that when all atoms are displaced by some constant vector $\vec{\delta}$, all physical observables and their derivatives stay the same:

$$E^{\mathrm{BO}}(\{\mathbf{R}\} + \vec{\delta}) = E^{\mathrm{BO}}(\{\mathbf{R}\}), \qquad \frac{\partial E^{\mathrm{BO}}(\{\mathbf{R}\} + \vec{\delta})}{\partial R_{\kappa\alpha,p}} = \frac{\partial E^{\mathrm{BO}}(\{\mathbf{R}\})}{\partial R_{\kappa\alpha,p}}. \tag{2.138}$$

This displacement can also be expanded using Taylor series:

$$\frac{\partial E^{\mathrm{BO}}(\{\mathbf{R}\} + \vec{\delta})}{\partial R_{\kappa\alpha,p}} = \frac{\partial E^{\mathrm{BO}}(\{\mathbf{R}\})}{\partial R_{\kappa\alpha,p}} + \sum_{\kappa'\alpha',p} \delta_{\alpha'} \frac{\partial^2 E^{\mathrm{BO}}(\{\mathbf{R}\})}{\partial R_{\kappa'\alpha',p'} \partial R_{\kappa\alpha,p}} + \mathcal{O}(\delta^2), \tag{2.139}$$

with the second term on the right-hand side vanishing:

$$\begin{aligned} &\sum_{\alpha'} \delta_{\alpha'} \sum_{\kappa',p'} \frac{\partial^2 E^{\mathrm{BO}}(\{\mathbf{R}\})}{\partial R_{\kappa'\alpha',p'} \partial R_{\kappa\alpha,p}} = 0, \quad \forall \delta_{\alpha'} \in \mathbb{R}, \\ &\Rightarrow \sum_{\kappa',p'} \frac{\partial^2 E^{\mathrm{BO}}(\{\mathbf{R}\})}{\partial R_{\kappa'\alpha',p'} \partial R_{\kappa\alpha,p}} = \sum_{\kappa',p'} C^{\kappa\alpha,p}_{\kappa'\alpha',p'} = 0. \end{aligned} \tag{2.140}$$

This is called the *acoustic sum rule*. Since all interatomic force constants are evaluated for the equilibrium configuration $\mathbf{R} = \mathbf{R}^{\mathrm{eq}}$, this means that the force acting in the direction α on the ion κ, p is unaffected by the sum of movement of all other atoms κ', p' in all directions α'. Since collective displacements of atoms correspond to $\mathbf{q} = \Gamma = \vec{0}$, the same will be true for the dynamical matrix:

$$\sum_{\kappa',p'} \frac{e^{i\Gamma\cdot\vec{0}}}{M_\kappa} C^{\kappa\alpha,0}_{\kappa'\alpha',p'} \frac{e^{i\Gamma\cdot\mathbf{T}'_p}}{M_{\kappa'}} = \sum_{\kappa'} D^{\kappa\alpha}_{\kappa'\alpha'}(\Gamma) = 0 \tag{2.141}$$

If the unit cell contains two or more atoms of the same type, the rest of the modes $(N_{\mathrm{n.at.}} - 1) \times 3$ should approach non-zero values as $|\mathbf{q}| \to 0$. In classical terms, there is movement of atoms within the unit cell and the center of mass within that unit cell is also moving. At $|\mathbf{q}| = 0$ the unit cells are not moving in unison but rather like a standing wave with zero group velocity. However since there is a restitution force acting on the atoms in the unit cell they are vibrating with a non-zero frequency. This behavior is similar to optical waves, therefore these modes are called the *optical* modes.

When $|\mathbf{q}| = 0$ it is impossible to distinguish transversal and longitudinal directions of motion for optical modes. However, when $\mathbf{q}$ is still small but non-zero, there will be two transversal components in the plane perpendicular to $\mathbf{q}$ and one longitudinal parallel to $\mathbf{q}$. If there are at least two atoms with a different charge (and mass), an electric field between them is also generated. This macroscopic electric field $V_{\mathbf{E}} = e\mathbf{E} \cdot \mathbf{r}$ is not invariant after translation and therefore incompatible with Born von-Karman periodic conditions. The range of dipole-dipole Coulomb interaction between the moving ions is much greater than the boundaries of the unit cell.

Such electric field will result in lifting the degeneracy around $|\mathbf{q}| = 0$ but not exactly at $|\mathbf{q}| = 0$. For any direction of $\mathbf{q}$ there will always be one longitudinal component (that lies along the direction of $\mathbf{q}$) and two transversal components (that lie in the plane perpendicular to $\mathbf{q}$). The frequency of the non-degenerate longitudinal optical component $\omega_{\mathbf{q}}^{\mathrm{LO}}$ will be slightly higher than the 2-fold degenerate transversal optical components $\omega_{\mathbf{q}}^{\mathrm{TO}}$. This phenomena is often referred to as LO-TO splitting. When observing plots that show a phonon dispersion in 1BZ, this splitting is often 'present' at Γ point as well, due to the scale of the plot and being 'zoomed out', but it should be noted that they are degenerate only at exactly Γ and nowhere else. The magnitude of the splitting greatly depends on the direction when moving away from Γ.

Imaginary phonon frequencies: saddle points and anharmonic behavior

In the harmonic approximation, the interatomic force constants $C_{\kappa'\alpha'p'}^{\kappa\alpha,p}$ can be written as a Hessian matrix that consists of second derivatives of E^{BO}. Since they are evaluated at equilibrium position of atoms, where the energy surface E^{BO} exhibits a minimum, this matrix is positive definite, meaning that all its eigenvalues $\omega_{\mathbf{q}\nu}^2$ are positive. Since those eigenvalues physically represent the harmonic frequencies of ionic movement, only the positive values of $\sqrt{\omega_{\mathbf{q}\nu}^2}$ should be taken.

If however, all values of $\omega_{\mathbf{q}\nu}^2$ are negative, this means that the atomic configuration in E^{BO} is extremal, but it is the maximal value instead of minimal. This would be a case of unstable equilibrium configuration. In the third case, where some $\omega_{\mathbf{q}\nu}^2$ are positive and some are negative means that the chosen ionic configuration for E^{BO} is a *saddle* point. The frequencies for which $\omega_{\mathbf{q}\nu}^2$ is negative are called silent or *imaginary* frequencies.

The discussion in this section assumed that there are no temperature effects i.e. that the crystal is at $T = 0$ K. In practice, temperature effects can vary depending on the material. In some materials it has minimal effects on the configuration of ions at equilibrium and the only difference between $T = 0$ K and the room temperature is a small effect of thermal expansion. In other materials, temperature effects can lead to phase transitions where the configuration of ions is changed beyond simple temperature expansion. In the later case, the harmonic approximation usually fails when considering their configurations at temperatures other than $T = 0$ K.

Phonons in the second quantization

The Hamiltonian for ionic vibration can also be written in the second quantization using the well known ladder operators $\hat{a}_{\mathbf{q}\nu}$ and $\hat{a}^{\dagger}_{\mathbf{q}\nu}$, which destroy and create a $\mathbf{q}\nu$-phonon respectively. The ionic displacements $\Delta R_{\kappa\alpha,p}$ are then expressed as:

$$\Delta R_{\kappa\alpha,p} = N_{\mathrm{uc}}^{-1/2} \sum_{\mathbf{q}\nu} \frac{e^{i\mathbf{q}\cdot\mathbf{T}_p}\xi_{\kappa\alpha,\nu}(\mathbf{q})}{(2M_\kappa\omega_{\mathbf{q}\nu}/\hbar)^{1/2}} \left(\hat{a}_{\mathbf{q}\nu} + \hat{a}^{\dagger}_{-\mathbf{q}\nu}\right). \tag{2.142}$$

This transforms the phonon Hamiltonian H_{ph}:

$$H_{\mathrm{ph}} = \sum_{\kappa\alpha,p} \left(\frac{P^2_{\kappa\alpha,p}}{2M_\kappa} + \frac{1}{2} \sum_{\kappa'\alpha',p'} C^{\kappa\alpha,p}_{\kappa'\alpha',p'} \Delta R_{\kappa\alpha,p} \Delta R_{\kappa'\alpha',p'} \right), \tag{2.143}$$

to:

$$H_{\mathrm{ph}} = \sum_{\mathbf{q}\nu} \hbar\omega_{\mathbf{q}\nu} \left(\hat{a}^{\dagger}_{\mathbf{q}\nu}\hat{a}_{\mathbf{q}\nu} + \frac{1}{2} \right). \tag{2.144}$$

Since $\omega_{\mathbf{q}\nu}$ appears in the denominator for the expression of ionic displacements $\Delta R_{\kappa\alpha,p}$ in Eq. (2.142), the summation over acoustic modes at Γ point ($|\mathbf{q}| = 0$, $\omega_{\mathbf{q}\nu} = \omega_{\Gamma\mathrm{A}} = 0$) is skipped i.e. it is assumed that they contain zero amplitudes.

2.8.2 Frozen phonon method

In the harmonic approximation there are several ways to compute the dynamical matrix (interatomic force constants). The simplest and earliest one is the *frozen phonon* method which uses finite, periodic displacements of atoms from their equilibrium configuration and was performed as early as in the 1980s [89, 90, 91]. In the first step, the equilibrium configuration of ions is obtained, using either ab initio methods like DFT, or using empirical lattice parameters. In most DFT codes, forces are calculated on all atoms and all directions, so second derivatives are obtained directly from calculating forces on a system when one atom is displaced without the need to displace atoms in pairs.

Procedure for frozen phonon calculation using DFT is as follows. One should perform a calculation for displacing one atom κ, along one direction α in unit cell p for $\pm\Delta R$ amount. After DFT calculation is complete, forces on all the rest κ', p' atoms along α' directions are stored as $F_{\kappa'\alpha',p}(\Delta \mathrm{R}_{\kappa\alpha,\mathrm{p}})$ and process is repeated for all displacements $\pm\Delta R_{\kappa\alpha,p}$ until all $F_{\kappa'\alpha',p}(\Delta \mathrm{R}_{\kappa\alpha,\mathrm{p}})$ are obtained[18]. Interatomic force constants $C^{\kappa\alpha,p}_{\kappa'\alpha',p'}$ are then calculated using these displacements with the central finite difference formula :

$$C^{\kappa\alpha,p}_{\kappa'\alpha',p'} = -\frac{\partial^2 E^{\mathrm{BO}}(\{\mathbf{R}\})}{\partial R_{\kappa'\alpha',p'}\partial R_{\kappa\alpha,p}} = -\frac{F_{\kappa'\alpha',p'}(+\Delta R_{\kappa\alpha,p}) - F_{\kappa'\alpha',p'}(-\Delta R_{\kappa\alpha,p})}{2\Delta R}. \tag{2.145}$$

Since DFT can only produce the ground state, the displaced atoms are said to be static and in their ground state or 'frozen in time', therefore the name - frozen

[18]This process can be significantly reduced by skipping calculations for elements that are equivalent due to symmetry rules.

phonons. One can reduce the number of these calculations by using symmetry properties of the crystal and determine how many interatomic force constants will be unique and obtain the rest using the group theory. The simplicity of this method is in its implementation, since it doesn't require anything more than a standard DFT. However, for a chosen grid of $\mathbf{q}$ vectors the Born von-Karman cell has to contain at least the same number of unit cells. Moreover, the calculations for one $\mathbf{q}$ grid are all coupled in a sense that if one desires to perform calculations on a denser grid, the whole procedure has to be repeated on a supercell that corresponds to that grid. The scaling of computational workload is very unfavorable when linear dimensions of the supercell are increased as they scale as $3\times N_{\mathrm{at}}^{\mathrm{UC}}\times\mathcal{R}_{\mathrm{IFC}}^{9}$ where $\mathcal{R}_{\mathrm{IFC}}$ is the range of the interatomic force constants and scales as $\mathcal{R}_{\mathrm{IFC}}^{3}\propto N_{\mathrm{at}}^{\mathrm{SC}}$ where $N_{\mathrm{at}}^{\mathrm{SC}}$ is the number of atoms in the supercell [92].This poor scaling of computational resources becomes a problem especially when matrices in the long wavelength limit ($|\mathbf{q}|\to 0$) are required.

2.8.3 Density functional perturbation theory - DFPT

The density functional perturbation theory (DFPT) avoids the computational burden of supercells, and is able to perform all the calculation using only the atoms in the unit cell. This method can be formulated either using the linear response theory formulated by Baroni et at. [93, 94, 95, 92] as implemented in Quantum Espresso code by Giannozzi et al [96, 97] or the variational method formulated by Gonze et al. [98, 99, 100, 101, 102] as implemented in Abinit code [103, 104]. Both methods give the same result within the error of numerical accuracy. Since it doesn't require supercells, besides the reduced computational load, the DFPT computation can be performed for arbitrary $\mathbf{q}$, since calculations for each $\mathbf{q}$ are now decoupled from any kind of predetermined grid. This means that unlike the frozen-phonon, which computes interatomic forces in real space, and then obtains dynamical matrices by Fourier transform to reciprocal space, the DFPT obtains dynamical matrices directly. Because phonon dispersion is usually a rather smooth function of $\mathbf{q}$, dynamical matrices can be easily interpolated for a denser $\mathbf{q}$ grid. The interpolation is done by Fourier transform of dynamical matrices from reciprocal to real space which will return the interatomic constants for a supercell. These interatomic constants can be used to determine the dynamical matrices (and then the phonon frequencies) for any $\mathbf{q}$ point that was not on the original grid. In the long wavelength limit, the dynamical matrices are separated into analytic and non analytic part. The analytic part for which the macroscopic electric field is zero is easily obtained. To obtain the non analytic part, which contains the effects of macroscopic electric field, the required macroscopic dielectric constant ε_{∞} and Born effective charges Z^{*} can be easily obtained with DFPT [93, 94, 95, 98, 99, 100, 101, 102, 92]. The non-analytic part is essential to properly produce the LO-TO splitting in the phonon structure.

Hellman-Feynman theorem

One can begin with the BO Hamiltonian H^{BO}, which is

$$\begin{aligned} H^{\mathrm{BO}}(\{\mathbf{R}\}) &= T_{\mathrm{el}}(\{\mathbf{r}\}) + V_{\mathrm{el-ion}}(\{\mathbf{R}\},\mathbf{r}) + V_{\mathrm{el-el}}(\mathbf{r},\mathbf{r}') \\ &\quad + V_{\mathrm{ion-ion}}(\{\mathbf{R}\}), \\ T_{\mathrm{el}}(\{\mathbf{r}\}) &= \sum_{i,p} \frac{-\hbar^2\nabla_{i,p}^2}{2m_e}, \\ V_{\mathrm{el-ion}}(\{\mathbf{R}\},\{\mathbf{r}\}) &= -\sum_{\kappa,i,p\geq p'} Z_\kappa e^2 v_{\mathrm{c}}(\mathbf{r}_{i,p'} - \mathbf{R}_{\kappa,p}), \\ V_{\mathrm{el-el}}(\{\mathbf{r}\},\{\mathbf{r}'\}) &= \sum_{i>j,p\geq p'} e^2 v_{\mathrm{c}}(\mathbf{r}_{i,p} - \mathbf{r}_{j,p'}), \\ V_{\mathrm{ion-ion}}(\{\mathbf{R}\}) &= \sum_{\kappa>\kappa',p\geq p'} Z_{\kappa,p} Z_{\kappa',p'} e^2 v_{\mathrm{c}}(\mathbf{R}_{\kappa,p} - \mathbf{R}_{\kappa',p'}), \end{aligned} \tag{2.146}$$

where indices i,j and κ,κ' take into account all electrons and ions, in one unit cell, p,p' go over all unit cells, v_{c} is the Coulomb potential $v_{\mathrm{c}} = (4\pi\epsilon_0)^{-1}|\mathbf{r}|^{-1}$, and $\{\mathbf{r}\}$ and $\{\mathbf{R}\}$ are collective coordinates of all electrons and ions, respectively.

In the ground state, the BO energy can be expressed as a functional of electron density:

$$E^{\mathrm{BO}} = T_{\mathrm{el}}[n] + \int \mathrm{d}\mathbf{r}\, n_{\mathbf{R}}(\mathbf{r}) V_{\mathrm{el-ion}} + \int \mathrm{d}\mathbf{r}\, n_{\mathbf{R}}(\mathbf{r}) V_{\mathrm{el-el}} + V_{\mathrm{ion-ion}}, \tag{2.147}$$

where $n_{\mathbf{R}}(\mathbf{r}) = \Psi^*(\{\mathbf{R}\},\mathbf{r})\Psi(\{\mathbf{R}\},\mathbf{r})$ is the electron charge density in the ground state for ionic configuration $\{\mathbf{R}\}$ and $V_{\mathrm{ion-ion}}$ depends only on ionic coordinates and not on the electron density.

Hellman-Feynman theorem [105] states that the first derivative of the eigenvalues of the Hamiltonian H_λ, which depends on a parameter λ is given by the expectation value of the derivative of the Hamiltonian:

$$\frac{\partial E_\lambda}{\partial \lambda} = \langle \Psi_\lambda | \frac{H_\lambda}{\partial \lambda} | \Psi_\lambda \rangle \tag{2.148}$$

when $H_\lambda \Psi_\lambda = E_\lambda \Psi_\lambda$. In the BO approximation, and in the case for ionic vibrations, this parameter λ can be replaced with the ionic positions $\{\mathbf{R}\}$. This means that the force acting on one ion from Eq. (2.122) can also be obtained as:

$$\mathbf{F}_{\kappa,p} = -\frac{\partial E^{\mathrm{BO}}(\{\mathbf{R}\})}{\partial \mathbf{R}_{\kappa,p}} = \langle \Psi(\{\mathbf{R}\}) | \frac{\partial H^{\mathrm{BO}}}{\partial \mathbf{R}_{\kappa,p}} | \Psi(\{\mathbf{R}\}) \rangle \tag{2.149}$$

Inserting Eq. (2.147) into Eq. (2.149), the force on one ion in BO approximation is obtained:

$$\mathbf{F}_{\kappa,p} = -\int \mathrm{d}\mathbf{r}\, n_{\mathbf{R}} \frac{\partial V_{\mathrm{el-ion}}}{\partial \mathbf{R}_{\kappa,p}} - \frac{\partial V_{\mathrm{ion-ion}}}{\partial \mathbf{R}_{\kappa,p}} \tag{2.150}$$

Interatomic force constants are then obtained by differentiating forces in Eq. (2.150):

$$\begin{aligned} C^{\kappa\alpha,p}_{\kappa'\alpha',p'} &= \frac{\partial^2 E^{\mathrm{BO}}}{\partial R_{\kappa'\alpha',p'}\partial R_{\kappa\alpha,p}} = -\frac{\partial F_{\kappa\alpha,p}}{\partial R_{\kappa'\alpha',p'}} = \\ &= \int \mathrm{d}\mathbf{r}\,\frac{\partial n_{\mathbf{R}}}{\partial R_{\kappa'\alpha',p'}}\frac{\partial V_{\mathrm{el-ion}}}{\partial \mathbf{R}_{\kappa\alpha,p}} + \int \mathrm{d}\mathbf{r}\, n_{\mathbf{R}}\frac{\partial^2 V_{\mathrm{el-ion}}}{\partial \mathbf{R}_{\kappa'\alpha',p'}\partial \mathbf{R}_{\kappa\alpha,p}} \\ &+ \frac{\partial^2 V_{\mathrm{ion-ion}}}{\partial \mathbf{R}_{\kappa'\alpha',p'}\partial \mathbf{R}_{\kappa\alpha,p}}. \end{aligned} \tag{2.151}$$

This result was first given by De Cicco and Johnson (1969) [106] and by Pick, Cohen, and Martin (1970) [107] and it shows that in the BO approximation, the interatomic force constants depend not only on electron charge density in the ground state but also on its linear response to ionic movement $\partial n_{\mathbf{R}}/\partial R_{\kappa\alpha,p}$.

The electron-ion potential $V^{\mathrm{ion-ion}}$ is just a sum over individual Coulomb potentials of ions so its second derivatives are disconnected from the electron density. The potential $V^{\mathrm{el-ion}}$, is local in $\mathbf{r}$ when $\mathbf{R}_\kappa$ are fixed parameters, so the computation of its first and second derivatives over $R_{\kappa\alpha,p}$ is straightforward.

The most involved part of the procedure is obtaining the derivative of electronic density $\frac{\partial n_{\mathbf{R}}}{\partial R_{\kappa'\alpha',p'}}$. The Kohn-Sham scheme in DFT claims that the ground state density of an interacting system is the same as the ground state density of a corresponding non-interacting auxiliary system. Using the Kohn-Sham scheme one can obtain $\frac{\partial n_{\mathbf{R}}}{\partial R_{\kappa'\alpha',p'}}$ by perturbing the Kohn-Sham Hamiltonian which describes this auxiliary non-interacting system.

Perturbations of Kohn-Sham Hamiltonian: The Sternheimer equation

Within density functional theory, the electronic density of the system is obtained from the Kohn-Sham Hamiltonian H^{KS}:

$$H^{\mathrm{KS}}\Psi_{\mathbf{k}m} = \left[\frac{p^2}{2m_e} + V^{\mathrm{KS}}(\mathbf{r},\{\mathbf{R}\})\right]\Psi_{\mathbf{k}m} = \varepsilon_{\mathbf{k}m}\Psi_{\mathbf{k}m}, \tag{2.152}$$

where V_{KS} is the effective Kohn-Sham potential from Eq. (2.60) in Sec. 2.7.2 that describes local potential acting on the auxiliary system of non-interacting electrons. Contributions to V_{KS} include: the external potential V_{ext}, Hartree electronic screening V_{H} and the exchange-correlation potential V_{xc}:

$$\begin{aligned} V^{\mathrm{KS}} &= V_{\mathrm{ext}} + V_{\mathrm{H}} + V_{\mathrm{xc}}, \\ V_{\mathrm{ext}} &= -\sum_{\kappa,p} Z_\kappa e^2 v_{\mathrm{c}}(\mathbf{r} - \mathbf{R}_\kappa - \mathbf{T}_p), \\ V_{\mathrm{H}} &= \frac{e^2}{4\pi\epsilon_0}\sum_p \int_{\mathrm{sc}} \mathrm{d}\mathbf{r}'\,\frac{n(\mathbf{r}',\{\mathbf{R}\})}{|\mathbf{r} - \mathbf{r}' - \mathbf{T}_p|}, \\ V_{\mathrm{xc}} &= \left.\frac{\delta E^{\mathrm{xc}}[n]}{\delta n}\right|_{n(\mathbf{r},\{\mathbf{R}\})} \end{aligned} \tag{2.153}$$

The electron density $n(\mathbf{r})$ in this case is expressed using a sum of Kohn-Sham states, where index $\mathbf{R}$ compared to one found in Eq. (2.147), Eq. (2.149), Eq. (2.150) and Eq. (2.151) is dropped since the equilibrium configuration $\{\mathbf{R}_{\text{eq}}\}$ is assumed:

$$n(\mathbf{r}) = \sum_{\mathbf{k}m}^{\text{occ.}} \Psi^*_{\mathbf{k}m}\Psi_{\mathbf{k}m} = \sum_{\mathbf{k}m}^{\text{occ.}} u^*_{\mathbf{k}m}u_{\mathbf{k}m}, \tag{2.154}$$

where m goes over occupied states only. One can define a differential operator Δ^λ that acts on function F_λ that depends on some set of parameters $\lambda = \{\lambda_1, \lambda_2, \dots\}$ as:

$$\Delta^\lambda F_\lambda = \sum_i \partial_{\lambda_i} F_\lambda \delta\lambda_i \tag{2.155}$$

and replace λ_i with ionic positions $R_{\kappa\alpha,p}$ to expand the Kohn-Sham Hamilotnian, wave-function, energy and electronic density to linear order around the equilibrium configuration $\{\mathbf{R}_{\text{eq}}\}$:

$$\begin{aligned} H^{\text{KS}} &= H_0^{\text{KS}} + \Delta^{\mathbf{R}} V^{\text{KS}}, \\ \Psi_{\mathbf{k}m} &= \Psi^0_{\mathbf{k}m} + \Delta^{\mathbf{R}}\Psi_{\mathbf{k}m}, \\ \varepsilon_{\mathbf{k}m} &= \varepsilon^0_{\mathbf{k}m} + \Delta^{\mathbf{R}}\varepsilon_{\mathbf{k}m}, \\ n(\mathbf{r}) &= n^0(\mathbf{r}) + \Delta^{\mathbf{R}} n(\mathbf{r}), \end{aligned} \tag{2.156}$$

which transforms the Kohn-Sham equation Eq. (2.152) to:

$$\left(H_0^{\text{KS}} - \varepsilon^0_{\mathbf{k}m}\right)\left|\Delta^{\mathbf{R}}\Psi_{\mathbf{k}m}\right\rangle = -\left(\Delta^{\mathbf{R}}V^{\text{KS}} - \Delta^{\mathbf{R}}\varepsilon_{\mathbf{k}m}\right)\left|\Psi^0_{\mathbf{k}m}\right\rangle. \tag{2.157}$$

The Eq. (2.157) is also known in atomic physics as the *Sternheimer equation*, named after Sternheimer who used it in 1954 to calculate atomic polarizabilities [108]. Self-consistent version of this equation was introduced by Mahan in 1980 [109] to calculate atomic polarizabilities within DFT using linear density approximation.

Using first-order perturbation theory, the linear response to $\Delta^{\mathbf{R}}$ for $\varepsilon_{\mathbf{k}m}$, V^{KS}, $n(\mathbf{r})$, and $\Psi_{\mathbf{k}m}$ can be obtained as:

$$\begin{aligned} \Delta^{\mathbf{R}}\varepsilon_{\mathbf{k}m} &= \left\langle\Psi^0_{\mathbf{k}m}\right| \Delta^{\mathbf{R}}V^{\text{KS}} \left|\Psi^0_{\mathbf{k}m}\right\rangle, \\ \Delta^{\mathbf{R}}V^{\text{KS}} &= \Delta^{\mathbf{R}}V_{\text{ext}} + \int_{\text{sc}} \mathrm{d}\mathbf{r}' \, \frac{e^2\Delta^{\mathbf{R}}n(\mathbf{r}')}{4\pi\epsilon_0|\mathbf{r}-\mathbf{r}'|} + \left.\frac{\mathrm{d}V_{\text{xc}}[n]}{\mathrm{d}n}\right|_{n=n(\mathbf{r})} \Delta^{\mathbf{R}}n(\mathbf{r}), \\ \Delta^{\mathbf{R}}n(\mathbf{r}) &= \sum_{\mathbf{k}m}^{\text{occ.}} \left[(\Delta^{\mathbf{R}}\Psi^{0*}_{\mathbf{k}m})\Psi^0_{\mathbf{k}m} + \Psi^{0*}_{\mathbf{k}m}(\Delta^{\mathbf{R}}\Psi^0_{\mathbf{k}m})\right] \\ &= 2\,\text{Re}\sum_{\mathbf{k}m}^{\text{occ.}} \Psi^{0*}_{\mathbf{k}m}\Delta^{\mathbf{R}}\Psi^0_{\mathbf{k}m} \\ \Delta^{\mathbf{R}}\Psi_{\mathbf{k}m} &= \sum_{\mathbf{k}'m'\neq\mathbf{k}m} \Psi^0_{\mathbf{k}'m'} \frac{\left\langle\Psi^0_{\mathbf{k}'m'}\right| \Delta^{\mathbf{R}}V^{\text{KS}} \left|\Psi^0_{\mathbf{k}m}\right\rangle}{\varepsilon^0_{\mathbf{k}m} - \varepsilon^0_{\mathbf{k}'m'}}. \end{aligned} \tag{2.158}$$

Projection on unoccupied states only

The linear response to ionic movement of electron density $\Delta^{\mathbf{R}} n(\mathbf{r})$ in Eq. (2.158) has one sum over occupied states and another over both occupied and unoccupied:

$$\Delta^{\mathbf{R}} n(\mathbf{r}) = 2\,\mathrm{Re} \sum_{\mathbf{k}m}^{\text{occ.}} \sum_{\mathbf{k}'m' \neq \mathbf{k}m} \Psi^{0*}_{\mathbf{k}m} \Psi^{0}_{\mathbf{k}'m'} \frac{\langle \Psi^0_{\mathbf{k}'m'} | \, \Delta^{\mathbf{R}} V^{\mathrm{KS}} \, | \Psi^0_{\mathbf{k}m} \rangle}{\varepsilon^0_{\mathbf{k}m} - \varepsilon^0_{\mathbf{k}'m'}}. \tag{2.159}$$

If one separates the sum over all states for $\Delta^{\mathbf{R}} n(\mathbf{r})$ as a sum of occupied and unoccupied states: $\sum_{\mathbf{k}'m' \neq \mathbf{k}m} = \sum^{\text{occ.}}_{\mathbf{k}'m' \neq \mathbf{k}m} + \sum^{\text{unocc.}}_{\mathbf{k}'m' \neq \mathbf{k}m}$ the terms which contain $\sum^{\text{occ.}}_{\mathbf{k}m} \sum^{\text{occ.}}_{\mathbf{k}'m' \neq \mathbf{k}m}$ would cancel each other since the expectation values in their numerators are the same:

$$\langle \Psi_{\mathbf{k}'m'} | \, \Delta^{\mathbf{R}} V^{\mathrm{KS}} \, | \Psi_{\mathbf{k}m} \rangle = \langle \Psi_{\mathbf{k}m} | \, \Delta^{\mathbf{R}} V^{\mathrm{KS}} \, | \Psi_{\mathbf{k}'m'} \rangle \tag{2.160}$$

and their denominators have the opposite signs: $\varepsilon^0_{\mathbf{k}m} - \varepsilon^0_{\mathbf{k}'m'}$ and $\varepsilon^0_{\mathbf{k}'m'} - \varepsilon^0_{\mathbf{k}m}$, respectively.

The linear response to electron density $\Delta^{\mathbf{R}} n(\mathbf{r})$ has only contributions from matrix elements that connect occupied to unoccupied states:

$$\Delta^{\mathbf{R}} n(\mathbf{r}) = 2\,\mathrm{Re} \sum_{\mathbf{k}m}^{\text{occ.}} \Psi^{*}_{\mathbf{k}m} \sum_{\mathbf{k}'m'}^{\text{unocc.}} \Psi_{\mathbf{k}'m'} \frac{\langle \Psi^0_{\mathbf{k}'m'} | \, \Delta^{\mathbf{R}} V^{\mathrm{KS}} \, | \Psi^0_{\mathbf{k}m} \rangle}{\varepsilon^0_{\mathbf{k}m} - \varepsilon^0_{\mathbf{k}'m'}}. \tag{2.161}$$

In other words, the electron-density linear response $\Delta^{\mathbf{R}} n(\mathbf{r})$, does not respond to any perturbations that connect occupied states only. One can define an operators P_v and P_c that project to occupied and unoccupied states:

$$\begin{aligned} P_v &= \sum_{v'}^{\text{occ.}} \left| \Psi^{(0)}_{\mathbf{k}v'} \right\rangle \left\langle \Psi^{(0)}_{\mathbf{k}v'} \right| \\ P_c &= \sum_{c'}^{\text{unocc.}} \left| \Psi^{(0)}_{\mathbf{k}c'} \right\rangle \left\langle \Psi^{(0)}_{\mathbf{k}c'} \right|, \\ P_v P_c &= P_c P_v = 0 \\ P_v &+ P_c = 1, \end{aligned} \tag{2.162}$$

and express $\Delta^{\mathbf{R}} n(\mathbf{r})$ as:

$$\Delta^{\mathbf{R}} n(\mathbf{r}) = 2\,\mathrm{Re} \sum_{\mathbf{k}v}^{\text{occ.}} \Psi^{*}_{\mathbf{k}v} \left(P_c \Delta^{\mathbf{R}} \Psi_{\mathbf{k}v} \right). \tag{2.163}$$

Since it has been shown that only $P_c \Delta^{\mathbf{R}} \Psi_{\mathbf{k}v}$ is required for $\Delta^{\mathbf{R}} n(\mathbf{r})$, one can apply projection P_c from the left on the Sternheimer equation (2.157):

$$\left(H^{\mathrm{KS}}_0 - \varepsilon^0_{\mathbf{k}v} \right) P_c \left| \Delta^{\mathbf{R}} \Psi^0_{\mathbf{k}v} \right\rangle = -P_c \Delta^{\mathbf{R}} V^{\mathrm{KS}} \left| \Psi^0_{\mathbf{k}v} \right\rangle, \tag{2.164}$$

where $[H^{\mathrm{KS}}_0, P_c] = [\Delta^{\mathbf{R}} \varepsilon_{\mathbf{k}v}, P_c] = 0$ and $P_c \left| \Psi^{(0)}_{\mathbf{k}v} \right\rangle = 0$. Even though Eq. (2.164) doesn't connect occupied states, one can ensure to avoid singularities by adding

αP_v in parenthesis on the left-hand-side, since $P_c P_v = 0$, where α is a small but non-zero parameter. This transforms Eq. (2.164) to:

$$\begin{aligned} P_c \left|\Delta^{\mathbf{R}}\Psi^0_{\mathbf{k}v}\right\rangle &= G_{\mathbf{k}v}(\varepsilon^{(0)}_{\mathbf{k}v}) P_c \Delta^{\mathbf{R}} V^{\mathrm{KS}} \left|\Psi^0_{\mathbf{k}v}\right\rangle, \\ G_{\mathbf{k}v}(\omega) &= \left[H^{\mathrm{KS}}_0 + \alpha P_v - \varepsilon^0_{\mathbf{k}v}\right]^{-1} \end{aligned} \tag{2.165}$$

In semiconductors and insulators, where the electronic ground state has a well defined number of occupied states and a reasonably wide band gap, one can make a clear separation in sums in Eq. (2.161) and Eq. (2.163). In metals however, even infinitesimal perturbations such as ionic movement can change the orbital occupation number of electrons which can influence the Fermi level which separates occupied and occupied states. This case has been discussed by de Gironcoli in 1995 [110] in detail. Popular approach is to apply broadening the Kohn-Sham energy levels using some smearing function: Gaussian, Lorentzian, Fermi-Dirac distribution, which has a direct influence on electronic density and any derivative of it. The rest of this chapter is limited only to the case of insulators and semiconductors when there is a well defined gap in the electronic structure.

Projection on one unit cell: decoupling of individual q-points

One of the main advantages of DFPT over the frozen phonon method is the ability to decouple perturbations of different $\mathbf{q}$, making calculation for any $\mathbf{q}$ independent of all other $\mathbf{q}'$ and avoid the use of large super cells. One can introduce projectors $P^{\mathbf{k}+\mathbf{q}}$ which project onto $\mathbf{k}+\mathbf{q}$ manyfold of states, and by translational invariance commute with H^{KS}. Projectors $P^{\mathbf{k}+\mathbf{q}}$ also commute with projectors $P_{v/c}$ and their product is $P^{\mathbf{k}+\mathbf{q}} P_{v/c} = P^{\mathbf{k}+\mathbf{q}}_{v/c}$. Projecting Eq. (2.164) over $\mathbf{k}+\mathbf{q}$ manifold results in:

$$P^{\mathbf{k}+\mathbf{q}}_c \left(H^{\mathrm{KS}} + \alpha P^{\mathbf{k}+\mathbf{q}}_v - \varepsilon^0_{\mathbf{k}v}\right) \left|\Delta^{\mathbf{R}}\Psi^0_{\mathbf{k}v}\right\rangle = -P^{\mathbf{k}+\mathbf{q}}_c \Delta^{\mathbf{R}} V^{\mathrm{KS}} \left|\Psi^0_{\mathbf{k}v}\right\rangle. \tag{2.166}$$

where $\left|\Delta^{\mathbf{R}}\Psi_{\mathbf{k}+\mathbf{q}v}\right\rangle = P^{\mathbf{k}+\mathbf{q}}_v \left|\Delta^{\mathbf{R}}\Psi_{\mathbf{k}v}\right\rangle$, and v signifies an occupied state. If one were to take the Fourier transform of $\Delta^{\mathbf{R}} V^{\mathrm{KS}}$ as:

$$\Delta^{\mathbf{R}} V^{\mathrm{KS}} = \sum_{\mathbf{q}} e^{i\mathbf{q}\cdot\mathbf{r}} \Delta^{\mathbf{q}} v^{\mathrm{KS}}_{\mathbf{q}} \tag{2.167}$$

where $v^{\mathrm{KS}}_{\mathbf{q}}$ is a lattice-periodic function, the Eq. (2.166) transforms into:

$$\begin{aligned} \left(H^{\mathrm{KS}}_{\mathbf{k}+\mathbf{q}} + \alpha \sum_{v'}^{\text{occ.}} \left|u_{\mathbf{k}+\mathbf{q}v'}\right\rangle \left\langle u_{\mathbf{k}+\mathbf{q}v'}\right| - \varepsilon^0_{\mathbf{k}v}\right) P^{\mathbf{k}+\mathbf{q}}_c \left|\Delta^{\mathbf{q}} u_{\mathbf{k}v}\right\rangle \\ = -P^{\mathbf{k}+\mathbf{q}}_c \Delta^{\mathbf{q}} v^{\mathrm{KS}}_{\mathbf{q}} \left|u_{\mathbf{k}v}\right\rangle, \end{aligned} \tag{2.168}$$

where $u_{\mathbf{k}v}$ are lattice-periodic functions, $H^{\mathrm{KS}}_{\mathbf{k}+\mathbf{q}} = e^{-i(\mathbf{k}+\mathbf{q})\cdot\mathbf{r}} H^{\mathrm{KS}} e^{+i(\mathbf{k}+\mathbf{q})\cdot\mathbf{r}}$ and projection operator $P^{\mathbf{k}+\mathbf{q}}_c$ can also be written as:

$$P^{\mathbf{k}+\mathbf{q}}_c = 1 - P^{\mathbf{k}+\mathbf{q}}_v = 1 - \sum_{v'}^{\text{occ.}} \left|u_{\mathbf{k}+\mathbf{q}v'}\right\rangle \left\langle u_{\mathbf{k}+\mathbf{q}v'}\right|. \tag{2.169}$$

Fourier $\mathbf{q}$-components for electron-density $\Delta^{\mathbf{q}} n_{\mathbf{q}}(\mathbf{r})$ response and unit-cell potential response $\Delta^{\mathbf{q}} v_{\mathbf{q}}^{\mathrm{KS}}(\mathbf{r})$ are:

$$\begin{aligned}\Delta^{\mathbf{q}} n_{\mathbf{q}}(\mathbf{r}) &= 2\,\mathrm{Re}\sum_{\mathbf{k}v} u^*_{\mathbf{k}v}(\mathbf{r})\Delta^{\mathbf{q}} u_{\mathbf{k}+\mathbf{q}v}(\mathbf{r}) \\ \Delta^{\mathbf{q}} v_{\mathbf{q}}^{\mathrm{KS}}(\mathbf{r}) &= \Delta^{\mathbf{q}} v_{\mathbf{q}}^{\mathrm{ext}} + \int \mathrm{d}\mathbf{r}'\,\frac{e^2 \Delta^{\mathbf{q}} n_{\mathbf{q}}(\mathbf{r}')}{|\mathbf{r}-\mathbf{r}'|} e^{-i\mathbf{q}(\mathbf{r}-\mathbf{r}')} \\ &\quad + \left.\frac{\mathrm{d}v^{\mathrm{xc}}[n]}{\mathrm{d}n}\right|_{n=n(\mathbf{r})} \Delta^{\mathbf{q}} n_{\mathbf{q}}(\mathbf{r})\end{aligned} \tag{2.170}$$

Eq. (2.168) and Eq. (2.170) form a set of self-consistent equations which are used to obtain linear responses for:

- electron density $\Delta^{\mathbf{q}} n_{\mathbf{q}}(\mathbf{r})$,
- wave functions $\Delta^{\mathbf{q}} u_{\mathbf{k}+\mathbf{q}v}(\mathbf{r})$,
- and Kohn-Sham effective potential $\Delta^{\mathbf{R}} v_{\mathbf{q}}^{\mathrm{KS}}(\mathbf{r})$,

to a perturbation of ionic displacement connected to vector $\mathbf{q}$.

Since these equations are solved in terms of lattice periodic functions only, there is no need to use supercells. Equivalently, this means that all $\mathbf{q}$ perturbations are decoupled from each other. This is convenient, since calculations for any $\mathbf{q}$ (or a grid of $\mathbf{q}$-s) can be done independently from any other $\mathbf{q}'$ (or a grid of different $\mathbf{q}$-s). This makes DFPT much more flexible than the frozen phonon method, where calculations on one $\mathbf{q}$-grid are predetermined by the size of the supercell, and if a different $\mathbf{q}'$-grid is chosen (with a different supercell) calculations must be repeated even for the points that appear on both grids.

Interpolation of Dynamic matrices: Fourier transform of Interatomic force constants

The Fourier transform of interatomic force constants $\tilde{C}^{\kappa\alpha}_{\kappa'\alpha'}(\mathbf{q})$ will be:

$$\begin{aligned}\tilde{C}^{\kappa\alpha}_{\kappa'\alpha'}(\mathbf{q}) &= (N_{\mathrm{uc}})^{-1} \sum_{pp'} e^{-i\mathbf{q}\cdot\mathbf{T}_p} C^{\kappa\alpha,p}_{\kappa'\alpha',p'} e^{+i\mathbf{q}\cdot\mathbf{T}_{p'}} \\ &= \frac{\partial^2 E^{\mathrm{BO}}}{\partial R_{\kappa'\alpha'}(-\mathbf{q}) \partial R_{\kappa\alpha}(\mathbf{q})}\end{aligned} \tag{2.171}$$

where $\partial/\partial R_{\kappa\alpha}(\mathbf{q}) = \sum_p e^{-i\mathbf{q}\cdot\mathbf{T}_p} \partial/\partial R_{\kappa\alpha,p}$. Using Eq. (2.151) one can separate the contributions to $\tilde{C}^{\kappa\alpha}_{\kappa'\alpha'}(\mathbf{q})$ from electron-ion potential $V^{\mathrm{el-ion}}$:

$$\begin{aligned}\tilde{C}^{\kappa\alpha}_{\kappa'\alpha'}(\mathbf{q})_{\mathrm{el-ion}} &= \int \mathrm{d}\mathbf{r}\,\frac{\partial n(\mathbf{r})}{\partial R_{\kappa'\alpha'}(-\mathbf{q})} \frac{\partial V_{\mathrm{el-ion}}}{\partial R_{\kappa\alpha}(\mathbf{q})} \\ &\quad + \int \mathrm{d}\mathbf{r}\, n(\mathbf{r}) \frac{\partial^2 V_{\mathrm{el-ion}}}{\partial R_{\kappa'\alpha'}(-\mathbf{q}) \partial R_{\kappa\alpha}(\mathbf{q})},\end{aligned} \tag{2.172}$$

and ion-ion potential $V^{\text{ion}-\text{ion}}$:

$$\tilde{C}^{\kappa\alpha}_{\kappa'\alpha'}(\mathbf{q})_{\text{ion}-\text{ion}} = \int \mathrm{d}\mathbf{r}\, \frac{\partial^2 V_{\text{ion}-\text{ion}}}{\partial R_{\kappa'\alpha'}(-\mathbf{q})\partial R_{\kappa\alpha}(\mathbf{q})}. \tag{2.173}$$

The derivative $\partial n(\mathbf{r})/\partial R_{\kappa'\alpha'}(-\mathbf{q})$ is obtained from the DFPT loop as individual components of $\Delta^{\mathbf{q}} n_{\mathbf{q}}(\mathbf{r})$. The derivatives $\partial V^{\text{el}-\text{ion}}/\partial R_{\kappa\alpha,\mathbf{q}}$ are already obtained as components of $\Delta_{\mathbf{q}} v^{\text{el}-\text{ion}}_{\mathbf{q}}$ in Eq. (2.170) and the second derivative is simply obtained as components of the double variation $\Delta^{-\mathbf{q}}\Delta^{\mathbf{q}} v^{\text{el}-\text{ion}}_{\mathbf{q}}$. The ion-ion potential $V^{\text{ion}-\text{ion}}$ does not depend on electronic structure so it does not appear in the DFPT self-consistent equations. This term, as well as its derivatives can be computed separately from the electronic terms. The procedure is straightforward and it includes obtaining the Ewald term E_{Ew} which already obtained in most codes during DFT procedure, and computing its second derivatives to obtain $\tilde{C}^{\kappa\alpha}_{\kappa'\alpha'}(\mathbf{q})_{\text{ion}-\text{ion}}$ is done once without the need for self-consistency.

The dynamic matrix is then obtained as:

$$D^{\kappa\alpha}_{\kappa'\alpha'}(\mathbf{q}) = (M_\kappa M_{\kappa'})^{-1/2} \left[\tilde{C}^{\kappa\alpha}_{\kappa'\alpha'}(\mathbf{q})_{\text{el}-\text{ion}} + \tilde{C}^{\kappa\alpha}_{\kappa'\alpha'}(\mathbf{q})_{\text{ion}-\text{ion}}\right]. \tag{2.174}$$

Finally, eigenvectors $\xi_{\kappa\alpha,\nu}(\mathbf{q})$ and eigenvalues $\omega_{\mathbf{q}\nu}$ of $D^{\kappa\alpha}_{\kappa'\alpha'}(\mathbf{q})$ give phonon polarization vectors and phonon frequencies for ionic perturbation corresponding to vector $\mathbf{q}$, respectively.

Interatomic force constants in real space can be obtained by inverse Fourier transform of dynamical matrices, considering that dynamical matrices were obtained for a dense grid of $\mathbf{q}$-vectors to ensure the convergence. Since the phonon dispersion is a rather smooth function for $\mathbf{q}$, interpolation to a denser $\mathbf{q}$-grid can be done by an inverse Fourier transform from real space interatomic force constants. Dense $\mathbf{q}$ grid of Dynamical matrices is then used to produce phonon density of states and dispersion relation.

The DFPT equations Eq. (2.168) and Eq. (2.170) are solved self-consistently, using ground state calculations for a grid of $\mathbf{k}$ and $\mathbf{k}+\mathbf{q}$ vectors, hence the computational load is the same as the one for a ground state calculation. One should always converge a DFT calculation first, before proceeding to DFPT procedure.

Convergence of DFPT calculations

One way to converge DFPT calculations, is to take a look at the acoustic sum rule, which stems from the translational invariance, and states that for zone center $\mathbf{q} = \Gamma$ perturbations, acoustic modes should have zero frequency or:

$$\sum_{\kappa'} D^{\kappa\alpha}_{\kappa'\alpha'}(\Gamma) = 0. \tag{2.175}$$

This was established in Eq. (2.140) and Eq. (2.141) when total energy in BO approximation E^{BO} was obtained by minimizing the BO energy surface using wave functions that describe all electrons $\Psi(\{\mathbf{r}\},\{\mathbf{R}\})$. Since DFPT relies on DFT, for all terms in the effective Kohn-Sham potential a collective translation of the ions

is possible except for the exchange-correlation potential, which uses a fixed grid in real space in the DFT implementation. Using a denser **k**-grid and/or larger kinetic energy cutoff (more plane waves in the wavefunction expansion for plane wave basis codes) will help acoustic modes approach zero but it will never land there exactly. One simple fix for this is to modify the dynamical matrices:

$$D^{\kappa\alpha}_{\kappa'\alpha'}(\Gamma)_{\text{new}} = D^{\kappa\alpha}_{\kappa'\alpha'}(\Gamma) - \delta_{\rho\kappa'} \sum_{\rho} D^{\kappa\alpha}_{\rho\alpha'}(\Gamma). \tag{2.176}$$

This will modify the phonon frequencies at Γ only. If one wishes to obtain them at $\mathbf{q} \to 0$, other dynamical matrices for $\mathbf{q} \neq 0$ should also be corrected. Since phonon frequencies only approach zero at Γ one should check the convergence for different **k** grids and kinetic energy cutoffs, and try to obtain a reasonably small values for acoustic modes at Γ. Once the correction in Eq. (2.176) is small enough, one should continue for rest **q** point using the same **k**-grid and kinetic energy cutoff.

The second sum rule that could be used for convergence is the charge neutrality for Born effective charges and it states that the sum of Born effective charges in the unit cell must be zero:

$$\sum_{\kappa} Z^{*}_{\kappa\alpha,\alpha'} = 0, \tag{2.177}$$

where Born effective charges tensor $Z^{*}_{\kappa\alpha,\alpha'}$ is defined as proportionality coefficient to the linear order that relates the polarization per unit cell created along direction α' and the displacement of ion κ. The charge neutrality sum rule in Eq. (2.177) will be violated because numerical calculations have finite basis for Kohn-Sham wave functions (they take finite number of plane waves in plane wave implementations), or because of the discretization of the real space integrals used for exchange-correlation potentials. This can be fixed by either redistributing excess charges evenly among atoms:

$$^{\text{new}}Z^{*}_{\kappa\alpha,\alpha'} = Z^{*}_{\kappa\alpha,\alpha'} - N_{\text{at}} \sum_{\kappa} Z^{*}_{\kappa\alpha,\alpha'}, \tag{2.178}$$

or developing a weighing strategy to redistribute the charges to each atom in proportion to their mean electronic charge. However, numerical results for sum of Born effective charges in Eq. (2.177), should converge to a reasonably small value when basis for Kohn-Sham functions and number of **k**-points in the electronic calculations is sufficiently large.

2.8.4 Self-constistent phonon method - SCPH

Since the standard approach based on the use of harmonic approximation and DFPT is not sufficient to describe phonons in some materials, a more sophisticated approach is needed. One can therefore use the self-consistent phonon method (SCPH) following the methodology and the implementation of Ref. [111]. This section, serves as a brief overview of the main ideas of SCPH and its implementation.

In the BO approximation, the dynamics of lattice ions is described by the Hamiltonian $H = T + U$, where T is their kinetic energy, while U is the potential energy

which is a function of the displacements from the equilibrium position. The potential energy can be expanded as $U = U_0 + U_2 + U_3 + U_4 + \ldots$, where the term U_n is of $n-$th order with respect to atomic displacements and the term U_1 is missing because it contains forces which are zero in equilibrium. Keeping the terms U_0 and U_2 only is the standard harmonic approximation. In this case, phonon frequencies are obtained from diagonalization of the corresponding dynamical matrix.

To obtain the phonon frequencies in general case when the terms beyond U_2 are included, one can make use of many body Green's function theory. The Hamiltonian is divided into $H = H_0 + H_1$ where $H_0 = T + U_0 + U_2$ is the harmonic part of the Hamiltonian whose solution is known, while the anharmonic terms $H_1 = U_3 + U_4 + \ldots$ constitute the interaction part. The phonon Green's function G_0 for the Hamiltonian H_0 is known, while the Dyson equation relates G_0, the phonon Green's function G of the Hamiltonian H and the self-energy Σ. The Dyson equation has to be complemented with the equation for self-energy. The self-energy is in principle given by a diagrammatic expansion involving an infinite number of Feynman diagrams. In practice one selects only the most relevant diagrams for the problem at hand. To obtain the renormalized phonon frequencies, it turns out that the most relevant diagram is the loop diagram originating from the quartic term U_4 (shown in Fig. 1(a) in Ref. [111]). The Green's function and the self-energy can then be found self-consistently and the renormalized phonon frequency is determined from the pole of the Green's function.

To perform the calculation within the SCPH method, one also has to obtain all relevant force constants that appear in the U_n terms in the expansion of U. The second-order force constants are obtained from a supercell density functional theory calculations and the finite displacement method. While the finite displacement method can in principle be used to obtain higher order force constants, a different strategy yields more stable results for the force constants. Namely, finite-temperature ab initio molecular dynamics calculation is performed to obtain various atomic configurations and the corresponding total energy and forces in these configurations. The force constants that appear in anharmonic terms in U are then fitted to the data obtained, where great care has to be taken to avoid overfitting the data.

Details of the full calculation protocol for $CsPbX_3$ (X=Cl, Br, I), are reported in Sec. 4.3.4.

2.9 Electron-phonon interaction

A detailed review on electron-phonon interactions from first principles was done recently by Giustino [44]. In that review, there are two approaches: one using an approximation that electronic system can be described by sharp quasiparticle excitations, and another, more involved using field-theoretic approach that doesn't rely on such approximation and was intensively covered by Marini in Ref. [112]. This section borrows some elements from that review in the sharp quasiparticle approximation in order to derive the practical approach for calculation of electron-phonon effects on electron energy levels first used used by Allen and Heine [113] and Alen and Cardona [114, 115] called Allen-Heine-Cardona theory.

The total Hamiltonian can be rewritten using the second quantization as:

$$H^{\mathrm{TOT}} = H_{\mathrm{el.}} + H_{\mathrm{ion.}} + H_{\mathrm{el-ion}}, \tag{2.179}$$

where $H_{\mathrm{el.}}$, $H_{\mathrm{ion.}}$ are Hamiltonians that describe the ionic and electronic systems, and $H_{\mathrm{el-ion}}$ is the Hamiltonian that describes the electron-ion interaction.

The ionic Hamiltonian $H_{\mathrm{ion.}}$ can be written in the second quantization as in Eq. (2.144):

$$H_{\mathrm{ph}} = \sum_{\mathbf{q}\nu} \hbar\omega_{\mathbf{q}\nu} \left(\hat{a}^{\dagger}_{\mathbf{q}\nu} \hat{a}_{\mathbf{q}\nu} + \frac{1}{2} \right), \tag{2.180}$$

where $\hat{a}^{\dagger}_{\mathbf{q}\nu}$ ($\hat{a}_{\mathbf{q}\nu}$) is the creation(annihilation) operator for a phonon in the state $\mathbf{q}\nu$, and $\hbar\omega_{\mathbf{q}\nu}$ is the energy of that photon in the BO and harmonic approximation, obtained by solving the Eq. (2.129), where dynamical matrices $D^{\kappa'\alpha'}_{\kappa\alpha}(\mathbf{q})$ have the form of a Hessian.

The electronic Hamiltonian in sharp quasiparticle approximation H_e can be approximated using the Kohn-Sham Hamiltonian H^{KS} in the first quantization:

$$H_{\mathrm{el.}} = H^{\mathrm{KS}} = -\frac{\hbar^2}{2m_e}\nabla^2 + V^{\mathrm{KS}}(\mathbf{r}, \{\mathbf{R}^{\mathrm{eq}}\}), \tag{2.181}$$

and in the second quantization, when diagonalized by Kohn-Sham one electron functions $|\Psi_{\mathbf{k}n}\rangle$:

$$H_{\mathrm{el.}} = \sum_{\mathbf{k}n,\mathbf{k}'n'} \langle \Psi_{\mathbf{k}n} | \, H^{\mathrm{KS}} \, | \Psi_{\mathbf{k}'n'} \rangle \, \hat{c}^{\dagger}_{\mathbf{k}n} \hat{c}_{\mathbf{k}'n'} = \sum_{\mathbf{k}n} \varepsilon^{\mathrm{KS}}_{\mathbf{k}n} \hat{c}^{\dagger}_{\mathbf{k}n} \hat{c}_{\mathbf{k}n}. \tag{2.182}$$

where $\hat{c}^{\dagger}_{\mathbf{k}n}$ ($\hat{c}_{\mathbf{k}n}$) is the creation(annihilation) operator for an electron in state $\mathbf{k}n$, and $\varepsilon^{\mathrm{KS}}_{\mathbf{k}n}$ is the Kohn-Sham energy of state $\mathbf{k}n$. The electronic wave functions $\Psi_{\mathbf{k}n}(\mathbf{r})$ are normalized to the volume of a supercell that contains N_{uc} unit cells of volume V_{uc}, and can be written using Bloch waves and Bloch factors:

$$\Psi_{\mathbf{k}n}(\mathbf{r}) = (N_{\mathrm{uc}} V_{\mathrm{uc}})^{-1/2} e^{i\mathbf{k}\cdot\mathbf{r}} u_{\mathbf{k}n}(\mathbf{r}), \tag{2.183}$$

where $u_{\mathbf{k}n}$ are unit cell periodic functions normalized to the volume of a unit cell:

$$\begin{aligned}
\langle \Psi_{\mathbf{k}n}(\mathbf{r}) | \Psi_{\mathbf{k}'n'}(\mathbf{r}) \rangle &= N_{\mathrm{uc}}^{-1} \int_{\mathrm{sc}} \frac{\mathrm{d}\mathbf{r}}{V_{\mathrm{uc}}} e^{-i\mathbf{k}\cdot\mathbf{r}} u^*_{\mathbf{k}n}(\mathbf{r}) u_{\mathbf{k}'n'}(\mathbf{r}) e^{i\mathbf{k}'\cdot\mathbf{r}} \\
&= N_{\mathrm{uc}}^{-1} \sum_p \int_{\mathrm{uc}} \frac{\mathrm{d}\mathbf{r}}{V_{\mathrm{uc}}} e^{-i\mathbf{k}\cdot(\mathbf{r}+\mathbf{T}_p)} u^*_{\mathbf{k}n}(\mathbf{r}+\mathbf{T}_p) u_{\mathbf{k}'n'}(\mathbf{r}+\mathbf{T}_p) e^{i\mathbf{k}'\cdot(\mathbf{r}+\mathbf{T}_p)} \\
&= N_{\mathrm{uc}}^{-1} \sum_p e^{-i(\mathbf{k}-\mathbf{k}')\cdot\mathbf{T}_p} \int_{\mathrm{uc}} \frac{\mathrm{d}\mathbf{r}}{V_{\mathrm{uc}}} e^{-i(\mathbf{k}-\mathbf{k}')\cdot\mathbf{r}} u^*_{\mathbf{k}n}(\mathbf{r}) u_{\mathbf{k}'n'}(\mathbf{r}) \\
&= \delta_{\mathbf{k},\mathbf{k}'} \int_{\mathrm{uc}} \frac{\mathrm{d}\mathbf{r}}{V_{\mathrm{uc}}} e^{-i(\mathbf{k}-\mathbf{k}')\cdot\mathbf{r}} u^*_{\mathbf{k}n}(\mathbf{r}) u_{\mathbf{k}'n'}(\mathbf{r}) \\
&= \delta_{\mathbf{k},\mathbf{k}'} \langle \mathbf{k}n | \mathbf{k}'n' \rangle_{\mathrm{uc}} = \delta_{\mathbf{k},\mathbf{k}'} \delta_{nn'},
\end{aligned} \tag{2.184}$$

where $N_{\mathrm{uc}}^{-1} \sum_p e^{-i(\mathbf{k}'-\mathbf{k})\cdot\mathbf{T}_p} = \delta_{\mathbf{k},\mathbf{k}'}$, $u_{\mathbf{k}n}(\mathbf{r}+\mathbf{T}_p) = u_{\mathbf{k}n}(\mathbf{r})$ is a consequence of translational invariance and V_{uc} is the volume of the unit cell.

In order to obtain the electron-ion part of the Hamiltonian, one can perturb the electronic potential V^{KS} from the electronic Hamiltonian $H_{\mathrm{el.}}$, with respect to ionic displacements around equilibrium configuration $\{\mathbf{R}^{\mathrm{eq}}\}$. The Kohn-Sham effective potential V^{KS} can be expanded in terms of ionic displacement $\Delta R_{\kappa\alpha,p} = R_{\kappa\alpha,p} - R^{\mathrm{eq}}_{\kappa\alpha,p}$ in Taylor series:

$$\begin{aligned}
V^{\mathrm{KS}}(\mathbf{r}, \{\mathbf{R}\}) = V^{\mathrm{KS}}(\{\mathbf{R}^{\mathrm{eq}}\}) &+ \sum_{\kappa\alpha,p} \partial_{\kappa\alpha,p} V^{\mathrm{KS}} \Delta R_{\kappa\alpha,p} \\
&+ \frac{1}{2} \sum_{\kappa\alpha,p} \sum_{\kappa'\alpha',p'} \partial_{\kappa\alpha,p} \partial_{\kappa'\alpha',p'} V^{\mathrm{KS}} \Delta R_{\kappa\alpha,p} \Delta R_{\kappa'\alpha',p'} + \dots
\end{aligned} \tag{2.185}$$

The expansion in Eq. (2.185) is similar to the Taylor expansion for E^{BO} in Eq. (2.121) in Sec. 2.8.1 about phononic structure. In that section, E^{BO} was a result of a minimizing procedure for Hamiltonian H^{BO} that contained all ionic and potential energies of the interacting system. This minima let to the equilibrium configuration of ions, which then led to vanishing of the first derivative of E^{BO} with respect to displacement from that equilibrium position. In Eq. (2.185), one is interested in change of the local Kohn-Sham potential V^{KS}, when ions are displaced from their equilibrium position. The first derivatives of $\partial_{\kappa\alpha,p} V^{\mathrm{KS}}$ do not vanish in this case, since they doesn't represent a force acting on ions.

Derivatives can be transformed by expanding $\Delta R_{\kappa\alpha,p}$ using the ladder operators from Eq. (2.142):

$$\begin{aligned}
\sum_{\kappa\alpha,p} \partial_{\kappa\alpha,p} V^{\mathrm{KS}} \Delta R_{\kappa\alpha,p} &= \sum_{\kappa\alpha,p} \partial_{\kappa\alpha,p} V^{\mathrm{KS}} \sum_{\mathbf{q}\nu} \frac{N_{\mathrm{uc}}^{-1/2} \xi_{\kappa\alpha,\nu}(\mathbf{q}) e^{i\mathbf{q}\cdot\mathbf{T}_p}}{(2M_\kappa \omega_{\mathbf{q}\nu}/\hbar)^{1/2}} \left(\hat{a}_{\mathbf{q}\nu} + \hat{a}^\dagger_{-\mathbf{q}\nu} \right) \\
&= N_{\mathrm{uc}}^{-1/2} \sum_{\mathbf{q}\nu} e^{i\mathbf{q}\cdot\mathbf{r}} \Delta_{\mathbf{q}\nu} v^{\mathrm{KS}} \left(\hat{a}_{\mathbf{q}\nu} + \hat{a}^\dagger_{-\mathbf{q}\nu} \right),
\end{aligned} \tag{2.186}$$

where:

$$\begin{aligned}\Delta_{\mathbf{q}\nu} v^{\mathrm{KS}} &= \sum_{\kappa\alpha} \frac{\xi_{\kappa\alpha,\nu}(\mathbf{q}) e^{i\mathbf{q}\cdot\mathbf{r}}}{(2M_\kappa \omega_{\mathbf{q}\nu}/\hbar)^{1/2}} \partial_{\kappa\alpha,\mathbf{q}} v^{\mathrm{KS}}, \\ \partial_{\kappa\alpha,\mathbf{q}} v^{\mathrm{KS}} &= \sum_p e^{-i\mathbf{q}\cdot(\mathbf{r}-\mathbf{T}_p)} \partial_{\kappa\alpha,p} V^{\mathrm{KS}},\end{aligned} \tag{2.187}$$

and new label v^{KS} is used instead of V^{KS} in order to emphasize that all partial derivatives are over $\partial/\partial R_{\kappa\alpha}(\mathbf{q})$ instead of $\partial/\partial R_{\kappa\alpha,p}$. Eq. (2.187) can be also seen as a Fourier transform, that replaces sums over $(\kappa\alpha) \to \nu$ (since $N_\kappa \times N_\alpha = N_\nu$) and $p \to \mathbf{q}$ (since $N_{\mathrm{uc}} = N_p = N_{\mathbf{q}}$), and introduces second-quantization operators $\hat{a}_{\mathbf{q}\nu}$ and $\hat{a}^\dagger_{-\mathbf{q}\nu}$. The electron-phonon Hamiltonian in the second quantization $H_{\mathrm{el-ph}}$ will be the perturbation of V^{KS} from the equilibrium configuration of ions:

$$H_{\mathrm{el-ph}} = \sum_{\mathbf{k}n,\mathbf{k}'n'} \langle \Psi_{\mathbf{k}n} | \, V^{\mathrm{KS}}(\{\mathbf{R}\}) - V^{\mathrm{KS}}(\{\mathbf{R}^{\mathrm{eq}}\}) \, | \Psi_{\mathbf{k}'n'} \rangle \, \hat{c}^\dagger_{\mathbf{k}n} \hat{c}_{\mathbf{k}'n'}. \tag{2.188}$$

From Eq. (2.185) one can see that electron-phonon interaction in Eq. (2.188) will contain terms from a Taylor expansion of V^{KS} with respect to ionic displacements.

From Eq. (2.186) one can see that first-order terms will introduce sum over one set of $\mathbf{q}\nu$ corresponding to coupling to phonon operators $(\hat{a}_{\mathbf{q}\nu} + \hat{a}^\dagger_{-\mathbf{q}\nu})$. Using the normalization relations, the first-order term in brackets will transform as:

$$\begin{aligned}&\sum_{\mathbf{k}n,\mathbf{k}'n'} \langle \Psi_{\mathbf{k}n} | \, N_{\mathrm{uc}}^{-1/2} \sum_{\mathbf{q}\nu} e^{i\mathbf{q}\cdot\mathbf{r}} \Delta_{\mathbf{q}\nu} v^{\mathrm{KS}} \, | \Psi_{\mathbf{k}'n'} \rangle = \\ &\sum_{\mathbf{k}n,\mathbf{k}'n'} \sum_{\mathbf{q}\nu} N_{\mathrm{uc}}^{-1} \sum_p e^{-i(\mathbf{k}-\mathbf{q}-\mathbf{k}')\cdot\mathbf{T}_p} \\ &\times \int_{\mathrm{uc}} \frac{\mathrm{d}\mathbf{r}}{V_{\mathrm{uc}}} e^{-i(\mathbf{k}-\mathbf{q}-\mathbf{k}')\cdot\mathbf{r}} u_{\mathbf{k}n} N_{\mathrm{uc}}^{-1/2} \Delta_{\mathbf{q}\nu} v^{\mathrm{KS}} u_{\mathbf{k}'n'} = \\ &\sum_{\mathbf{k}n,\mathbf{k}'n'} \sum_{\mathbf{q}\nu} \delta_{\mathbf{k}-\mathbf{q},\mathbf{k}'} \, \langle \mathbf{k}n | \, N_{\mathrm{uc}}^{-1/2} \Delta_{\mathbf{q}\nu} v^{\mathrm{KS}} \, | \mathbf{k}'n' \rangle_{\mathrm{uc}} = \\ &\sum_{\mathbf{k}nn'} \sum_{\mathbf{q}\nu} \langle \mathbf{k}n | \, N_{\mathrm{uc}}^{-1/2} \Delta_{\mathbf{q}\nu} v^{\mathrm{KS}} \, | \mathbf{k}-\mathbf{q}n' \rangle_{\mathrm{uc}} = \\ &\sum_{\mathbf{k}nn'} \sum_{\mathbf{q}\nu} \langle \mathbf{k}+\mathbf{q}n | \, N_{\mathrm{uc}}^{-1/2} \Delta_{\mathbf{q}\nu} v^{\mathrm{KS}} \, | \mathbf{k}n' \rangle_{\mathrm{uc}} \, .\end{aligned} \tag{2.189}$$

Similarly, for the second-order, there will be two sums over $\mathbf{q}\nu$ and $\mathbf{q}'\nu'$ that couple to a product of operators $(\hat{a}_{\mathbf{q}\nu} + \hat{a}^\dagger_{-\mathbf{q}\nu})(\hat{a}_{\mathbf{q}'\nu'} + \hat{a}^\dagger_{-\mathbf{q}'\nu'})$. The second-order term in brackets will transform in an similar manner as the first term:

$$\begin{aligned}&\frac{1}{2} \sum_{\mathbf{k}n,\mathbf{k}'n'} \langle \Psi_{\mathbf{k}n} | \, N_{\mathrm{uc}}^{-1} \sum_{\mathbf{q}\nu} \sum_{\mathbf{q}'\nu'} e^{i\mathbf{q}'\cdot\mathbf{r}} \Delta_{\mathbf{q}'\nu'} e^{i\mathbf{q}\cdot\mathbf{r}} \Delta_{\mathbf{q}\nu} v^{\mathrm{KS}} \, | \Psi_{\mathbf{k}'n'} \rangle = \\ &\frac{1}{2} \sum_{\mathbf{k}n,\mathbf{k}'n'} \sum_{\mathbf{q}\nu} \sum_{\mathbf{q}'\nu'} \delta_{\mathbf{k}-\mathbf{q}-\mathbf{q}',\mathbf{k}'} \, \langle \mathbf{k}n | \, N_{\mathrm{uc}}^{-1} \Delta_{\mathbf{q}'\nu'} \Delta_{\mathbf{q}\nu} v^{\mathrm{KS}} \, | \mathbf{k}'n' \rangle_{\mathrm{uc}} = \\ &\frac{1}{2} \sum_{\mathbf{k}nn'} \sum_{\mathbf{q}\nu} \sum_{\mathbf{q}'\nu'} \langle \mathbf{k}+\mathbf{q}+\mathbf{q}'n | \, N_{\mathrm{uc}}^{-1} \Delta_{\mathbf{q}'\nu'} \Delta_{\mathbf{q}\nu} v^{\mathrm{KS}} \, | \mathbf{k}n' \rangle_{\mathrm{uc}} \, .\end{aligned} \tag{2.190}$$

By including the terms up to second-order with respect to atomic displacements, electron-phonon Hamiltonian $H_{\mathrm{el-ph}}$ takes the form

$$\begin{aligned} H_{\mathrm{el-ph}} &= N_{\mathrm{uc}}^{-1/2} \sum_{\mathbf{k}mn} \sum_{\mathbf{q}\nu} g^{\mathrm{Fan}}_{mn,\nu}(\mathbf{k},\mathbf{q}) \hat{c}^{\dagger}_{\mathbf{k}+\mathbf{q}m} \hat{c}_{\mathbf{k}n} (\hat{a}^{\dagger}_{-\mathbf{q}\nu} + \hat{a}_{\mathbf{q}\nu}) \\ &+ N_{\mathrm{uc}}^{-1} \sum_{\mathbf{k}mn} \sum_{\mathbf{q}\mathbf{q}'\nu\nu'} g^{\mathrm{DW}}_{mn,\nu\nu'}(\mathbf{k},\mathbf{q},\mathbf{q}') \hat{c}^{\dagger}_{\mathbf{k}+\mathbf{q}+\mathbf{q}'m} \hat{c}_{\mathbf{k}n} \times \\ &\times (\hat{a}^{\dagger}_{-\mathbf{q}\nu} + \hat{a}_{\mathbf{q}\nu})(\hat{a}^{\dagger}_{-\mathbf{q}'\nu'} + \hat{a}_{\mathbf{q}'\nu'}), \end{aligned} \tag{2.191}$$

where $g^{\mathrm{Fan}}_{nm,\nu}(\mathbf{k},\mathbf{q})$ and $g^{\mathrm{DW}}_{nm,\nu\nu'}(\mathbf{k},\mathbf{q},\mathbf{q}')$ are first-order Fan and second-order Debye-Waller (DW) matrix elements of electron-phonon interaction given as:

$$\begin{aligned} g^{\mathrm{Fan}}_{mn,\nu}(\mathbf{k},\mathbf{q}) &= \langle \mathbf{k}+\mathbf{q}m | \, \Delta_{\mathbf{q}\nu} v^{\mathrm{KS}} \, | \mathbf{k}n \rangle_{\mathrm{uc}} \\ &= \sum_{\kappa\alpha} \frac{\xi_{\kappa\alpha,\nu}(\mathbf{q})}{(2M_{\kappa}\omega_{\mathbf{q}\nu}/\hbar)^{1/2}} \langle \mathbf{k}+\mathbf{q}m | \, \frac{\partial v^{\mathrm{KS}}}{\partial R_{\kappa\alpha}(\mathbf{q})} \, | \mathbf{k}n \rangle_{\mathrm{uc}} , \end{aligned} \tag{2.192}$$

and

$$\begin{aligned} g^{\mathrm{DW}}_{mn,\nu\nu'}(\mathbf{k},\mathbf{q},\mathbf{q}') &= \langle \mathbf{k}+\mathbf{q}+\mathbf{q}'m | \, \frac{1}{2} \Delta_{\mathbf{q}\nu} \Delta_{\mathbf{q}'\nu'} v^{\mathrm{KS}} \, | \mathbf{k}n \rangle_{\mathrm{uc}} \\ &= \frac{1}{2} \sum_{\kappa\kappa'\alpha\alpha'} \frac{\xi_{\kappa\alpha,\nu}(\mathbf{q})}{(2M_{\kappa}\omega_{\mathbf{q}\nu}/\hbar)^{1/2}} \frac{\xi_{\kappa'\alpha',\nu'}(\mathbf{q}')}{(2M'_{\kappa}\omega_{\mathbf{q}'\nu'}/\hbar)^{1/2}} \\ &\times \langle \mathbf{k}+\mathbf{q}+\mathbf{q}'m | \, \frac{\partial^2 v^{\mathrm{KS}}}{\partial R_{\kappa'\alpha'}(\mathbf{q}') \partial R_{\kappa\alpha}(\mathbf{q})} \, | \mathbf{k}n \rangle_{\mathrm{uc}} , \end{aligned} \tag{2.193}$$

respectively. Matrix elements $g^{\mathrm{Fan}}_{mn,\nu}(\mathbf{k},\mathbf{q})$ and $g^{\mathrm{DW}}_{mn,\nu\nu'}(\mathbf{k},\mathbf{q},\mathbf{q}')$ have the physical dimension of energy, and measure the probability of an electron transitioning from one state to another due to interaction with a phonon. Fan term $g^{\mathrm{Fan}}_{mn,\nu}(\mathbf{k},\mathbf{q})$ measures the probability of interacting with one phonon $\mathbf{q}\nu$ and DW term of interacting with two phonons $\mathbf{q}\nu$ and $\mathbf{q}'\nu'$.

The first-order matrix elements $g^{\mathrm{Fan}}_{mn,\nu}(\mathbf{k},\mathbf{q})$ can be obtained in harmonic approximation using DFPT, as derivatives $\partial_{\kappa\alpha,\mathbf{q}} v^{\mathrm{KS}}$ are already obtained at the end of the self-consistent procedure that solves Sternheimer equation Eq. (2.168) in search for density response $\Delta^{\mathbf{q}} n(\mathbf{r})$. This is described in approaches by both Baroni et al. [93, 94, 95, 92] and Gonze et al. [98, 99, 100, 101, 102].In order to save on memory and space, $\partial_{\kappa\alpha,\mathbf{q}} v^{\mathrm{KS}}$ are not saved by default of DFPT procedure in most codes (like for e.g. Quantum Espresso [97], and Abinit [104]), however there is usually an option to change this. The end result of DFPT, which are $\omega_{\mathbf{q}\nu}$ and $\xi_{\kappa\alpha,\nu}(\mathbf{q})$ are always saved by default, and when combined with $\partial_{\kappa\alpha,\mathbf{q}} v^{\mathrm{KS}}$, the computation of $g^{\mathrm{Fan}}_{mn,\nu}(\mathbf{k},\mathbf{q})$ is straightforward using Eq. (2.192).

The second-order terms in Eq. (2.193) would require solving the second-order Sternheimer equation, like the one in Eq. (A.11) in A.3 of the Appendix, which is much more involved and usually avoided in the literature. However, Allen and Heine [113] and Allen and Cardona [114, 115] used rigid-ion approximation and translation invariance to obtain second-order DW term, diagonal in $\mathbf{k}n$. This approach became known as the Allen-Heine-Cardona theory.

2.9.1 Allen-Heine-Cardona theory

This section provides a brief overview of the Allen-Heine-Cardona (AHC) theory that is used to describe the phonon-induced band gap renormalization in semiconductor materials. Using the AHC formulation, a procedure for self-consistent calculation of phonon-induced renormalizations of band energies and their broadening will be presented in Chapter 4.

In the work of Allen, Heine and Cardona[113, 114, 115] the ionic displacements were treated as perturbation within the Reyleigh-Schrödinger perturbation theory (RSPT) for the Kohn-Sham Hamiltonian. Within RSPT, only terms diagonal in $\mathbf{k}n$ are considered, which constrains the DW terms to $\mathbf{q}+\mathbf{q}' = 0$ case. This simplification along with rigid-ion approximation is the basis of the Allen-Heine-Cardona (AHC) formulation for temperature dependent renormalization of Kohn-Sham energy levels $\Delta E^{\mathrm{AHC}}_{\mathbf{k}n}$:

$$
\begin{aligned}
\Delta E^{\mathrm{AHC}}_{\mathbf{k}n}(T) &= \frac{1}{2}\lambda^2 E^{\mathrm{FAN}}_{\mathbf{k}n}(T) + \frac{1}{2}\lambda^2 E^{\mathrm{DW}}_{\mathbf{k}n}(T) \\
&= N_{\mathrm{uc}}^{-1} \sum_{\mathbf{q}\nu} \frac{2n_{\mathbf{q}\nu}(T)+1}{2\omega_{\mathbf{q}\nu}/\hbar} \\
&\times \Bigg\{ \sum_{\kappa\kappa'\alpha\alpha'} \frac{\xi_{\kappa\alpha,\nu}(-\mathbf{q})}{(M_\kappa)^{1/2}} \frac{\xi_{\kappa'\alpha',\nu}(\mathbf{q})}{(M_{\kappa'})^{1/2}} \\
&\qquad \times 2\,\mathrm{Re} \sum_{n'\neq n} \frac{\langle u_{\mathbf{k}n}| \frac{\partial v^{\mathrm{KS}}}{\partial R_{\kappa\alpha}(-\mathbf{q})} |u_{\mathbf{k}+\mathbf{q}'n'}\rangle \langle u_{\mathbf{k}+\mathbf{q}'n'}| \frac{\partial v^{\mathrm{KS}}}{\partial R_{\kappa'\alpha'}(\mathbf{q})} |u_{\mathbf{k}n}\rangle}{\varepsilon_{\mathbf{k}n} - \varepsilon_{\mathbf{k}+\mathbf{q}n'} + i\delta} \\
&\quad - \sum_{\kappa\kappa'\alpha\alpha'} \left[\frac{\xi_{\kappa\alpha,\nu}(-\mathbf{q})\xi_{\kappa\alpha',\nu}(\mathbf{q})}{2M_\kappa} + \frac{\xi_{\kappa'\alpha,\nu}(-\mathbf{q})\xi_{\kappa'\alpha',\nu}(\mathbf{q})}{2M_{\kappa'}} \right] \\
&\qquad \times 2\,\mathrm{Re} \sum_{n'\neq n} \frac{\langle u_{\mathbf{k}n}| \frac{\partial v^{\mathrm{KS}}}{\partial R_{\kappa\alpha}(\Gamma)} |u_{\mathbf{k}n'}\rangle \langle u_{\mathbf{k}n'}| \frac{\partial v^{\mathrm{KS}}}{\partial R_{\kappa'\alpha'}(\Gamma)} |u_{\mathbf{k}n}\rangle}{\varepsilon_{\mathbf{k}n} - \varepsilon_{\mathbf{k}n'} + i\delta} \Bigg\}.
\end{aligned}
\tag{2.194}
$$

where $i\delta$ is a small parameter, introduced to avoid numerical divergence if the denominator becomes too small, while parameter $\lambda \to 1$ that originates from RSPT is kept in order to emphasize that one is dealing with second-order terms. Derivation of Eq. (2.194) can be obtained by following A.3, A.4, and A.5 of the Appendix, respectively. Eq. (2.194) is also called adiabatic AHC formula because phonon energies $\hbar\omega_{\mathbf{q}\nu}$ were neglected in the denominator:

$$
\varepsilon_{\mathbf{k}n} - \varepsilon_{\mathbf{k}+\mathbf{q}n'} \pm \hbar\omega_{\mathbf{q}\nu} \approx \varepsilon_{\mathbf{k}n} - \varepsilon_{\mathbf{k}+\mathbf{q}n'}. \tag{2.195}
$$

Adiabatic formula has been first used with semiempirical calculations [113, 114, 115] and more recently using DFT with pseudopotentials [116, 117]. The same equation as Eq. (2.194) can be obtained using more sophisticated approach using many-body formalism and field-theory, using the same approximations[112, 44].

2.9.2 Fan term in the non-adiabatic case

Following the many-body perturbation theory procedure, energy renormalization of electronic levels due to ionic movement in solids can be obtained following procedures in Refs. [112, 44]. In many-body language, renormalization $\frac{1}{2}\lambda^2 E^{(2)}_{\mathbf{k}n}(T)$ which is purely real, is replaced by electron-phonon self-energy $\Sigma_{\mathbf{k}n}(T)$ which is a complex number. Up to the second order this self-energy will contain two terms, Fan $\Sigma^{\mathrm{Fan}}_{\mathbf{k}n}(T)$ and Debye-Weller $\Sigma^{\mathrm{DW}}_{\mathbf{k}n}(T)$. In present discussion, the Debye-Weller term is identical to $\frac{1}{2}\lambda^2 E^{\mathrm{DW}}_{\mathbf{k}n}(T)$, however the Fan terms requires some attention.

Following Mahan 2000 [Chapter 3.4, Eq. (3.212)] [118], one can perform a similar procedure for one-phonon self-energy to obtain:

$$\Sigma^{\mathrm{Fan}}_{\mathbf{k}n}(i\omega, T) = -\frac{1}{\beta N_q}\sum_{m,\mathbf{q}\nu} |g_{nm,\nu}(\mathbf{k},\mathbf{q})|^2 \sum_j D^{(0)}_{\mathbf{q}\nu}(i\omega_j) G^{(0)}_{\mathbf{k}+\mathbf{q}m}(i\omega - i\omega_j), \tag{2.196}$$

where $\beta = (k_{\mathrm{B}}T)^{-1}$, k_{B} is the Boltzman constant, T is the temperature, N_q is the number of $\mathbf{q}$-points in the sum, and $G^{(0)}_{\mathbf{k}+\mathbf{q}m}(i\omega - i\omega_j)$ and $D^{(0)}_{\mathbf{q}\nu}(i\omega_j)$ are electronic and phononic Green's functions at finite temperatures, respectively:

$$\begin{aligned} G^{(0)}_{\mathbf{k}+\mathbf{q}m}(i\omega - i\omega_j) &= \frac{1}{i\omega - i\omega_j - \varepsilon_{\mathbf{k}+\mathbf{q}n} + \varepsilon_F}, \\ D^{(0)}_{\mathbf{q}\nu}(i\omega_j) &= \frac{1}{i\omega_j - \omega_{\mathbf{q}\nu}} - \frac{1}{i\omega_j + \omega_{\mathbf{q}\nu}}, \end{aligned} \tag{2.197}$$

where ε_F is the Fermi energy, $i\omega_j$ are Matsubara frequencies and $\hbar = 1$ for simplicity. Again, following Mahan 2000 [Chapter 3.5 Eq. (3.216)] [118] one can use the summation over all Matsubara frequencies:

$$\begin{aligned} &-\frac{1}{\beta}\sum_j D^{(0)}_{\mathbf{q}\nu}(i\omega_j) G^{(0)}_{\mathbf{k}+\mathbf{q}m}(i\omega - i\omega_j) = \\ &\frac{n_{\mathbf{q}\nu}(T) + 1 - f_{\mathbf{k}+\mathbf{q}m}}{i\omega - \varepsilon_{\mathbf{k}+\mathbf{q}m} - \omega_{\mathbf{q}\nu}} + \frac{n_{\mathbf{q}\nu}(T) + f_{\mathbf{k}+\mathbf{q}m}}{i\omega - \varepsilon_{\mathbf{k}+\mathbf{q}m} + \omega_{\mathbf{q}\nu}}, \end{aligned} \tag{2.198}$$

where $n_{\mathbf{q}\nu}(T)$ and $f_{\mathbf{k}m}$ are Bose-Einstein and Fermi-Dirac occupation numbers for $\mathbf{q}\nu$-phonon and $\mathbf{k}m$-electron, respectively. At this point, one can perform analytic continuation for $i\omega$ by simply performing a rotation to the real axis as $i\omega \to \omega + i\delta$, where δ is some arbitrary small real parameter. This transforms $\Sigma^{\mathrm{Fan}}_{\mathbf{k}n}(T)$ to:

$$\begin{aligned} \Sigma^{\mathrm{Fan}}_{\mathbf{k}n}(\omega, T) = &\frac{1}{N_q}\sum_{m\mathbf{q}\nu} |g_{nm,\nu}(\mathbf{k},\mathbf{q})|^2 \times \\ &\times \left[\frac{n_{\mathbf{q}\nu}(T) + 1 - f_{\mathbf{k}+\mathbf{q}m}}{\omega - \varepsilon_{\mathbf{k}+\mathbf{q}m} - \omega_{\mathbf{q}\nu} + i\delta} + \frac{n_{\mathbf{q}\nu}(T) + f_{\mathbf{k}+\mathbf{q}m}}{\omega - \varepsilon_{\mathbf{k}+\mathbf{q}m} + \omega_{\mathbf{q}\nu} + i\delta}\right]. \end{aligned} \tag{2.199}$$

Diagonal terms for Debye-Waller part of self-energy $\Sigma^{\mathrm{DW}}_{\mathbf{k}n} = \Sigma^{\mathrm{DW}}_{\mathbf{k}nm}\delta_{nm}\delta_{\mathbf{q},-\mathbf{q}'}\delta_{\nu\nu'}$ can

be obtained from rigid-ion approximation and rewritten from Eq. (2.191) as:

$$\begin{aligned}\Sigma^{\mathrm{DW}}_{\mathbf{k}n}(T) &= -\frac{1}{N_{\mathbf{q}}}\sum_{m\mathbf{q}\nu} g^{\mathrm{ria}}_{nm,\nu}(\mathbf{k},\mathbf{q})\left[2n_{\mathbf{q}\nu}(T)+1\right],\\ g^{\mathrm{ria}}_{nm,\nu}(\mathbf{k},\mathbf{q}) &= \sum_{\kappa\kappa'\alpha\alpha'}\left[\frac{\xi_{\kappa\alpha,\nu}(-\mathbf{q})\xi_{\kappa\alpha',\nu}(\mathbf{q})}{2M_\kappa\omega_{\mathbf{q}\nu}/\hbar}+\frac{\xi_{\kappa'\alpha,\nu'}(-\mathbf{q})\xi_{\kappa'\alpha',\nu}(\mathbf{q})}{2M_{\kappa'}\omega_{\mathbf{q}\nu}/\hbar}\right]\\ &\quad\times \mathrm{Re}\,\frac{\langle u_{\mathbf{k}n}|\frac{\partial v^{\mathrm{KS}}}{\partial R_{\kappa\alpha}(\Gamma)}|u_{\mathbf{k}m}\rangle\langle u_{\mathbf{k}m}|\frac{\partial v^{\mathrm{KS}}}{\partial R_{\kappa'\alpha'}(\Gamma)}|u_{\mathbf{k}n}\rangle}{\varepsilon_{\mathbf{k}n}-\varepsilon_{\mathbf{k}m}+i\delta}.\end{aligned} \tag{2.200}$$

Sometimes $\Sigma^{\mathrm{DW}}_{\mathbf{k}n}$ and $\Sigma^{\mathrm{Fan}}_{\mathbf{k}n}$ terms are referred as static and dynamic terms, respectively, based on their dependence on ω.

2.9.3 Solving the AHC equation

Fan renormalization term has adiabatic and static $\frac{1}{2}\lambda^2 E^{\mathrm{Fan}}_{\mathbf{k}n}(T)$ and non-adiabatic and dynamic $\Sigma^{\mathrm{Fan}}_{\mathbf{k}n}(\omega,T)$ form presented Eq. (2.194) (also Eq. (A.45) in the Appendix) and Eq. (2.199), respectively. In the adiabatic and static case, the renormalization neglects phononic energies in the denominator, but the calculation is straightforward, if all ingredients of Eq. (A.56) are known. For the non-adiabatic case, there are a few methods of solution.

Optimization method - direct solution

In the non-adiabatic case, the energy renormalization is expressed as a solution for optimization equation, provided that non-diagonal terms in band indices $\Sigma_{\mathbf{k}nm}(\omega,T)$ can be neglected:

$$\omega = \varepsilon_{\mathbf{k}n} + \Sigma^{\mathrm{Fan}}_{\mathbf{k}n}(\omega,T) + \Sigma^{\mathrm{DW}}_{\mathbf{k}n}(T), \tag{2.201}$$

where ω is a complex number whore real part represents the renormalized energy level $\mathrm{Re}\,\omega = E_{\mathbf{k}n}(T)$. Since one is considering electrons that interact with ionic vibrations, one can expect that there will be some uncertainty or *smearing* of their energy levels. The imaginary part of ω will represent the half-width of that smearing centered around ω. Because $\Sigma^{\mathrm{DW}}_{\mathbf{k}n}$ is not dependent on ω, and purely real, the main focus will be on the $\Sigma^{\mathrm{Fan}}_{\mathbf{k}n}(\omega,T)$ term, which is dependent on ω, and complex.

Spectral function method

Besides direct solving for ω from Eq. (2.201), one can search for a peak in the spectral function $A_{\mathbf{k}n}(\omega,T)$:

$$\begin{aligned}A_{\mathbf{k}n}(\omega,T) &= -\frac{1}{\pi}|\,\mathrm{Im}\,G_{\mathbf{k}n}(\omega,T)|\\ &= -\frac{1}{\pi}\,\mathrm{Im}\,\frac{1}{\omega-\varepsilon_{\mathbf{k}n}-\Sigma_{\mathbf{k}n}(\omega,T)}\\ &= -\frac{1}{\pi}\frac{\mathrm{Im}\,\Sigma_{\mathbf{k}n}(\omega,T)}{[\omega-\varepsilon_{\mathbf{k}n}-\mathrm{Re}\,\Sigma_{\mathbf{k}n}(\omega,T)]^2+[\mathrm{Im}\,\Sigma_{\mathbf{k}n}(\omega,T)]^2},\end{aligned} \tag{2.202}$$

where $\Sigma_{\mathbf{k}n} = \Sigma^{\text{Fan}}_{\mathbf{k}n} + \Sigma^{\text{DW}}_{\mathbf{k}n}$. This spectral function should produce a well defined peak near $\varepsilon_{\mathbf{k}n}$ and perhaps a small satellite. In practice, one performs a numerical calculation for a mesh of ω points. In order to check if the range of ω-mesh is sufficient one can check if the spectral function integrates to unity:

$$\int \mathrm{d}\omega \, A_{\mathbf{k}n}(\omega, T) = 1. \tag{2.203}$$

Linear QP approximation

Similarly to the quasi-particle (QP) approximation in GW method for electron-electron self-energy, explained in Sec. 2.7.5, one can make a similar approximation in the case of electron-phonon self-energy. Eq. (2.201) can be split for real and imaginary parts of ω. The Fan term can approximated by Taylor expansion for ω around $\varepsilon_{\mathbf{k}n}$:

$$\Sigma^{\text{Fan}}_{\mathbf{k}n}(\omega, T) = \Sigma^{\text{Fan}}_{\mathbf{k}n}(\varepsilon_{\mathbf{k}n}, T) + \left.\frac{\partial \Sigma^{\text{Fan}}_{\mathbf{k}n}}{\partial \omega}\right|_{\omega=\varepsilon_{\mathbf{k}n}} (\omega - \varepsilon_{\mathbf{k}n}) + \dots \tag{2.204}$$

Keeping only the first derivative in Taylor expansion of $\Sigma^{\text{Fan}}_{\mathbf{k}n}$ and inserting it into Eq. (2.201), one obtains the linear quasi-particle equation for energy renormalization $\omega^{\text{QPL}} = E^{\text{QPL}}_{\mathbf{k}n} + i\Gamma_{\mathbf{k}n}(T)$. The real part of ω^{QPL} is the renormalized energy level:

$$\begin{aligned} E^{\text{QPL}}_{\mathbf{k}n}(T) = \varepsilon_{\mathbf{k}n} &+ Z_{\mathbf{k}n} \left[\operatorname{Re}\Sigma^{\text{Fan}}_{\mathbf{k}n}(\varepsilon_{\mathbf{k}n}, T) + \operatorname{Re}\Sigma^{\text{DW}}_{\mathbf{k}n}(T)\right] \\ &- \left(Z_{\mathbf{k}n} \left.\frac{\partial \operatorname{Im}\Sigma^{\text{Fan}}_{\mathbf{k}n}}{\partial \omega}\right|_{\omega=\varepsilon_{\mathbf{k}n}}\right) \Gamma_{\mathbf{k}n} \quad , \end{aligned} \tag{2.205}$$

where

$$Z_{\mathbf{k}n} = \left(1 - \left.\frac{\partial \operatorname{Re}\Sigma^{\text{Fan}}_{\mathbf{k}n}}{\partial \omega}\right|_{\omega=\varepsilon_{\mathbf{k}n}}\right)^{-1}, \tag{2.206}$$

while the imaginary part represents smearing $\Gamma_{\mathbf{k}n}$:

$$\begin{aligned} \Gamma_{\mathbf{k}n}(T) = Z_{\mathbf{k}n} &\operatorname{Im}\Sigma^{\text{Fan}}_{\mathbf{k}n}(\varepsilon_{\mathbf{k}n}, T) \\ &+ Z_{\mathbf{k}n} \left.\frac{\partial \operatorname{Im}\Sigma^{\text{Fan}}_{\mathbf{k}n}}{\partial \omega}\right|_{\omega=\varepsilon_{\mathbf{k}n}} (E^{\text{QPL}}_{\mathbf{k}n} - \varepsilon_{\mathbf{k}n}). \end{aligned} \tag{2.207}$$

Equations (2.205) and (2.207) are decoupled only in the case when $\partial \operatorname{Im}\Sigma^{\text{Fan}}_{\mathbf{k}n}/\partial\omega$ is zero or negligible around $\omega = \varepsilon_{\mathbf{k}n}$. Decoupled linear QP equations are:

$$\begin{aligned} E^{\text{QPL}}_{\mathbf{k}n}(T) &= \varepsilon_{\mathbf{k}n} + Z_{\mathbf{k}n} \left[\operatorname{Re}\Sigma^{\text{Fan}}_{\mathbf{k}n}(\varepsilon_{\mathbf{k}n}, T) + \operatorname{Re}\Sigma^{\text{DW}}_{\mathbf{k}n}(T)\right], \\ \Gamma_{\mathbf{k}n}(T) &= Z_{\mathbf{k}n} \operatorname{Im}\Sigma^{\text{Fan}}_{\mathbf{k}n}(\varepsilon_{\mathbf{k}n}, T). \end{aligned} \tag{2.208}$$

Besides neglecting $\partial \operatorname{Im}\Sigma^{\text{Fan}}_{\mathbf{k}n}/\partial\omega$ at $\omega = \varepsilon_{\mathbf{k}n}$, there are a few more checks to be performed in order to use the linear QP approximation. This involves checking if renormalization factor is $Z_{\mathbf{k}n} \leq 1$. For constant $\Sigma^{\text{Fan}}_{\mathbf{k}n}$ around $\varepsilon_{\mathbf{k}n}$, the renormalization

factor $Z_{\mathbf{k}n} = 1$, which corresponds to on-the-mass-shell (OTMS) approximation for the real part. When $\Sigma^{\text{Fan}}_{\mathbf{k}n}$ is smooth and decreasing with ω around $\varepsilon_{\mathbf{k}n}$, then $\partial \operatorname{Re}\Sigma^{\text{Fan}}_{\mathbf{k}n}/\partial\omega$ will be negative and $Z_{\mathbf{k}n} < 1$. If $\Sigma^{\text{Fan}}_{\mathbf{k}n}$ is smooth and increasing with ω around $\varepsilon_{\mathbf{k}n}$, then $\partial \operatorname{Re}\Sigma^{\text{Fan}}_{\mathbf{k}n}/\partial\omega$ will be positive and $Z_{\mathbf{k}n} > 1$, which points to a breakdown of linear QP approximation. The case where $\partial \operatorname{Re}\Sigma^{\text{Fan}}_{\mathbf{k}n}/\partial\omega$ rapidly changes sign around $\varepsilon_{\mathbf{k}n}$ usually points to an underconverged calculation for $\Sigma^{\text{Fan}}_{\mathbf{k}n}$.

Besides $Z_{\mathbf{k}n} \leq 1$, one should also check if the spectral function $A_{\mathbf{k}n}$ has any satellites and if the peak is symmetric. If both are true, then the spectral function $A_{\mathbf{k}n}$ can also be simplified using linear QP approximation, where it becomes a symmetric Lorentzian centered around $E^{\text{QPL}}_{\mathbf{k}n}$ with half-width $\Gamma_{\mathbf{k}n}$:

$$\begin{aligned} A^{\text{QPL}}_{\mathbf{k}n}(\omega, T) &= -\frac{1}{\pi}\frac{Z_{\mathbf{k}n}\operatorname{Im}\Sigma_{\mathbf{k}n}(\varepsilon_{\mathbf{k}n}, T)}{[\omega - \varepsilon_{\mathbf{k}n} - Z_{\mathbf{k}n}\operatorname{Re}\Sigma_{\mathbf{k}n}(\varepsilon_{\mathbf{k}n}, T)]^2 + [Z_{\mathbf{k}n}\operatorname{Im}\Sigma_{\mathbf{k}n}(\varepsilon_{\mathbf{k}n}, T)]^2} \\ &= -\frac{1}{\pi}\frac{Z_{\mathbf{k}n}\Gamma_{\mathbf{k}n}}{(\omega - E^{\text{QPL}}_{\mathbf{k}n})^2 + \Gamma^2_{\mathbf{k}n}}, \end{aligned} \tag{2.209}$$

OTMS approximation

For the simplest solution for Eq. (2.201), is to approximate the solution to real axis by simply inserting the bare value $\varepsilon_{\mathbf{k}n}$ into $\Sigma^{\text{Fan}}_{\mathbf{k}n}$: and obtain renormalization in the so-called on-the-mass-shell (OTMS) approximation:

$$E^{\text{otms}}_{\mathbf{k}n}(T) = \varepsilon_{\mathbf{k}n} + \operatorname{Re}\Sigma^{\text{Fan}}_{\mathbf{k}n}(\varepsilon_{\mathbf{k}n}, T) + \operatorname{Re}\Sigma^{\text{DW}}_{\mathbf{k}n}(T). \tag{2.210}$$

Eq. (2.210) assumes that one is dealing with sharp excitations and that there is no smearing, so one can imagine that possible energies form an infinitely thin shell in $\mathbf{k}n$ space for fixed T.

AHC equation in practice

The sum over electronic states in Eq. (2.194), Eq. (2.199), and Eq. (2.200) contains both occupied and unoccupied states and one should perform a convergence test w.r.t. number of unoccupied bands that are included in that sum. One can use the Sternheimer equation, Eq. (2.168), Sec. 2.8.3, from the DFPT procedure to calculate contribution to unoccupied states from $P_c^{\mathbf{k}+\mathbf{q}}|\Delta^{\mathbf{q}}u_{\mathbf{k}n}\rangle$ and $P_c^{\mathbf{k}+\mathbf{q}}\Delta^{\mathbf{q}}v^{\text{KS}}|u_{\mathbf{k}n}\rangle$, which was first demonstrated by Gonze et al. 2011 [119]. However, since one is using DFPT equation which is adiabatic and static, these terms can only have the same form as the ones for $\frac{1}{2}\lambda E_{\mathbf{k}n}(T)$ from Eq. (2.194) (Eq. (A.45) in the Appendix A.3). Although non-adiabatic Fan term would require a proper summation for all bands, one can approximate that the contribution which stems from highly occupied states is much smaller so that static and adiabatic treatment is justified for them. The convergence test in this case is performed to check which unoccupied states give significant contribution and which can be treated as static and adiabatic.

The convergence of $\Delta E_{\mathbf{k}n}(T)$ w.r.t. the number of $\mathbf{q}'$-points in practice has proven to be very slow [120], which makes these kind of calculations demanding and in some cases not tractable. At present, there are several schemes used to interpolate

$g^{\mathrm{Fan}}_{nn',\nu'}(\mathbf{k}, -\mathbf{q}')$ in order to increase the $\mathbf{q}$-grid density at reduced computational cost. Interpolation of $\xi_{\kappa\alpha,\nu}(\mathbf{q})$ and $\omega_{\mathbf{q}\nu}$ is routinely performed and available in most DFPT codes. It involves Fourier transform of dynamical matrices $D^{\kappa\alpha}_{\kappa'\alpha'}(\mathbf{q})$ and then directly solving for $\xi_{\kappa\alpha,\nu}(\mathbf{q})$ and $\omega_{\mathbf{q}\nu}$ at interpolated $\mathbf{q}$ points, which is described in more detail in Sec. 2.8.3 Significantly more involved part of interpolation are transition matrix elements $\langle u_{\mathbf{k}n}| \partial v^{\mathrm{KS}}/\partial R_{\kappa\alpha}(-\mathbf{q}') |u_{\mathbf{k}+\mathbf{q}'n'}\rangle$. Several strategies for this have been developed with much success, however this topic exceeds the reach of this work and more information can be found in Ref. [121, 122].

Finally, one should address the numerical parameter $i\delta$ in the numerator of Eq. (2.194) and Eq. (2.199). This parameter is expected to be small, and standard value of δ was set to 100 meV in works from Refs. [123, 117]. However, Ponce et al 2015 [120], showed that this parameter has to also be included in convergence tests. At $T \to 0$ the parameter should indeed be arbitrary small, however, given the connection of the imaginary part of $\Sigma^{\mathrm{Fan}}_{\mathbf{k}n}$ to the broadening parameter $i\Gamma_{\mathbf{k}n}$ the choice for δ in the case of finite temperatures should be carefully discussed. Indeed, Green's functions $G^{(0)}_{\mathbf{k}+\mathbf{q}m}$ and $D^{(0)}_{\mathbf{q}\nu}$ used in Eq. (2.196) have their 'bare' forms.

Using 'dressed' Green's function instead of 'bare' ones is one of the results of this thesis, as it removes some ambiguity since $i\delta$ is then replaced by $\mathrm{Im}\,\Sigma_{\mathbf{k}n}$ (or $\Gamma_{\mathbf{k}n}$), so real and imaginary parts of $\Sigma^{\mathrm{Fan}}_{\mathbf{k}n}(\omega, T)$ are solved self-consistently. More detail on this procedure is presented Sec. 4.2.

2.10 Elements of Group theory

This section serves as a brief introduction to the language and notation of point groups used in the thesis (O_{h}, T_{d}, Double groups). The notation in this section follows Refs. [124, 50].

2.10.1 Basic definitions

Definition of a group: A set of elements and a binary composition called a product, will form a group G when these four conditions are fulfilled:

- Product of any two elements of the group is also an element of that group (closure):
  $(\forall A, B \in G): \quad AB \in G.$

- Associative law is valid for all members of group G:
  $\forall A, B, C \in G: \quad (AB)C = A(BC).$

- A unique unit or identity element E exists, so that product with any A gives A:
  $(\exists E \in G)(\forall A \in G): \quad AE = EA = A.$

- For every $A \in G$ there is a unique inverse element A^{-1}, so the product AA^{-1} gives unit or identity element E:

$(\forall A)(\exists A^{-1}): \quad AA^{-1} = A^{-1}A = E,$
specially $E = E^{-1}: \quad EE^{-1} = E^{-1}E = E.$

In general, products do not commute but if they do the group is called Abelian group: *if* $\forall(A, B \in G): \quad AB = BA$, *then* G *is Abelian.*

Depending on the number of elements, groups can be infinite or finite. The number of elements in the group G is the *order of the group*, often labeled as $|G|$. If collection of elements g in a group G also forms a group, then g is a *subgroup* of G. Order of group g must be a divisor of the order of group G, i.e. $|G|/|g| = d$, where d is an integer.

One example of an infinite group is the full group of rotations. Sphere can be rotated by any angle around any axis that contains the center of the sphere. Finite group example would be a group of all permutations of three numbers (123), or a group of rotations that rotate a square back to it's original position.

For finite groups, if any element X is multiplied by itself n times, the identity element E is recovered: $X^n = E$. This will be true also for $2n, 3n, 4n, \ldots$, so the smallest integer n is *the order of element* X.

Rearrangement theorem: If $E, A_1, A_2, \ldots, A_k \ldots, A_h$ are elements of group G then for any $A_k \in G$, an assembly of elements $A_kE, A_kA_1, A_kA_2, \ldots, A_kA_k \ldots, A_kA_h$ contains each element of the group once and only once.

A set of elements that can reproduce the whole group by multiplication are called *group generators* which can be used to construct *multiplication tables*. By rearrangement theorem, every row and column of the multiplication table will contain each element once and only once.

Conjugation and class

Definition of conjugation: Two elements $A, B \in G$ are said to be conjugate if there exists an element $X \in G$ for which $A = XBX^{-1}$. **Theorem:** If A is conjugate to B and B is conjugate to C, then A is also conjugate to C:
$A = XBX^{-1} \wedge B = YCY^{-1} : A = XYCX^{-1}Y^{-1} = (XY)C(XY)^{-1}$.
Theorem: Elements of group G can be split into *conjugation classes* $C_1, C_2, \ldots, C_r$, where r is the number of conjugate classes, with the following properties:

- Every element of G is in some class once and only once: $G = C_1 + C_2 + \ldots + C_r$,
- All elements of a class are mutually conjugate and consequently have the same element order,
- An element that commutes with all elements of the group is in a class by itself and is called a self-conjugate element (in non-Abelian group identity E is always self-conjugate and in a class by itself, but in Abelian group every element is self-conjugate and in a class by itself).
- the number of elements in a class $|C_i|$ is a divisor of the order of the group $|G|$,

- $C_iC_j = \sum_{k=1}^{r} h_{ij,k}C_k$ where $h_{ij,k} = h_{ji,k}$ are called the *class multiplication coefficients* which can be either a positive integer or zero.

Cosets

Definition: If g is a subgroup of G, and X is an element of G, then gX is a *right coset* of g, while Xg is a *left coset* of g, and X is called a *coset representative*. A coset isn't necessarily a subgroup, but it will be if $X \in g$ by the rearrangement theorem. Two cosets of the same subgroup will have exactly the same elements or no elements in common.

The concept of cosets becomes more clear if one imagines a space group that contains a point group and a group of translations. Applying a translation to a subgroup of rotations is a coset of that subgroup of rotations. If the symmetry group contains only pure translations and rotations they are called symmorphic, otherwise if it contains at least one symmetry operation that involves a translation followed by a rotation they are called non-symmorphic.

2.10.2 Representation

Homomorphism and Isomorphism

Definition: Two groups G_1 and G_2, can have a mapping f which maps elements from G_1 onto G_2, $f : G_1 \to G_2$ while preserving multiplication $f(g_1)f(g_2) = f(g_1g_2)$, where g_1 and g_2 are elements of G_1 and G_2, respectively. If there is a 1-to-1 correspondence ($|G_1| = |G_2|$), they are *isomorphic*. Otherwise, if there is many-to-one correspondence, they are *homomorphic*.

The mapping f can be seen as a mathematical representation of group elements and multiplication (e.g. matrix representation of elements and their multiplication). If representations are isomorphic they are called faithful, if they are homomorphic they are called unfaithful.

In quantum mechanics, faithful representations of groups are important because one wants to establish a 1-to-1 correspondence in order to faithfully apply symmetry operations on operators and wave functions.

Matrix group

Definition: Matrix group Γ is a group of non-singular matrices (non-singular matrices have an inverse). If all matrices are unitary (inverse matrix is the adjoint of the same matrix), then it is called a *unitary matrix group*.

Two matrices M_1, M_2 are said to be *conjugate* if there exists a non-singular matrix S such that $M_2 = SM_1S^{-1}$.

Two matrix groups Γ_1, Γ_2 are *equivalent* if there exists a non-singular matrix S for which $\Gamma_2 = S\Gamma_1S^{-1}$. If follows from this that Γ_1 and Γ_2 must also be isomorphic. However, if two matrix groups are isomorphic, they don't have to be equivalent: they can be isomorphic and have different dimensions, and in turn, not equivalent.

Theorem : Every matrix group is equivalent to a unitary matrix group.
In other words, any matrix group Γ can be transformed into an equivalent unitary matrix group Γ_U. Non-singular matrices S that transform matrices from one unitary group to another, equivalent, and also unitary group, will also be unitary matrices $S^{-1} = S^\dagger$.
Definition: Trace of a matrix M is a sum of it's diagonal elements, written as $\mathrm{tr}\{M\}$. Character of a matrix group Γ is a function χ defined for all elements as $M \in \Gamma$ as: $\chi(M) = \mathrm{tr}\{M\}$.
Theorem: If Γ is a matrix group with identity E then $\chi(E) = \mathrm{tr}\{E\} = \dim E$, and if M_1 and M_2 are in the same conjugation class in Γ, then $\chi(M_1) = \chi(M_2)$.
Theorem: Two matrix groups are isomorphic and have the same character group if and only if they are equivalent.

Reducible and irreducible representations

Definition: If all the matrices in the representation can be transformed by some non-singular matrix to equivalent representation in which, all the matrices have the same block form, then that representation is called *reducible*. Otherwise it is *irreducible*. The blocks in the reducible representation will themselves form a representation. Irreducible representation cannot be expressed in terms of representations of lower dimensionality. Any reducible representation Γ_R can be expressed in block forms of some irreducible representations Γ_i, $i = 1, 2, 3, \ldots$:

$$\Gamma_R = \begin{bmatrix} \Gamma_1 & \mathcal{O} & \mathcal{O} & \ldots \\ \mathcal{O} & \Gamma_2 & \mathcal{O} & \ldots \\ \mathcal{O} & \mathcal{O} & \Gamma_3 & \ldots \\ \vdots & \vdots & \vdots & \ddots \end{bmatrix}, \tag{2.211}$$

Or in shorthand notation:

$$\Gamma_R = \Gamma_1 + \Gamma_2 + \Gamma_3 + \ldots \tag{2.212}$$

Schur's lemma Let two irreducible representations Γ and Γ' of group G have the property: $\Gamma(g)S = S\Gamma'(g)$ for all elements $g \in G$, then either S is a zero matrix or S is a non-singular matrix so Γ and Γ' are equivalent.
Theorem: Representation is irreducible if and only if the only matrices that commute with all matrices of the representation are scalar multiples of the unit matrix.
Theorem: For any group G of order $|G|$ with elements $g_1, g_2, \ldots g_{|G|}$, the representation $\Gamma(G)$ will be irreducible if and only if:

$$\frac{1}{|G|} \sum_{i=1}^{|G|} |\chi(g_i)|^2 = 1, \tag{2.213}$$

where $\chi(g_i)$ is the character of matrix $\Gamma(g_i)$.

Theorem The number of irreducible representations is the same as the number of classes r and

$$\sum_{i=1}^{r} d_i^2 = |G|, \tag{2.214}$$

where $d_i = \dim \Gamma_i(G)$ and $\Gamma_i(G)$ are irreducible representations of G.
Definition: *Character table* of a group G is an $r \times r$ square array whose entries are $\chi^i(C_t)$, where C_t is a class of elements of G and $i, t = 1, 2, \ldots, r$. Examples of character tables for point groups T_d and O_h can be found in Appendix C and in Figure 2.1.

Basis of a representation

Definition: Representation of a group G is defined by a homomorphism γ which maps G to a group $T(G)$ of non-singular linear operators acting on a finite dimensional vector space $\mathbf{V}$ over the complex field. This is represented as $\gamma g = T(g)$ for all $g \in G$.

If γ is a representation it follows:

- $T(g_1)[T(g_2)\mathbf{x}] = T(g_1 g_2)\mathbf{x}$ for all $\mathbf{x} \in \mathbf{V}$ and $g_1, g_2 \in G$,
- $T(E)\mathbf{x} = \mathbf{x}$ for all $\mathbf{x} \in \mathbf{V}$, i.e. T_E is the identity operator,
- $[T(g)]^{-1}\mathbf{x} = T(g^{-1})\mathbf{x}$ for all $\mathbf{x} \in \mathbf{V}$ and $g \in G$,

and specially if γ is isomorphism, then $T(G)$ is a faithful representation.

Suppose that there is a basis of linearly independent vectors $\mathbf{x}_1, \mathbf{x}_2, \ldots, \mathbf{x}_n$ spanning over some vector space $\mathbf{V}$, and define matrices $\Gamma_\mathbf{x}(g)$ as:

$$T(g)\mathbf{x}_i = \sum_{j=1}^{d} [\Gamma_\mathbf{x}(g)]_{ij}\mathbf{x}_j, \tag{2.215}$$

where $\Gamma_\mathbf{x}(g)$ is the matrix representation of element g in the basis $\mathbf{x}$ of $\mathbf{V}$ obtained by the mapping γ. Set of all distinct non-singular matrices $\Gamma_\mathbf{x}(g)$ for all $g \in G$ form a unitary matrix group as a consequence of the homomorphic mapping $\gamma : \gamma g = T_\mathbf{x}(g)$, $\forall g \in G$.

Orthogonality relations

Assume that for some group G, of order $|G|$, and number of classes r, there are r irreducible representations $\Gamma_1, \Gamma_2, \ldots, \Gamma_r$, with dimensionality $d_1, d_2, \ldots, d_r$, respectively. These irreducible representations can be mapped onto matrices $D^{\Gamma_i}(g)_{\mu\nu}$, where g is the element in G and μ, ν are indices of the matrix.
Theorem: The orthogonality relation for matrix elements is

$$\frac{1}{|G|} \sum_{g}^{|G|} D^{\Gamma_i}(g)_{\mu\nu} D^{\Gamma_j}(g^{-1})_{\mu'\nu'} = \frac{\delta^{ij}}{d_i} \delta_{\mu\mu'} \delta_{\nu\nu'}, \tag{2.216}$$

where δ^{ij} is 1 for equivalent representations Γ_i, Γ_j and 0 for non equivalent. If the matrix group is unitary, then

$$\frac{1}{|G|}\sum_{g}^{|G|} D^{\Gamma_i}(g)_{\mu\nu}[D^{\Gamma_j}(g)_{\mu'\nu'}]^{\dagger} = \frac{\delta^{ij}}{d_i}\delta_{\mu\mu'}\delta_{\nu\nu'}, \tag{2.217}$$

where † makes the matrix adjoint: $[D^{\Gamma_j}(g)_{\mu'\nu'}]^{\dagger} = D^{\Gamma_j}(g)^{*}_{\nu'\mu'}$.
Theorem: The orthogonality relation for characters is (summation over group elements)

$$\frac{1}{|G|}\sum_{g}^{|G|} \chi^{\Gamma_i}(g)\chi^{\Gamma_j}(g^{-1}) = \delta^{ij}, \tag{2.218}$$

and if the matrix representation is unitary:

$$\frac{1}{|G|}\sum_{g}^{|G|} \chi^{\Gamma_i}(g)\chi^{\Gamma_j}(g)^{*} = \delta^{ij}. \tag{2.219}$$

Since all elements g_k of class C_k have the same character, the orthogonality theorem can be also expressed by visualizing the character table where classes and irreducible representations form a square table as seen in Figure 2.1.

When visualizing the character table, one can imagine a ruler that multiplies two characters from the same column with their class order $|C_k|$ but different (or same) rows and moves horizontally through the whole table, or equivalently using the following theorem:
Theorem: The orthogonality relation for characters is (summation goes over all classes C_k, $k = 1, \ldots, r$, where $|C_k|$ is the order of C_k):

$$\frac{1}{|G|}\sum_{r}^{k} \chi^{\Gamma_i}(g_k)\chi^{\Gamma_j}(g_k^{-1})|C_k| = \delta^{ij}, \tag{2.220}$$

and if the matrix representation is unitary:

$$\frac{1}{|G|}\sum_{k}^{r} \chi^{\Gamma_i}(g_k)\chi^{\Gamma_j}(g_k)^{*}|C_k| = \delta^{ij}. \tag{2.221}$$

Similarly, one can image the same ruler multiplying two characters from the same row, but different (or same) column with square roots their respectable class orders $\sqrt{|C_k|}$ and $\sqrt{|C_{k'}|}$ and moves vertically through the whole table, or equivalently using the following theorem:
Theorem: The orthogonality relation for characters is (summation over irreducible representations Γ_i for elements g_k in class C_k of order $|C_k|$)

$$\frac{1}{|G|}\sum_{i}^{r} \sqrt{|C_k|}\chi^{\Gamma_i}(g_k)\chi^{\Gamma_i}(g_{k'}^{-1})\sqrt{|C_{k'}|} = \delta_{kk'}, \tag{2.222}$$

and if the matrix representation is unitary:

$$\frac{1}{|G|}\sum_{i}^{r}\sqrt{|C_k|}\chi^{\Gamma_i}(g_k)\chi^{\Gamma_i}(g_{k'})^*\sqrt{|C_{k'}|}=\delta_{kk'}. \tag{2.223}$$

Using the above orthogonality relations of character combined with Eq. (2.214), one can deduce whether some representation is irreducible or not. If the representation is reducible, it will not obey the character orthogonal theorem. If the representation is indeed irreducible, obtained characters can be inserted into the character table and aid in finding the remaining irreducible representations.

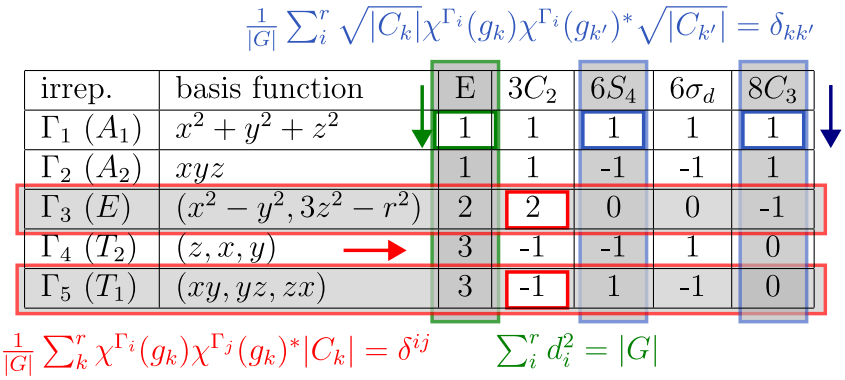

Figure 2.1. Visual example for using character orthogonality rules on T_d point group.

Character table and orthogonality relations

Figure 2.1 illustrates a character table of point group T_d and how to use character orthogonality rules with it. First two columns show names of irreducible representations and their respectable basis functions. Rest of the columns show the values of characters of their respective class in each representation. Classes are labeled using Schoenflies notation where E is the identity element, C_n is rotation by $2\pi/n$, σ_d is a reflection on a diagonal plane, and S_n is an improper rotation (rotation followed by a reflection in horizontal plane) by $2\pi/n$ and each preceding number shows the class order (for example, class $8C_3$ has 8 elements which represent rotation by $2\pi/3$). Adding all class orders one obtains the order of T_d point group

$$|G| = 1+3+6+6+8 = 24.$$

The red and blue rectangles depict an imaginary ruler that slides horizontally and vertically, respectively, while multiplying characters from the table for the summation. The red rectangle corresponds to Eq. (2.221), or in this case:

$$\frac{1}{24}\left[2\cdot 3\cdot 1+2\cdot(-1)\cdot 3+0\cdot 1\cdot 6+0\cdot(-1)\cdot 6+(-1)\cdot 0\cdot 8\right]=0.$$

The blue rectangle corresponds to Eq. (2.223), or in this case:

$$\frac{1}{24}\left[1\cdot 1+(-1)\cdot 1+0\cdot(-1)+(-1)\cdot 0+1\times 0\right]\sqrt{6}\sqrt{8}=0.$$

Finally, the green rectangle corresponds to Eq. (2.214), or in this case: $1^2+1^2+2^2+3^2+3^2=24$.

2.10.3 Double groups

The vector space $\mathbf{V}$ of the representation can be a space that spans over basis vectors or functions. In 3-dimensional space, rotations of geometric vectors is represented by 3×3 matrix group of unitary matrices $SO(3)$. From the full rotation group one can deduce that the character of a rotation around z-axes for angle α is:

$$\chi_l(\alpha)=\frac{\sin[(l+1/2)\alpha]}{\sin(\alpha/2)} \tag{2.224}$$

where l is the orbital angular momentum number connected to the orbital momentum operator $\mathbf{L}$ and takes integer values. Basis functions of the full rotation group are the spherical harmonics $Y_l^m(\theta,\phi)$, where m has integer value for projection of L onto the z-axis and has values of $m=-l,-l+1,\ldots,-1,0,1,\ldots l-1,l$. When spin-orbit interaction is included, the total momentum becomes $\mathbf{J}=\mathbf{L}+\mathbf{S}$, where $\mathbf{S}$ is the spin angular momentum that projects on z-axis with half-integer values $m_s=-1/2,+1,2$, allowing only half-integer values of $j=|l-s|,|l-s|+1,\ldots,l+s$ and it's z-axis projection $m_j=-j,-j+1,\ldots,j-1,j$. Replacing $l\to j$ in Eq. (2.224) one obtains the formula for characters when j has half-integer value. The characters of rotation by $\alpha+2\pi$ are:

$$\chi_j(\alpha)=\frac{\sin[(j+1/2)(\alpha+2\pi)]}{\sin[(\alpha+2\pi)/2]}=\frac{\sin[(j+1/2)\alpha]\cos[(j+1/2)2\pi]}{\sin(\alpha/2)\cos(\pi)}, \tag{2.225}$$

which leads to:

$$\chi_j(\alpha+2\pi)=\chi_j(\alpha)(-1)^{2j}. \tag{2.226}$$

This implies that 2π rotations and any rotations followed by 2π rotations should change sign if and only if j is half-integer. In order to include rotations for both integer and half-integer values of j, instead of $SO(3)$ one uses it's double cover, the $SU(2)$ group. The smallest dimension of $SO(3)$ representation is $d=1$ and it always returns identity after 2π rotation. Matrix representations are called single valued, therefore the name single (valued) groups. For $SU(2)$, the smallest dimension of representation is $d=2$, whose basis vectors are called spinors, and these matrices change sign after 2π rotation. Matrix representations are called double valued, therefore the name double (valued) groups.

The generators of $SU(2)$ group are 2×2 complex matrices called the Pauli matrices:

$$\sigma_x=\begin{bmatrix}0&1\\1&0\end{bmatrix},\quad \sigma_y=\begin{bmatrix}0&-i\\i&0\end{bmatrix},\quad \sigma_z=\begin{bmatrix}1&0\\0&-1\end{bmatrix}, \tag{2.227}$$

and they are the basis for the simplest representation of half-integer spin representation i.e. the $D_{1/2}$ representation.

To construct a double group G^d from single group G, one has to include $|G|$ more elements, which are constructed as a coset of G: $\mathcal{R}G$, where $\mathcal{R}$ represents 2π rotations. Even though number of elements and rank of a double group is doubled $|G^d| = 2|G|$, the number of classes r and irreducible representations will not necessary be also doubled. Rotations by π that have another perpendicular axes in it's class will share the class with rotations by $\pi + 2\pi$, otherwise $\pi + 2\pi$ rotations will be in a separate class. Rotations for all other angles will have a separate class when followed by a 2π rotation. All irreducible representations of G will also be irreducible representations of G^d, and will have the same characters for α and $\alpha + 2\pi$ rotations. For the rest of irreducible representations, characters must change sign after 2π rotation.

All rules and theorems for single groups also apply to double groups. Using Eq. (2.214), one can deduce the dimensions of the remaining irreducible representations. Among them, 2-dimensional $D_{1/2}$ representation must be one of them.

Double valued basis of spinors Ψ consists of two wave functions $\psi_\uparrow$ and $\psi_\downarrow$ for $+1/2$ and $-1/2$ spins, respectively, and they can be also represented as:

$$\begin{aligned}\Psi &= \psi_\uparrow + \psi_\downarrow = \psi_{+1/2}\,|\alpha\rangle + \psi_{-1/2}\,|\beta\rangle \\ &= \begin{bmatrix}\psi_{+1/2}\\ 0\end{bmatrix} + \begin{bmatrix}0\\ \psi_{-1/2}\end{bmatrix} = \begin{bmatrix}\psi_{+1/2}\\ \psi_{-1/2}\end{bmatrix}.\end{aligned} \tag{2.228}$$

The inclusion of double groups and spinors is essential for describing the spin-orbit coupling between electronic angular momentum and spin. In solid-state the inclusion of spin changes the degeneracy of states and can also introduce the spin splitting effect in crystals. Connecting the states to their corresponding irreducible representations Γ_i (non-degenerate to 1-dimensional representations and set of d-degenerate states to a d-dimensional representation) one can obtain the irreducible representations to which these states transform when spin is included by multiplying those single representations with $D_{1/2}$ representation. The product $\Gamma_i \otimes D_{1/2}$ should return Γ_j^d representation that appears only for double groups. If the product returns more than one representation, this corresponds to spin splitting of the states, each corresponding to irreducible representations found in that product. Examples for these products for T_d and O_h point groups can be found in B.1 and B.2 of the Appendix, respectively.

Character tables for T_d and O_h double groups can be found in Appendix C. Therein, the spinor $D_{1/2}$ representation is labeled as Γ_6 and Γ_6^+ for T_d and O_h, respectively.

Chapter 3

Construction of symmetry-adapted Kane Hamiltonians

This chapter is dedicated to construction of symmetry-adapted Hamiltonians relying on Kane's $\mathbf{k} \cdot \mathbf{p}$ theory presented in Sec. 2.6 and closely follows published work of the author (Ref. [46]). However, present chapter is limited to only the parts that concern bulk phase of the CdSe zincblende crystal along with cubic $CsPbX_3$ (X=Cl, Br, I). The procedure that is used to obtain band gaps for $CsPbX_3$ (X=Cl, Br, I) which follows Ref. [45] will be described later, in Chapter 4. The full discussion on nanostructures is contained in Chapter 5: for CdSe they are described in Sec. 5.4 and segments of Ref. [46], while for $CsPbX_3$ (X=Cl, Br, I) they can be found in Sec. 5.5 and in Ref. [47].

3.1 Introduction

Kane model proved to be both practical and successful in treating the electronic states in semiconductors [53, 55, 125, 51]. It is based on the representation of the single-particle wavefunction in terms of Bloch functions of the bulk material at a certain point in the Brillouin zone (typically the Γ point) and slowly varying envelope functions. The $\mathbf{k} \cdot \mathbf{p}$ Hamiltonian for a nanostructure is then an operator that acts on the column of envelope functions corresponding to each of the bulk bands.

Despite the success in using the $\mathbf{k}\cdot\mathbf{p}$ method for description of bulk band structure around a certain point in the Brillouin zone (usually the Γ point) and for treating the semiconductor nanostructures, there is still no systematic way to construct the $\mathbf{k} \cdot \mathbf{p}$ Hamiltonian for a given material and obtain the parameters of the Hamiltonian. The parameters of most conventional $\mathbf{k}\cdot\mathbf{p}$ Hamiltonians (such as the 8-band Hamiltonian [125, 126, 127]) for a few most common classes of semiconductors can be found in the literature [128, 129] and were obtained from the band gap and effective masses in the valence and conduction band. Parameters of $\mathbf{k} \cdot \mathbf{p}$ Hamiltonians with larger number of bands (such as, for example, the 30-band Hamiltonian [130, 131, 132, 133, 134])

are typically obtained by fitting to the calculated band structure of the material. However, given a relatively large number of fitting parameters, it is questionable if the fit gives unique parameters. It is also not clear what part of the Brillouin zone should be used in the fitting procedure, since it is not expected that the $\mathbf{k}\cdot\mathbf{p}$ method describes the bulk band structure throughout the whole Brillouin zone.

Given the fact that new classes of semiconductor materials and nanostructures based upon them emerge or find new applications quite often, it would be of significant interest to develop the procedure for construction of desired $\mathbf{k}\cdot\mathbf{p}$ Hamiltonians. Since all parameters of the $\mathbf{k}\cdot\mathbf{p}$ Hamiltonian are related to momentum matrix elements between single-particle wave functions of the bulk, it is in principle possible to obtain them from electronic structure calculation of the bulk material. This is indeed done when $\mathbf{k}\cdot\mathbf{p}$ is used as a method for interpolation of ab initio calculated band structure to a more dense grid of $\mathbf{k}$-points [135, 136, 137, 138]. However, there is a certain shortcoming of this approach when it comes to the construction of $\mathbf{k}\cdot\mathbf{p}$ Hamiltonians that should be used in future applications. Namely, due to the symmetry of the crystalline material the energy levels in characteristic points in the Brillouin zone are degenerate and for this reason the choice of Bloch wave functions from the Hilbert space spanned by the degenerate states is not unique. As a consequence, one may end up with different forms of the final $\mathbf{k}\cdot\mathbf{p}$ Hamiltonian depending on the particular choice of Bloch functions from this space. The number of Hamiltonian parameters in these forms might be significantly larger than the true number of parameters imposed by the symmetry of the crystal (demonstrated in B.3 of the Appendix and section II-C of the Supplementary Information of Ref. [46]).

This chapter is organized as follows. Sec. 3.2 starts by describing the procedure for construction of symmetry-adapted Hamiltonians based on Kane model found in Sec. 2.6. In Sec. 3.3 this procedure is applied for Hamiltonians that are based on zincblende CdSe and cubic $CsPbX_3$ (X=Cl, Br, I). Sec. 3.4 contains computational details for zincblende CdSe in the case of DFT and G_0W_0 calculations, in Sections 3.4.1 and 3.4.2, respectively. Computational details for cubic $CsPbX_3$ (X=Cl, Br, I) calculations are found in Chapter 4, which focuses on these materials, or more precisely in Sec. 4.3. Finally, numerical results showing the obtained electronic structures for zincblende CdSe and cubic $CsPbX_3$ (X=Cl, Br, I) are presented in Sec. 3.5 followed by conclusion in Sec. 3.6.

3.2 Construction of symmetry-adapted Hamiltonian

In Sec. 2.6, Kane model with Löwdin's perturbation was used to construct a $\mathbf{k}\cdot\mathbf{p}$ Hamiltonian, from which the so-called $\mathbf{k}\cdot\mathbf{p}$ parameters emerged $\mathbf{p}_{nm}$, and $P_{nm,ij}$ which are to be obtained using Bloch functions $\Psi_{\mathbf{k}_0 n}$ and energies $E_{\mathbf{k}_0 n}$ at point $\mathbf{k}_0$, which is referred to as *the unperturbed point* in 1BZ. Bands which are considered in the Hamiltonian directly, are called *main bands*, while the remaining bands enter the Hamiltonian as a second-order perturbation $P_{nm,ij}$ where they appear in the denominator and are called *remote bands*. The $\mathbf{k}\cdot\mathbf{p}$ equation from Sec. 2.6 that is

used to construct the Hamiltonian from ab initio methods in this chapter is:

$$\begin{aligned}
\sum_m H_{nm} B_m^{(a)} &= \sum_m \left(H_{nm}^{(0)} \delta_{nm} + H_{nm}^{(1)} + H_{nm}^{(2)} \right) B_m^{(a)} = E_{\mathbf{k}n} B_m^{(a)}, \\
H_{nm}^{(0)} &= E_{\mathbf{k}_0 m} + \frac{\hbar^2}{2m_e} (\mathbf{k} - \mathbf{k}_0)^2, \\
H_{nm}^{(1)} &= \frac{\hbar}{m_e} (\mathbf{k} - \mathbf{k}_0) \cdot \mathbf{p}_{nm}, \\
H_{nm}^{(2)} &= \sum_{ij} \frac{\hbar (\mathbf{k} - \mathbf{k}_0)_i}{m_e} P_{nm,ij} \frac{\hbar (\mathbf{k} - \mathbf{k}_0)_j}{m_e}, \\
\mathbf{p}_{nm} &= \langle \Psi_{\mathbf{k}_0 n} | \, \mathbf{p}_{\mathrm{soc}} \, | \Psi_{\mathbf{k}_0 m} \rangle = \hbar \mathbf{k}_0 \delta_{nm} + \langle u_{\mathbf{k}_0 n} | \, \mathbf{p}_{\mathrm{soc}} \, | u_{\mathbf{k}_0 m} \rangle \,, \\
P_{nm,ij} &= \sum_{r \neq [m,n]} \frac{(\mathbf{p}_{nm})_i (\mathbf{p}_{nm})_j}{(E_{\mathbf{k}_0 n} + E_{\mathbf{k}_0 m})/2 - E_{\mathbf{k}_0 r}}, \qquad i,j = x,y,z \quad ,
\end{aligned} \tag{3.1}$$

where main bands are labeled with m, n indices, while remote bands are labeled with r indices, and $H_{nm}^{(0)}$, $H_{nm}^{(1)}$, and $H_{nm}^{(2)}$ are matrix elements of zeroth, first and second -order terms in the Hamiltonian $\mathcal{H}$, respectively. Since $\mathbf{k} \cdot \mathbf{p}$ theory is applicable only in small region around $\mathbf{k}_0$ the relativistic term for electron kinetic energy is neglected since it is negligible in the 1BZ. For similar reason, SOC modification to momentum operator $\mathbf{p}_{\mathrm{soc}}$ can also be neglected $\mathbf{p}_{\mathrm{soc}} \approx \mathbf{p}$, while SOC contributions are contained to zero-th order in energies $E_{\mathbf{k}_0 n}$ and in eigenstates $\Psi_{\mathbf{k}_0 n}$.

In Sec. 2.4, it was shown that any $\mathbf{k}$ point in 1BZ has symmetry operations which form a group $G_{\mathbf{k}}$ which is a sub group of the whole crystal symmetry G_Γ. Unperturbed point $\mathbf{k}_0$ is often chosen as a point with full crystal symmetry or some other high symmetry point, and often the main bands in the Hamiltonian will be degenerate. The allowed degeneracies depend on the dimensions of the irreducible representations contained in the point group $G_{\mathbf{k}_0}$ which correspond to these states. When degenerate states are included the issue of uniqueness of the Hamiltonian arises.

Let d be the degeneracy of the set of eigenstates $|\phi_1\rangle, |\phi_2\rangle, \ldots, |\phi_d\rangle$ at $\mathbf{k}_0$ and let $\mathcal{H}_d$ be Hilbert space spanned by these states. The states $|\phi_1\rangle, |\phi_2\rangle, \ldots, |\phi_d\rangle$ will form an orthonormal basis of $\mathcal{H}_d$ but any other orthonormal basis may be chosen. Different basis would give different momentum matrix elements $\mathbf{p}_{nm}$ which would result in a different form in $H_{nm}^{(1)}$ and $H_{nm}^{(2)}$. This arbitrary choice might not lead to a minimal number of unique parameters in the Hamiltonian, which would be imposed by the group $G_{\mathbf{k}_0}$.

Eigenstates $\Psi_{\mathbf{k}_0 n}$ obtained from DFT might not give the desired form of the Hamiltonian H_{nm}, in a sense that this initial form will appear to have more parameters than the ones found in literature for the same structure. Indeed, this is often the case however, the desired form of H_{nm} can be obtained by applying a unitary transformation to those eigenstates.

If a set of eigenstates $|\phi_1\rangle, |\phi_2\rangle, \ldots, |\phi_d\rangle$ was obtained from DFT, it cannot be deduced from DFT alone to which irreducible representation this set will correspond to. This set will form matrices $\Gamma(g)$ of some irreducible representation of the group

$G_{\mathbf{k}_0}$ which are given as:

$$\Gamma_{mn}(g) = \langle \phi_m | \, P(g) \, | \phi_n \rangle \,, \tag{3.2}$$

where g is an element of the group $G_{\mathbf{k}_0}$ and $P(g)$ is the operator that applies the symmetry operation g on the given eigenstate. The matrices $\Gamma(g)$ are obtained by direct calculation from Eq. (3.2). Once $\Gamma(g)$ matrices for all g are obtained, their characters are compared with the known character tables of $G_{\mathbf{k}_0}$ in order to identify which irreducible representation they belong to. Conventional matrices $\Gamma^{'}(g)$ can be found in group theory literature or databases of point groups. Since there are many ways to represent $\Gamma^{'}(g)$, they might differ from the source. For the results found in this chapter, the Bilbao crystallographic server was used. Matrices $\Gamma^{'}(g)$ and $\Gamma(g)$ are connected by a unitary transformation U:

$$U^{\dagger}\Gamma(g)U = \Gamma^{'}(g), \tag{3.3}$$

which is true for every $g \in G_{\mathbf{k}_0}$. This same unitary transformation U from Eq. (3.3) also transforms basis set $|\phi_i\rangle$ to a new basis $|\psi_j\rangle$, where $i, j = 1, 2, \ldots, d$:

$$\begin{aligned} |\psi_j\rangle &= \sum_{i=1}^{d} U_{ij} \, |\phi_i\rangle \,, \\ \langle \psi_j | &= \sum_{i=1}^{d} \langle \phi_i | \, U^{*}_{ji}. \end{aligned} \quad , \tag{3.4}$$

In the new basis $|\psi_j\rangle$, operator $P(g)$ from Eq. (3.2) will produce the conventional $\Gamma^{'}(g)$ matrices:

$$\begin{aligned} P(g)_{ij} &= \langle \psi_i | \, P(g) \, | \psi_j \rangle \\ &= \sum_{km} \langle \phi_k | \, U^{\dagger}_{ki} P(g) U_{mj} \, | \phi_m \rangle \\ &= \sum_{km} U^{\dagger}_{ki} \, \langle \phi_k | \, P(g) \, | \phi_m \rangle \, U_{mj} \\ &= \sum_{km} U^{*}_{ik} \Gamma(g)_{km} U_{mj} \\ &= \Gamma^{'}(g)_{ij}. \end{aligned} \tag{3.5}$$

In the $|\psi_j\rangle$ basis, the block in H_{mn} that corresponds to these degenerate states will have a more convenient, *symmetry-adapted* form in which relevant parameters and their symmetry can easily be identified. If H_{mn} has several sets of degenerate states α with degeneracy d_α, a corresponding U^{α} must be obtained for each of those degenerate sets and transform their basis in order to obtain a full symmetry-adapted Hamiltonian:

$$\left|\psi^{\alpha}_{j}\right\rangle = \sum_{i}^{d_\alpha} U^{\alpha}_{ij} \left|\phi^{\alpha}_{j}\right\rangle \tag{3.6}$$

Furthermore, in the new symmetry adapted basis $\left|\psi^{\alpha}_{j}\right\rangle$, the Hamiltonian $\mathcal{H}$ can be divided in blocks $\mathcal{B}(\Gamma^{'}_{\alpha}, \Gamma^{'}_{\beta})$ which consist of first and second-order terms that contain

products from degenerate sets $|\psi^\alpha\rangle$ (d_α degenerate) and $|\psi^\alpha\rangle$ (d_β degenerate) which transform in accordance with the irreducible representations $\Gamma^{'}_{\alpha}$ (d_α dimensional) and $\Gamma^{'}_{\beta}$ (d_β dimensional), respectively.

As mentioned in Sec. 2.6 and explained in detail in Ref. [48, 51], Luttinger used the method of invariants, which is a systematic way to obtain the minimal number of parameters just by symmetry properties for $\mathcal{B}(\Gamma^{'}_{\alpha}, \Gamma^{'}_{\beta})$ blocks. This method however, is unable to produce the numerical value for such parameters. Using this procedure to transform initial Hamiltonian from ab initio methods to symmetry adapted form links the Luttinger method (from 1955.) to modern numerical ab initio calculations and enables the reconstruction of Luttinger parameters for any symmetry and any material.

Equivalently, one can transform the H_{mn} directly using a block diagonal matrix that contains all unitary transforms for all states, degenerate and non-degenerate:

$$\mathcal{H}^{\text{sym.ad.}} = U^\dagger \mathcal{H}^{\text{init}} U, \qquad U = \text{diag}(U^1, U^2, \ldots U^\alpha, \ldots), \tag{3.7}$$

where $\mathcal{H}^{\text{sym.ad}}$ and $\mathcal{H}^{\text{init}}$ are the symmetry-adapted and initial Hamiltonian. For non-degenerate states, or states that do not need to be transformed that block would just be an identity matrix $U^\alpha = \mathbb{1}$.

The procedure of obtaining a unitary transformation U which connects $\Gamma^{'}(g)$ and $\Gamma(g)$ has been developed in Ref. [139] and will be outlined here. One firsts obtains a set of coefficients r_{ab} as:

$$r_{ab} = \sqrt{\frac{n_\Gamma}{|G|}} \left(\sum_{g \in G} \Gamma_{aa}(g) \Gamma^{'}_{bb}(g^{-1}) \right)^{1/2}, \tag{3.8}$$

where $\Gamma_{aa}(g)$ and $\Gamma^{'}_{bb}(g)$ are known matrix elements for the symmetry operation (group element) g and its inverse g^{-1}, respectively, $|G|$ is the order of the group G, while n_Γ is the dimension of the representations Γ and $\Gamma^{'}$. This will produce multiple r_{ab}, but only the pairs (a, b) for which $r_{ab} > 0$ can be chosen. In Ref.[139], it was proven that such a pair must exist. The matrix U is then obtained from:

$$U_{ij} = \frac{1}{r_{ab}} \frac{n_\Gamma}{|G|} \sum_{g \in G} \Gamma_{ia}(g^{-1}) \Gamma^{'}_{bj}(g). \tag{3.9}$$

To summarize, obtaining a symmetry-adapted Hamiltonian H_{mn} from any ab initio method is done by the following steps:

- Perform ab initio calculation of the band structure for bulk.
- Chose the unperturbed point $\mathbf{k}_0$ in the 1BZ that is most suited for the $\mathbf{k} \cdot \mathbf{p}$ expansion and extract the band energies $E_{\mathbf{k}_0 n}$ and their eigenstates $\Psi_{\mathbf{k}_0 n}$ obtained in the previous step.
- Select the states that enter the Hamiltonian H_{mn} and identify their corresponding irreducible representations within the point group $G_{\mathbf{k}_0}$ by calculating $\Gamma^\alpha(g)$ from Eq. (3.2) and comparing their characters with the ones in the literature or irreducible representation databases.

- Once all $\Gamma^{\alpha}(g)$ for each degenerate set of states α are obtained, match them with the corresponding $\Gamma^{'}(g)$ matrices found in literature or some irreducible representation database.

- Calculate U^{α} for each set of degenerate states $|\phi^{\alpha}\rangle$ using $\Gamma^{\alpha}(g)$ with their corresponding $\Gamma^{'}(g)$ from Eq. (3.8) and Eq. (3.9).

- Apply U^{α} to $|\phi^{\alpha}\rangle$ and obtain symmetry-adapted basis functions $|\psi^{\alpha}\rangle$ using Eq. (3.6).

- Evaluate the momentum matrix elements in $|\psi^{\alpha}\rangle$ basis to obtain the symmetry-adapted Hamiltonian, or equivalently transform $\mathcal{H}^{\text{init}}$ with block diagonal $U = \text{diag}(U_1, U_2, \ldots, U_{\alpha}, \ldots)$ using Eq. (3.7).

It is obvious that this method is not limited to any particular crystal symmetry or only high symmetry $\mathbf{k}_0$ points. However, it is most advantageous for crystals and $\mathbf{k}_0$ points with the higher order. If one had to calculate several materials that share the same symmetry, one would only need to keep track of minimal number of required parameters and their numerical value while keeping the analytical form of the Hamiltonian fixed. Since DFT and similar ab initio procedures can be computationally demanding, all these parameters can be obtained for one material, and then stored in a database where they could be available for others to use for much less computationally demanding $\mathbf{k} \cdot \mathbf{p}$ calculations. Moreover, these same parameters can be used for $\mathbf{k} \cdot \mathbf{p}$ Hamiltonians that use Burt-Foreman envelope function method for nanostructures, as seen in Sec. 5.2, where from a numerical point, the computational resource requirements can be significantly reduced with a fully symmetric and a minimal set of parameters.

3.3 Analytical results: Blocks of the Hamiltonian

Blocks of symmetry-adapted Hamiltonian are considered for CdSe and $CsPbX_3$ (X=Cl, Br, I). The former CdSe, is a zincblende crystal with T_{d} symmetry, while the later $CsPbX_3$, is a cubic perovskite with O_{h} symmetry[1]. Both materials have a direct gap, CdSe at the Γ point and $CsPbX_3$ at the R point, which will be considered as their respectable unperturbed points $\mathbf{k}_0$. Hamiltonian of two sizes is considered: a smaller, here referred as a standard 4×4 (8×8) Hamiltonian and a larger, here referred as an extended 13×13 (26×26) Hamiltonian for the case when SOC is omitted (included).

When SOC is included, previously obtained states without SOC, that correspond to irreducible representations of a single point group, will either split or become double degenerate states, that correspond to irreducible representations of double point groups. This splitting or turning into double degenerate states corresponds to multiplying single irreducible representations with spinor representation of that point group. Multiplication table of single irreducible representations with spinor

[1] O_{h} contains all symmetry operations of T_{d}, plus inversion.

representation for T_{d} (O_{h}) can be found in Eq. (B.14) in B.1 [Eq. (B.27) in B.1] of the Appendix. The case when degenerate bands are split into two sets of degenerate bands due to inclusion of SOC is referred to as spin splitting of the bands.

Labels of bands are as follows: CBM and VBM are conduction band minima and valence band maxima, and CBMx (VBMx) are bands that are x levels higher (lower) than CBM (VBM). Bands that are included in the Hamiltonians are presented in Figure 3.1, where splitting due to inclusion of SOC is illustrated. The Hamiltonian

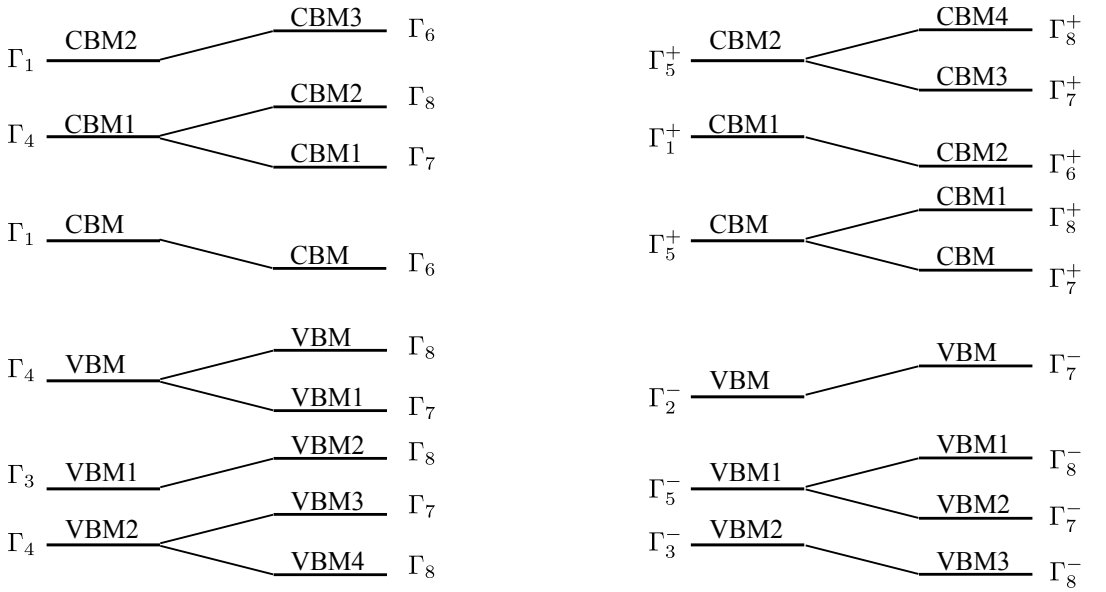

Figure 3.1. Bands that are included in the extended Hamiltonian and their double group partners for CdSe (T_{d} group, left) and $CsPbX_3$ (O_{h} group, right). Bands: Γ_1, Γ_1^+, and Γ_2^- non-degenerate, Γ_3, Γ_3^-, Γ_7, and $\Gamma_7^\pm$ are 2-fold degenerate, Γ_4 and $\Gamma_5^\pm$ are 3-fold degenerate, Γ_8 and $\Gamma_8^\pm$ are 4-fold degenerate. Notation follows the one found in Ref. [124].

is divided into blocks, where each block $\mathcal{B}(\Gamma_a, \Gamma_b)$ contains first and second-order $\mathbf{k}\cdot\mathbf{p}$ parameters in symmetry adapted basis, connecting Γ_a and Γ_b (non) degenerate states. If these blocks connect the same states they are absolutely diagonal. If they connect two same irreducible representations from different states they are irrep diagonal. The rest are off-diagonal blocks.

Figure 3.2 and Figure 3.3 illustrate blocks $\mathcal{B}(\Gamma_\alpha, \Gamma_\beta)$ that are present in the CdSe Hamiltonian when SOC is omitted and included. Absolutely diagonal and irrep-diagonal states are represented with colored squares while off-diagonals are represented with gray squares. In the case of the zincblende CdSe, the T_{d} point group doen't have inversion. So states do not have any parity, hence there are irrep-diagonal blocks that connect valence and conduction states in the extended Hamiltonian. When symmetry adaptation procedure is applied, each block is obtained with the smallest number of parameters, and this number is determined by the point group of the crystal. Analytical expressions for all the elements of all blocks of the $\mathbf{k}\cdot\mathbf{p}$ Hamiltonian are given in Sec. B.1 of the Appendix as well as in Supplementary Information of Ref. [46], in the case of T_{d}, and in Sec. B.2 of the

Appendix for O_h point group. It can be checked that the same form of the blocks of the Hamiltonian is obtained when Luttinger's method of invariants is applied [54, 51]. Also, the standard four-band Hamiltonian obtained there coincides with the second-order four-band Kane Hamiltonian [51]. The standard eight-band Hamiltonian obtained in Ref. [46] coincides with Weiler eight-band Hamiltonian [126, 51], after an appropriate unitary transformation is made. Numerical parameters for all Hamiltonians as well as unitary transformation that leads to Weiler Hamiltonian can be found in Supplementary Information of Ref. [46].

The advantage of symmetry-adapted form over the initial form of the $\mathbf{k}\cdot\mathbf{p}$ Hamiltonian is illustrated in the Appendix B.3. The number of parameters can be drastically reduced after the unitary transform which brings initial Hamiltonian into the symmetry-adapted form. Namely, 1 and 5 parameters in the symmetry-adapted form for the first and the second-order terms, respectively, compared to 5 and 49 first and second-order terms, respectively, in the initial form, just for the simplest 4×4 Hamiltonian. This shows clear advantage in terms of simplicity for any use of these Hamiltonians like for e.g. in calculating electronic structure for nanostructures.

In the case of cubic perovskite $CsPbX_3$, where O_h group is just T_d with inversion around the center, irreducible representations can have different parity (+ or −). Since the $\mathbf{p}$ corresponds to irreducible representation Γ_{15}^-, which has odd parity, states connected with the same parity will only have second-order terms, while states connected with opposite parity will have only first-order terms, according to symmetry rules. All conduction states have + parity while all valence states have − parity, so there will be no irrep-diagonal states that mix conduction and valence electrons.

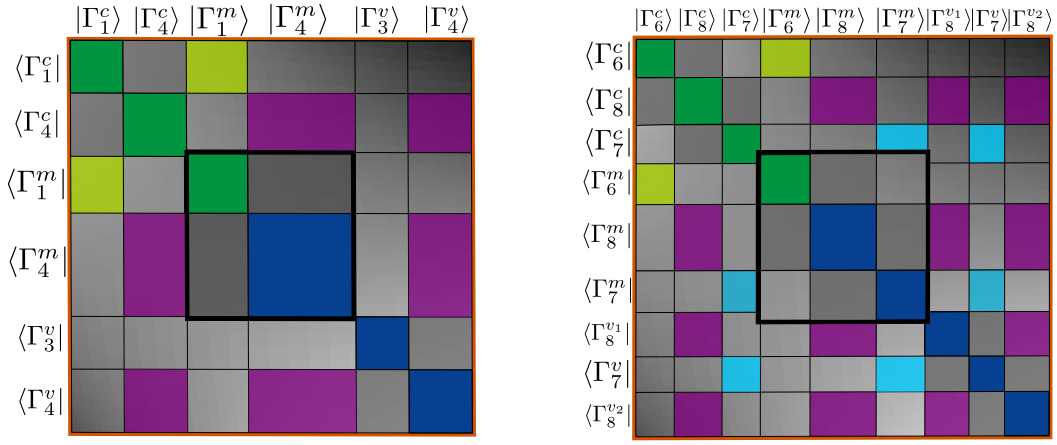

Figure 3.2. The matrix form of $\mathbf{k}\cdot\mathbf{p}$ Hamiltonian obtained when SOC is omitted (left); included (right) for zincblende CdSe. Labels of the bands are based on their corresponding irreducible representations with superscripts which denote bands that form the gap -m, bands that correspond to higher conduction states -c, and lower valence states -v. Each block of the matrix contains the terms that originate from matrix elements between the states that transform according to irreducible representation specified on the left and above the matrix. The central square marked with thick black lines denotes the smaller standard Hamiltonian.

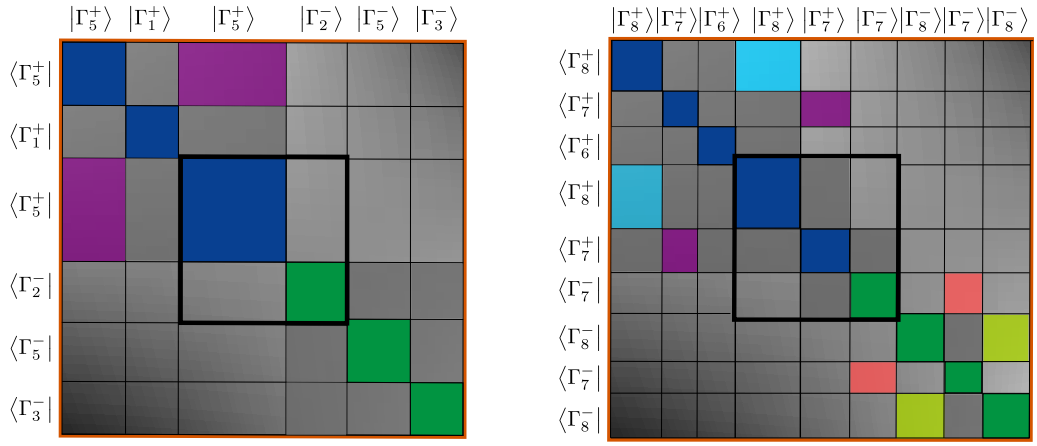

Figure 3.3. The matrix form of $\mathbf{k}\cdot\mathbf{p}$ Hamiltonian obtained when SOC is omitted (left); included (right) for cubic perovskite $CsPbX_3$. Labels of the bands are based on their corresponding irreducible representations. In this case conduction states have + parity, while all valence states have − parity. Each block of the matrix contains the terms that originate from matrix elements between the states that transform according to irreducible representation specified on the left and above the matrix. The central square marked with thick black lines denotes the smaller standard Hamiltonian.

All $\mathcal{B}(\Gamma_a, \Gamma_b)$ blocks for T_d single and double point group as well as for O_h double group can be found in B.1 and B.2 of the Appendix, respectively. Point group character tables for both T_d and O_h are in Appendix C.

3.4 Computation details

This section lists computational details for CdSe cubic crystal used for this chapter, namely ones used in DFT and G_0W_0 calculations. Relevant parameters and codes used for DFT with semi-local functional as well as hybrid functional for $CsPbX_3$ (X=Cl,Br,I) can be found in Chapter 4 in Sections 4.3.1 and 4.3.2, respectively and in Ref. [45].

Numerical parameters for symmetry-adapted $\mathbf{k}\cdot\mathbf{p}$ Hamiltonian blocks for zinc-blende CdSe, obtained using DFT with semi-local functional PBEsol and using the G_0W_0, can be found in Ref. [46]. Numerical parameters for symmetry-adapted $\mathbf{k}\cdot\mathbf{p}$ Hamiltonian blocks for cubic $CsPbX_3$ (X=Cl, Br, I) $\mathbf{k}\cdot\mathbf{p}$ Hamiltonians, obtained using DFT with semi-local functional PBEsol (for Cl, Br) and PBE (for I) can be found in Ref. [140].

3.4.1 DFT

The band energies and wave functions were obtained from DFT where exchange-correlation energy was modeled using the Perdew-Burke-Ernzerhof generalized gradient approximation revised for solids (PBEsol) [76]. Calculations were performed

using the Quantum Espresso code [96, 97]. Core electrons were modeled using fully relativistic optimized norm-conserving Vanderbilt pseudopotentials [141, 142].

For CdSe, the $10 \times 10 \times 10$ grid in reciprocal space of the Brillouin zone was used, while the kinetic energy cutoff of the plane waves used to represent the wave functions was 90 Ry. The lattice constant of $a = 6.096$ Å, obtained by minimization of the energy of the structure, was used in all subsequent calculations.

3.4.2 $\mathbf{G_0W_0}$

The G_0W_0 calculations for zincblende CdSe were performed using the Yambo code [87, 88], with input Kohn-Sham wave functions obtained from previous DFT calculation on the $4\times4\times4$ grid in reciprocal space. Plasmon-pole approximation was used to account for the frequency dependence of the dielectric function. Kinetic energy cutoff used for the calculation of dielectric function in G_0W_0 calculation was 50 Ry. The corresponding number of bands was 400 (800), while the number of bands used in the evaluation of self-energy was 300 (600) in the case when spin-orbit interaction is omitted (included). It is estimated that these values yield numerical accuracy of 20 meV or better for band energy corrections.

3.5 Numerical results

In Figure 3.4 the plot for the band structure of zinc-blende CdSe is shown. Results are obtained from a standard DFT calculation and from diagonalizing the $\mathbf{k}\cdot\mathbf{p}$ Hamiltonian for a path in $\mathbf{k}$-space. Two cases for Hamiltonian size are presented: standard 4×4 (8×8) and extended 13×13 (26×26) when the SOC is omitted (included).

The expected result, that the extended Hamiltonian would produce a band structure that is quantitatively and qualitatively closer to the full DFT than the standard one is confirmed on the plot. The preferred strategy to adding states to standard Hamiltonian is to add them symmetrically around the main states, until enough states ensure that qualitative trend of the band structure is followed in the whole 1BZ and that adding more states doesn't give significant improvement, since more states would require more computational resources for nanostructures. Adding more valence than conduction states or vice-versa to the standard Hamiltonian could lead to closing of the gap at points away from $\mathbf{k}_0$ which is the Γ point in this case. In this case this was more prone to happen if the number of conduction states added was greater than the number of valence states added. If such spurious states were to occur, this would prevent any further application of the $\mathbf{k}\cdot\mathbf{p}$ Hamiltonian to the nanostructure. Opting for 13(26) states in the extended Hamiltonian was a compromise between (a) accurate description of the band structure in the largest area of the 1BZ as possible, (b) to use a reasonable amount of bands to do so and (c) to avoid appearance of any spurious states that would close the gap.

The accuracy of standard and extended Hamiltonians, against the DFT in terms of band structure is presented in Figure 3.5. Results show the maximal absolute dif-

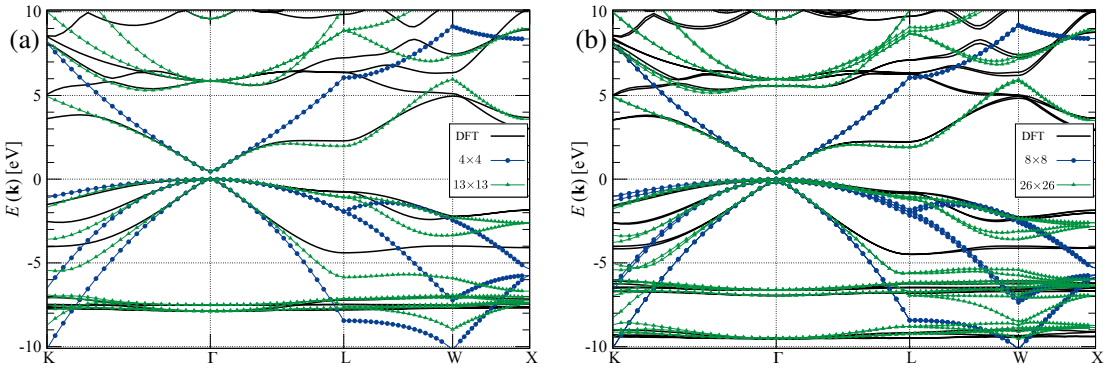

Figure 3.4. Band structure of zincblende CdSe calculated using DFT and using standard and extended $\mathbf{k} \cdot \mathbf{p}$ Hamiltonian when the effects of spin-orbit interaction are: (a) omitted; (b) included.

ference between $\mathbf{k} \cdot \mathbf{p}$ and DFT band structure when moving away from the $\mathbf{k}_0$ point (Γ in this case) within a sphere of radius k_r in the 1BZ. The standard (extended) Hamiltonian produce a band structure that differs no more than 4 eV (1.75 eV) inside the sphere inscribed in the 1BZ, with a difference not greater than 45 meV (35 meV) inside a sphere of radius $k_r = 0.2$ in units of $2\pi/a$, where a is the lattice constant. Figure 3.5 shows that in the reasonable vicinity of $\mathbf{k}_0$, in any direction, the extended Hamiltonian produces a significantly better band structure to the one obtained with the standard Hamiltonian, when compared to DFT. If only the low field electrical properties or the optical properties at photon energies just above the gap are needed, the standard Hamiltonian is usually sufficient. However, if optical properties in a wider range of energies (which would be relevant in the case of solar cells), or transport at larger electrical field (which would be relevant in field-effect transistors) is required, the extended Hamiltonian provides a good description for all relevant electronic states.

So far, the results considered only the Hamiltonians constructed from wave functions and energies obtained from DFT using PBEsol functional. It is well known that the DFT typically underestimates the band gap when compered to the experimental result. In this case, the DFT gap using PBEsol functionals is 0.47 eV and 0.40 eV when SOC is omitted and included, respectively, which is not a good value when compared to the experimental one of 1.71 eV [143]. Since the methodology of $\mathbf{k} \cdot \mathbf{p}$ in general, is by no means limited to only DFT wave functions and energies, it would be useful to construct these same Hamiltonians with parameters that provide a much closer gap to the experimental result. One way to do so, is to calculate the band structure using many-body perturbation theory in the GW approximation [80], mentioned in Sec. 2.7.5. Here, the G_0W_0 variant of GW approximation is used, in which the self-energy is obtained from Green's function G_0 of an electron in DFT Kohn-Sham potential, without further iterations. The G_0W_0 calculation provides band gaps of 1.77 eV and 1.60 eV, without and with SOC, respectively, which is in a much better agreement with the experimental value.

The energies $E^{\mathrm{GW}}_{\mathbf{k}_0 n}$ obtained from G_0W_0 method are used to obtain $P_{nm,ij}$ param-

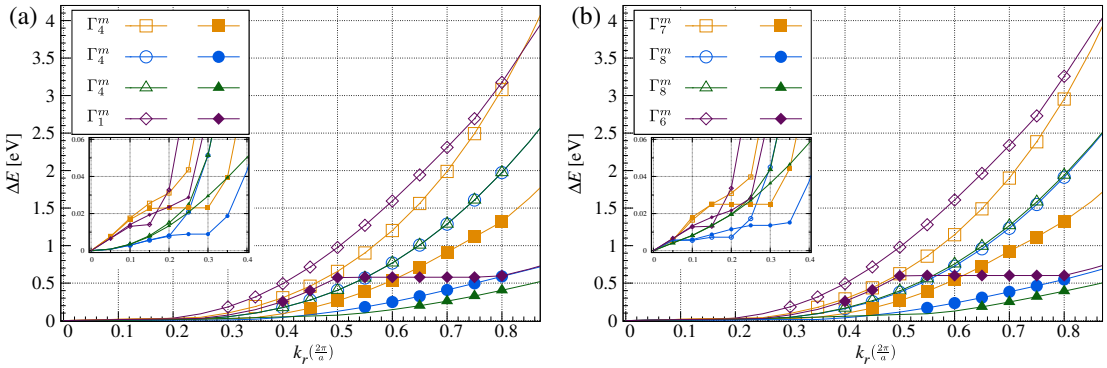

Figure 3.5. Maximal absolute difference ΔE between the band energy obtained from DFT and $\mathbf{k}\cdot\mathbf{p}$ within the region of the Brillouin zone in the shape of a sphere of radius k_r centered at Γ when the effects of spin-orbit interaction are: (a) omitted; (b) included. The difference is shown for main bands where the results obtained using standard $\mathbf{k}\cdot\mathbf{p}$ Hamiltonian are shown using empty symbols, while the results obtained using the extended $\mathbf{k}\cdot\mathbf{p}$ Hamiltonian are shown using filled symbols. Insets show a zoom of the same graph in the region around $k_r = 0$.

eters for standard and extended Hamiltonians. The band structure obtained from these parameters when SOC included is presented in Figure 3.6.

Besides the G_0W_0 method, one could perform a DFT calculation using hybrid functional like PBE0 (described in Sec. 2.7.3) which has proved to be much more useful when obtaining electronic structure for the cubic phase of cesium-lead-halide perovskites $CsPbX_3$ (X=Cl, Br, I). The computational resources required for hybrid functional are similar to those of the G_0W_0 method. However since the cubic phase of perovskites has 5 atoms per unit cell, compared to 2 atoms which are present in the zincblende CdSe case, it wasn't computationally feasible to obtain energies for higher states that are required for second-order parameters $P_{nm,ij}$ to converge. In this case, the correction to DFT obtained parameters is only to the zero-th order i.e. energies $E_{\mathbf{k}n}$ are replaced with the ones obtained from hybrid DFT calculation while first and second-order parameters $\mathbf{p}_{nm}$ and $P_{nm,ij}$ remain the same as the ones obtained from the standard DFT calculation. Furthermore, because the cubic phase for these perovskites is only observed at high temperatures, another correction has to be included to the zero-th order parameters. At high temperatures where the cubic phase is formed for $CsPbX_3$ perovskites, phonon-induced renormalization for band energies is significant and it will be discussed in detail in Chapter 4. This phonon-induced renormalization is introduced with the electron-phonon self-energy $\Sigma(T)$ which has a strong temperature dependence. In Figures 3.7, 3.8 and 3.9 band structure obtained from standard (8×8) and extended (26×26) Hamiltonians with PBE0 energies and $\Sigma(T)$ is compared to the one obtained from standard DFT.

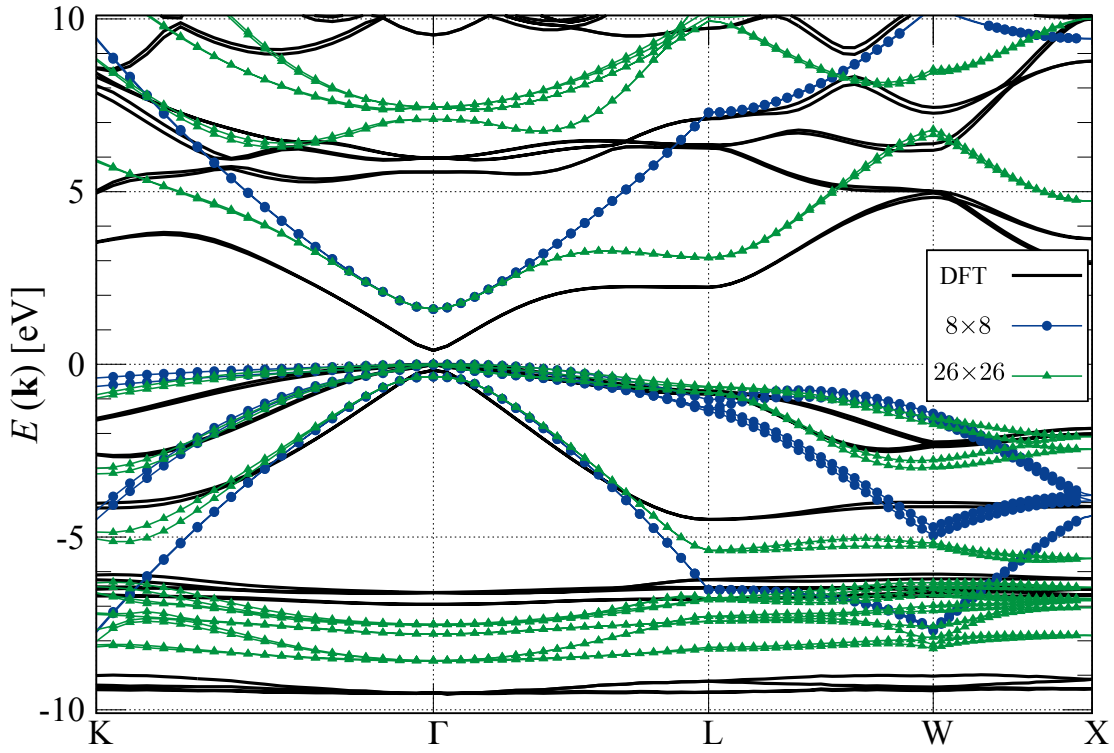

Figure 3.6. Band structure of zincblende CdSe calculated using standard and extended $\mathbf{k}\cdot\mathbf{p}$ Hamiltonian parametrized starting from band energies obtained in G_0W_0 calculation. DFT results are given for comparison.

3.6 Conclusion

In conclusion, this chapter presented a method that allows automatic construction of $\mathbf{k}\cdot\mathbf{p}$ Hamiltonians in their symmetry-adapted form starting from output of ab initio band structure calculation of bulk material. This method was then applied to construct the $\mathbf{k}\cdot\mathbf{p}$ Hamiltonians for zincblende CdSe and cubic $CsPbX_3$ (X=Cl, Br, I) materials. While construction and parameterization of $\mathbf{k}\cdot\mathbf{p}$ Hamiltonians is usually believed to be a rather difficult and time consuming task, it is the author's expectation that the method presented in this chapter will change the situation and that it will be straightforward in the future to obtain $\mathbf{k}\cdot\mathbf{p}$ Hamiltonians for new materials and apply them to study electronic properties of nanostructures based on these materials without the need to perform any kind of fitting.

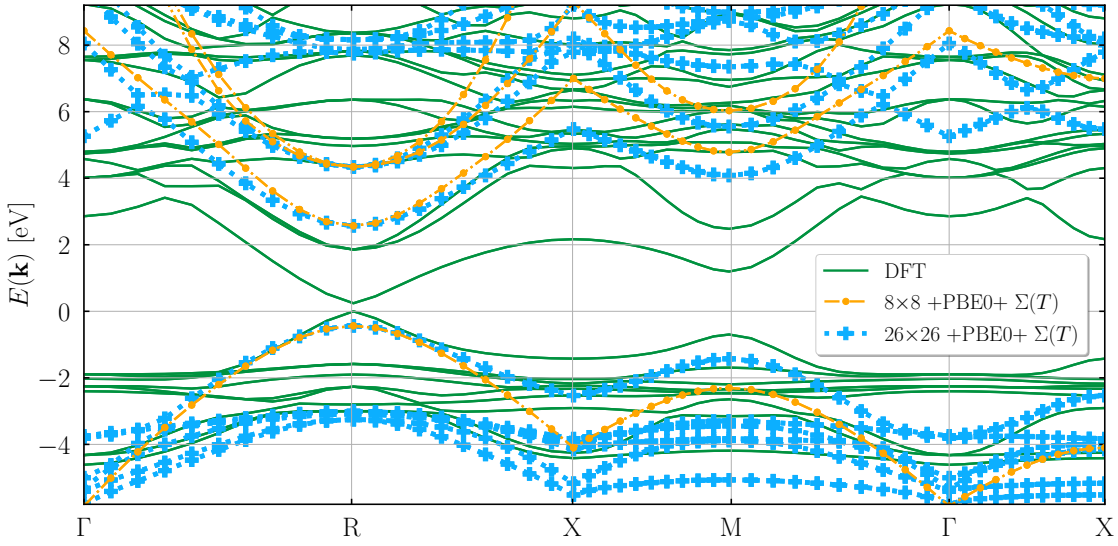

Figure 3.7. Band structure of the cubic phase of $CsPbCl_3$ calculated using standard and extended $\mathbf{k}\cdot\mathbf{p}$ Hamiltonian parametrized using band energies obtained using hybrid PBE0 functional and self-energy correction $\Sigma(T)$ at T=320 K that stems from the phonon-induced renormalization of band energies. DFT results obtained with PBEsol functional are also given for comparison.

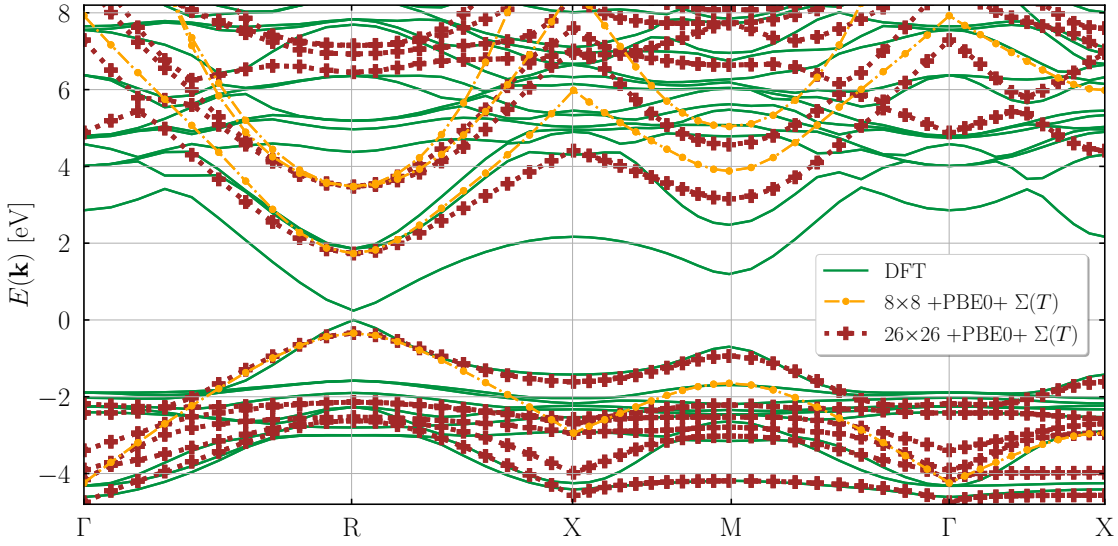

Figure 3.8. Band structure of the cubic phase of $CsPbBr_3$ calculated using standard and extended $\mathbf{k}\cdot\mathbf{p}$ Hamiltonian parametrized using band energies obtained using hybrid PBE0 functional and self-energy correction $\Sigma(T)$ at T=400 K that stems from the phonon-induced renormalization of band energies. DFT results obtained with PBEsol functional are also given for comparison.

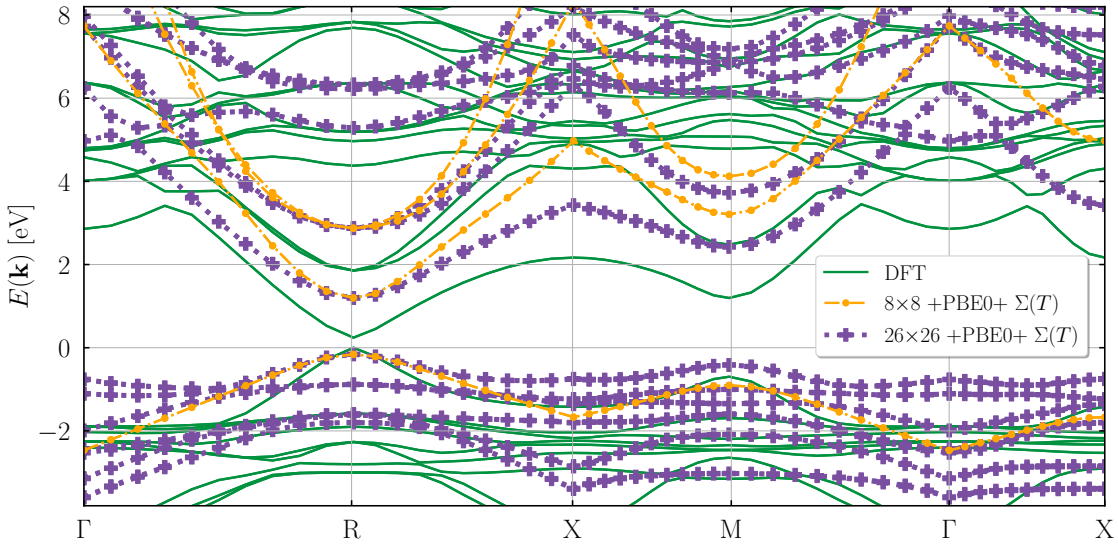

Figure 3.9. Band structure of the cubic phase of $CsPbI_3$ calculated using standard and extended $\mathbf{k} \cdot \mathbf{p}$ Hamiltonian parametrized using band energies obtained using hybrid PBE0 functional and self-energy correction $\Sigma(T)$ at T=300 K that stems from the phonon-induced renormalization of band energies. DFT results obtained with PBE functional are also given for comparison.

Chapter 4

Temperature dependence of band gap in halide perovskites

Present chapter, follows the paper that describes electronic structure calculations of the temperature dependence of the band gap and band energies for halide perovskite materials $CsPbX_3$ (X = Cl, Br or I) in cubic crystal structure[45]. These materials were first considered in Chapter 3 in their bulk phase, while results considering nanostructures based on them are reserved for Chapter 5 (more precisely Sec. 5.5).

4.1 Introduction

Halide-lead perovskite materials are relevant for applications in many electronic devices, which by design should be able to perform at wide range of temperatures. At low temperatures, an orthorhombic structure has been observed, followed by a narrow range for tetragonal structure before the phase transition to cubic structure which has been observed around and above room temperature i.e.: 320 K, 403 K and 300 K, for $CsPbCl_3$, $CsPbBr_3$ and $CsPbI_3$, respectively. When designing any kind of electronic device, the first step would be to obtain an accurate electronic structure at all possible temperatures for all materials that this device is based on. However, there are several challenges that need to be addressed when dealing with halide-lead perovskites that can be made of three main points. First, for many other semiconductors, standard local or semi-local approximations to density functional theory (DFT) underestimate the material band gap [41, 144, 145] and more sophisticated approaches, such as the use of GW approximation [146, 147, 148] or hybrid functionals [149, 150], are necessary. Second, in the case of case of halide-lead perovskites, electronic structure calculations become more demanding, as one has to take into account the effects of spin-orbit interaction due to presence of heavy atoms such as lead [41, 144, 145]. Third, temperature effects on the band gap and the overall electronic structure of perovskites are rather pronounced [38, 151, 152, 153, 154, 155, 156] and one cannot simply assign the electronic structure calculated for fixed atoms in the crystal lattice as the electronic structure at higher temperatures. First two points have been addressed previously in the literature, however the third

point still requires some discussion and will be the main focus of this chapter.

The most successful theory for treating the temperature effects on the electronic structure of semiconductors is the Allen-Heine-Cardona (AHC) theory [113, 114, 115], described in Sec. 2.9. Within this theory, one expands the Hamiltonian up to second-order terms in atomic displacements from the equilibrium position and perturbatively evaluates the change in band energies. In conjunction with the methods for electronic structure calculation for fixed atomic positions, this theory was used to study the temperature dependence of the band gap and zero temperature band gap renormalization in a variety of semiconductors [120, 157, 117, 158, 115, 159]. However, the theory can be straightforwardly applied to a particular material only if its crystal structure at a given temperature is the same as at zero temperature.

As mentioned, halide-lead perovskite materials $CsPbX_3$ (X = Cl, Br or I) exhibit cubic structure at high temperatures only [160, 161, 33, 162, 163, 164]. As the temperature is lowered they transform to a tetragonal structure and finally to an orthorhombic structure [160, 161, 33, 162]. Therefore, the cubic structure is not a stable structure at zero temperature. When one attempts to calculate the phonon dispersion in the material by assuming a cubic structure at zero temperature, phonon modes of imaginary frequencies are obtained [165, 162, 166, 167] and it is not clear how to treat such phonons within AHC theory.

Previous works on the effects of temperature on halide perovskite semiconductors have not addressed other bands than the conduction band minimum (CBM) and the valence band maximum (VBM). While these two bands are most relevant for the determination of the band gap of the material, there is a significant interest to know the energies of the other bands. These are important, for example, to understand the optical response of the material in the ultraviolet spectral range relevant for ultraviolet detectors [10]. On the theoretical side, the knowledge of band energies at characteristic points in the Brillouin zone is necessary to construct multiband Hamiltonians [130, 132, 133, 46] that can further be used to predict the electronic states in halide perovskite nanostructures. While the renormalization of energies of the other bands can in principle be obtained in the same way as for CBM and VBM within AHC theory, certain issues, related to the energy level broadening parameter δ, arise. On the one hand, band renormalization for other bands converges linearly with respect to δ when $\delta \to 0$ in contrast to Lorentzian convergence of CBM and VBM [120], which makes it more challenging to obtain the convergence of other bands. On the other hand, other bands typically exhibit larger broadening of energy levels than the CBM and VBM. Consequently, it is questionable if one should evaluate the $\delta \to 0$ limit for other bands at all. Preferably, the broadening of the energy levels should be evaluated simultaneously with the band energy renormalization.

In this chapter, following calculations for lead halide perovskites are performed: electronic structure calculations for cubic and orthorhombic phase, phononic structure for cubic phase using harmonic and anharmonic treatment, and temperature dependent electron-phonon renormalization of the electronic structure. Electronic structure calculations (without the effects of phonon-induced band renormalization) are performed using a hybrid functional that satisfies the Koopmans condition.

Phononic structure is obtained using density functional perturbation theory (DFPT) and self-consistent phonon (SCPH) theory. Electron-phonon renormalization of electronic structure is performed using AHC theory that introduces temperature dependence of the electronic structure. The challenge of treating phonons within AHC theory is overcome by performing phonon band structure calculations at a finite temperature within the framework of SCPH theory, where all phonon modes remain stable. The challenge of the choice of energy level broadening is overcome by performing the calculation in which energy levels and their broadening are determined self-consistently. The obtained temperature dependence of the band gap for cubic structure is compared to experimental results from the literature. Calculation of orthorhombic structure at zero temperature is shown also. Finally the chapter ends with a comment on overall temperature dependence of the band gap of $CsPbX_3$ materials from zero to high temperatures.

This chapter is organized as follows. Sec. 4.2 starts with explaining the self-consistent Migdal approximation and describes the self-consistent method, based on AHC theory found in Sec. 2.9 that was used to obtain the main results in this chapter. Sec. 4.3, contains computational details and results necessary for the next section. Computational details and obtained results start with results from standard DFT with semi-local functionals in Sec. 4.3.1 followed by hybrid functional calculations in 4.3.2. Next, DFPT compuational details and results are shown for harmonic phonons in Sec. 4.3.3, followed by anharmonic calculations performed using self-consistent phonon calculations (SCPH) in Sec. 4.3.4. Sec. 4.4 contains the main results that include temperature renormalization of electron bands using on-the-mass-shell (OTMS) approach in Sec. 4.4.1 and self-consistent procedure (SCP) based on Migdal approximation in Sec. 4.4.2. In Sec. 4.4.3 results from Sec. 4.4 are compared with experiments. Chapter ends with discussion and conclusions in Sec. 4.5.

4.2 Self-consistent Migdal approximation

The non-adiabatic and dynamic Fan term from Eq. (2.199) from Sec. 2.9.2 that described Allen-Heine-Cardona theory was:

$$\begin{aligned}
\Sigma^{\text{Fan}}_{\mathbf{k}n}(\omega, T) =& \frac{1}{N_q} \sum_{m,\mathbf{q}\nu} \left| g^{\text{Fan}}_{nm,\nu}(\mathbf{k}, \mathbf{q}) \right|^2 \times \\
& \times \left[\frac{n_{\mathbf{q}\nu}(T) + 1 - f_{\mathbf{k}+\mathbf{q}m}}{\omega - \varepsilon_{\mathbf{k}+\mathbf{q}m} - \omega_{\mathbf{q}\nu} + i\delta} + \frac{n_{\mathbf{q}\nu}(T) + f_{\mathbf{k}+\mathbf{q}m}}{\omega - \varepsilon_{\mathbf{k}+\mathbf{q}m} + \omega_{\mathbf{q}\nu} + i\delta} \right] \\
=& \frac{1}{N_q} \sum_{m,\mathbf{q}\nu} \left| g^{\text{Fan}}_{nm,\nu}(\mathbf{k}, \mathbf{q}) \right|^2 \times \\
& \times \Big[(n_{\mathbf{q}\nu}(T) + 1 - f_{\mathbf{k}+\mathbf{q}m}) G^{(0)}_{\mathbf{k}+\mathbf{q}m}(\omega - \omega_{\mathbf{q}\nu}) + \\
& (n_{\mathbf{q}\nu}(T) + f_{\mathbf{k}+\mathbf{q}m}) G^{(0)}_{\mathbf{k}+\mathbf{q}m}(\omega + \omega_{\mathbf{q}\nu}) \Big],
\end{aligned} \tag{4.1}$$

where $g^{\rm Fan}_{mn,\nu}(\mathbf{k},\mathbf{q})$ is the electron-phonon matrix element that contains probability of transition between $\mathbf{k}+\mathbf{q}m$ and $\mathbf{k}n$ electron states by scattering from $\mathbf{q}\nu$-phonon with frequency $\omega_{\mathbf{q}\nu}$, $n_{\mathbf{q}\nu}(T)$ is the Bose-Einstein factor for $\mathbf{q}\nu$ phonons at temperature T and $f_{\mathbf{k}+\mathbf{q}m}$ is the Fermi-Dirac occupation factor for $\mathbf{k}+\mathbf{q}m$ state with $\varepsilon_{\mathbf{k}+\mathbf{q}m}$ as the Kohn-Sham energy of that state and δ is a positive real infinitesimal. The matrix element $g^{\rm Fan}_{nm,\nu}(\mathbf{k},\mathbf{q})$ was given in Eq. (2.192) in Sec. 2.9, as well as in Eq. (A.40) in A.4 of the Appendix, and can be expanded as:

$$\begin{aligned} g^{\rm Fan}_{mn,\nu}(\mathbf{k},\mathbf{q}) &= \langle \mathbf{k}+\mathbf{q}m| \, \Delta_{\mathbf{q}\nu} v^{\rm KS} \, |\mathbf{k}n\rangle_{\rm uc} \\ &= \sum_{\kappa\alpha} \frac{\xi_{\kappa\alpha,\nu}(\mathbf{q})}{(2M_\kappa \omega_{\mathbf{q}\nu}/\hbar)^{1/2}} \langle \mathbf{k}+\mathbf{q}m| \, \frac{\partial v^{\rm KS}}{\partial R_{\kappa\alpha}(\mathbf{q})} \, |\mathbf{k}n\rangle_{\rm uc} \,, \end{aligned} \tag{4.2}$$

where $\kappa = 1 \ldots N_{\rm at}$ and $\alpha = x, y, z$ are ion and directional indices, $\xi_{\kappa\alpha,\nu}(\mathbf{q})$ and $\omega_{\mathbf{q}\nu}$ are eigenvectors and energies for $\mathbf{q}\nu$-phonons, respectively, and term in brackets is the transition matrix element between electron states $\mathbf{k}+\mathbf{q}m$ and $\mathbf{k}n$ induced by phonon with vector $\mathbf{q}$. Similarly, from Eq. (2.200) one obtains the Debye-Waller term in the rigid-ion approximation:

$$\begin{aligned} \Sigma^{\rm DW}_{\mathbf{k}n}(T) &= -\frac{1}{N_{\mathbf{q}}} \sum_{m\mathbf{q}\nu} g^{\rm ria}_{nm,\nu}(\mathbf{k},\mathbf{q}) \left[2n_{\mathbf{q}\nu}(T)+1\right], \\ g^{\rm ria}_{nm,\nu}(\mathbf{k},\mathbf{q}) &= \sum_{\kappa\kappa'\alpha\alpha'} \left[\frac{\xi_{\kappa\alpha,\nu}(-\mathbf{q})\xi_{\kappa\alpha',\nu}(\mathbf{q})}{2M_\kappa\omega_{\mathbf{q}\nu}/\hbar} + \frac{\xi_{\kappa'\alpha,\nu'}(-\mathbf{q})\xi_{\kappa'\alpha',\nu}(\mathbf{q})}{2M_{\kappa'}\omega_{\mathbf{q}\nu}/\hbar} \right] \\ &\quad \times \mathrm{Re}\, \frac{\langle u_{\mathbf{k}n}| \frac{\partial v^{\rm KS}}{\partial R_{\kappa\alpha}(\Gamma)} |u_{\mathbf{k}m}\rangle \langle u_{\mathbf{k}m}| \frac{\partial v^{\rm KS}}{\partial R_{\kappa'\alpha'}(\Gamma)} |u_{\mathbf{k}n}\rangle}{\varepsilon_{\mathbf{k}n} - \varepsilon_{\mathbf{k}m} + i\delta}. \end{aligned} \tag{4.3}$$

Using on-the-mass-shell approximation (OTMS), the renormalized Kohn-Sham state $E^{\rm OTMS}_{\mathbf{k}n}(T)$ can be simply obtained as:

$$E^{\rm OTMS}_{\mathbf{k}n}(T) = \varepsilon_{\mathbf{k}n} + \mathrm{Re}\, \Sigma^{\rm Fan}_{\mathbf{k}n}(\varepsilon_{\mathbf{k}n}, T) + \mathrm{Re}\, \Sigma^{\rm DW}_{\mathbf{k}n}(T), \tag{4.4}$$

or by applying one of the solution methods described in Sec. 2.9.3.

As discussed in Chapter 2, Sec. 2.9.3, there are challenges in obtaining converged result for band energy renormalization via the AHC theory for bands other than VBM and CBM using Eqs. (4.1), (4.3) and (4.4). The convergence with respect to energy level broadening parameter δ as $\delta \to 0$ is a slow linear convergence[120] and hence one needs to use rather small δ, which in turn requires large number of q-points in the summation. The broadening of the energy levels obtained from the imaginary part of the self-energy is on the order of 100 meV or more. It is therefore questionable if the $\delta \to 0$ limit is relevant at all. It is certainly more appropriate to self-consistently determine the renormalization and broadening of the energy levels. One way to achieve this will be explained in this section.

The terms $(\omega - \varepsilon_{\mathbf{k}+\mathbf{q}m} \pm \omega_{\mathbf{q}\nu} + i\delta)^{-1}$ represent the retarded Green's function of a bare electron $G^{(0)}_{\mathbf{k}+\mathbf{q}m}(\omega \pm \omega_{\mathbf{q}\nu})$, while $\Sigma^{\rm Fan}_{\mathbf{k}n}(\omega, T)$ itself is the self-energy in the so-called Migdal approximation. A more accurate approximation is the self-consistent

Migdal approximation where the bare Green's function $G^{(0)}$ is replaced with the dressed Green's function G. With this, $\Sigma^{\rm Fan}_{\mathbf{k}n}(\omega,T)$ would take the form

$$\begin{aligned}\Sigma^{\rm Fan}_{\mathbf{k}n}(\omega) =& \frac{1}{N_q}\sum_{m,\mathbf{q}\nu}\left|g^{\rm Fan}_{nm,\nu}(\mathbf{k},\mathbf{q})\right|^2\times \\ &\times\left[(n_{\mathbf{q}\nu}(T)+1-f_{\mathbf{k}+\mathbf{q}m})G_{\mathbf{k}+\mathbf{q}m}(\omega-\omega_{\mathbf{q}\nu})+\right. \\ &\left.(n_{\mathbf{q}\nu}(T)+f_{\mathbf{k}+\mathbf{q}m})G_{\mathbf{k}+\mathbf{q}m}(\omega+\omega_{\mathbf{q}\nu})\right].\end{aligned} \tag{4.5}$$

One can in principle find the Green's function, the self-energy, the spectral function and hence the energy level renormalization and broadening by self-consistently solving Eq. (4.5) and the Dyson equation. However, this requires evaluation of all these quantities at wave vectors throughout the whole Brillouin zone in each step of the self-consistent procedure, which is a highly demanding computational task. A significant simplification that decouples different $\mathbf{k}n$ states can be made as follows.

The Green's function in Eq. (4.5) is given as

$$G_{\mathbf{k}+\mathbf{q}m}(\omega)=\frac{1}{\omega-\varepsilon_{\mathbf{k}+\mathbf{q}m}-\Sigma_{\mathbf{k}+\mathbf{q}m}(\omega)}. \tag{4.6}$$

One can then make a replacement $\Sigma_{\mathbf{k}+\mathbf{q}m}(\omega)\to\Sigma_{\mathbf{k}n}(\omega)=\Sigma^{\rm Fan}_{\mathbf{k}n}(\omega)+\Sigma^{\rm DW}_{\mathbf{k}n}$ in Eq. 4.6. Such a replacement is justified by the fact that the dominant contribution to the sum in Eq. (4.5) comes from the terms in the sum that have $m=n$ and small value of $\mathbf{q}$. For such terms $\Sigma_{\mathbf{k}+\mathbf{q}m}(\omega)\approx\Sigma_{\mathbf{k}n}(\omega)$. It is therefore appropriate to replace the self-energy for all terms in the sum with self-energy of the dominant terms. The expression for $\Sigma^{\rm Fan}_{\mathbf{k}n}$ then reads

$$\begin{aligned}\Sigma^{\rm Fan}_{\mathbf{k}n}(\omega) =& \frac{1}{N_q}\sum_{m,\mathbf{q}\nu}\left|g^{\rm Fan}_{nm,\nu}(\mathbf{k},\mathbf{q})\right|^2\times \\ &\times\left[\frac{n_{\mathbf{q}\nu}(T)+1-f_{\mathbf{k}+\mathbf{q}m}}{\omega-\varepsilon_{\mathbf{k}+\mathbf{q}m}-\omega_{\mathbf{q}\nu}-\Sigma_{\mathbf{k}n}(\omega-\omega_{\mathbf{q}\nu})}+\right. \\ &\left.\frac{n_{\mathbf{q}\nu}(T)+f_{\mathbf{k}+\mathbf{q}m}}{\omega-\varepsilon_{\mathbf{k}+\mathbf{q}m}+\omega_{\mathbf{q}\nu}-\Sigma_{\mathbf{k}n}(\omega+\omega_{\mathbf{q}\nu})}\right].\end{aligned} \tag{4.7}$$

It is important to note that Eq. (4.7) does not contain the self-energies of the states other than $\mathbf{k}n$, which is a consequence of the approximation used for $\Sigma_{\mathbf{k}+\mathbf{q}m}(\omega)$. The self-energy $\Sigma^{\rm Fan}_{\mathbf{k}n}(\omega)$ can now be obtained using a self-consistent procedure (SCP) as follows. One starts with some initial guess for $\Sigma_{\mathbf{k}n}(\omega)$ and evaluates $\Sigma^{\rm Fan}_{\mathbf{k}n}(\omega)$ using Eq. (4.5) and the total self-energy as the sum of the Fan and the Debye-Waller term. New value of $\Sigma^{\rm Fan}_{\mathbf{k}n}(\omega)$ is then calculated again using Eq. (4.7) and the procedure is repeated until the convergence of $\Sigma^{\rm Fan}_{\mathbf{k}n}(\omega)$ is reached. The spectral function is then obtained as

$$A_{\mathbf{k}n}(\omega)=-\frac{1}{\pi}\,{\rm Im}\,\frac{1}{\omega-\varepsilon_{\mathbf{k}n}-\Sigma_{\mathbf{k}n}(\omega)} \tag{4.8}$$

and the renormalized energy $E_{\mathbf{k}n}$ is obtained as the energy $\omega_{\rm max}$ at which the spectral function reaches a maximum. This procedure for evaluation of renormalized energies

is similar in spirit to the procedure suggested in Ref. [44] (Eq. 166 therein), where approximations that also lead to decoupling of different $\mathbf{k}n$ states were used. The difference between these procedures is that here the full frequency dependence of self-energies is considered rather than the energy of the renormalized state and its broadening only.

It is worth mentioning that, it is rather challenging to treat the electron-phonon interaction in real materials beyond the approximations mentioned. These approximations all contain the assumption that electron-phonon interaction is not too strong. Full nonperturbative treatment of electron-phonon interaction has so far only been performed for model Hamiltonians, such as the Holstein or Fröhlich model. In a recent study of the Holstein model [168] it was shown that for relatively weak electron-phonon coupling the spectral functions in the Migdal and self-consistent Migdal approximation are similar to the spectral functions obtained using more advanced approaches, such as the cumulant expansion method and the dynamical mean field theory. Moreover, self-consistent Migdal approximation performs overall only somewhat worse than the cumulant expansion method, which is not the case for the Migdal approximation that gives inaccurate results starting from moderate values of electron-phonon coupling. Based on the knowledge gained from the Holstein model, one can infer about the accuracy of the OTMS and SCP results for real perovskite materials. It is expected that the SCP results which are based on the self-consistent Migdal approximation should in principle be more accurate than the OTMS results which are based on the Migdal approximation. On the other hand, it will be shown in Sec. 4.4 that OTMS and SCP results are not too different. This suggests that the regime where electron-phonon coupling is considered to be relatively weak, it is appropriate to apply either the Migdal or the self-consistent Migdal approximation.

In both the OTMS and SCP approach, as typically done in the literature [44], only the diagonal (intraband) self-energies $\Sigma_{\mathbf{k}n}(\omega)$ were evaluated and not the off-diagonal (interband) self-energies $\Sigma_{\mathbf{k}nm}(\omega)$ (with $n \neq m$). In the case of OTMS approach one is actually interested in diagonal self-energies only because they directly determine the band energy renormalization, see Eq. (4.4). On the other hand, introduction of off-diagonal self-energies in the SCP approach would strongly increase the computational burden of the whole procedure. On physical grounds, it should be noted that band energy renormalization due to interband electron-phonon scattering processes is already described by the diagonal self-energies [via the $m \neq n$ terms in the sum in Eq. (4.1)]. Hence, inclusion of non-diagonal self-energies would represent only a higher order effect.

4.3 Computational details

4.3.1 DFT with semi-local functionals

Density functional theory calculations of the electronic structure of the $CsPbX_3$ materials were performed using the semi-local PBEsol [76] functional in case of $CsPbCl_3$ and $CsPbBr_3$, while the PBE functional [73] was used in case of $CsPbI_3$. Calculations were performed using the plane wave code Quantum Espresso [96, 97].

Norm-conserving fully relativistic pseudopotentials [142, 141] were used to treat the effect of core electrons. The effects of spin-orbit interaction were included. The wave functions were represented on a $4\times4\times4$ reciprocal space $k-$point grid with a kinetic energy cutoff of 50 Ry for $CsPbCl_3$ and $CsPbBr_3$ and a cutoff of 40 Ry for $CsPbI_3$. Taking a note, a different functional was used for $CsPbI_3$ because the gap obtained using the PBEsol functional at the optimized lattice constant obtained from this functional is nearly zero, which prevents the use of this functional in further DFPT calculations.

The optimized lattice constants for the cubic structure obtained from the calculations are respectively 10.6 a_0, 11.1 a_0 and 12.1 a_0 (in units of first Bohr radius a_0) for $CsPbCl_3$, $CsPbBr_3$ and $CsPbI_3$. We note that the lattice constants obtained for $CsPbCl_3$ and $CsPbBr_3$ are in excellent agreement with the experimental lattice constant at the lowest temperature where the material exhibits a cubic structure (which are 10.59 a_0 at 320 K for $CsPbCl_3$ and 11.10 a_0 at 403 K for $CsPbBr_3$, see Ref. [164]). This agreement is reasonable in case of $CsPbI_3$ (experimental lattice constant is 11.67 a_0 at 300 K, see Ref. [169]) and would be better if the PBEsol functional, which gives the lattice constant of 11.8 a_0, were used. However, as noted before, the use of PBEsol functional for $CsPbI_3$ closes the gap of the material and hence this functional was not used for $CsPbI_3$. While the agreements obtained are somewhat fortuitous because standard DFT calculations are performed at zero temperature, the lattice constants obtained were used in further calculations because they are in good agreement with experimental lattice constants. The direct band gaps at the R-point obtained for $CsPbCl_3$, $CsPbBr_3$ and $CsPbI_3$ are respectively 0.59 eV, 0.22 eV and 0.21 eV. These gaps are well below the experimental band gaps, see Figure 4.1. This is expected because it is well known that semi-local functionals underestimate the band gap [84].

Calculations for the orthorhombic structure of $CsPbX_3$ material that is stable at zero temperature were performed as following. The coordinates of the initial structure were taken from The Materials Project website [170] as structures numbered 675524, 567629, and 1120768 for $CsPbCl_3$, $CsPbBr_3$ and $CsPbI_3$, respectively, and were further relaxed (cif files for the initial and relaxed structures are included in Supplementary Information of Ref. [45]). $CsPbCl_3$ orthorhombic structure corresponds to space group number 38 (Amm2) with 10 atoms per primitive cell, while $CsPbBr_3$ and $CsPbI_3$ orthorhombic structures both correspond to space group number 62 (Pmna) with 20 atoms per primitive cell. The same density functionals, k-point grid dimension, and the plane wave kinetic energy cutoff were used as in the case of the cubic structure. PBEsol functional was used for optimization of atomic coordinates and the dimensions of the unit cell for all three materials (since the gap of orthorhombic $CsPbI_3$ does not close when the PBEsol functional is used in the calculation). The calculations were performed using the Quantum Espresso code [96, 97] with variable cell relaxation option. The band gaps obtained for orthorhombic $CsPbCl_3$, $CsPbBr_3$ and $CsPbI_3$ are respectively 1.1 eV, 0.83 eV and 0.62 eV.

4.3.2 Hybrid functional calculations

To overcome the band gap problem of semi-local functionals, electronic structure calculation was performed using a hybrid functional. In particular, PBE0 functional was used [78, 171] whose parameter α is chosen to satisfy the Koopmans condition. We take the values of α for $CsPbX_3$ materials that were calculated in Ref. [79]. Hybrid functional calculations were also performed using the Quantum Espresso code [96, 97, 172]. The calculation parameters common to standard semi-local DFT calculation were set to the same values. In addition, for cubic structures a $4 \times 4 \times 4$ reciprocal $q-$points grid was used to sample the Fock operator and the Gygi-Baldereschi method [173] was used to treat the singularity at $q \to 0$. For orthorhombic structures that have a larger unit cell than cubic structures, $3 \times 3 \times 2$ k- and q-points grid was used in the case of $CsPbBr_3$ and $CsPbI_3$, while for $CsPbCl_3$ a $4 \times 4 \times 4$ k- and q-points grid was used.

In hybrid functional calculations, obtained values of the band gap of the cubic phase are: 2.4 eV, 1.5 eV and 0.96 eV for $CsPbCl_3$, $CsPbBr_3$ and $CsPbI_3$. These values are closer to experimental values than the values obtained from semi-local functionals. However, these values are still smaller than the experimental band gaps, see Figure 4.1. Such a result indicates that temperature effects might play a significant role and that it is important to investigate them.

In case of orthorhombic structure, band gaps of 3.0 eV, 2.4 eV and 1.5 eV, respectively for $CsPbCl_3$, $CsPbBr_3$ and $CsPbI_3$, were obtained. These results are in good agreement with experimental gaps of the low-temperature orthorhombic structures, which are 3.056 eV for $CsPbCl_3$ (Ref. [174]), 2.25 eV for $CsPbBr_3$ (Ref. [175]) and 1.72 eV for $CsPbI_3$ (Ref. [176]).

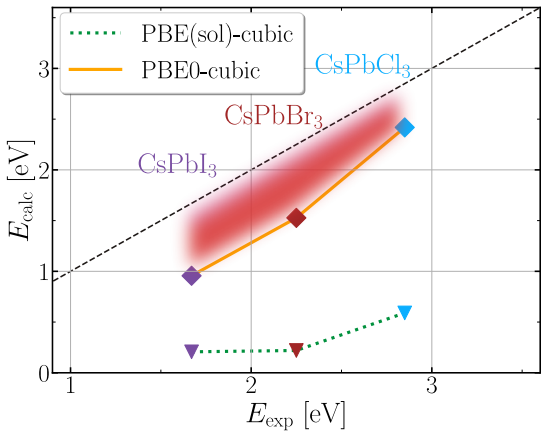

Figure 4.1. Comparision of experimental and theoretical results for the electronic gap for $CsPbX_3$ (X = Cl, Br or I) calculated without taking temperature effects into account. The line $x = y$ represents the experimental results for lowest temperature of the cubic structure. The symbols denote calculated values for the cubic structure using the PBE (PBEsol) functional for $CsPbI_3$ ($CsPbCl_3$ and $CsPbBr_3$) (inverted triangles) and PBE0 functional modified to satisfy the Koopmans condition (diamonds).

4.3.3 DFPT

To take into account the effect of temperature on electronic band structure, it is necessary to calculate the phonon frequencies and eigenvectors and the electron-phonon coupling constants. For this reason, DFPT calculations of phonons in harmonic approximation were performed. The same density functional, kinetic energy cutoff and the reciprocal space $k-$point grid were used as in DFT calculations. The calculations were performed using the Abinit code [103, 177, 178, 104].

The phonon band structures obtained from calculations for cubic $CsPbX_3$ materials are presented in Figure 4.2 (dashed line), where phonons with imaginary frequencies are presented using negative values. Since cubic structure is not stable at zero temperature, there is a significant number of phonon modes with imaginary frequencies. It is therefore a challenge to include such modes in the calculation of phonon-induced band renormalization.

4.3.4 SCPH

Standard DFPT calculations of phonon band structure assume a zero temperature and the harmonic approximation. As discussed in Section. 2.8.3, this leads to phonon modes with imaginary frequencies for the cubic structure. To overcome this issue, one has to take into account the anharmonic effects and the effects of temperature. This can be naturally accomplished using the self-consistent phonon method [179, 111].

The calculations based on the SCPH method were performed for cubic ABX_3 (X=Cl, Br, I) perovskites using the following protocol. The calculations were performed using the ALAMODE code [180, 111], while DFT calculations and ab initio molecular dynamics simulations were performed using the Quantum Espresso code [96, 97]. One first has to be obtain all relevant force constants. (i) Harmonic force constants were obtained by performing the DFT calculation of $2 \times 2 \times 2$ cubic supercell, where a shifted $4 \times 4 \times 4$ $k-$point grid was employed. Other parameters of the DFT calculation are the same as in Sec. 4.3.1. An atom is displaced by 0.01 Å in a certain direction and new atomic forces are calculated. The harmonic force constants are then obtained from these forces using a least square fit implemented in the ALAMODE code. (ii) To obtain anharmonic force constants, one first generates representative atomic structures which will be used for evaluation of forces and subsequent force constant fitting. Ab initio molecular dynamics was perfomed for NVT ensemble in 2000 steps at a temperature of 500 K with a timestep of 2 fs for a $2 \times 2 \times 2$ cubic supercell. To gain on computational speed in this calculation the kinetic energy cut-off is reduced to 30 Ry and $k-$point grid consisting of Γ point only was used. This is justified in this place, since the goal is only to get configurations where atoms are displaced from their equilibrium positions, rather than to extract physical quantities from the molecular dynamics simulation. Then, 30 snapshots were selected from the simulation which are equally spaced from timestep 500 to timestep 2000. (iii) For the snapshots obtained, each atom was additionally displaced by up to 0.1 Å in each direction. For these 30 snapshots, the atomic forces

were accurately computed from DFT by using 50 Ry kinetic energy cutoff and a shifted $4 \times 4 \times 4$ $k-$point grid. (iv) With the forces obtained a fitting of the force constants using the adaptive LASSO method is performed, following Refs. [181, 111]. In the fitting, there is a restriction that fourth order force constants are zero beyond third neighbor atoms, that the fifth and sixth order constants are nonzero for nearest neighbors only and that higher order constants are equal to zero. (v) The force constants obtained in the previous step are used as input for the SCPH method calculation. In the SCPH method calculation, the off-diagonal elements of the self-energy are neglected and $4 \times 4 \times 4$ grid was used to represent the self-energy in reciprocal space.

The phonon band structure obtained from the SCPH method is presented in Figure 4.2. Phonon frequencies that are non-negative throughout the whole Brillouin zone were obtained. Also, with an increase of temperature, a small but non negligible shift in frequencies is present. These shifts are negative for the three highest bands and positive for the rest. It will be shown, in Sec. 4.4.1, that these shifts are large enough to have a significant contribution to the renormalization of electronic bands.

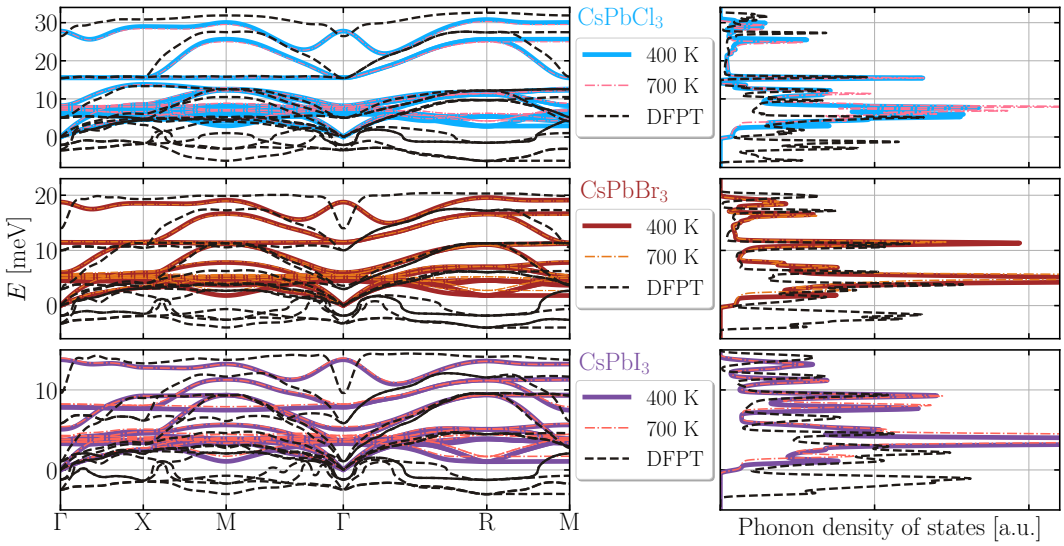

Figure 4.2. Phonon dispersion (left column) and phonon density of states (in arbitrary units) for $CsPbX_3$ (X = Cl, Br or I, in rows from top to bottom) obtained using the SCPH method at $T = 400\,\mathrm{K}$ (solid line) and $T = 700\,\mathrm{K}$ (dot-dashed line), as well as using DFPT with harmonic approximation (dashed line).

4.4 Results

The calculations, in the following sections, were performed using the author's code which takes DFPT results from the Abinit code. These results include variations of the Kohn–Sham potential with respect to ionic displacements and the interatomic force constants, that are then used to calculate first and second-order matrix ele-

ments of electron–phonon interaction. In all band energy renormalization calculations bare band energies that appear in Eq. (4.1) and Eq. (4.3) were taken from DFT calculations reported in Sec. 4.3.1.

4.4.1 Band energy renormalization with OTMS approach

This section applies the AHC procedure using the OTMS approach, briefly described in Sec. 4.2 and in detail in Sec 2.9.2 and Sec. 2.9.3 on cubic $CsPbX_3$ perovskites. The results can be also found in Ref. [45] were author's own code was used which takes DFPT results from the Abinit code to produce phonon-induced renormalization.

Convergence with respect to N_q

In order to obtain reliable results, one has to use enough q-points in the summations in Eq. (4.1) and Eq. (4.3) and check the sensitivity of the results to the value of δ in Eq. (4.1). It has been shown in Ref. [120] that the band energy renormalization for polar materials converges as $1/N_q$ with the number of points N_q and that a Lorentzian type convergence for CBM and VBM energies of polar materials is obtained while decreasing δ.

In Ref. [38] phonon modes obtained within the harmonic approximation were used, however, the phonon modes with imaginary frequencies were simply disregarded. In such an approach it remains unclear whether one should disregard only the phonons at certain q-points where their frequency becomes imaginary or one should disregard the whole phonon mode that produces an imaginary frequency in at least one point in the Brillouin zone. To understand whether the approach where imaginary phonon frequencies are discarded can provide reasonably good results, the convergence tests with respect to N_q and δ were performed in three cases: (i) assuming phonon frequencies from DFPT and disregarding the contribution from phonons with imaginary frequencies; (ii) assuming phonon frequencies from DFPT and disregarding the contribution from the whole phonon bands that exhibit imaginary frequencies at any q-point; (iii) assuming phonon frequencies obtained from the SCPH method. These three cases will be referred to as cases (i), (ii) and (iii) in what follows.

Figure 4.3 shows the results for the band gap renormalization obtained using the OTMS approach in each of these cases. It can be seen that, in case (i) the behavior with respect to N_q is not convergent and one obtains unphysically large band gap renormalizations. In this case several phonon bands cross zero energy at several different points in the Brillouin zone (see left column in Figure 4.2), which leads to divergence of Fan matrix elements due to $\omega_{\mathbf{q}\nu}$ term in the denominator, see Eq. (4.2). The convergence is better in case (ii) when such phonon bands are simply disregarded, however one obtains band gap renormalization which is underestimated with respect to case (iii). In case (iii), the convergence with respect to δ and N_q is obtained.

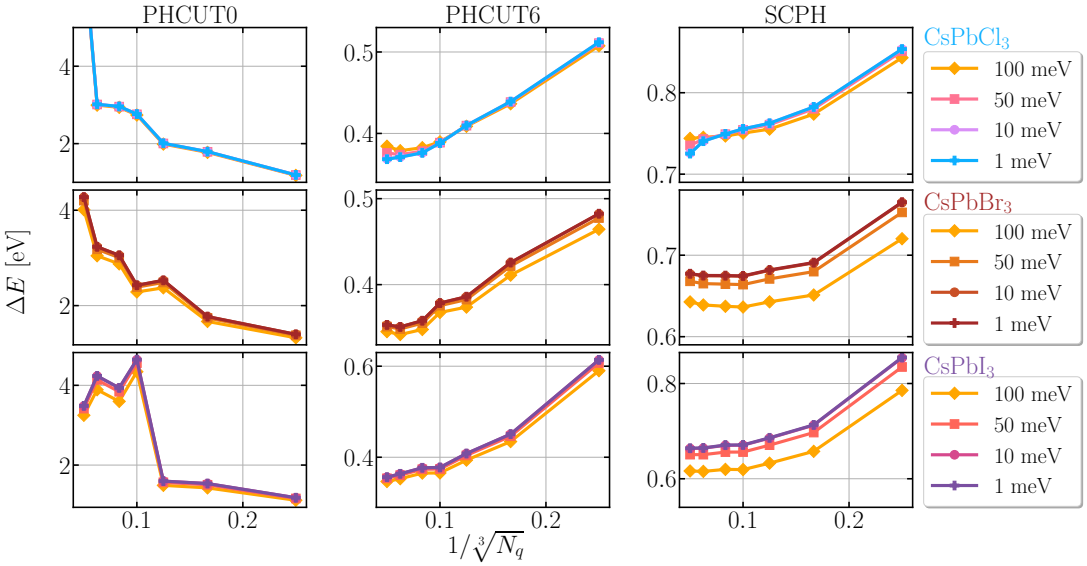

Figure 4.3. Dependence of band gap renormalization obtained using the OTMS approach on the number of q-points N_q and on the small parameter δ (whose value is specified in the legend) for $CsPbX_3$ (X = Cl, Br or I, in rows from top to bottom) materials at $T = 400$K. The column labeled as PHCUT0 denotes the result obtained assuming phonon frequencies from DFPT and disregarding the contribution from phonons with imaginary frequencies [case (i) discussed in the text], while the column labeled as PHCUT6 denotes the results obtained assuming phonon frequencies from DFPT and disregarding the contribution from the whole bands that exhibit imaginary frequencies at any q-point [case (ii) in the text]. The column labeled as SCPH denotes the result obtained by taking phonon frequencies from the SCPH method [case (iii) in the text].

.

Contributions of phonons to VBM and CBM

Figure 4.4 shows a decomposition of the CBM and VBM renormalization into contributions from phonons of different energies $\hbar\omega_{\mathrm{ph}}$. Most of the contributions come from the region where the density of phonon states is highest and these contributions come mostly from lower bands. Lower energy phonons also tend to have larger electron-phonon coupling matrix elements due to the $\omega_{\mathbf{q}\nu}$ term in the denominator in Eq. (4.2). This fact also contributes to prevalent contribution of lower energy phonons to band energy renormalization. Since most of these lower energy phonons turn into imaginary frequency phonons within DFPT calculation, the results obtained in case (ii) are underestimated in comparison to the results in case (iii). The contributions of the first-order Fan and second-order Debye-Waller terms in Eq. (4.4) to band energy renormalization are now analyzed. In line with previous literature results for other materials [113, 182], one can find that these two terms have opposite signs and that both of these terms have significant absolute values, see Figure 4.5. For these reasons, accurate calculation of each of these terms is necessary to obtain reliable final result for band energy renormalization.

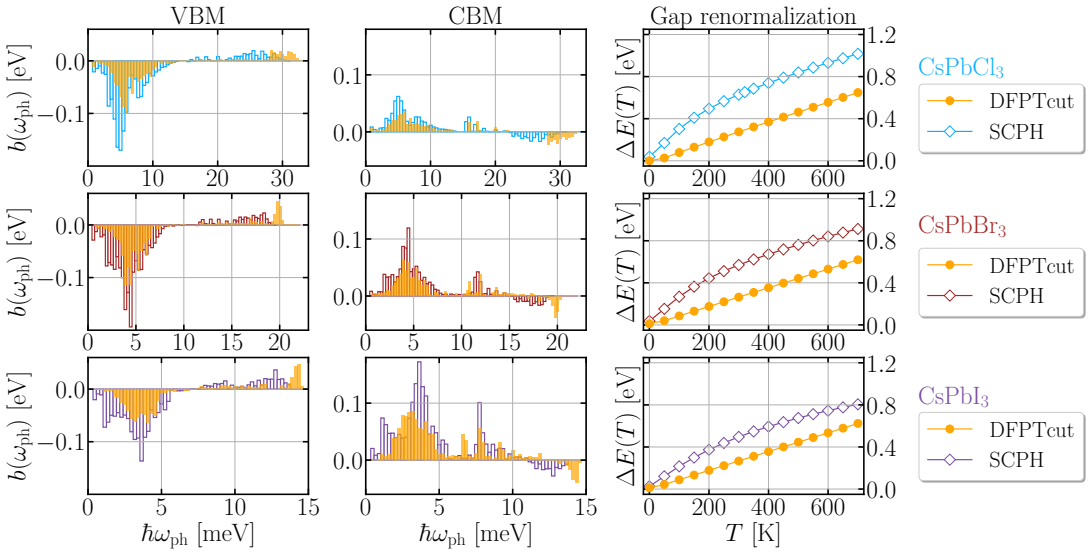

Figure 4.4. Contributions from phonons of different frequencies to VBM (left column) and CBM (middle column) renormalization at $T = 400\,\mathrm{K}$ and temperature dependent gap renormalization (right column) for $CsPbX_3$ (X = Cl, Br or I, in rows from top to bottom) obtained using the OTMS approach. The results in case (ii) are shown as filled bins, while the results in case (iii) are shown as transparent bins. The value of each bin $b(\omega_i)$ represents the contribution of all phonons with frequencies from the range $(\omega_i - \Delta\omega/2, \omega_i + \Delta\omega/2)$ to band energy renormalization, so that $\Delta E_{\mathbf{k}n} = \sum_i b(\omega_i)$. Filled circles in the right column correspond to case (ii), while empty deltoids correspond to case (iii).

Linearity of temperature dependence

There is also the linearity of the temperature dependence of the band gap renormalization that should be discussed. One can notice from Eq. (4.4) [with self-energies given by Eqs. (4.1) and (4.3)] that the temperature dependence originates only from the Bose term in these equations. When phonon energies are small the temperature dependence of the Bose term is linear. As a consequence, the temperature dependence of band energy renormalization is also linear in case (ii), as can be seen in Figure 4.4 On the other hand, in case (iii) the phonon frequencies also depend on temperature and the temperature dependence of the band gap is determined by the ratio of the Bose term (which contains temperature dependent phonon frequency) and the phonon frequency [which comes from the Fan matrix element, see Eqs. (4.2) and (4.1)]. The Bose term increases the gap with temperature as in case (ii), however, most of the temperature dependent frequencies (especially the ones where density of phonon states is largest) increase with temperature. They then tend to decrease the renormalization, which leads to nonlinear dependence in case (iii), as seen in Figure 4.4.

The temperature dependence of the band gap of the investigated materials using the OTMS approach is among the results presented in Figure 4.9. For the reasons

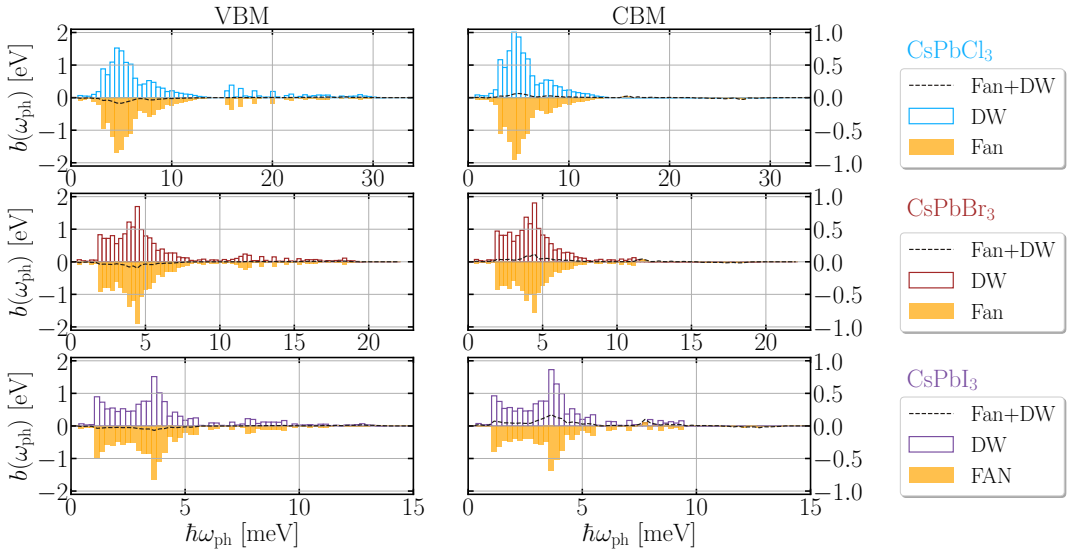

Figure 4.5. Contributions from Fan and Debye-Waller terms of phonons at different frequencies to VBM (left column) and CBM (right column) renormalization at $T = 400$ K for $CsPbX_3$ (X = Cl, Br or I, in rows from top to bottom) obtained using the OTMS approach. The value of each bin $b(\omega_i)$ represents the contribution of all phonons with frequencies from the range $(\omega_i - \Delta\omega/2, \omega_i + \Delta\omega/2)$ to band energy renormalization, so that $\Delta E_{\mathbf{k}n} = \sum_i b(\omega_i)$.

previously discussed, these results and all subsequent results were obtained by taking the phonon frequencies obtained from the calculation based on the SCPH method. In all calculations reported in this and the next section renormalized band energies were obtained by adding the phonon-induced renormalization to the band energies calculated using the hybrid functional as described in Sec. 4.3.2.

Bands other than VBM and CBM

The OTMS approach can be used in principle to determine the renormalization of bands other than the CBM and the VBM. As discussed in the introduction and Sec. 4.2 (and hinted at the end of Sec. 2.9.3), band renormalization for other bands exhibits a slow linear convergence with respect to δ when $\delta \to 0$ in contrast to Lorentzian convergence of CBM and VBM. As a consequence, one has to go to rather small values of δ to reach convergence. However, for small values of δ, large values of N_q are needed, which introduces a large computational burden. This behavior is illustrated in Figure S1, Figure S9 and Figure S14 in the Supplementary Information of Ref. [45], for the cases of $CsPbCl_3$, $CsPbBr_3$, and $CsPbI_3$, respectively. For larger values of δ (100 meV and 50 meV in the figure) good convergence with respect to N_q is achieved but the result still depends on δ and one therefore needs to go to smaller δ to achieve convergence with respect to δ. However, for smaller values of δ (10 meV and 1 meV), convergence with respect to N_q could not be achieved with grids up to $20 \times 20 \times 20$. As also discussed in the introduction and Sec. 4.2, it is questionable if

the limit $\delta \to 0$ of the energy level broadening parameter gives accurate results given the fact that the energy levels of higher bands can exhibit significant broadening. For all these reasons, it is more desirable to self-consistently determine the energy level broadening. These results are the subject of Sec. 4.4.2.

4.4.2 Band energy renormalization using the SCP approach

Results for band energy renormalization obtained using the SCP approach are presented in this section. The frequency dependence of the self-energy and the spectral function for several bands at the R point in the case of $CsPbBr_3$ material at $T = 400$ K is presented in Figure 4.6 (the same results for $CsPbCl_3$ and $CsPbI_3$ are presented respectively in Figures S4 and S17 in Supplementary Information of Ref. [45]). Naming of the bands in ascending order of energies at the R point is as VBM4 (2×), VBM3 (4×), VBM2 (2×), VBM1 (4×), VBM (2×), CBM (2×), CBM1 (4×), CBM2 (2×), CBM3 (2×), CBM4 (4×), where the numbers in brackets denote their degeneracy. The spectral functions of the CBM and VBM are relatively narrow and symmetric, while the spectral functions of other bands (CBM1 and VBM1 in Figure 4.6 and CBM2-4, VBM2-4 in Figures S10 and S12 in Supplementary Information of Ref. [45] in case of $CsPbBr_3$, see also Figures S2, S4 and S6 for $CsPbCl_3$, as well as Figures S15, S17 and S19 for $CsPbI_3$ material) are wider and somewhat asymmetric. Such a result confirms that it was necessary to go beyond the OTMS approach in the $\delta \to 0$ limit to obtain accurate results for bands other than CBM and VBM. There is even a difference between the OTMS and SCP result for CBM and VBM which leads to band gap difference between the two approaches on the order of 100 meV at $T = 400$ K (see Sec. 4.4.3 for more details).

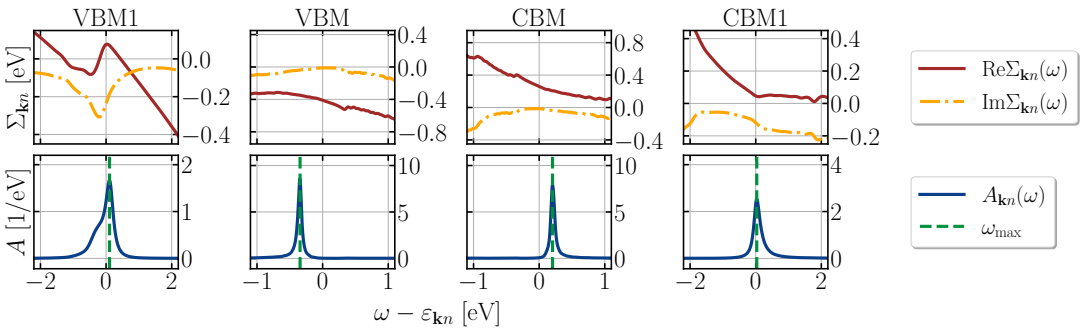

Figure 4.6. The frequency dependence of the self-energy and the spectral function for bands VBM1, VBM, CBM and CBM1 at the R point in the case of $CsPbBr_3$ material at $T = 400$ K

.

Convergence with respect to N_q

In Figure 4.7 one can observe that convergence with respect to N_q was achieved with a $20 \times 20 \times 20$ grid. Convergence is achieved both for real part of self-energy

that corresponds to band energy renormalization and for imaginary part of the self-energy that is related to energy level broadening. As expected, it is easier to reach convergence for energy levels that exhibit larger broadening, that is, for states other than CBM and VBM (Figure 4.7 and Figures S11 and S13 in Supplementary Information of Ref. [45], see also Figures S3, S5 and S7 for $CsPbCl_3$ material, as well as Figures S16, S18 and S20 for $CsPbI_3$ material). CBM and VBM states exhibit lowest broadening due to the fact that single phonon emission processes from these states are not possible. Hence the total scattering rate from these states, which is related to energy level broadening, is determined by phonon absorption processes only. On the other hand, for bands higher than CBM (lower than VBM), there is always a nearby other band below (above) it to which phonon emission is also possible. Hence, these states exhibit higher electron-phonon scattering rates than CBM and VBM, which leads to larger broadening of these states.

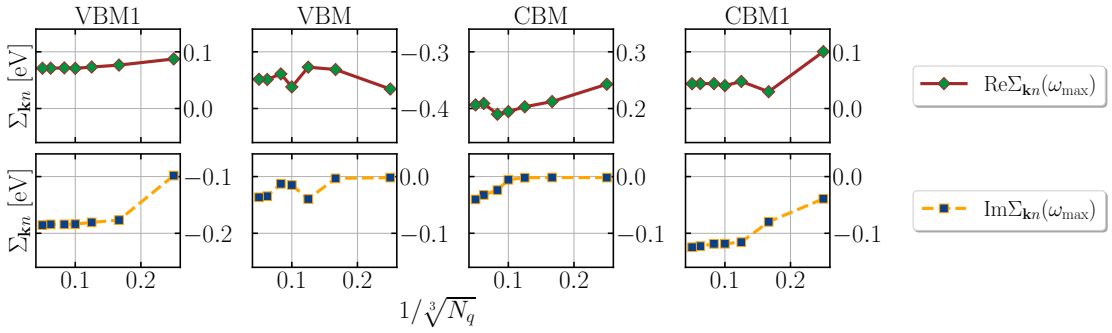

Figure 4.7. The dependence of the real and imaginary part of self-energy at the renormalized energy on the size of the q-points grid. The results are presented for $CsPbBr_3$ material at $T = 400\,\mathrm{K}$ for bands VBM1, VBM, CBM and CBM1 at the R point.

Temperature dependence at R-point

The final results for temperature dependence of band energies and the imaginary part of self-energies (that are related to energy level broadening) at the R point for the $CsPbBr_3$ material are presented in Figure 4.8. The same results for $CsPbCl_3$ and $CsPbI_3$ are presented in Figure S8 and Figure S21, respectively, in the Supplementary Information of Ref. [45]. The results indicate that the temperature dependence of band energies is most pronounced for the CBM and the VBM and that it is much weaker for the other bands. The energy level broadenings increase as the temperature increases and this dependence is nearly linear for most bands.

The temperature dependence of the band gap calculated within the SCP approach is presented in Figure 4.9. The results suggest that the gap renormalization and the band gap are somewhat smaller in the SCP approach than in the case of the OTMS approach. The largest difference between the two approaches is at highest temperatures. Such a difference originates from the fact that the spectral function within the SCP approach takes a relatively broad asymmetric shape at these

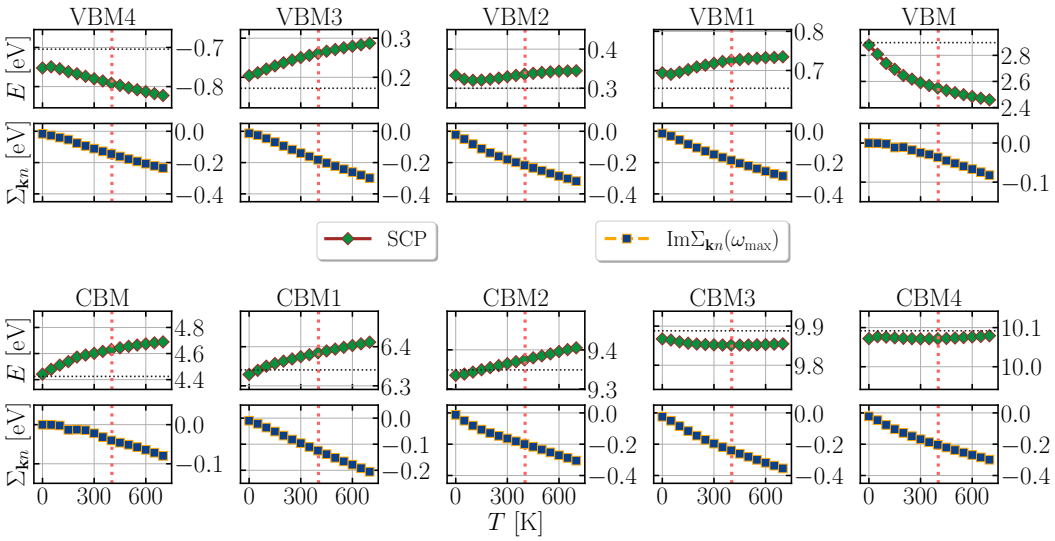

Figure 4.8. Temperature dependence of the band energy and the imaginary part of the self-energy for VBM and VBMx (CBM and CBMx) bands (where $x = 1, 2, 3, 4$) calculated using the SCP approach. The results are shown for $CsPbBr_3$ at the R point. Vertical and horizontal dotted lines represent the temperature of the phase transition to cubic structure $T_c = 403\,\mathrm{K}$ and band energy from PBE0 calculations, respectively.

temperatures, while the OTMS approach inherently assumes a narrow symmetric Lorentzian spectral function. The comparison of the temperature dependence of the band gap within the SCP approach with experiments will be discussed in Sec. 4.4.3.

Temperature dependence at Γ, X, M points

To gain insight into the effect of temperature on band energies throughout the Brillouin zone, SCP calculations of the spectral function and band energy renormalization at points Γ, X and M in the Brillouin zone were also performed for the three investigated materials. The results are presented in Figures S23 - S85 in Supplementary Information of Ref. [45]. All energy levels at X and M points are twofold degenerate, while the degeneracy of the bands at Γ is as follows: VBM4 (4×), VBM3 (2×), VBM2 (4×), VBM1 (2×), VBM (4×), CBM (2×), CBM1 (4×), CBM2 (2×), CBM3 (2×), CBM4 (4×). One can see (Figures S29, S36, S43, S50, S57, S64, S71, S78, and S85 in Supplementary Information of Ref. [45]) that in most cases the real and the imaginary part of the self-energy are smooth and continuous when the temperature changes. The exception are VBM2 for $CsPbCl_3$ between $T = 50\,\mathrm{K}$ and $T = 100\,\mathrm{K}$, and VBM1 for $CsPbBr_3$ and $CsPbI_3$ between $T = 550\,\mathrm{K}$ and $T = 600\,\mathrm{K}$, all three at the X point (Figures S50, S57, and S64 in Supplementary Information of Ref. [45], respectively). In these cases, the spectral function has two competing maxima (see Figures S87 - S89 in Supplementary Information of Ref. [45]) that are well inside the range of its half-width and the change of temperature changes the

dominant maximum. It should be noted that for all of the examined points, the changes of state energies are such that the band gap remains determined by the R point VBM and CBM. However, the increase of the temperature can change the ordering of the bands: at certain points in the Brillouin zone some neighbouring bands below (above) VBM1 (CBM1) will swap places with respect to their order obtained from the PBE0 functional calculations. Nevertheless, for simplicity, the bands are labeled based on their ordering obtained from zero temperature PBE0 functional calculations. When it comes to energy level broadening, it turns out that it is lowest for the VBM and CBM bands (with imaginary part of the self-energy well below 100 meV for these states and significantly above 100 meV for the other states), as in the case of the R point. The CBM and VBM states at these points are well separated in energy from the other bands (see the material band structures in Fig. S86 in Supplementary Information of Ref. [45]) which restricts the phase space for electron scattering. The exception to this behaviour is the VBM state at the Γ point which is rather broad. In this case, there are several bands that are close in energy to the VBM state at Γ. The hole can scatter to these bands which contributes to the increase of energy level broadening.

4.4.3 Comparison of the temperature dependence of the band gap with experiments

In this section, the results for the band gap and its temperature dependence are compared with available experimental results from the literature.

In case of $CsPbBr_3$ band gap of 2.08 eV and 2.20 eV was obtained from SCP and OTMS, respectively, at a temperature of 400 K. This result is close to the experimental value of 2.36 eV from Ref. [183], obtained at 403 K. Presented calculation gives the band gap of $CsPbCl_3$ of 3.01 eV and 3.07 eV from SCP and OTMS, respectively, at a temperature of 320 K. This result is in good agreement with experimental value of 2.85 eV from Ref. [184]. For the $CsPbI_3$ material, band gap of 1.35 eV and 1.45 eV was obtained from SCP and OTMS, respectively, at a temperature of 300 K, which is in reasonable agreement with experimental values of 1.67 eV (Ref. [185]) and 1.73 eV (Ref. [186]).

High temperatures with cubic structure

Next, one can focus on the slope of the temperature dependence of the band gap. In the range of temperatures where the material is in the cubic form, the calculated temperature dependence is nearly linear. Therefore, for the purpose of comparison with experiment, it is sufficient to discuss its slope. In case of $CsPbBr_3$, the obtained slope $\left(\frac{\mathrm{d}E_g}{\mathrm{d}T}\right)_{\mathrm{ph}}$ is 0.50 $\frac{\mathrm{meV}}{\mathrm{K}}$ and 0.80 $\frac{\mathrm{meV}}{\mathrm{K}}$ from SCP and OTMS, respectively, in the temperature range from 400 K to 700 K. For $CsPbCl_3$, the calculation yields the slope of 0.68 $\frac{\mathrm{meV}}{\mathrm{K}}$ and 0.96 $\frac{\mathrm{meV}}{\mathrm{K}}$ from SCP and OTMS, respectively, in the temperature range from 320 K to 700 K. Finally, for $CsPbI_3$ a slope $\left(\frac{\mathrm{d}E_g}{\mathrm{d}T}\right)_{\mathrm{ph}}$ of 0.41 $\frac{\mathrm{meV}}{\mathrm{K}}$ and

$0.77\,\frac{\mathrm{meV}}{\mathrm{K}}$ was obtained from SCP and OTMS, respectively, in the temperature range from 300 K to 700 K.

To compare the slope of the temperature dependence to experiment, one also has to take into account the effect of thermal expansion, which is not included in the calculation with a fixed lattice constant. The slope of the temperature dependence of the band gap from the effect of thermal expansion is given as

$$\left(\frac{\mathrm{d}E_g}{\mathrm{d}T}\right)_{\mathrm{TE}} = \left(\frac{\mathrm{d}E_g}{\mathrm{d}a}\right)\left(\frac{\mathrm{d}a}{\mathrm{d}T}\right), \tag{4.9}$$

where $\frac{\mathrm{d}E_g}{\mathrm{d}a}$ is the slope of the dependence of the band gap on the lattice constant and $\frac{\mathrm{d}a}{\mathrm{d}T}$ is the slope of the temperature dependence of the lattice constant, which is related to linear thermal expansion coefficient as

$$\alpha = \frac{1}{a}\frac{\mathrm{d}a}{\mathrm{d}T}. \tag{4.10}$$

Estimation of $\frac{\mathrm{d}E_g}{\mathrm{d}a}$ was done by calculating the gap dependence of the lattice constant using DFT with the same semi-local functional used in Sec. 4.3.1. Obtained values are respectively: 2.1, 2.4 and 1.1 $\frac{\mathrm{eV}}{\mathrm{\AA}}$ for $CsPbBr_3$, $CsPbCl_3$ and $CsPbI_3$. Literature values of linear thermal expansion coefficients are respectively $0.26 \cdot 10^{-4}\,\mathrm{K}^{-1}$, $(0.22-0.30)\cdot 10^{-4}\mathrm{K}^{-1}$ and $(0.39-0.40)\cdot 10^{-4}\mathrm{K}^{-1}$ for $CsPbBr_3$, $CsPbCl_3$ and $CsPbI_3$ (Ref. [187]). From Eqs. (4.9) and (4.10) one then obtains that $\left(\frac{\mathrm{d}E_g}{\mathrm{d}T}\right)_{\mathrm{TE}}$ is respectively equal to 0.32 $\frac{\mathrm{meV}}{\mathrm{K}}$, 0.35 $\frac{\mathrm{meV}}{\mathrm{K}}$ and 0.29 $\frac{\mathrm{meV}}{\mathrm{K}}$ for $CsPbBr_3$, $CsPbCl_3$ and $CsPbI_3$. The results suggest that the contribution from thermal expansion is smaller than the contribution from phonon-induced band gap renormalization for all the materials studied.

The total slope of the temperature dependence of the band gap can be estimated by adding contributions from phonon-induced band gap renormalization and from thermal expansion

$$\frac{\mathrm{d}E_g}{\mathrm{d}T} = \left(\frac{\mathrm{d}E_g}{\mathrm{d}T}\right)_{\mathrm{TE}} + \left(\frac{\mathrm{d}E_g}{\mathrm{d}T}\right)_{\mathrm{ph}}. \tag{4.11}$$

Finally, the obtained slopes $\frac{\mathrm{d}E_g}{\mathrm{d}T}$ are: 0.81 $\frac{\mathrm{meV}}{\mathrm{K}}$ (1.12 $\frac{\mathrm{meV}}{\mathrm{K}}$), 1.02 $\frac{\mathrm{meV}}{\mathrm{K}}$ (1.31 $\frac{\mathrm{meV}}{\mathrm{K}}$), and 0.70 $\frac{\mathrm{meV}}{\mathrm{K}}$ (1.06 $\frac{\mathrm{meV}}{\mathrm{K}}$) from SCP (OTMS) results, respectively for $CsPbBr_3$, $CsPbCl_3$ and $CsPbI_3$.

Experimental data for the temperature dependence of the band gap of the cubic structure and its slope are relatively scarce. Ref. [188] reports the slope of (0.85 ± 0.05) $\frac{\mathrm{meV}}{\mathrm{K}}$ for $CsPbI_3$ based on the measurements in the temperature range from 570 K to 620 K. This value is in the range between results shown from SCP and OTMS for the same material. The slope of 0.341 $\frac{\mathrm{meV}}{\mathrm{K}}$ was reported for $CsPbBr_3$ in Ref. [155] in the temperature range from 380 K to 435 K where the material exhibits a phase transition from tetragonal to cubic structure. This slope is significantly smaller than the one estimated here. It is however questionable if the comparison of these slopes is meaningful given the fact that experimental data cover only a very small initial part of the temperature range where the material is cubic. For

the $CsPbCl_3$ material, author is not aware of any literature data with temperature dependence of the band gap in the cubic phase. Overall, further experimental measurements of the temperature dependence of the band gap in a broader temperature range in the cubic phase are certainly desirable.

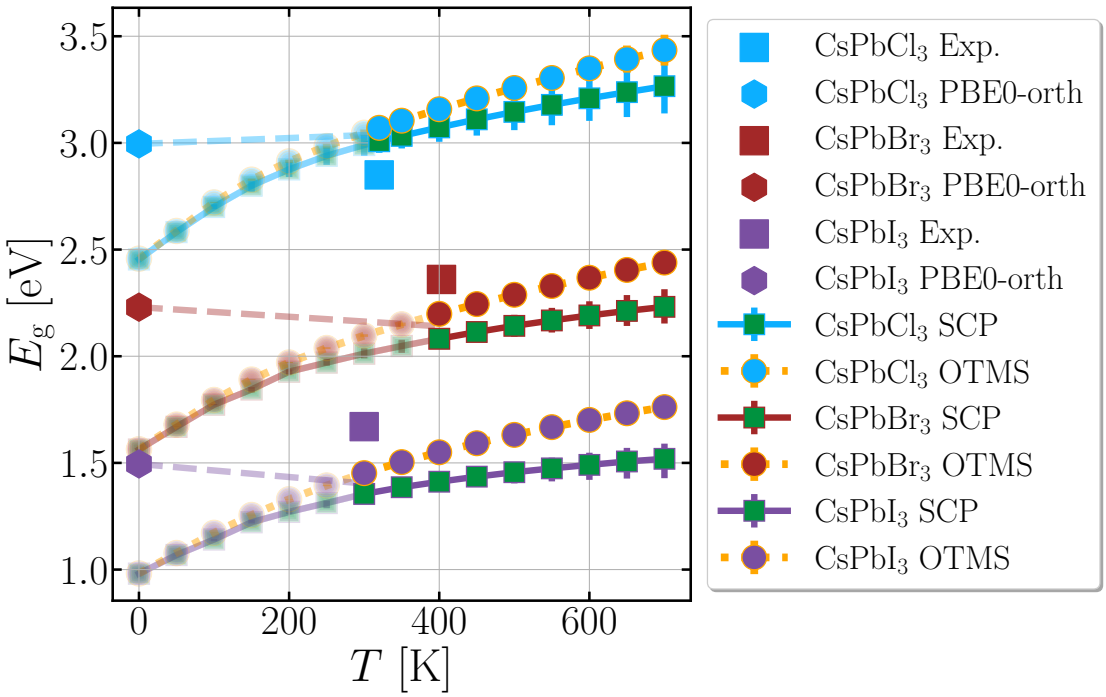

Figure 4.9. Temperature dependence of the calculated band gap of $CsPbX_3$ materials (X = Cl, Br or I, from top to bottom). The calculated band gap of orthorhombic structures at zero temperature is represented by hexagons, while the band gaps of the cubic structure calculated using the SCP (OTMS) approach are represented by full (dotted) lines and two color squares (circles). Experimental results are represented by single color squares with the values of 2.85 eV (Ref. [184]), 2.36 eV (Ref. [183]), and 1.67 eV (Ref. [185]) respectively, at temperatures of 320 K, 403 K and 300 K, respectively, for $CsPbCl_3$, $CsPbBr_3$ and $CsPbI_3$, respectively. Dashed lines are used as a guide to the eye to connect the zero temperature result for the band gap of orthorhombic structure with the result at the lowest temperature where the material exhibits a cubic structure.

Low temperatures with orthorhombic structure

Finally, the temperature dependence of the band gap at lower temperatures when the materials exhibit an orthorhombic or a tetragonal structure is addressed. Experimental results at these temperatures generally indicate that temperature dependence of the band gap is rather weak. For example, it was reported in Ref. [176] that the band gap of $CsPbBr_3$ ($CsPbI_3$) increases by about 60 meV (80 meV) from 0 K to 300 K. In Ref. [184] a similar result was obtained for $CsPbBr_3$, while in case

of $CsPbCl_3$ the changes of the band gap in this temperature range were smaller than 20 meV. In Refs. [189, 190, 191], a comparably weak temperature dependence of the gap was observed for nanocrystals based on $CsPbX_3$ materials in the same temperature range. For all the three materials, the band gap at zero temperature is only slightly (by less than 100 meV) lower or even slightly larger than at lowest temperature where the material exhibits a cubic structure, see the reference to the values of experimental band gaps at the end of Sec. 4.3.2 for orthorhombic structure and the beginning of this section for cubic structure. Presented calculations of the band gap of orthorhombic structure at zero temperature and of the cubic structure are in line with such behavior, see the dashed lines in Figure 4.9. Since the orthorhombic and tetragonal structure have a larger unit cell than the cubic structure, temperature dependent electronic structure calculations of these structures were not performed due to larger computational cost and the fact that experimental results indicate a rather weak temperature dependence in this range of temperatures.

4.5 Discussion and conclusions

Next, one can discuss previous computational works where the effects of temperature on electronic structure of halide perovskites were investigated. In Ref. [151] the effects of temperature were included by performing finite temperature ab initio molecular dynamics with a sufficiently large supercell and by calculating the average band gap change from many molecular dynamics snapshots. Excellent agreement with experimental band gaps of cubic inorganic halide perovskites at the lowest temperature where the material exhibits a cubic structure was obtained. On the computational side, this approach is rather demanding as it would require a separate molecular dynamics simulation at each temperature to obtain the temperature dependence of the band gap. This approach inherently assumes classical phonons which is likely a good approximation at room temperature because the dominant phonon modes that determine the electronic structure renormalization have energies which are significantly smaller than thermal energy k_BT at room temperature. In Refs. [167, 192] the effects of temperature were also included by taking an average over many different configurations with atoms displaced from their equilibrium positions. In Refs. [152, 153] the authors exploited the special displacements method [193, 194] which enables the calculation of the band gap at a given temperature from a single calculation of a large supercell with atoms displaced from their equilibrium positions in accordance with a particular pattern. In Ref. [38], AHC theory, the finite difference approach, as well as the approach with average over many different atomic configurations sampled using a Monte Carlo approach were used to study temperature dependence of the band gap of cubic methylammonium lead iodide perovskite. However, AHC theory was applied by simply excluding imaginary phonon modes, while from this section (that relies on Ref. [45]) one can find that such a procedure does not give reliable results in case of inorganic halide perovskites that are investigated.

Several advantages are mentioned here, as well as shortcomings, of the approach

based on AHC theory over other approaches. To obtain temperature dependence of the electronic structure, the most demanding steps of the procedure - DFPT calculations and extraction of force constants for the application of the SCPH method - need to be performed only once, that is, they do not have to be repeated for each temperature. On the other hand, in all approaches based on atomic displacements (sampled either from molecular dynamics, Monte Carlo or using the special displacements) the whole computational procedure has to be repeated at each temperature. Within AHC approach it is straightforward to obtain the renormalization of states other than CBM or VBM, while in the methods based on supercell calculations this is either impossible or one has to exploit a certain type of unfolding procedure, such as the one used in Ref. [193]. It should be mentioned that the approach based on AHC theory certainly has its limitations. Being based on expansion up to second-order terms with respect to atomic displacements, it is not expected to be highly accurate in conditions when such an expansion is not sufficient. On the other hand, the approaches based on atomic displacements usually do not have such a limitation.

In conclusion, this chapter shows ab initio calculations of temperature dependent electronic structure of inorganic halide perovskite materials $CsPbX_3$. The challenge that comes from the fact that cubic structure is not stable at zero temperature and that one obtains phonon modes with imaginary frequencies in a standard DFPT calculation was overcome by using the SCPH method that gives the phonon spectrum with real non-negative frequencies. The challenge of obtaining the energies of bands other than the CBM and the VBM in the calculations based on AHC theory was addressed by exploiting a self-consistent procedure for evaluation of relevant self-energies and spectral functions. The obtained band gaps at the lowest temperature where the material exhibits a cubic structure are in good agreement with experiment. Also, one can see that there is good agreement of calculated and experimental temperature dependence of the band gap for the $CsPbI_3$ material where reliable experimental data are available in the literature. Results of this chapter also suggest that the band gaps at the lowest temperature where the material exhibits a cubic structure are similar to the band gaps at zero temperature where the material exhibits an orthorhombic structure. Such a finding is consistent with experimental data that suggest a rather weak temperature dependence at lower temperatures where the material exhibits an orthorhombic or a tetragonal structure. Finally, it was shown that temperature dependence of band energies at the R point is most pronounced for the CBM and the VBM, while it is less pronounced for higher and lower bands.

Chapter 5

Nanostructures

Present chapter follows published results in Ref. [46] in the case of CdSe and expands upon the results and methods published in Ref. [47] for halide perovskites $CsPbX_3$ (X=Cl, Br, I). Although this chapter is dedicated to nanostructures, it relies on bulk phase results obtained in both Chapter 3 and Chapter 4 as they are one of the necessary steps in computing these results.

5.1 Introduction

Most electronic and optical devices consist of semiconductor materials, and over the years, general improvements of these devices made them smaller in size and more power efficient. The size of a bulk phase, can be as small as few micrometers, however, as one enters the scale of a few dozen nanometers or less, the electronic properties of the material start to change from the bulk counterpart. Materials at these scales are called *nanostructures* or nanocrystals, and their properties become very dependent on their size and shape. This dependence makes it possible to fine tune electronic properties, like the band gap of a material, to desired values, allowing one to replicate the electronic properties of a much more expensive or less durable material using more cost effective and/or more durable materials. Working with nanostructures whose electronic properties change with their size introduces new challenges for investigating and modeling semiconductor materials.

This chapter is dedicated to discussing methods for obtaining the electronic structure and using them on CdSe and $CsPbX_3$ (X=Cl, Br, I) halide perovskite nanostructures, whose bulk phase properties were previously explored in Chapters 3 and 4, respectively. Modeling of bulk phase materials rested on the translational invariance and periodic conditions of Bloch theorem, where the whole crystal structure can be reduced to one unit cell that is infinitely replicated without overlap in all 3 directions in real space. Calculations limited to one unit unit cell were able to produce electronic, phononic, and electron-phonon properties with much success using methods explained in Chapter 2, in Sections 2.7, 2.8, and 2.9, respectively.

On the other hand, Chapter 3 dealt with symmetry adaptation of $\mathbf{k} \cdot \mathbf{p}$ Hamiltonian in Kane model, in order to reduce the computational burden of DFT and explore the limits where $\mathbf{k} \cdot \mathbf{p}$ theory is a good approximation for electronic struc-

ture compared to DFT. In a sense, the true usefulness of the method developed in Chapter 3 will become evident in the present chapter. Namely, the translational invariance and periodicity is violated for nanostructures, since the crystal is reduced to a size where it can no longer be considered as infinite. The Bloch theorem doesn't hold anymore, so one has limited choice when it comes to modeling the electronic structure. One choice is to use DFT by making the computational cell the size of the actual nanostructure with added vacuum on its edges. This choice rapidly increases the computational resources with increase in size and creates a problem of implementing this vacuum space on computational level. Another choice is to modify the Bloch theorem and still use the $\mathbf{k}\cdot\mathbf{p}$ method with Kohn-Sham states, but for nanostructures. Using the $\mathbf{k}\cdot\mathbf{p}$ method, nanostructures can be modeled using feasible resources that range from a simple desktop personal computer to the ones required at DFT or DFPT level.

One such method that modifies the $\mathbf{k}\cdot\mathbf{p}$ model for nanostructures is the *Burt-Foreman envelope function method*. This method effectively replaces the plane wave $e^{i\mathbf{k}\cdot\mathbf{r}}$ with an envelope function in Bloch theorem, found in Chapter 2, Eq. (2.12), while still keeping the one-electron formalism. This way, after some derivation and a few approximations, the one-electron equation obtained for states in the nanostructure resembles the Kane model, however the solution requires solving for envelope functions instead. These envelope functions can also be represented in plane wave basis and the solution will consist of solving for amplitudes in that expansion. Square moduli of envelope functions also follow the ones obtained from DFT wave functions for the corresponding nanostructure [46]. Finally, this method can be easily implemented using the same symmetry-adapted Hamiltonians used for bulk in Chapter 3, making the calculations more transferable and easily implemented by simply using minimal number of $\mathbf{k}\cdot\mathbf{p}$ parameters with symmetry-adapted form of Hamiltonian.

This chapter is organized as follows. First the Burt-Foreman method is presented in Sec. 5.2. Sec. 5.3 derives the solution in plane wave basis for quantum dots, wires and wells. This methodology is applied and tested in Sec. 5.4, where results for CdSe quantum wells are compared with the same ones obtained from DFT. This comparison with DFT is performed in order to benchmark the applicability of $\mathbf{k}\cdot\mathbf{p}$ envelope function method on nanostructures. After this validation, in Sec. 5.5 the same methods are applied on lead-halide perovskites $CsPbX_3$ (X=Cl, Br, I), where besides the dependence of size and shape of the nanostructures (dots, wires and wells), these materials also show temperature dependence. Finally, Sec. 5.6 concludes the chapter with final discussion on the obtained results.

5.2 Burt-Foreman envelope function method

Nanostructures can be classified by the number of dimensions in which the bulk material is confined. When confinement is in one-dimension only, these nanostructures are referred to as quantum wells, in two-dimensions they are called quantum wires, and when confined in all three-dimensions - quantum dots. In this chapter a few assumptions will be made. First, the confinement is always made along a direction

of unit cell vectors (direct and reciprocal). Second, the nanostructure consists of an integer number of unit cells in the confinement direction (in order for chemical formula to remain the same as for bulk). Third, the effects of interaction with surrounding material and the nanostrucure is neglected at their interface and the material is not distorted in any way. At that interface it behaves as in the bulk.

In Chapter 2, Sec. 2.4, it was shown that in bulk, under the assumption that the crystal is not bounded and spans to infinity in all directions, the translational invariance introduces the electron crystal momentum $\mathbf{k}$ which was used as a continuous quantum number and the generator of translations using plane waves. The electron was described as *nearly free* using the Bloch functions $\Psi_{\mathbf{k}n}(\mathbf{r}) = u_{\mathbf{k}n}(\mathbf{r})e^{i\mathbf{k}\cdot\mathbf{r}}$ which contain a plane wave $e^{i\mathbf{k}\cdot\mathbf{r}}$ multiplied by a periodic Bloch factor $u_{\mathbf{k}n}(\mathbf{r})$. Bloch factors are invariant when translated by direct (reciprocal) lattice vectors $\mathbf{R}$ ($\mathbf{G}$) which translate any point from one unit cell (Brillouin zone) to their equivalent in another unit cell (Brillouin zone), i.e.: $u_{\mathbf{k}n}(\mathbf{r}+\mathbf{R}) = u_{\mathbf{k}n}(\mathbf{r})$ ($u_{\mathbf{k}+\mathbf{G}n}(\mathbf{r}) = u_{\mathbf{k}n}(\mathbf{r})$).

When dealing with nanostructures, the crystal is confined in one, two, or three directions, and infinite crystal approximation is not valid anymore so the full translational invariance, that was present in bulk, is lost in directions where confinement is present. Consequently, the electron crystal momentum $\mathbf{k}$ as defined in bulk (or rather, the components of $\mathbf{k}$ that are limited to 1BZ), is not a good quantum number in nanostructures. The nearly free electron can not be modulated by Bloch factors that are periodic inside one unit cell, but rather by some factors that are periodic over the whole direction of confinement. However, since the confinement itself contains unit cells which are described by Bloch functions, perhaps these Bloch functions can become modulators for some *function* that would describe a nearly free electron within the nanostructure. This *function* should be position dependent and change as it moves along the space: it should vanish (or be negligible) outside of the nanostructure and be slowly varying when compared to the bulk Bloch functions inside the nanostructure, but still follow or envelope the trend of Bloch function[1], therefore it is often called an *envelope function*.

In this formulation, the confinement, as a result, generates a *new* unit cell, one that (along the direction of the confinement) contains integer number of bulk unit cells as well the surrounding space filled with non-interacting material or vacuum that spans to infinity.

In bulk, Bloch wave functions are a product of plane waves which have the periodicity of the unit cell and Bloch factors $u_{\mathbf{k}n}(\mathbf{r})$ which would change with $\mathbf{r}$ as it moves along the atoms within the unit cell. This would suggest that plane waves are smoother than the Bloch factors. In nanostructure, envelope functions would have the periodicity of the *new* unit cell, that contains the nanostructure itself (made from several unit cells) as well as the empty space. Therefore, it follows that envelope functions are smoother than Bloch functions which would describe one bulk unit cell and much smoother than Bloch factors. This is an important assumption that will be relevant in the derivation of the envelope function equations. The larger the number of unit cells that is contained in the nanostructure the smoother the envelope

[1]Another way of thinking is to imagine a periodic system of non-interacting nanostructures what are separated by some infinitely space filled with non-interacting material or vacuum.

function would be, and for very large nanostrutures all results should approach the ones found in bulk.

Michael Burt [195, 196] proposed and later Bradley Foreman [197, 198] refined the idea of *exact envelope function* theory, now known as Burt-Foreman envelope function theory that, requires for envelope functions to be continuous and infinitely differentiable. Even though $\mathbf{k}$ is not a good quantum number, bulk Bloch functions at any $\mathbf{k}$ form a complete set, so a set can be chosen at any $\mathbf{k}_0$ in 1BZ to form the total wavefunction $\Psi(\mathbf{r})$ in a nanostructure:

$$\Psi^{\text{nano}} \equiv \Psi(\mathbf{r}) = \sum_m \psi_m(\mathbf{r})\Psi^{\text{bulk}}_{\mathbf{k}_0 m}(\mathbf{r}) = \sum_m \psi_m(\mathbf{r})u_{\mathbf{k}_0 m}(\mathbf{r})e^{i\mathbf{k}_0\cdot\mathbf{r}}, \tag{5.1}$$

where $\psi_m(\mathbf{r})$ are the envelope functions and summation is made over all possible states of an electron m. It wouldn't be wrong to write $\Psi_{\mathbf{k}_0}(\mathbf{r})$ in order to distinguish at which $\mathbf{k}$ a set of Bloch functions was used, but because sets are never mixed the indices referring to $\mathbf{k}$ are dropped for simplicity. The following is obtained when momentum operator $\mathbf{p} = -i\hbar\nabla$ and its square $p^2 = -\hbar^2\nabla^2$ act on $\Psi(\mathbf{r})$:

$$\begin{aligned}
\mathbf{p}\Psi(\mathbf{r}) &= \sum_m \left[(\mathbf{p}\psi_m)u_m + \psi_m(\mathbf{p}u_m) + \hbar\mathbf{k}_0\psi_m u_m\right] e^{i\mathbf{k}_0\cdot\mathbf{r}}, \\
p^2\Psi(\mathbf{r}) &= \sum_m \left[(p^2\psi_m) + 2(\mathbf{p}\psi_m)(\hbar\mathbf{k}_0 + \mathbf{p})\right] u_m e^{i\mathbf{k}_0\cdot\mathbf{r}} \\
&\quad + \sum_m \psi_m(p^2 + \hbar^2k_0^2 + 2\hbar\mathbf{k}_0\cdot\mathbf{p})u_m e^{i\mathbf{k}_0\cdot\mathbf{r}}.
\end{aligned} \tag{5.2}$$

The one-electron Hamiltonian $\mathcal{H}^{(1e)} = [p^2/(2m_e) + V]$ from Eq. (2.11) (Chapter 2, Sec. 2.4), can also be adapted for nanostructures using Ψ from Eq. (5.1). The general equation $\mathcal{H}^{(1e)}\Psi = E\Psi$ in this case is:

$$\begin{aligned}
&\sum_m \left[\frac{(p^2\psi_m)}{2m_e} + \frac{(\mathbf{p}\psi)}{m_e}(\hbar\mathbf{k}_0 + \mathbf{p})\right] u_m e^{i\mathbf{k}_0\cdot\mathbf{r}} \\
&+ \sum_m \psi_m \left[\frac{p^2 + \hbar k_0^2}{2m_e} + \frac{\hbar\mathbf{k}_0\cdot\mathbf{p}}{m_e} + V(\mathbf{r})\right] u_m e^{i\mathbf{k}_0\cdot\mathbf{r}} = E\sum_m \psi_m u_m e^{i\mathbf{k}_0\cdot\mathbf{r}}.
\end{aligned} \tag{5.3}$$

Assuming that $\psi_m(\mathbf{r})$ is much smoother than $u_m(\mathbf{r})$, allows for an approximation that ψ_m can be brought outside of the integral over d$\mathbf{r}$ when limits of that integral are within the bulk unit cell[2] like they are in Eq. (2.17), i.e. $\langle u_n|\,\psi_m\,|u_m\rangle \approx \psi_m\,\langle u_n|u_m\rangle$. The Eq. (5.3) is first multiplied by $e^{-i\mathbf{k}_0\cdot\mathbf{r}}$, then multiplied by $\langle u_n|$ from the right, and after integration over one bulk unit cell the following is obtained:

$$\sum_m \left[\left(\psi_m E_m + \frac{p^2\psi_m}{2m_e}\right)\delta_{nm} + \mathbf{p}_{nm}\cdot\frac{\mathbf{p}\psi_m}{m_e}\right] = E\psi_n, \tag{5.4}$$

[2]This statement, of course, should not be true for nanostructures that contain one bulk unit cell. The size limit of the nanostructure at which this is a good approximation is also not clear, since it would depend on the size, type and number of atoms inside the unit cell, so comparison with a more sophisticated method is always necessary in order to claim a valid result.

where $\mathbf{p}_{nm} = \hbar\mathbf{k}_0 + \langle u_n | \mathbf{p} | u_m \rangle$ and $\langle u_n | (p^2 + \hbar k_0^2)/(2m_e) + \hbar\mathbf{k}_0 \cdot \mathbf{p}/m_e + V | u_m \rangle = E_m \delta_{nm}$ were used. After applying the Löwdin's perturbation, the second-order $\mathbf{k} \cdot \mathbf{p}$ equation for envelope functions is obtained:

$$\begin{aligned} &\sum_m \left[\left(\psi_m E_m + \frac{p^2 \psi_m}{2m_e} \right) \delta_{nm} + \mathbf{p}_{nm} \cdot \frac{\mathbf{p}\psi_m}{m_e} + H^{(2)}_{nm} \right] = E\psi_n, \\ &H^{(2)}_{nm} = \sum_{ij} \frac{(\mathbf{p})_i}{m_e} P_{nm,ij} \frac{(\mathbf{p}\psi_m)_j}{m_e}, \\ &P_{nm,ij} = \sum_{r \neq [m,n]} \frac{(\mathbf{p}_{nm})_i (\mathbf{p}_{nm})_j}{(E_n + E_m)/2 - E_{\mathbf{k}_0 r}}, \qquad i,j = x,y,z \quad , \end{aligned} \tag{5.5}$$

Eq. (5.5) is rather similar to Eq. (2.32), and would become identical if momentum operator that acts on envelopes ψ_m is replaced with electron momentum at some $\mathbf{k}-\mathbf{k}_0$ i.e. $(\mathbf{p}\psi_m) \to (\mathbf{k}-\mathbf{k}_0)\psi_m$, or equivalently envelopes are reduced to plane waves with an amplitude of $B^{(a)}_m$ with periodicity of a bulk unit cell $\psi_m \to B^{(a)}_m e^{i(\mathbf{k}-\mathbf{k}_0)\cdot\mathbf{r}}$. If SOC would be included, the procedure would remain the same, except that $\Psi(\mathbf{r})$ would be a two component spinor and bulk parameters $\mathbf{p}_{nm}$ would become $\mathbf{p}_{nm} = \hbar\mathbf{k}_0 + \langle u_n | \mathbf{p}_{\text{soc}} | u_m \rangle$.

5.3 Envelopes in plane wave basis

In this section, a solution for one-, two- and three- dimensional confinement will be presented, which correspond to quantum wells, wires and dots, respectively. In order to simplify the derivation, it will be assumed that the nanostructure is placed at the centre of an imaginary box with infinitely thin walls which has a cuboid shape, and that the dimensions of this box allow for some non-interacting material to fill the voids of this box only along directions of confinement.

One way to solve Eq. (5.5) is to expand ψ_m as a set of plane waves and their corresponding amplitudes. In the plane wave basis, the problem effectively reduces to an infinite array of nanostructures centered inside their respected imaginary boxes, separated by a non-interacting material in the direction of the confinement. To further simplify the solution, it is assumed that this non-interacting material has identical properties as the original bulk material i.e. its $\mathbf{k} \cdot \mathbf{p}$ parameters $\mathbf{p}_{nm}$ and $P_{nm,ij}$ are the same however, the energy levels E^B_m are shifted by some amount ΔE in order to create a gap large enough to avoid any overlap with states of the examined nanostructure material $E^B_m = E_m \pm \Delta E$. This is justified when there are no contacts between different materials and non-interacting material is just supposed to imitate vacuum where all envelope functions (and by extension, full wave functions of electrons that they modulate) vanish. Band energies can be expressed as position dependent, using a step function $\chi(\mathbf{r})$ which returns 0 and 1 when $\mathbf{r}$ is inside the non-interacting material and the nanostructure, respectively:

$$E_m(\mathbf{r}) = \chi(\mathbf{r}) E_m + [1 - \chi(\mathbf{r})] E^B_m. \tag{5.6}$$

Effectively, the nanostructure of volume V_Q is now placed at the center of a box-shaped unit cell that has a volume of V_B and there are infinite amount of identical neighboring unit cells .This is reminiscent of a boxed particle problem in quantum mechanics, or rather an infinite 3D well, where solutions are also expressed in the plane wave basis and E_m^B is analogous to the infinite well potential. The envelope function $\psi_m(\mathbf{r})$ can be written as a set of plane waves:

$$\begin{aligned}\psi_m(\mathbf{r}) &= \frac{1}{V_B^{1/2}}\sum_q W_q^{(m)} e^{i\mathbf{k}_q\cdot\mathbf{r}} \\ &= \frac{1}{(L_xL_yL_z)^{1/2}}\sum_{\mathbf{q}} W_q^{(m)} e^{i(k_q^x x + k_q^y y + k_q^z z)} \\ &= \sum_q W_q^{(m)} \prod_{\alpha=x,y,z} \frac{1}{L_\alpha^{1/2}} e^{ik_q^\alpha \alpha}, \quad k_q^\alpha = \frac{2\pi}{L_\alpha} q_\alpha,\end{aligned} \tag{5.7}$$

where L_α, $\alpha = x, y, z$ is the box unit cell length along direction α, while q_α can have positive and negative integer values: $q_\alpha = 0, \pm1, \pm2, \pm3 \ldots, \pm N_{\text{pw}}^\alpha$, and N_{pw}^α is the necessary value for converging the numerical results along the direction α. This gives a total number of plane waves $N_{\text{pw}}^{\text{tot}} = \prod_{\alpha=x,y,z}(2N_{\text{pw}}^\alpha + 1)$, where N_{pw}^α is positive non-zero integer for confined dimensions. Envelope function $\psi_m(\mathbf{r}) = \psi_m(\mathbf{r} + \mathbf{R}_L)$ will now be periodic over a set of vectors $\mathbf{R}_L = \sum_\alpha R_\alpha \mathbf{e}_\alpha$, $R_\alpha = L_\alpha a_L$. Inserting Eq. (5.7) into Eq. (5.5) and multiplying with $V_B^{-1/2} e^{-i\mathbf{k}_s\cdot\mathbf{r}}$ from the left, then integrating over whole box unit cell space $\int_{V_B} \mathrm{d}\mathbf{r}$ the general form of envelope function $\mathbf{k}\cdot\mathbf{p}$ equation in plane wave basis is obtained:

$$\begin{aligned}&\sum_{m,q}\left[\frac{\hbar^2}{2m_0}\sum_{\alpha=x,y,z} k_q^\alpha k_q^\alpha \delta_{sq} + \mathcal{J}^{sq}(E_m)\right]\delta_{nm} W_q^{(m)} \\ &+ \sum_{m,q}\left[\frac{\hbar}{m_0}\sum_{\alpha=x,y,z} k_q^\alpha \mathbf{e}_\alpha\cdot\mathbf{p}_{nm}^\alpha + H_{nm}^{(2)}(s,q)\right]\delta_{sq} W_q^{(m)} = E W_s^{(n)}, \\ &H_{nm}^{(2)}(s,q) = \sum_{ij=x,y,z} \frac{\hbar k_s^i}{m_e} P_{nm,ij} \frac{\hbar k_q^j}{m_e},\end{aligned} \tag{5.8}$$

where

$$\begin{aligned}&\mathcal{J}^{sq}(E) = E_B\delta_{sq} + (E - E_B)\mathcal{J}^{sq}, \quad E_B = E \pm \Delta E_B, \\ &\mathcal{J}^{sq} = \frac{1}{V_B}\int_{V_B}\chi(\mathbf{r})\prod_{\alpha=x,y,z}\mathrm{d}\alpha\, e^{-i\Delta k_{sq}^\alpha \alpha} = \frac{1}{V_B}\int_{V_Q}\prod_{\alpha=x,y,z}\mathrm{d}\alpha\, e^{-i\Delta k_{sq}^\alpha \alpha}, \\ &\delta_{sq} = \frac{1}{V_B}\int_{V_B}\prod_{\alpha=x,y,z}\mathrm{d}\alpha\, e^{-i\Delta k_{sq}^\alpha \alpha}, \quad \Delta k_{sq}^\alpha = \frac{2\pi}{L_\alpha}(s_\alpha - q_\alpha).\end{aligned} \tag{5.9}$$

The integral $\mathcal{J}^{sq}$ (Kronecker delta δ_{sq}) from Eq. (5.9), can also be identified as a Fourier transform of $\chi(\mathbf{r})$ function from Eq. (5.6) ($f = 1$ function) integrated inside the full volume of the box unit cell V_B.

Quantum dot with cuboid shape

In the case of cuboid geometry, the integral can be separated as a product of three independent integrals:

$$\begin{aligned}\mathcal{J}^{sq} &= \prod_{\alpha=x,y,z} \mathcal{J}^{sq}_{\alpha} = \prod_{\alpha=x,y,z} \frac{1}{L_\alpha} \int_{-l_\alpha/2}^{+l_\alpha/2} \mathrm{d}\alpha\, e^{-i\Delta k^\alpha_{sq}\alpha}, \\ \mathcal{J}^{sq}_{\alpha} &= \frac{l_\alpha}{L_\alpha}\delta_{sq} + \frac{1-\delta_{sq}}{iL_\alpha \Delta k^\alpha_{sq}}(e^{+i\Delta k^\alpha_{sq} l_\alpha/2} - e^{-i\Delta k^\alpha_{sq} l_\alpha/2}).\end{aligned} \tag{5.10}$$

Quantum dot with ellipsoid shape

In the case of ellipsoid geometry, the integral $\mathcal{J}^{sq}$ can be solved by first transforming the ellipsoid into a sphere of unit radius by scaling the axes, and then by introducing spherical coordinates. It is assumed that $l_\alpha/2$ is the length of the semi-axis of the ellipsoid in direction $\alpha = x, y, z$, then new coordinates $\alpha_t = \alpha \times (2/l_\alpha)$ and $q^\alpha_{sq} = \Delta k^\alpha_{sq} \times (l_\alpha/2)$ are introduced to transform the nanostructure to a spherical shape, and a new set of spherical coordinates are obtained $(x_t, y_t, z_y) \to (r_t, \theta_t, \phi_t)$. The $\mathcal{J}^{sq}$ integral in the case of ellipsoid geometry is:

$$\begin{aligned}\mathcal{J}^{sq} &= \frac{1}{L_x L_y L_z}\frac{l_x}{2}\frac{l_y}{2}\frac{l_z}{2}\left\{\frac{4\pi}{3}\delta(\mathbf{q}_t) + 2\pi\frac{\delta(\mathbf{q}_t)-1}{iq_t}\left[I(+iq_t) - I(-iq_t)\right]\right\}, \\ I(\beta) &= \int_0^1 r_t e^{\beta r_t}\,\mathrm{d}r_t = \frac{e^\beta(\beta-1)+1}{\beta^2},\end{aligned} \tag{5.11}$$

where $\mathbf{q}_t = \sum_\alpha \Delta k^\alpha_{sq}\mathbf{e}_\alpha l_\alpha/2$ and $I(\beta)$ is solved by integrating by parts.

Quantum wire with elliptical base

If the confinement is two-dimensional like in the case of quantum wires, one direction can be chosen as non-confined one and let it be the z direction. In the non-confined direction z, that component of the plane wave becomes independent of q as the non-interacting material vanishes in that direction thus the translational invariance is restored $k^z_q \to (\mathbf{k} - \mathbf{k}_0)_z$. The integral $\mathcal{J}^{sq}$ from Eq. (5.10) will have the non-confined component equal to unity: $J^{sq}_z = 1$. In the case of rectangle geometry, confined components $\mathcal{J}^{sq}_\alpha$ are the same as for cuboid shape in Eq. (5.10). In the case of elliptic geometry, the solution is similar as for the case of ellipsoid, assuming that $l_\alpha/2$ are the semi-axes of the ellipse in the direction α. First the ellipse is transformed to a circle by scaling the axes $\alpha_t = \alpha_t \times (2/l_\alpha)$, $k^\alpha_t = \Delta k^\alpha_{sq} \times (l_\alpha/2)$, $\alpha = x, y$, and then polar coordinates are introduced $(x_t, y_t) \to (\rho, \Phi)$. The $s \neq q$

term of $\mathcal{J}^{sq}$ is then:

$$\begin{aligned}\mathcal{J}^{sq}(s \neq q) &= \frac{(l_x/2)(l_y/2)}{L_x L_y} \int_0^1 \mathrm{d}\rho\, \rho \int_0^{2\pi} \mathrm{d}\Phi\, e^{-ik'_\rho \rho \cos\Phi} \\ &= \frac{(l_x/2)(l_y/2)}{L_x L_y} \int_0^{k_\rho} \frac{\mathrm{d}(k_\rho \rho)}{k'_\rho} \frac{(k_\rho \rho)}{k_\rho} 2\pi J_0(k_\rho \rho) \\ &= 2\pi \frac{(l_x/2)(l_y/2)}{L_x L_y} \frac{J_1(k_\rho)}{k_\rho},\end{aligned} \tag{5.12}$$

where $k_\rho = \sqrt{(k_t^x)^2 + (k_t^y)^2}$, J_0 and J_1 are the spherical Bessel functions of the 0-th and 1-st order, respectively, which obey the relations:

$$\begin{aligned}&J_0(x) = \frac{1}{2\pi} \int_0^{2\pi} \mathrm{d}\Phi\, e^{-ix\cos\Phi}, \quad J_n(x) = \frac{1}{2\pi i^n} \int_0^{2\pi} \mathrm{d}\Phi\, e^{-ix\cos\Phi} e^{in\Phi}, \\ &\int_0^\infty J_n(x)\,\mathrm{d}x = 1, \qquad\qquad \frac{\mathrm{d}}{\mathrm{d}x}\left[x^m J_m(x)\right] = x^m J_{m-1}.\end{aligned} \tag{5.13}$$

Combining both the $s = q$ and $s \neq q$ terms, the $\mathcal{J}^{sq}$ for quantum wire with an elliptic base is:

$$\mathcal{J}^{sq} = \delta(k_\rho) \frac{(l_x/2)(l_y/2)\pi}{L_x L_y} + [1 - \delta(k_\rho)] \frac{2\pi(l_x/2)(l_y/2)}{L_x L_y} \frac{J_1(k_\rho)}{k_\rho}. \tag{5.14}$$

For quantum wires, the envelope function $\mathbf{k} \cdot \mathbf{p}$ equation Eq. (5.8) will have the form:

$$\begin{aligned}&\sum_m \left[\frac{\hbar^2}{2m_0}(\mathbf{k} - \mathbf{k}_0)_z^2 \delta_{nm} + \frac{\hbar}{m_0}(\mathbf{k} - \mathbf{k}_0)_z \cdot \mathbf{p}_{nm}^z\right] \delta_{sq} W_q^{(m)} \\ &+ \sum_{m,q} \left[\frac{\hbar^2}{2m_0} \sum_{\alpha=x,y} k_q^\alpha k_q^\alpha \delta_{sq} + \mathcal{J}^{sq}(E_m)\right] \delta_{nm} W_q^{(m)} \\ &+ \sum_{m,q} \left[\frac{\hbar}{m_0} \sum_{\alpha=x,y} k_q^\alpha \mathbf{e}_\alpha \cdot \mathbf{p}_{nm}^\alpha + H_{nm}^{(2)}(s,q)\right] \delta_{sq} W_q^{(m)} = E W_s^{(n)},\end{aligned} \tag{5.15}$$

$$\begin{aligned}H_{nm}^{(2)}(s,q) &= \sum_{ij} \frac{\hbar \mathcal{K}_s^i}{m_e} P_{nm,ij} \frac{\hbar \mathcal{K}_q^j}{m_e}, \\ \mathcal{K}_q &= (\mathbf{k} - \mathbf{k}_0)_z + \sum_{\alpha=x,y} k_q^\alpha \mathbf{e}_\alpha.\end{aligned}$$

Quantum well

For quantum wells, the confinement is present in just one direction. There is only one possible geometry, which is linear. Assuming that confinement direction is z,

the $\mathcal{J}^{sq}$ integral from Eq. (5.10) reduces to $\mathcal{J}^{sq} = \mathcal{J}_z^{sq}$. The envelope function $\mathbf{k}\cdot\mathbf{p}$ equation Eq. (5.8) for quantum wells will be:

$$\begin{aligned}
&\sum_m \left[\frac{\hbar^2}{2m_0}\sum_{\alpha=x,y}(\mathbf{k}-\mathbf{k}_0)_\alpha^2\delta_{nm} + \frac{\hbar}{m_0}\sum_{\alpha=x,y}(\mathbf{k}-\mathbf{k}_0)_\alpha\cdot\mathbf{p}_{nm}^\alpha\right]\delta_{sq}W_q^{(m)} \\
&+\sum_{m,q}\left[\frac{\hbar^2}{2m_0}k_q^z k_q^z\delta_{sq} + \mathcal{J}^{sq}(E_m)\right]\delta_{nm}W_q^{(m)} \\
&+\sum_{m,q}\left[\frac{\hbar}{m_0}k_q^z\mathbf{e}_x\cdot\mathbf{p}_{nm}^z + H_{nm}^{(2)}(s,q)\right]\delta_{sq}W_q^{(m)} = EW_s^{(n)},
\end{aligned} \tag{5.16}$$

$$H_{nm}^{(2)}(s,q) = \sum_{ij}\frac{\hbar\mathcal{K}_s^i}{m_e}P_{nm,ij}\frac{\hbar\mathcal{K}_q^j}{m_e}, \quad \mathcal{K}_q = \sum_{\alpha=x,y}(\mathbf{k}-\mathbf{k}_0)_\alpha + k_q^z\mathbf{e}_x.$$

Convergence tests: size of the box and the number of plane waves

Since the nanostructure is placed inside of a box unit cell with non-interacting material, the volume of this box V_B should theoretically approach infinity. However, this would also require an infinite amount of plane waves $N_{\text{pw}}^{\text{tot}}$ in the expansion in Eq. (5.7) which would not be computationally feasible within a numerical calculation. The nanostructure $\mathbf{k}\cdot\mathbf{p}$ Hamiltonian matrix scales with number of bands N_{bands} and $N_{\text{pw}}^{\text{tot}}$, so the square matrix that needs to be diagonalized will have $(N_{\text{pw}}^{\text{tot}}\times N_{\text{band}})^2$ elements when using envelopes. Because this number can become very large in some cases, diagonalizing such matrices becomes unfeasible for desktop computers, it is important to study how much computational resources is needed to ensure the convergence of the results. This topic is explored in author's published work in Ref. [47].

In Ref. [47], this convergence is explored for $CsPbBr_3$ quantum wells using 8×8 and 26×26 bulk Hamiltonians. There, convergence tests show that for quantum well nanostrucure centered inside of a box with non-interacting material, size of that box should be at least several bulk unit cells larger than the nanostructure along the confinement direction. Then, the number of plane waves N_{pw} used should be equal to the number of bulk unit cells that make up the box, along the direction of confinement. For example, a quantum well of size $l = 6a$, should be centered inside of a box with linear dimension of $L = 3l = 18a = N_{\text{B}}a$, where a is the length of a unit cell along the direction of the confinement, the number of sufficient plane waves is $N_{\text{pw}} = N_{\text{B}} = 18$ in order to ensure convergence of the numeric results for the band gap. This gives $N_{\text{pw}}^{\text{tot}} = 2\times N_{\text{pw}} + 1 = 37$ total plane waves and a square matrix with $(37\times N_{\text{band}})^2$ elements to be diagonalized.

Another result from Ref. [47], is that a divergence for band gaps was observed for 26×26 Hamiltonian when $N_{\text{pw}} > N_{\text{B}}$. This divergence wasn't observed with 8×8 Hamiltonians that have much less parameters. Therefore in most cases, a fixed value of $N_{\text{pw}} = N_{\text{B}}$ should be kept. For large wells, where the band gap is asymptotically approaching bulk values, convergence is much faster than for smaller or intermediate

wells, therefore number of plane waves can be smaller than the number of unit cells that make up the size of the box along the confinement direction $N_{\mathrm{pw}} < N_{\mathrm{B}}$. Although this is not very much useful for quantum wells, since available computational resources are almost always met for modern desktop computers, in the case of wires and dots this information is important in order to avoid costly calculations for very large nanostructures[3] that can easily exert computational resources with $N_{\mathrm{pw}} = N_{\mathrm{B}}$ only to obtain the same result with $N_{\mathrm{pw}} < N_{\mathrm{B}}$.

5.4 Comparison of DFT and Burt-Foreman envelope method

This section, combines the symmetry-adapted Hamiltonians from Chapter 3 with $\mathbf{k} \cdot \mathbf{p}$ methodology of envelope functions from Sec. 5.2. In Chapter 3, and Ref. [45], results from $\mathbf{k} \cdot \mathbf{p}$ using Kane method for band structure were compared to the ones obtained with DFT in order to benchmark the $\mathbf{k} \cdot \mathbf{p}$ method and determine how accurate it is w.r.t. the number of bands included in the Hamiltonian and distance from the unperturbed point $\mathbf{k}_0$ in the case of bulk zinc-blende CdSe. In this section, a similar approach is taken in order to compare $\mathbf{k} \cdot \mathbf{p}$ results obtained using Burt-Foreman method for quantum wells with DFT results. Even though DFT is a powerful tool for computing electronic structure, it does have limitations regarding the size of the unit cell which it computes. In the case of nanostructures, these unit cells can become so large that the computation either becomes unfeasible due to large memory requirements or feasible only for simplest crystals and low dimensions of confinement. In the later case, the computational time is much longer than in the case of bulk. For that reason, $\mathbf{k} \cdot \mathbf{p}$ is a good method that can drastically reduce the computational resources and produce reliable results for the electronic structure. However, reducing computational resources comes with the cost since perturbative approach is unable to produce the results in same detail as a non-perturbative, direct DFT calculation. As in the case for bulk, some fair comparison is needed in order to understand the limitations of the $\mathbf{k} \cdot \mathbf{p}$ method for nanostructures. For this comparison, quantum wells made from stacked zinc-blende CdSe layers were calculated using DFT and $\mathbf{k} \cdot \mathbf{p}$ envelope method. All these finding were published in Ref. [46].

Computational details for CdSe quantum wells

Within DFT, calculation of electronic states was performed by considering a slab whose surfaces are perpendicular to the [001] direction. The slab was terminated with Cd layer at both surfaces and pseudohydrogen atoms of charge 1.5 were added in order to passivate the dangling bonds at surfaces. Pseudohydrogen atoms were positioned at a distance of 1.58 Å from the corresponding Cd atom. For slabs the width of $\leq 6a$ ($\geq 6a$), the vacuum region of the width equal to $3a$ (half of the

[3] That is, the ones whose gap is approaching bulk values asymptotically when their size is increased.

slab width) was added on both sides of the quantum well, to avoid the interaction of the quantum well with its images caused by the periodic boundary conditions in the calculation. The calculations were performed for quantum wells containing from 1 to 18 CdSe unit cells. The size of the quantum well here is defined as the distance between the two pseudohydrogen passivating layers. In order to lower the computational cost and therefore extend the range of well widths, only the case when SOC is omitted is considered.

Within $\mathbf{k} \cdot \mathbf{p}$ method, the ΔE for the non-interacting material was set at $\Delta E =$ 5 eV, the length of the box was $L_z = 20$ nm and $N_{pw} = 50$. These values were chosen to be sufficiently large so that the further increase would not affect the results.

Band gap comparisons between DFT and $\mathbf{k} \cdot \mathbf{p}$

Figure 5.1 shows the dependence of the band gap as a function of well width obtained from DFT and $\mathbf{k} \cdot \mathbf{p}$ envelope method. As mentioned, SOC was omitted in DFT calculations in order to reduce the computational resources, hence only $\mathbf{k} \cdot \mathbf{p}$ results without SOC are presented for a fair comparison, both using the standard 4×4 and extended 13×13 Hamiltonian. The agreement between DFT and $\mathbf{k} \cdot \mathbf{p}$ results as well as between regular and extended Hamiltonian within $\mathbf{k} \cdot \mathbf{p}$ is excellent. For quantum well widths of three lattice constants and larger the band gap differences are smaller than 20 meV. The agreement is quite satisfactory even for rather thin wells of 1 and 2 unit cells, where one might expect for $\mathbf{k} \cdot \mathbf{p}$ to not perform quite well. This is even more impressive when taken into consideration that, the calculation of the quantum well electronic structure in $\mathbf{k} \cdot \mathbf{p}$ can take only a few seconds on a single-core desktop computer, regardless of the width of the well. However, DFT calculations can take minutes or hours depending on the width of the well when using a high performance computing cluster with several nodes containing multi-core processors each. For example, the DFT results presented here were obtained for approximately 3 min using 32 cores and 21 hours using 64 cores for narrowest and widest well, respectively. When this computational requirement gets scaled for nanostructures with more than one dimensional confinement such as wires and dots, and for crystals with more atoms in the unit cell, the advantages of $\mathbf{k} \cdot \mathbf{p}$ over DFT become even more pronounced. Since the periodicity is present only in one direction for quantum wires, or there is none in the case of quantum dots, with increase in supercell sizes, the number of atoms inside them can become so large that these problems become computationally intractable for DFT. On the other hand, $\mathbf{k} \cdot \mathbf{p}$ is almost routinely used to study quantum dots and wires, see for example Refs. [199, 200, 201, 202, 203, 204].

Next, the origin of surprisingly good agreement between DFT and $\mathbf{k} \cdot \mathbf{p}$ for thin wells is discussed. Within $\mathbf{k} \cdot \mathbf{p}$ the atomistic wavefunction (shown in Figure 5.2 in full lines) is represented in terms of the product of slowly varying envelope functions (shown in Figure 5.2 in dashed lines) and rapidly varying bulk Bloch functions, while the only additional approximation in $\mathbf{k} \cdot \mathbf{p}$ with respect to the atomistic method (DFT in our case) comes from truncation of the wavefunction expansion to a limited set of bands. For this reason, the excellent agreement between $\mathbf{k} \cdot \mathbf{p}$ and DFT results for

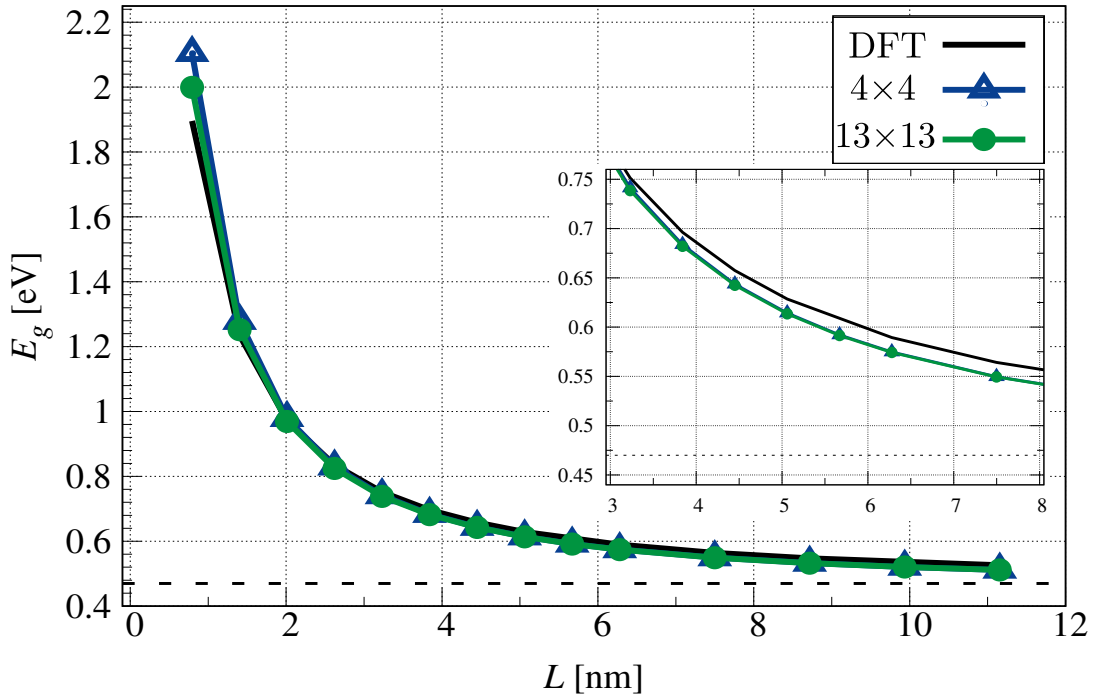

Figure 5.1. Dependence of zincblende CdSe quantum well band gap on well width. The results obtained from DFT without the effects of spin-orbit coupling and from standard 4×4 and extended 13×13 $\mathbf{k} \cdot \mathbf{p}$ models are presented. The inset shows the zoom of the same dependence to the narrower range in the figure. The horizontal dashed line denotes the bulk DFT band gap.

wide wells is expected because basis functions used in $\mathbf{k}\cdot\mathbf{p}$ provide a good basis set in this case. In the case of very thin wells, one could argue that the representation of the wavefunction in terms of the product of envelope functions and bulk Bloch functions for a few bands only cannot be a good representation because the system is rather different from bulk and therefore the basis formed from bulk Bloch functions cannot be a good basis. The results for CdSe wells confirm that such an argument is certainly valid to some extent because the agreement between DFT and $\mathbf{k}\cdot\mathbf{p}$ becomes somewhat worse for quite thin wells. Nevertheless, the agreement between DFT and $\mathbf{k}\cdot\mathbf{p}$ is quite satisfactory even then. It should be noted as well that the use of pseudohydrogen surface passivation also contributes in making the wave functions of thin wells closer to wave functions of bulk material.

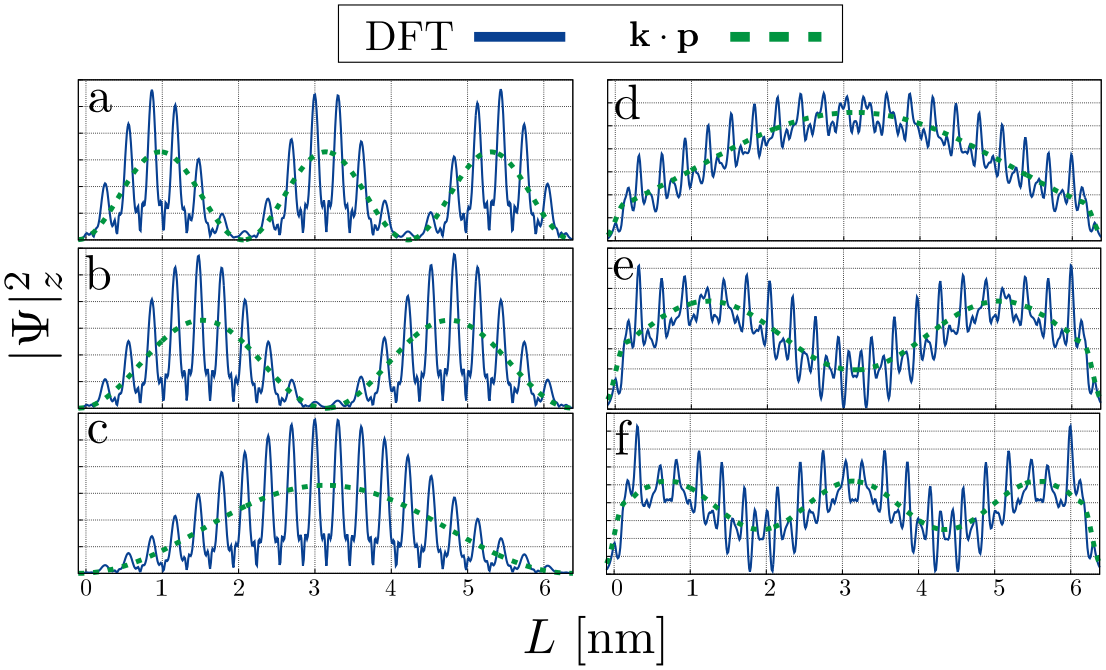

Figure 5.2. The wavefunction moduli squared of quantum well states obtained from DFT without the effects of spin-orbit coupling and the 4-band $\mathbf{k}\cdot\mathbf{p}$ model. The DFT wave functions are presented by performing the in-plane average of wavefunction moduli squared. The $\mathbf{k}\cdot\mathbf{p}$ wave functions are presented by a sum $\sum_n |\Psi_n(z)|^2$. The wave functions that are presented in the figure correspond to the following states: a) VBM-4, b) degenerate VBM-3 and VBM-2, c) degenerate VBM-1 and VBM, d) CBM, e) CBM+1, f) CBM+2, where VBM (valence band maximum) denotes the highest energy state in the valence band, while CBM (conduction band minimum) denotes the lowest energy state in the conduction band.

Band gap obtained from $\mathbf{k}\cdot\mathbf{p}$ with G_0W_0 energies

Upon confirming the accuracy of the $\mathbf{k}\cdot\mathbf{p}$ method when compared to DFT with PBEsol functional for CdSe quantum wells, one can continue by performing the same calculations with SOC included and improved gap values using G_0W_0 self-energy

corrections to $E_{\mathbf{k}_0 n}$. These energies were also used in obtaining the second-order $\mathbf{k}\cdot\mathbf{p}$ parameters (all the parameters of these Hamiltonians are given in Sections III-F and III-H of Supplementary Information in Ref. [46]). Furthermore, to obtain an accurate quasi-particle band gap, a correction which takes into account the dielectric mismatch between the quantum well and the vacuum, i.e. the image charge effect is added to the band gap. This correction was added using the analytical formula presented in Ref. [205], which was also recently applied in a DFT study of CdSe nanoplatelets [206]. The results obtained are presented in Figure 5.3 along with the results obtained from $\mathbf{k}\cdot\mathbf{p}$ Hamiltonians parametrized from DFT using PBEsol functional, which are given for comparison. As expected, a significantly larger band gaps using $\mathbf{k}\cdot\mathbf{p}$ Hamiltonians parametrized from G_0W_0 calculation of bulk are obtained. Noting that the focus here is on the single particle energies and that the reported gaps are the quasiparticle band gaps. To obtain the optical gap, one would additionally need to consider excitonic effects, which was also recently done for CdSe nanoplatelets in Ref. [206].

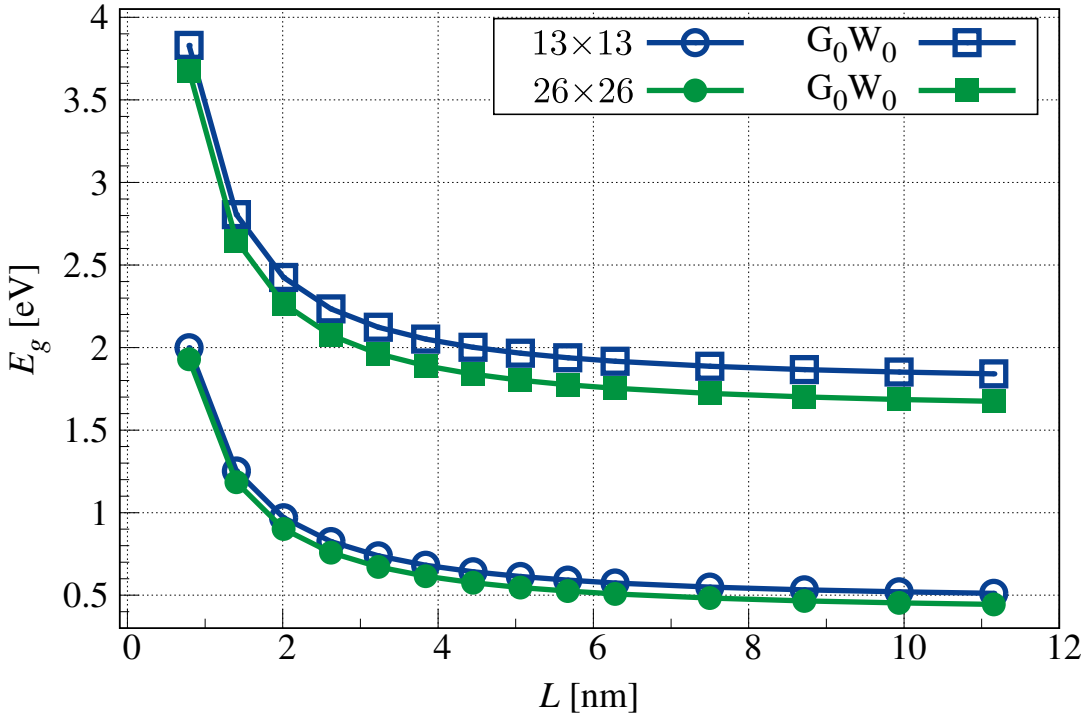

Figure 5.3. Well width dependence of zincblende CdSe quantum well band gap calculated using the $\mathbf{k}\cdot\mathbf{p}$ method. The parameters of the $\mathbf{k}\cdot\mathbf{p}$ Hamiltonian were extracted from G_0W_0 calculation of bulk band structure. The results obtained with and without the effects of spin-orbit interaction are shown respectively in full and empty squares. The results obtained from $\mathbf{k}\cdot\mathbf{p}$ Hamiltonians parametrized from DFT are shown for comparison in full (the case with spin-orbit interaction) and empty (the case without spin-orbit interaction) circles.

5.5 Temperature dependent band gaps of perovskite nanostructures

Sec. 5.4 served as a check for the present methodology, where DFT results were used as a benchmark for $\mathbf{k}\cdot\mathbf{p}$ envelope function method, where band gaps and wavefunction square moduli were compared for CdSe quantum wells. Having performed necessary checks, the same method can be applied for other materials, like the ones in Ref. [207].

This section combines the symmetry-adapted Hamiltonians from Chapter 3 with methodology of $\mathbf{k}\cdot\mathbf{p}$ that uses envelope functions from Sec. 5.2 with results obtained for temperature dependent electronic structure from Chapter 4 in order to produce the final result of this thesis i.e. the temperature dependent band gap of halide-lead perovskite nanostructures. Results are presented for quantum dots and wires of different shapes as well as for quantum wells.

Parameters for $\mathbf{k}\cdot\mathbf{p}$ Hamiltonian, $\mathbf{p}_{nm}$ and $P_{nm,ij}$ are obtained from DFT wave functions obtained using PBE (PBEsol) functional for cubic $CsPbI_3$ ($CsPbCl_3$ and $CsPbBr_3$), while E_m parameters are obtained from PBE0 functionals with temperature renormalization self-energies $\Sigma(T)$ obtained from self-consistent method, as described in Chapter 4.

5.5.1 Quantum dot with cubic shape

For cubic halide-lead perovskites, cubic shape quantum dots are consist of cubic unit cells with lattice constant a =10.6, 11.1 and 12.1 for $CsPbX_3$, X=Cl, Br, and I, respectively. These unit cells are considered to be stacked together to form a cube shaped nanostructure that is confined in all three directions.

Figure 5.4 (5.5 and 5.6) shows band energies obtained using 8×8 and 26×26 Hamiltonians for nanostructures at the temperature of phase transition to cubic structure $T = 320$ K ($T = 400$ K and $T = 300$ K). Comparing the 8×8 and 26×26 results, one can see that for very small dots ($l = 2a$ and $l = 6a$) band energies are very distinct between the two, while this difference becomes less pronounced with intermediate dots ($l = 6a$ and $l = 8a$). This trend is continued with the increase of size of the dot, until band energies start to band together and it becomes hard to distinguish them individually, so one cannot make a fair comparison between the 8×8 and 26×26 results, like for the case of large dots ($l = 10a$ and $l = 12a$). Even though gap values are very close between 8×8 and 26×26 results, the rest of the bands show much discrepancy especially for small and intermediate dots. If one were to investigate phenomena other than the band gap itself, like absorption, where one must account on all possible transitions between all valence and conduction states, the higher resolution of 26×26 over 8×8 Hamiltonian would be very beneficial. In the following discussion, results will be mostly focused on the band gap itself.

Figure 5.7 (5.8 and 5.9) shows band edges and gaps for $CsPbCl_3$ ($CsPbBr_3$ and $CsPbI_3$) depending on the nanostructure size, obtained at the temperature of phase transition to cubic structure $T = 320$ K ($T = 400$ K and $T = 300$ K) and several temperatures above. As previously discussed, $\mathbf{k}\cdot\mathbf{p}$ results for very small

nanostructures are not expected to be good, as discussed in Sec. 5.4 and Sec. 5.2, and are deliberately left out of the plot. Similarly, Figure 5.10(5.11 and 5.12) shows band edges and gaps for $CsPbCl_3$($CsPbBr_3$ and $CsPbI_3$) depending on the temperature, for a few selected sizes of the nanostructure: $l = 4a, 6a, 8a, 16a$, where l is the length of one edge of the cube and a is the lattice constant. On both mentioned figures for $CsPbCl_3$($CsPbBr_3$ and $CsPbI_3$), one can see that both 8×8 and 26×26 Hamiltonians produce very similar results: almost identical for VBM, with discrepancy for CBM (and therefore band gap) not greater than 0.4 meV, 0.2 meV and 0.05 meV in the case of very small ($4a \leq l < 8a$), intermediate ($8a \leq l < 12a$) and large ($12a \leq l$) dots, while keeping consistent slopes with across all sizes and temperatures, with 26×26 Hamiltonians producing somewhat smaller values for the band gap in all cases. The same conclusion can be made for spherical shape quantum dots found in Appendix D.1.

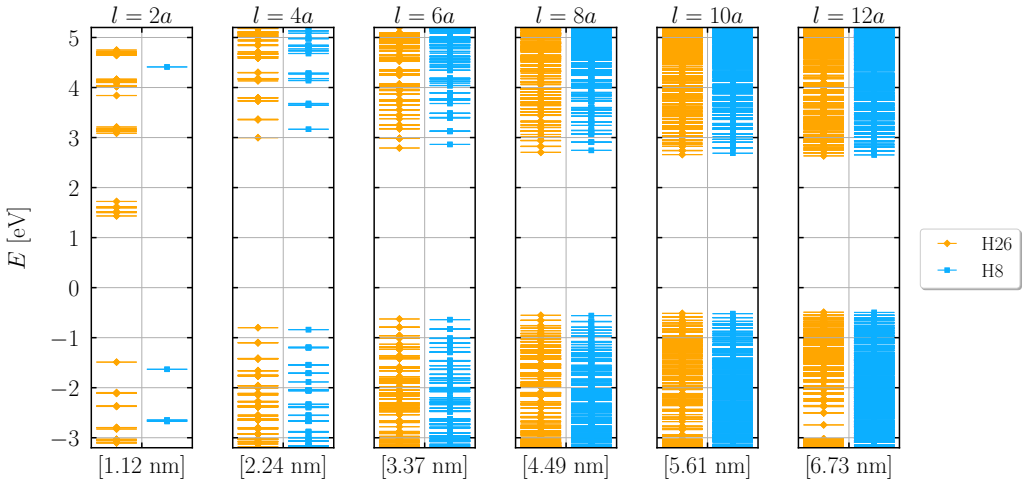

Figure 5.4. Comparison of band energies between 8×8 and 26×26 Hamiltonian for $CsPbCl_3$ cubic quantum dots of different sizes at $T = 400$ K, where l is the length of one edge of the cube, and H8(H26) are results obtained from 8×8(26×26) Hamiltonian.

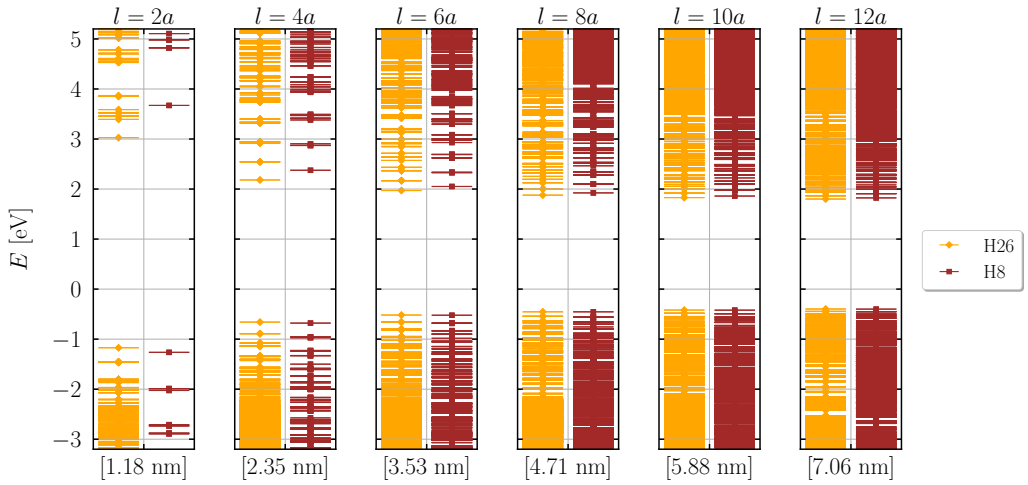

Figure 5.5. Comparison of band energies between 8×8 and 26×26 Hamiltonian for $CsPbBr_3$ cubic quantum dots of different sizes at $T = 400$ K, where l is the length of one edge of the cube, and H8(H26) are results obtained from 8×8(26×26) Hamiltonian.

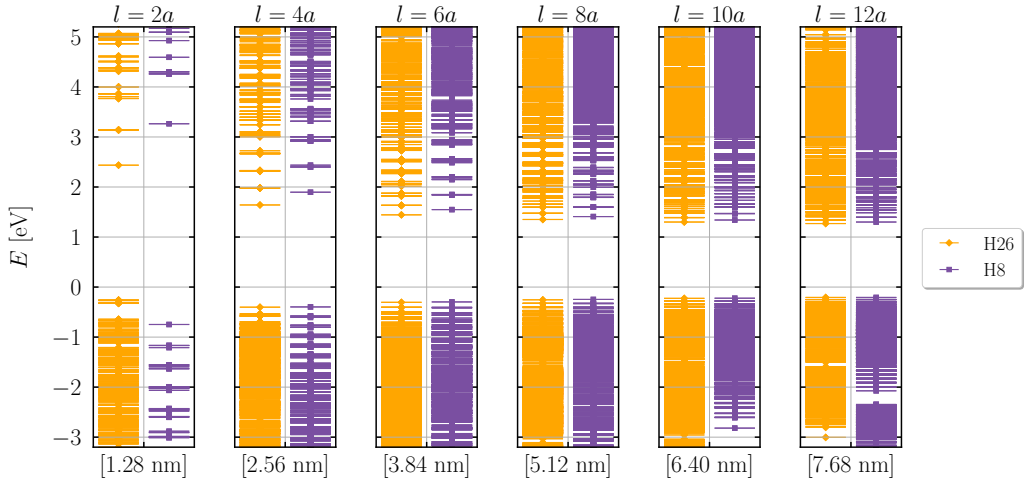

Figure 5.6. Comparison of band energies between 8×8 and 26×26 Hamiltonian for $CsPbI_3$ cubic quantum dots of different sizes at $T = 300$ K, where l is the length of one edge of the cube, and H8(H26) are results obtained from 8×8(26×26) Hamiltonian.

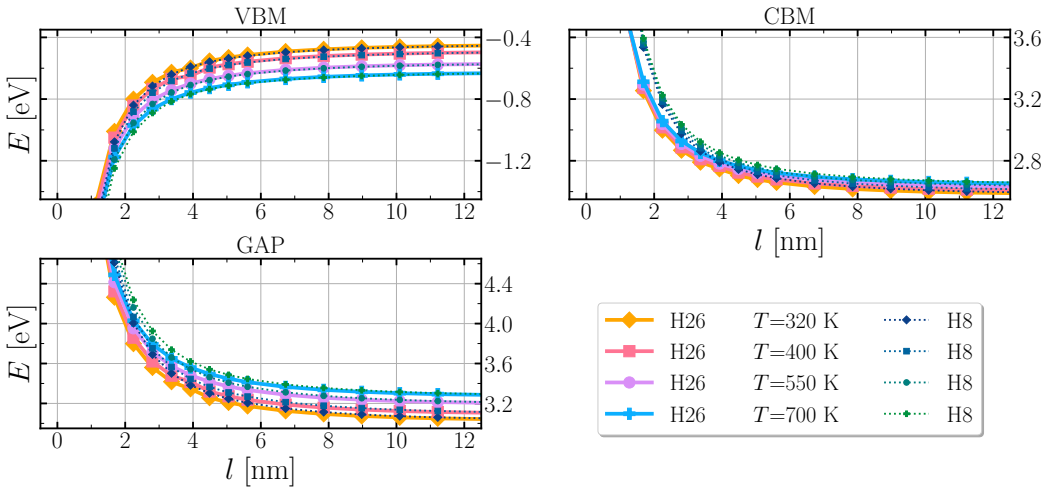

Figure 5.7. Energies of band edges and gap for $CsPbCl_3$ cubic quantum dots of different sizes at several selected temperatures, where l is the length of one edge of the cube, and VBM (CBM) are valence band maximum (conduction band minimum).

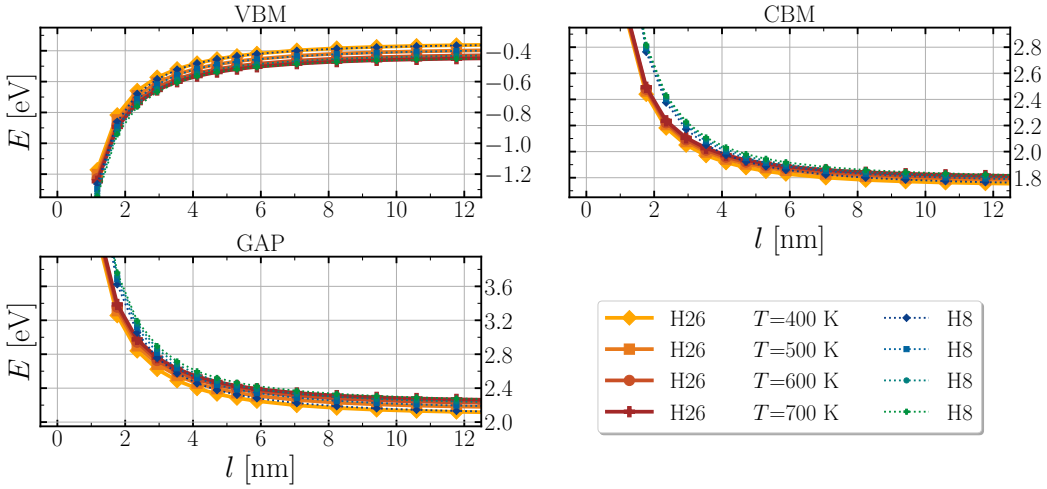

Figure 5.8. Energies of band edges and gap for $CsPbBr_3$ cubic quantum dots of different sizes at several selected temperatures, where l is the length of one edge of the cube, and VBM (CBM) are valence band maximum (conduction band minimum).

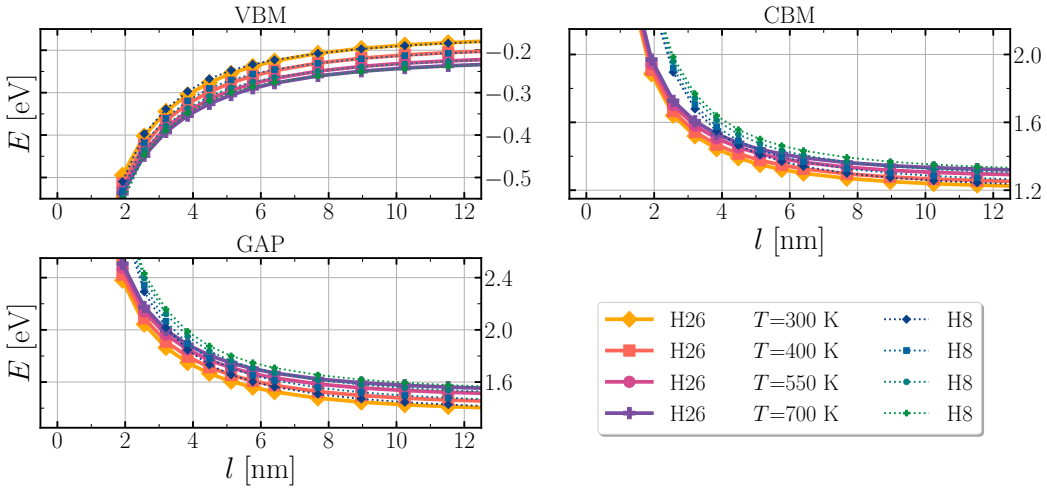

Figure 5.9. Energies of band edges and gap for $CsPbI_3$ cubic quantum dots of different sizes at several selected temperatures, where l is the length of one edge of the cube, and VBM (CBM) are valence band maximum (conduction band minimum).

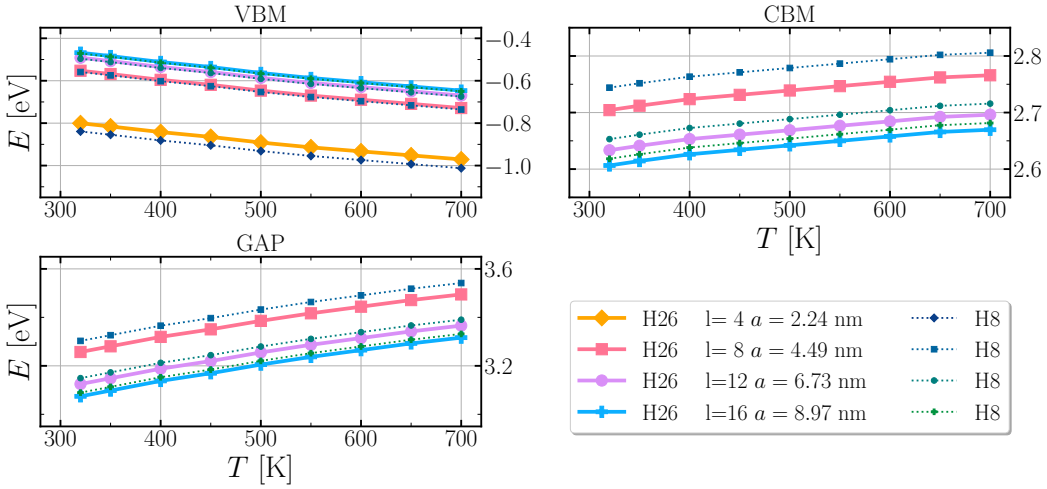

Figure 5.10. Energies of band edges and gap for $CsPbCl_3$ cubic quantum dots at different temperatures for several selected sizes, where l is the length of one edge of the cube, and VBM (CBM) are valence band maximum (conduction band minimum).

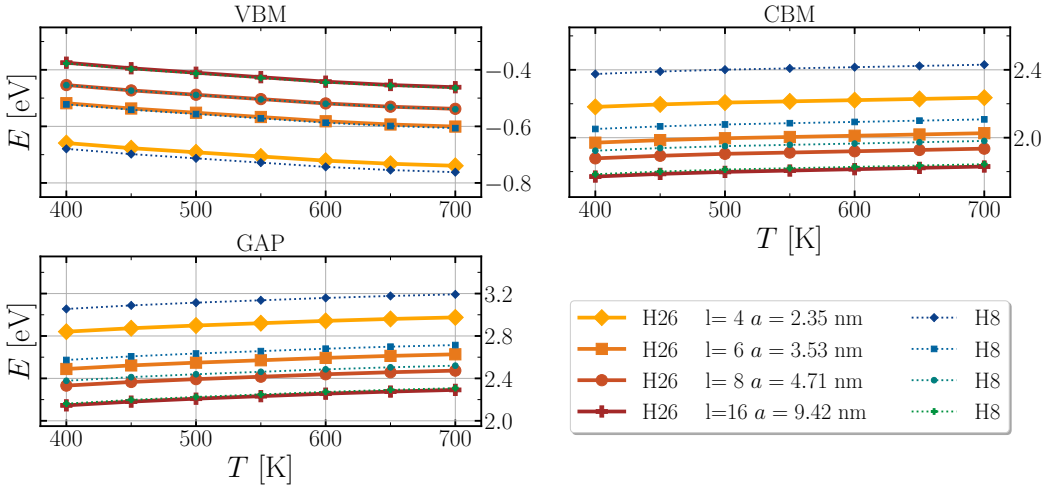

Figure 5.11. Energies of band edges and gap for $CsPbBr_3$ cubic quantum dots at different temperatures for several selected sizes, where l is the length of one edge of the cube, and VBM (CBM) are valence band maximum (conduction band minimum).

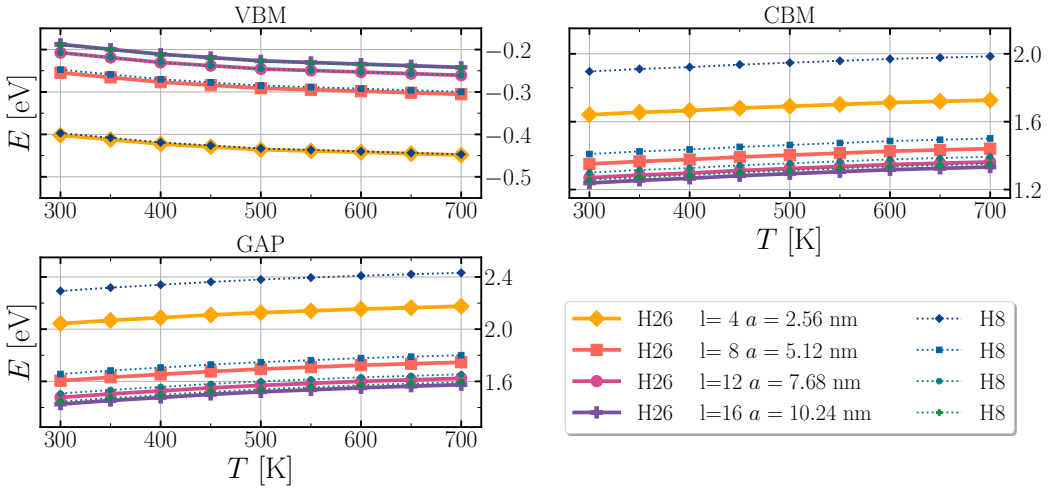

Figure 5.12. Energies of band edges and gap for $CsPbI_3$ cubic quantum dots at different temperatures for several selected sizes, where l is the length of one edge of the cube, and VBM (CBM) are valence band maximum (conduction band minimum).

5.5.2 Quantum wire with square base

For cubic halide-lead perovskites, squared shape quantum wires consist of cubic unit cells with lattice constant a =10.6, 11.1 and 12.1 for $CsPbX_3$, X=Cl, Br, and I, respectively. Unit cell of the nanostructure is formed by expanding the supercell to include equal number of unit cells in x and y directions and form a cuboid of $m \times a, m \times a, a$ dimensions in x, y, z directions, respectively, where the base of the cuboid is a square with length $l = ma$. This way, x and y are directions of confinement and z is the direction that resembles bulk periodic conditions. The same discussion for energies of the band gaps and edges as the one for quantum dots from Sec. 5.5.1 can be made here, except that discrepancies between 8×8 and 26×26 Hamiltonians are less pronounced and curvature slopes are less steep when decreasing the dimensions of the nanostructure. Both 8×8 and 26×26 Hamiltonians produce very similar results: almost identical for VBM, with discrepancy for CBM (and therefore band gap) not greater than 0.2 meV, 0.1 meV and 0.05 meV in the case of very small ($4a \leq l < 8a$), intermediate ($8a \leq l < 12a$) and large ($12a \leq l$) dots, while keeping consistent slopes across all sizes and temperatures, with 26×26 Hamiltonians producing somewhat smaller values for the band gap in all cases. The same conclusion can be made for quantum wires with circular base found in Appendix D.2.

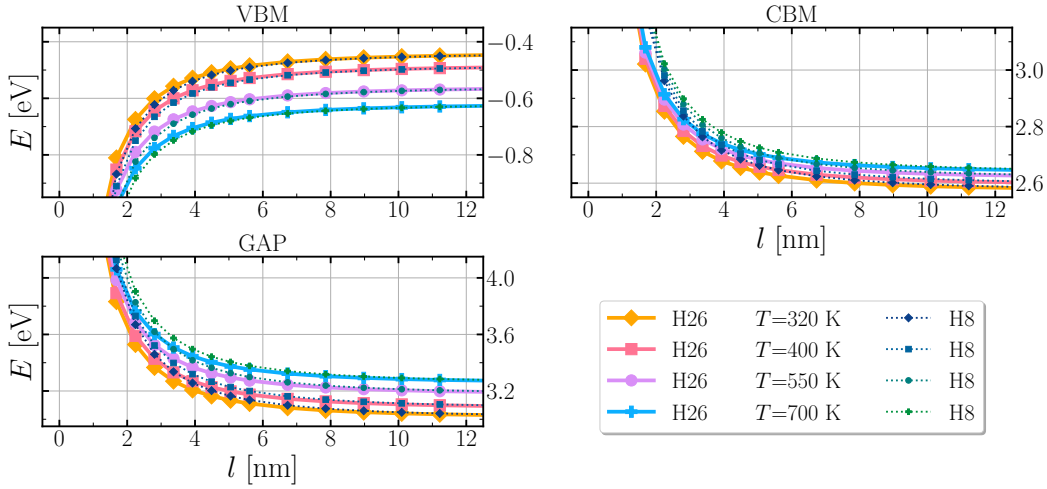

Figure 5.13. Energies of band edges and gap for $CsPbCl_3$ squared quantum wires of different sizes at several selected temperatures, where l is the length of the edge of the square base of the wire, and VBM (CBM) are valence band maximum (conduction band minimum).

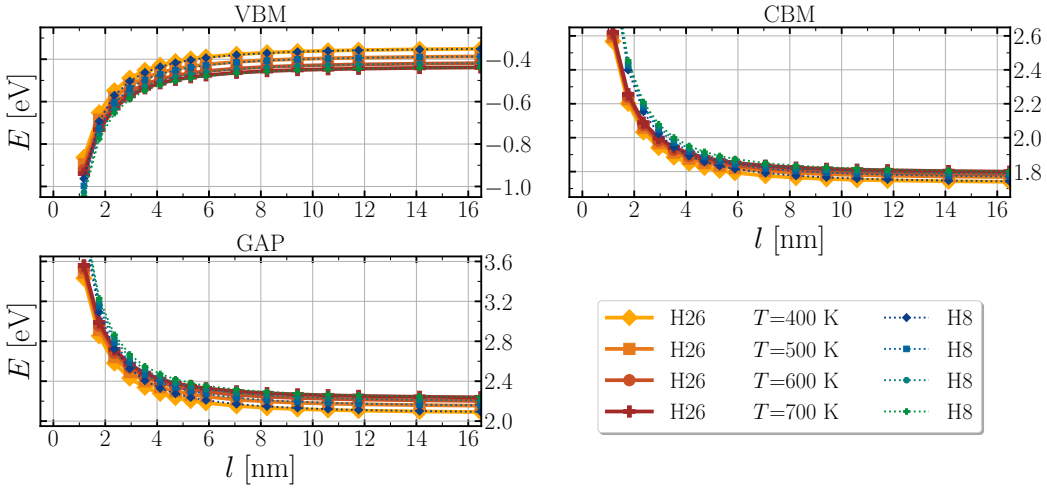

Figure 5.14. Energies of band edges and gap for $CsPbBr_3$ squared quantum wires of different sizes at several selected temperatures,where l is the length of the edge of the square base of the wire, and VBM (CBM) are valence band maximum (conduction band minimum).

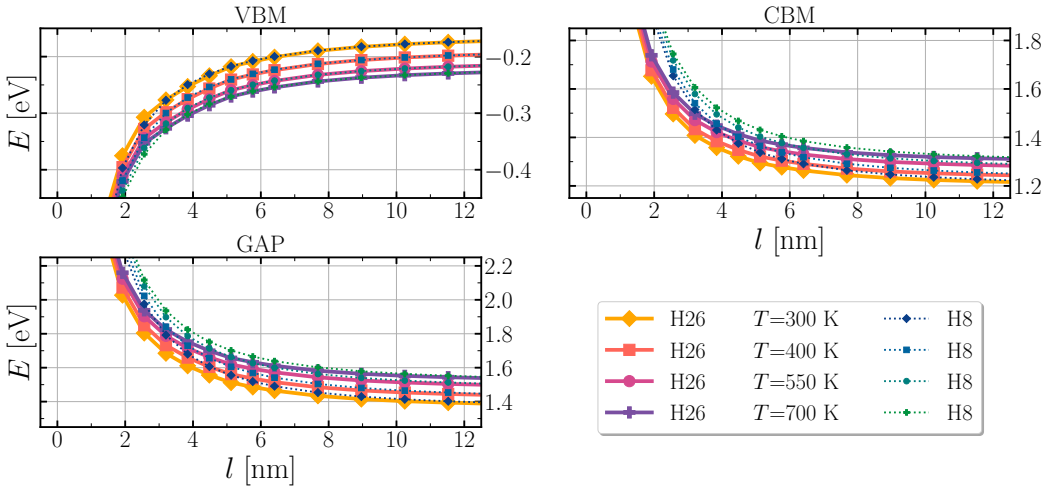

Figure 5.15. Energies of band edges and gap for $CsPbI_3$ squared quantum wires of different sizes at several selected temperatures, where l is the length of the edge of the square base of the wire, and VBM (CBM) are valence band maximum (conduction band minimum).

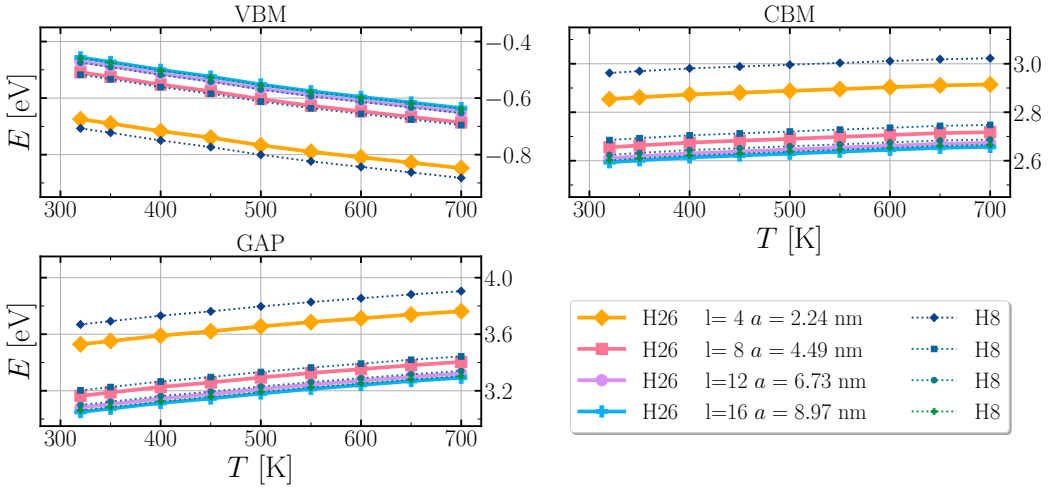

Figure 5.16. Energies of band edges and gap for $CsPbCl_3$ squared quantum wires at different temperatures for several selected sizes, where l is the length of the edge of the square base of the wire, and VBM (CBM) are valence band maximum (conduction band minimum).

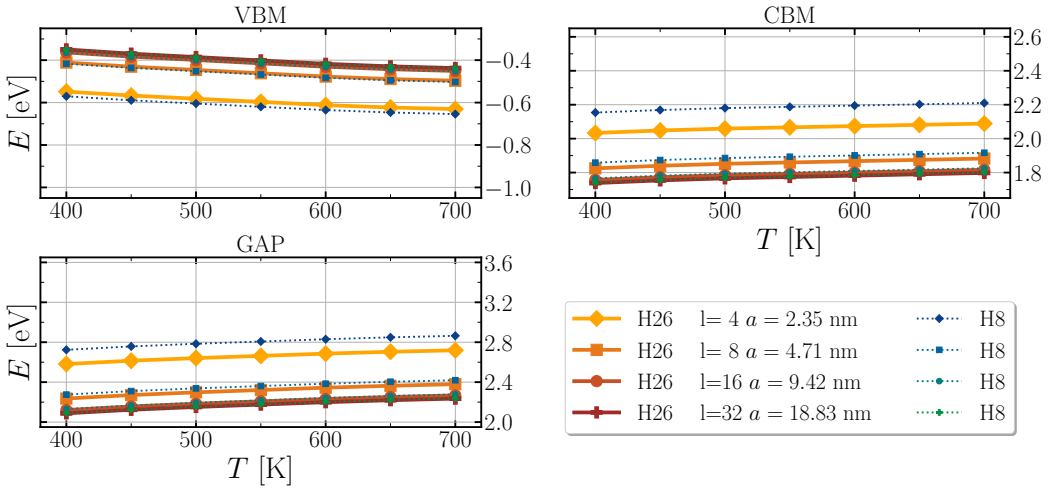

Figure 5.17. Energies of band edges and gap for $CsPbBr_3$ squared quantum wires at different temperatures for several selected sizes,where l is the length of the edge of the square base of the wire, and VBM (CBM) are valence band maximum (conduction band minimum).

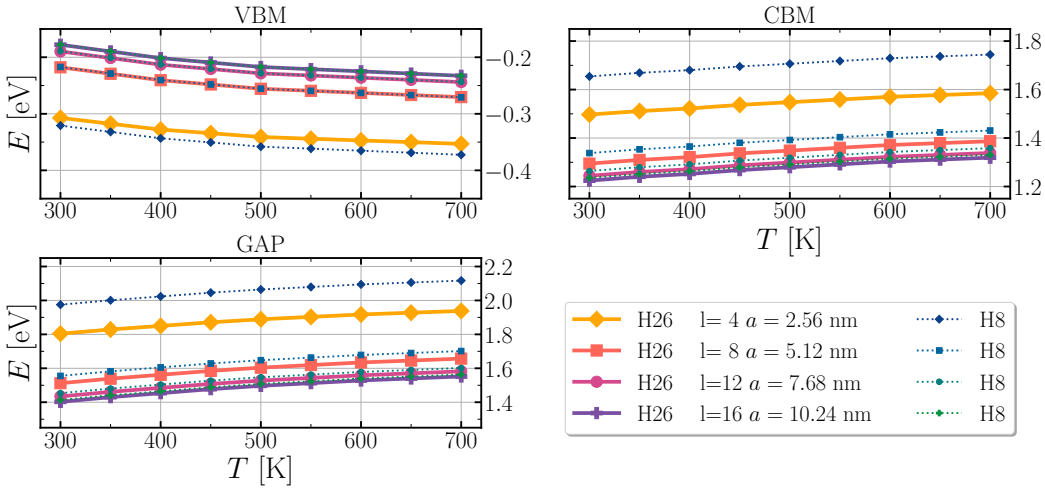

Figure 5.18. Energies of band edges and gap for $CsPbI_3$ squared quantum wire at different temperatures for several selected sizes, where l is the length of the edge of the square base of the wire, and VBM (CBM) are valence band maximum (conduction band minimum).

5.5.3 Quantum well

For cubic halide-lead perovskites, quantum wells consist of cubic unit cells with lattice constant a =10.6, 11.1 and 12.1 for $CsPbX_3$, X=Cl, Br, and I, respectively. Unit cell of the nanostructure is formed by expanding the supercell to include m number of unit cells in z direction and form a cuboid of $a, a, m \times a$ dimensions in x, y, z directions, respectively. This way, z is the direction of confinement and x, y plane resembles bulk periodic conditions. The same discussion for energies of the band gaps and edges as the one for quantum dots from Sec. 5.5.1 and Sec. 5.5.2 can be made here, except that discrepancies between 8×8 and 26×26 Hamiltonians are less pronounced and curvature slopes are even less steep when decreasing the dimensions of the nanostructure. Both 8×8 and 26×26 Hamiltonians produce very similar results: almost identical for VBM, with discrepancy for CBM (and therefore band gap) not greater than 0.1 meV, 0.05 meV and 0.001 meV in the case of very small ($4a \leq l < 8a$), intermediate ($8a \leq l < 12a$) and large ($12a \leq l$) dots, while keeping consistent slopes with across all sizes and temperatures, with 26×26 Hamiltonians producing somewhat smaller values for the band gap in all cases.

5.6 Conclusion

In conclusion, this chapter started with the derivation of Burt-Foreman envelope method and proceeded with solution by using plane wave basis. In the plane wave basis, integrals $J^{sq}(E)$ have emerged that were dependent on the geometry of the nanostructure. These integrals were analytically solved for cuboid and ellipsoid quantum dots, quantum wires with ellipsoid and rectangle shape and for quantum

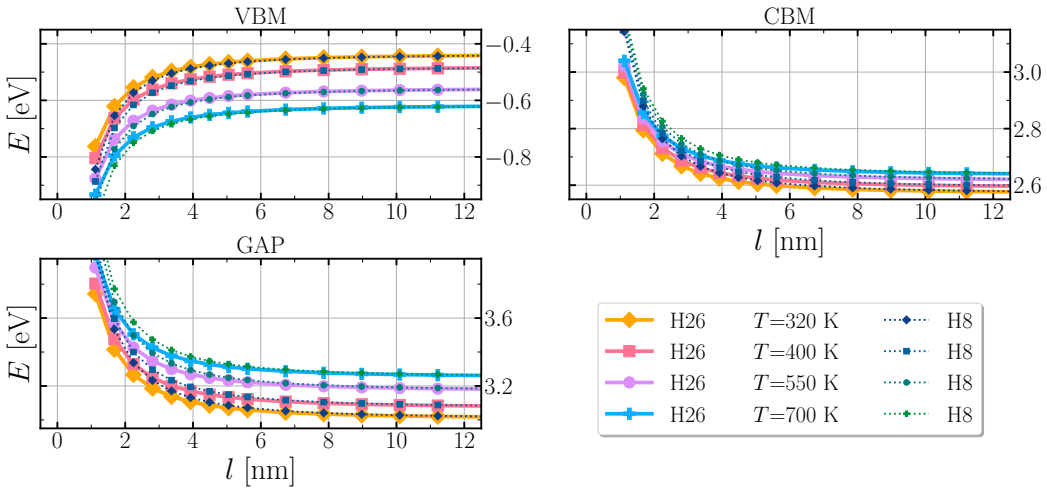

Figure 5.19. Energies of band edges and gap for $CsPbCl_3$ quantum wells of different sizes at several selected temperatures, where l is the size of the well, and VBM (CBM) are valence band maximum (conduction band minimum).

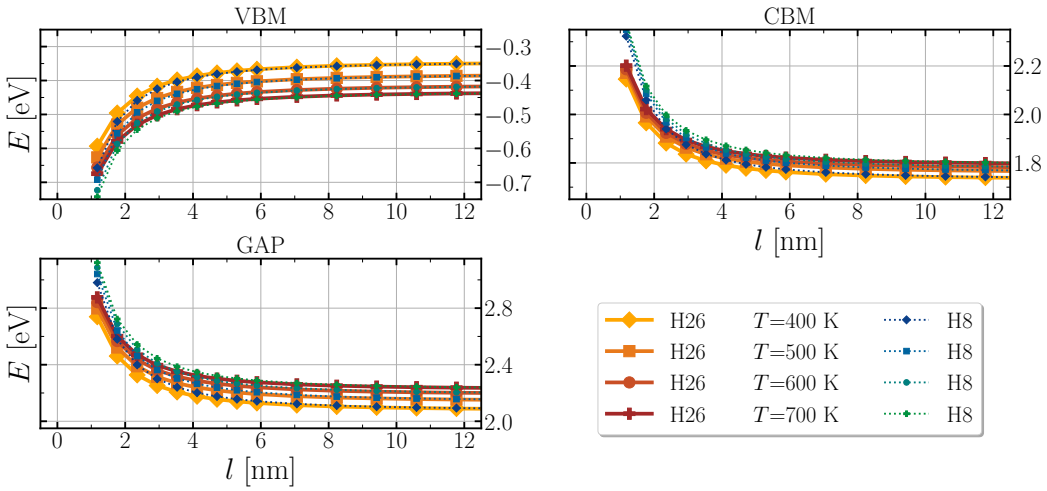

Figure 5.20. Energies of band edges and gap for $CsPbBr_3$ quantum wells of different sizes at several selected temperatures, where l is the size of the well, and VBM (CBM) are valence band maximum (conduction band minimum).

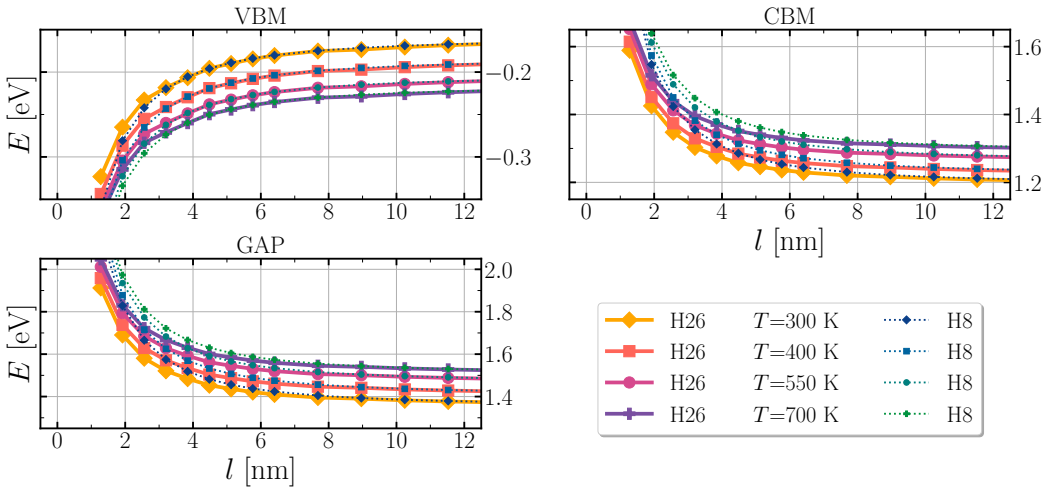

Figure 5.21. Energies of band edges and gap for $CsPbI_3$ quantum wells of different sizes at several selected temperatures, where l is the size of the well, and VBM (CBM) are valence band maximum (conduction band minimum).

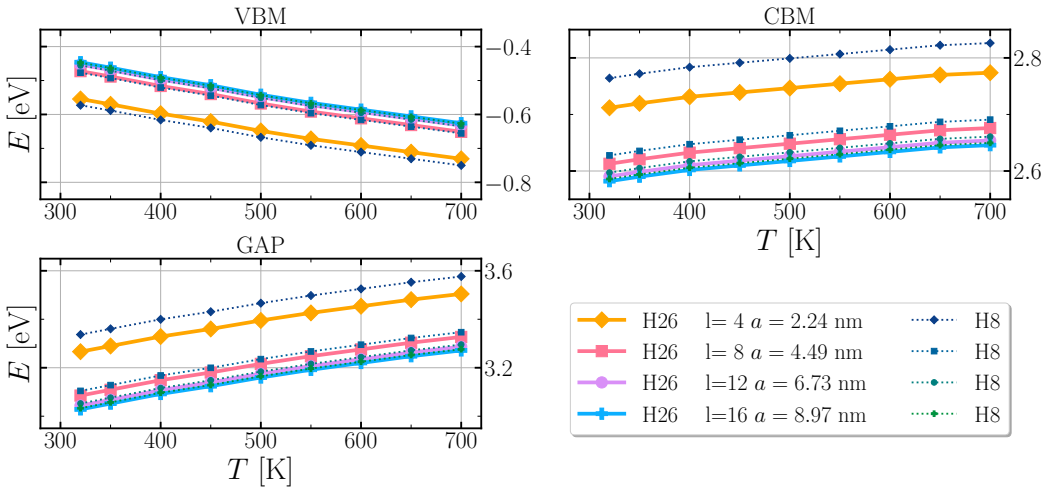

Figure 5.22. Energies of band edges and gap for $CsPbCl_3$ quantum wells at different temperatures for several selected sizes, where l is the size of the well, and VBM (CBM) are valence band maximum (conduction band minimum).

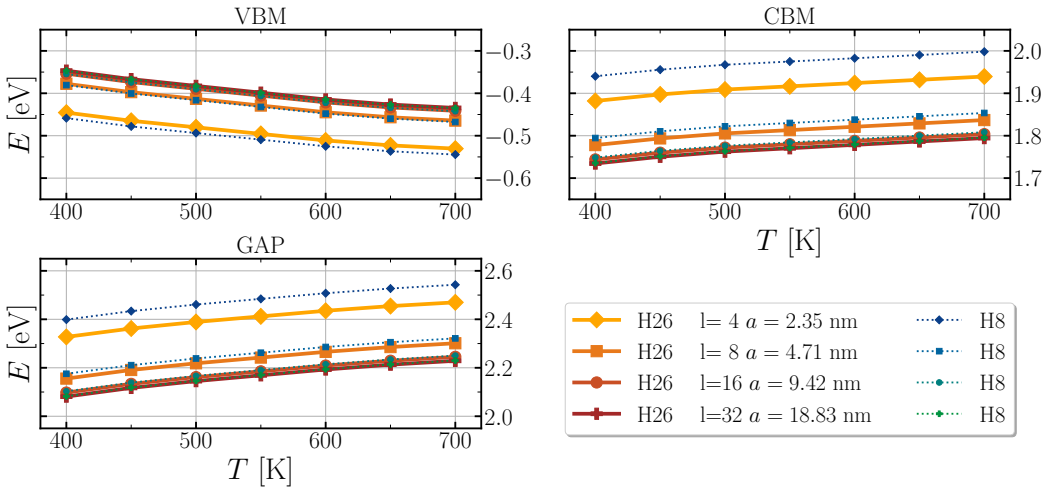

Figure 5.23. Energies of band edges and gap for $CsPbBr_3$ quantum wells at different temperatures for several selected sizes, where l is the size of the well, and VBM (CBM) are valence band maximum (conduction band minimum).

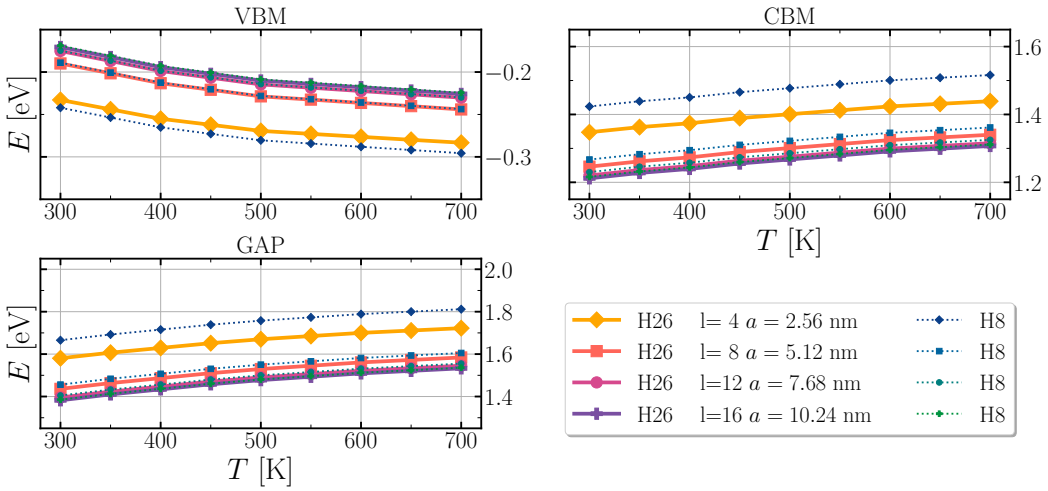

Figure 5.24. Energies of band edges and gap for $CsPbI_3$ quantum wells at different temperatures for several selected sizes, where l is the size of the well, and VBM (CBM) are valence band maximum (conduction band minimum).

wells. Continuing with zincblende CdSe materials, which were used to perform a precision test between for envelope function method in plane wave basis by using DFT calculations as a benchmark for quantum wells and obtaining excellent agreement for band gaps and squared moduli of wave functions. This is an important result, considering that DFT calculations require far more computational resources than $\mathbf{k} \cdot \mathbf{p}$ envelope method. For unit cells that contain more atoms and nanostructures that are confined in more than one dimension, DFT calculations easily exceed available computational resources, while $\mathbf{k} \cdot \mathbf{p}$ envelope method can be applied in most cases using desktop computers. Considering the computational resources, this chapter also addresses the numerical convergence tests that have to be performed when using plane wave basis and provides some insight on how to estimate required computational resources for $\mathbf{k} \cdot \mathbf{p}$ envelope method calculations. Band gaps for zincblende CdSe quantum wells were then calculated using G_0W_0 energies and image charge effects were added to account for dielectric mismatch between the well and the surrounding material. Combining methodology from Chapter 3 with envelope functions in plane wave basis and electronic structure results from Chapter 4, temperature dependent band gaps for lead-halide perovskite nanostructures were obtained. These results include band gaps for quantum dots (cubic and spherical shape), wires (with square and circular base) and wells. Hamiltonians that include only bands near the gap (8) produce satisfactory results for band gaps at much less computational cost when compared to the ones that take more bands around the gap into account (26). Since the temperature band energy renormalization is taken from bulk calculations, these corrections enter the $\mathbf{k} \cdot \mathbf{p}$ Hamiltonian at zero-th order. Therefore, all slopes and trends considering temperature changes for band energies are conserved when moving from bulk to nanostructure. Comparing the slopes of energy levels that change with size of the nanostructure, quantum dots had the steepest slopes, followed by quantum wires and then wells for the same material, which is consistent with the literature [51]. Finally, the results for halide-perovskites lack the correction for dielectric mismatch, as this would require a careful analytical and numerical effort that is planned for future.

Chapter 6

Conclusion

Present chapter concludes the results of this thesis. The main goal of this work was obtaining the electronic structure of perovskite nanostructures. What seemed as a straightforward task at first, proved to be challenging as one step after another, there were some challenges that required deeper understanding or some sort of modification of standard methods. At this point, a brief summary of the obtained results in this thesis is shown, followed with suggestions for possible research in the future.

6.1 Summary

The goal of this thesis is to obtain the electronic structure of inorganic halide perovskite nanocrystals. Halide perovskites have been praised as a low-cost, easily produced materials in laboratory conditions that can range from bulk crystals to nanocrystals with extremely modular shape and band gap. Their low-cost combined with promising performance makes them an excellent candidate for semiconductor-based devices like solar cells, LEDs, photodetectors, lasers and more. Even though the stability and performance of these devices have seen rapid improvement, their stability, efficiency and lifetime are the main reason they are sill not used for industrial and commercial purposes. In order to improve the device performance and lifetime, obtaining a good picture for electronic properties of these materials is necessary. This study focused on the electronic structure of inorganic variants with formula $CsPbX_3$ (X=Cl, Br, I) in their cubic phase. Even though DFT is routinely used for electronic structure calculations for many bulk semiconductors, calculation of nanostructures would require methods like $\mathbf{k} \cdot \mathbf{p}$ that can deal with these larger systems while keeping the computational resources at DFT level. Since $\mathbf{k} \cdot \mathbf{p}$ is a perturbative method, it relies on DFT results as a source of unperturbed parameters like Kohn-Sham states. Furthermore, in order for $\mathbf{k} \cdot \mathbf{p}$ to be successful for nanocrystals, it has to provide accurate results for bulk phase, something which is directly reliant on DFT results, meaning that DFT error in band gap for halide perovskites should be addressed first. Finally, once proper band gaps are obtained, one can proceed to apply $\mathbf{k} \cdot \mathbf{p}$ method on nanocrystals and obtain their electronic structure.

First, in order to obtain $\mathbf{k} \cdot \mathbf{p}$ parameters, one must perform a DFT calculation

that produces Kohn-Sham wave functions and energies. This way, an initial $\mathbf{k}\cdot\mathbf{p}$ Hamiltonian was obtained that didn't have identical analytical form as the ones found in literature, for crystal structures that share O_h symmetry, obtained using theory of invariants that relies on crystal symmetry [48, 51]. Namely, the required number of parameters determined by the symmetry of the crystal was at first glance much smaller than the ones initially obtained directly from DFT. Although the initial calculation provides a good result with all symmetries, this is not so obvious from its analytical form. For this reason, a method for obtaining analytical form of $\mathbf{k}\cdot\mathbf{p}$ Hamiltonian identical to the ones found in literature, purely from ab initio DFT calculations was developed. This method was named symmetry-adaptation, and was published in Ref. [46] and presented in Chapter 3, where CdSe material was considered, for which various analytical forms were widely used in literature, as a check for the methodology. The key of symmetry-adaptation of one Hamiltonian obtained numerically, into another Hamiltonian found in the literature, was to find a unitary transform that will perform a rotation on Kohn-Sham states after which the symmetry-adapted Hamiltonian will be produced. Besides this, Chapter 3 contains a small benchmark for $\mathbf{k}\cdot\mathbf{p}$ Hamiltonian performance. This benchmark compared the maximum deviation of $\mathbf{k}\cdot\mathbf{p}$ electronic structure from DFT result, when moving away from the unperturbed point in the 1BZ. This check confirmed that $\mathbf{k}\cdot\mathbf{p}$ Hamiltonians with more bands should produce a better dispersion relation. Based on this, band structures for CdSe and $CsPbX_3$ (X=Cl, Br, I) were produced using more refined band energies obtained from GW and hybrid-DFT, respectively.

Next topic, was to address the issue of underestimated band gap for cubic halide perovskites when using DFT with local and semi-local functionals, which was done in Chapter 4 and published in Ref. [45]. Namely, for lead based halide perovskites, main contributors to VBM and CBM are $6s$ and $6p$ Pb orbitals, respectively, which makes inclusion of SOC a requirement. However, inclusion of SOC reduces the band gap around 1 eV compared to no-SOC calculation, which gives a reasonable estimate of the band gap. Therefore, an error in local or semi-local treatment and the error of omitting the SOC cancel each other to produce a decent band gap for halide perovskites. However, SOC treatment results in underestimated band gap for local and semi-local DFT. Furthermore, there is the issue of the cubic structure stability, which is not at all stable at zero temperatures that ground state calculations provided by DFT assume. Temperatures at which halide perovskite transition to cubic structure are rather high (for $CsPbX_3$ they are 320 K, 403K and 300 K for X= Cl, Br, and I, respectively) and its effects cannot be neglected. Indeed, early DFPT calculations that are based on the harmonic approximation indicated presence of imaginary (silent or negative) phonon modes at R and M points in 1BZ, which points to strong anharmonic effects. Therefore, a combination of more sophisticated method than semi-local DFT is required for the electronic structure, and the inclusion of temperature and anharmonic effects. For electronic strucure calculations a hybrid-DFT using PBE0 modified with Koopmans' conditions for mixing parameter α has proven to provide good results for cubic halide perovkites. The most dominant temperature effect is the electron-phonon interaction that contributes to significant renormalization and broadening of the electron bands. One widely used

method for electron band renormalization is the AHC theory that treats phonon vibrations as a perturbation of the static lattice. Chapter 4 goes through necessary steps, required to provide an accurate estimate for band gaps. They include: (1) addressing the strong anharmonicity in lattice vibrations, (2) considering the non-linearity of temperature effects on bands, and (3) resolving the connection between band broadening and renormalization.

The strong anharmonicity (1) can be treated using using the SCPH method that considers many-body effects as opposed to harmonic and independent phonon treatment of DFPT. In Ref. [38], contribution of soft modes was simply disregarded, a solution that was also considered here, but proved to greatly underestimate the renormalization. Furthermore, Ref. [38], was rather ambiguous about whether whole soft mode should be disregarded or just points where that mode becomes negative. Performing a check it was shown that only the disregard of the whole soft mode contributions will provide converged results. Using SCPH, anharmonic frequencies are produced which correct the error of DFPT phonon structure by not just correcting the silent modes, but providing more accurate results for higher modes as well. Also, it was shown that the largest contribution to renormalization was indeed from phonons in the range of intermediate frequencies, where the density of phonon states is highest. In harmonic approximation, most of these states are lost to the soft region, further proving that their neglect cannot be justified.

Next, the AHC theory was previously routinely used for structures that are stable at zero temperature and have phonons that can be treated with harmonic approximation. This results in equation that uses electron-phonon matrix elements and phonon frequencies at their zero temperature values, and the only temperature dependent term in the equation for band renormalization is the Bose-Einstein factor. This would produce linear trend of band renormalization with temperature, making renormalization at very high temperature unrealistic. However, the introduction of temperature dependence in phononic frequencies reduces the growth of Bose-Einstein factor, to produce a non-linear trend of temperature effects that point towards saturation with extremely high temperatures.

Until this point, renormalization and broadening effects have been considered separate within the AHC theory, as it has been done routinely in the literature. Namely, the AHC theory can be derived using many-body perturbation theory, using bare electron and phonon Green functions. This way, renormalization has a small parameter $i\delta$ (where δ is purely real) in the denominator that prevents divergence and provides smoothening. Previously in the literature, this parameter was usually set to 0.1 eV for calculation of both renormalization and broadening [117]. In Ref. [120], it was established that as $\delta \to 0$, the renormalization should converge as a Lorentzian or linearly with increasing q-grid density. However, due to anharmonicity, the δ broadening should not be arbitrary small, especially at high temperatures and there should be an established connection between renormalization and broadening (3) of the bands. To resolve this issue, a self-consistent procedure based on the self-consistent Migdal approximation was developed. In AHC theory bare electron Green function was replaced with a dressed one, which coupled the real and imaginary parts of electron-phonon self-energy that represent

renormalization and broadening, respectively. This way, real and imaginary parts must be solved self-consistently and the matter was further simplified by considering only intraband transitions to the first-order, while interband transitions were considered to be of the higher order. The results show that VBM and CBM renormalization have a smaller, non-zero broadening, compared to the rest of the bands that show greater broadening which results in band diffusion and overlap at high temperatures. The renormalized band gaps show excellent agreement with experimental data for temperatures where cubic structure is formed. However, due to limited experimental data on band gap slopes that do not cover a wide range of temperatures, meaningful for comparison, one cannot draw a full conclusion. The obtained value of the band gap slope with temperature for $CsPbI_3$ agrees with the experiment (range from 570 K to 620 K) while underestimating it for $CsPbBr_3$ (data range from 380 K to 435 K, which covers around the point of transition to cubic structure) and having no experimental data for $CsPbCl_3$ for comparison. When going to even lower temperatures, PBE0 calculations with Koopmans' condition for α parameter for orthorhombic structure of halide perovskites indicate a very weak temperature dependence with the band gap, which is consistent with the literature.

Finally, once good band gaps of bulk perovskite structure are obtained, one can proceed by using them to calculate the electronic structure of nanostructures which is done in Chapter 5. For this, a modified $\mathbf{k} \cdot \mathbf{p}$ Kane method was used, which is based on Burt-Foreman envelope method, where envelopes were expanded in plane wave basis. Presented method considers that the surrounding material has the same properties as the nanostructure, but with a wide enough band gap that prevents mixing of states. This produces a certain integral that depends only on the shape and size of the nanostrucure. In general, analytical formula for this integral is given for quantum wells, wires with rectangular and elliptical cross sections, and dots of cuboid and ellipsoid shape.

Before using envelope functions on nanostructures it is a good idea to benchmark this method against a more reliable one. Since cubic perovskite materials would be too computationally expensive to calculate using DFT, CdSe was again selected as a test material in order to check the performance of the $\mathbf{k} \cdot \mathbf{p}$ envelope method. Also, the symmetry-adaptation method developed in Chapter 3 has shown to be very useful for envelopes, since it provides the minimum number of $\mathbf{k} \cdot \mathbf{p}$ parameters one has to keep track of while constructing the Hamiltonians. Using $\mathbf{k} \cdot \mathbf{p}$ envelopes, the computational cost is reduced for several orders of magnitude while showing excellent agreement with DFT band gap results for quantum wells, in the case for wide wells, and somewhat worse but satisfactory agreement for very thin wells. After this check, SOC along with GW corrections were included to produce band gaps of CdSe quantum wells, which was also published in Ref. [46].

Finally, with great confidence in the test proven $\mathbf{k} \cdot \mathbf{p}$ envelope method one can proceed to calculate the electronic structure of halide perovskite nanostructures. These results are shown for a range of temperatures where the cubic phase is present as well as for various shapes and sizes of the nanostrucures. These include quantum wells of various widths, wires with circular and square cross section with different diameters and edge lengths, respectively, and quantum dots in the shape of a sphere

and cube with different diameters and edge lengths. The results for quantum wells were published in Ref. [47], while the rest of the results are first published in this thesis.

6.2 Future plans

After finishing this work on the electronic structure of perovskite nanocrystals, there are still some unanswered points that can be a topic of further research. What follows are some ideas on what the further work can expand on based on the work already done for this thesis.

In Chapter 3, the symmetry-adaptation procedure was done only for two point groups T_d and O_h. This can easily be extended to include matrix blocks $\mathcal{B}(\Gamma_m, \Gamma_n)$ for all point groups and their irreducible representations Γ_α which correspond to first and second-order $\mathbf{k} \cdot \mathbf{p}$ parameters formed by Kohn-Sham states that also form a basis of those irreducible representations Γ_α. Furthermore, an automated procedure that uses theory of invariants directly to obtain these analytical forms can be developed as well using some programming language. This two can be combined to automate the gathering of numerical data, performing a unitary transformations to symmetry-adapted basis and checking against the result that theory of invariants would produce. This could be streamlined into some open source library that will be available to anyone and create a database of $\mathbf{k} \cdot \mathbf{p}$ parameters for various materials. Being an open source project, other groups may contribute to its development and further application. This kind of tool could prove quite useful for any researcher that needs a quick estimate for an electronic structure of some bulk or nanocrystal without the need of extensive knowledge in physics or coding.

Chapter 4 produces simple Kohn-Sham band gaps, which although useful doesn't provide enough information about optical gap that absorption experiments measure. Indeed, in order to extend these results to include absorption gaps and capture exciton quasi particles, one would need to solve BSE equation, which is quite challenging for materials with this many atoms. However, given that photovoltaic devices operate in the high temperature regime, a simpler approach using the perturbation theory and Fermi golden rule can be used to obtain absorption spectrum.

In pursuit of band renormalization, electron-phonon matrix elements were obtained for dense $\mathbf{k}, \mathbf{q}$-grids in order to converge results. However, if one were to investigate charge carrier transport properties a much finer $\mathbf{k}, \mathbf{q}$-grid is required. Indeed, these calculations are computationally demanding but one option is to perform an interpolation of electron-phonon matrix elements using Wannier basis, which was recently done in Ref. [121]. One can also adapt the method from Ref. [122], which is insensitive to band curvature and can be performed without extremely dense $\mathbf{k}, \mathbf{q}$-grids[1] in order to obtain relaxation times and charge carrier mobility. Although these two methods rely on the assumption that the electron-phonon interaction is weak, they can be useful for halide perovskites where this is not the case, by developing

[1]Some studies for Si required up to 85×10^3 and 200×10^3 inequivalent $\mathbf{k}$ and $\mathbf{q}$ points, respectively.

certain modifications.

Chapter 5 provides only Kohn-Sham gaps for halide perovskites without the dielectric mismatch correction between the nanostructure and the surrounding material. This is the first issue that would have to be addressed. Ingredients would require the dielectric constant for bulk halide perovskites, which can be either obtained from literature or calculated using DFPT, and a good theoretical model that can be used on provided nanocrystal geometries. In bulk the carrier separation energy is small at room temperature so charge separation is very likely due to just lattice vibration. In nanostructures however, this is not always the case due to the confinement effects.

Appendix A

Analytical Derivations

A.1 Time-independent perturbation theory

In this section, a quick overview of Reyleigh-Schrödinger perturbation theory is presented. More details on this subject can be found in many standard Quantum Mechanics textbooks like the ones found in Ref. [208, 209, 210].

Very few problems in quantum mechanics can be solved exactly and for this reason many approximation strategies were developed from the very start. One such is the time-independent or stationary or Reyleigh-Schrödinger perturbation theory. It starts form Hamiltonian that can be solved exactly $H^{(0)}$ with eigenfunctions $\Psi_n^{(0)}$ that produce discrete energy levels $E^{(0)}$. Perturbed problem can be written as $H = H^{(0)} \sum_i \lambda^i H^{(i)}$, $i = 1, 2, 3, \ldots$ where λ is some arbitrary small parameter and $H^{(n)}$ is the perturbed part of the total Hamiltonian H of the i-th order. Similarly, the expectation value for some discrete level E_n and its eigenfunction Ψ_n will be equal to $E_n = E_n^{(0)} + \sum_i \lambda^i E_n^{(i)}$ and $\Psi_n = \Psi_n^{(0)} + \sum_i \lambda^i \Psi_n^{(i)}$, respectively. Writing down:

$$\begin{aligned}\left(H^{(0)} + \sum_i \lambda^i H^{(i)}\right)\left(\Psi_n^{(0)} + \sum_i \lambda^i \Psi_n^{(i)}\right) = \left(E_n^{(0)} + \sum_i \lambda^i E_n^{(i)}\right) \\ \times \left(\Psi_n^{(0)} + \sum_i \lambda^i \Psi_n^{(i)}\right),\end{aligned} \tag{A.1}$$

and performing multiplication by grouping terms to their corresponding order for λ, for $i = 1$ one obtains:

$$\lambda\left(H^{(0)}\Psi_n^{(1)} + H^{(1)}\Psi_n^{(0)}\right) = \lambda\left(E_n^{(0)}\Psi_n^{(1)} + E_n^{(1)}\Psi_n^{(0)}\right). \tag{A.2}$$

Eq. (A.2) can be multiplied by $\Psi_n^{(0)}$ from the right and integrated to obtain $E_n^{(1)}$:

$$E_n^{(1)} = H_{nn}^{(1)} = \left\langle \Psi_n^{(0)} \right| H^{(1)} \left| \Psi_n^{(0)} \right\rangle, \tag{A.3}$$

where $\left\langle \Psi_n^{(0)} \middle| \Psi_n^{(1)} \right\rangle = 0$ and the fact that $H^{(0)}$ is Hermitian $\left\langle \Psi_n^{(0)} \middle| H^{(0)} \middle| \Psi_n^{(1)} \right\rangle = E_n^{(0)} \left\langle \Psi_n^{(0)} \middle| \Psi_n^{(1)} \right\rangle = 0$ was used.

Unperturbed functions $\Psi^{(0)}$ can be used as a basis for expressing perturbed functions $\Psi_n^{(i)} = \sum_s C_{nm}^{(i)} \Psi_m^{(0)}$, and if inserted in Eq. (A.2), $C_{nr}^{(1)}$ coefficients can be obtained by multiplying from the right by $\left|\Psi_r^{(0)}\right\rangle$, with $r \neq n$:

$$C_{nr}^{(1)} = \frac{H_{nr}^{(1)}}{E_n^{(0)} - E_r^{(0)}}, \quad r \neq n, \tag{A.4}$$

which leads to first-order perturbation in wavefunction $\Psi_n^{(1)}$:

$$\Psi_n^{(1)} = \sum_r C_{nr}^{(1)} \Psi_r^{(0)} = \sum_{r \neq n} \Psi_r^{(0)} \frac{H_{nr}^{(1)}}{E_n^{(0)} - E_r^{(0)}}. \tag{A.5}$$

In order for perturbation approximation to be valid, coefficients $C_{nr}^{(i)}$ must satisfy $|C_{nr}^{(i)}| << 1$ for all i and nr.

For energy levels that are degenerate without the perturbation, the same procedure can be performed noting that the state $\Phi_n^{(0)}$ for l-fold degenerate level E_n will be represented as a sum of degenerate partners:

$$\Phi_n^{(0)} = \sum_d^l C_{n,d}^{(0)} \Psi_{nd}^{(0)}, \tag{A.6}$$

and the first-order correction will be:

$$\Psi_{nd}^{(1)} = \sum_r \sum_{d'}^l C_{nd,rd'}^{(1)} \Psi_{rd'}^{(0)} \tag{A.7}$$

The energy correction in the first-order $E_n^{(1)}$ will be obtained by solving a system of l equations:

$$\sum_{d'}^l C_{n,d'}^{(0)} \left(E_n^{(1)} \delta_{dd'} - \left\langle \Psi_{nd}^{(0)} \right| H^{(1)} \left| \Psi_{rd'}^{(0)} \right\rangle \right) = 0, \quad d, d' = 1, 2, 3, \ldots l. \tag{A.8}$$

From Eq. (A.5), one can conclude that $C_{nn} = 0$, which can also be shown using the condition that $\langle \Psi_n | \Psi_n \rangle = 1$. Expansion of $\langle \Psi_n | \Psi_n \rangle$ gives:

$$\begin{aligned}
\langle \Psi_n | \Psi_n \rangle &= \left(\left\langle \Psi_n^{(0)} \right| + \sum_i \lambda^i \left\langle \Psi_n^{(i)} \right| \right) \left(\left| \Psi_n^{(0)} \right\rangle + \sum_i \lambda^i \left| \Psi_n^{(i)} \right\rangle \right) \\
&= \left\langle \Psi_n^{(0)} \middle| \Psi_n^{(0)} \right\rangle \\
&+ \lambda \left(\left\langle \Psi_n^{(0)} \middle| \Psi_n^{(1)} \right\rangle + \left\langle \Psi_n^{(1)} \middle| \Psi_n^{(0)} \right\rangle \right) \\
&+ \lambda^2 \left(\left\langle \Psi_n^{(0)} \middle| \Psi_n^{(2)} \right\rangle + \left\langle \Psi_n^{(2)} \middle| \Psi_n^{(0)} \right\rangle + \left\langle \Psi_n^{(1)} \middle| \Psi_n^{(1)} \right\rangle + \left\langle \Psi_n^{(1)} \middle| \Psi_n^{(1)} \right\rangle \right) \\
&+ \lambda^3 \left(\left\langle \Psi_n^{(0)} \middle| \Psi_n^{(3)} \right\rangle + \ldots \right) + \ldots \\
&= 1 + \sum_i \mathcal{O}(\lambda^i).
\end{aligned} \tag{A.9}$$

Since $\lambda \neq 0$, all the terms in parenthesis must vanish. For the first-order terms:

$$C_{nn}^{(1)} + C_{nn}^{(1)*} = 2\,\mathrm{Re}\, C_{nn}^{(i)} = 0, \tag{A.10}$$

the condition is that the real part of $C_{nn}^{(1)}$ is zero. It is possible to rotate the perturbed wavefunction Ψ_n, by multiplying it with some phase $e^{i\alpha}$ (where α will depend on λ), to make $C_{nr}^{(1)}$ coefficients purely real, therefore the imaginary part of $C_{nn}^{(1)}$ will also vanish.

For second-order terms in λ, one can write a similar equation to Eq. (A.2):

$$\lambda^2 \left(H^{(0)}\Psi_n^{(2)} + H^{(1)}\Psi_n^{(1)} + H^{(2)}\Psi_n^{(0)}\right) = \lambda^2 \left(E_n^{(0)}\Psi_n^{(2)} + E_n^{(1)}\Psi_n^{(1)} + E_n^{(2)}\Psi_n^{(0)}\right). \tag{A.11}$$

Using the same procedure of multiplying by $\Psi_n^{(0)}$ from the right and integrating, the second-order correction of energy is obtained $E_n^{(2)}$:

$$E_n^{(2)} = H_{nn}^{(2)} + \sum_{r\neq n} \frac{H_{nr}^{(1)} H_{rn}^{(1)}}{E_n^{(0)} - E_r^{(0)}}. \tag{A.12}$$

If there are no perturbations in the Hamiltonian to the second-order, then $H^{(2)} = 0$.

One can continue and obtain corrections of E_n to an arbitrary order. What is important is to notice that that for i-th order of correction for energy levels, the correction in eigenfunctions is needed to the order of $(i-1)$.

A.2 Effective-mass equation as a perturbation

Periodic system of non-interacting electrons is described by a simple Hamiltonian $H = p^2/(2m_e) + V$ which can be solved using Bloch functions $\Psi_{\mathbf{k}n} = e^{i\mathbf{k}\cdot\mathbf{r}} u_{\mathbf{k}n}$ where $u_{\mathbf{k}n}$ are unit cell periodic Bloch factors, $H\Psi_{\mathbf{k}n} = E_{\mathbf{k}n}\Psi_{\mathbf{k}n}$, to obtain energies $E_{\mathbf{k}n}$, where $\mathbf{k}n$ is the state of electron ($\mathbf{k}$ is a vector in 1BZ and n is the energy level). For $H_{\mathbf{k}} = e^{-i\mathbf{k}\cdot\mathbf{r}} H e^{i\mathbf{k}\cdot\mathbf{r}}$ one obtains:

$$\begin{aligned} H_{\mathbf{k}} u_{\mathbf{k}n} &= E_{\mathbf{k}n} u_{\mathbf{k}n}, \\ H_{\mathbf{k}} &= \frac{(\mathbf{p} + \hbar\mathbf{k})^2}{2m_e} + V(\mathbf{r}). \end{aligned} \tag{A.13}$$

Suppose that for some $\mathbf{k}_0$ that all $u_{\mathbf{k}_0 n}$ and $E_{\mathbf{k}_0 n}$ can be obtained. For any other $\mathbf{k}$, Bloch factors can be expressed in the basis of $u_{\mathbf{k}_0 n}$ as:

$$u_{\mathbf{k}n} = \sum_m B_m^{(n)} u_{\mathbf{k}_0 m}. \tag{A.14}$$

In Eq. (A.13), $H_{\mathbf{k}}$ can be transformed as:

$$H_{\mathbf{k}} = H_{\mathbf{k}_0} + \frac{(\hbar k - \hbar k_0)^2}{2m_e} + \frac{\hbar(\mathbf{k} - \mathbf{k}_0)\cdot\mathbf{p}}{m_e}. \tag{A.15}$$

Using the static perturbation theory, where unperturbed Hamiltonian is $H^{(0)} = H_{\mathbf{k}_0} + (\hbar k - \hbar k_0)^2/(2m_e)$ and perturbation $H^{(1)} = \hbar(\mathbf{k}-\mathbf{k}_0)\cdot\mathbf{p}/m_e$, one obtains first and second-order corrections for level E_n:

$$\begin{aligned} E^{(1)}_{\mathbf{k}n} &= H^{(1)}_{nn} = \frac{\hbar(\mathbf{k}-\mathbf{k}_0)\cdot\mathbf{p}_{nn}}{m_e}, \\ E^{(2)}_{\mathbf{k}n} &= \sum_{r\neq n} \frac{H^{(1)}_{nr}H^{(1)}_{rn}}{E_{\mathbf{k}_0 n} - E_{\mathbf{k}_0 r}}, \\ \mathbf{p}_{nr} &= \langle \Psi_{\mathbf{k}_0 n} | \, \mathbf{p} \, | \Psi_{\mathbf{k}_0 r} \rangle \\ &= \hbar\mathbf{k}_0\delta_{nr} + \langle u_{\mathbf{k}_0 n} | \, \mathbf{p} \, | u_{\mathbf{k}_0 r} \rangle \, . \end{aligned} \tag{A.16}$$

The total energy in effective-mass approximation for $E_{\mathbf{k}n}$ is:

$$E_{\mathbf{k}n} = E_{\mathbf{k}_0 n} + \frac{\hbar^2(\mathbf{k}-\mathbf{k}_0)^2}{2m_e} + \frac{\hbar}{m_e}(\mathbf{k}-\mathbf{k}_0)\cdot\mathbf{p}_{nn} + \sum_{r\neq n}\frac{|\hbar(\mathbf{k}-\mathbf{k}_0)\cdot\mathbf{p}_{nr}|^2}{m_e^2(E_{\mathbf{k}_0 n} - E_{\mathbf{k}_0 r})}. \tag{A.17}$$

In the case that $\mathbf{k}_0 n$ state is l-fold degenerate, there will be l states $\left|\Psi^{(s)}_{\mathbf{k}_0 n}\right\rangle$, $s = 1, 2, \ldots, l$ with same energy $E_{\mathbf{k}_0 n}$. Moving away from $\mathbf{k}_0$ to point $\mathbf{k}$, the degeneracy is in general lifted, so $E^{(s)}_{\mathbf{k}n}$ is obtained from a system of l equations:

$$\sum_d \left[H^{(0)}_{sd} + H^{(1)}_{sd} + H^{(2)}_{sd}\right] C_d = E^{(s)}_{\mathbf{k}n} C_s, \quad s, d = 1, 2, 3, \ldots l \tag{A.18}$$

where:

$$\begin{aligned} H^{(0)}_{sd} &= \left(E_{\mathbf{k}_0 n} + \frac{\hbar^2(\mathbf{k}-\mathbf{k}_0)^2}{2m_e}\right)\delta_{sd}, \\ H^{(1)}_{sd} &= \frac{\hbar}{m_e}(\mathbf{k}-\mathbf{k}_0)\cdot\mathbf{p}^{(s,d)}_{nn}, \\ H^{(2)}_{sd} &= \sum_{r\neq n}\frac{\hbar^2}{m_e^2}\frac{(\mathbf{k}-\mathbf{k}_0)\cdot\mathbf{p}^{(s,\ )}_{nr}\mathbf{p}^{(\ ,d)}_{rn}\cdot(\mathbf{k}-\mathbf{k}_0)}{E_{\mathbf{k}_0 n} - E_{\mathbf{k}_0 r}}, \\ \mathbf{p}^{(s,d)}_{nn} &= \left\langle \Psi^{(s)}_{\mathbf{k}_0 n}\right| \mathbf{p} \left|\Psi^{(d)}_{\mathbf{k}_0 n}\right\rangle, \end{aligned} \tag{A.19}$$

A.3 Displacement of ions as a perturbation

Using stationary perturbation theory, one can introduce the displacement of ions as a perturbation on energy levels of an electron. In this case, the unperturbed Hamiltonian is the Kohn-Sham Hamiltonian $H^{(0)} \equiv H^{\mathrm{KS}}$ which is diagonalized by Kohn-Sham wave functions $\Psi^{(0)}_{\mathbf{k}n}(\mathbf{r})$ and energies $E^{(0)}_{\mathbf{k}n} \equiv \varepsilon_{\mathbf{k}n}$ for an electron in state $\mathbf{k}n$. The perturbation for displacement of ion κ in unit cell p along the direction α in the i-th order is:

$$\lambda^i F^{(i)} = \frac{\lambda^i}{i!}\left(\prod_i \sum_{\kappa\alpha,p} \Delta R_{\kappa\alpha,p}\partial_{\kappa\alpha,p}\right) F^0, \quad F = H, \Psi_{\mathbf{k}n}, \tag{A.20}$$

where λ is the strength of the perturbation, and $\Delta R_{\kappa\alpha,p}$ is the displacement itself in units of length. The expectation value of the energy level $E_{\mathbf{k}n}$ perturbed by ionic displacement will be:

$$\begin{aligned}
E_{\mathbf{k}n} = \langle \Psi_{\mathbf{k}n} | \, H \, | \Psi_{\mathbf{k}n} \rangle &= \left\langle \Psi^{(0)}_{\mathbf{k}n} + \sum_i \lambda^i \Psi^{(i)}_{\mathbf{k}n} \right| H^{(0)} + \sum_i \lambda^i H^{(i)} \left| \Psi_{\mathbf{k}n} + \sum_i \lambda^i \Psi^{(i)}_{\mathbf{k}n} \right\rangle \\
&= \left\langle \Psi^{(0)}_{\mathbf{k}n} \right| H^{(0)} \left| \Psi^{(0)}_{\mathbf{k}n} \right\rangle \\
&+ \lambda \left[\left\langle \Psi^{(0)}_{\mathbf{k}n} \right| H^{(1)} \left| \Psi^{(0)}_{\mathbf{k}n} \right\rangle + \left\langle \Psi^{(0)}_{\mathbf{k}n} \right| H^{(0)} \left| \Psi^{(1)}_{\mathbf{k}n} \right\rangle + \left\langle \Psi^{(1)}_{\mathbf{k}n} \right| H^{(0)} \left| \Psi^{(0)}_{\mathbf{k}n} \right\rangle \right] \\
&+ \lambda^2 \left[\left\langle \Psi^{(0)}_{\mathbf{k}n} \right| H^{(2)} \left| \Psi^{(0)}_{\mathbf{k}n} \right\rangle + \left\langle \Psi^{(0)}_{\mathbf{k}n} \right| H^{(1)} \left| \Psi^{(1)}_{\mathbf{k}n} \right\rangle + \left\langle \Psi^{(1)}_{\mathbf{k}n} \right| H^{(1)} \left| \Psi^{(0)}_{\mathbf{k}n} \right\rangle \right] \\
&+ \lambda^3 \left[\ldots \right] + \ldots
\end{aligned} \tag{A.21}$$

Expanding the expectation value in orders of λ:

$$E_{\mathbf{k}n} = E^{(0)}_{\mathbf{k}n} + \lambda E^{(1)}_{\mathbf{k}n} + \frac{1}{2!}\lambda^2 E^{(2)}_{\mathbf{k}n} + \frac{1}{3!}\lambda^3 E^{(3)}_{\mathbf{k}n} + \ldots, \tag{A.22}$$

allows one to obtain the terms individually (to the second-order):

$$\begin{aligned}
E^{(0)}_{\mathbf{k}n} &= \left\langle \Psi^{(0)}_{\mathbf{k}n} \right| H^{(0)} \left| \Psi^{(0)}_{\mathbf{k}n} \right\rangle, \\
E^{(1)}_{\mathbf{k}n} &= \left\langle \Psi^{(0)}_{\mathbf{k}n} \right| H^{(1)} \left| \Psi^{(0)}_{\mathbf{k}n} \right\rangle, \\
E^{(2)}_{\mathbf{k}n} &= \left\langle \Psi^{(0)}_{\mathbf{k}n} \right| H^{(2)} \left| \Psi^{(0)}_{\mathbf{k}n} \right\rangle + 2\,\mathrm{Re} \left\langle \Psi^{(0)}_{\mathbf{k}n} \right| H^{(1)} \left| \Psi^{(1)}_{\mathbf{k}n} \right\rangle.
\end{aligned} \tag{A.23}$$

The first-order correction to the wave-function is written as:

$$\left| \Psi^{(1)}_{\mathbf{k}n} \right\rangle = \sum_{\mathbf{k}'n' \neq \mathbf{k}n} \frac{\left| \Psi^{(0)}_{\mathbf{k}'n'} \right\rangle \left\langle \Psi^{(0)}_{\mathbf{k}'n'} \right| H^{(1)} \left| \Psi^{(0)}_{\mathbf{k}n} \right\rangle}{E^{(0)}_{\mathbf{k}n} - E^{(0)}_{\mathbf{k}'n'}}. \tag{A.24}$$

In the case where more than one ion is displaced, each λ should match the displacement $\Delta R_{\kappa\alpha,p}$ of ion κ in unit cell p along the direction α. This transforms λ to $\lambda_{\kappa\alpha,p}$ and $H^{(1)}$ to:

$$\lambda H^{(1)} \to \sum_{\kappa\alpha,p} \lambda \frac{\partial H^{\mathrm{KS}}}{\partial R_{\kappa\alpha,p}} \Delta R_{\kappa\alpha,p} = \sum_{\kappa\alpha,p} \lambda_{\kappa\alpha,p} \frac{\partial H^{\mathrm{KS}}}{\partial R_{\kappa\alpha,p}} = \sum_{\kappa\alpha,p} \lambda_{\kappa\alpha,p} \frac{\partial V^{\mathrm{KS}}}{\partial R_{\kappa\alpha,p}}, \tag{A.25}$$

where $\lambda_{\kappa\alpha,p} = \lambda \Delta R_{\kappa\alpha,p}$. One can also define a Fourier transform for the first:

$$\begin{aligned}
\sum_p \lambda_{\kappa\alpha,p} \frac{\partial V^{\mathrm{KS}}}{\partial R_{\kappa\alpha,p}} &= \sum_{\mathbf{q}} e^{i\mathbf{q}\cdot\mathbf{r}} \\
&\quad \times N_{\mathrm{uc}}^{-1} \sum_p e^{-i\mathbf{q}\cdot(\mathbf{r}-\mathbf{T}_p)} \lambda_{\kappa\alpha,p} \frac{\partial V^{\mathrm{KS}}(\mathbf{r}-\mathbf{T}_p)}{\partial R_{\kappa\alpha,p}} \\
&= \sum_{\mathbf{q}} e^{i\mathbf{q}\cdot\mathbf{r}} \tilde{\lambda}_{\kappa\alpha}(\mathbf{q}) \frac{\partial v^{\mathrm{KS}}}{\partial R_{\kappa\alpha}(\mathbf{q})},
\end{aligned} \tag{A.26}$$

and the second derivative of V^{KS}:

$$\begin{aligned}\sum_{pp'} \lambda_{\kappa\alpha,p}\lambda_{\kappa'\alpha',p'} \frac{\partial^2 V^{\mathrm{KS}}}{\partial R_{\kappa\alpha,p}\partial R_{\kappa'\alpha',p'}} &= \sum_{\mathbf{q}\mathbf{q}'} e^{i(\mathbf{q}+\mathbf{q}')\cdot\mathbf{r}} \\ &\times N_{\mathrm{uc}}^{-2} \sum_{pp'} e^{-i(\mathbf{q}+\mathbf{q}')\cdot\mathbf{r}} e^{i\mathbf{q}\cdot\mathbf{T}_p} e^{i\mathbf{q}'\cdot\mathbf{T}_{p'}} \\ &\times \lambda_{\kappa\alpha,p}\lambda_{\kappa\alpha,p} \frac{\partial^2 V^{\mathrm{KS}}(\mathbf{r}-\mathbf{T}_p-\mathbf{T}_{p'})}{\partial R_{\kappa\alpha,p}\partial R_{\kappa'\alpha',p'}} \\ &= \sum_{\mathbf{q}\mathbf{q}'} e^{i(\mathbf{q}+\mathbf{q}')\cdot\mathbf{r}} \tilde{\lambda}_{\kappa\alpha}(\mathbf{q})\tilde{\lambda}_{\kappa'\alpha'}(\mathbf{q}') \\ &\times \frac{\partial^2 v^{\mathrm{KS}}}{\partial R_{\kappa\alpha}(\mathbf{q})\partial R_{\kappa'\alpha'}(\mathbf{q}')},\end{aligned} \tag{A.27}$$

where v^{KS} is used to emphasize that all partial derivatives are over $\partial/\partial R_{\kappa\alpha}(\mathbf{q})$ instead of $\partial/\partial R_{\kappa\alpha,p}$. Matrix elements that correspond to the perturbation designated by $\tilde{\lambda}_{\kappa\alpha}(\mathbf{q})$ are:

$$\begin{aligned}\left\langle \Psi^{(0)}_{\mathbf{k}'n'} \right| e^{i\mathbf{q}\cdot\mathbf{r}} \frac{\partial v^{\mathrm{KS}}}{\partial R_{\kappa\alpha}(\mathbf{q})} \left| \Psi^{(0)}_{\mathbf{k}n} \right\rangle &= \frac{1}{N_{\mathrm{uc}}V_{\mathrm{uc}}} \int_{\mathrm{sc}} \mathrm{d}\mathbf{r} u^*_{\mathbf{k}'n'} e^{-i(\mathbf{k}'-\mathbf{k}-\mathbf{q})\cdot\mathbf{r}} \frac{\partial v^{\mathrm{KS}}}{\partial R_{\kappa\alpha}(\mathbf{q})} u_{\mathbf{k}n} \\ &= \frac{1}{V_{\mathrm{uc}}} \int_{\mathrm{uc}} \mathrm{d}\mathbf{r} u^*_{\mathbf{k}'n'} e^{-i(\mathbf{k}'-\mathbf{k}-\mathbf{q})\cdot\mathbf{r}} \frac{\partial v^{\mathrm{KS}}}{\partial R_{\kappa\alpha}(\mathbf{q})} u_{\mathbf{k}n} \\ &\times \frac{1}{N_{\mathrm{uc}}} \sum_p e^{i(\mathbf{k}'-\mathbf{k}-\mathbf{q})\cdot\mathbf{T}_p} \\ &= \frac{1}{V_{\mathrm{uc}}} \int_{\mathrm{uc}} \mathrm{d}\mathbf{r} u^*_{\mathbf{k}+\mathbf{q}n'} \frac{\partial v^{\mathrm{KS}}}{\partial R_{\kappa\alpha}(\mathbf{q})} u_{\mathbf{k}n} \\ &= \left\langle u_{\mathbf{k}+\mathbf{q}n'} \right| \frac{\partial v^{\mathrm{KS}}}{\partial R_{\kappa\alpha}(\mathbf{q})} \left| u_{\mathbf{k}n} \right\rangle_{\mathrm{uc}} \\ &= \left\langle u_{\mathbf{k}n'} \right| \frac{\partial v^{\mathrm{KS}}}{\partial R_{\kappa\alpha}(\mathbf{q})} \left| u_{\mathbf{k}-\mathbf{q}n} \right\rangle_{\mathrm{uc}},\end{aligned} \tag{A.28}$$

where integral over the whole volume was reduced to sum of integrals over one unit cell: $\int_{\mathrm{sc}} \mathrm{d}\mathbf{r} \to \sum_p \int_{\mathrm{uc}} \mathrm{d}\mathbf{r}$ and $\mathbf{r} \to \mathbf{r} - \mathbf{T}_p$ for every $\mathbf{r}$ under the integral and $1/(N_{\mathrm{uc}}) \sum_p e^{i(\mathbf{k}'-\mathbf{k}-\mathbf{q})\cdot\mathbf{T}_p} = \delta(\mathbf{k}'-\mathbf{k}-\mathbf{q})$. Eq. (A.28) can be interpreted also as a probability of an electron to transition from $\mathbf{k}'n'$ to $\mathbf{k}'n'$ state, induced by phonon at $\mathbf{q}$, or, that electron loses $\hbar\mathbf{q}$ portion of its crystal momentum when scattered from a phonon at $\mathbf{q}$. The sum over $\kappa\alpha$ and $\mathbf{q}$ for elements diagonal in $\mathbf{k}n$ gives the

first-order energy correction:

$$\begin{aligned}\lambda E^{(1)}_{\mathbf{k}n} &= \sum_{\kappa\alpha}\sum_{\mathbf{q}} \tilde{\lambda}_{\kappa\alpha}(\mathbf{q}) \left\langle \Psi^{(0)}_{\mathbf{k}n} \right| e^{i\mathbf{q}\cdot\mathbf{r}} \frac{\partial v^{\mathrm{KS}}}{\partial R_{\kappa\alpha}(\mathbf{q})} \left| \Psi^{(0)}_{\mathbf{k}n} \right\rangle \\ &= \sum_{\kappa\alpha}\sum_{\mathbf{q}} \tilde{\lambda}_{\kappa\alpha}(\mathbf{q}) \left\langle u_{\mathbf{k}+\Gamma n} \right| \frac{\partial v^{\mathrm{KS}}}{\partial R_{\kappa\alpha}(\mathbf{q})} \left| u_{\mathbf{k}n} \right\rangle_{\mathrm{uc}} \delta_{\mathbf{q},\Gamma} \\ &= \sum_{\kappa\alpha} \tilde{\lambda}_{\kappa\alpha}(\Gamma) \left\langle u_{\mathbf{k}+\Gamma n} \right| \frac{\partial v^{\mathrm{KS}}}{\partial R_{\kappa\alpha}(\Gamma)} \left| u_{\mathbf{k}n} \right\rangle_{\mathrm{uc}} .\end{aligned} \tag{A.29}$$

Eq. (A.29) shows that the correction of electronic level to the first-order may contain only perturbation from Γ phonons[1]. This result can also be derived using Hellman-Feynman theorem:

$$\sum_{\kappa\alpha,p} \frac{\partial \varepsilon_{\mathbf{k}n}}{\partial R_{\kappa\alpha,p}} = \sum_{\kappa\alpha,p} \left\langle \Psi^{(0)}_{\mathbf{k}n} \right| \frac{\partial H^{\mathrm{KS}}}{\partial R_{\kappa\alpha,p}} \left| \Psi^{(0)}_{\mathbf{k}n} \right\rangle = \sum_{\kappa\alpha} \left\langle u_{\mathbf{k}n} \right| \frac{\partial v^{\mathrm{KS}}}{\partial R_{\kappa\alpha}(\Gamma)} \left| u_{\mathbf{k}n} \right\rangle . \tag{A.30}$$

Using Eq. (A.5), the corresponding first-order correction to the wave-function can be expressed as:

$$\tilde{\lambda}_{\kappa\alpha}(\mathbf{q}) \left| \Psi^{(1)}_{\mathbf{k}n}(\mathbf{q}) \right\rangle = \tilde{\lambda}_{\kappa\alpha}(\mathbf{q}) \sum_{\mathbf{k}'n'\neq\mathbf{k}n} \frac{\left| \Psi^{(0)}_{\mathbf{k}'n'} \right\rangle \left\langle \Psi^{(0)}_{\mathbf{k}'n'} \right| e^{i\mathbf{q}\cdot\mathbf{r}} \frac{\partial v^{\mathrm{KS}}}{\partial R_{\kappa\alpha}(\mathbf{q})} \left| \Psi^{(0)}_{\mathbf{k}n} \right\rangle}{E^{(0)}_{\mathbf{k}n} - E^{(0)}_{\mathbf{k}'n'}}. \tag{A.31}$$

Expansion of the left- and right- hand side (LHS and RHS), respectively gives:

$$\begin{aligned}\mathrm{LHS} &= \tilde{\lambda}_{\kappa\alpha}(\mathbf{q}) \left| \Psi^{(1)}_{\mathbf{k}n} \right\rangle = \tilde{\lambda}_{\kappa\alpha}(\mathbf{q}) e^{i\mathbf{q}\cdot\mathbf{r}} \left| \frac{\partial \Psi^{(0)}_{\mathbf{k}n}}{\partial R_{\kappa\alpha}(\mathbf{q})} \right\rangle \\ &= \tilde{\lambda}_{\kappa\alpha}(\mathbf{q}) e^{i(\mathbf{k}+\mathbf{q})\cdot\mathbf{r}} \left| \frac{\partial u_{\mathbf{k}n}}{\partial R_{\kappa\alpha}(\mathbf{q})} \right\rangle \\ \mathrm{RHS} &= \tilde{\lambda}_{\kappa\alpha}(\mathbf{q}) \sum_{\mathbf{k}'n'\neq\mathbf{k}n} \frac{\left| \Psi^{(0)}_{\mathbf{k}'n'} \right\rangle \left\langle \Psi^{(0)}_{\mathbf{k}'n'} \right| e^{i\mathbf{q}\cdot\mathbf{r}} \frac{\partial v^{\mathrm{KS}}}{\partial R_{\kappa\alpha}(\mathbf{q})} \left| \Psi^{(0)}_{\mathbf{k}n} \right\rangle}{E^{(0)}_{\mathbf{k}n} - E^{(0)}_{\mathbf{k}'n'}} \\ &= \tilde{\lambda}_{\kappa\alpha}(\mathbf{q}) \sum_{n'\neq n} e^{i(\mathbf{k}+\mathbf{q})\cdot\mathbf{r}} \frac{\left| u_{\mathbf{k}+\mathbf{q}n'} \right\rangle \left\langle u_{\mathbf{k}+\mathbf{q}n'} \right| \frac{\partial v^{\mathrm{KS}}}{\partial R_{\kappa\alpha}(\mathbf{q})} \left| u_{\mathbf{k}n} \right\rangle}{E^{(0)}_{\mathbf{k}n} - E^{(0)}_{\mathbf{k}+\mathbf{q}n'}}.\end{aligned} \tag{A.32}$$

Finally, the correction of the lattice periodic function $u^{\mathbf{q}}_{\mathbf{k}n}$ for components $\kappa\alpha$ is:

$$\left| u^{\mathbf{q}}_{\mathbf{k}n} \right\rangle_{\kappa\alpha} = \left| \frac{\partial u_{\mathbf{k}n}}{\partial R_{\kappa\alpha}(\mathbf{q})} \right\rangle = \sum_{n'\neq n} \frac{\left| u_{\mathbf{k}+\mathbf{q}n'} \right\rangle \left\langle u_{\mathbf{k}+\mathbf{q}n'} \right| \frac{\partial v^{\mathrm{KS}}}{\partial R_{\kappa\alpha}(\mathbf{q})} \left| u_{\mathbf{k}n} \right\rangle}{E^{(0)}_{\mathbf{k}n} - E^{(0)}_{\mathbf{k}+\mathbf{q}n'}}. \tag{A.33}$$

[1]Calculating first-order corrections may seem redundant because once the time-averages are taken, averaged displacement in first-order vanishes anyway since $\langle \tilde{\lambda}_{\kappa\alpha}(\mathbf{q}) \rangle = \lambda \langle \Delta R_{\kappa\alpha}(\mathbf{q}) \rangle = 0$ for all $\mathbf{q}$. Nevertheless this extra step was done for the reason of pedagogical consistency.

The second-order correction $\frac{1}{2}\lambda^2 E^{(2)}_{\mathbf{k}n}$ has two terms. One is $\lambda^2 \left\langle \Psi^{(0)}_{\mathbf{k}n} \right| H^{(2)} \left| \Psi^{(0)}_{\mathbf{k}n} \right\rangle$ which transforms as:

$$\frac{1}{2}\sum_{\kappa\alpha}\sum_{\kappa'\alpha'}\sum_{\mathbf{q}\mathbf{q}'}\tilde{\lambda}_{\kappa\alpha}(\mathbf{q})\tilde{\lambda}_{\kappa'\alpha'}(\mathbf{q}')\left\langle \Psi^{(0)}_{\mathbf{k}n}\right| e^{i(\mathbf{q}+\mathbf{q}')\cdot\mathbf{r}}\frac{\partial^2 v^{\mathrm{KS}}}{\partial R_{\kappa\alpha}(\mathbf{q})\partial R_{\kappa'\alpha'}(\mathbf{q}')}\left|\Psi^{(0)}_{\mathbf{k}n}\right\rangle =$$

$$\frac{1}{2}\sum_{\kappa\alpha}\sum_{\kappa'\alpha'}\sum_{\mathbf{q}\mathbf{q}'}\tilde{\lambda}_{\kappa\alpha}(\mathbf{q})\tilde{\lambda}_{\kappa'\alpha'}(\mathbf{q}')\left\langle u_{\mathbf{k}n}\right| \frac{\partial^2 v^{\mathrm{KS}}}{\partial R_{\kappa\alpha}(\mathbf{q})\partial R_{\kappa'\alpha'}(\mathbf{q}')}\left|u_{\mathbf{k}n}\right\rangle_{\mathrm{uc}}\delta_{\mathbf{q},-\mathbf{q}'} = \tag{A.34}$$

$$\frac{1}{2}\sum_{\kappa\alpha}\sum_{\kappa'\alpha'}\sum_{\mathbf{q}'}\tilde{\lambda}_{\kappa\alpha}(-\mathbf{q}')\tilde{\lambda}_{\kappa'\alpha'}(\mathbf{q}')\left\langle u_{\mathbf{k}n}\right| \frac{\partial^2 v^{\mathrm{KS}}}{\partial R_{\kappa\alpha}(-\mathbf{q}')\partial R_{\kappa'\alpha'}(\mathbf{q}')}\left|u_{\mathbf{k}n}\right\rangle_{\mathrm{uc}},$$

and the other is $2\lambda^2 \,\mathrm{Re}\left\langle \Psi^{(0)}_{\mathbf{k}n}\right| H^{(1)} \left|\Psi^{(1)}_{\mathbf{k}n}\right\rangle$ which transforms as:

$$2\sum_{\kappa\alpha}\sum_{\kappa'\alpha'}\sum_{\mathbf{q}\mathbf{q}'}\tilde{\lambda}_{\kappa\alpha}(\mathbf{q})\tilde{\lambda}_{\kappa'\alpha'}(\mathbf{q}')\,\mathrm{Re}\left\langle \Psi^{(0)}_{\mathbf{k}n}\right| e^{i\mathbf{q}\cdot\mathbf{r}}\frac{\partial v^{\mathrm{KS}}}{\partial R_{\kappa\alpha}(\mathbf{q})}\left|\Psi^{(1)}_{\mathbf{k}n}(\mathbf{q}')\right\rangle \tag{A.35}$$

Matrix element $\left\langle \Psi^{(0)}_{\mathbf{k}n}\right| e^{i\mathbf{q}\cdot\mathbf{r}}\frac{\partial v^{\mathrm{KS}}}{\partial R_{\kappa\alpha}(\mathbf{q})}\left|\Psi^{(1)}_{\mathbf{k}n}(\mathbf{q}')\right\rangle$ can be expanded using Eq. (A.31):

$$\left\langle \Psi^{(0)}_{\mathbf{k}n}\right| e^{i\mathbf{q}\cdot\mathbf{r}}\frac{\partial v^{\mathrm{KS}}}{\partial R_{\kappa\alpha}(\mathbf{q})}\left|\Psi^{(1)}_{\mathbf{k}n}(\mathbf{q}')\right\rangle =$$

$$\frac{1}{N_{\mathrm{uc}}V_{\mathrm{uc}}}\int_{\mathrm{sc}}\mathrm{d}\mathbf{r}\,u^*_{\mathbf{k}n}\frac{\partial v^{\mathrm{KS}}}{\partial R_{\kappa\alpha}(\mathbf{q})}e^{i(\mathbf{q}+\mathbf{q}')\cdot\mathbf{r}}\sum_{n'\neq n}u^*_{\mathbf{k}+\mathbf{q}'n'}\frac{\left\langle u_{\mathbf{k}+\mathbf{q}'n'}\right|\frac{\partial v^{\mathrm{KS}}}{\partial R_{\kappa'\alpha'}(\mathbf{q}')}\left|u_{\mathbf{k}n}\right\rangle}{E^{(0)}_{\mathbf{k}n}-E^{(0)}_{\mathbf{k}+\mathbf{q}'n'}} =$$

$$\frac{1}{V_{\mathrm{uc}}}\int_{\mathrm{uc}}\mathrm{d}\mathbf{r}\,u^*_{\mathbf{k}n}\frac{\partial v^{\mathrm{KS}}}{\partial R_{\kappa\alpha}(\mathbf{q})}e^{i(\mathbf{q}+\mathbf{q}')\cdot\mathbf{r}}\delta_{\mathbf{q},-\mathbf{q}'}\sum_{n'}u^*_{\mathbf{k}+\mathbf{q}'n'}\frac{\left\langle u_{\mathbf{k}+\mathbf{q}'n'}\right|\frac{\partial v^{\mathrm{KS}}}{\partial R_{\kappa'\alpha'}(\mathbf{q}')}\left|u_{\mathbf{k}n}\right\rangle}{E^{(0)}_{\mathbf{k}n}-E^{(0)}_{\mathbf{k}+\mathbf{q}'n'}} = \tag{A.36}$$

$$\sum_{n'\neq n}\frac{\left\langle u_{\mathbf{k}n}\right|\frac{\partial v^{\mathrm{KS}}}{\partial R_{\kappa\alpha}(-\mathbf{q}')}\left|u_{\mathbf{k}+\mathbf{q}'n'}\right\rangle\left\langle u_{\mathbf{k}+\mathbf{q}'n'}\right|\frac{\partial v^{\mathrm{KS}}}{\partial R_{\kappa'\alpha'}(\mathbf{q}')}\left|u_{\mathbf{k}n}\right\rangle}{E^{(0)}_{\mathbf{k}n}-E^{(0)}_{\mathbf{k}+\mathbf{q}'n'}}$$

Finally, the second-order correction $\frac{1}{2}\lambda^2 E^{(2)}_{\mathbf{k}n}$ will be:

$$\frac{1}{2}\lambda^2 E^{(2)}_{\mathbf{k}n} = \frac{1}{2}\lambda^2 E^{\mathrm{DW}}_{\mathbf{k}n} + \frac{1}{2}\lambda^2 E^{\mathrm{Fan}}_{\mathbf{k}n},$$

$$\frac{1}{2}\lambda^2 E^{\mathrm{DW}}_{\mathbf{k}n} = \frac{1}{2}\sum_{\kappa\kappa'\alpha\alpha'}\sum_{\mathbf{q}'}\tilde{\lambda}_{\kappa\alpha}(-\mathbf{q}')\tilde{\lambda}_{\kappa'\alpha'}(\mathbf{q}')\left\langle u_{\mathbf{k}n}\right|\frac{\partial^2 v^{\mathrm{KS}}}{\partial R_{\kappa\alpha}(-\mathbf{q}')\partial R_{\kappa'\alpha'}(\mathbf{q}')}\left|u_{\mathbf{k}n}\right\rangle \tag{A.37}$$

$$\frac{1}{2}\lambda^2 E^{\mathrm{Fan}}_{\mathbf{k}n} = 2\,\mathrm{Re}\sum_{\kappa\kappa'\alpha\alpha'}\sum_{\mathbf{q}'n'\neq n}\tilde{\lambda}_{\kappa\alpha}(-\mathbf{q}')\tilde{\lambda}_{\kappa'\alpha'}(\mathbf{q}'),$$
$$\times\frac{\left\langle u_{\mathbf{k}n}\right|\frac{\partial v^{\mathrm{KS}}}{\partial R_{\kappa\alpha}(-\mathbf{q}')}\left|u_{\mathbf{k}+\mathbf{q}'n'}\right\rangle\left\langle u_{\mathbf{k}+\mathbf{q}'n'}\right|\frac{\partial v^{\mathrm{KS}}}{\partial R_{\kappa'\alpha'}(\mathbf{q}')}\left|u_{\mathbf{k}n}\right\rangle}{E^{(0)}_{\mathbf{k}n}-E^{(0)}_{\mathbf{k}+\mathbf{q}'n'}}.$$

Until this point, the strength of the perturbation has been expressed with $\tilde{\lambda}_{\kappa\alpha}(\mathbf{q})$ in order to keep track of order of λ in energy corrections. When $\lambda \to 1$ they become $\Delta R_{\kappa\alpha}(\mathbf{q})$. Remembering that in the second quantization in real space these terms are:

$$\Delta R_{\kappa\alpha,p} = N_{\mathrm{uc}}^{-1/2} \sum_{\mathbf{q}\nu} \frac{e^{i\mathbf{q}\cdot\mathbf{T}_p} \xi_{\kappa\alpha,\nu}(\mathbf{q})}{(2M_\kappa \omega_{\mathbf{q}\nu}/\hbar)^{1/2}} \left(\hat{a}_{\mathbf{q}\nu} + \hat{a}^\dagger_{-\mathbf{q}\nu} \right), \tag{A.38}$$

so $\Delta R_{\kappa\alpha}(\mathbf{q})$ can be obtained with Fourier transform:

$$\begin{aligned}
\Delta R_{\kappa\alpha}(\mathbf{q}) &= \frac{1}{N_{\mathrm{uc}}} \sum_p e^{-i\mathbf{q}\cdot\mathbf{T}_p} \Delta R_{\kappa\alpha,p} \\
&= N_{\mathrm{uc}}^{-1/2} \sum_{\mathbf{q}'\nu} \frac{\xi_{\kappa\alpha,\nu}(\mathbf{q})}{(2M_\kappa \omega_{\mathbf{q}\nu}/\hbar)^{1/2}} \left(\hat{a}_{\mathbf{q}'\nu} + \hat{a}^\dagger_{-\mathbf{q}'\nu} \right) \frac{1}{N_{\mathrm{uc}}} \sum_p e^{-i(\mathbf{q}-\mathbf{q}')\cdot\mathbf{T}_p} \\
&= N_{\mathrm{uc}}^{-1/2} \sum_{\mathbf{q}'\nu} \frac{\xi_{\kappa\alpha,\nu}(\mathbf{q})}{(2M_\kappa \omega_{\mathbf{q}'\nu}/\hbar)^{1/2}} \left(\hat{a}_{\mathbf{q}'\nu} + \hat{a}^\dagger_{-\mathbf{q}'\nu} \right) \delta_{\mathbf{q},\mathbf{q}'} \\
&= N_{\mathrm{uc}}^{-1/2} \sum_{\nu} \frac{\xi_{\kappa\alpha,\nu}(\mathbf{q})}{(2M_\kappa \omega_{\mathbf{q}\nu}/\hbar)^{1/2}} \left(\hat{a}_{\mathbf{q}\nu} + \hat{a}^\dagger_{-\mathbf{q}\nu} \right),
\end{aligned} \tag{A.39}$$

where $\xi_{\kappa\alpha,\nu}(\mathbf{q})$ and $\omega_{\mathbf{q}\nu}$ are polarization vectors and phonon frequencies of mode ν obtained from phonon structure and $\hat{a}_{\mathbf{q}\nu}(\hat{a}^\dagger_{-\mathbf{q}\nu})$ are destruction (creation) operators of phonon $\mathbf{q}\nu(-\mathbf{q}\nu)$.

Electron-phonon matrix elements of the first-order $g_{nn',\nu}(\mathbf{k},\mathbf{q})$ can be defined as probability of scattering of electron from one state $\mathbf{k}n$ to another $\mathbf{k}'n'$ by phonon $\mathbf{q}\nu$ where $\mathbf{k}-\mathbf{k}' = \mathbf{q}$, and expressed as a sum of perturbation for all ions κ and directions α:

$$g_{nn',\nu}(\mathbf{k},\mathbf{q}) = \sum_{\kappa\alpha} \frac{\xi_{\kappa\alpha,\nu}(\mathbf{q})}{(2M_\kappa \omega_{\mathbf{q}\nu}/\hbar)^{1/2}} \left\langle u_{\mathbf{k}+\mathbf{q}n} \right| \frac{\partial v^{\mathrm{KS}}}{\partial R_{\kappa\alpha}(\mathbf{q})} \left| u_{\mathbf{k}n'} \right\rangle, \tag{A.40}$$

which is the same as Eq. (2.192) after expansion. For $g_{nn',\nu\nu'}(\mathbf{k},\mathbf{q},\mathbf{q}')$ second-order terms, one obtains:

$$\begin{aligned}
g_{nn',\nu\nu'}(\mathbf{k},\mathbf{q},\mathbf{q}') = \frac{1}{2} \sum_{\kappa\kappa'\alpha\alpha'} & \frac{\xi_{\kappa\alpha,\nu}(\mathbf{q})}{(2M_\kappa \omega_{\mathbf{q}\nu}/\hbar)^{1/2}} \frac{\xi_{\kappa'\alpha',\nu'}(\mathbf{q}')}{(2M_{\kappa'} \omega_{\mathbf{q}'\nu'}/\hbar)^{1/2}} \\
& \times \left\langle u_{\mathbf{k}+\mathbf{q}+\mathbf{q}'n} \right| \frac{\partial^2 v^{\mathrm{KS}}}{\partial R_{\kappa\alpha}(\mathbf{q}) \partial R_{\kappa'\alpha'}(\mathbf{q}')} \left| u_{\mathbf{k}n'} \right\rangle.
\end{aligned} \tag{A.41}$$

Expression in Eq. (A.41) is the same as Eq. (2.193) after expansion.

When Kohn-Sham Hamiltonian is expressed using second-quantization $H^{(0)} = H^{\mathrm{KS}} = \sum_{\mathbf{k}n} \varepsilon_{\mathbf{k}n} \hat{c}^\dagger_{\mathbf{k}n} \hat{c}_{\mathbf{k}n}$, the perturbation of electronic states by ionic displacement,

to the second-order, is expressed as:

$$
\begin{aligned}
H^{(1)} &= N_{\mathrm{uc}}^{-1/2} \sum_{\mathbf{k}mn} \sum_{\mathbf{q}\nu} g_{mn,\nu}(\mathbf{k},\mathbf{q}) \hat{c}^{\dagger}_{\mathbf{k}+\mathbf{q}m} \hat{c}_{\mathbf{k}n} \left(\hat{a}_{\mathbf{q}\nu} + \hat{a}^{\dagger}_{-\mathbf{q}\nu} \right), \\
H^{(2)} &= N_{\mathrm{uc}}^{-1} \sum_{\mathbf{k}mn} \sum_{\mathbf{q}\nu,\mathbf{q}'\nu'} g_{mn,\nu\nu'}(\mathbf{k},\mathbf{q},\mathbf{q}') \hat{c}^{\dagger}_{\mathbf{k}+\mathbf{q}+\mathbf{q}'m} \hat{c}_{\mathbf{k}n} \\
&\quad \times \left(\hat{a}_{\mathbf{q}\nu} + \hat{a}^{\dagger}_{-\mathbf{q}\nu} \right) \left(\hat{a}_{\mathbf{q}'\nu'} + \hat{a}^{\dagger}_{-\mathbf{q}'\nu'} \right),
\end{aligned}
\tag{A.42}
$$

which is the same as Eq. (2.191).

Since ions are moving in time, one should take time-averaged values of $\lambda E^{(1)}_{\mathbf{k}n}$ and $\lambda^2 E^{(2)}_{\mathbf{k}n}$. Time-average of $\Delta R_{\kappa\alpha}(\mathbf{q})$ is zero, since ion will spent the same time any two opposite directions, therefore $\left\langle \lambda E^{(1)}_{\mathbf{k}n} \right\rangle = 0$. For $\left\langle \lambda^2 E^{(2)}_{\mathbf{k}n} \right\rangle$ one makes use of the following contraction (found in Mahan 2000 [118]):

$$
\left\langle (\hat{a}^{\dagger}_{-\mathbf{q}\nu} + \hat{a}_{\mathbf{q}\nu})(\hat{a}^{\dagger}_{-\mathbf{q}'\nu'} + \hat{a}_{\mathbf{q}'\nu'}) \right\rangle = \delta_{-\mathbf{q},\mathbf{q}'} \delta_{\nu,\nu'} (n_{\mathbf{q}'\nu'}(T) + n_{\mathbf{q}\nu}(T) + 1), \tag{A.43}
$$

where $n_{\mathbf{q}\nu}(T)$ is the Bose-Einstein distribution factor that introduces the temperature dependence T. Using this contraction, the second-order corrections to $E_{\mathbf{k}n}$ in Reyleigh-Schrödinger perturbation theory will be:

$$
\begin{aligned}
\frac{1}{2}\lambda^2 E^{\mathrm{DW}}_{\mathbf{k}n}(T) &= N_{\mathrm{uc}}^{-1} \sum_{\mathbf{q}'\nu'} \frac{2n_{\mathbf{q}'\nu'}(T)+1}{2\omega_{\mathbf{q}'\nu'}/\hbar} \sum_{\kappa\kappa'\alpha\alpha'} \frac{\xi_{\kappa\alpha,\nu'}(-\mathbf{q}')}{(M_\kappa)^{1/2}} \frac{\xi_{\kappa'\alpha',\nu'}(\mathbf{q}')}{(M_{\kappa'})^{1/2}} \\
&\quad \times \frac{1}{2} \left\langle u_{\mathbf{k}n} \right| \frac{\partial^2 v^{\mathrm{KS}}}{\partial R_{\kappa\alpha}(-\mathbf{q}') \partial R_{\kappa'\alpha'}(\mathbf{q}')} \left| u_{\mathbf{k}n} \right\rangle \\
&= \sum_{\mathbf{q}'\nu'} g_{nn,\nu\nu}(\mathbf{k},-\mathbf{q}',\mathbf{q}') \left[2n_{\mathbf{q}'\nu'}(T) + 1 \right],
\end{aligned}
\tag{A.44}
$$

and

$$
\begin{aligned}
\frac{1}{2}\lambda^2 E^{\mathrm{Fan}}_{\mathbf{k}n}(T) &= N_{\mathrm{uc}}^{-1} \sum_{\mathbf{q}'\nu'} \frac{2n_{\mathbf{q}'\nu'}(T)+1}{2\omega_{\mathbf{q}'\nu'}/\hbar} \sum_{\kappa\kappa'\alpha\alpha'} \frac{\xi_{\kappa\alpha,\nu'}(-\mathbf{q}')}{(M_\kappa)^{1/2}} \frac{\xi_{\kappa'\alpha',\nu'}(\mathbf{q}')}{(M_{\kappa'})^{1/2}} \\
&\quad \times 2\,\mathrm{Re} \sum_{n' \neq n} \frac{\left\langle u_{\mathbf{k}n} \right| \frac{\partial v^{\mathrm{KS}}}{\partial R_{\kappa\alpha}(-\mathbf{q}')} \left| u_{\mathbf{k}+\mathbf{q}'n'} \right\rangle \left\langle u_{\mathbf{k}+\mathbf{q}'n'} \right| \frac{\partial v^{\mathrm{KS}}}{\partial R_{\kappa'\alpha'}(\mathbf{q}')} \left| u_{\mathbf{k}n} \right\rangle}{E^{(0)}_{\mathbf{k}n} - E^{(0)}_{\mathbf{k}+\mathbf{q}'n'}} \\
&= \sum_{\mathbf{q}'\nu'} \sum_{n' \neq n} \left| g_{nn'}(\mathbf{k},\mathbf{q}) \right|^2 \left[2n_{\mathbf{q}'\nu'}(T) + 1 \right],
\end{aligned}
\tag{A.45}
$$

where $n_{\mathbf{q}\nu}(T) = n_{-\mathbf{q}\nu}(T)$ and $\omega_{-\mathbf{q}\nu} = \omega_{\mathbf{q}\nu}$ were used.

The first-order electron-phonon matrix elements $g_{nm,\nu}(\mathbf{k},\mathbf{q})$ are obtained as a part of the DFPT routine. The second-order terms $g_{nn,\nu\nu}(\mathbf{k},\mathbf{q},-\mathbf{q})$ are more involved and are not part of the DFPT routine. In order to compute $g_{nn,\nu\nu}(\mathbf{k},\mathbf{q},-\mathbf{q})$, Allen and Heine made use of the rigid-ion approximation [113, 114, 115], which allows one to express second-order terms $g_{nn,\nu\nu}(\mathbf{k},\mathbf{q},-\mathbf{q})$ using first-order terms $g_{nm,\nu}(\mathbf{k},\mathbf{q})$.

A.4 Collective displacement of ions

In the case of collective displacements of all ions by some ΔR along γ-direction, $\Delta R_{\kappa\gamma,p}$ are constant for all p unit cells. In the reciprocal space, this corresponds to Γ perturbation $\Delta R_{\kappa\alpha}(\mathbf{q}) = \Delta R \delta_{\alpha\gamma}\delta_{\mathbf{q},\Gamma}$. Moving all ions in γ-direction by ΔR is equivalent to just moving the system of reference by $-\Delta R\mathbf{e}_\gamma$, therefore in this case, by the principle of translation invariance, there is no perturbation so $\lambda E^{(1)}_{\mathbf{k}n}$ and $\lambda^2 E^{(2)}_{\mathbf{k}n}$ from Eq. (A.29) and Eq. (A.37), respectively, should vanish.

From $\lambda E^{(1)}_{\mathbf{k}n} = 0$:

$$\begin{aligned} \lambda E^{(1)}_{\mathbf{k}n} = \Delta R \sum_\kappa \langle u_{\mathbf{k}+\Gamma n}| \frac{\partial v^{\mathrm{KS}}}{\partial R_{\kappa\gamma}(\Gamma)} |u_{\mathbf{k}n}\rangle = 0, \\ \Rightarrow \sum_\kappa \langle u_{\mathbf{k}n}| \frac{\partial v^{\mathrm{KS}}}{\partial R_{\kappa\gamma}(\Gamma)} |u_{\mathbf{k}n}\rangle = 0. \end{aligned} \tag{A.46}$$

From $\frac{1}{2}\lambda^2 E^{(2)}_{\mathbf{k}n} = 0$ one obtains:

$$\begin{aligned} \frac{1}{2}\lambda^2 E^{(2)}_{\mathbf{k}n} = (\Delta R)^2 \sum_{\kappa\kappa'\gamma} \Bigg[\frac{1}{2} \langle u_{\mathbf{k}n}| \frac{\partial^2 v^{\mathrm{KS}}}{\partial R_{\kappa\gamma}(\Gamma)\partial R_{\kappa'\gamma}(\Gamma)} |u_{\mathbf{k}n}\rangle \\ + 2\,\mathrm{Re} \sum_{n'\neq n} \frac{\langle u_{\mathbf{k}n}| \frac{\partial v^{\mathrm{KS}}}{\partial R_{\kappa\gamma}(\Gamma)} |u_{\mathbf{k}'n'}\rangle \langle u_{\mathbf{k}n'}| \frac{\partial v^{\mathrm{KS}}}{\partial R_{\kappa'\gamma}(\Gamma)} |u_{\mathbf{k}n}\rangle}{E^{(0)}_{\mathbf{k}n} - E^{(0)}_{\mathbf{k}n'}} \Bigg] = 0, \end{aligned} \tag{A.47}$$

where κ and κ' can be decoupled in the sum, or equivalently, one can take a derivative $\partial/\partial R_{\kappa'\beta}$ of Eq. (A.46) to obtain:

$$\begin{aligned} \sum_\kappa \Bigg[\langle u_{\mathbf{k}n}| \frac{\partial^2 v^{\mathrm{KS}}}{\partial R_{\kappa\gamma}(\Gamma)\partial R_{\kappa'\beta}(\Gamma)} |u_{\mathbf{k}n}\rangle \\ + 2\,\mathrm{Re} \sum_{n'\neq n} \frac{\langle u_{\mathbf{k}n}| \frac{\partial v^{\mathrm{KS}}}{\partial R_{\kappa\gamma}(\Gamma)} |u_{\mathbf{k}+\mathbf{q}'n'}\rangle \langle u_{\mathbf{k}+\mathbf{q}n'}| \frac{\partial v^{\mathrm{KS}}}{\partial R_{\kappa'\beta}(\Gamma)} |u_{\mathbf{k}n}\rangle}{E^{(0)}_{\mathbf{k}n} - E^{(0)}_{\mathbf{k}n'}} \Bigg] = 0. \end{aligned} \tag{A.48}$$

From Eq. (A.48) one can obtain the second-order derivatives of v^{KS} for perturbations in Γ using only first-order derivatives:

$$\begin{aligned} \sum_\kappa \langle u_{\mathbf{k}n}| \frac{\partial^2 v^{\mathrm{KS}}}{\partial R_{\kappa\gamma}(\Gamma)\partial R_{\kappa'\beta}(\Gamma)} |u_{\mathbf{k}n}\rangle = \\ -2\,\mathrm{Re} \sum_\kappa \sum_{n'\neq n} \frac{\langle u_{\mathbf{k}n}| \frac{\partial v^{\mathrm{KS}}}{\partial R_{\kappa\gamma}(\Gamma)} |u_{\mathbf{k}n'}\rangle \langle u_{\mathbf{k}n'}| \frac{\partial v^{\mathrm{KS}}}{\partial R_{\kappa'\beta}(\Gamma)} |u_{\mathbf{k}n}\rangle}{E^{(0)}_{\mathbf{k}n} - E^{(0)}_{\mathbf{k}n'}}. \end{aligned} \tag{A.49}$$

A.5 Rigid-ion approximation

In order to express electron-phonon matrix of second-order using first-order elements, Allen and Heine [113, 114, 115] used the rigid-ion approximation for the

second-order derivatives. Rigid-ion potential is local and expressed as a sum of individual ion-centered Coulomb potentials:

$$V^{\mathrm{ri}}(\mathbf{r}) = \sum_{\kappa,p} Z_\kappa v_c(\mathbf{R}_\kappa + \mathbf{T}_p - \mathbf{r}), \tag{A.50}$$

where κ and p are ion and unit cell indices, respectively. The second-order derivative of V^{ri} will be:

$$\frac{\partial^2 V_{\mathrm{el-ion}}}{\partial R_{\kappa\alpha,p}\partial R_{\kappa'\alpha',p'}} = 0, \quad \text{if} \quad \kappa \neq \kappa' \quad \text{and} \quad p \neq p'. \tag{A.51}$$

For Hamiltonians that consist of rigid-ion potential only $H^{\mathrm{ri}} = T + V^{\mathrm{ri}}$, the dynamical matrix $D^{\kappa\alpha}_{\kappa'\alpha'}(\mathbf{q})_{\mathrm{ri}}$ will be:

$$\begin{aligned} D^{\kappa\alpha}_{\kappa'\alpha'}(\mathbf{q})_{\mathrm{ri}} &= \frac{\delta_{\kappa\kappa'}}{N_{\mathrm{uc}}} \sum_{p,p'} \delta_{pp'} \frac{e^{-i\mathbf{q}\cdot\mathbf{T}_p}}{M_\kappa^{1/2}} \frac{\partial^2 V^{\mathrm{ri}}}{\partial R_{\kappa\alpha,p}\partial R_{\kappa'\alpha',p'}} \frac{e^{i\mathbf{q}\cdot\mathbf{T}_{p'}}}{M_{\kappa'}^{1/2}} \\ &= \frac{\delta_{\kappa\kappa'}}{M_\kappa^{1/2} M_{\kappa'}^{1/2}} \sum_{p} \delta_{p0} e^{-i\mathbf{q}\cdot\mathbf{T}_p} \frac{\partial^2 V^{\mathrm{ri}}}{\partial R_{\kappa\alpha,p}\partial R_{\kappa'\alpha',0}} \\ &= \frac{\delta_{\kappa\kappa'}}{M_\kappa^{1/2} M_{\kappa'}^{1/2}} \frac{\partial^2 V^{\mathrm{ri}}}{\partial R_{\kappa\alpha,0}\partial R_{\kappa'\alpha',0}} \\ &= \delta_{\kappa\kappa'} D^{\kappa\alpha}_{\kappa'\alpha'}(\Gamma). \end{aligned} \tag{A.52}$$

Inserting (A.52) into Eq. (A.44), one would obtain the rigid-ion approximation for $\frac{1}{2}\lambda^2 E^{\mathrm{DW}}_{\mathbf{k}n}(T)$:

$$\begin{aligned} \frac{1}{2}\lambda^2 E^{\mathrm{DW}}_{\mathbf{k}n}(T)_{\mathrm{ria}} &= N_{\mathrm{uc}}^{-1} \sum_{\mathbf{q}'\nu'} \frac{2n_{\mathbf{q}'\nu'}(T)+1}{2\omega_{\mathbf{q}'\nu'}/\hbar} \sum_{\kappa\kappa'\alpha\alpha'} \xi_{\kappa\alpha,\nu'}(-\mathbf{q}')\xi_{\kappa'\alpha',\nu'}(\mathbf{q}') \\ &\quad \times \frac{1}{2} \left\langle u_{\mathbf{k}n} \right| D^{\kappa\alpha}_{\kappa'\alpha'}(\mathbf{q})_{\mathrm{ri}} \left| u_{\mathbf{k}n} \right\rangle \\ &= N_{\mathrm{uc}}^{-1} \sum_{\mathbf{q}'\nu'} \sum_{\kappa\kappa'\alpha\alpha'} \xi_{\kappa\alpha,\nu'}(-\mathbf{q}')\xi_{\kappa'\alpha',\nu'}(\mathbf{q}') \\ &\quad \times \frac{1}{2} \left\langle u_{\mathbf{k}n} \right| \delta_{\kappa\kappa'} D^{\kappa\alpha}_{\kappa'\alpha'}(\Gamma)_{\mathrm{ri}} \left| u_{\mathbf{k}n} \right\rangle . \end{aligned} \tag{A.53}$$

When V^{ri} is used for the second derivative instead of v^{KS} in Eq. (A.49), one obtains:

$$\begin{aligned} &\sum_\kappa \left\langle u_{\mathbf{k}n} \right| D^{\kappa\gamma}_{\kappa'\beta}(\Gamma) \left| u_{\mathbf{k}n} \right\rangle \delta_{\kappa\kappa'} = \frac{1}{M_{\kappa'}} \left\langle u_{\mathbf{k}n} \right| D^{\kappa'\gamma}_{\kappa'\beta}(\Gamma) \left| u_{\mathbf{k}n} \right\rangle = \\ &-2\,\mathrm{Re} \sum_\kappa \sum_{n'\neq n} \frac{\left\langle u_{\mathbf{k}n} \right| \frac{\partial v^{\mathrm{KS}}}{\partial R_{\kappa\gamma}(\Gamma)} \left| u_{\mathbf{k}n'} \right\rangle \left\langle u_{\mathbf{k}n'} \right| \frac{\partial v^{\mathrm{KS}}}{\partial R_{\kappa'\beta}(\Gamma)} \left| u_{\mathbf{k}n} \right\rangle}{E^{(0)}_{\mathbf{k}n} - E^{(0)}_{\mathbf{k}n'}}, \end{aligned} \tag{A.54}$$

which can be used to transform Eq. (A.54) to:

$$\begin{aligned}\frac{1}{2}\lambda^2 E^{\mathrm{DW}}_{\mathbf{k}n}(T)_{\mathrm{ria}} &= N_{\mathrm{uc}}^{-1}\sum_{\mathbf{q}'\nu'}\frac{2n_{\mathbf{q}'\nu'}(T)+1}{2\omega_{\mathbf{q}'\nu'}/\hbar}\sum_{\kappa\kappa'\alpha\alpha'}\xi_{\kappa\alpha,\nu'}(-\mathbf{q}')\xi_{\kappa'\alpha',\nu'}(\mathbf{q}') \\ &\times\frac{1}{2}\left\langle u_{\mathbf{k}n}\right| D^{\kappa\alpha}_{\kappa'\alpha'}(\Gamma)\delta_{\kappa\kappa'}\left|u_{\mathbf{k}n}\right\rangle \\ &= N_{\mathrm{uc}}^{-1}\sum_{\mathbf{q}'\nu'}\frac{-1}{2\omega_{\mathbf{q}'\nu'}/\hbar}\left[2n_{\mathbf{q}'\nu'}(T)+1\right] \\ &\times\sum_{\kappa\kappa'\alpha\alpha'}\left[\frac{\xi_{\kappa\alpha,\nu'}(-\mathbf{q}')\xi_{\kappa\alpha',\nu'}(\mathbf{q}')}{2M_\kappa}+\frac{\xi_{\kappa'\alpha,\nu'}(-\mathbf{q}')\xi_{\kappa'\alpha',\nu'}(\mathbf{q}')}{2M_{\kappa'}}\right] \\ &\times 2\,\mathrm{Re}\sum_{n'\neq n}\frac{\left\langle u_{\mathbf{k}n}\right|\frac{\partial v^{\mathrm{KS}}}{\partial R_{\kappa\alpha}(\Gamma)}\left|u_{\mathbf{k}n'}\right\rangle\left\langle u_{\mathbf{k}n'}\right|\frac{\partial v^{\mathrm{KS}}}{\partial R_{\kappa'\alpha'}(\Gamma)}\left|u_{\mathbf{k}n}\right\rangle}{E^{(0)}_{\mathbf{k}n}-E^{(0)}_{\mathbf{k}n'}}.\end{aligned} \tag{A.55}$$

Using rigid-ion approximation, the total renormalization of energy level $E_{\mathbf{k}n} = E^{(0)}_{\mathbf{k}n} + \Delta E_{\mathbf{k}n}(T)$ due to ionic movement is:

$$\begin{aligned}\Delta E_{\mathbf{k}n}(T) &= \frac{1}{2}\lambda^2 E^{\mathrm{FAN}}_{\mathbf{k}n}(T)+\frac{1}{2}\lambda^2 E^{\mathrm{DW}}_{\mathbf{k}n}(T) \\ &= N_{\mathrm{uc}}^{-1}\sum_{\mathbf{q}'\nu'}\frac{2n_{\mathbf{q}'\nu'}(T)+1}{2\omega_{\mathbf{q}'\nu'}/\hbar} \\ &\times\left\{\sum_{\kappa\kappa'\alpha\alpha'}\frac{\xi_{\kappa\alpha,\nu'}(-\mathbf{q}')}{(M_\kappa)^{1/2}}\frac{\xi_{\kappa'\alpha',\nu'}(\mathbf{q}')}{(M_{\kappa'})^{1/2}}\right. \\ &\quad\times 2\,\mathrm{Re}\sum_{n'\neq n}\frac{\left\langle u_{\mathbf{k}n}\right|\frac{\partial v^{\mathrm{KS}}}{\partial R_{\kappa\alpha}(-\mathbf{q}')}\left|u_{\mathbf{k}+\mathbf{q}'n'}\right\rangle\left\langle u_{\mathbf{k}+\mathbf{q}'n'}\right|\frac{\partial v^{\mathrm{KS}}}{\partial R_{\kappa'\alpha'}(\mathbf{q}')}\left|u_{\mathbf{k}n}\right\rangle}{E^{(0)}_{\mathbf{k}n}-E^{(0)}_{\mathbf{k}+\mathbf{q}'n'}} \\ &\quad-\sum_{\kappa\kappa'\alpha\alpha'}\left[\frac{\xi_{\kappa\alpha,\nu'}(-\mathbf{q}')\xi_{\kappa\alpha',\nu'}(\mathbf{q}')}{2M_\kappa}+\frac{\xi_{\kappa'\alpha,\nu'}(-\mathbf{q}')\xi_{\kappa'\alpha',\nu'}(\mathbf{q}')}{2M_{\kappa'}}\right] \\ &\quad\left.\times 2\,\mathrm{Re}\sum_{n'\neq n}\frac{\left\langle u_{\mathbf{k}n}\right|\frac{\partial v^{\mathrm{KS}}}{\partial R_{\kappa\alpha}(\Gamma)}\left|u_{\mathbf{k}n'}\right\rangle\left\langle u_{\mathbf{k}n'}\right|\frac{\partial v^{\mathrm{KS}}}{\partial R_{\kappa'\alpha'}(\Gamma)}\left|u_{\mathbf{k}n}\right\rangle}{E^{(0)}_{\mathbf{k}n}-E^{(0)}_{\mathbf{k}n'}}\right\}.\end{aligned} \tag{A.56}$$

Eq. (A.56) was originally derived by Allen, Heine and Cardona [113, 114, 115], and is often referred as Allen-Heine-Cardona (AHC) equation. The sum in Eq. (A.56) assumes that there are as many $\mathbf{q}'$-vectors as unit cells N_{uc} and that they are commensurable. If one wishes to include non-commensurable $\mathbf{q}'$-grid, the sum can be replaced with an integral, $N_{\mathrm{uc}}^{-1}\sum_{\mathbf{q}'} \to \int \mathrm{d}\mathbf{q}'$.

Eq. (A.56) is also adiabatic, since the difference of energy levels between $\mathbf{k}n$ and $\mathbf{k}+\mathbf{q}'n'$ doesn't include phononic frequencies:

$$E^{(0)}_{\mathbf{k}n} - E^{(0)}_{\mathbf{k}+\mathbf{q}'n'} \pm \hbar\omega_{\mathbf{q}'\nu'} \approx E^{(0)}_{\mathbf{k}n} - E^{(0)}_{\mathbf{k}+\mathbf{q}'n'}. \tag{A.57}$$

Furthermore, all energy levels are treated as sharp excitations without any smearing caused by ionic movements, which is sometimes also referred as on-the-mass-shell

(OTMS) approximation. This is a good approximation for low temperatures $T \to 0$ and for materials with weak electron-phonon interaction. For all other cases, a non-adiabatic formula is preferred.

Appendix B

Blocks found in Kane Hamiltonians

Using either numerical calculation described in Chapter 3 or analytical approach from theory of invariants found in Ref. [48, 51], one can obtain the following $\mathbf{k}\cdot\mathbf{p}$ Hamiltonians. Irreducible representations follow the notation found in Ref. [124].

B.1 T_d point group $\mathcal{B}(\Gamma_a, \Gamma_b)$ blocks

Analytical expressions for all possible blocks $\mathcal{B}(\Gamma_m, \Gamma_n)$ of the $\mathbf{k}\cdot\mathbf{p}$ Hamiltonian in the case of single T_d group are listed below:

$$\mathcal{B}(\Gamma_1, \Gamma_1) = C_1 k^2, \tag{B.1}$$

$$\mathcal{B}(\Gamma_1, \Gamma_2) = \mathcal{B}(\Gamma_1, \Gamma_5) = \mathcal{B}(\Gamma_2, \Gamma_4) = 0, \tag{B.2}$$

$$\mathcal{B}(\Gamma_1, \Gamma_3) = C_2 \begin{bmatrix} (k_z^2 + \omega^2 k_x^2 + \omega k_y^2) & (k_z^2 + \omega k_x^2 + \omega^2 k_y^2) \end{bmatrix}, \quad \omega = e^{i2\pi/3}, \tag{B.3}$$

$$\mathcal{B}(\Gamma_1, \Gamma_4) = C_3 \begin{bmatrix} k_z & k_x & k_y \end{bmatrix} + C_4 \begin{bmatrix} k_x k_y & k_y k_z & k_z k_x \end{bmatrix}, \tag{B.4}$$

$$\mathcal{B}(\Gamma_2, \Gamma_2) = C_5 k^2, \tag{B.5}$$

$$\mathcal{B}(\Gamma_2, \Gamma_3) = C_6 \begin{bmatrix} -(k_z^2 + \omega^2 k_x^2 + \omega k_y^2) & (k_z^2 + \omega k_x^2 + \omega^2 k_y^2) \end{bmatrix}, \tag{B.6}$$

$$\mathcal{B}(\Gamma_2, \Gamma_5) = C_7 \begin{bmatrix} k_z & k_x & k_y \end{bmatrix} + C_8 \begin{bmatrix} k_x k_y & k_y k_z & k_z k_x \end{bmatrix}, \tag{B.7}$$

$$\begin{aligned} \mathcal{B}(\Gamma_3, \Gamma_3) = {} & C_9 \begin{bmatrix} k^2 & 0 \\ 0 & k^2 \end{bmatrix} \\ & + C_{10} \begin{bmatrix} 0 & (k_z^2 + \omega^2 k_x^2 + \omega k_y^2) \\ (k_z^2 + \omega k_x^2 + \omega^2 k_y^2) & 0 \end{bmatrix}, \end{aligned} \tag{B.8}$$

$$\begin{aligned}\mathcal{B}(\Gamma_3,\Gamma_4) = C_{11}&\begin{bmatrix} k_z & \omega k_x & \omega^2 k_y \\ k_z & \omega^2 k_x & \omega k_y \end{bmatrix} \\ + C_{12}&\begin{bmatrix} k_x k_y & \omega k_y k_z & \omega^2 k_z k_x \\ k_x k_y & \omega^2 k_y k_z & \omega k_z k_x \end{bmatrix},\end{aligned} \tag{B.9}$$

$$\begin{aligned}\mathcal{B}(\Gamma_3,\Gamma_5) = C_{13}&\begin{bmatrix} k_z & \omega k_x & \omega^2 k_y \\ -k_z & -\omega^2 k_x & -\omega k_y \end{bmatrix} \\ + C_{14}&\begin{bmatrix} k_x k_y & \omega k_y k_z & \omega^2 k_z k_x \\ -k_x k_y & -\omega^2 k_y k_z & -\omega k_z k_x \end{bmatrix}\end{aligned} \tag{B.10}$$

$$\begin{aligned}\mathcal{B}(\Gamma_4,\Gamma_4) = C_{15}&\begin{bmatrix} 0 & k_y & k_x \\ k_y & 0 & k_z \\ k_x & k_z & 0 \end{bmatrix} \\ + C_{16}&\begin{bmatrix} 0 & k_z k_x & k_y k_z \\ k_z k_x & 0 & k_x k_y \\ k_y k_z & k_x k_y & 0 \end{bmatrix} \\ + C_{17}&\begin{bmatrix} 2k_z^2 - k_x^2 - k_y^2 & 0 & 0 \\ 0 & 2k_x^2 - k_y^2 - k_z^2 & 0 \\ 0 & 0 & 2k_y^2 - k_z^2 - k_x^2 \end{bmatrix} \\ + C_{18}&\begin{bmatrix} k^2 & 0 & 0 \\ 0 & k^2 & 0 \\ 0 & 0 & k^2 \end{bmatrix},\end{aligned} \tag{B.11}$$

$$\begin{aligned}\mathcal{B}(\Gamma_4,\Gamma_5) = C_{19}&\begin{bmatrix} 0 & k_y & -k_x \\ -k_y & 0 & k_z \\ k_x & -k_z & 0 \end{bmatrix} \\ + C_{20}&\begin{bmatrix} 0 & k_z k_x & -k_y k_z \\ -k_z k_x & 0 & k_x k_y \\ k_y k_z & -k_x k_y & 0 \end{bmatrix} \\ + C_{21}&\begin{bmatrix} k_x^2 - k_y^2 & 0 & 0 \\ 0 & k_y^2 - k_z^2 & 0 \\ 0 & 0 & k_z^2 - k_x^2 \end{bmatrix},\end{aligned} \tag{B.12}$$

$$\begin{aligned}\mathcal{B}(\Gamma_5,\Gamma_5) = {} & C_{22}\begin{bmatrix}0 & k_y & k_x\\ k_y & 0 & k_z\\ k_x & k_z & 0\end{bmatrix}\\ & + C_{23}\begin{bmatrix}0 & k_zk_x & k_yk_z\\ k_zk_x & 0 & k_xk_y\\ k_yk_z & k_xk_y & 0\end{bmatrix}\\ & + C_{24}\begin{bmatrix}2k_z^2-k_x^2-k_y^2 & 0 & 0\\ 0 & 2k_x^2-k_y^2-k_z^2 & 0\\ 0 & 0 & 2k_y^2-k_z^2-k_x^2\end{bmatrix}\\ & + C_{25}\begin{bmatrix}k^2 & 0 & 0\\ 0 & k^2 & 0\\ 0 & 0 & k^2\end{bmatrix},\end{aligned} \tag{B.13}$$

When spin-orbit interaction is included, the states transform according to the representations of the double point group T_{d}, which means that only the Γ_6, Γ_7 and Γ_8 states are relevant. The spinor representation corresponds to Γ_6 and multiplying all single irreducible representations gives the following products:

$$\begin{aligned}&\Gamma_6 \otimes \Gamma_6 \to \Gamma_6,\\ &\Gamma_2 \otimes \Gamma_6 \to \Gamma_7,\\ &\Gamma_3 \otimes \Gamma_6 \to \Gamma_8,\\ &\Gamma_4 \otimes \Gamma_6 \to \Gamma_7 + \Gamma_8,\\ &\Gamma_5 \otimes \Gamma_6 \to \Gamma_6 + \Gamma_8.\end{aligned} \tag{B.14}$$

Since the matrices that are obtained have some parts that appear more than once, the following shortened notation is introduced:

$$\Upsilon = k_z^2 + \omega k_x^2 + \omega^2 k_y^2, \quad \omega = e^{i2\pi/3}, \quad \zeta = e^{i\pi/4} \tag{B.15}$$

$$\Sigma(z,x,y) = \begin{bmatrix} z & x-iy \\ x+iy & -z \end{bmatrix}, \tag{B.16}$$

$$\Delta(z,x,y) = \zeta \begin{bmatrix} z & \omega^2 x - i\omega y \\ \omega^2 x + i\omega y & -z \end{bmatrix}, \tag{B.17}$$

$$\Lambda(z,x,y) = \begin{bmatrix} -i\omega x - \omega^2 y & z \\ iz & \omega x + i\omega^2 y \end{bmatrix}, \tag{B.18}$$

$$\Xi(z,x,y) = -\zeta \begin{bmatrix} z & \omega^2 x - i\omega y \\ \omega^2 x + i\omega y & -z \end{bmatrix} = -\Delta(z,x,y), \tag{B.19}$$

$$\begin{aligned}\Omega_1(z,x,y) &= -i\begin{bmatrix}-i\omega^2 x-\omega y & z\\ iz & \omega^2 x+i\omega y\end{bmatrix},\\ \Omega_2(z,x,y) &= +i\begin{bmatrix}-\omega x-i\omega^2 y & z\\ iz & i\omega x+\omega^2 y\end{bmatrix}.\end{aligned} \tag{B.20}$$

Using the notation from equations (B.15) through (B.20) all the relevant blocks $\mathcal{B}(\Gamma_m,\Gamma_n)$ of the Hamiltonian in case of double point group T_d are listed below:

$$\mathcal{B}(\Gamma_6,\Gamma_6) = C_1^d k^2, \tag{B.21}$$

$$\mathcal{B}(\Gamma_7,\Gamma_7) = C_2^d k^2, \tag{B.22}$$

$$\mathcal{B}(\Gamma_6,\Gamma_7) = C_3^d \Sigma(k_z,k_x,k_y) + C_4^d \Sigma(k_xk_y,k_yk_z,k_zk_x) \tag{B.23}$$

$$\begin{aligned}\mathcal{B}(\Gamma_6,\Gamma_8) = {}& \frac{C_5^d}{\sqrt{2}}\begin{bmatrix}-\zeta\Upsilon^* & 0 & 0 & \Upsilon\\ 0 & -\zeta\Upsilon^* & -i\Upsilon & 0\end{bmatrix}\\ &+ C_6^d\begin{bmatrix}\Delta(k_z,k_x,k_y) & \Lambda(k_z,k_x,k_y)\end{bmatrix}\\ &+ C_7^d\begin{bmatrix}\Delta(k_xk_y,k_yk_z,k_zk_x) & \Lambda(k_xk_y,k_yk_z,k_zk_x)\end{bmatrix}\end{aligned} \tag{B.24}$$

$$\begin{aligned}\mathcal{B}(\Gamma_7,\Gamma_8) = {}& +\frac{C_8^d}{\sqrt{2}}\begin{bmatrix}\zeta\Upsilon^* & 0 & 0 & \Upsilon\\ 0 & \zeta\Upsilon^* & -i\Upsilon & 0\end{bmatrix}\\ &+ C_9^d\begin{bmatrix}-\Delta(k_z,k_x,k_y) & \Lambda(k_z,k_x,k_y)\end{bmatrix}\\ &+ C_{10}^d\begin{bmatrix}-\Delta(k_xk_y,k_yk_z,k_zk_x) & \Lambda(k_xk_y,k_yk_z,k_zk_x)\end{bmatrix}\end{aligned}, \tag{B.25}$$

$$\begin{aligned}\mathcal{B}(\Gamma_8,\Gamma_8) = {}& C_{11}^d k^2\\ &+ C_{12}^d\begin{bmatrix}0 & 0 & 0 & -\Upsilon^*\\ 0 & 0 & i\Upsilon^* & 0\\ 0 & \Upsilon & 0 & 0\\ -i\Upsilon & 0 & 0 & 0\end{bmatrix}\\ &+ C_{13}^d\begin{bmatrix}\Sigma(k_z,k_x,k_y) & 0\\ 0 & \Sigma(k_z,k_y,k_x)\end{bmatrix}\\ &+ C_{14}^d\begin{bmatrix}0 & \Omega_1(k_z,k_x,k_y)\\ \Omega_2(k_z,k_x,k_y) & 0\end{bmatrix}\\ &+ C_{15}^d\begin{bmatrix}\Sigma(k_xk_y,k_yk_z,k_zk_x) & 0\\ 0 & \Sigma(k_xk_y,k_zk_x,k_yk_z)\end{bmatrix}\\ &+ C_{16}^d\begin{bmatrix}0 & \Omega_1(k_xk_y,k_yk_z,k_zk_x)\\ \Omega_2(k_xk_y,k_yk_z,k_zk_x) & 0\end{bmatrix}\end{aligned}, \tag{B.26}$$

B.2 $O_{\rm h}$ point group $\mathcal{B}(\Gamma_a, \Gamma_b)$ blocks

The spinor representation in $O_{\rm h}$ corresponds to Γ_6^+ and multiplying all single irreducible representations gives the following products:

$$\begin{aligned}
&\Gamma_6^\pm \otimes \Gamma_6^+ \to \Gamma_6^\pm,\\
&\Gamma_2^\pm \otimes \Gamma_6^+ \to \Gamma_7^\pm,\\
&\Gamma_3^\pm \otimes \Gamma_6^+ \to \Gamma_8^\pm,\\
&\Gamma_4^\pm \otimes \Gamma_6^+ \to \Gamma_7^\pm + \Gamma_8^\pm,\\
&\Gamma_5^\pm \otimes \Gamma_6^+ \to \Gamma_6^\pm + \Gamma_8^\pm.
\end{aligned} \tag{B.27}$$

One can introduce short notations:

$$\Upsilon = k_z^2 + \omega k_x^2 + \omega^2 k_y^2, \quad \omega = e^{i2\pi/3}, \quad \zeta = e^{i\pi/4}, \tag{B.28}$$

and

$$\Sigma(z,x,y) = \begin{bmatrix} z & x - iy \\ x + iy & -z \end{bmatrix} = z\sigma_z + x\sigma_x + y\sigma_y, \tag{B.29}$$

to write all possible blocks $\mathcal{B}(\Gamma_m, \Gamma_n)$ of the $\mathbf{k}\cdot\mathbf{p}$ Hamiltonian for double $O_{\rm h}$ group:

$$\mathcal{B}(\Gamma_6^\pm, \Gamma_6^\pm) = k^2\ C, \tag{B.30}$$

$$\mathcal{B}(\Gamma_6^\pm, \Gamma_6^\mp) = 0, \tag{B.31}$$

$$\mathcal{B}(\Gamma_7^\pm, \Gamma_7^\pm) = k^2\ C, \tag{B.32}$$

$$\mathcal{B}(\Gamma_7^\pm, \Gamma_7^\mp) = \Sigma(k_z, k_x, k_y)\ C, \tag{B.33}$$

$$\mathcal{B}(\Gamma_6^\pm, \Gamma_7^\pm) = \Sigma(k_x k_y, k_y k_z, k_z k_x)\ C \tag{B.34}$$

$$\mathcal{B}(\Gamma_6^\pm, \Gamma_7^\mp) = 0 \tag{B.35}$$

$$\begin{aligned}
\mathcal{B}(\Gamma_6^\pm, \Gamma_8^\mp) = {}& k_z \begin{bmatrix} 1 & 0 & 0 & -\zeta \\ 0 & -1 & i\zeta & 0 \end{bmatrix} C_z \\
&+ k_x \begin{bmatrix} 0 & \omega^2 & -i\omega\zeta & 0 \\ \omega^2 & 0 & 0 & -\omega\zeta \end{bmatrix} C_x \\
&+ k_y \begin{bmatrix} 0 & -i\omega & -\omega^2\zeta & 0 \\ i\omega & 0 & 0 & -i\omega^2\zeta \end{bmatrix} C_y
\end{aligned} \tag{B.36}$$

$$\begin{aligned}
\mathcal{B}(\Gamma_7^\pm, \Gamma_8^\pm) = {}& \begin{bmatrix} -i\zeta\Upsilon^* & 0 & 0 & \Upsilon \\ 0 & -i\zeta\Upsilon^* & i\Upsilon & 0 \end{bmatrix} C_\Upsilon \\
&+ k_x k_y \begin{bmatrix} 1 & 0 & 0 & -\zeta \\ 0 & -1 & i\zeta & 0 \end{bmatrix} C_{xy} \\
&+ k_y k_z \begin{bmatrix} 0 & \omega^2 & -i\omega\zeta & 0 \\ \omega^2 & 0 & 0 & -\omega\zeta \end{bmatrix} C_{yz} \\
&+ k_z k_x \begin{bmatrix} 0 & -i\omega & -\omega^2\zeta & 0 \\ i\omega & 0 & 0 & -i\omega^2\zeta \end{bmatrix} C_{zx}
\end{aligned} \tag{B.37}$$

$$\begin{aligned}\mathcal{B}(\Gamma_7^{\pm},\Gamma_8^{\mp}) = k_z &\begin{bmatrix}1 & 0 & 0 & \zeta\\ 0 & -1 & -i\zeta & 0\end{bmatrix} C_z\\ + k_x &\begin{bmatrix}0 & \omega^2 & i\omega\zeta & 0\\ \omega^2 & 0 & 0 & \omega\zeta\end{bmatrix} C_x\\ + k_y &\begin{bmatrix}0 & -i\omega & \omega^2\zeta & 0\\ i\omega & 0 & 0 & i\omega^2\zeta\end{bmatrix} C_y\end{aligned} \tag{B.38}$$

$$\begin{aligned}\mathcal{B}(\Gamma_6^{\pm},\Gamma_8^{\pm}) = &\begin{bmatrix}i\zeta\Upsilon^* & 0 & 0 & \Upsilon\\ 0 & i\zeta\Upsilon^* & i\Upsilon & 0\end{bmatrix} C_\Upsilon\\ k_xk_y &\begin{bmatrix}1 & 0 & 0 & \zeta\\ 0 & -1 & -i\zeta & 0\end{bmatrix} C_{xy}\\ + k_yk_z &\begin{bmatrix}0 & \omega^2 & i\omega\zeta & 0\\ \omega^2 & 0 & 0 & \omega\zeta\end{bmatrix} C_{yz}\\ + k_zk_x &\begin{bmatrix}0 & -i\omega & \omega^2\zeta & 0\\ i\omega & 0 & 0 & i\omega^2\zeta\end{bmatrix} C_{zx}\end{aligned} \tag{B.39}$$

$$\begin{aligned}\mathcal{B}(\Gamma_8^{\pm},\Gamma_8^{\mp}) = k_z &\begin{bmatrix}1 & 0 & 0 & 0\\ 0 & -1 & 0 & 0\\ 0 & 0 & -1 & 0\\ 0 & 0 & 0 & 1\end{bmatrix} C_z\\ + k_x &\begin{bmatrix}0 & 1 & 0 & 0\\ 1 & 0 & 0 & 0\\ 0 & 0 & 0 & -i\\ 0 & 0 & i & 0\end{bmatrix} C_x\\ + k_y &\begin{bmatrix}0 & -i & 0 & 0\\ i & 0 & 0 & 0\\ 0 & 0 & 0 & 1\\ 0 & 0 & 1 & 0\end{bmatrix} C_y\\ + k_z &\begin{bmatrix}0 & 0 & 0 & 1\\ 0 & 0 & -i & 0\\ 0 & 1 & 0 & 0\\ -i & 0 & 0 & 0\end{bmatrix} C'_z\\ + k_x &\begin{bmatrix}0 & 0 & i\omega^2 & 0\\ 0 & 0 & 0 & \omega^2\\ -\omega & 0 & 0 & 0\\ 0 & -i\omega & 0 & 0\end{bmatrix} C'_x\\ + k_y &\begin{bmatrix}0 & 0 & \omega & 0\\ 0 & 0 & 0 & i\omega\\ -i\omega^2 & 0 & 0 & 0\\ 0 & -\omega^2 & 0 & 0\end{bmatrix} C'_y\end{aligned} \tag{B.40}$$

$$
\begin{aligned}
\mathcal{B}(\Gamma_8^{\pm},\Gamma_8^{\pm}) = k^2\ C & \\
&+ \begin{bmatrix} 0 & 0 & 0 & -\Upsilon^* \\ 0 & 0 & -i\Upsilon^* & 0 \\ 0 & \Upsilon & 0 & 0 \\ i\Upsilon & 0 & 0 & 0 \end{bmatrix} C_{\Upsilon} \\
&+ k_x k_y \begin{bmatrix} 1 & 0 & 0 & 0 \\ 0 & -1 & 0 & 0 \\ 0 & 0 & 1 & 0 \\ 0 & 0 & 0 & -1 \end{bmatrix} C_{xy} \\
&+ k_y k_z \begin{bmatrix} 0 & 1 & 0 & 0 \\ 1 & 0 & 0 & 0 \\ 0 & 0 & 0 & i \\ 0 & 0 & -i & 0 \end{bmatrix} C_{yz} \\
&+ k_z k_x \begin{bmatrix} 0 & -i & 0 & 0 \\ i & 0 & 0 & 0 \\ 0 & 0 & 0 & -1 \\ 0 & 0 & -1 & 0 \end{bmatrix} C_{zx} \\
&+ k_x k_y \begin{bmatrix} 0 & 0 & 0 & 1 \\ 0 & 0 & -i & 0 \\ 0 & -1 & 0 & 0 \\ i & 0 & 0 & 0 \end{bmatrix} C'_{xy} \\
&+ k_y k_z \begin{bmatrix} 0 & 0 & i\omega^2 & 0 \\ 0 & 0 & 0 & \omega^2 \\ \omega & 0 & 0 & 0 \\ 0 & i\omega & 0 & 0 \end{bmatrix} C'_{yz} \\
&+ k_z k_x \begin{bmatrix} 0 & 0 & \omega & 0 \\ 0 & 0 & 0 & i\omega \\ i\omega^2 & 0 & 0 & 0 \\ 0 & \omega^2 & 0 & 0 \end{bmatrix} C'_{zx}
\end{aligned}
\tag{B.41}
$$

B.3 Comparison of DFT-obtained and symmetry-adapted 4×4 Hamiltonian

Two analytical forms of the 4×4 Hamiltonian, made from degenerate states corresponding to Γ_4 and Γ_1 irreps that lie below and above the gap respectively, in the case of CdSe, are presented here. Both Hamiltonians give the same physics, overall, and they are connected by an unitary transformation U, that is used to transform initial DFT basis $|\phi_i\rangle$ to the symmetry-adapted basis $|\psi_j\rangle$. To give more clarity and justify the whole procedure of transforming the initial DFT basis, we will compare inital DFT-form $H^{\text{init}}_{\text{DFT}}$, obtained from groups of degenerate states $|\phi_i\rangle$ and symmetry-adapted form $H^{\text{sym}}_{\text{adap}}$, that is made out of transformed groups of degenerate

states $|\psi_j\rangle$.

Initial DFT-form $H_{\mathrm{DFT}}^{\mathrm{init}}$ of the 4×4 Hamiltonian is given as:

$$
\begin{aligned}
H_{\mathrm{DFT}}^{\mathrm{init}} = \frac{k^2}{2m_0} &+ \begin{bmatrix} E_{\Gamma_1} & 0 & 0 & 0 \\ 0 & E_{\Gamma_4} & 0 & 0 \\ 0 & 0 & E_{\Gamma_4} & 0 \\ 0 & 0 & 0 & E_{\Gamma_4} \end{bmatrix} \\
&+ \frac{\hbar}{m_0} \begin{bmatrix} 0 & P_{01}^{(1)} & P_{02}^{(1)} & P_{03}^{(1)} \\ P_{01}^{(1)*} & 0 & 0 & 0 \\ P_{02}^{(1)*} & 0 & 0 & 0 \\ P_{03}^{(1)*} & 0 & 0 & 0 \end{bmatrix} \\
&+ \frac{\hbar^2}{m_0^2} \begin{bmatrix} P_{00}^{(2)} & P_{01}^{(2)} & P_{02}^{(2)} & P_{03}^{(2)} \\ P_{01}^{(2)*} & P_{11}^{(2)} & P_{12}^{(2)} & P_{13}^{(2)} \\ P_{02}^{(2)*} & P_{12}^{(2)*} & P_{22}^{(2)} & P_{23}^{(2)} \\ P_{03}^{(2)*} & P_{13}^{(2)*} & P_{23}^{(2)*} & P_{33}^{(2)} \end{bmatrix},
\end{aligned}
$$

where:

$$
\begin{aligned}
P_{0i}^{(1)} &= C_{0i}^{x(1)} k_x + C_{0i}^{y(1)} k_y + C_{0i}^{z(1)} k_z, \quad i = 1, 2, 3; \\
P_{0i}^{(2)} &= C_{0i}^{xy(2)} k_x k_y + C_{0i}^{yz(2)} k_y k_z + C_{0i}^{zx(2)} k_z k_x, \quad i = 1, 2, 3; \\
P_{ij}^{(2)} &= C_{ij}^{xx(2)} k_x^2 + C_{ij}^{yy(2)} k_y^2 + C_{ij}^{zz(2)} k_z^2 \\
&\quad + C_{ij}^{xy(2)} k_x k_y + C_{ij}^{yz(2)} k_y k_z + C_{ij}^{zx(2)} k_z k_x, \quad i, j = 1, 2, 3; \\
P_{00}^{(2)} &= C_{33}^{zz(2)} k^2.
\end{aligned}
$$

If we count the number of parameters $C_{0i}^{m(1)}$ for 1st order and $C_{ij}^{mn(2)}$ for 2nd order terms $(m, n = x, y, z)$ in the last four expressions, we can tell that $H_{\mathrm{DFT}}^{\mathrm{init}}$ has a total number of $3 \times 3 + 3 \times 3 + 6 \times 6 + 1 = 55$ parameters. Of course, this number can be reduced but the procedure could be rather cumbersome especially if a great number of materials with different symmetries is to be processed.

Symmetry-adapted form $H^{\text{sym}}_{\text{adap}}$ of the 4×4 Hamiltonian is given as:

$$
\begin{aligned}
H^{\text{sym}}_{\text{adap}} = \frac{k^2}{2m_0} + &\begin{bmatrix} E_{\Gamma_1} & 0 & 0 & 0 \\ 0 & E_{\Gamma_4} & 0 & 0 \\ 0 & 0 & E_{\Gamma_4} & 0 \\ 0 & 0 & 0 & E_{\Gamma_4} \end{bmatrix} + \frac{\hbar}{m_0} \begin{bmatrix} 0 & C_3 k_z & C_3 k_x & C_3 k_y \\ C_3^* k_z & C_{15} k_y & C_{15} k_x & \\ C_3^* k_x & C_{15} k_y & 0 & C_{15} k_z \\ C_3^* k_y & C_{15} k_x & C_{15} k_z & 0 \end{bmatrix} \\
&+ \frac{\hbar^2}{m_0} C_{18} \begin{bmatrix} 0 & 0 & 0 & 0 \\ 0 & k^2 & 0 & 0 \\ 0 & 0 & k^2 & 0 \\ 0 & 0 & 0 & k^2 \end{bmatrix} \\
&+ \frac{\hbar^2}{m_0} C_{17} \begin{bmatrix} 0 & 0 & 0 & 0 \\ 0 & 2k_z^2 - k_x^2 - k_y^2 & 0 & 0 \\ 0 & 0 & 2k_x^2 - k_y^2 - k_z^2 & 0 \\ 0 & 00 & & 2k_y^2 - k_z^2 - k_x^2 \end{bmatrix} \\
&+ \frac{\hbar^2}{m_0} \begin{bmatrix} C_4 k_x k_y & C_4 k_y k_z & C_4 k_z k_x & C_1 k^2 \\ C_4^* k_x k_y & 0 & C_{16} k_z k_x & C_{16} k_y k_z \\ C_4^* k_y k_z & C_{16} k_z k_x & 0 & C_{16} k_x k_y \\ C_4^* k_z k_x & C_{16} k_y k_z & C_{16} k_x k_y & 0 \end{bmatrix},
\end{aligned}
$$

where $C_{15} = 0$ if the block is formed from two same Γ_4 irreps as it is in the 4×4 case. This gives for $H^{\text{sym}}_{\text{adap}}$, a total number of $1 + 5 = 6$ parameters, for 1st and 2nd order $\mathbf{k} \cdot \mathbf{p}$ terms. This way, if we were to process a large number of crystals, we could group them according to their symmetry group, and compare the individual parameters.

Unlike symmetry-adapted form $H^{\text{sym}}_{\text{adap}}$, initial DFT-form $H^{\text{init}}_{\text{DFT}}$ clearly demonstrates much more parameters than symmetry of the crystal CdSe would suggest, even for the simplest 4×4 case. We note also, that this procedure can be used to generate standardized analytical forms of $\mathbf{k} \cdot \mathbf{p}$ Hamiltonians for crystals of any kind of symmetry, at any point $\mathbf{k}_0$ in Brillouin zone. Of course, benefits of this method will be greater if the symmetry point group $G_{\mathbf{k}_0}$ at $\mathbf{k}_0$ is of the higher order.

Having a symmetry-adapted Hamiltonian form also gives great advantage when it comes to calculation of nanostructures. Numerical codes for calculating nanostructures using $\mathbf{k} \cdot \mathbf{p}$ Hamiltonians of a certain point group could be easily adapted to another material of the same point group by just changing numerical values of the parameters, that can be easily obtained using ab inito calculation for bulk material and the procedure described in Sec. 3.2 and Ref. [46].

Appendix C

Point group tables

irrep.	basis function	E	$3C_2$	$6S_4$	$6\sigma_d$	$8C_3$
Γ_1 (A_1)	$x^2+y^2+z^2$	1	1	1	1	1
Γ_2 (A_2)	xyz	1	1	-1	-1	1
Γ_3 (E)	$(x^2-y^2, 3z^2-r^2)$	2	2	0	0	-1
Γ_4 (T_2)	(z,x,y)	3	-1	-1	1	0
Γ_5 (T_1)	(xy,yz,zx)	3	-1	1	-1	0

Table C.1: Character table for the T_d point group [50, 211].

irrep.	basis function	E	$3C_2$ $3\overline{C}_2$	$6S_4$	$6\sigma_d$ $6\overline{\sigma}_d$	$8C_3$	$\overline{E}$	$6\overline{S}_4$	$8\overline{C}_3$
Γ_1 (A_1)	$x^2+y^2+z^2$	1	1	1	1	1	1	1	1
Γ_2 (A_2)	xyz	1	1	-1	-1	1	1	-1	1
Γ_3 (E)	$(x^2-y^2, 3z^2-r^2)$	2	2	0	0	-1	2	0	-1
Γ_4 (T_2)	(z,x,y)	3	-1	-1	1	0	3	-1	0
Γ_5 (T_1)	(xy,yz,zx)	3	-1	1	-1	0	3	1	0
Γ_6 $(\overline{E}_1)$	$\phi_{1/2,-1/2}, \phi_{1/2,+1/2}$	2	0	$\sqrt{2}$	0	1	-2	$-\sqrt{2}$	-1
Γ_7 $(\overline{E}_2)$	$\Gamma_2 \times \Gamma_6$	2	0	$-\sqrt{2}$	0	1	-2	$\sqrt{2}$	-1
Γ_8 $(\overline{F})$	$\phi_{3/2,-3/2}, \phi_{3/2,-1/2}$ $\phi_{3/2,+1/2}, \phi_{3/2,+3/2}$	4	0	0	0	-1	-4	0	1

Table C.2: Character table for the double T_d point group [211]. Wave functions $\phi_{1/2,\pm1/2}$ and $\phi_{3/2,\pm1/2}, \phi_{3/2,\pm3/2}$ are the basis functions for the square of total angular momentum $\mathbf{J}^2$ and its z-component J_z: $\phi_{J,m_J}(m_J = -J, -J+1, \ldots, J-1, J)$, for $J = 1/2$ and $J = 3/2$, respectively.

Irrep.	Basis function	E	$3C_4^2$	$6C_2'$	$8C_3$	$6C_4$	i	$3iC_4^2$	$6iC_2'$	$8iC_3$	$6iC_4$
Γ_1^+ (Γ_1, A_{1g})	1	1	1	1	1	1	1	1	1	1	1
Γ_1^- (Γ_1', A_{1u})	$xyz[x^4(y^2-z^2)$ $+y^4(z^2-x^2)$ $+z^4(x^2-y^2)]$	1	1	1	1	1	-1	-1	-1	-1	-1
Γ_2^+ (Γ_2, A_{2g})	$x^4(y^2-z^2)$ $+y^4(z^2-x^2)$ $+z^4(x^2-y^2)$	1	1	-1	1	-1	1	1	-1	1	-1
Γ_2^- (Γ_2', A_{2u})	xyz	1	1	-1	1	-1	-1	-1	1	-1	1
Γ_3^+ $(\Gamma_{12}^+, \Gamma_{12}, E_g)$	x^2-y^2, $3z^2-r^2$	2	2	0	-1	0	2	2	0	-1	0
Γ_3^- $(\Gamma_{12}^-, \Gamma_{12}', E_u)$	$xyz(x^2-y^2)$, $xyz(3z^2-r^2)$	2	2	0	-1	0	-2	-2	0	1	0
Γ_4^+ $(\Gamma_{15}^+, \Gamma_{15}', T_{2g})$	$xy(x^2-y^2)$, $yz(y^2-z^2)$, $zx(z^2-x^2)$	3	-1	-1	0	1	3	-1	-1	0	1
Γ_4^- $(\Gamma_{15}^-, \Gamma_{15}, T_{1u})$	z, x, y	3	-1	-1	0	1	-3	1	1	0	-1
Γ_5^+ $(\Gamma_{25}^+, \Gamma_{25}', T_{2g})$	xy, yz, zx	3	-1	1	0	-1	3	-1	1	0	-1
Γ_5^- $(\Gamma_{25}^-, \Gamma_{25}, T_{2u})$	$z(x^2-y^2)$, $x(y^2-z^2)$, $y(z^2-x^2)$	3	-1	1	0	-1	-3	1	-1	0	1

Table C.3: Character table for the O_h point group [211, 50].

Irrep Basis f.	E	$3C_4^2$ $3\overline{C^2}_4$	$8C_3$	$6C_2'$ $6\overline{C}_2'$	$6C_4$	$\overline{E}$	$8\overline{C}_3$	$6\overline{C}_4$	i	$3iC_4^2$ $3i\overline{C^2}_4$	$8iC_3$	$6iC_2'$ $6i\overline{C}_2'$	$6iC_4$	$\bar{i}$	$8i\overline{C}_3$	$6i\overline{C}_4$
Γ_1^+ (A_{1g})	1	1	1	1	1	1	1	1	1	1	1	1	1	1	1	1
Γ_1^- (A_{1u})	1	1	1	1	1	1	1	1	-1	-1	-1	-1	-1	-1	-1	-1
Γ_2^+ (A_{2g})	1	1	1	-1	-1	1	1	-1	1	1	1	-1	-1	1	1	-1
Γ_2^- (A_{2u})	1	1	1	-1	-1	1	1	-1	-1	-1	-1	1	1	-1	-1	1
Γ_3^+ (E_g)	2	2	-1	0	0	2	-1	0	2	2	-1	0	0	2	-1	0
Γ_3^- (E_u)	2	2	-1	0	0	2	-1	0	-2	-2	1	0	0	-2	1	0
Γ_4^+ (T_{2g})	3	-1	0	-1	1	3	0	1	3	-1	0	-1	1	3	0	1
Γ_4^- (T_{1u})	3	-1	0	-1	1	3	0	1	-3	1	0	1	-1	-3	0	-1
Γ_5^+ (T_{2g})	3	-1	0	1	-1	3	0	1	3	-1	0	1	-1	3	0	1
Γ_5^- (T_{2u})	3	-1	0	1	-1	3	0	1	-3	1	0	-1	1	-3	0	-1
Γ_6^+ (E_{1g}) $\phi_{1/2,-1/2}$, $\phi_{1/2,+1/2}$	2	0	1	0	$\sqrt{2}$	-2	-1	$-\sqrt{2}$	2	0	1	0	$\sqrt{2}$	-2	-1	$-\sqrt{2}$
Γ_6^- (E_{1u}) $\Gamma_1^- \times \Gamma_6^+$	2	0	1	0	$\sqrt{2}$	-2	-1	$-\sqrt{2}$	-2	0	-1	0	$-\sqrt{2}$	2	1	$\sqrt{2}$
Γ_7^+ (E_{2g}) $\Gamma_2^+ \times \Gamma_6^+$	2	0	1	0	$-\sqrt{2}$	-2	-1	$\sqrt{2}$	2	0	1	0	$-\sqrt{2}$	-2	-1	$\sqrt{2}$
Γ_7^- (E_{2u}) $\Gamma_2^- \times \Gamma_6^+$	2	0	1	0	$-\sqrt{2}$	-2	-1	$\sqrt{2}$	-2	0	-1	0	$\sqrt{2}$	2	1	$-\sqrt{2}$
Γ_8^+ (F_g) $\phi_{3/2,-3/2}$, $\phi_{3/2,-1/2}$, $\phi_{3/2,+1/2}$, $\phi_{3/2,+3/2}$	4	0	-1	0	0	-4	1	0	4	0	-1	0	0	-4	1	0
Γ_8^- (F_u) $\Gamma_1^- \times \Gamma_8^+$	4	0	-1	0	0	-4	1	0	-4	0	1	0	0	4	-1	0

Table C.4: Character table for the double O_{h} point group [211, 50].

Appendix D

$CsPbX_3$ nanostructure gaps for different geometries

D.1 Quantum dot with spherical shape

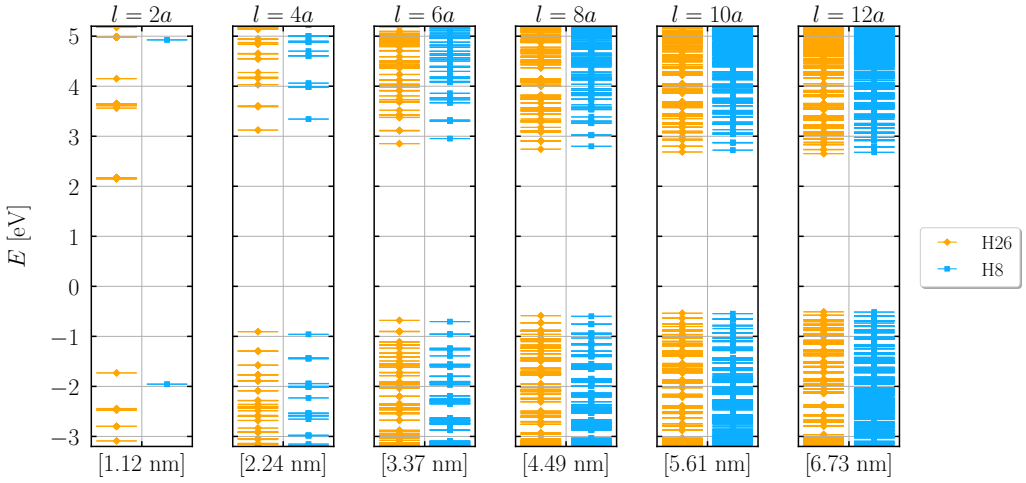

Figure D.1. Comparison of band energies between 8×8 and 26×26 Hamiltonian for $CsPbCl_3$ spherical quantum dots of different sizes at $T = 400$ K, where l is the length of one edge of the cube, and H8(H26) are results obtained from 8×8(26×26) Hamiltonian.

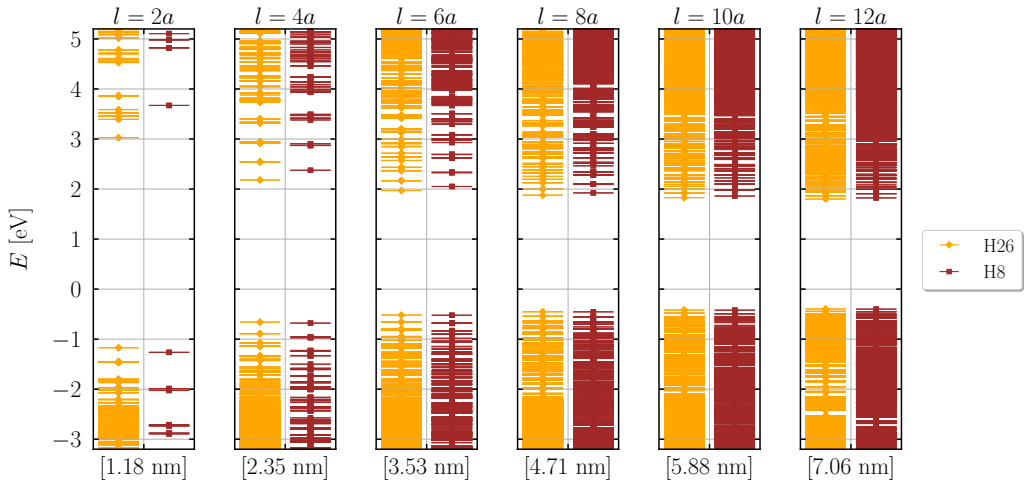

Figure D.2. Comparison of band energies between 8×8 and 26×26 Hamiltonian for $CsPbBr_3$ spherical quantum dots of different sizes at $T = 400$ K, where l is the length of one edge of the cube, and H8(H26) are results obtained from 8×8(26×26) Hamiltonian.

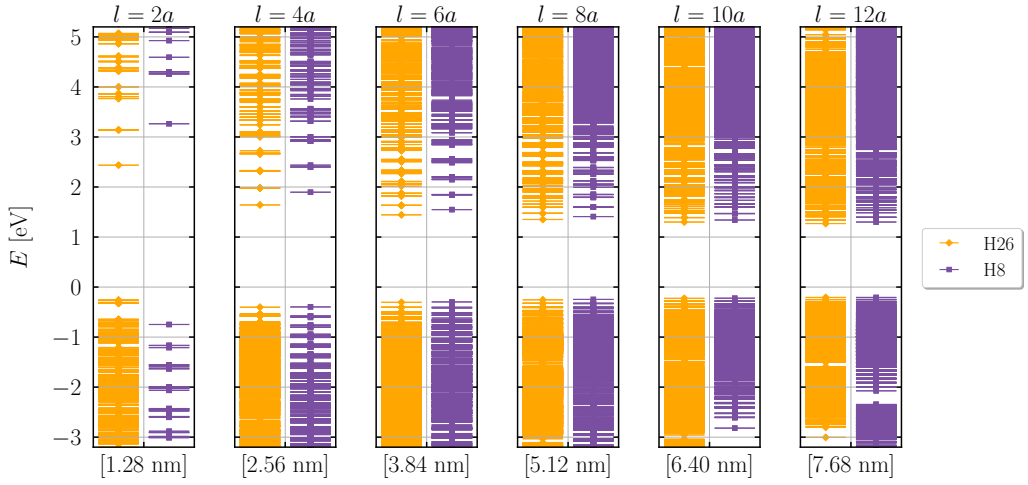

Figure D.3. Comparison of band energies between 8×8 and 26×26 Hamiltonian for $CsPbI_3$ spherical quantum dots of different sizes at $T = 300$ K, where l is the length of one edge of the cube, and H8(H26) are results obtained from 8×8(26×26) Hamiltonian.

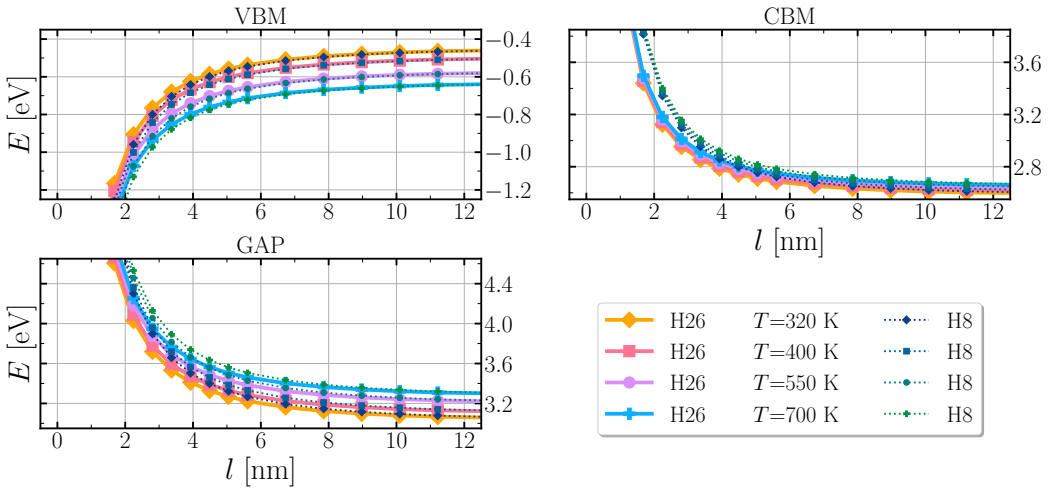

Figure D.4. Energies of band edges and gap for spherical $CsPbCl_3$ quantum dots of different sizes at several selected temperatures, where l is the diameter of the sphere, and VBM (CBM) are valence band maximum (conduction band minimum).

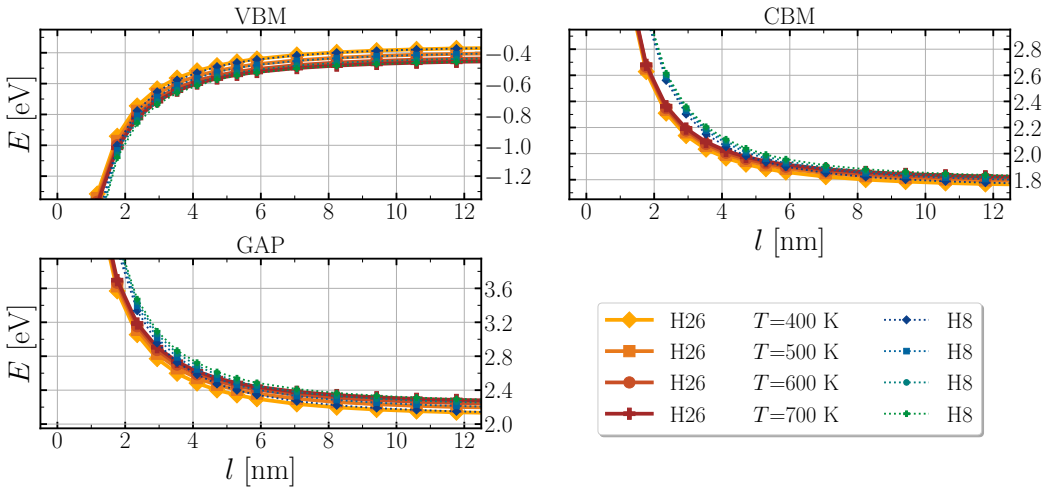

Figure D.5. Energies of band edges and gap for spherical $CsPbBr_3$ quantum dots of different sizes at several selected temperatures, where l is the diameter of the sphere, and VBM (CBM) are valence band maximum (conduction band minimum).

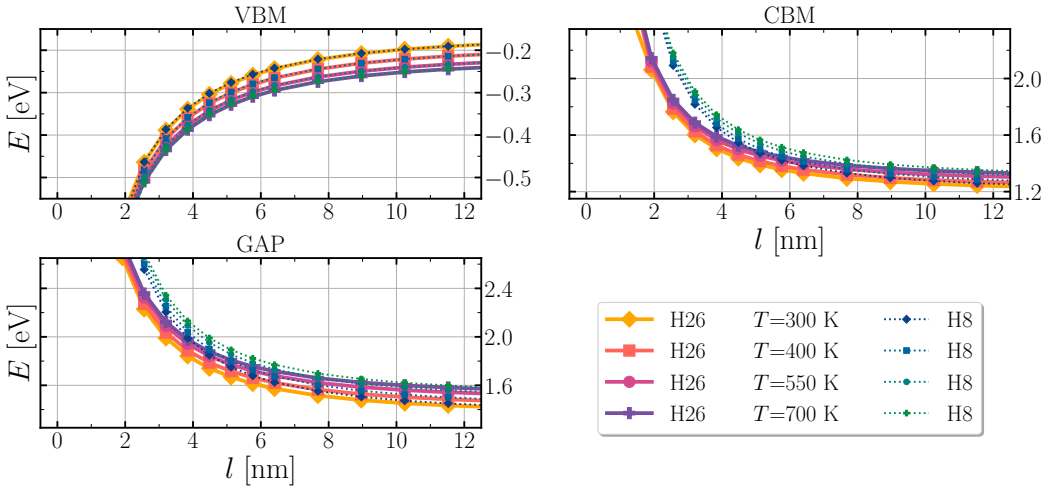

Figure D.6. Energies of band edges and gap for spherical $CsPbI_3$ quantum dots of different sizes at several selected temperatures, where l is the diameter of the sphere, and VBM (CBM) are valence band maximum (conduction band minimum).

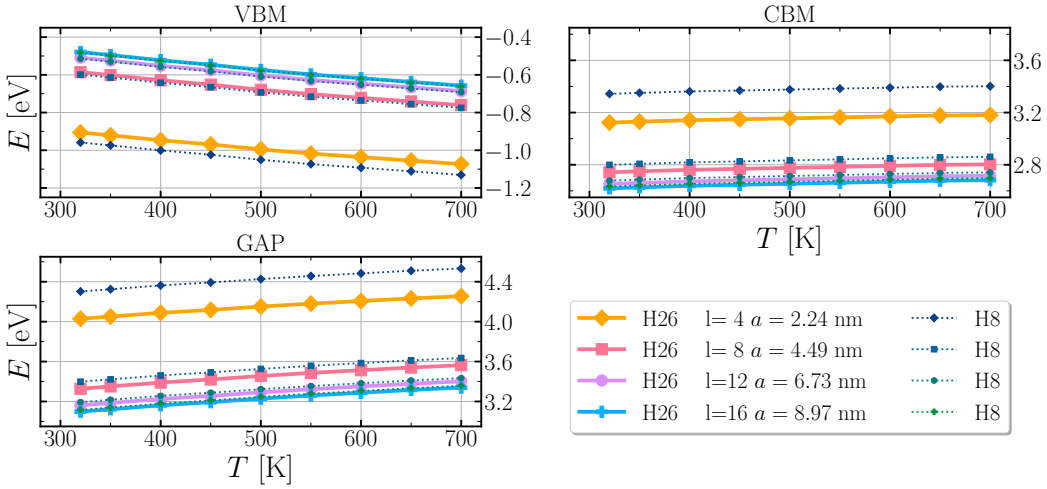

Figure D.7. Energies of band edges and gap for $CsPbCl_3$ spherical quantum dots at different temperatures for several selected sizes, where l is the length of one edge of the cube, and VBM (CBM) are valence band maximum (conduction band minimum).

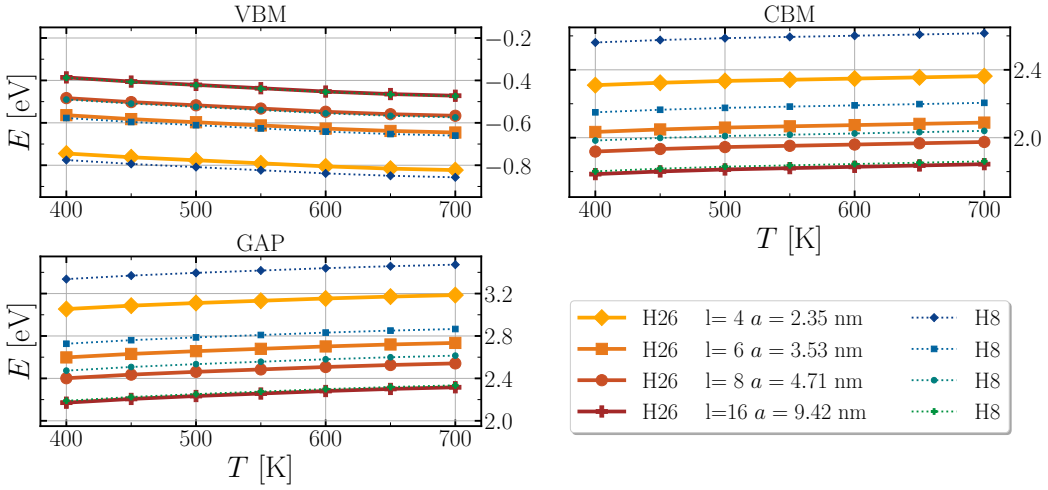

Figure D.8. Energies of band edges and gap for $CsPbBr_3$ spherical quantum dots at different temperatures for several selected sizes, where l is the length of one edge of the cube, and VBM (CBM) are valence band maximum (conduction band minimum).

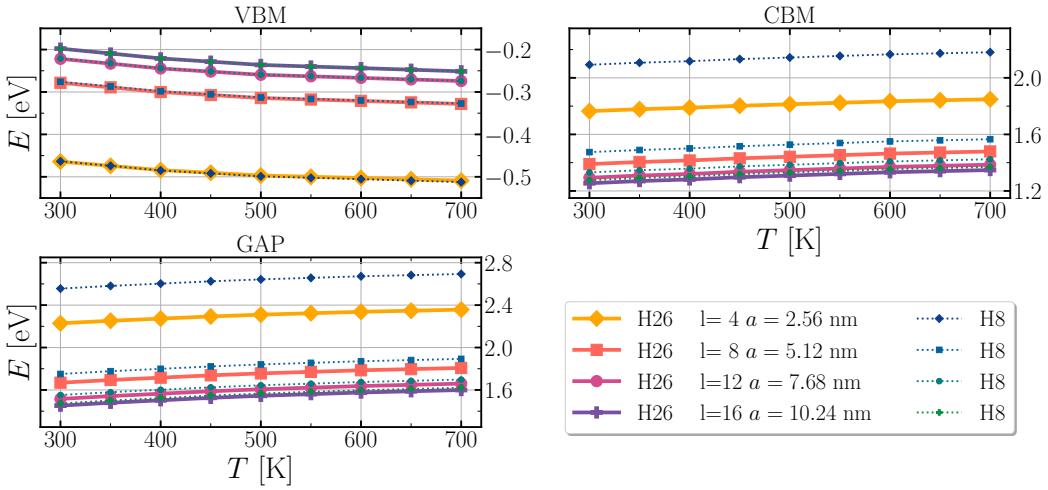

Figure D.9. Energies of band edges and gap for $CsPbI_3$ spherical quantum dots at different temperatures for several selected sizes, where l is the length of one edge of the cube, and VBM (CBM) are valence band maximum (conduction band minimum).

D.2 Quantum wire with circular base

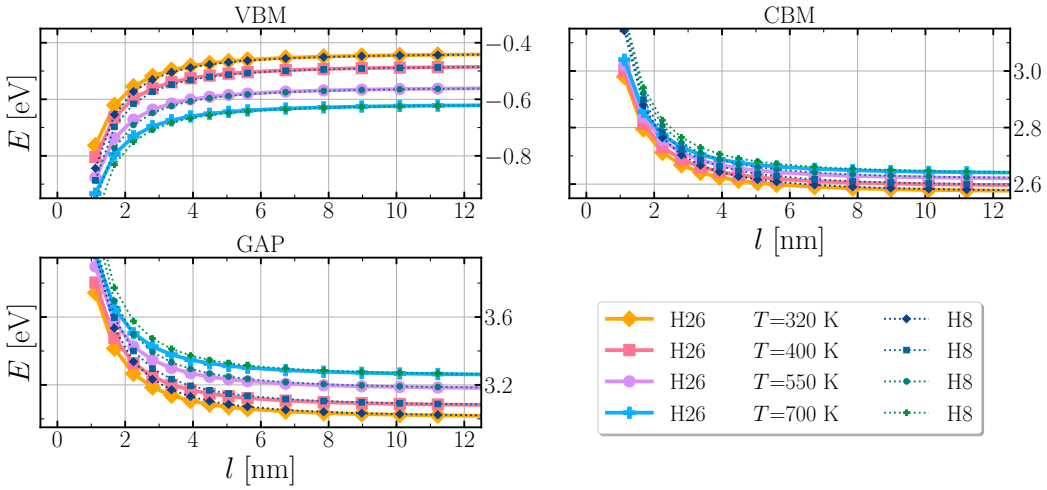

Figure D.10. Energies of band edges and gap for $CsPbCl_3$ quantum wires of different cross section sizes at several selected temperatures, where l is the diameter of the circular base of the wire, and VBM (CBM) are valence band maximum (conduction band minimum).

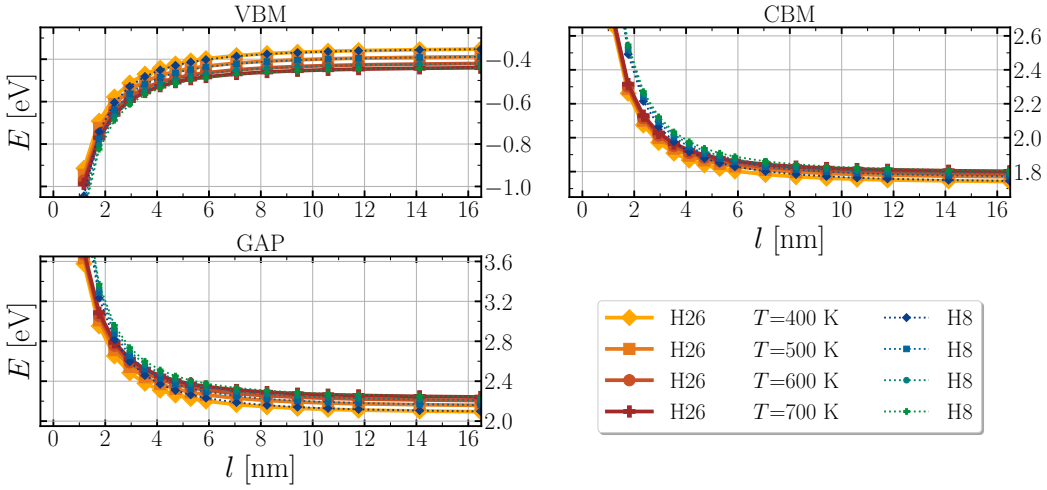

Figure D.11. Energies of band edges and gap for $CsPbBr_3$ circular quantum wire of different sizes at several selected temperatures, where l is the diameter of the circular base of the wire, and VBM (CBM) are valence band maximum (conduction band minimum).

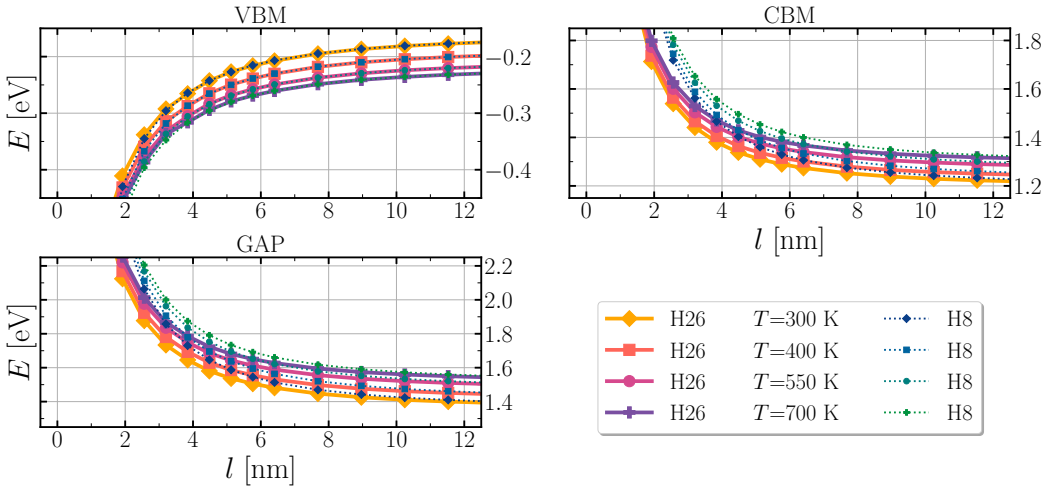

Figure D.12. Energies of band edges and gap for $CsPbI_3$ circular quantum wire of different sizes at several selected temperatures, where l is the diameter of the circular base of the wire, and VBM (CBM) are valence band maximum (conduction band minimum).

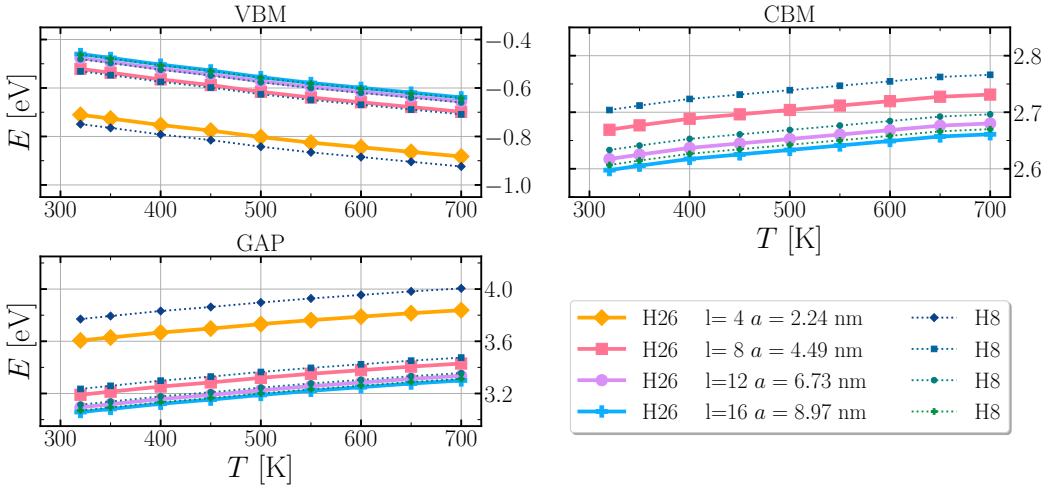

Figure D.13. Energies of band edges and gap for $CsPbCl_3$ circular quantum wire at different temperatures for several selected sizes, where l is the diameter of the circular base of the wire, and VBM (CBM) are valence band maximum (conduction band minimum).

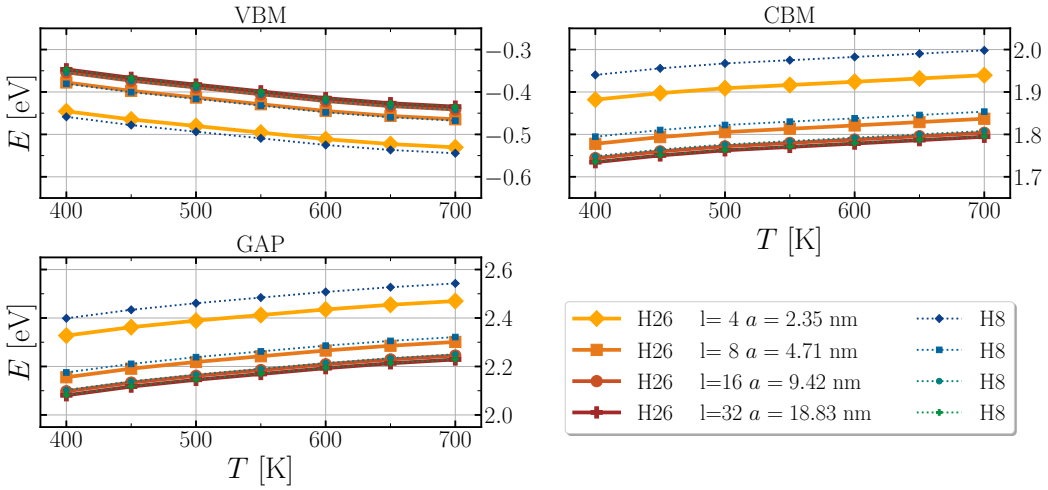

Figure D.14. Energies of band edges and gap for $CsPbBr_3$ circular quantum wire at different temperatures for several selected sizes, where l is the diameter of the circular base of the wire, and VBM (CBM) are valence band maximum (conduction band minimum).

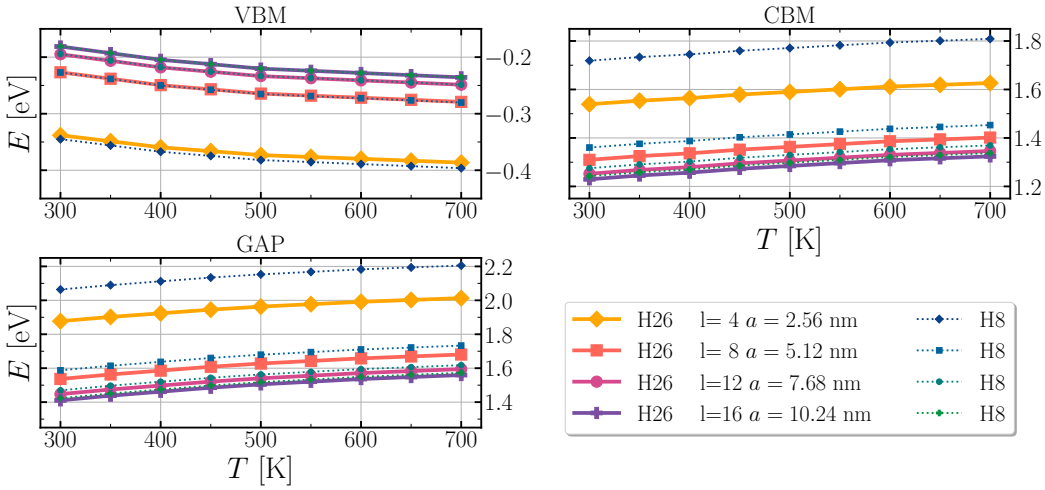

Figure D.15. Energies of band edges and gap for $CsPbI_3$ circular quantum wire at different temperatures for several selected sizes, where l is the diameter of the circular base of the wire, and VBM (CBM) are valence band maximum (conduction band minimum).

Bibliography

[1] T. Nie, Z. Fang, X. Ren, Y. Duan and S. Liu, *Nano-Micro Lett.*, 2023, **15**, 70.

[2] L. Zhang, L. Mei, K. Wang, Y. Lv, S. Zhang, Y. Lian, X. Liu, Z. Ma, G. Xiao, Q. Liu, S. Zhai, S. Zhang, G. Liu, L. Yuan, B. Guo, Z. Chen, K. Wei, A. Liu, S. Yue, G. Niu, X. Pan, J. Sun, Y. Hua, W.-Q. Wu, D. Di, B. Zhao, J. Tian, Z. Wang, Y. Yang, L. Chu, M. Yuan, H. Zeng, H.-L. Yip, K. Yan, W. Xu, L. Zhu, W. Zhang, G. Xing, F. Gao and L. Ding, *Nano-Micro Lett.*, 2023, **15**, 177.

[3] M. M. Lee, J. Teuscher, T. Miyasaka, T. N. Murakami and H. J. Snaith, *Science*, 2012, **338**, 643–647.

[4] M. Liu, M. B. Johnston and H. J. Snaith, *Nature*, 2013, **501**, 395–398.

[5] A. K. Jena, A. Kulkarni and T. Miyasaka, *Chem. Rev.*, 2019, **119**, 3036–3103.

[6] M. Aldamasy, Z. Iqbal, G. Li, J. Pascual, F. Alharthi, A. Abate and M. Li, *Phys. Chem. Chem. Phys.*, 2021, **23**, 23413–23427.

[7] X.-K. Liu, W. Xu, S. Bai, Y. Jin, J. Wang, R. H. Friend and F. Gao, *Nat. Mater.*, 2021, **20**, 10–21.

[8] K. Xing, S. Cao, X. Yuan, R. Zeng, H. Li, B. Zou and J. Zhao, *Phys. Chem. Chem. Phys.*, 2021, **23**, 17113–17128.

[9] M. Ahmadi, T. Wu and B. Hu, *Adv. Mater.*, 2017, **29**, 1605242.

[10] T. M. H. Nguyen, S. Kim and C. W. Bark, *J. Mater. Chem. A*, 2021, **9**, 1269–1276.

[11] L. Lei, Q. Dong, K. Gundogdu and F. So, *Adv. Funct. Mater.*, 2021, **31**, 2010144.

[12] H. Wei and J. Huang, *Nat. Commun.*, 2019, **10**, 1066.

[13] S. Svanström, A. García Fernández, T. Sloboda, T. J. Jacobsson, H. Rensmo and U. B. Cappel, *Phys. Chem. Chem. Phys.*, 2021, **23**, 12479–12489.

[14] H. Xie, S. Hao, J. Bao, T. J. Slade, G. J. Snyder, C. Wolverton and M. G. Kanatzidis, *J. Am. Chem. Soc.*, 2020, **142**, 9553–9563.

[15] X. Liu, J. Qiu, Q. Huang, X. Chen, J. Yu and J. Bao, *Phys. Chem. Chem. Phys.*, 2023, **25**, 11620–11629.

[16] A. Kojima, K. Teshima, Y. Shirai and T. Miyasaka, *J. Am. Chem. Soc.*, 2009, **131**, 6050–6051.

[17] National renewable energy laboratory. Best research-cell effiencies (2024). Available from `https://www.nrel.gov/pv/cell-efficiency.html`.

[18] Z.-K. Tan, R. S. Moghaddam, M. L. Lai, P. Docampo, R. Higler, F. Deschler, M. Price, A. Sadhanala, L. M. Pazos, D. Credgington, F. Hanusch, T. Bein, H. J. Snaith and R. H. Friend, *Nat. Nanotechnol.*, 2014, **9**, 687–692.

[19] Z. Xiao, Z. Song and Y. Yan, *Adv. Mater.*, 2019, **31**, 1803792.

[20] W. Xiang and W. Tress, *Adv. Mater.*, 2019, **31**, 1902851.

[21] N. C. Giebink, G. P. Wiederrecht, M. R. Wasielewski and S. R. Forrest, *Phys. Rev. B*, 2011, **83**, 195326.

[22] W. Shockley and H. J. Queisser, *J. Appl. Phys.*, 1961, **32**, 510–519.

[23] S. Rühle, *Sol. Energy*, 2016, **130**, 139–147.

[24] Q. Han, Y.-T. Hsieh, L. Meng, J.-L. Wu, P. Sun, E.-P. Yao, S.-Y. Chang, S.-H. Bae, T. Kato, V. Bermudez and Y. Yang, *Science*, 2018, **361**, 904–908.

[25] Z. Fang, Q. Zeng, C. Zuo, L. Zhang, H. Xiao, M. Cheng, F. Hao, Q. Bao, L. Zhang, Y. Yuan, W.-Q. Wu, D. Zhao, Y. Cheng, H. Tan, Z. Xiao, S. Yang, F. Liu, Z. Jin, J. Yan and L. Ding, *Sci. Bull.*, 2021, **66**, 621–636.

[26] H. Li and W. Zhang, *Chem. Rev.*, 2020, **120**, 9835–9950.

[27] F. Fu, J. Li, T. C. Yang, H. Liang, A. Faes, Q. Jeangros, C. Ballif and Y. Hou, *Adv. Mater.*, 2022, **34**, 2106540.

[28] J. Liu, Y. He, L. Ding, H. Zhang, Q. Li, L. Jia, J. Yu, T. W. Lau, M. Li, Y. Qin, X. Gu, F. Zhang, Q. Li, Y. Yang, S. Zhao, X. Wu, J. Liu, T. Liu, Y. Gao, Y. Wang, X. Dong, H. Chen, P. Li, T. Zhou, M. Yang, X. Ru, F. Peng, S. Yin, M. Qu, D. Zhao, Z. Zhao, M. Li, P. Guo, H. Yan, C. Xiao, P. Xiao, J. Yin, X. Zhang, Z. Li, B. He and X. Xu, *Nature*, 2024, **635**, 596–603.

[29] Q. A. Akkerman, G. Rainò, M. V. Kovalenko and L. Manna, *Nat. Mater.*, 2018, **17**, 394–405.

[30] I. Chung, J.-H. Song, J. Im, J. Androulakis, C. D. Malliakas, H. Li, A. J. Freeman, J. T. Kenney and M. G. Kanatzidis, *J. Am. Chem. Soc.*, 2012, **134**, 8579–8587.

[31] L. N. Quan, M. Yuan, R. Comin, O. Voznyy, E. M. Beauregard, S. Hoogland, A. Buin, A. R. Kirmani, K. Zhao, A. Amassian, D. H. Kim and E. H. Sargent, *J. Am. Chem. Soc.*, 2016, **138**, 2649–2655.

[32] M. Roknuzzaman, K. Ostrikov, H. Wang, A. Du and T. Tesfamichael, *Sci. Rep.*, 2017, **7**, 14025.

[33] A. Marronnier, G. Roma, S. Boyer-Richard, L. Pedesseau, J.-M. Jancu, Y. Bonnassieux, C. Katan, C. C. Stoumpos, M. G. Kanatzidis and J. Even, *ACS Nano*, 2018, **12**, 3477–3486.

[34] A. E. Maughan, A. M. Ganose, M. A. Almaker, D. O. Scanlon and J. R. Neilson, *Chem. Mater.*, 2018, **30**, 3909–3919.

[35] L. D. Whalley, J. M. Skelton, J. M. Frost and A. Walsh, *Phys. Rev. B*, 2016, **94**, 220301.

[36] A. M. A. Leguy, J. M. Frost, A. P. McMahon, V. G. Sakai, W. Kockelmann, C. Law, X. Li, F. Foglia, A. Walsh, B. C. O'Regan, J. Nelson, J. T. Cabral and P. R. F. Barnes, *Nat. Commun.*, 2015, **6**, 7124.

[37] J. M. Frost and A. Walsh, *Acc. Chem. Res.*, 2016, **49**, 528–535.

[38] W. A. Saidi, S. Poncé and B. Monserrat, *J Phys. Chem. Lett.*, 2016, **7**, 5247–5252.

[39] J. M. Frost, K. T. Butler and A. Walsh, *APL Mater.*, 2014, **2**, 081506.

[40] C. Quarti, E. Mosconi, J. M. Ball, V. D'Innocenzo, C. Tao, S. Pathak, H. J. Snaith, A. Petrozza and F. De Angelis, *Energy Environ. Sci.*, 2016, **9**, 155–163.

[41] L. D. Whalley, J. M. Frost, Y.-K. Jung and A. Walsh, *J. Chem. Phys.*, 2017, **146**, 220901.

[42] T. Chen, B. J. Foley, B. Ipek, M. Tyagi, J. R. D. Copley, C. M. Brown, J. J. Choi and S.-H. Lee, *Phys. Chem. Chem. Phys.*, 2015, **17**, 31278–31286.

[43] A. A. Bakulin, O. Selig, H. J. Bakker, Y. L. Rezus, C. Müller, T. Glaser, R. Lovrincic, Z. Sun, Z. Chen, A. Walsh, J. M. Frost and T. L. C. Jansen, *J. Phys. Chem. Lett.*, 2015, **6**, 3663–3669.

[44] F. Giustino, *Rev. Mod. Phys.*, 2017, **89**, 015003.

[45] M. Jocić and N. Vukmirović, *Phys. Chem. Chem. Phys.*, 2023, **25**, 29017–29031.

[46] M. Jocić and N. Vukmirović, *Phys. Rev. B*, 2020, **102**, 085121.

[47] M. Jocić and N. Vukmirović, *Facta Univ.- Ser. Phys. Chem. Tech.*, 2024, **22**, 001–011.

[48] G. Bir and G. Pikus, *Symmetry and Strain-induced Effects in Semiconductors*, Wiley, New York, 1974.

[49] N. Ashcroft and N. Mermin, *Solid State Physics*, Saunders College Publishing, Fort Worth, 1976.

[50] M. S. Dresselhaus, G. Dresselhaus and A. Jorio, *Group Theory: Application to the Physics of Condensed Matter*, Springer-Verlag Berlin Heidelberg, 2008.

[51] L. C. Lew Yan Voon and M. Willatzen, *The k·p Method: Electronic Properties of Semiconductors*, Springer-Verlag Berlin Heidelberg, 2009.

[52] G. Dresselhaus, A. F. Kip and C. Kittel, *Phys. Rev.*, 1955, **98**, 368–384.

[53] J. M. Luttinger and W. Kohn, *Phys. Rev.*, 1955, **97**, 869–883.

[54] J. M. Luttinger, *Phys. Rev.*, 1956, **102**, 1030–1041.

[55] E. Kane, *J. Phys. Chem. Solids*, 1956, **1**, 82 – 99.

[56] E. Kane, *J. Phys. Chem. Solids*, 1957, **1**, 249–261.

[57] E. Kane, *Semiconductors and Semimetals*, Elsevier, 1966, vol. 1, pp. 75–100.

[58] P. Löwdin, *J. Chem. Phys.*, 1951, **19**, 1396–1401.

[59] R. M. Martin, *Electronic Structure: Basic Theory and Practical Methods*, Cambridge University Press, 2004.

[60] R. M. Martin, L. Reining and D. M. Ceperley, *Interacting Electrons: Theory and Computational Approaches*, Cambridge University Press, 2016.

[61] F. Giustino, *Materials Modelling Using Density Functional Theory: Properties and Predictions*, Oxford University Press, 2014.

[62] P. Hohenberg and W. Kohn, *Phys. Rev.*, 1964, **136**, B864–B871.

[63] M. Levy, *Proceedings of the National Academy of Sciences*, 1979, **76**, 6062–6065.

[64] E. H. Lieb, *Int. J. Quantum Chem.*, 1983, **24**, 243–277.

[65] R. M. Dreizler and E. K. U. Gross, *Density Functional Theory*, Springer Berlin Heidelberg, 1990.

[66] D. R. Hamann, M. Schlüter and C. Chiang, *Phys. Rev. Lett.*, 1979, **43**, 1494–1497.

[67] N. Troullier and J. L. Martins, *Phys. Rev. B*, 1991, **43**, 1993–2006.

[68] D. Vanderbilt, *Phys. Rev. B*, 1990, **41**, 7892–7895.

[69] P. E. Blöchl, *Phys. Rev. B*, 1994, **50**, 17953–17979.

[70] O. Gunnarsson, M. Jonson and B. I. Lundqvist, *Phys. Rev. B*, 1979, **20**, 3136–3164.

[71] V. Sahni, K. P. Bohnen and M. K. Harbola, *Physical Review A*, 1988, **37**, 1895–1907.

[72] R. Parr and Y. Weitao, *Density-Functional Theory of Atoms and Molecules*, Oxford University Press, 1994.

[73] J. P. Perdew, K. Burke and M. Ernzerhof, *Phys. Rev. Lett.*, 1996, **77**, 3865–3868.

[74] A. D. Becke, *Physical Review A*, 1988, **38**, 3098–3100.

[75] C. Lee, W. Yang and R. G. Parr, *Phys. Rev. B*, 1988, **37**, 785–789.

[76] J. P. Perdew, A. Ruzsinszky, G. I. Csonka, O. A. Vydrov, G. E. Scuseria, L. A. Constantin, X. Zhou and K. Burke, *Phys. Rev. Lett.*, 2008, **100**, 136406.

[77] J. Tao, J. P. Perdew, V. N. Staroverov and G. E. Scuseria, *Phys. Rev. Lett.*, 2003, **91**, 146401.

[78] J. P. Perdew, M. Ernzerhof and K. Burke, *J. Chem. Phys.*, 1996, **105**, 9982–9985.

[79] T. Bischoff, J. Wiktor, W. Chen and A. Pasquarello, *Phys. Rev. Mater.*, 2019, **3**, 123802.

[80] L. Hedin, *Phys. Rev.*, 1965, **139**, A796–A823.

[81] M. Shishkin and G. Kresse, *Phys. Rev. B*, 2007, **75**, 235102.

[82] C. Rostgaard, K. W. Jacobsen and K. S. Thygesen, *Phys. Rev. B*, 2010, **81**, 085103.

[83] E. E. Salpeter and H. A. Bethe, *Phys. Rev.*, 1951, **84**, 1232–1242.

[84] J. P. Perdew, *Int. J. Quantum Chem.*, 1985, **28**, 497–523.

[85] A. Marini, R. Del Sole and G. Onida, *Phys. Rev. B*, 2002, **66**, 115101.

[86] G. Onida, L. Reining and A. Rubio, *Rev. Mod. Phys.*, 2002, **74**, 601–659.

[87] A. Marini, C. Hogan, M. Grüning and D. Varsano, *Comp. Phys. Comm.*, 2009, **180**, 1392 – 1403.

[88] D. Sangalli, A. Ferretti, H. Miranda, C. Attaccalite, I. Marri, E. Cannuccia, P. Melo, M. Marsili, F. Paleari, A. Marrazzo, G. Prandini, P. Bonfà, M. O. Atambo, F. Affinito, M. Palummo, A. Molina-Sánchez, C. Hogan, M. Grüning, D. Varsano and A. Marini, *J. Phys.: Condens. Matter*, 2019, **31**, 325902.

[89] M. T. Yin and M. L. Cohen, *Phys. Rev. Lett.*, 1980, **45**, 1004–1007.

[90] J. Ihm, M. Yin and M. L. Cohen, *Solid State Commun.*, 1981, **37**, 491–494.

[91] M. T. Yin and M. L. Cohen, *Phys. Rev. B*, 1982, **26**, 3259–3272.

[92] S. Baroni, S. de Gironcoli, A. Dal Corso and P. Giannozzi, *Rev. Mod. Phys.*, 2001, **73**, 515–562.

[93] S. Baroni, P. Giannozzi and A. Testa, *Phys. Rev. Lett.*, 1987, **58**, 1861–1864.

[94] S. Baroni, P. Giannozzi and A. Testa, *Phys. Rev. Lett.*, 1987, **59**, 2662–2665.

[95] P. Giannozzi, S. de Gironcoli, P. Pavone and S. Baroni, *Phys. Rev. B*, 1991, **43**, 7231–7242.

[96] P. Giannozzi, S. Baroni, N. Bonini, M. Calandra, R. Car, C. Cavazzoni, D. Ceresoli, G. L. Chiarotti, M. Cococcioni, I. Dabo, A. D. Corso, S. de Gironcoli, S. Fabris, G. Fratesi, R. Gebauer, U. Gerstmann, C. Gougoussis, A. Kokalj, M. Lazzeri, L. Martin-Samos, N. Marzari, F. Mauri, R. Mazzarello, S. Paolini, A. Pasquarello, L. Paulatto, C. Sbraccia, S. Scandolo, G. Sclauzero, A. P. Seitsonen, A. Smogunov, P. Umari and R. M. Wentzcovitch, *J. Phys.-Condens. Matter*, 2009, **21**, 395502.

[97] P. Giannozzi, O. Andreussi, T. Brumme, O. Bunau, M. B. Nardelli, M. Calandra, R. Car, C. Cavazzoni, D. Ceresoli, M. Cococcioni, N. Colonna, I. Carnimeo, A. D. Corso, S. de Gironcoli, P. Delugas, R. A. DiStasio, A. Ferretti, A. Floris, G. Fratesi, G. Fugallo, R. Gebauer, U. Gerstmann, F. Giustino, T. Gorni, J. Jia, M. Kawamura, H.-Y. Ko, A. Kokalj, E. Küçükbenli, M. Lazzeri, M. Marsili, N. Marzari, F. Mauri, N. L. Nguyen, H.-V. Nguyen, A. O. de-la Roza, L. Paulatto, S. Poncé, D. Rocca, R. Sabatini, B. Santra, M. Schlipf, A. P. Seitsonen, A. Smogunov, I. Timrov, T. Thonhauser, P. Umari, N. Vast, X. Wu and S. Baroni, *J. Phys.-Condens. Matter*, 2017, **29**, 465901.

[98] X. Gonze, D. C. Allan and M. P. Teter, *Phys. Rev. Lett.*, 1992, **68**, 3603–3606.

[99] X. Gonze, *Phys. Rev. A*, 1995, **52**, 1096–1114.

[100] X. Gonze, P. Ghosez and R. W. Godby, *Phys. Rev. Lett.*, 1995, **74**, 4035–4038.

[101] X. Gonze, *Phys. Rev. B*, 1997, **55**, 10337–10354.

[102] X. Gonze and C. Lee, *Phys. Rev. B*, 1997, **55**, 10355–10368.

[103] X. Gonze, B. Amadon, P.-M. Anglade, J.-M. Beuken, F. Bottin, P. Boulanger, F. Bruneval, D. Caliste, R. Caracas, M. Côté, T. Deutsch, L. Genovese, P. Ghosez, M. Giantomassi, S. Goedecker, D. Hamann, P. Hermet, F. Jollet, G. Jomard, S. Leroux, M. Mancini, S. Mazevet, M. Oliveira, G. Onida,

Y. Pouillon, T. Rangel, G.-M. Rignanese, D. Sangalli, R. Shaltaf, M. Torrent, M. Verstraete, G. Zerah and J. Zwanziger, *Comput. Phys. Commun.*, 2009, **180**, 2582–2615.

[104] X. Gonze, B. Amadon, G. Antonius, F. Arnardi, L. Baguet, J.-M. Beuken, J. Bieder, F. Bottin, J. Bouchet, E. Bousquet, N. Brouwer, F. Bruneval, G. Brunin, T. Cavignac, J.-B. Charraud, W. Chen, M. Côté, S. Cottenier, J. Denier, G. Geneste, P. Ghosez, M. Giantomassi, Y. Gillet, O. Gingras, D. R. Hamann, G. Hautier, X. He, N. Helbig, N. Holzwarth, Y. Jia, F. Jollet, W. Lafargue-Dit-Hauret, K. Lejaeghere, M. A. L. Marques, A. Martin, C. Martins, H. P. C. Miranda, F. Naccarato, K. Persson, G. Petretto, V. Planes, Y. Pouillon, S. Prokhorenko, F. Ricci, G.-M. Rignanese, A. H. Romero, M. M. Schmitt, M. Torrent, M. J. van Setten, B. V. Troeye, M. J. Verstraete, G. Zérah and J. W. Zwanziger, *Comput. Phys. Commun.*, 2020, **248**, 107042.

[105] R. P. Feynman, *Phys. Rev.*, 1939, **56**, 340–343.

[106] P. DeCicco and F. Johnson, *Proceedings of the Royal Society of London. A. Mathematical and Physical Sciences*, 1969, **310**, 111–119.

[107] R. M. Pick, M. H. Cohen and R. M. Martin, *Phys. Rev. B*, 1970, **1**, 910–920.

[108] R. M. Sternheimer, *Phys. Rev.*, 1954, **96**, 951–968.

[109] G. D. Mahan, *Phys. Rev. A*, 1980, **22**, 1780–1785.

[110] S. de Gironcoli, *Phys. Rev. B*, 1995, **51**, 6773–6776.

[111] T. Tadano and S. Tsuneyuki, *Phys. Rev. B*, 2015, **92**, 054301.

[112] A. Marini, S. Poncé and X. Gonze, *Phys. Rev. B*, 2015, **91**, 224310.

[113] P. B. Allen and V. Heine, *J. Phys. C: Solid State Phys.*, 1976, **9**, 2305–2312.

[114] P. B. Allen and M. Cardona, *Phys. Rev. B*, 1981, **23**, 1495–1505.

[115] P. B. Allen and M. Cardona, *Phys. Rev. B*, 1983, **27**, 4760–4769.

[116] A. Marini, *Phys. Rev. Lett.*, 2008, **101**, 106405.

[117] F. Giustino, S. G. Louie and M. L. Cohen, *Phys. Rev. Lett.*, 2010, **105**, 265501.

[118] G. D. Mahan, *Many-particle physics. Third edition.*, Springer US, 2000.

[119] X. Gonze, P. Boulanger and M. Côté, *Ann. Phys.*, 2010, **523**, 168–178.

[120] S. Poncé, Y. Gillet, J. Laflamme Janssen, A. Marini, M. Verstraete and X. Gonze, *J. Chem. Phys.*, 2015, **143**, 102813.

[121] N. Vukmirović, *Phys. Rev. B*, 2021, **104**, 085203.

[122] N. Vukmirović, *Comput. Phys. Commun.*, 2025, **312**, 109583.

[123] S. Zollner, M. Cardona and S. Gopalan, *Phys. Rev. B*, 1992, **45**, 3376–3385.

[124] C. Bradley and A. Cracknell, *The Mathematical Theory of Symmetry in Solids: Representation Theory for Point Groups and Space Groups*, Oxford University Press, 2010.

[125] C. R. Pidgeon and R. N. Brown, *Phys. Rev.*, 1966, **146**, 575–583.

[126] M. H. Weiler, R. L. Aggarwal and B. Lax, *Phys. Rev. B*, 1978, **17**, 3269–3283.

[127] T. B. Bahder, *Phys. Rev. B*, 1990, **41**, 11992–12001.

[128] I. Vurgaftman, J. R. Meyer and L. R. Ram-Mohan, *J. Appl. Phys.*, 2001, **89**, 5815–5875.

[129] I. Vurgaftman and J. R. Meyer, *J. Appl. Phys.*, 2003, **94**, 3675–3696.

[130] M. El Kurdi, G. Fishman, S. Sauvage and P. Boucaud, *J. Appl. Phys.*, 2010, **107**, 013710.

[131] S. Richard, F. Aniel and G. Fishman, *Phys. Rev. B*, 2004, **70**, 235204.

[132] S. Boyer-Richard, F. Raouafi, A. Bondi, L. Pédesseau, C. Katan, J.-M. Jancu and J. Even, *Appl. Phys. Lett.*, 2011, **98**, 251913.

[133] Z. Song, W. Fan, C. S. Tan, Q. Wang, D. Nam, D. H. Zhang and G. Sun, *New J. Phys.*, 2019, **21**, 073037.

[134] N. A. Čukarić, M. Ž. Tadić, B. Partoens and F. M. Peeters, *Phys. Rev. B*, 2013, **88**, 205306.

[135] C. Persson and C. Ambrosch-Draxl, *Comp. Phys. Comm.*, 2007, **177**, 280 – 287.

[136] K. Berland and C. Persson, *Comput. Mater. Sci.*, 2017, **134**, 17 – 24.

[137] T. Shishidou and T. Oguchi, *Phys. Rev. B*, 2008, **78**, 245107.

[138] C. J. Pickard and M. C. Payne, *Phys. Rev. B*, 1999, **59**, 4685–4693.

[139] M. Mozrzymas, M. Studziński and M. Horodecki, *J. Phys. A-Math. Theor.*, 2014, **47**, 505203.

[140] Numerical values of parameters for symmetry-adapted Hamiltonian in the case of cubic halide perovskites are available at: `https://www.scl.rs/mjocic/CsPbX3_kp_parameters/Ham_blocks_CsPbX3.zip`.

[141] D. R. Hamann, *Phys. Rev. B*, 2013, **88**, 085117.

[142] M. van Setten, M. Giantomassi, E. Bousquet, M. Verstraete, D. Hamann, X. Gonze and G.-M. Rignanese, *Comp. Phys. Comm.*, 2018, **226**, 39 – 54.

[143] S. Ninomiya and S. Adachi, *J. Appl. Phys.*, 1995, **78**, 4681–4689.

[144] W.-J. Yin, J.-H. Yang, J. Kand, Y. Yan and S.-H. Wei, *J. Mater. Chem. A*, 2015, **3**, 8926–8942.

[145] J. Even, L. Pedesseau, C. Katan, M. Kepenekian, J.-S. Lauret, D. Sapori and E. Deleporte, *J. Phys. Chem. C*, 2015, **119**, 10161–10177.

[146] F. Brivio, K. T. Butler, A. Walsh and M. van Schilfgaarde, *Phys. Rev. B*, 2014, **89**, 155204.

[147] A. Amat, E. Mosconi, E. Ronca, C. Quarti, P. Umari, M. K. Nazeeruddin, M. Grätzel and F. De Angelis, *Nano Lett.*, 2014, **14**, 3608–3616.

[148] P. Umari, E. Mosconi and F. De Angelis, *Sci. Rep.*, 2014, **4**, 4467.

[149] M. H. Du, *J. Mater. Chem. A*, 2014, **2**, 9091–9098.

[150] J. Feng and B. Xiao, *J. Phys. Chem. Lett.*, 2014, **5**, 1278–1282.

[151] J. Wiktor, U. Rothlisberger and A. Pasquarello, *J. Phys. Chem. Lett.*, 2017, **8**, 5507–5512.

[152] H. Wang, A. Tal, T. Bischoff, P. Gono and A. Pasquarello, *npj Comput. Mater.*, 2022, **8**, 237.

[153] J. Ning, L. Zheng, W. Lei, S. Wang, J. Xi and J. Yang, *Phys. Chem. Chem. Phys.*, 2022, **24**, 16003–16010.

[154] A. Francisco-López, B. Charles, O. J. Weber, M. I. Alonso, M. Garriga, M. Campoy-Quiles, M. T. Weller and A. R. Goñi, *J. Phys. Chem. Lett.*, 2019, **10**, 2971–2977.

[155] G. Mannino, I. Deretzis, E. Smecca, A. La Magna, A. Alberti, D. Ceratti and D. Cahen, *J. Phys. Chem. Lett.*, 2020, **11**, 2490–2496.

[156] M. Mladenović and N. Vukmirović, *Phys. Chem. Chem. Phys.*, 2018, **20**, 25693–25700.

[157] J. Park, W. A. Saidi, B. Chorpening and Y. Duan, *J. Phys. Chem. C*, 2021, **125**, 22231–22238.

[158] A. Miglio, V. Brousseau-Couture, E. Godbout, G. Antonius, Y.-H. Chan, S. G. Louie, M. Côté, M. Giantomassi and X. Gonze, *npj Comput. Mater.*, 2020, **6**, 167.

[159] R. D. King-Smith, R. J. Needs, V. Heine and M. J. Hodgson, *EPL*, 1989, **10**, 569–574.

[160] S. Hirotsu, J. Harada, M. Iizumi and K. Gesi, *J. Phys. Soc. Jpn.*, 1974, **37**, 1393–1398.

[161] S. Plesko, R. Kind and J. Roos, *J. Phys. Soc. Jpn.*, 1978, **45**, 553–557.

[162] R. X. Yang, J. M. Skelton, E. L. da Silva, J. M. Frost and A. Walsh, *J. Phys. Chem. Lett.*, 2017, **8**, 4720–4726.

[163] D. Trots and S. Myagkota, *J. Phys. Chem. Solids*, 2008, **69**, 2520–2526.

[164] C. K. Møller, *Nature*, 1958, **182**, 1436–1436.

[165] X. Zhou and Z. Zhang, *AIP Adv.*, 2020, **10**, 125015.

[166] T. Tadano and W. A. Saidi, *Phys. Rev. Lett.*, 2022, **129**, 185901.

[167] C. E. Patrick, K. W. Jacobsen and K. S. Thygesen, *Phys. Rev. B*, 2015, **92**, 201205.

[168] P. Mitrić, V. Janković, N. Vukmirović and D. Tanasković, *Phys. Rev. B*, 2023, **107**, 125165.

[169] G. E. Eperon, G. M. Paternò, R. J. Sutton, A. Zampetti, A. A. Haghighirad, F. Cacialli and H. J. Snaith, *J. Mater. Chem. A*, 2015, **3**, 19688–19695.

[170] A. Jain, S. P. Ong, G. Hautier, W. Chen, W. D. Richards, S. Dacek, S. Cholia, D. Gunter, D. Skinner, G. Ceder and K. A. Persson, *APL Materials*, 2013, **1**, 011002.

[171] C. Adamo and V. Barone, *J. Chem. Phys.*, 1999, **110**, 6158–6170.

[172] L. Lin, *J. Chem. Theory Comput.*, 2016, **12**, 2242–2249.

[173] F. Gygi and A. Baldereschi, *Phys. Rev. B*, 1986, **34**, 4405–4408.

[174] M. Baranowski, P. Plochocka, R. Su, L. Legrand, T. Barisien, F. Bernardot, Q. Xiong, C. Testelin and M. Chamarro, *Photonics Res.*, 2020, **8**, A50–A55.

[175] Z. Liu, J. A. Peters, C. C. Stoumpos, M. Sebastian, B. W. Wessels, J. Im, A. J. Freeman and M. G. Kanatzidis, Hard X-Ray, Gamma-Ray, and Neutron Detector Physics XV, 2013, p. 88520A.

[176] Z. Yang, A. Surrente, K. Galkowski, A. Miyata, O. Portugall, R. J. Sutton, A. A. Haghighirad, H. J. Snaith, D. K. Maude, P. Plochocka and R. J. Nicholas, *ACS Energy Lett.*, 2017, **2**, 1621–1627.

[177] X. Gonze, F. Jollet, F. Abreu Araujo, D. Adams, B. Amadon, T. Applencourt, C. Audouze, J.-M. Beuken, J. Bieder, A. Bokhanchuk, E. Bousquet, F. Bruneval, D. Caliste, M. Côté, F. Dahm, F. Da Pieve, M. Delaveau, M. Di Gennaro, B. Dorado, C. Espejo, G. Geneste, L. Genovese,

A. Gerossier, M. Giantomassi, Y. Gillet, D. Hamann, L. He, G. Jomard, J. Laflamme Janssen, S. Le Roux, A. Levitt, A. Lherbier, F. Liu, I. Lukačević, A. Martin, C. Martins, M. Oliveira, S. Poncé, Y. Pouillon, T. Rangel, G.-M. Rignanese, A. Romero, B. Rousseau, O. Rubel, A. Shukri, M. Stankovski, M. Torrent, M. Van Setten, B. Van Troeye, M. Verstraete, D. Waroquiers, J. Wiktor, B. Xu, A. Zhou and J. Zwanziger, *Comput. Phys. Commun.*, 2016, **205**, 106–131.

[178] X. Gonze, B. Amadon, G. Antonius, F. Arnardi, L. Baguet, J.-M. Beuken, J. Bieder, F. Bottin, J. Bouchet, E. Bousquet *et al.*, *Comput. Phys. Commun.*, 2019, **248**, 107042.

[179] N. R. Werthamer, *Phys. Rev. B*, 1970, **1**, 572–581.

[180] T. Tadano, Y. Gohda and S. Tsuneyuki, *J. Phys.-Condens. Matter*, 2014, **26**, 225402.

[181] F. Zhou, W. Nielson, Y. Xia and V. Ozoliņš, *Phys. Rev. Lett.*, 2014, **113**, 185501.

[182] S. Poncé, G. Antonius, Y. Gillet, P. Boulanger, J. Laflamme Janssen, A. Marini, M. Côté and X. Gonze, *Phys. Rev. B*, 2014, **90**, 214304.

[183] J. B. Hoffman, A. L. Schleper and P. V. Kamat, *J. Am. Chem. Soc.*, 2016, **138**, 8603–8611.

[184] M. Sebastian, J. A. Peters, C. C. Stoumpos, J. Im, S. S. Kostina, Z. Liu, M. G. Kanatzidis, A. J. Freeman and B. W. Wessels, *Phys. Rev. B*, 2015, **92**, 235210.

[185] C. C. Stoumpos, C. D. Malliakas and M. G. Kanatzidis, *Inorg. Chem.*, 2013, **52**, 9019–9038.

[186] G. E. Eperon, S. D. Stranks, C. Menelaou, M. B. Johnston, L. M. Herz and H. J. Snaith, *Energy Environ. Sci.*, 2014, **7**, 982–988.

[187] T. Haeger, R. Heiderhoff and T. Riedl, *J. Mater. Chem. C*, 2020, **8**, 14289–14311.

[188] R. J. Sutton, M. R. Filip, A. A. Haghighirad, N. Sakai, B. Wenger, F. Giustino and H. J. Snaith, *ACS Energy Lett.*, 2018, **3**, 1787–1794.

[189] B. T. Diroll, H. Zhou and R. D. Schaller, *Adv. Funct. Mater.*, 2018, **28**, 1800945.

[190] R. Saran, A. Heuer-Jungemann, A. G. Kanaras and R. J. Curry, *Adv. Opt. Mater.*, 2017, **5**, 1700231.

[191] J. Yi, X. Ge, E. Liu, T. Cai, C. Zhao, S. Wen, H. Sanabria, O. Chen, A. M. Rao and J. Gao, *Nanoscale Adv.*, 2020, **2**, 4390–4394.

[192] T. Lanigan-Atkins, X. He, M. J. Krogstad, D. M. Pajerowski, D. L. Abernathy, G. N. M. N. Xu, Z. Xu, D.-Y. Chung, M. G. Kanatzidis, S. Rosenkranz, R. Osborn and O. Delaire, *Nat. Mater.*, 2021, **20**, 977–983.

[193] M. Zacharias and F. Giustino, *Phys. Rev. Res.*, 2020, **2**, 013357.

[194] M. Zacharias and F. Giustino, *Phys. Rev. B*, 2016, **94**, 075125.

[195] M. G. Burt, *J. Phys. Condens. Matter*, 1992, **4**, 6651–6690.

[196] M. G. Burt, *J. Phys. Condens. Matter*, 1999, **11**, 53–83.

[197] B. A. Foreman, *Phys. Rev. B*, 2005, **72**, 165345.

[198] B. A. Foreman, *Phys. Rev. B*, 2007, **76**, 045327.

[199] M. A. Cusack, P. R. Briddon and M. Jaros, *Phys. Rev. B*, 1996, **54**, R2300–R2303.

[200] S.-S. Li, J.-B. Xia, Z. L. Yuan, Z. Y. Xu, W. Ge, X. R. Wang, Y. Wang, J. Wang and L. L. Chang, *Phys. Rev. B*, 1996, **54**, 11575–11581.

[201] A. D. Andreev and E. P. O'Reilly, *Phys. Rev. B*, 2000, **62**, 15851–15870.

[202] S. Tomić, A. G. Sunderland and I. J. Bush, *J. Mater. Chem.*, 2006, **16**, 1963–1972.

[203] N. Vukmirović, D. Indjin, V. D. Jovanović, Z. Ikonić and P. Harrison, *Phys. Rev. B*, 2005, **72**, 075356.

[204] N. Vukmirović and S. Tomić, *J. Appl. Phys.*, 2008, **103**, 103718.

[205] Y. Cho and T. C. Berkelbach, *Phys. Rev. B*, 2018, **97**, 041409.

[206] Q. Zhou, Y. Cho, S. Yang, E. A. Weiss, T. C. Berkelbach and P. Darancet, *Nano Lett.*, 2019, **19**, 7124–7129.

[207] D. Danilović, A. R. Milosavljević, P. Sapkota, R. Dojčilovi´ c, D. Tošić, N. Vukmirović, M. Jocić, V. Djoković, S. Ptasinska and D. K. Božanić, *J. Phys. Chem. C*, 2022, **126**, 13739–13747.

[208] L. D. Landau, E. M. Lifshitz, J. B. Sykes, J. S. Bell and M. E. Rose, *Physics Today*, 1958, **11**, 56–59.

[209] B. H. Bransden and C. J. Joachain, *Quantum mechanics*, Prentice Hall, Harlow, England, 2nd edn, 2000.

[210] J. J. Sakurai and J. Napolitano, *Modern Quantum Mechanics*, Cambridge University Press, 2nd edn, 2017.

[211] L. Elcoro, B. Bradlyn, Z. Wang, M. G. Vergniory, J. Cano, C. Felser, B. A. Bernevig, D. Orobengoa, G. de la Flor and M. I. Aroyo, *J. Appl. Crystallogr.*, 2017, **50**, 1457–1477.

Биографија и библографија аутора

Милан Јоцић је рођен 1992. године у Нишу, где је завршио и основну школу 2007. године. Исте године је уписао Гимназију ,,Светозар Марковић" у Нишу и завршио је 2011. године.

Школске 2011/2012. године је уписао основне студије физике на Природно-математичком факултету Универитета у Нишу, на Департману за физику. Дипломирао је 2014. године са просечном оценом 9.13/, а након тога је на истом факултету уписао мастер студије, модул Општа физика. У октобру 2016. године је одбранио мастер рад из предмета Квантна механика код доц. др Ненада Љ. Милојевића под називом *,,Трансфер електрона у судару протона са хелијумом (Electron Transfer in Proton-helium collision)"*, чиме је завршио мастер студије са просечном оценом 9.85.

Школске 2016/2017. године је уписао докторске академске студије физике на Природно-математичком факултету Универзитета у Нишу. Од маја 2017. године ради као истраживач-приправник потом постаје истраживач-сарадник на Институту за физику у Београду. Под менторством др Ненада Вукмировића успешно објављује два рада у врхунским међународним часописима М21 категорије и један у међународном часопису М51 категорије, на којима се базирају резултати ове тезе као и један у међународном часопису М22 категорије, чији резултати нису део ове тезе:

- M. Jocić and N. Vukmirović, *Ab Initio Construction of Symmetry-adapted k·p Hamiltonians for the Electronic Structure of Semiconductors,* Phys. Rev. B 102, 085121 (2020).
  doi: 10.1103/PhysRevB.102.085121 (M21)
- M. Jocić and N. Vukmirović, *Ab-initio Calculations of Temperature Dependent Electronic Structures of Inorganic Halide Perovskite Materials,* Phys. Chem. Chem. Phys. **25**, 29017 (2023).
  doi: 10.1039/d3cp02054a (M21)
- M. Jocić and N. Vukmirović, *Temperature Dependence of the Electronic Band Gap of CsPbBr3 Quantum Wells Obtained Using k·p Method*, Facta Univ.- Ser. Phys. Chem. Tech. **22**, 1 (2024)
  doi: 10.2298/FUPCT2401001J (M51)
- D. Danilović, A. Milosavljević, P. Sapkota, R. Dojcilović, D. Tošić, N. Vukmirović, M. Jocić, V. Đoković, S. Ptasinska, and D. K. Božanić:
  "Electronic Properties of Silver–Bismuth Iodide Rudorffite Nanoplatelets"
  J. Phys. Chem. C **126**, 13739-13747 (2022).
  doi: 10.1021/acs.jpcc.2c03208 (M22)

ИЗЈАВА О АУТОРСТВУ

Изјављујем да је докторска дисертација, под насловом

Електронска својства перовскитних нанокристала

која је одбрањена на Природно-математичком факултету Универзитета у Нишу:

- резултат сопственог истраживачког рада;
- да ову дисертацију, ни у целини, нити у деловима, нисам пријављивао/ла на другим факултетима, нити универзитетима;
- да нисам повредио/ла ауторска права, нити злоупотребио/ла интелектуалну својину других лица.

Дозвољавам да се објаве моји лични подаци, који су у вези са ауторством и добијањем академског звања доктора наука, као што су име и презиме, година и место рођења и датум одбране рада, и то у каталогу Библиотеке, Дигиталном репозиторијуму Универзитета у Нишу, као и у публикацијама Универзитета у Нишу.

У Нишу, _____.

Потпис аутора дисертације:

_____

Милан М. Јоцић

ИЗЈАВА О ИСТОВЕТНОСТИ ШТАМПАНОГ И ЕЛЕКТРОНСКОГ ОБЛИКА ДОКТОРСКЕ ДИСЕРТАЦИЈЕ

Наслов дисертације:

Електронска својства перовскитних нанокристала

Изјављујем да је електронски облик моје докторске дисертације, коју сам предао/ла за уношење у **Дигитални репозиторијум Универзитета у Нишу,** истоветан штампаном облику.

У Нишу, _____.

Потпис аутора дисертације:

_____

Милан М. Јоцић

ИЗЈАВА О КОРИШЋЕЊУ

Овлашћујем Универзитетску библиотеку „Никола Тесла“ да у Дигитални репозиторијум Универзитета у Нишу унесе моју докторску дисертацију, под насловом:

Електронска својства перовскитних нанокристала

Дисертацију са свим прилозима предао/ла сам у електронском облику, погодном за трајно архивирање.

Моју докторску дисертацију, унету у Дигитални репозиторијум Универзитета у Нишу, могу користити сви који поштују одредбе садржане у одабраном типу лиценце Креативне заједнице (Creative Commons), за коју сам се одлучио/ла.

1. Ауторство **(CC BY)**
2. Ауторство – некомерцијално **(CC BY-NC)**
3. **Ауторство – некомерцијално – без прераде (CC BY-NC-ND)**
4. Ауторство – некомерцијално – делити под истим условима **(CC BY-NC-SA)**
5. Ауторство – без прераде **(CC BY-ND)**
6. Ауторство – делити под истим условима **(CC BY-SA)**

У Нишу, _____.

Потпис аутора дисертације:

_____

Милан М. Јоцић